



Guan, Qingwen (2024) *Tailoring self-sorting behavior in multicomponent supramolecular systems using functional dipeptide diastereomers*. PhD thesis

<https://theses.gla.ac.uk/84811/>

Copyright and moral rights for this work are retained by the author

A copy can be downloaded for personal non-commercial research or study, without prior permission or charge

This work cannot be reproduced or quoted extensively from without first obtaining permission in writing from the author

The content must not be changed in any way or sold commercially in any format or medium without the formal permission of the author

When referring to this work, full bibliographic details including the author, title, awarding institution and date of the thesis must be given

Enlighten: Theses

<https://theses.gla.ac.uk/>  
[research-enlighten@glasgow.ac.uk](mailto:research-enlighten@glasgow.ac.uk)



University  
of Glasgow

**Tailoring self-sorting behavior in multicomponent  
supramolecular systems using functional dipeptide  
diastereomers**

**Qingwen Guan**

Submitted in fulfilment of the requirements for the Degree of Doctor of  
Philosophy

School of Chemistry  
College of Science and Engineering  
University of Glasgow

October 2024

## Abstract

---

Multi-component supramolecular systems are essential for tailoring materials to meet specific application needs, mimicking natural processes where molecular self-sorting forms complex, multi-layered structures within cells for vital functions. In these systems, self-sorting is carefully controlled to program desired properties into the final product, balancing the retention of key characteristics with the introduction of new structural or functional properties. While these self-sorted systems are promising for creating advanced materials, their complexity makes them difficult to fully understand and control.

In Chapter 2, we extensively employed characterization techniques such as small-angle scattering (SAS), cryo-transmission electron microscopy (cryo-TEM), rheology, and various spectroscopic methods to investigate the self-sorting behavior of mixtures of diastereoisomers of naphthyl diphenylalanine. We examined how their composition ratio affects the properties of functionalized dipeptide hydrogels in different phases. These studies demonstrated how significant structural features and interactions at varying ratios influence the physical and optical properties of gels, such as viscosity, gelation time, turbidity, and spectral characteristics.

In Chapter 3, we delved deeper into stacking patterns and their impact on the properties of a library of naphthyl dipeptide diastereomeric mixtures. Using differently substituted naphthalene rings, we developed multicomponent systems with varying self-assembled nanostructures or gelation capabilities. Analysis at molecular, microscopic, and holistic levels revealed that each component within the two-component systems could independently form self-assembled nanostructures, thus exhibiting self-sorting behaviors at different scales. These findings illustrate that the peptide's stereochemistry plays a pivotal role in self-assembly, enabling the design of self-sorting, low molecular weight gel (LMWG) systems.

In Chapter 4, we described the optical properties of the dipeptide-based pre-gel solutions using advanced characterization methods such as synchrotron radiation circular dichroism (SRCD) and Mueller Matrix Polarimetry (MMP). MMP analysis captured comprehensive polarization data, confirming significant differences in molecular orientation and electronic interactions between homochiral and heterochiral systems. These findings indicate that mixing diastereoisomers alters the optical properties, affecting circular birefringence and dichroism, and suggesting shifts in chiral order and molecular interactions.

# Table of Contents

<b>Abstract.....</b>	<b>1 -</b>
<b>Table of Contents .....</b>	<b>2 -</b>
<b>Acknowledgments .....</b>	<b>4 -</b>
<b>Declaration of Authorship.....</b>	<b>5 -</b>
<b>List of Publications.....</b>	<b>6 -</b>
<b>List of Abbreviations .....</b>	<b>7 -</b>
<b>Chapter 1: Literature Review .....</b>	<b>10 -</b>
1.1 Introduction to Low Molecular Weight Gelators.....	10 -
1.1.1 Gelation of LMWGs .....	10 -
1.1.2 Design of LMWGs.....	11 -
1.1.3 Factors Affecting Gelation of LMWGs .....	13 -
1.1.4 Impact of Chirality on Self-Assembly .....	15 -
1.2 Introduction to Multicomponent Supramolecular Systems .....	18 -
1.3 Design of Self-Sorting Binary Supramolecular Systems.....	22 -
1.3.1 Temperature-Induced Self-Sorting .....	23 -
1.3.2 pH-Induced Self-Sorting.....	23 -
1.3.3 Self-Sorting Induced by Chiral Difference .....	24 -
1.3.4 Self-Sorting Induced by Structural Difference .....	26 -
1.4 Characterization Techniques for Multicomponent Supramolecular Systems.....	27 -
1.4.1 Molecular-Level Characterization .....	27 -
1.4.2 Nanometer-Scale Characterization .....	30 -
1.4.3 Microscale Characterization .....	35 -
1.4.4 Macroscale Characterization.....	37 -
1.5 Aims and Objectives .....	40 -
1.6 References.....	41 -
<b>Chapter 2: Self-Sorting in Diastereomeric Mixtures of Functionalized Dipeptides.....</b>	<b>53 -</b>
2.1 Introduction.....	54 -
2.2 Results and Discussion.....	55 -
2.2.1 Self-Sorting in Pre-Gel Solutions at High pH.....	55 -
2.2.2 Self-Sorting in Gels at Low pH.....	69 -
2.3 Conclusions .....	76 -
2.4 Experimental Section .....	77 -
2.4.1 Sample Preparation Protocols .....	77 -
2.4.2 Characterization .....	78 -
2.5 References.....	83 -
<b>Chapter 3: A Comprehensive Study on Self-Sorting in a Library of Naphthyl Diphenylalanine Diastereomers.....</b>	<b>88 -</b>
3.1 Introduction.....	89 -
3.2 Results and Discussion.....	90 -
3.2.1 7MeO2NapFF .....	92 -
3.2.2 6Br2NapFF.....	115 -

3.2.3 1NapFF.....	- 128 -
3.2.4 6CN2NapFF .....	- 143 -
3.2.5 4Cl1NapFF.....	- 156 -
3.3 Impact of the Mixing Approach on Multicomponent Systems.....	- 169 -
3.4 Conclusions.....	- 173 -
3.5 Experimental Section .....	- 175 -
3.5.1 Sample Preparation Protocols .....	- 175 -
3.5.2 Characterization .....	- 176 -
3.6 References.....	- 178 -
<b>Chapter 4: Mueller Matrix Polarimetry Study in Diastereomeric Mixtures of Functionalized Dipeptides .....</b>	<b>- 182 -</b>
4.1 Introduction.....	- 183 -
4.2 Results and Discussion.....	- 184 -
4.2.1 SRCD Studies for 2NapFF Pre-Gel Solutions .....	- 184 -
4.2.2 MMP Studies for 2NapFF Pre-Gel Solutions .....	- 185 -
4.2.3 MMP Analysis of Other Diastereomeric Dipeptide Solutions.....	- 197 -
4.3 Conclusions.....	- 212 -
4.4 Experimental Section .....	- 213 -
4.4.1 Preparation of Solutions.....	- 213 -
4.4.2 Basics of Mueller Matrix Analysis .....	- 214 -
4.4.3 SRCD and MMP Measurement .....	- 215 -
4.5 References.....	- 217 -
<b>Chapter 5: Conclusions and Outlooks .....</b>	<b>- 221 -</b>
5.1 Conclusions.....	- 221 -
5.2 Outlooks .....	- 222 -
<b>Appendices .....</b>	<b>- 223 -</b>
A2 Appendix for Chapter 2.....	- 223 -
A2.1 Materials.....	- 223 -
A2.2 Synthesis of Dipeptides.....	- 225 -
A2.3 Additional Figures and Tables .....	- 241 -
A3 Appendix for Chapter 3.....	- 249 -
A3.1 Materials.....	- 249 -
A3.2 Synthesis of Dipeptides.....	- 250 -
A3.3 Additional Figures and Tables .....	- 326 -
A4 Appendix for Chapter 4.....	- 337 -
A4.1 Additional Figures.....	- 337 -

## Acknowledgments

---

I would like to express my profound gratitude to my supervisor, Professor Dave J. Adams, for his invaluable guidance, steadfast support, and insightful feedback throughout my academic journey. His mentorship has not only been inspiring but also transformative.

I extend my heartfelt thanks to all current and former members of our laboratory: Bart, Tom, Santanu, Lisa, Dan, Libby, Valentina, Courtenay, Jacquelyn, Chloe, Rebecca, Max, Simona, Dipankar, Alex, Emma, Rui, Fin, Amina, Nick, Ziyao, and Connor. Your collegiality, assistance, and encouragement have been pivotal to my professional and personal growth.

Special recognition is due to the technicians of the School of Chemistry - Dr. Giovanni Rossi, David Adam, Alec Mungall, Jim Gallagher, Andrew Monaghan, Claire Wilson, and Rahul Kumar. Your expertise and steadfast support were crucial in enabling the successful execution of experiments and data collection.

I am also immensely grateful to Professor Annela M. Seddon, Dr. Adam Squires, Wanli Liu, Professor Honggang Cui, Tian Xu, and the scientists at the B23 beamline - Professor Giuliano Siligardi and Dr. Tiberiu-Marius Gianga, for their generous assistance with SANS, SAXS, cryo-TEM, and SRCD techniques.

My deepest appreciation extends to my family, whose unwavering love, encouragement, and support have sustained me through the ups and downs of this demanding yet fulfilling journey.

Finally, I acknowledge the crucial financial support from the China Scholarship Council (grant no. 202006440011), which was indispensable in completing this research.

## **Declaration of Authorship**

---

I declare that, except where explicit reference is made to the contribution of others, that this thesis is the result of my work and has not been submitted for any other degree at the University of Glasgow or any other institution.

Qingwen Guan

## List of Publications

---

1. **Guan, Q.**; McAulay, K.; Xu, T.; Rogers, S. E.; Edwards-Gayle, C.; Schweins, R.; Cui, H.; Seddon, A. M.; Adams, D. J. Self-sorting in Diastereomeric Mixtures of Functionalized Dipeptides. *Biomacromolecules* 2023, 24 (6), 2847-2855.
2. Li, W.; **Guan, Q.**; Li, M.; Saiz, E.; Hou, X. Nature-inspired Strategies for the Synthesis of Hydrogel Actuators and Their Applications. *Progress in Polymer Science* 2023, 140, 101665.
3. Li, M.; **Guan, Q.**; Li, C.; Saiz, E. Self-powered Hydrogel Sensors. *Device* 2023, 1 (1), 100007.

## List of Abbreviations

---

1D: one-dimensional

$^1\text{H}$ : proton-1

1Nap: 1-naphthyloxy

2D: two-dimensional

2Nap: 2-naphthyloxy

4Cl1Nap: 4-chloro-1-naphthyloxy

6Br2Nap: 6-bromo-2-naphthyloxy

6CN2Nap: 6-cyano-2-naphthyloxy

7MeO2Nap: 7-methoxy-2-naphthyloxy

$^{13}\text{C}$ : carbon-13

A: absorbance

AFM: Atomic force microscopy

Å: angstrom

Azo: azobenzene

Boc: tert-butyloxy carbonyl

C: cylinder

CB: circular birefringence

CD: circular dichroism

Cbz: carboxybenzyl

CLSM: Confocal laser scanning microscopy

Cryo-TEM: cryogenic transmission electron microscopy

C-terminus: carboxyl terminus

D: depolarization

$\text{D}_2\text{O}$ : deuterium oxide

$\delta$ : chemical shift

$\text{DMSO-d}_6$ : deuterated dimethyl sulfoxide

DSC: Differential scanning calorimetry

EC: elliptical cylinder

FEC: flexible elliptical cylinder

FC: flexible cylinder  
Fmoc: fluorenylmethoxycarbonyl  
FUV: far-ultraviolet  
fXRD: fibre X-ray diffraction  
GdL: glucono delta-lactone  
G': "storage" or "elastic" modulus  
G'': "loss" or "plastic" modulus  
HCl: hydrochloric acid  
HC: hollow cylinder  
HT: high tension  
IBCF: iso-butyl chloroformate  
I(Q): scattering intensity  
IR: Infrared spectroscopy  
*J*: coupling constant  
 $\lambda_{em}$ : emission wavelength  
 $\lambda_{ex}$ : excitation wavelength  
LB: linear birefringence  
LB': 45° linear birefringence  
LD: linear dichroism  
LD': 45° linear dichroism  
LiOH: lithium hydroxide  
LMWG: low molecular weight gelator  
M: molar concentration or molarity, 1 M = 1 mol/L  
mdeg: millidegrees  
MMP: Mueller Matrix Polarimetry  
NMR: nuclear magnetic resonance spectroscopy  
NaCl: sodium chloride  
NaOH: sodium hydroxide  
NMM: N-methyl morpholine  
N-terminus: amino terminus  
Phe or F: phenylalanine  
pH: the potential of hydrogen  
PL: power law

PMP: Partially Modulated Polarization  
POM: Polarized optical microscopy  
ppm: parts per million  
PTZ: phenothiazine  
Pyr: pyrene  
Q: scattering vector  
SANS: small-angle neutron scattering  
SAS: Small-angle scattering  
SAXS: small-angle X-ray scattering  
SEM: Scanning Electron Microscopy  
SLD: scattering length density  
SRCD: Synchrotron Radiation Circular Dichroism  
 $\tan\delta$ : loss factor,  $\tan\delta=G''/G'$   
TFA: trifluoroacetic acid  
 $\theta$ : scattering angle  
THF: tetrahydrofuran  
TLC: thin-layer chromatography  
 $T_g$ : phase transition temperature  
UV-Vis: ultraviolet-visible spectroscopy  
VUV: vacuum ultraviolet  
w/w: weight per weight  
wt%: weight percentage  
XRD: X-ray diffraction

## Chapter 1: Literature Review

---

### 1.1 Introduction to Low Molecular Weight Gelators

Gels are versatile materials that consist of a solid three-dimensional network that encapsulates a liquid, allowing them to hold substantial volumes of fluid.<sup>1</sup> This structure endows gels with unique viscoelastic properties, combining the flow behavior of liquids (viscosity) with the strength of solids (elasticity).<sup>2</sup> Despite being mostly liquid, often comprising up to 99% of their weight, gels maintain a solid-like behavior. In these systems, the gelator is dispersed throughout a suitable liquid, where the liquid forms the continuous phase and the solid forms the discontinuous phase.<sup>3</sup> The strength and viscosity of gels are enhanced either through self-assembly or through cross-linking within their structure. Gels are classified by the type of liquid they contain, such as organic gels, hydrogels, and xerogels (referred to as aerogels when dried, but expanded). Additionally, gels are categorized as either natural or synthetic, with synthetic varieties including polymer and supramolecular gels.

Among synthetic gels, polymer gels are distinguished by their cross-linking processes, which can be either physical or chemical. Chemical polymer gel networks, cross-linked by covalent bonds, are thermally irreversible and cannot be redissolved.<sup>4</sup> In contrast, supramolecular gels, which are bonded non-covalently, offer significant advantages over traditional polymer gels. These low molecular weight gels (LMWGs) can fracture and reorganize at low strains and dynamically adapt to temperature changes. This makes them particularly effective for applications that require rapid recovery and self-healing, such as controlled release systems.<sup>5-7</sup> Furthermore, LMWGs respond quickly to various environmental stimuli, making them valuable in fields like sensor technologies.<sup>6-9</sup> Their dynamic, reversible behavior combined with the ease of modification renders them highly suitable for innovative applications where flexibility and responsiveness are essential.

#### 1.1.1 Gelation of LMWGs

Supramolecular gels are crafted from low molecular weight gelators (LMWGs) that engage in non-covalent interactions, such as hydrogen bonding,  $\pi$ - $\pi$  interactions, van der Waals forces, electrostatic and hydrophobic interactions.<sup>10, 11</sup> These gelators, typically found in concentrations ranging from 0.1 wt% to 10 wt% and with molecular weights under 2,000 Daltons, can self-

assemble into one-dimensional structures like fibers and sheets (Figure 1-1).<sup>7, 12, 13</sup> This self-assembly is often initiated by external factors, including pH changes,<sup>14-18</sup> temperature variations (through heat-cool cycles),<sup>19-23</sup> or the addition of specific divalent cations<sup>14, 24, 25</sup> or anti-solvents.<sup>17, 26, 27</sup> These triggers decrease the solubility of the gelators, enhance intermolecular interactions, and lead to aggregation. The resulting aggregates then entangle or cross-link to create a three-dimensional network that traps the solvent, converting the liquid solution into a semi-solid gel.

The gelation process unfolds through a series of structured, hierarchical assemblies, beginning with molecular stacking and advancing to the formation of continuous networks (Figure 1-1).<sup>28, 29</sup> Initially, one-dimensional molecular interactions prompt self-assembly, leading to the creation of nanostructures and subsequently, one-dimensional fibers, which are often more effective than other configurations.<sup>29</sup> The delicate balance between molecular dissolution and aggregation in the solution is key to determining whether gelation will occur. In water, noncovalent interactions such as hydrogen bonding,  $\pi$ - $\pi$  stacking, and electrostatic forces facilitate self-assembly, although their relatively weak nature means that the hydrophobic interactions often take a dominant role during anisotropic aggregation. The transition from secondary to tertiary structure is crucial for gel formation, and fiber cross-linking through entanglement or branching plays an essential role in stabilizing the liquid phase.<sup>28</sup> The assembly of these fibers is controlled by a balance of weak physical forces. Unlike the structured three-dimensional order seen in crystallization, the self-assembled fiber network predominantly expands along a single axis, such as the direction of  $\pi$ - $\pi$  stacking.<sup>12</sup> This growth pattern resembles radial branches in a K-tree structure, highlighting the complexity and directionality of gel network formation.

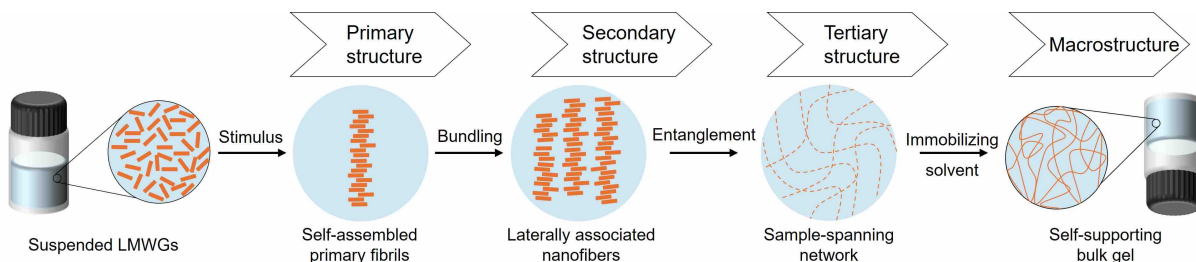


**Figure 1-1.** Hierarchical self-assembly of LMWGs to form supramolecular gels.

## 1.1.2 Design of LMWGs

The characteristics of typical LMWGs include: (i) Molecules must exhibit dual solubility-both partial solubility and partial insolubility in a solvent-to facilitate effective interactions that are crucial for forming a stable network. (ii) These molecules engage in various weak intermolecular forces that collectively contribute to the gel's stability. Non-polar interactions, driven by hydrophobic groups such as aromatic rings or long fatty chains, promote aggregation, while polar hydrophilic groups like peptide or urea bonds provide additional stabilization. (iii) Directional non-covalent interactions between molecules lead to the anisotropic assembly of nanoscale fibers, a process influenced by the molecules' asymmetry or distinct regions that favor assembly. (iv) The molecules typically display chirality, which affects how they assemble and influences the properties of the final material.<sup>30, 31</sup> LMWGs encompass a diverse range of structures including surfactants, functionalized sugars, oligopeptides, simple alkanes, modified amino acids, dendrimers, and peptide fatty amides.<sup>32-38</sup> The principles behind the design of LMWGs are poorly understood, and many have been discovered accidentally. Further exploration often involves minor modifications to known structures; however, these adjustments can sometimes inhibit gel formation. The absence of clear guidelines for self-assembly and gelation complicates the development of specialized gelators tailored for specific applications.

Surfactant properties, specifically the balance between hydrophilic and hydrophobic traits, facilitate their self-assembly in water.<sup>39</sup> LMWGs capable of forming hydrogels typically feature both hydrophilic segments, ensuring water compatibility, and hydrophobic regions, which encourage self-assembly. Peptide amphiphiles are increasingly used as building blocks for creating nanomaterials in biomedicine, optoelectronics, and catalysis, combining the simplicity of small molecules with the functionality of peptides.<sup>40</sup> Aromatic peptide amphiphiles are usually composed of four segments: the N-terminal aromatic hydrophobic head, linker segment, dipeptide sequence, and C-terminal hydrophilic tail (Figure 1-2).<sup>37, 41</sup> These components are designed to influence the structural features of the self-assembly of aromatic peptide amphiphiles.<sup>42</sup> In water, these structures can form cylindrical, worm-like micelles, with the hydrophobic head at the core and the hydrophilic tail on the surface. The assembly of these aromatic peptide hydrogels is predominantly driven by intermolecular hydrogen bonding and hydrophobic interactions from amino acid side chains. The assembly is further stabilized through hydrogen bonds, electrostatic forces, and van der Waals interactions.

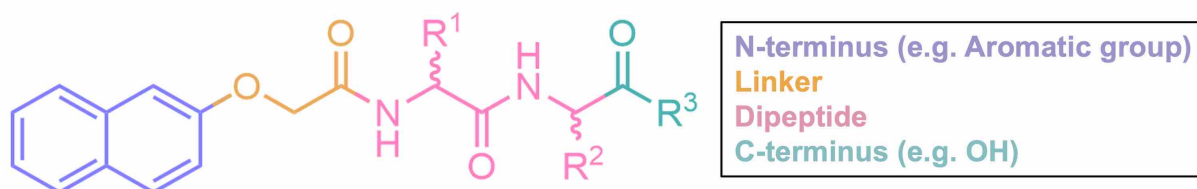


**Figure 1-2.** Schematic representation of an aromatic peptide amphiphile, featuring naphthalene (Nap) dipeptide as a typical example.

To create efficient dipeptide hydrogels, the N-terminus of the dipeptide is often modified with a large aromatic group.<sup>37</sup> These aromatic moieties aid in peptide self-assembly and stabilize its structure and function through  $\pi$ - $\pi$  stacking and hydrophobic interactions.<sup>43</sup> Common aromatics include naphthalene (Nap) derivatives, fluorenylmethoxycarbonyl (Fmoc), Phenyl (Phe), pyrene (Pyr), carboxybenzyl (Cbz), phenothiazine (PTZ), and azobenzene (Azo).<sup>30, 44</sup> The choice of amino acids is vital as it determines the chemical characteristics of the peptides, ranging from hydrophobic to hydrophilic, neutral to charged (e.g. positive or negative), and acidic to basic, thus providing high programmability for the gels.<sup>37</sup> A protected conjugated naphthyl dipeptide, featuring a hydrophobic aromatic ring and a hydrophilic -OH group, illustrates this versatility.<sup>45</sup> Under alkaline conditions, cylindrical micelles formed by the anionic form of LMWGs transform into a gel network as they protonate and increase contact points. Altering the amino acids and substituents on the naphthalene ring can significantly modify the formed structure, gelation ability, and gel performance.<sup>46, 47</sup>

### 1.1.3 Factors Affecting Gelation of LMWGs

The self-assembly process of carbohydrate LMWGs is affected by factors such as heating temperature, pH, solvent composition, salt presence, gelator concentration, and mechanical agitation.<sup>12, 48-52</sup> These variables significantly influence the nanostructure and microstructure of the gels, which ultimately determine their properties.<sup>29</sup>

Consider temperature as an example: factors such as the exact heating level, duration of heat exposure, cooling rate, final cooling temperature, and the time before evaluating the gel are all crucial in determining its gelation capability and ultimate characteristics.<sup>9, 53-55</sup> pH variations also significantly affect the self-assembly of Fmoc-diphenylalanine (Fmoc-FF) into fibrils, causing shifts in the pH at which these changes occur (Figure 1-3a).<sup>56</sup> At high pH, the reduced electrostatic repulsion among negatively charged molecules facilitates the formation of a flexible fibril network, resulting in weak hydrogels. Conversely, at an intermediate pH, the

structure changes to non-gelling, flat, rigid ribbons due to decreased charge repulsion, which promotes a more ordered assembly. Below a certain pH (the apparent  $pK_a$  of C-terminal carboxylic acid), gels derived from 2NapFF solutions strengthen due to increased entanglement and fiber formation as the charge diminishes, stabilizing their mechanical properties.<sup>57</sup> As the concentration of 2NapFF increases from a minimal 0.001 wt% to 1.0 wt%, the structure evolves from spherical micelles to worm-like micelles, and finally to associations of these worm-like structures (Figure 1-3b).<sup>24</sup> Additionally, applying heat-cool cycles to this dipeptide solution significantly boosts viscosity and results in more rigid, self-supporting materials by reorganizing the micelles (Figure 1-3c).<sup>58</sup> This process decreases their flexibility, as indicated by increased Kuhn lengths, reduces their radii, and extends their overall length due to partial dehydration of the micellar core. These temperature-driven modifications are crucial for material processing, electrospinning, and ensuring experimental consistency in laboratories with variable temperatures. By manipulating solvent ratios and temperature cycles, the mechanical strength and recovery ability of Fmoc-leucine-glycine (FmocLG) gels after mechanical stress can be significantly altered,<sup>59</sup> attributed to the alterations in the gelation process and the resultant large-scale network structure of the self-assembled fibers (Figure 1-3d).

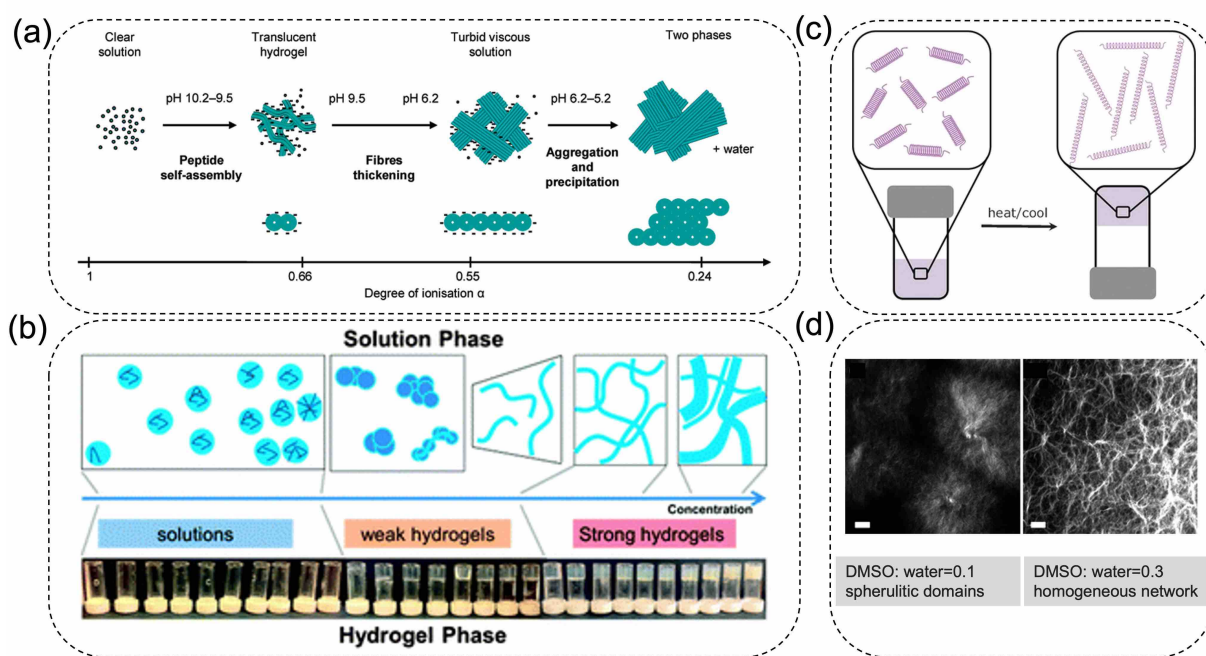


**Figure 1-3.** Representative examples illustrating factors influencing self-assembly. (a) Proposed self-assembly mechanism of Fmoc-FF with decreasing pH above the critical gelation concentration, illustrating the impact of peptide ionization degree ( $\alpha$ ). At high pH, diminished electrostatic repulsion facilitates the formation of flexible fibrils into weak hydrogels, while at intermediate pH, decreased repulsion promotes the transition to non-gelling, flat, rigid ribbons,

enabling more structured assembly. (Reproduced with permission from Ref.<sup>56</sup> Copyright 2009, American Chemical Society). (b) Structural transformations of 2NapFF self-assemblies in solution phase with concentrations increasing from 0.001 wt% to 1.0 wt%, alongside inversion vial tests for 2NapFF solutions with added calcium nitrate. (Reproduced with permission from Ref.<sup>24</sup> Copyright 2016, The Royal Society of Chemistry). (c) Simple heat-cool cycles consisting of heating to 40°C for 2 minutes followed by cooling to 25°C significantly influence the properties of a 2NapFF solution at high pH. After treatment, the micelles exhibit increased rigidity and elongation, becoming longer and thinner. These changes are evidenced by an increased Kuhn length, indicating reduced flexibility, and a decreased radius. (Reproduced with permission from Ref.<sup>58</sup> Copyright 2017, Wiley-VCH). (d) Confocal microscopic images showcasing microstructural differences in FmocLG gels formed at various volume fractions of DMSO:H<sub>2</sub>O ( $\phi_{\text{DMSO}}$ ) at a FmocLG concentration of 5 mg/mL. At  $\phi_{\text{DMSO}}=0.10$ , fibers are dispersed in spherulitic domains; at  $\phi_{\text{DMSO}}=0.30$ , fibers form a homogeneous network. Scale bars represent 10  $\mu\text{m}$ . (Reproduced with permission from Ref.<sup>59</sup> Copyright 2011, The Royal Society of Chemistry).

The properties of hydrogels are influenced by several factors, including the average thickness and strength of the fibers,<sup>35, 46, 60, 61</sup> the type of cross-linking,<sup>10, 51, 62</sup> the degree of branching (which relates to the spacing between cross-linking points),<sup>49, 62-64</sup> and the distribution of fibers on a larger scale.<sup>26, 65</sup> These characteristics primarily stem from the molecular structure, as molecular interactions play a crucial role in the assembly process.<sup>37, 40, 66</sup> Managing the microstructure effectively is essential to enhance gel properties; however, the techniques to achieve precise control are still under development. Additionally, the performance of supramolecular gels is shaped by preparation methods,<sup>14, 17, 51, 67</sup> storage conditions,<sup>10</sup> aging<sup>68</sup> and the properties of the solvents used.<sup>69</sup> Evaluations of these gels focus on their durability, the concentration required for gel formation, the uniformity of component distribution, the reversibility of transitions between gel and solution states, and the ability to adjust structural configurations.

### 1.1.4 Impact of Chirality on Self-Assembly

Chirality significantly influences supramolecular self-assembly by regulating molecular structure organization.<sup>31, 42</sup> In organic synthesis, chirality information embedded in molecular-level building blocks is transformed into nanoscale gel-phase structures through hierarchical

assembly.<sup>70-74</sup> This is especially evident in LMWGs, where molecular-level chirality is used to adjust macroscopic material properties, departing from traditional polymer gel methodologies.<sup>20, 31</sup> For instance, Garcia et al. demonstrated that diastereomeric tripeptides containing D- and L-amino acids self-assemble into hydrogels more efficiently than their enantiomeric counterparts due to their amphiphilic nature and ability to form stable  $\beta$ -sheet structures.<sup>20</sup>

Chirality in LMWGs crucially impacts the gelation process by influencing specific non-covalent interactions.<sup>75</sup> Basak et al. found that enantiomeric isomers of the tripeptide Phe-Phe-Leu, labeled with ferrocene and pyrene, form robust, structurally intact aggregates more readily than achiral peptides, resulting in a uniform nanofibrillar structure through selective molecular recognition. This significantly affected the gel network morphology and stability (Figure 1-4).<sup>23</sup> Additionally, Adams' group challenged the conventional belief that racemic mixtures cannot form gels by showing that both racemic and enantiomeric forms of the functionalized dipeptide 2NapFF effectively gel under high pH conditions, highlighting the critical role of optical activity in self-assembly.<sup>35</sup>

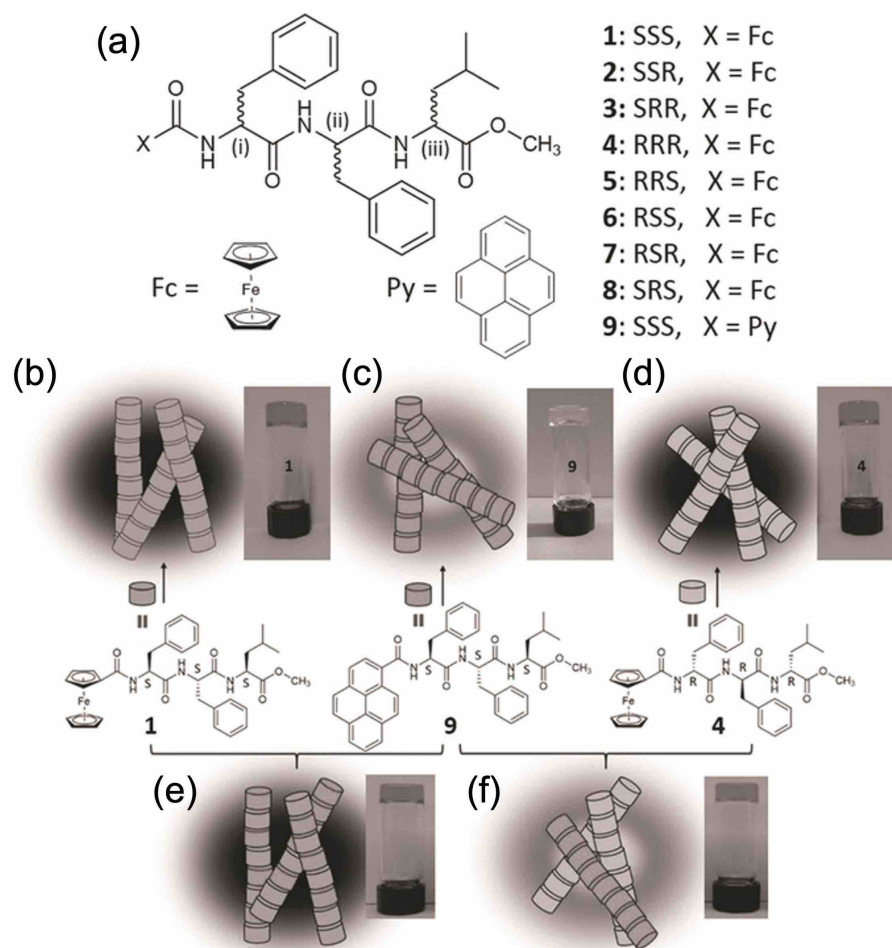


**Figure 1-4.** (a) Chemical structures of the stereoisomers of the tripeptides, labeled with ferrocene (Fc) ((1–8) and pyrene (Py) (9). Py is noted for its high fluorescence, while Fc serves as a fluorescent quencher. (b-d) Illustration of the self-assembly of single-component homochiral gelators 1, 9, and 4 into nanofibers, where 1 and 4 generate non-fluorescent nanofibers and 9 produces fluorescent nanofibers. (e) A two-component system comprising gelators 1 and 9, both with S-type chiral centers, forms non-fluorescent fibers, indicating the co-assembly of the mixed peptide chains. (f) A two-component system consisting of gelators 4 and 9, with opposing chiral centers, produces fluorescent fibers, demonstrating self-sorting during fiber formation. (Reproduced with permission from Ref.<sup>23</sup> Copyright 2017, Wiley-VCH).

Chirality plays a crucial role in directing the twist of fibers, which influences the physical properties of the gel, including its strength and morphology.<sup>72, 76, 77</sup> The chiral arrangement dictates the directional twist, impacting how the fibers align and interact, thereby affecting the gel's macroscopic properties like mechanical strength and stability. The assembly path is supported by a blend of hydrophobic and hydrogen bonding interactions, which guide the elongation and eventual maturation of the fibers into robust nanotubes. These processes

underscore the complex interplay between molecular interactions and macroscopic structure formation in chiral self-assembling systems. It can also introduce entirely new structures and properties into mixtures of enantiomers. For example, Nagy et al. demonstrated that racemic mixtures facilitate hydrophobic interactions, which are impossible in pure enantiomeric assemblies, significantly enhancing inter-residue interactions and mechanical rigidity.<sup>78</sup> In practical applications, the Smith group illustrated the pivotal role of molecular chirality in gel properties by incorporating specific chiral amines (R-amines) into dendritic L-lysine molecules, markedly improving the gel's thermodynamic stability.<sup>22</sup> Concurrently, Ślęczkowski et al. showed that specific chiral solvents can act as additives, influencing the assembly of chiral molecules and even altering the stereochemical preferences of monomers.<sup>79</sup>

Additionally, Liu's group synthesized chiral supramolecular organic gels with left-handed helical morphologies by co-assembling achiral gelators with chiral diamides, highlighting the role of chirality transfer in intermolecular chain interactions.<sup>80</sup> Feringa et al.'s findings revealed that chirality can be transferred from one self-assembly system to another and magnified in molecular form, paving the way for the design of functional supramolecular materials.<sup>81</sup> Palmans et al. exemplified that adding a small percentage of chiral "sergeant" molecules to achiral "soldier" molecules robustly amplifies chirality and forms highly ordered chiral nanostructures.<sup>82</sup> van Gestel et al. demonstrated that the "majority-rules" effect strongly biases the helical assembly of C<sub>3</sub>-symmetrical molecules towards the majority enantiomer.<sup>83</sup> These studies enhance our understanding of molecular-level chirality in supramolecular self-assembly and highlight its potential for creating innovative supramolecular materials with tailored morphologies and properties.

## 1.2 Introduction to Multicomponent Supramolecular Systems

Supramolecular gels can be classified into two categories based on the number of components: single-component and multi-component gels. Single-component gels are created from a single gelator through non-covalent interactions, whereas multi-component gels consist of two or more compounds that self-assemble into stable supramolecular aggregates via synergistic non-covalent interactions.<sup>84-86</sup> These aggregates can further organize into three-dimensional networks. While most supramolecular gels utilize a single gelator, the combination of multiple gelators enhances complexity and functionality.<sup>8, 14, 38, 87, 88</sup>

Molecular self-assembly is the spontaneous formation of stable structures through non-covalent interactions under near-thermodynamic minimum or kinetically metastability.<sup>29, 55</sup> Multi-component self-assembly is an adaptable approach for designing supramolecular gels, providing benefits such as molecular complexity,<sup>89, 90</sup> tunable mechanical properties,<sup>47, 91, 92</sup> in-situ material formation,<sup>93, 94</sup> novel functionality,<sup>93, 95</sup> and diverse morphologies.<sup>14, 27, 62, 96, 97</sup> This method holds significant potential in materials science, biology, engineering, and medicine.<sup>7, 42, 97</sup> However, the inherent uncertainty in bottom-up self-assembly complicates control over size, morphology, and properties. A thoughtful design of the self-assembly process can help achieve desired structures and functions.

The two-component supramolecular assembly represents the simplest and most extensively studied multi-component gel system, involving the integration of two distinct building blocks into an ordered structure.<sup>85, 86, 97</sup> Preparation methods for these gels can be categorized based on the gelation capabilities of the components (Figure 1-5a):<sup>8, 86</sup> (1) Non-gelator systems, where neither compound can individually form a gel, yet mixing them leads to a stable gel. This method facilitates complex formation before self-assembly, enabling better control and fine-tuning.<sup>86, 98, 99</sup> (2) Gelator and non-gelator systems, where one component can gel independently while the other cannot. Additives in this system can alter the gel's thermodynamic and mechanical properties, making the resulting two-component gels markedly different from single-component gels.<sup>17, 47, 100</sup> (3) Two-gelator systems, where each component can independently form a gel, resulting in properties that differ from single-component gels. In these systems, adjusting the molecular structure of either component can introduce new functions,<sup>47, 52, 101, 102</sup> while varying their ratios can create new supramolecular aggregates,<sup>52, 62, 91, 103, 104</sup> enhancing the potential for smart soft materials.<sup>101, 105, 106</sup>

Incorporating a non-gelator into a gelator can alter the self-assembly process, affecting the gel's thermodynamic and mechanical properties and potentially introducing new functions.<sup>107</sup> Non-gelators may include substances like surfactants, polymers, or long-chain amines.<sup>29</sup> In a gelator-non-gelator system, three typical assembly modes exist (Figure 1-5b):<sup>108</sup> first, all components self-assemble into a gel network; second, the non-gelator adheres to the surfaces of the gelator's nanofibers; and third, the additive dissolves in the solution, surrounded by the fiber network. When designing a two-component system, combining the non-gelator with the gelator can help achieve the desired functionality.<sup>88, 107</sup>

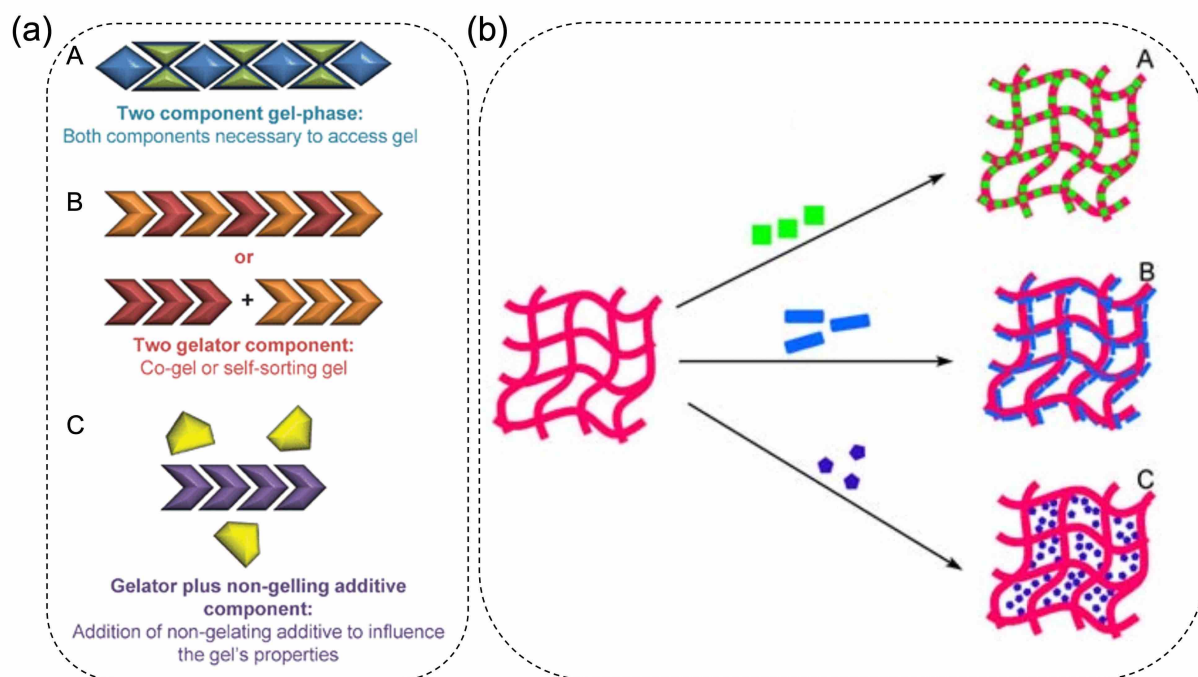


**Figure 1-5.** (a) Schematic diagram showing the three primary classifications of two-component supramolecular gels. (Reproduced with permission from Ref.<sup>86</sup> Copyright 2012, The Royal Society of Chemistry). (b) Cartoon outlining three assembly modes for supramolecular gelators when paired with non-gelling additives. In Case A, all components self-assemble into a unified gel network. In Case B, the additives attach to the surface of the gel network. In Case C, the additives remain in the solvent phase, encircled by the fiber networks. (Reproduced with permission from Ref.<sup>108</sup> Copyright 2011, Springer Nature).

In a two-gelator system, each component can serve independently as a gelator. This multi-component gel often exhibits superior properties compared to a single-component gel, sometimes leading to the development of new materials.<sup>7, 84</sup> The assembly process for two gelators typically involves four modes (Figure 1-6):<sup>99, 109, 110</sup> orthogonal self-assembly (self-sorting), where components segregate into distinct structural regions; cooperative self-assembly, where building blocks adhere to a common self-assembly pattern; random self-assembly, lacking any specific order; and destructive self-assembly, where partial binding and mismatching result in structural defects.

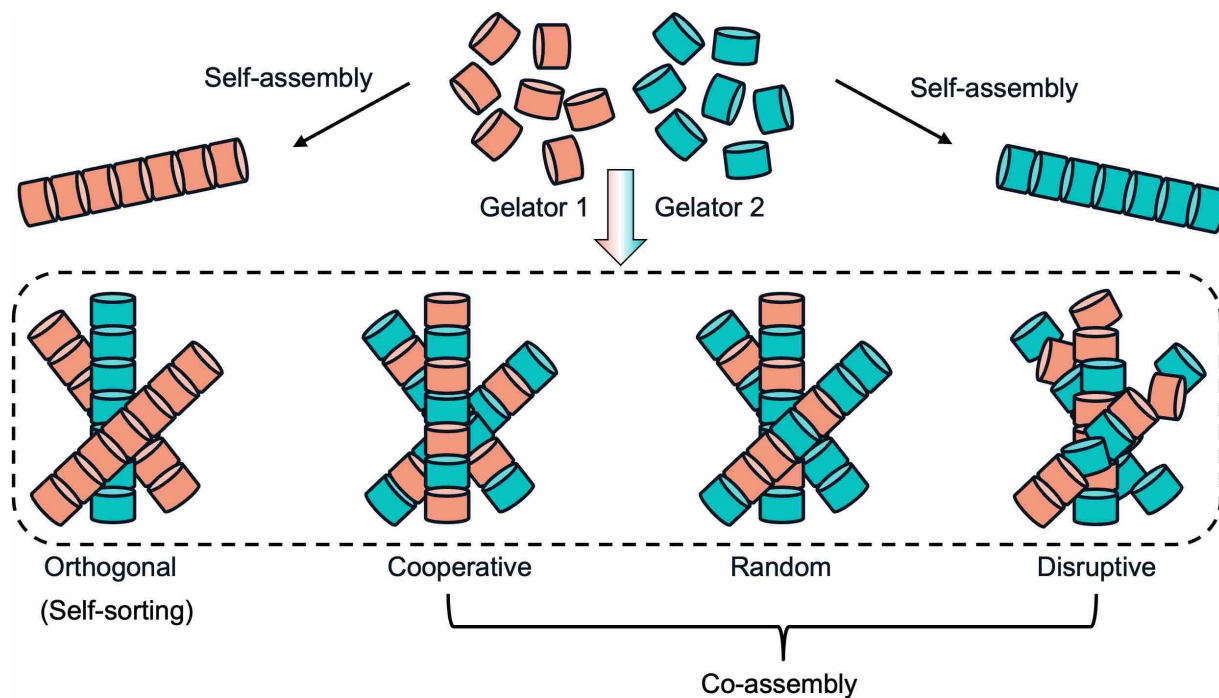


**Figure 1-6.** Overview of common assembly mechanisms in two-gelator supramolecular systems. Orthogonal self-assembly: each fiber is composed of only one type of gelator molecule; Cooperative self-assembly: two types of gelator molecules combine in a specific ratio and sequence to form fibers, allowing the components to be ordered; Random self-assembly: fibers are formed with a variable amount of gelator; Destructive self-assembly: mixing the components disrupts the system's ability to form self-assembled structures.

Assembly may also result in a combination of these possibilities, or predominantly, but not exclusively, in a single assembly.<sup>104, 111</sup> All these possibilities provide opportunities to make exciting new materials.

Most research focuses on two extremes: (1) co-assembly, where components combine through supramolecular interactions to form complex aggregates containing both gelators;<sup>62, 91, 95, 97, 112</sup> and (2) self-sorting, where molecules can distinguish between themselves and others, enabling the coexistence of pure assemblies from individual gelators.<sup>15, 102, 113-115</sup> Primary fibers from different components interact in distinct ways at the nanometre level, including lateral associations that are either homogeneous or heterogeneous, as shown in Figure 1-7.<sup>85</sup> At a larger scale of several microns, these fibers can be distributed in different spatial patterns, resulting in various microstructures. These structures may include intertwined (Figure 1-8a) or interpenetrating ((Figure 1-8b)) arrangements, often dominated by a single component. The self-sorting gel's network of intertwined fibers creates an extensive surface area between the fibers.

Additionally, distinct fiber domains formed by separate components may coexist, as illustrated in Figure 1-8c.<sup>38, 85</sup> To develop multi-responsive gels, combinations of gelators with differing responses can be explored,<sup>87</sup> as well as various self-assembly modes.<sup>92</sup> In multi-component systems, gelators with diverse structural patterns may enhance self-sorting, while similar structural components may facilitate co-assembly.

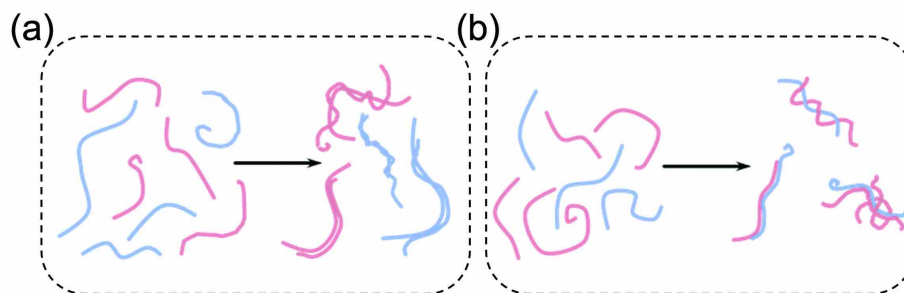


**Figure 1-7.** Schematic diagram illustrating how the self-sorting primary fibers may assemble into (a) homo-aggregates or (b) hetero-aggregates via lateral association. (Reproduced with permission from Ref.<sup>85</sup> Copyright 2018, The Royal Society of Chemistry).

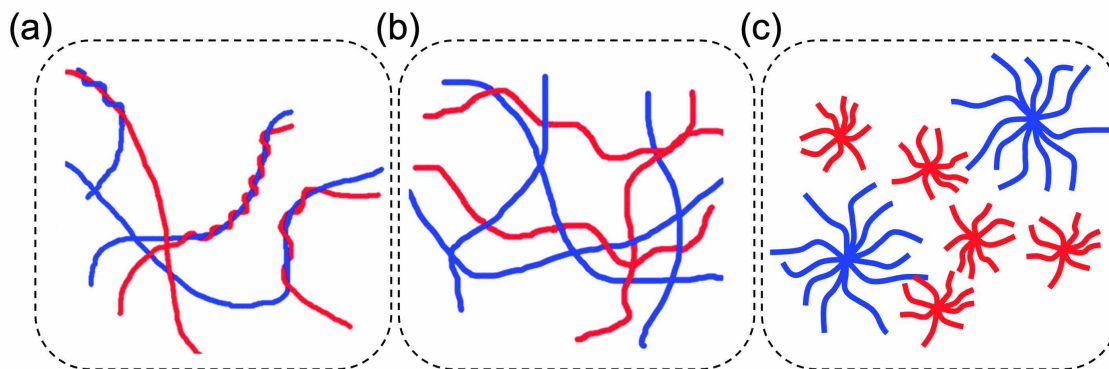


**Figure 1-8.** Illustration of networks on the multi-micron scale formed from a two-gelator self-sorting system: (a) an intertwining fibrous network (hetero-aggregates), (b) an interpenetrating network (homo-aggregates), and (c) the coexistence of fibrous domains formed by individual components. (Figures (a) and (b) are reproduced with permission from Ref.<sup>38</sup> Copyright 2015, The Royal Society of Chemistry).

### 1.3 Design of Self-Sorting Binary Supramolecular Systems

Self-sorting is a fundamental process in biological systems, essential for the organized assembly of molecules such as DNA and the precise folding of proteins.<sup>106, 116</sup> This mechanism ensures that each molecule interacts selectively, guiding critical functions in living organisms. Self-sorting events are essential in supramolecular assembly and have promoted the development of

highly ordered functional materials with complex structures and functions.<sup>84</sup> Artificial self-sorting LMWG systems can be developed by precisely controlling their molecular structure and selecting appropriate triggers.<sup>31, 115, 117, 118</sup> These approaches lead to materials with highly ordered and complex functions, driving innovation and broadening the scope of applications in functional material design.

### **1.3.1 Temperature-Induced Self-Sorting**

In traditional self-sorting systems, materials are prepared by heating a solution containing two types of gelators to temperatures above their solubility limits.<sup>68, 119-123</sup> As the solution cools, one type of gelator starts to aggregate at a higher temperature, initiating the formation of a self-sorting network.<sup>124</sup> However, designing these thermally induced self-sorting patterns is challenging because there is no direct correlation between the molecular structure and the assembly temperature. Wakabayashi et al. demonstrated that adding immiscible hydrophobic substituents to peptide amphiphiles makes it possible to control the self-sorting and co-assembly of molecular pairs.<sup>125</sup> Self-sorting is achieved through a standard heating-cooling process, while co-assembly requires an additional high-temperature incubation. This is particularly effective with longer hydrophobic tails, resulting in varied morphologies highlighting the tunable balance between hydrophobic interactions and immiscibility. This method underscores the significance of structural differences and dynamic behavior in achieving precise self-sorting using thermal triggers. Despite the promising potential of these techniques, there are several challenges. These include unpredictable gelation temperatures of LMWGs and the risk of irreversible chemical changes in gelators at high temperatures.<sup>126, 127</sup> These issues make the development of materials more complex, requiring continued research to refine and optimize these methods.

### **1.3.2 pH-Induced Self-Sorting**

Gradual pH adjustments are crucial for precisely controlling the assembly dynamics of dipeptide-based LMWGs.<sup>14, 15, 47, 87, 105, 128-130</sup> The effectiveness of this method stems from the direct correlation between the  $pK_a$  values of gelators and their hydrophobicity.<sup>45, 131</sup> Experimental findings suggest that optimal assembly occurs when there is approximately a one-unit difference between the  $pK_a$  values of the components.<sup>15, 47, 87</sup> For example, in an alkaline system with two different gelators, each characterized by distinct  $pK_a$  values, the slow hydrolysis of glucono- $\delta$ -lactone (GdL) gradually lowers the pH.<sup>16</sup> This change sequentially

triggers the self-assembly of each gelator: the gelator with the higher  $pK_a$  starts to aggregate first, followed by the second gelator forming a distinct interpenetrating network as the pH further decreases (Figure 1-9).<sup>15</sup>

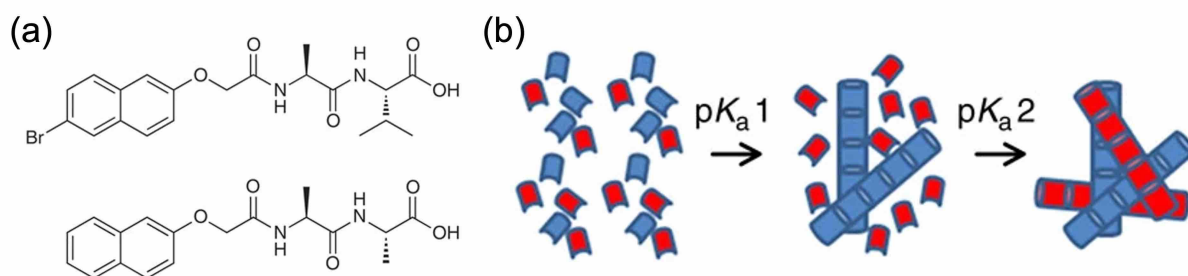


**Figure 1-9.** (a) Chemical structures of two gelators with distinct apparent  $pK_a$ . (b) Schematic illustration of the GdL-triggered sequential self-assembly process that forms a self-sorting fibrous network. (Adapted with permission from Ref.<sup>15</sup> Copyright 2013, Springer Nature).

This technique showcases how self-assembly can be precisely manipulated across different scales, emphasizing the significant influence of molecular structure on assembly sequencing. It highlights that even molecules with similar structures can have different behaviors due to slight differences in  $pK_a$  values.<sup>45, 47</sup> By adjusting the amount of GdL or temperature, researchers can finely control the assembly sequence, offering more flexibility and predictability than traditional methods relying on controlled cooling rates.<sup>27, 132</sup> The Smith group further advanced this approach by developing a multicomponent gel system that employed two distinct pH triggers—GdL and diphenyliodonium nitrate (DPIN). This system controls the self-assembly of two different gelators based on their  $pK_a$  values, allowing for the formation of a sophisticated secondary network structure through strategic pH adjustments.<sup>132</sup> This method significantly improves over conventional heat-induced gelation techniques, facilitating the development of more complex structures.

### 1.3.3 Self-Sorting Induced by Chiral Difference

Enantiomeric molecules are highly effective in creating self-sorting multicomponent systems through stereoselective self-assembly.<sup>31, 86, 115-118, 122</sup> These molecules, which are mirror images of each other, selectively interact and assemble according to their specific configurations. This capability facilitates the precise organization of components within a system. Racemic mixtures often form aggregates that could hinder or disrupt the chiral structure and the gelation process.<sup>133, 134</sup> However, under certain conditions, these mixtures can form aggregates in a more controlled way, illustrating how structural differences between chiral isomers directly influence their

molecular stacking and facilitate the orderly assembly of enantiomers through targeted supramolecular interactions.<sup>31, 117</sup>

In systems composed of pure enantiomers, interactions foster self-sorting and enhance the stacking of similar molecules.<sup>135-138</sup> Adhikari and colleagues demonstrated that the chirality of Fmoc-protected amino acids—glutamic acid and lysine—affects the orientation of chiral helical nanofibers formed in hydrogel systems (Figure 1-10a).<sup>122</sup> Their studies revealed that homochiral combinations in two-component hydrogels produce either co-assembled left-handed or right-handed fibers, a finding confirmed by circular dichroism and atomic force microscopy. Additionally, experiments with racemic mixtures in four-component hydrogels showed that each chiral form preferentially aligns with its identical counterpart, allowing for the coexistence of distinct helical orientations (Figure 1-10b). Introducing helices of varying chirality can alter stacking patterns, potentially initiating supramolecular self-sorting critical for creating homochiral structures, which markedly influence the material's macroscopic properties.<sup>116, 137</sup> In two-component gel systems, the non-covalent interactions between weak or reversible enantiomers play a crucial role in maintaining structural stability.<sup>117, 139</sup> Through chiral recognition, scientists can manipulate energy transfer and assembly processes in multicomponent systems, achieving a higher level of structural precision in self-sorting systems.<sup>140</sup> The chiral effects and self-sorting of enantiomers are vital for defining structure and function. Chirality recognition between gelators can also be used to construct a self-sorting system.<sup>23, 141</sup>

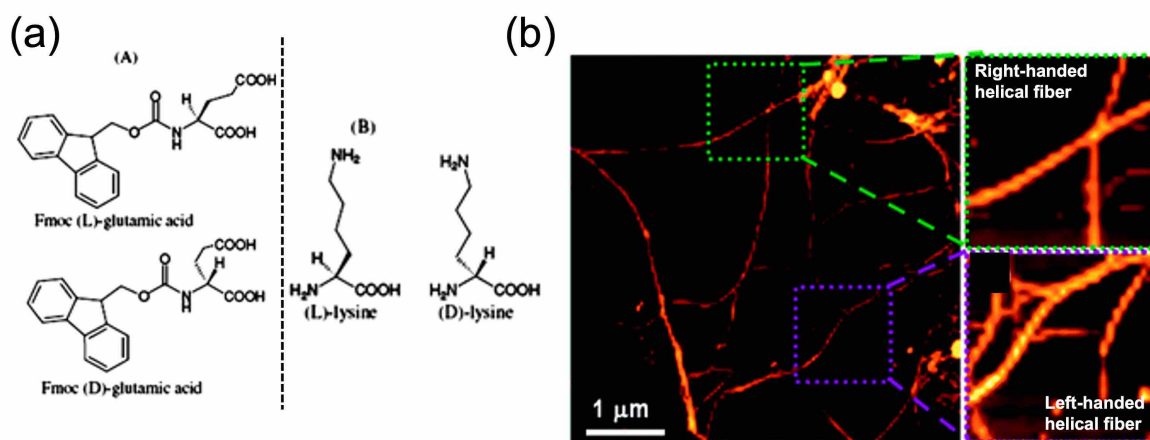


**Figure 1-10.** (a) Molecular structures of the gelators in binary hydrogels: (A) Fmoc-Glu and (B) Lys. (b) AFM visualization of the mixed enantiomers in a complex (four-component) hydrogel [Fmoc-(L+D)Glu + (L+D)Lys], showing both left- and right-handed helical structures. (Adapted with permission from Ref.<sup>122</sup> Copyright 2011, The Royal Society of Chemistry).

This approach utilizes the self-sorting of enantiomeric mixtures to facilitate supramolecular assembly, helping to develop new materials with specific functionalities and organized structures. However, managing interactions among various chiral components presents challenges, with the instability of racemates introducing unpredictability in structural design.

### **1.3.4 Self-Sorting Induced by Structural Difference**

The design of multicomponent gels benefits greatly from understanding the differences and complementarity in molecular structures, particularly for achieving self-sorting or co-assembly behavior.<sup>17, 27, 90, 142, 143</sup> Research indicates that markedly different structural motifs encourage self-sorting in these systems, whereas components with similar structures are likely to co-assemble.<sup>14, 68, 123, 133, 144-146</sup> For example, Onogi et al. developed self-sorting supramolecular nanofibrillar hydrogels from peptide gelators and amphiphilic phosphates (Figure 1-11). Employing novel fluorescent probes and advanced imaging techniques, they accomplished real-time in situ imaging of two- and three-dimensional fibers. This approach revealed the orthogonal interactions between fibers, showcasing the variations in formation rates and the stability of their physical and chemical properties within the gel. Liu et al. developed two hydrogels with opposite handedness of supramolecular structures by using gelators LPF and LPFEG, which differ in peripheral substituents but share a chiral phenylalanine core.<sup>106</sup> These two gelators form self-sorting double-network nanofibers with adjustable chiroptical activities by varying their molar ratios. Although even minor variations in molecular structure can substantially affect the assembly mode in multicomponent systems, they also add complexity and challenges to the design process.<sup>17, 144, 147</sup> This necessitates careful consideration and precision in the architectural design of these materials to ensure desired outcomes.

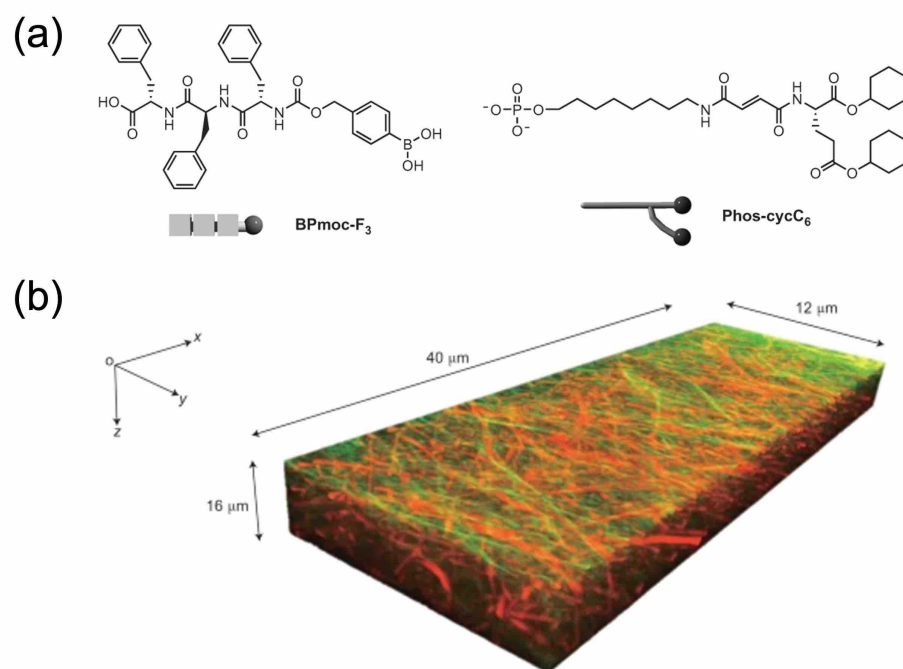


**Figure 1-11.** (a) Molecular structures of the gelators: BPmoc-F<sub>3</sub> and Phos-cycC<sub>6</sub>. (b) Three-dimensional confocal laser scanning microscopy (CLSM) image of hydrogels, illustrating the self-sorted supramolecular nanofibers. (Adapted with permission from Ref.<sup>114</sup> Copyright 2016, Springer Nature).

## 1.4 Characterization Techniques for Multicomponent Supramolecular Systems

The self-assembly of gelators spans multiple levels, from molecular to multi-micrometer scales. At the nanoscale, interactions between native fibers, such as lateral connections, play a crucial role in shaping their structure. As observations expand to the multi-micron scale, the arrangement of these fibers may show uniform or varied patterns, leading to various microstructures. Due to the hierarchical and complex nature of these systems, studying and assessing their properties requires a range of characterization techniques. Particularly when comparing single-component and multi-component systems, it's vital to analyze the differences or similarities to understand how the two-component systems assemble. Multiple complementary techniques are used for cross-validation to obtain accurate results.

### 1.4.1 Molecular-Level Characterization

At the molecular level, several techniques such as ultraviolet-visible absorption spectroscopy, fluorescence spectroscopy, circular dichroism, infrared spectroscopy, and nuclear magnetic resonance are employed to analyze the molecular arrangement, non-covalent interactions, and dynamic behaviors of gelators.

In self-sorting two-component systems, the ultraviolet-visible (UV-Vis) spectrum typically mirrors the additive results of the individual components' spectra, showing no new peaks that would suggest the formation of charge transfer complexes.<sup>123, 148, 149</sup> Co-assembly between molecules often results in the formation of new structures that adjust energy levels and significantly alter the absorption spectrum.<sup>62, 150</sup> These changes not only signal charge transfer but also aid in identifying co-assembly behavior. By mixing molecules that function as electron donors and acceptors, specific charge transfer complexes are formed.<sup>151</sup> These complexes are crucial for promoting and sustaining the co-assembly state. Furthermore, the temperature-dependent properties of UV/Vis spectroscopy allow for detailed studies of multicomponent supramolecular systems. By tracking absorbance against temperature, researchers can identify phase transition temperatures ( $T_g$ ). For example, research by Sugiyasu et al. demonstrated that the dissociation temperature in a self-sorting system corresponds with those of the individual components, suggesting that each gelator self-assembles independently without affecting the aggregation-dissociation processes of the others (Figure 1-12).<sup>149</sup> Moreover, the spectra of the two-component gel showed an overlap of the individual spectra of 4Thio and Pery without new peaks, indicating no chemical interactions between them and reinforcing their self-sorting behavior.

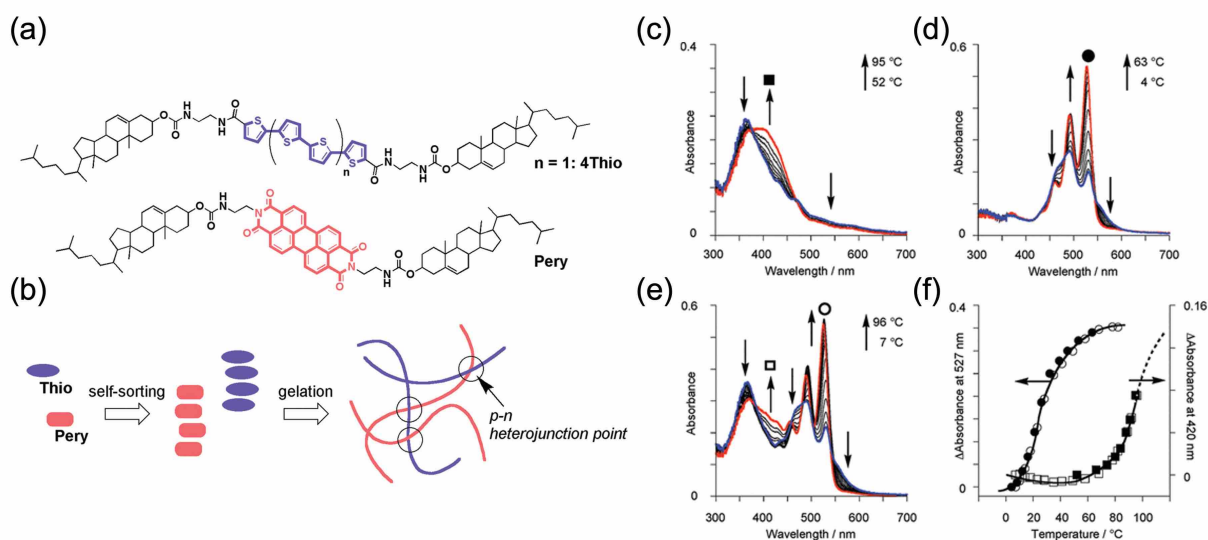


**Figure 1-12.** (a) Chemical structures of 4Thio and Pery. (b) Schematic representation of self-sorting binary gels, illustrating the formation of functional nanocables at the p–n heterojunction points. Temperature-dependent UV-Vis spectra for (c) 4Thio gel, (d) Pery gel, (e) 4Thio/Pery self-sorting gel, and (f) absorbance as a function of temperature. The dissociation temperature for the Pery gel is approximately 25 °C, whereas for the 4Thio gel, it is assumed to be around 95 °C due to its high stability under the experimental conditions. (Adapted with permission from Ref. <sup>149</sup> Copyright 2008, American Chemical Society).

Fluorescence spectroscopy is a valuable tool for observing structural changes and studying energy transfer effects, indicating molecules' proximity within a structure. For effective energy transfer to occur, the donor and acceptor molecules must be close to each other, a condition often met by thorough mixing or co-assembly of fibers. This proximity is crucial in multicomponent supramolecular co-assembly and intertwined self-sorting systems.<sup>152, 153</sup> However, fluorescence spectroscopy alone cannot distinguish between these two types of assembly due to similar energy transfer characteristics.

Chirality in gelator molecules can be converted into gel-phase assemblies, ranging in size from nanometres to micrometers, through hierarchical assembly processes.<sup>20, 31, 62, 76</sup> Circular dichroism (CD) spectroscopy is the primary method for examining the formation of nanoscale chiral structures in these gelators molecules.<sup>31, 106</sup> CD spectroscopy generally shows a simple overlap of the spectra from individual components in self-sorting systems.<sup>119, 149</sup> In contrast, co-assembly systems often produce spectra that deviate from the expected combinations of components.<sup>27, 47, 62</sup> For accurate CD spectral analysis, it is essential to maintain high tension (HT) voltage below a specific threshold and keep absorbance under 0.2.<sup>154, 155</sup> The HT

(High Tension) voltage in a CD spectrometer controls the energy applied to the detector and the photomultiplier tube. It influences the sensitivity and response of the detector to the signal, which is critical for accurate measurements. If the HT voltage is too high, it can saturate the detector, leading to distorted readings. The absorbance, which is directly related to sample concentration, needs to stay below 0.2 to ensure linearity in measurements. Higher concentrations increase absorbance, potentially causing detector saturation if the HT voltage is not adjusted accordingly, impacting the signal-to-noise ratio. Furthermore, the thermal sensitivity of self-assembled fibers makes temperature-dependent CD spectroscopy a useful technique for understanding the assembly behaviors of nanoscale chiral aggregates in dual-component systems.<sup>88, 106</sup>

Infrared spectroscopy (IR) is a powerful tool for verifying the presence of hydrogen bonds by observing shifts in characteristic peaks between a gelator's hydrated and gel phases. It also provides insights into the molecular organization of the gelator and identifies non-covalent interactions essential for gel formation.<sup>17, 52, 53, 62, 156</sup> In certain binary supramolecular systems dominated by self-sorting, IR can detect subtle interactions with the second gelator to assess co-assembly.<sup>14, 111</sup> In multicomponent systems, a clear divergence between the IR spectrum and the linear sum of the individual components' spectra usually indicates co-assembly.<sup>146</sup> In contrast, spectral overlay suggests self-sorting.<sup>17, 157</sup> It is important to note that the OH stretching peak of water can mask other critical peaks, such as the NH stretching peak. To overcome this, IR spectroscopy often uses dehydrated samples or deuterium water as a solvent, enhancing the reliability of the results.

Nuclear magnetic resonance (NMR) spectroscopy is crucial for analyzing supramolecular systems, particularly in observing gelation processes. In the gel state, the restricted mobility of gelator molecules reduces their visibility in NMR scans. NMR is handy in slow gelation processes, as it can distinguish between self-sorting, characterized by a sequential disappearance of peaks, and co-assembly, where peaks vanish simultaneously.<sup>15, 27, 68, 148</sup> In a self-sorting system, the presence of one component may influence the assembly behavior of another. Temperature-dependent NMR demonstrates that the stabilization of one of the gelators in a binary gel at various temperatures mirrors its behavior when gelled alone, suggesting that the presence of the second gelator does not impact its assembly process.<sup>68</sup>

## **1.4.2 Nanometer-Scale Characterization**

### 1.4.2.1 Microscopy

Supramolecular gels consist of aggregate networks that self-assemble from molecular blocks, with aggregate sizes ranging from a few nanometres to a few micrometers. Electron microscopy and X-ray/neutron scattering are excellent tools for gaining insight into these structures.

Scanning Electron Microscopy (SEM) and Transmission Electron Microscopy (TEM) are powerful techniques used to visualize the intricate details of supramolecular assemblies. SEM scans the surface of a sample with a focused electron beam, capturing images that reveal the morphology, structural details, and composition of these assemblies.<sup>153, 158, 159</sup> On the other hand, TEM achieves visualization at the sub-nanometre level, clearly depicting the superstructures formed by gelators through non-covalent interactions and providing insights into the gelation process by analyzing the size and shape of the aggregates.<sup>160-162</sup> In the study of self-sorting systems, it's common to observe structures of two distinct sizes.<sup>14, 68, 106, 130, 144, 163, 164</sup> Conversely, co-assembly systems often produce unique morphologies that are different from those observed in single-component systems (Figure 1-13).<sup>52, 62, 165</sup> Electron microscope images of LMWGs can show aggregates that are either uniform or vary significantly, highlighting the complex nature of these assemblies.<sup>15, 27, 166</sup> However, both SEM and TEM typically require the sample to be dried using methods like vacuum or freeze-drying to remove solvents, which results in a "dry gel." This drying process can alter the non-covalent forces within the gel, potentially changing the self-assembled structures or causing crystallization.<sup>167, 168</sup> Therefore, the images produced may not fully represent the actual state of the aggregate structures, which is a significant limitation of these techniques that must be considered when interpreting results.

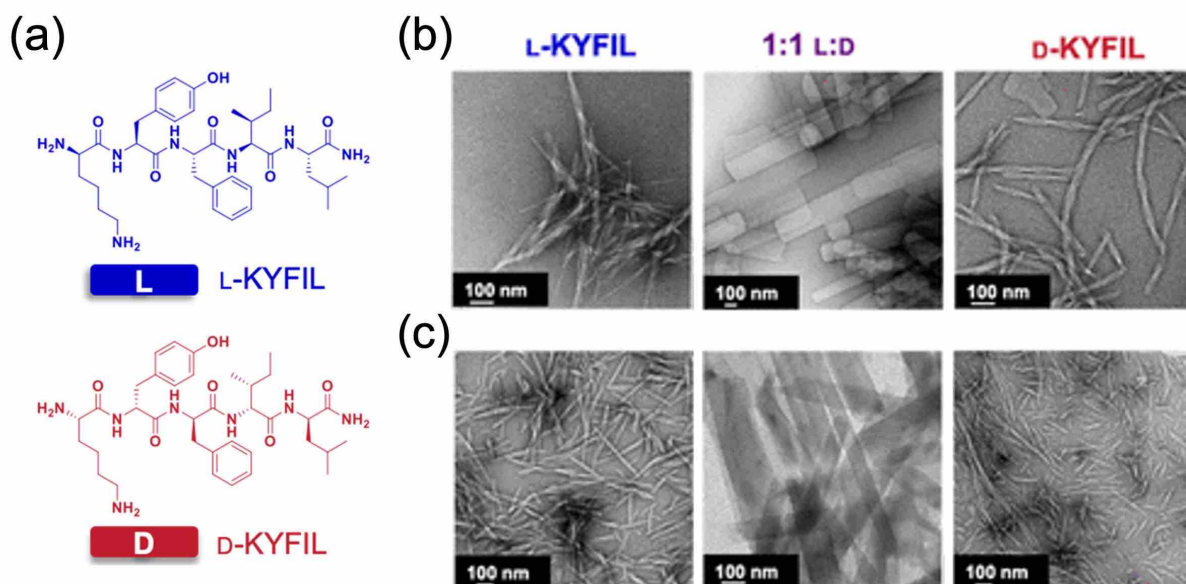


**Figure 1-13.** (a) Chemical structures of L- and D-KYFIL peptides. TEM images of (b) 0.75% (w/v) and (c) 1.5% (w/v) L-, 1:1 volume ratio L:D- and D-KYFIL hydrogels in PBS at pH 7.4. The pure L- and D-KYFIL hydrogels exhibit twisted nanofibers, whereas the 1:1 blend forms micron-scale sheets. (Adapted with permission from Ref.<sup>52</sup> Copyright 2023, American Chemical Society).

Atomic force microscopy (AFM) allows for the detailed observation of three-dimensional surface topography of supramolecular systems ranging from the nanometre to the submillimetre scale, without the need to dehydrate samples.<sup>62, 144, 164, 169-171</sup> A significant limitation, however, is that the probe tip can compress the nanostructures of soft materials. This compression can distort the appearance of structures, making them seem wider and shallower than they truly are, which can lead to measurement inaccuracies. It is crucial to consider this factor when analyzing images from soft material samples using AFM.

Cryogenic transmission electron microscopy (cryo-TEM) is a favored technique for examining thermally cured liquid or semi-liquid samples, providing high-resolution images that reveal both the fundamental properties of structures and the coexistence of self-assembled structures in supramolecular systems.<sup>62, 120, 171-174</sup> Unlike indirect methods like scattering techniques, which depend on theoretical models and can struggle with complex systems containing multiple aggregates or a wide size range, cryo-TEM offers data that is more direct and easier to interpret, making it crucial for analyzing intricate systems effectively. Cryo-TEM provides two major advantages for studying supramolecular LMWGs. First, it maintains samples in their hydrated state, avoiding the distortions caused by drying under a high vacuum and better preserving their

original condition. Second, rapid freezing techniques within a cryogenic medium allow cryo-TEM to quickly "freeze" gels, preventing nanoscale structural changes.<sup>175, 176</sup> However, cryo-TEM has a drawback: the thin films required for this technique can limit the visualization of entire gel networks, often only revealing isolated structural components instead of comprehensive networks.<sup>62, 176, 177</sup> Additionally, the highly regular structures sometimes observed may be artifacts resulting from shear forces during sample preparation, rather than true representations of the network. These aspects must be meticulously considered when analyzing cryo-TEM images.

### 1.4.2.2 Small-Angle Scattering

Small-angle scattering (SAS), encompassing small-angle X-ray scattering (SAXS) and small-angle neutron scattering (SANS), is a technique for analyzing structures at the mesoscale, ranging from 1 to 1000 nanometers.<sup>178-180</sup> One of the key advantages of SAS is its non-destructive approach, allowing researchers to study samples in their natural, hydrated state without the need for drying. This method is particularly useful for investigating primary structures such as fibrils.<sup>85, 181</sup>

The basic mechanism of SAS involves a beam of X-rays or neutrons being directed at a sample. As the beam interacts with the sample, it is deflected at small angles, typically between 0.1 to 10 degrees (Figure 1-14).<sup>88, 178, 181</sup> The scattered beams are then detected and analyzed. The pattern and angle of scattering provide detailed insights into the size and shape of structures within the sample; larger structures tend to scatter beams at narrower angles. A small fraction of the beam is elastically scattered to a detector, and the intensity of this scattering, represented as  $I(Q)$  where  $Q$  is the scattering vector correlated with the angle, reveals extensive information about the size, shape, and distribution of scatterers. This effectively maps the spatial frequency of the structure under observation. The scattering vector  $Q$  is calculated using Equation A1-1.

$$Q = \frac{4\pi}{\lambda} \cdot \sin\left(\frac{2\theta}{2}\right) \quad \text{Equation A1-1}$$

where  $\lambda$  represents the wavelength of the neutrons, and  $2\theta$  is the scattering angle.

In an isotropic scattering system, the scattering intensity detected at any point on the detector remains uniform within expected statistical deviations.<sup>182</sup> By averaging this data over the azimuthal angle  $\phi$ , a one-dimensional scattering pattern,  $I(Q)$ , is derived. This pattern directly reflects the scattering vector  $Q$ , offering a streamlined and straightforward depiction of scattering behavior.

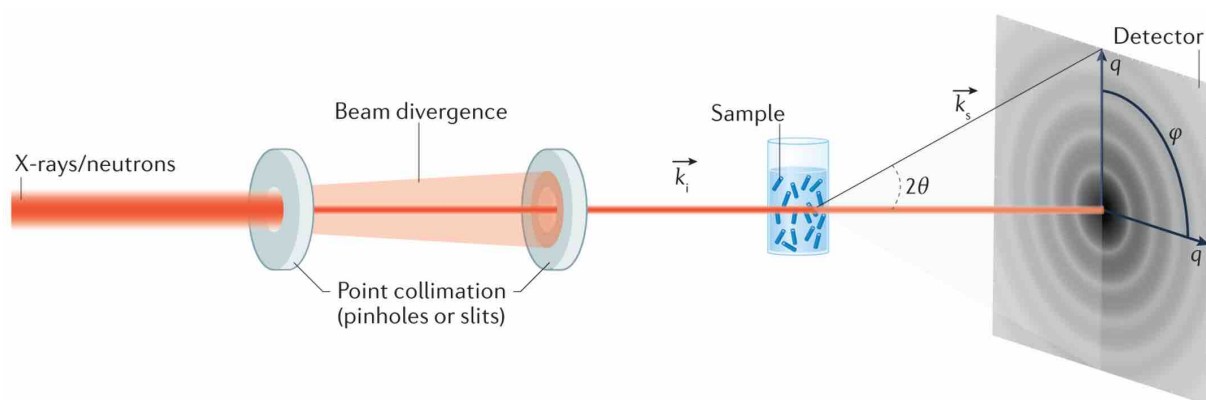


**Figure 1-14.** Schematic illustration of small-angle scattering. This diagram shows the scattered ( $k_s$ ) and transmitted ( $k_i$ ) X-rays/neutrons wave vector, momentum transfer vector ( $q$ , where  $q=k_s-k_i$ ), and the azimuthal angle ( $\varphi$ ). (Reproduced with permission from Ref.<sup>182</sup> Copyright 2021, Springer Nature)

Achieving adequate contrast is crucial for strong scattering and high-quality data in scattering techniques.<sup>178, 183</sup> SANS often uses deuterated solvents to enhance this contrast, leveraging the differences in scattering length densities between hydrogen and deuterium.<sup>178</sup> Similarly, in SAXS, contrast is derived from variations in electron density.<sup>184</sup> Structural parameters of materials are typically deduced by fitting the scattering data to appropriate models, which facilitates detailed analysis of their microscopic structures.<sup>17, 49, 167, 178</sup> Model fitting in SAS analysis is not universally applicable and can be limited by the context of the analysis and differences in how data fits various models, as evidenced by functionalized dipeptide data fitting differently due to solvent contrast variations.<sup>58</sup>

SAS is critical for identifying the packing arrangement in multicomponent systems, particularly when there are notable differences in the scattering profiles of the components or when a newly formed network differs significantly from its individual components.<sup>15, 17, 47, 148</sup> For instance, in a self-sorting system, the scattering profile often reveals distinct peaks characteristic of each gelator (Figure 1-15).<sup>15</sup> The data are more accurately interpreted using a combination of models based on each component. Conversely, if the scattering from a co-assembled system closely aligns with that of a single component, it suggests that this component primarily dominates the co-assembled structure.<sup>88</sup> Additionally, selectively deuterating one of the gelators to match the contrast can reduce its impact on the overall scattering of the system.<sup>88, 105</sup> If the scattering profile of a hybrid system closely resembles that of one of the gelators, it indicates a self-sorting assembly mode.<sup>15</sup> However, it is important to remember that scattering data may not always provide detailed insights into the types or densities of cross-links within the network.

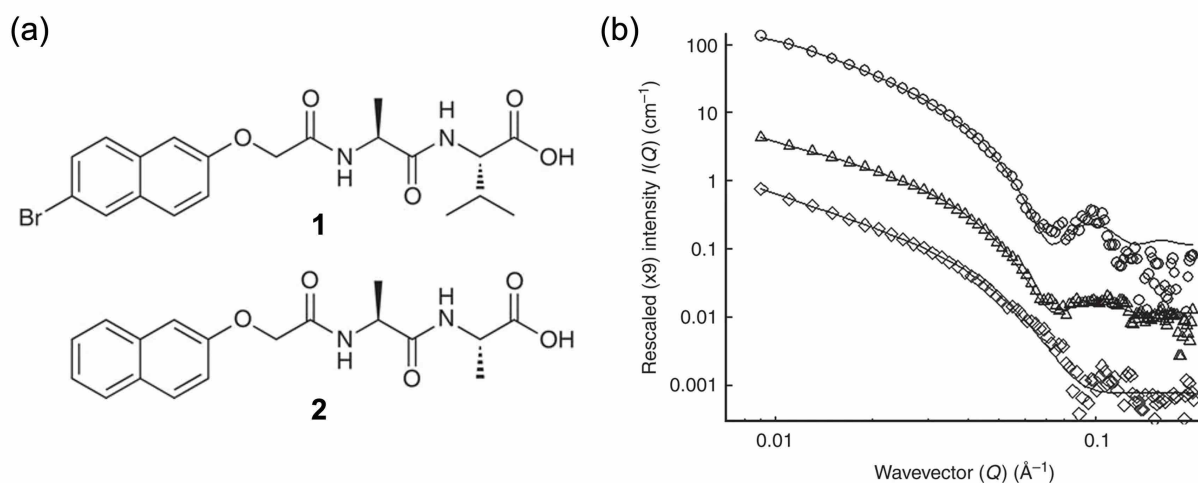


**Figure 1-15.** (a) Chemical structures of gelators **1** and **2**. (b) SANS data for gels **1** (circles), **2** (diamonds), and the two-component systems of **1** and **2** (triangles). The scattering of the binary gel shows characteristic peaks associated with pure **1** and pure **2**: a slow decay at low  $Q$  corresponding to **2**; and a steep weak peak corresponding to **1** near  $Q_{\text{max}} \approx 0.1 \text{ \AA}^{-1}$  ( $63 \text{ \AA}$ ), indicating the presence of a certain degree of core-shell structure. (Adapted with permission from Ref.<sup>15</sup> Copyright 2013, Springer Nature).

### 1.4.2.3 X-Ray Diffraction

X-ray diffraction (XRD) is a critical method for examining the morphologies and packing arrangement of supramolecular self-assemblies.<sup>21, 86, 185-187</sup> In situations where electron microscopy does not provide sufficient resolution to distinguish assembly patterns in binary gels, fiber X-ray diffraction (fXRD) serves as an effective alternative.<sup>15, 47</sup> This technique assesses whether the co-assembly process alters the original structure or results in a new, distinct form.<sup>27</sup> In multi-component gels that self-sort, fXRD can reveal overlapping diffraction signatures of each individual components.<sup>15, 130</sup>

### 1.4.3 Microscale Characterization

In the realm of microscopy, fluorescence confocal microscopy and polarized light microscopy are invaluable for exploring the morphologies of supramolecular self-assemblies at the microscopic scale.<sup>10, 27, 35, 49</sup> Polarized optical microscopy (POM), despite its resolution limit of 0.2 microns, effectively reveals the aggregate structure and uniformity of microstructures.<sup>188, 189</sup> Confocal microscopy, on the other hand, specializes in producing three-dimensional reconstructions of objects with complex geometries. Unlike traditional microscopy, confocal

microscopy yields clearer internal images by eliminating the overlap of information from different depths, providing a more precise view of the internal architecture.<sup>190-192</sup> It is beneficial for examining the surface contours of opaque materials and the internal structures of transparent ones.<sup>177, 193 17, 27</sup>

Confocal laser scanning microscopy (CLSM)<sup>153, 171, 193</sup> and super-resolution microscopy<sup>102, 114, 177, 194</sup> have significantly enhanced our ability to analyze microscopic structures. These advanced imaging techniques enable the real-time monitoring of structural changes in gels under natural conditions and can identify complex patterns of network formations. For instance, Kubota et al. demonstrated the selective formation of interpenetrating and parallel self-sorting networks using a method called dynamic covalent oxime chemistry, as verified through CLSM.<sup>195</sup> Their observations indicated that upon the addition of O-benzylhydroxylamine, short peptide nanofibers began to form and elongate both near and on Phos-MecycC<sub>5</sub> nanofibers, as well as randomly in the surrounding water, creating an interpenetrating network (Figure 1-16b). Additionally, in parallel networks, these fibers formed and extended along the lipid nanofibers without merging, thus preserving their structural independence (Figure 1-16c). Although they typically require the introduction of dyes, which might affect the assembly process, their detailed visualization of fine fibrous textures is invaluable.

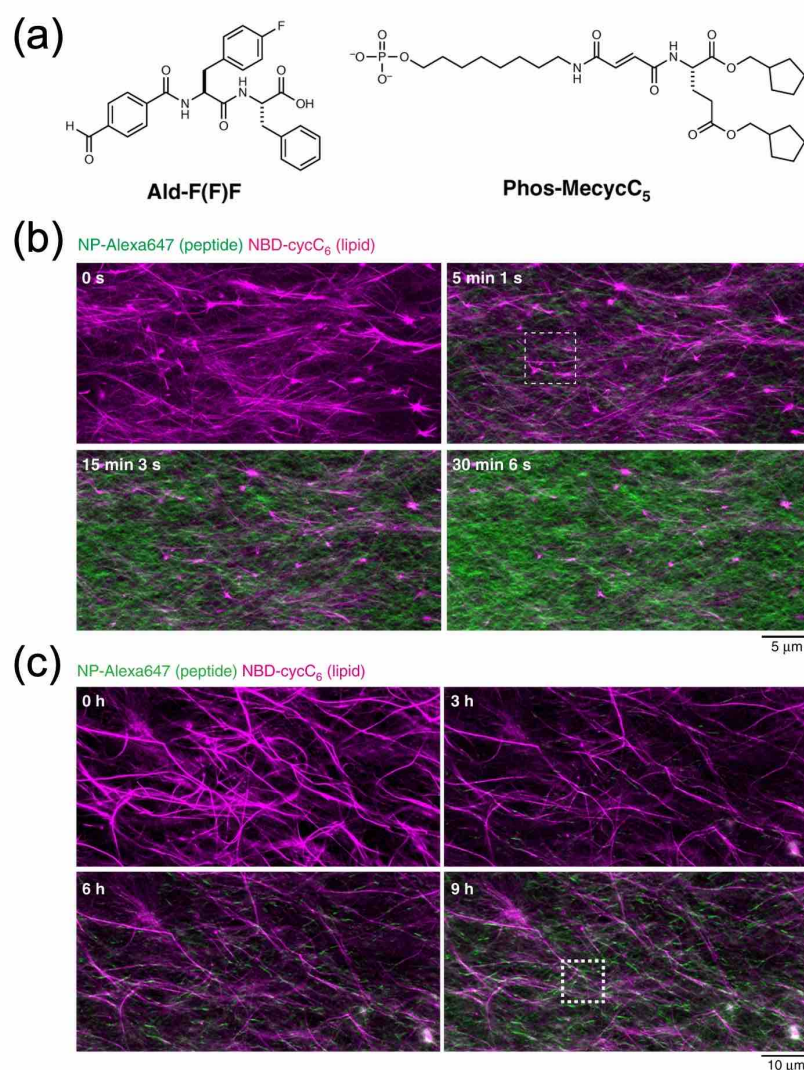


**Figure 1-16.** (a) Molecular structures of Ald-F(F)F peptide and Phos-MecycC<sub>5</sub> lipid hydrogelators. (b) Real-time high-resolution Airyscan CLSM imaging of the development of the interpenetrating self-sorting network. (c) Real-time high-resolution Airyscan CLSM imaging of the development of the parallel self-sorting network. Fluorescent markers NP-Alexa647 and NBD-cycC<sub>6</sub> were utilized to highlight peptide and lipid nanofibers, respectively. (Adapted with permission from Ref.<sup>195</sup> Copyright 2020, Springer Nature).

## 1.4.4 Macroscale Characterization

### 1.4.4.1 Rheology

Rheology examines how substances deform and flow under external forces. Shear viscosity reveals information about the self-assembly of pre-gel solutions and helps differentiate between solution types, such as Newtonian and non-Newtonian fluids. Shear thickening, or rheopectic

behavior, suggests that at certain shear rates, the internal structure of the solution changes, increasing resistance and raising the apparent viscosity. In contrast, shear thinning, or pseudoplastic behavior, indicates that the self-assembled structures align perpendicularly to the applied shear stress, reducing anisotropy and lowering the apparent viscosity.<sup>88</sup>

Rheological measurements can also characterize the mechanical properties of gels, providing insights into their network structures.<sup>196</sup> By analyzing the storage modulus ( $G'$ ) and loss modulus ( $G''$ ) across variables like frequency, strain, temperature, and time, we can assess a material's response to stress and determine key mechanical properties such as the linear viscoelastic region (LVE), yield point, and flow point.<sup>3, 98, 197</sup> Additional parameters like reversibility,<sup>23, 59</sup> the rate and duration of self-assembly<sup>47, 148, 198</sup> can also be extracted from these tests. Generally, gels exhibit  $G'$  values that are approximately an order of magnitude higher than  $G''$ , with frequency sweeps showing frequency independence.<sup>10, 199</sup> The surface chemistry<sup>200</sup> and dimensions of the container<sup>26</sup> used for gel preparation can also influence the final gel properties, making it essential to specify both the container's property (e.g. surface hydrophobicity and chemical composition) and size.

Rheology is a crucial tool in studying supramolecular gels, providing insights into their structural dimensions, cross-linking density, dynamics, and mechanical and self-healing properties.<sup>98, 197, 198, 201</sup> For low molecular weight gels, various factors such as fiber size, morphology, crosslink density, and spatial distribution of fibers influence their rheological properties.<sup>29, 85</sup> Kinetic factors like the rate of gelation also play a crucial role; faster gelation typically results in more crosslinks but may reduce structural homogeneity, impacting the gel's rheological behavior.<sup>14, 59, 130</sup> In two-component systems, co-assembly can lead to new structures with distinct rheological behaviors compared to single-component systems.<sup>97, 99</sup> Experiments have shown that the modulus of two-component gels can increase, decrease, or stay the same, indicating that their properties can vary significantly through self-sorting and co-assembly processes.<sup>47, 62, 71, 91, 166, 202</sup> Therefore, careful interpretation is needed when linking rheological outcomes to specific assembly modes.

The rheological time sweep can be used to identify the assembly type for systems that undergo slow pH-triggered gelation. As the pH gradually decreases, the self-sorting network forms step by step, with  $G'$  and  $G''$  showing a multi-stage increase (Figure 1-17(b)).<sup>47, 148, 152</sup>

This process is often studied in conjunction with techniques like nuclear magnetic resonance ( $^1\text{H}$  NMR spectroscopy), where components progressively become NMR-invisible during

gelation.<sup>14, 15</sup> The degree of self-assembly can be tracked by monitoring the decrease in the integral values of characteristic  $^1\text{H}$  NMR peaks, which corresponds with an increase in modulus (Figure 1-17b).<sup>47, 148</sup> In cases of co-assembly, both gelators will become NMR-invisible simultaneously, and the modulus increases accordingly.

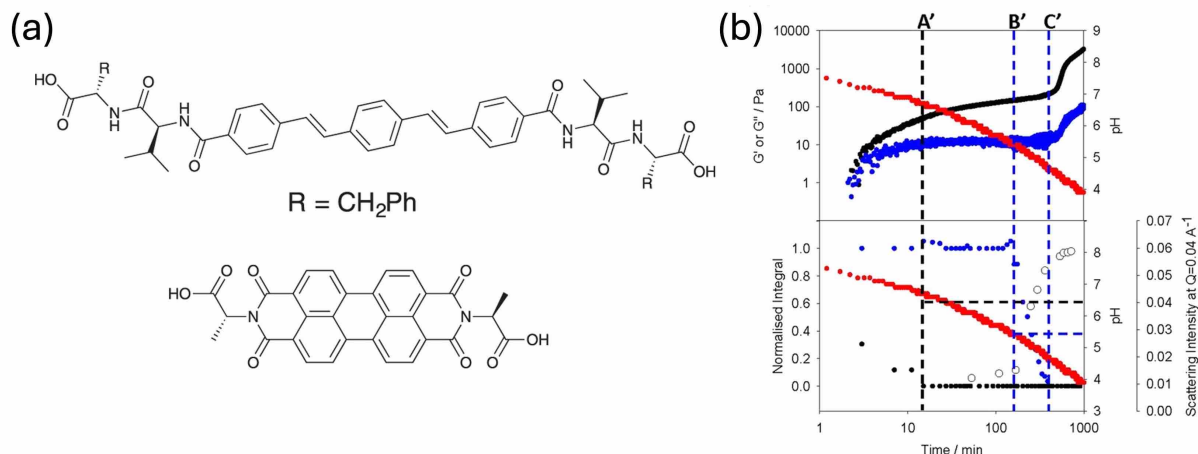


**Figure 1-17.** (a) The chemical structures of OPV3 (top) and PBI gelator (bottom). (b) The two-component gel network was monitored over time using various techniques. The top graph depicts changes in pH (red) alongside the rheological moduli,  $G'$  (black) and  $G''$  (blue). The bottom graph presents pH (red), the variation in the integral of the  $^1\text{H}$  NMR signal for the CH group of OPV3 gelator (black) and PBI gelator (blue), as well as the corresponding SAXS data (hollow circles). Ethanol served as an internal standard (IS), and the normalized value was determined by integrating the components against the internal standard at pD 11, before the addition of GdL. (Adapted with permission from Ref.<sup>148</sup> Copyright 2017, Springer Nature).

#### 1.4.4.2 Differential Scanning Calorimetry

Differential scanning calorimetry (DSC) is a method used to study the thermal properties of materials by measuring differences in heat flow between a sample and a reference. This technique is particularly effective for analyzing the absorption or release of heat during transitions from gel to sol phases.<sup>86, 188</sup> During these transitions, changes in heat content, or enthalpy, are identified by specific peaks on the DSC curve. To achieve clear results, samples are usually highly concentrated and display good crystallinity.<sup>203</sup> Moreover, DSC allows for the assessment of thermal reversibility in gels by cyclically heating and cooling the sample and monitoring shifts in these peaks.

DSC also plays a vital role in identifying packing preference in multi-component supramolecular systems.<sup>21, 68, 86, 117, 186, 204</sup> For example, in a two-component mixture, DSC can distinguish two separate temperature transitions, each corresponding to a different component.<sup>68</sup> This provides definitive evidence of two distinct network structures existing simultaneously. Additionally, researchers, such as Moffat, have shown that in two-component gels, the transition temperature of one gelator remains stable despite the presence of another, confirming that each component forms a thermally stable, independent network.<sup>144</sup> These findings emphasize the utility of DSC in analyzing the intricate interactions within multi-component systems, affirming its significance in the field of advanced materials research.

## 1.5 Aims and Objectives

Multicomponent gels offer precise control at molecular and network levels, allowing for the creation of advanced materials beyond the scope of single-component gels. These systems can be customized for specific properties through co-assembly and self-sorting mechanisms, which enhance functionality and stability. However, controlling the structural and functional variability in dual-component systems, especially due to changes in molar ratios, poses significant challenges. Current limitations in designing these gels for functions highlight the need for extensive research into their assembly mechanisms and properties. Consequently, developing innovative design strategies for multicomponent systems is crucial for further technological progress and application diversification in this area.

In Chapter 2, we explored the interactions between the diastereoisomers (L,L)-2NapFF and (L,D)-2NapFF upon mixing and their packing mode at different concentrations and pH levels, employing multi-scale characterization across molecular, fibril, network, and material levels. We anticipate three potential outcomes: either a mutual disruption leading to weak or no gel formation, independent self-assembly into distinct nanostructures, or co-assembly into a more robust gel system.

Chapter 3 builds on this analysis by testing the applicability of the methods used in Chapter 2 to other systems. It involves multi-scale characterization to determine if changes in the molecular structure of 2NapFF-achieved through selective substitutions on the naphthalene ring-align with established design principles. This could provide new insights into controlling the properties of solutions and gels formed by LMWGs.

In Chapter 4, we use Mueller matrix polarization methods and Synchrotron radiation circular dichroism spectroscopic techniques to thoroughly analyze and compare the optical properties of homochiral and heterochiral dipeptide systems involved in Chapters 2 and 3. This study focuses on their molecular orientation and interactions, aiming to enhance our understanding of the role of chiral materials in materials science and supramolecular chemistry. The findings are intended to offer theoretical and practical insights that could influence the design and application of future materials.

## 1.6 References

- (1) Martín-Illana, A.; Notario-Pérez, F.; Cazorla-Luna, R.; Ruiz-Caro, R.; Bonferoni, M. C.; Tamayo, A.; Veiga, M. D. Bigels as drug delivery systems: From their components to their applications. *Drug Discovery Today* **2022**, *27* (4), 1008-1026.
- (2) Dey, K.; Roca, E.; Ramorino, G.; Sartore, L. Progress in the mechanical modulation of cell functions in tissue engineering. *Biomaterials Science* **2020**, *8* (24), 7033-7081.
- (3) Yu, G.; Yan, X.; Han, C.; Huang, F. Characterization of supramolecular gels. *Chemical Society Reviews* **2013**, *42* (16), 6697-6722.
- (4) Seiffert, S.; Sprakel, J. Physical chemistry of supramolecular polymer networks. *Chemical Society Reviews* **2012**, *41* (2), 909-930.
- (5) Du, X.; Zhou, J.; Shi, J.; Xu, B. Supramolecular hydrogelators and hydrogels: From soft matter to molecular biomaterials. *Chemical Reviews* **2015**, *115* (24), 13165-13307.
- (6) Draper, E. R.; Adams, D. J. Photoresponsive gelators. *Chemical Communications* **2016**, *52* (53), 8196-8206.
- (7) Chivers, P. R.; Smith, D. K. Shaping and structuring supramolecular gels. *Nature Reviews Materials* **2019**, *4* (7), 463-478.
- (8) Li, L.; Sun, R.; Zheng, R. Tunable morphology and functionality of multicomponent self-assembly: A review. *Materials & Design* **2021**, *197*, 109209.
- (9) Panja, S.; Adams, D. J. Stimuli responsive dynamic transformations in supramolecular gels. *Chemical Society Reviews* **2021**, *50* (8), 5165-5200.
- (10) Adams, D. J. Personal perspective on understanding low molecular weight gels. *Journal of the American Chemical Society* **2022**, *144* (25), 11047-11053.
- (11) Nele, V.; Wojciechowski, J. P.; Armstrong, J. P.; Stevens, M. M. Tailoring gelation mechanisms for advanced hydrogel applications. *Advanced Functional Materials* **2020**, *30* (42), 2002759.
- (12) Draper, E. R.; Adams, D. J. Low-molecular-weight gels: The state of the art. *Chem* **2017**, *3* (3), 390-410.
- (13) Escuder, B.; Miravet, J. F. *Functional molecular gels*; Royal Society of Chemistry, 2013.
- (14) Tangsombun, C.; Smith, D. K. Self-sorting in multicomponent supramolecular gels using different assembly triggers and calcium ion-induced diffusion patterning. *Chemistry of Materials* **2024**, *36* (10), 5050-5062.
- (15) Morris, K. L.; Chen, L.; Raeburn, J.; Sellick, O. R.; Cotanda, P.; Paul, A.; Griffiths, P. C.; King, S. M.; O'Reilly, R. K.; Serpell, L. C.; Adams, D. J. Chemically programmed self-sorting of gelator networks. *Nature Communications* **2013**, *4* (1), 1480.

- (16) Adams, D. J.; Butler, M. F.; Frith, W. J.; Kirkland, M.; Mullen, L.; Sanderson, P. A new method for maintaining homogeneity during liquid–hydrogel transitions using low molecular weight hydrogelators. *Soft Matter* **2009**, *5* (9), 1856-1862.
- (17) Panja, S.; Dietrich, B.; Smith, A. J.; Seddon, A.; Adams, D. J. Controlling self-sorting versus co-assembly in supramolecular gels. *ChemSystemsChem* **2022**, *4* (4), e202200008.
- (18) Draper, E. R.; Adams, D. J. Controlling the assembly and properties of low-molecular-weight hydrogelators. *Langmuir* **2019**, *35* (20), 6506-6521.
- (19) Wu, S.; Zhang, Q.; Deng, Y.; Li, X.; Luo, Z.; Zheng, B.; Dong, S. Assembly pattern of supramolecular hydrogel induced by lower critical solution temperature behavior of low-molecular-weight gelator. *Journal of the American Chemical Society* **2020**, *142* (1), 448-455.
- (20) Garcia, A. M.; Iglesias, D.; Parisi, E.; Styan, K. E.; Waddington, L. J.; Deganutti, C.; De Zorzi, R.; Grassi, M.; Melchionna, M.; Vargiu, A. V.; Marchesan, S. Chirality effects on peptide self-assembly unraveled from molecules to materials. *Chem* **2018**, *4* (8), 1862-1876.
- (21) Loos, J. N.; Boott, C. E.; Hayward, D. W.; Hum, G.; MacLachlan, M. J. Exploring the tunable optical and mechanical properties of multicomponent low-molecular-weight gelators. *Langmuir* **2021**, *37* (1), 105-114.
- (22) Edwards, W.; Smith, D. K. Enantioselective component selection in multicomponent supramolecular gels. *Journal of the American Chemical Society* **2014**, *136* (3), 1116-1124.
- (23) Basak, S.; Singh, I.; Ferranco, A.; Syed, J.; Kraatz, H.-B. On the role of chirality in guiding the self-assembly of peptides. *Angewandte Chemie International Edition* **2017**, *56* (43), 13288-13292.
- (24) Cardoso, A. Z.; Mears, L. L. E.; Cattoz, B. N.; Griffiths, P. C.; Schweins, R.; Adams, D. J. Linking micellar structures to hydrogelation for salt-triggered dipeptide gelators. *Soft Matter* **2016**, *12* (15), 3612-3621.
- (25) Jia, X.; Chen, J.; Xu, W.; Wang, Q.; Wei, X.; Ma, Y.; Chen, F.; Zhang, G. Molecular dynamics study of low molecular weight gel forming salt-triggered dipeptide. *Scientific Reports* **2023**, *13* (1), 6328.
- (26) Hill, M. J. S.; Fuentes-Caparrós, A. M.; Adams, D. J. Effect of imposing spatial constraints on low molecular weight gels. *Biomacromolecules* **2023**, *24* (9), 4253-4262.
- (27) Ravarino, P.; Panja, S.; Bianco, S.; Koev, T.; Wallace, M.; Adams, D. J. Controlled annealing in adaptive multicomponent gels. *Angewandte Chemie International Edition* **2023**, *62* (4), e202215813.
- (28) Skilling, K. J.; Citossi, F.; Bradshaw, T. D.; Ashford, M.; Kellam, B.; Marlow, M. Insights into low molecular mass organic gelators: a focus on drug delivery and tissue engineering applications. *Soft Matter* **2014**, *10* (2), 237-256.
- (29) Raeburn, J.; Zamith Cardoso, A.; Adams, D. J. The importance of the self-assembly process to control mechanical properties of low molecular weight hydrogels. *Chemical Society Reviews* **2013**, *42* (12), 5143-5156.
- (30) Tomasini, C.; Castellucci, N. Peptides and peptidomimetics that behave as low molecular weight gelators. *Chemical Society Reviews* **2013**, *42* (1), 156-172.
- (31) Smith, D. K. Lost in translation? Chirality effects in the self-assembly of nanostructured gel-phase materials. *Chemical Society Reviews* **2009**, *38* (3), 684-694.
- (32) Dasgupta, A.; Mondal, J. H.; Das, D. Peptide hydrogels. *RSC Advances* **2013**, *3* (24), 9117-9149.
- (33) Feng, Y.; Liu, Z.-X.; Chen, H.; Fan, Q.-H. Functional supramolecular gels based on poly(benzyl ether) dendrons and dendrimers. *Chemical Communications* **2022**, *58* (63), 8736-8753.

- (34) Du, J.; You, Y.; Reis, R. L.; Kundu, S. C.; Li, J. Manipulating supramolecular gels with surfactants: Interfacial and non-interfacial mechanisms. *Advances in Colloid and Interface Science* **2023**, *318*, 102950.
- (35) McAulay, K.; Dietrich, B.; Su, H.; Scott, M. T.; Rogers, S.; Al-Hilaly, Y. K.; Cui, H.; Serpell, L. C.; Seddon, A. M.; Draper, E. R.; Adams, D. J. Using chirality to influence supramolecular gelation. *Chemical Science* **2019**, *10* (33), 7801-7806.
- (36) Morris, J.; Bietsch, J.; Bashaw, K.; Wang, G. Recently Developed Carbohydrate Based Gelators and Their Applications. *Gels* **2021**, *7* (1), 24.
- (37) Fleming, S.; Ulijn, R. V. Design of nanostructures based on aromatic peptide amphiphiles. *Chemical Society Reviews* **2014**, *43* (23), 8150-8177.
- (38) Raeburn, J.; Adams, D. J. Multicomponent low molecular weight gelators. *Chemical Communications* **2015**, *51* (25), 5170-5180.
- (39) Estroff, L. A.; Hamilton, A. D. Water gelation by small organic molecules. *Chemical Reviews* **2004**, *104* (3), 1201-1218.
- (40) Dasgupta, A.; Das, D. Designer peptide amphiphiles: self-assembly to applications. *Langmuir* **2019**, *35* (33), 10704-10724.
- (41) Li, L.; Xie, L.; Zheng, R.; Sun, R. Self-assembly dipeptide hydrogel: The structures and properties. *Frontiers in Chemistry* **2021**, *9*, 739791.
- (42) Sheehan, F.; Sementa, D.; Jain, A.; Kumar, M.; Tayarani-Najjaran, M.; Kroiss, D.; Ulijn, R. V. Peptide-based supramolecular systems chemistry. *Chem Rev* **2021**, *121* (22), 13869-13914.
- (43) Fichman, G.; Gazit, E. Self-assembly of short peptides to form hydrogels: Design of building blocks, physical properties and technological applications. *Acta Biomaterialia* **2014**, *10* (4), 1671-1682.
- (44) Li, L.; Xie, L.; Zheng, R.; Sun, R. Self-assembly dipeptide hydrogel: The structures and properties. *Front Chem* **2021**, *9*, 739791.
- (45) Chen, L.; Revel, S.; Morris, K.; L, C. S.; Adams, D. J. Effect of molecular structure on the properties of naphthalene-dipeptide hydrogelators. *Langmuir* **2010**, *26* (16), 13466-13471.
- (46) Chen, L.; Revel, S.; Morris, K.; C. Serpell, L.; Adams, D. J. Effect of molecular structure on the properties of naphthalene-dipeptide hydrogelators. *Langmuir* **2010**, *26* (16), 13466-13471.
- (47) Colquhoun, C.; Draper, E. R.; Eden, E. G.; Cattoz, B. N.; Morris, K. L.; Chen, L.; McDonald, T. O.; Terry, A. E.; Griffiths, P. C.; Serpell, L. C.; Adams, D. J. The effect of self-sorting and co-assembly on the mechanical properties of low molecular weight hydrogels. *Nanoscale* **2014**, *6* (22), 13719-13725.
- (48) Schnitzer, T.; Preuss, M. D.; van Basten, J.; Schoenmakers, S. M. C.; Spiering, A. J. H.; Vantomme, G.; Meijer, E. W. How subtle changes can make a difference: Reproducibility in complex supramolecular systems. *Angewandte Chemie International Edition* **2022**, *61* (41), e202206738.
- (49) Thomson, L.; McDowall, D.; Marshall, L.; Marshall, O.; Ng, H.; Homer, W. J. A.; Ghosh, D.; Liu, W.; Squires, A. M.; Theodosiou, E.; et al. Transferring micellar changes to bulk properties via tunable self-assembly and hierarchical ordering. *ACS Nano* **2022**, *16* (12), 20497-20509.
- (50) Ghosh, D.; Coulter, S. M.; Laverty, G.; Holland, C.; Douth, J. J.; Vassalli, M.; Adams, D. J. Metal cross-linked supramolecular gel noodles: Structural insights and antibacterial assessment. *Biomacromolecules* **2024**, *25* (5), 3169-3177.
- (51) Colquhoun, C.; Draper, E. R.; Schweins, R.; Marcello, M.; Vadukul, D.; Serpell, L. C.; Adams, D. J. Controlling the network type in self-assembled dipeptide hydrogels. *Soft Matter* **2017**, *13* (9), 1914-1919.

- (52) Duti, I. J.; Florian, J. R.; Kittel, A. R.; Amelung, C. D.; Gray, V. P.; Lampe, K. J.; Letteri, R. A. Peptide stereocomplexation orchestrates supramolecular assembly of hydrogel biomaterials. *Journal of the American Chemical Society* **2023**, *145* (33), 18468-18476.
- (53) Fuentes-Caparros, A. M.; de Paula Gomez-Franco, F.; Dietrich, B.; Wilson, C.; Brasnett, C.; Seddon, A.; Adams, D. J. Annealing multicomponent supramolecular gels. *Nanoscale* **2019**, *11* (7), 3275-3280.
- (54) Mohammed, Z. H.; Hember, M. W. N.; Richardson, R. K.; Morris, E. R. Kinetic and equilibrium processes in the formation and melting of agarose gels. *Carbohydrate Polymers* **1998**, *36* (1), 15-26.
- (55) Wang, J.; Liu, K.; Xing, R.; Yan, X. Peptide self-assembly: thermodynamics and kinetics. *Chemical Society Reviews* **2016**, *45* (20), 5589-5604.
- (56) Tang, C.; Smith, A. M.; Collins, R. F.; Ulijn, R. V.; Saiani, A. Fmoc-diphenylalanine self-assembly mechanism induces apparent pKa shifts. *Langmuir* **2009**, *25* (16), 9447-9453.
- (57) Wallace, M.; Iggo, J. A.; Adams, D. J. Using solution state NMR spectroscopy to probe NMR invisible gelators. *Soft Matter* **2015**, *11* (39), 7739-7747.
- (58) Draper, E. R.; Su, H.; Brasnett, C.; Poole, R. J.; Rogers, S.; Cui, H.; Seddon, A.; Adams, D. J. Opening a can of worm (-like micelle)s: the effect of temperature of solutions of functionalized dipeptides. *Angewandte Chemie* **2017**, *129* (35), 10603-10606.
- (59) Chen, L.; Raeburn, J.; Sutton, S.; Spiller, D. G.; Williams, J.; Sharp, J. S.; Griffiths, P. C.; Heenan, R. K.; King, S. M.; Paul, A.; et al. Tuneable mechanical properties in low molecular weight gels. *Soft Matter* **2011**, *7* (20), 9721-9727.
- (60) Gao, J.; Tang, C.; Elsayy, M. A.; Smith, A. M.; Miller, A. F.; Saiani, A. Controlling self-assembling peptide hydrogel properties through network topology. *Biomacromolecules* **2017**, *18* (3), 826-834.
- (61) McAulay, K.; Ucha, P. A.; Wang, H.; Fuentes-Caparrós, A. M.; Thomson, L.; Maklad, O.; Khunti, N.; Cowieson, N.; Wallace, M.; Cui, H. Controlling the properties of the micellar and gel phase by varying the counterion in functionalised-dipeptide systems. *Chemical Communications* **2020**, *56* (29), 4094-4097.
- (62) Yang, X.; Lu, H.; Tao, Y.; Zhang, H.; Wang, H. Controlling supramolecular filament chirality of hydrogel by co-assembly of enantiomeric aromatic peptides. *Journal of Nanobiotechnology* **2022**, *20* (1), 77.
- (63) Ozbas, B.; Kretsinger, J.; Rajagopal, K.; Schneider, J. P.; Pochan, D. J. Salt-Triggered Peptide Folding and Consequent Self-Assembly into Hydrogels with Tunable Modulus. *Macromolecules* **2004**, *37*, 7331.
- (64) Wang, H.; Yang, Z.; Adams, D. J. Controlling peptidebased hydrogelation. *Materials Today* **2012**, *15* (11), 500-507.
- (65) Panja, S.; Dietrich, B.; Adams, D. J. Controlling syneresis of hydrogels using organic salts. *Angewandte Chemie* **2022**, *134* (4), e202115021.
- (66) Jain, A.; McPhee, S. A.; Wang, T.; Nair, M. N.; Kroiss, D.; Jia, T. Z.; Ulijn, R. V. Tractable molecular adaptation patterns in a designed complex peptide system. *Chem* **2022**, *8* (7), 1894-1905.
- (67) Nowak, B. P.; Schlichter, L.; Ravoo, B. J. Mediating oxidation of thioethers with iodine—a mild and versatile pathway to trigger the formation of peptide hydrogels. *Angewandte Chemie International Edition* **2022**, *61* (22), e202201791.
- (68) Smith, M. M.; Smith, D. K. Self-sorting multi-gelator gels—mixing and ageing effects in thermally addressable supramolecular soft nanomaterials. *Soft Matter* **2011**, *7* (10), 4856-4860.
- (69) Draper, E. R.; Adams, D. J. Controlling supramolecular gels. *Nature Materials* **2024**, *23* (1), 13-15.

- (70) Bera, S.; Xue, B.; Rehak, P.; Jacoby, G.; Ji, W.; Shimon, L. J. W.; Beck, R.; Král, P.; Cao, Y.; Gazit, E. Self-assembly of aromatic amino acid enantiomers into supramolecular materials of high rigidity. *ACS Nano* **2020**, *14* (2), 1694-1706.
- (71) Nagy, K. J.; Giano, M. C.; Jin, A.; Pochan, D. J.; Schneider, J. P. Enhanced mechanical rigidity of hydrogels formed from enantiomeric peptide assemblies. *Journal of the American Chemical Society* **2011**, *133* (38), 14975-14977.
- (72) Marchesan, S.; Easton, C. D.; Styan, K. E.; Waddington, L. J.; Kushkaki, F.; Goodall, L.; McLean, K. M.; Forsythe, J. S.; Hartley, P. G. Chirality effects at each amino acid position on tripeptide self-assembly into hydrogel biomaterials. *Nanoscale* **2014**, *6* (10), 5172-5180.
- (73) Marchesan, S.; Easton, C. D.; Kushkaki, F.; Waddington, L.; Hartley, P. G. Tripeptide self-assembled hydrogels: unexpected twists of chirality. *Chemical Communications* **2012**, *48* (16), 2195-2197.
- (74) Ajayaghosh, A.; Varghese, R.; George, S. J.; Vijayakumar, C. Transcription and amplification of molecular chirality to oppositely biased supramolecular  $\pi$  helices. *Angewandte Chemie International Edition* **2006**, *45* (7), 1141-1144.
- (75) Smith, D. K. Supramolecular gels – a panorama of low-molecular-weight gelators from ancient origins to next-generation technologies. *Soft Matter* **2024**, *20* (1), 10-70.
- (76) Liu, M.; Zhang, L.; Wang, T. Supramolecular chirality in self-assembled systems. *Chemical Reviews* **2015**, *115* (15), 7304-7397.
- (77) Patterson, A. K.; El-Qarra, L. H.; Smith, D. K. Chirality-directed hydrogel assembly and interactions with enantiomers of an active pharmaceutical ingredient. *Chemical Communications* **2022**, *58* (24), 3941-3944.
- (78) Nagy-Smith, K.; Beltramo, P. J.; Moore, E.; Tycko, R.; Furst, E. M.; Schneider, J. P. Molecular, local, and network-level basis for the enhanced stiffness of hydrogel networks formed from coassembled racemic peptides: predictions from pauling and corey. *ACS Central Science* **2017**, *3* (6), 586-597.
- (79) Ślęczkowski, M. L.; Mabesoone, M. F. J.; Ślęczkowski, P.; Palmans, A. R. A.; Meijer, E. W. Competition between chiral solvents and chiral monomers in the helical bias of supramolecular polymers. *Nature Chemistry* **2021**, *13* (2), 200-207.
- (80) Lv, K.; Qin, L.; Wang, X.; Zhang, L.; Liu, M. A chiroptical switch based on supramolecular chirality transfer through alkyl chain entanglement and dynamic covalent bonding. *Physical Chemistry Chemical Physics* **2013**, *15* (46), 20197-20202.
- (81) de Jong, J. J. D.; Tiemersma-Wegman, T. D.; van Esch, J. H.; Feringa, B. L. Dynamic chiral selection and amplification using photoresponsive organogelators. *Journal of the American Chemical Society* **2005**, *127* (40), 13804-13805.
- (82) Palmans, A. R. A.; Vekemans, J. A. J. M.; Havinga, E. E.; Meijer, E. W. Sergeants-and-soldiers principle in chiral columnar stacks of disc-shaped molecules with C<sub>3</sub> symmetry. *Angewandte Chemie International Edition* **1997**, *36* (23), 2648-2651.
- (83) van Gestel, J.; Palmans, A. R. A.; Titulaer, B.; Vekemans, J. A. J. M.; Meijer, E. W. “Majority-Rules” operative in chiral columnar stacks of C<sub>3</sub>-symmetrical molecules. *Journal of the American Chemical Society* **2005**, *127* (15), 5490-5494.
- (84) Raymond, D. M.; Nilsson, B. L. Multicomponent peptide assemblies. *Chemical Society Reviews* **2018**, *47* (10), 3659-3720.
- (85) Draper, E. R.; Adams, D. J. How should multicomponent supramolecular gels be characterised? *Chemical Society Reviews* **2018**, *47* (10), 3395-3405.
- (86) Buerkle, L. E.; Rowan, S. J. Supramolecular gels formed from multi-component low molecular weight species. *Chemical Society Reviews* **2012**, *41* (18), 6089-6102.
- (87) Draper, E. R.; Eden, E. G. B.; McDonald, T. O.; Adams, D. J. Spatially resolved multicomponent gels. *Nature Chemistry* **2015**, *7* (10), 848-852.

- (88) Marshall, L. J.; Wallace, M.; Mahmoudi, N.; Ciccone, G.; Wilson, C.; Vassalli, M.; Adams, D. J. Hierarchical composite self-sorted supramolecular gel noodles. *Advanced Materials* **2023**, *35* (17), 2211277.
- (89) Loos, J. N.; D'Acierno, F.; Vijay Mody, U.; MacLachlan, M. J. Manipulating the self-assembly of multicomponent low molecular weight gelators (LMWGs) through molecular design. *ChemPlusChem* **2022**, *87* (4), e202200026.
- (90) Panja, S.; Dietrich, B.; Shebanova, O.; Smith, A. J.; Adams, D. J. Programming gels over a wide pH range using multicomponent systems. *Angewandte Chemie International Edition* **2021**, *60* (18), 9973-9977.
- (91) Halperin-Sternfeld, M.; Ghosh, M.; Sevostianov, R.; Grigoriants, I.; Adler-Abramovich, L. Molecular co-assembly as a strategy for synergistic improvement of the mechanical properties of hydrogels. *Chemical Communications* **2017**, *53* (69), 9586-9589.
- (92) Randle, R. I.; Ginesi, R. E.; Matsarskaia, O.; Schweins, R.; Draper, E. R. Process dependent complexity in multicomponent gels. *Macromolecular Rapid Communications* **2023**, *44* (4), 2200709.
- (93) Wu, B.; Zhao, S.; Yang, X.; Zhou, L.; Ma, Y.; Zhang, H.; Li, W.; Wang, H. Biomimetic heterodimerization of tetrapeptides to generate liquid crystalline hydrogel in a two-component system. *ACS Nano* **2022**, *16* (3), 4126-4138.
- (94) Giuri, D.; Marshall, L. J.; Dietrich, B.; McDowall, D.; Thomson, L.; Newton, J. Y.; Wilson, C.; Schweins, R.; Adams, D. J. Exploiting and controlling gel-to-crystal transitions in multicomponent supramolecular gels. *Chemical Science* **2021**, *12* (28), 9720-9725.
- (95) Ji, W.; Xue, B.; Yin, Y.; Guerin, S.; Wang, Y.; Zhang, L.; Cheng, Y.; Shimon, L. J. W.; Chen, Y.; Thompson, D.; et al. Modulating the electromechanical response of bio-inspired amino acid-based architectures through supramolecular co-assembly. *Journal of the American Chemical Society* **2022**, *144* (40), 18375-18386.
- (96) Edwards, W.; Smith, D. K. Chiral assembly preferences and directing effects in supramolecular two-component organogels. *Gels* **2018**, *4* (2), 31.
- (97) Makam, P.; Gazit, E. Minimalistic peptide supramolecular co-assembly: expanding the conformational space for nanotechnology. *Chemical Society Reviews* **2018**, *47* (10), 3406-3420.
- (98) Shakeel, A.; Farooq, U.; Gabriele, D.; Marangoni, A. G.; Lupi, F. R. Bigels and multi-component organogels: An overview from rheological perspective. *Food Hydrocolloids* **2021**, *111*, 106190.
- (99) Sasselli, I. R.; Syrgiannis, Z. Small molecules organic co-assemblies as functional nanomaterials. *European Journal of Organic Chemistry* **2020**, *2020* (33), 5305-5318.
- (100) Fichman, G.; Guterman, T.; Adler-Abramovich, L.; Gazit, E. Synergetic functional properties of two-component single amino acid-based hydrogels. *CrystEngComm* **2015**, *17* (42), 8105-8112.
- (101) Ji, W.; Yuan, C.; Chakraborty, P.; Makam, P.; Bera, S.; Rencus-Lazar, S.; Li, J.; Yan, X.; Gazit, E. Coassembly-induced transformation of dipeptide amyloid-like structures into stimuli-responsive supramolecular materials. *ACS Nano* **2020**, *14* (6), 7181-7190.
- (102) Shigemitsu, H.; Fujisaku, T.; Tanaka, W.; Kubota, R.; Minami, S.; Urayama, K.; Hamachi, I. An adaptive supramolecular hydrogel comprising self-sorting double nanofibre networks. *Nature Nanotechnology* **2018**, *13* (2), 165-172.
- (103) Guan, Q.; McAulay, K.; Xu, T.; Rogers, S. E.; Edwards-Gayle, C.; Schweins, R.; Cui, H.; Seddon, A. M.; Adams, D. J. Self-sorting in diastereomeric mixtures of functionalized dipeptides. *Biomacromolecules* **2023**, *24* (6), 2847-2855.
- (104) Draper, E. R.; Wallace, M.; Schweins, R.; Poole, R. J.; Adams, D. J. Nonlinear effects in multicomponent supramolecular hydrogels. *Langmuir* **2017**, *33* (9), 2387-2395.

- (105) Cross, E. R.; Sproules, S.; Schweins, R.; Draper, E. R.; Adams, D. J. Controlled tuning of the properties in optoelectronic self-sorted gels. *Journal of the American Chemical Society* **2018**, *140* (28), 8667-8670.
- (106) Liu, G.; Zhou, C.; Teo, W. L.; Qian, C.; Zhao, Y. Self-sorting double-network hydrogels with tunable supramolecular handedness and mechanical properties. *Angewandte Chemie International Edition* **2019**, *58* (28), 9366-9372.
- (107) Liu, M.; Ouyang, G.; Niu, D.; Sang, Y. Supramolecular gelatons: towards the design of molecular gels. *Organic Chemistry Frontiers* **2018**, *5* (19), 2885-2900.
- (108) Duan, P.; Li, Y.; Jiang, J.; Wang, T.; Liu, M. Towards a universal organogelator: A general mixing approach to fabricate various organic compounds into organogels. *Science China Chemistry* **2011**, *54* (7), 1051-1063.
- (109) Fleming, S.; Debnath, S.; Frederix, P. W.; Hunt, N. T.; Ulijn, R. V. Insights into the coassembly of hydrogelators and surfactants based on aromatic peptide amphiphiles. *Biomacromolecules* **2014**, *15* (4), 1171-1184.
- (110) Marshall, L. J.; Bianco, S.; Ginesi, R. E.; Dutch, J.; Draper, E. R.; Adams, D. J. Investigating multigelator systems across multiple length scales. *Soft Matter* **2023**, *19* (26), 4972-4981.
- (111) Xing, P.; Chu, X.; Li, S.; Xin, F.; Ma, M.; Hao, A. Switchable and orthogonal self-assemblies of anisotropic fibers. *New Journal of Chemistry* **2013**, *37* (12), 3949-3955.
- (112) Ji, W.; Yuan, H.; Xue, B.; Guerin, S.; Li, H.; Zhang, L.; Liu, Y.; Shimon, L. J. W.; Si, M.; Cao, Y.; et al. Co-assembly induced solid-state stacking transformation in amino acid-based crystals with enhanced physical properties. *Angewandte Chemie International Edition* **2022**, *61* (17), e202201234.
- (113) Yang, X.; Lu, H.; Wu, B.; Wang, H. Triggered Self-Sorting of Peptides to Form Higher-Order Assemblies in a Living System. *ACS Nano* **2022**, *16* (11), 18244-18252.
- (114) Onogi, S.; Shigemitsu, H.; Yoshii, T.; Tanida, T.; Ikeda, M.; Kubota, R.; Hamachi, I. In situ real-time imaging of self-sorted supramolecular nanofibres. *Nature Chemistry* **2016**, *8* (8), 743-752.
- (115) Li, L.; Zheng, R.; Sun, R. Understanding multicomponent low molecular weight gels from gelators to networks. *Journal of Advanced Research* **2024**.
- (116) Li, Y.-X.; Xu, L.; Kang, S.-M.; Zhou, L.; Liu, N.; Wu, Z.-Q. Helicity- and molecular-weight-driven self-sorting and assembly of helical polymers towards two-dimensional smectic architectures and selectively adhesive gels. *Angewandte Chemie International Edition* **2021**, *60* (13), 7174-7179.
- (117) Liu, Q.; Jin, B.; Li, Q.; Yang, H.; Luo, Y.; Li, X. Self-sorting assembly of artificial building blocks. *Soft Matter* **2022**, *18* (13), 2484-2499.
- (118) Safont-Sempere, M. M.; Fernández, G.; Würthner, F. Self-sorting phenomena in complex supramolecular systems. *Chemical Reviews* **2011**, *111* (9), 5784-5814.
- (119) Sugiyasu, K.; Kawano, S.-i.; Fujita, N.; Shinkai, S. Self-sorting organogels with p– n heterojunction points. *Chemistry of Materials* **2008**, *20* (9), 2863-2865.
- (120) Wang, Y.; de Kruijff, R. M.; Lovrak, M.; Guo, X.; Eelkema, R.; van Esch, J. H. Access to metastable gel states using seeded self-assembly of low-molecular-weight gelators. *Angewandte Chemie International Edition* **2019**, *58* (12), 3800-3803.
- (121) Wang, Y.; Piskorz, T. K.; Lovrak, M.; Mendes, E.; Guo, X.; Eelkema, R.; van Esch, J. H. Transient supramolecular hydrogels formed by aging-induced seeded self-assembly of molecular hydrogelators. *Advanced Science* **2020**, *7* (7), 1902487.
- (122) Adhikari, B.; Nanda, J.; Banerjee, A. Multicomponent hydrogels from enantiomeric amino acid derivatives: helical nanofibers, handedness and self-sorting. *Soft Matter* **2011**, *7* (19), 8913-8922.

- (123) Das, A.; Ghosh, S. A generalized supramolecular strategy for self-sorted assembly between donor and acceptor gelators. *Chemical Communications* **2011**, 47 (31), 8922-8924.
- (124) Fuentes-Caparrós, A. M.; de Paula Gómez-Franco, F.; Dietrich, B.; Wilson, C.; Brasnett, C.; Seddon, A.; Adams, D. J. Annealing multicomponent supramolecular gels. *Nanoscale* **2019**, 11 (7), 3275-3280.
- (125) Wakabayashi, R.; Imatani, R.; Katsuya, M.; Higuchi, Y.; Noguchi, H.; Kamiya, N.; Goto, M. Hydrophobic immiscibility controls self-sorting or co-assembly of peptide amphiphiles. *Chemical Communications* **2022**, 58 (4), 585-588.
- (126) Genaev, A. M.; Shchegoleva, L. N.; Salnikov, G. E.; Shernyukov, A. V.; Shundrin, L. A.; Shundrina, I. K.; Zhu, Z.; Koltunov, K. Y. Acid-catalyzed versus thermally induced C1-C1' bond cleavage in 1,1'-Bi-2-naphthol: An experimental and theoretical study. *The Journal of Organic Chemistry* **2019**, 84 (11), 7238-7243.
- (127) Koehler, K. C.; Anseth, K. S.; Bowman, C. N. Diels-alder mediated controlled release from a poly(ethylene glycol) based hydrogel. *Biomacromolecules* **2013**, 14 (2), 538-547.
- (128) Raeburn, J.; Alston, B.; Kroeger, J.; McDonald, T. O.; Howse, J. R.; Cameron, P. J.; Adams, D. J. Electrochemically-triggered spatially and temporally resolved multi-component gels. *Materials Horizons* **2014**, 1 (2), 241-246.
- (129) Draper, E. R.; Lee, J. R.; Wallace, M.; Jäckel, F.; Cowan, A. J.; Adams, D. J. Self-sorted photoconductive xerogels. *Chemical Science* **2016**, 7 (10), 6499-6505.
- (130) Ardoni, H. A. M.; Draper, E. R.; Citossi, F.; Wallace, M.; Serpell, L. C.; Adams, D. J.; Tovar, J. D. Kinetically controlled coassembly of multichromophoric peptide hydrogelators and the impacts on energy transport. *Journal of the American Chemical Society* **2017**, 139 (25), 8685-8692.
- (131) Tang, C.; Ulijn, R. V.; Saiani, A. Self-assembly and gelation properties of glycine/leucine Fmoc-dipeptides. *The European Physical Journal E* **2013**, 36, 1-11.
- (132) Cornwell, D. J.; Smith, D. K. Expanding the scope of gels – combining polymers with low-molecular-weight gelators to yield modified self-assembling smart materials with high-tech applications. *Materials Horizons* **2015**, 2 (3), 279-293.
- (133) Fuhrhop, J. H.; Boettcher, C. Stereochemistry and curvature effects in supramolecular organization and separation processes of micellar N-alkylaldonamide mixtures. *Journal of the American Chemical Society* **1990**, 112 (5), 1768-1776.
- (134) Hirst, A. R.; Smith, D. K.; Feiters, M. C.; Geurts, H. P. Two-component dendritic gel: Effect of stereochemistry on the supramolecular chiral assembly. *Chemistry–A European Journal* **2004**, 10 (23), 5901-5910.
- (135) Das, R. K.; Kandaneli, R.; Linnanto, J.; Bose, K.; Maitra, U. Supramolecular chirality in organogels: A detailed spectroscopic, morphological, and rheological investigation of gels (and xerogels) derived from alkyl pyrenyl urethanes. *Langmuir* **2010**, 26 (20), 16141-16149.
- (136) Spector, M. S.; Selinger, J. V.; Singh, A.; Rodriguez, J. M.; Price, R. R.; Schnur, J. M. Controlling the morphology of chiral lipid tubules. *Langmuir* **1998**, 14 (13), 3493-3500.
- (137) Messmore, B. W.; Sunkerkar, P. A.; Stupp, S. I. Mirror image nanostructures. *Journal of the American Chemical Society* **2005**, 127 (22), 7992-7993.
- (138) Cicchi, S.; Ghini, G.; Lascialfari, L.; Brandi, A.; Betti, F.; Berti, D.; Baglioni, P.; Di Bari, L.; Pescitelli, G.; Mannini, M. Self-sorting chiral organogels from a long chain carbamate of 1-benzyl-pyrrolidine-3, 4-diol. *Soft Matter* **2010**, 6 (8), 1655-1661.
- (139) Safont-Sempere, M. M.; Osswald, P.; Stolte, M.; Grüne, M.; Renz, M.; Kaupp, M.; Radacki, K.; Braunschweig, H.; Würthner, F. Impact of molecular flexibility on binding strength and self-sorting of chiral  $\pi$ -surfaces. *Journal of the American Chemical Society* **2011**, 133 (24), 9580-9591.

- (140) Yang, D.; Han, J.; Sang, Y.; Zhao, T.; Liu, M.; Duan, P. Steering triplet–triplet annihilation upconversion through enantioselective self-assembly in a supramolecular gel. *Journal of the American Chemical Society* **2021**, *143* (33), 13259-13265.
- (141) Afrasiabi, R.; Kraatz, H. B. Small-peptide-based organogel kit: Towards the development of multicomponent self-sorting organogels. *Chemistry—A European Journal* **2013**, *19* (47), 15862-15871.
- (142) Sahoo, J. K.; VandenBerg, M. A.; Ruiz Bello, E. E.; Nazareth, C. D.; Webber, M. J. Electrostatic-driven self-sorting and nanostructure speciation in self-assembling tetrapeptides. *Nanoscale* **2019**, *11* (35), 16534-16543.
- (143) Okesola, B. O.; Wu, Y.; Derkus, B.; Gani, S.; Wu, D.; Knani, D.; Smith, D. K.; Adams, D. J.; Mata, A. Supramolecular self-assembly to control structural and biological properties of multicomponent hydrogels. *Chemistry of Materials* **2019**, *31* (19), 7883-7897.
- (144) Moffat, J. R.; Smith, D. K. Controlled self-sorting in the assembly of ‘multi-gelator’ gels. *Chemical Communications* **2009**, (3), 316-318.
- (145) Das, A.; Molla, M. R.; Ghosh, S. Comparative self-assembly studies and self-sorting of two structurally isomeric naphthalene-diimide (NDI)-gelators. *Journal of Chemical Sciences* **2011**, *123*, 963-973.
- (146) Madhu, C.; Roy, B.; Makam, P.; Govindaraju, T. Bicomponent  $\beta$ -sheet assembly of dipeptide fluorophores of opposite polarity and sensitive detection of nitro-explosives. *Chemical Communications* **2018**, *54* (18), 2280-2283.
- (147) Ardoña, H. A. M.; Kale, T. S.; Ertel, A.; Tovar, J. D. Nonresonant and local field effects in peptidic nanostructures bearing oligo (p-phenylenevinylene) units. *Langmuir* **2017**, *33* (30), 7435-7445.
- (148) Castilla, A. M.; Draper, E. R.; Nolan, M. C.; Brasnett, C.; Seddon, A.; Mears, L. L. E.; Cowieson, N.; Adams, D. J. Self-sorted oligophenylvinylene and perylene bisimide hydrogels. *Scientific Reports* **2017**, *7* (1), 8380.
- (149) Sugiyasu, K.; Kawano, S.-i.; Fujita, N.; Shinkai, S. Self-sorting organogels with p–n heterojunction points. *Chemistry of Materials* **2008**, *20* (9), 2863-2865.
- (150) Behanna, H. A.; Donners, J. J. J. M.; Gordon, A. C.; Stupp, S. I. Coassembly of amphiphiles with opposite peptide polarities into nanofibers. *Journal of the American Chemical Society* **2005**, *127* (4), 1193-1200.
- (151) Rao, K. V.; George, S. J. Supramolecular alternate co-assembly through a non-covalent amphiphilic design: conducting nanotubes with a mixed D–A structure. *Chemistry – A European Journal* **2012**, *18* (45), 14286-14291.
- (152) Chen, L.; Revel, S.; Morris, K.; Adams, D. J. Energy transfer in self-assembled dipeptide hydrogels. *Chemical Communications* **2010**, *46* (24), 4267-4269.
- (153) Felip-León, C.; Díaz-Oltra, S.; Galindo, F.; Miravet, J. F. Chameleonic, light harvesting photonic gels based on orthogonal molecular fibrillization. *Chemistry of Materials* **2016**, *28* (21), 7964-7972.
- (154) Miles, A. J.; Wallace, B. A. Circular dichroism spectroscopy of membrane proteins. *Chemical Society Reviews* **2016**, *45* (18), 4859-4872.
- (155) Hoffmann, S. V.; Fano, M.; van de Weert, M. Circular dichroism spectroscopy for structural characterization of proteins. *Analytical Techniques in the Pharmaceutical Sciences* **2016**, 223-251.
- (156) Suzuki, M.; Yumoto, M.; Shirai, H.; Hanabusa, K. Supramolecular gels formed by amphiphilic low-molecular-weight gelators of N $\alpha$ ,N $\epsilon$ -Diacyl-L-Lysine derivatives. *Chemistry – A European Journal* **2008**, *14* (7), 2133-2144.

- (157) Abul-Haija, Y. M.; Roy, S.; Frederix, P. W.; Javid, N.; Jayawarna, V.; Ulijn, R. V. Biocatalytically triggered co-assembly of two-component core/shell nanofibers. *Small* **2014**, *10* (5), 973-979.
- (158) Bhattacharya, S.; Srivastava, A.; Pal, A. Modulation of viscoelastic properties of physical gels by nanoparticle doping: Influence of the nanoparticle capping agent. *Angewandte Chemie International Edition* **2006**, *45* (18), 2934-2937.
- (159) Shen, J.-S.; Mao, G.-J.; Zhou, Y.-H.; Jiang, Y.-B.; Zhang, H.-W. A ligand-chirality controlled supramolecular hydrogel. *Dalton Transactions* **2010**, *39* (30), 7054-7058.
- (160) Yao, S.; Beginn, U.; Gress, T.; Lysetska, M.; Würthner, F. Supramolecular polymerization and gel formation of bis (merocyanine) dyes driven by dipolar aggregation. *Journal of the American Chemical Society* **2004**, *126* (26), 8336-8348.
- (161) Patil, S. P.; Jeong, H. S.; Kim, B. H. A low-molecular-weight supramolecular hydrogel of riboflavin bolaamphiphile for VEGF-siRNA delivery. *Chemical Communications* **2012**, *48* (71), 8901-8903.
- (162) Brizard, A.; Stuart, M.; van Bommel, K.; Friggeri, A.; de Jong, M.; van Esch, J. Preparation of nanostructures by orthogonal self-assembly of hydrogelators and surfactants. *Angewandte Chemie International Edition* **2008**, *47* (11), 2063.
- (163) Singh, N.; Zhang, K.; Angulo-Pachón, C. A.; Mendes, E.; van Esch, J. H.; Escuder, B. Tandem reactions in self-sorted catalytic molecular hydrogels. *Chemical Science* **2016**, *7* (8), 5568-5572.
- (164) Tómasson, D. A.; Ghosh, D.; Kržišnik, Z.; Fasolin, L. H.; Vicente, A. A.; Martin, A. D.; Thordarson, P.; Damodaran, K. K. Enhanced mechanical and thermal strength in mixed-enantiomers-based supramolecular gel. *Langmuir* **2018**, *34* (43), 12957-12967.
- (165) Foster, J. A.; Edkins, R. M.; Cameron, G. J.; Colgin, N.; Fucke, K.; Ridgeway, S.; Crawford, A. G.; Marder, T. B.; Beeby, A.; Cobb, S. L. Blending gelators to tune gel structure and probe anion - induced disassembly. *Chemistry – A European Journal* **2014**, *20* (1), 279-291.
- (166) Chen, G.; Li, J.; Song, M.; Wu, Z.; Zhang, W.; Wang, Z.; Gao, J.; Yang, Z.; Ou, C. A mixed component supramolecular hydrogel to improve mice cardiac function and alleviate ventricular remodeling after acute myocardial infarction. *Advanced Functional Materials* **2017**, *27* (34), 1701798.
- (167) Mears, L. L. E.; Draper, E. R.; Castilla, A. M.; Su, H.; Zhuola; Dietrich, B.; Nolan, M. C.; Smith, G. N.; Douth, J.; Rogers, S.; et al. Drying affects the fiber network in low molecular weight hydrogels. *Biomacromolecules* **2017**, *18* (11), 3531-3540.
- (168) Mahler, A.; Reches, M.; Rechter, M.; Cohen, S.; Gazit, E. Rigid, self-assembled hydrogel composed of a modified aromatic dipeptide. *Advanced Materials* **2006**, *18* (11), 1365-1370.
- (169) Lebel, O.; Perron, M.-È.; Maris, T.; Zalzal, S. F.; Nanci, A.; Wuest, J. D. A new class of selective low-molecular-weight gelators based on salts of diaminotriazinecarboxylic acids. *Chemistry of Materials* **2006**, *18* (16), 3616-3626.
- (170) Qi, Z.; Malo de Molina, P.; Jiang, W.; Wang, Q.; Nowosinski, K.; Schulz, A.; Gradzielski, M.; Schalley, C. A. Systems chemistry: logic gates based on the stimuli-responsive gel–sol transition of a crown ether-functionalized bis(urea) gelator. *Chemical Science* **2012**, *3* (6), 2073-2082.
- (171) Sangji, M. H.; Lee, S. R.; Sai, H.; Weigand, S.; Palmer, L. C.; Stupp, S. I. Self-sorting vs coassembly in peptide amphiphile supramolecular nanostructures. *ACS Nano* **2024**, *18* (24), 15878-15887.
- (172) Wang, Y.; Lovrak, M.; Liu, Q.; Maity, C.; le Sage, V. A.; Guo, X.; Eelkema, R.; van Esch, J. H. Hierarchically compartmentalized supramolecular gels through multilevel self-sorting. *Journal of the American Chemical Society* **2018**, *141* (7), 2847-2851.

- (173) Mears, L. L.; Draper, E. R.; Castilla, A. M.; Su, H.; Zhuola; Dietrich, B.; Nolan, M. C.; Smith, G. N.; Douth, J.; Rogers, S. Drying affects the fiber network in low molecular weight hydrogels. *Biomacromolecules* **2017**, *18* (11), 3531-3540.
- (174) Boekhoven, J.; Brizard, A.; Stuart, M.; Florusse, L.; Raffy, G.; Del Guerzo, A.; Van Esch, J. Bio-inspired supramolecular materials by orthogonal self-assembly of hydrogelators and phospholipids. *Chemical science* **2016**, *7* (9), 6021-6031.
- (175) Yang, Z.; Gu, H.; Du, J.; Gao, J.; Zhang, B.; Zhang, X.; Xu, B. Self-assembled hybrid nanofibers confer a magnetorheological supramolecular hydrogel. *Tetrahedron* **2007**, *63* (31), 7349-7357.
- (176) McAulay, K.; Dietrich, B.; Su, H.; Scott, M. T.; Rogers, S.; Al-Hilaly, Y. K.; Cui, H.; Serpell, L. C.; Seddon, A. M.; Draper, E. R. Using chirality to influence supramolecular gelation. *Chemical Science* **2019**, *10* (33), 7801-7806.
- (177) Kubota, R.; Tanaka, W.; Hamachi, I. Microscopic imaging techniques for molecular assemblies: electron, atomic force, and confocal microscopies *Chemical Reviews* **2021**, *121* (22), 14281-14347.
- (178) McDowall, D.; Adams, D. J.; Seddon, A. M. Using small angle scattering to understand low molecular weight gels. *Soft Matter* **2022**, *18* (8), 1577-1590.
- (179) Hirst, A. R.; Coates, I. A.; Boucheteau, T. R.; Miravet, J. F.; Escuder, B.; Castelletto, V.; Hamley, I. W.; Smith, D. K. Low-molecular-weight gelators: elucidating the principles of gelation based on gelator solubility and a cooperative self-assembly model. *Journal of the American Chemical Society* **2008**, *130* (28), 9113-9121.
- (180) Banerjee, S.; Das, R. K.; Terech, P.; de Geyer, A.; Aymonier, C.; Loppinet-Serani, A.; Raffy, G.; Maitra, U.; Del Guerzo, A.; Desvergne, J.-P. Hybrid organogels and aerogels from co-assembly of structurally different low molecular weight gelators. *Journal of Materials Chemistry C* **2013**, *1* (20), 3305-3316.
- (181) Guilbaud, J.-B.; Saiani, A. Using small angle scattering (SAS) to structurally characterise peptide and protein self-assembled materials. *Chemical Society Reviews* **2011**, *40* (3), 1200-1210.
- (182) Jeffries, C. M.; Ilavsky, J.; Martel, A.; Hinrichs, S.; Meyer, A.; Pedersen, J. S.; Sokolova, A. V.; Svergun, D. I. Small-angle X-ray and neutron scattering. *Nature Reviews Methods Primers* **2021**, *1* (1), 70.
- (183) Hollamby, M. J. Practical applications of small-angle neutron scattering. *Physical chemistry chemical physics* **2013**, *15* (26), 10566-10579.
- (184) Doniach, S. Changes in biomolecular conformation seen by small angle X-ray scattering. *Chemical Reviews* **2001**, *101* (6), 1763-1778.
- (185) Ghosh, D.; Farahani, A. D.; Martin, A. D.; Thordarson, P.; Damodaran, K. K. Unraveling the self-assembly modes in multicomponent supramolecular gels using single-crystal X-ray diffraction. *Chemistry of materials* **2020**, *32* (8), 3517-3527.
- (186) Loos, J. N.; D'Acerno, F.; Vijay Mody, U.; MacLachlan, M. J. Manipulating the self-assembly of multicomponent low molecular weight gelators (LMWGs) through molecular design *ChemPlusChem* **2022**, *87* (4), e202200026.
- (187) Cornwell, D. J.; Smith, D. K. Expanding the scope of gels—combining polymers with low-molecular-weight gelators to yield modified self-assembling smart materials with high-tech applications. *Materials Horizons* **2015**, *2* (3), 279-293.
- (188) Terech, P.; Weiss, R. G. Low molecular mass gelators of organic liquids and the properties of their gels. *Chemical reviews* **1997**, *97* (8), 3133-3160.
- (189) Wang, G.; Cheuk, S.; Yang, H.; Goyal, N.; Reddy, P. V. N.; Hopkinson, B. Synthesis and Characterization of Monosaccharide-Derived Carbamates as Low-Molecular-Weight Gelators. *Langmuir* **2009**, *25* (15), 8696-8705.

- (190) Hirst, A. R.; Smith, D. K. Two-component gel-phase materials-highly tunable self-assembling systems. *Chemistry–A European Journal* **2005**, *11* (19), 5496-5508.
- (191) Weng, W.; Li, Z.; Jamieson, A. M.; Rowan, S. J. Control of gel morphology and properties of a class of metallo-supramolecular polymers by good/poor solvent environments. *Macromolecules* **2009**, *42* (1), 236-246.
- (192) Mallia, V. A.; Terech, P.; Weiss, R. G. Correlations of properties and structures at different length scales of hydro-and organo-gels based on N-alkyl-(R)-12-hydroxyoctadecylammonium chlorides. *The Journal of Physical Chemistry B* **2011**, *115* (43), 12401-12414.
- (193) Kubota, R.; Nakamura, K.; Torigoe, S.; Hamachi, I. The power of confocal laser scanning microscopy in supramolecular chemistry: In situ real-time imaging of stimuli-responsive multicomponent supramolecular hydrogels. *ChemistryOpen* **2020**, *9* (1), 67-79.
- (194) Dhiman, S.; Andrian, T.; Gonzalez, B. S.; Tholen, M. M.; Wang, Y.; Albertazzi, L. Can super-resolution microscopy become a standard characterization technique for materials chemistry? *Chemical Science* **2022**, *13* (8), 2152-2166.
- (195) Kubota, R.; Nagao, K.; Tanaka, W.; Matsumura, R.; Aoyama, T.; Urayama, K.; Hamachi, I. Control of seed formation allows two distinct self-sorting patterns of supramolecular nanofibers. *Nature Communications* **2020**, *11* (1), 4100.
- (196) Yan, C.; Pochan, D. J. Rheological properties of peptide-based hydrogels for biomedical and other applications. *Chemical Society Reviews* **2010**, *39* (9), 3528-3540.
- (197) Stojkov, G.; Niyazov, Z.; Picchioni, F.; Bose, R. K. Relationship between structure and rheology of hydrogels for various applications. *Gels* **2021**, *7* (4), 255.
- (198) Bianco, S.; Panja, S.; Adams, D. J. Using rheology to understand transient and dynamic gels. *Gels* **2022**, *8* (2), 132.
- (199) Zhang, M.; Xu, D.; Yan, X.; Chen, J.; Dong, S.; Zheng, B.; Huang, F. Self-healing supramolecular gels formed by crown ether based host-guest interactions. *Angewandte Chemie International Edition* **2012**, *51* (28), 7011-7015.
- (200) Angelerou, M. G. F.; Sabri, A.; Creasey, R.; Angelerou, P.; Marlow, M.; Zelzer, M. Surface-directed modulation of supramolecular gel properties. *Chemical Communications* **2016**, *52* (23), 4298-4300.
- (201) Kakehashi, R.; Tokai, N.; Nakagawa, M.; Kawasaki, K.; Horiuchi, S.; Yamamoto, A. Amidoamine oxide surfactants as low-molecular-weight hydrogelators: Effect of methylene chain length on aggregate structure and rheological behavior. *Gels* **2023**, *9* (3), 261.
- (202) Boothroyd, S.; Saiani, A.; Miller, A. F. Controlling network topology and mechanical properties of co-assembling peptide hydrogels. *Biopolymers* **2014**, *101* (6), 669-680.
- (203) Basit, H.; Pal, A.; Sen, S.; Bhattacharya, S. Two-component hydrogels comprising fatty acids and amines: structure, properties, and application as a template for the synthesis of metal nanoparticles. *Chemistry–A European Journal* **2008**, *14* (21), 6534-6545.
- (204) Dahan, E.; Sundararajan, P. R. Thermo-reversible gelation of rod-coil and coil-rod-coil molecules based on poly (dimethyl siloxane) and perylene imides and self-sorting of the homologous pair. *Soft Matter* **2014**, *10* (29), 5337-5349.

## **Chapter 2: Self-Sorting in Diastereomeric Mixtures of Functionalized Dipeptides**

---

This chapter is derived from the article titled "Self-sorting in Diastereomeric Mixtures of Functionalized Dipeptides" authored by Guan, Q.; McAulay, K.; Xu, T.; Rogers, S. E.; Edwards-Gayle, C.; Schweins, R.; Cui, H. G.; Seddon, A. M.; Adams, D. J., published in *Biomacromolecules* 2023, 24 (6), 2847-2855.

Guan, Q. conducted the synthesis and characterization (rheological experiments, microscopy, spectroscopy, and circular dichroism) of the gelators under examination. McAulay, K. and Seddon, A. M. assisted in collecting and processing SAXS and SANS data, while Xu, T. and Cui, H. gathered and processed Cryo-TEM images.

## 2.1 Introduction

Gels can be formed by the self-assembly of small molecules into fibers that entangle to give a network.<sup>1-3</sup> In most cases, such gels are formed from a single species. However, interesting and useful materials can be prepared from multicomponent systems. When two molecules that can self-assemble alone are mixed to form a gel, multiple possibilities are available.<sup>4,5</sup> Assuming a gel is still formed, first, the two molecules may mix in the self-assembled structures in either a specific or a random manner. Second, the two molecules may prefer to assemble independently, giving a self-sorted system (Figure 2-1). These possibilities refer to the primary self-assembled structures, with significant added complexity arising from how these structures can go on to further interact.<sup>6</sup>

Each of these systems has a potential use. For example, co-assembled systems can be used for cell work, whereby one component provides the matrix and the second component provides specific sites for cell adhesion or interaction.<sup>7,8</sup> Self-sorted systems have been used to form optoelectronic systems<sup>9-11</sup> and for advanced systems that can change properties on demand.<sup>12</sup> Self-sorting can even be triggered to occur within cells.<sup>13</sup>

A key issue is the design of such systems.<sup>4,5</sup> Limited methods exist that are known to drive a system towards a certain type of assembly. Specific mixing can be driven by mixing electron-rich and electron-poor gelators.<sup>14</sup> Aside from this, there are examples where different types of systems are formed, but little in the way of design rules.

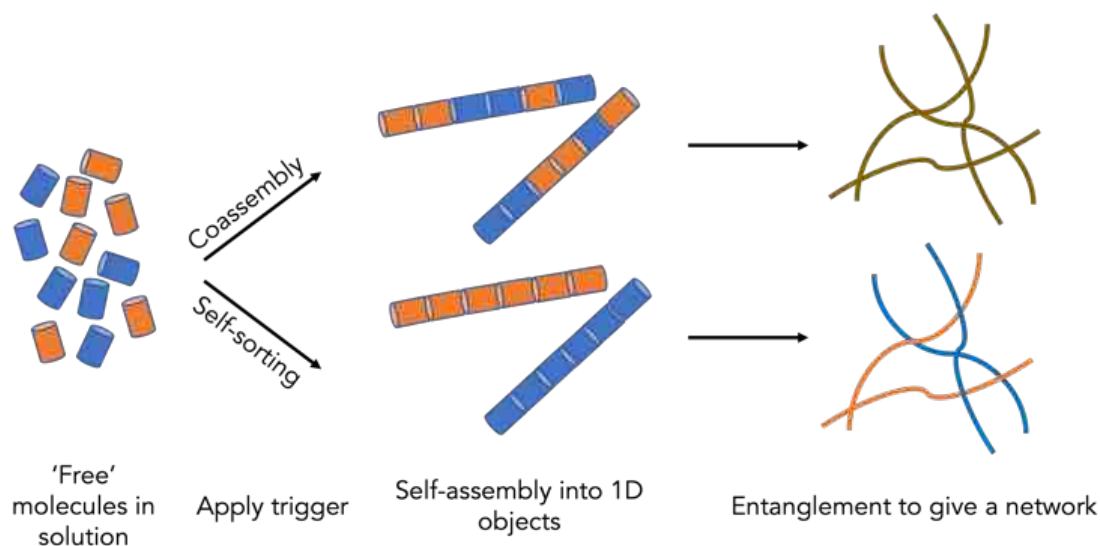


**Figure 2-1.** Cartoon showing how two gelators (shown as orange and blue) when mixed can form self-assembled fibers that (top) co-assemble and (bottom) self-sort.

For self-sorted systems, many cases rely on the gelators having sufficiently different molecular structures,<sup>15</sup> with the aim that structural mismatch favors this assembly. An important point is that most examples report a single set of conditions, which does not show that the design elements work across different concentrations and ratios. Further, the proof of what has been formed relies on spectroscopy at low concentrations or microscopy, which can only provide a small snapshot of the structures formed. Some examples exist where gelators of different chirality exist. Here, again, there are limited design rules with some mixtures giving more robust gels than using a gelator of a single chirality,<sup>16</sup> whilst other examples form mixtures where the different enantiomers or diastereomers disrupt the gelation.<sup>17</sup> There are examples where co-assembly or self-sorting can be controlled by chirality.<sup>18</sup>

One method we have used to form self-sorted hydrogels relies on controlling the kinetics of self-assembly. Mixing two gelators with different apparent  $pK_a$  values for their terminal carboxylic acids combined with a slow decrease in pH is an effective method of forming self-sorted systems.<sup>19</sup> There is however further complexity; at the initial high pH in water, micellar structures are formed, and we have found that in some cases there is evidence of mixing in the micellar phases leading to some mixing in the gel state as the pH is decreased.<sup>20</sup>

Here, we describe the systems prepared from two dipeptide-based gelators that differ only by the chirality of one of the amino acids. We provide firm evidence for self-sorting in the micellar and the gel phase using small-angle scattering and cryo-TEM, showing that complete self-sorting occurs across a range of relative concentrations.

## 2.2 Results and Discussion

### 2.2.1 Self-Sorting in Pre-Gel Solutions at High pH

2NapFF is a robust gelator, forming micellar structures at high pH and gels at low pH.<sup>21-23</sup> Where both phenylalanines are the *L*-enantiomer ((*L,L*)-2NapFF; Figure 2-2a), the small angle neutron scattering (SANS) data show that at high pH nanotubes are formed with a core radius of 1.7 nm and a wall thickness of 1.9 nm.<sup>21</sup> This is corroborated by cryo-TEM.<sup>21</sup> Gels are formed when the pH is decreased, where the core of the nanotubes collapse and lateral aggregation of the resulting cylindrical structures occurs.<sup>22</sup> We have also shown that the (*L,D*)-2NapFF diastereomer (Figure 2-2b) self-assembles into large, thin-walled rigid nanotubes at high pH with a core radius of 13.4 nm and a wall thickness of 1.4 nm as shown by SANS and again

corroborated by cryo-TEM.<sup>21</sup> When the pH is decreased, gels form where these structures persist. Considering the very different structures present in the single component systems at both high and low pH, we hypothesized that mixing (L,L)-2NapFF and (L,D)-2NapFF might result in self-sorted systems based on the morphology of self-assembled structure despite the similarity in molecular structure.

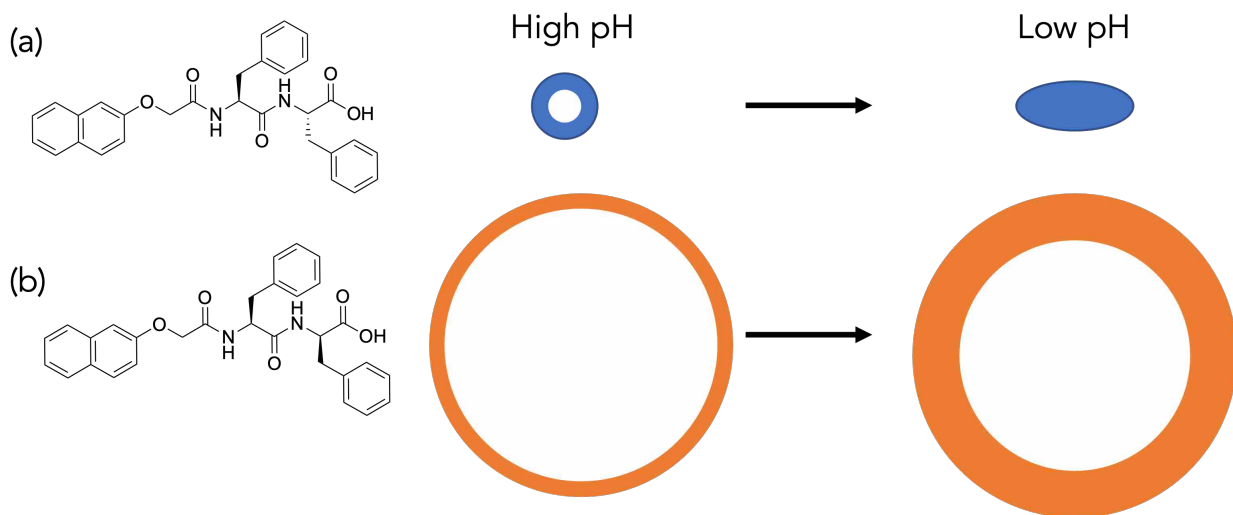


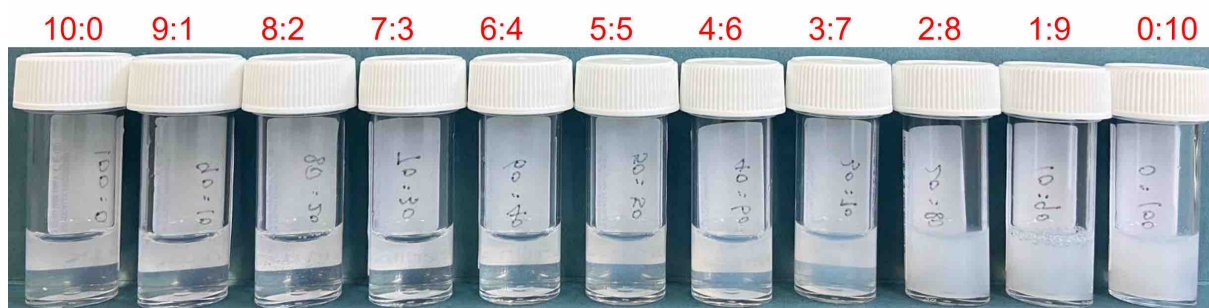
**Figure 2-2.** Chemical structures of (a) (L,L)-2NapFF and (b) (L,D)-2NapFF with to-scale cartoon of cross-sectional view of the nanotubes formed by each and the transition in structure on gelation. In the micellar state, (L,L)-2NapFF forms nanotubes with a core radius of 1.7 nm and a wall thickness of 1.9 nm; (L,D)-2NapFF forms nanotubes with a core radius of 13.4 nm and a wall thickness of 1.4 nm. On gelation, for (L,L)-2NapFF, the core collapses and lateral aggregation occurs leading to the apparent formation of elliptical cylinders, whereas for (L,D)-2NapFF large nanotubes persist as the pH decreases.

### 2.2.1.1 Microscopy, Rheology, and Spectroscopy

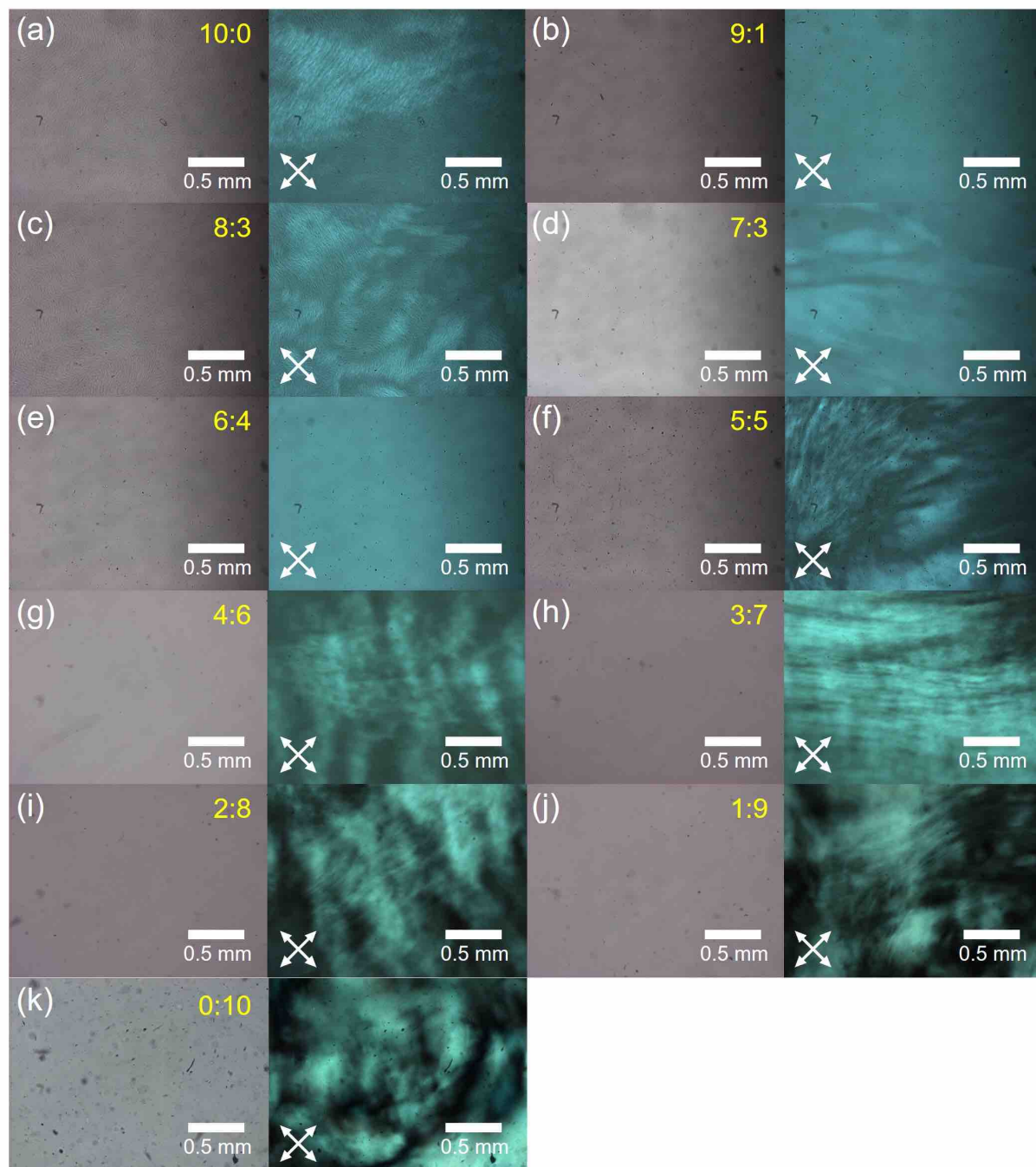
(L,L)-2NapFF and (L,D)-2NapFF were prepared as described previously.<sup>21</sup> Solutions of each were prepared at a concentration of 10 mg/mL and a pH of 10.5. At this concentration, both (L,L)-2NapFF and (L,D)-2NapFF form liquid crystal phases as shown by polarized microscopy, with (L,D)-2NapFF forming a more turbid solution by eye (Figure 2-3). The solutions of (L,L)-2NapFF and (L,D)-2NapFF at high pH were mixed to give solutions at several different ratios with a constant overall concentration of 2NapFF of 10 mg/mL. Visually, the turbidity decreased as the composition of the (L,L)-2NapFF increased.

Polarized light microscopy images (Figure 2-4) showed significant birefringence for ratios of (L,L)-2NapFF:(L,D)-2NapFF of 5:5 to 0:10. Birefringent domains are also observed in solutions for the other ratios excluded 9:1 and 6:4. The viscosity varied across the series, with the mixture at 6:4 (L,L)-2NapFF:(L,D)-2NapFF being the most viscous (Figure 2-5). The turbidity of the samples increased as the amount of (L,D)-2NapFF in the mixtures was increased (Figure 2-6).

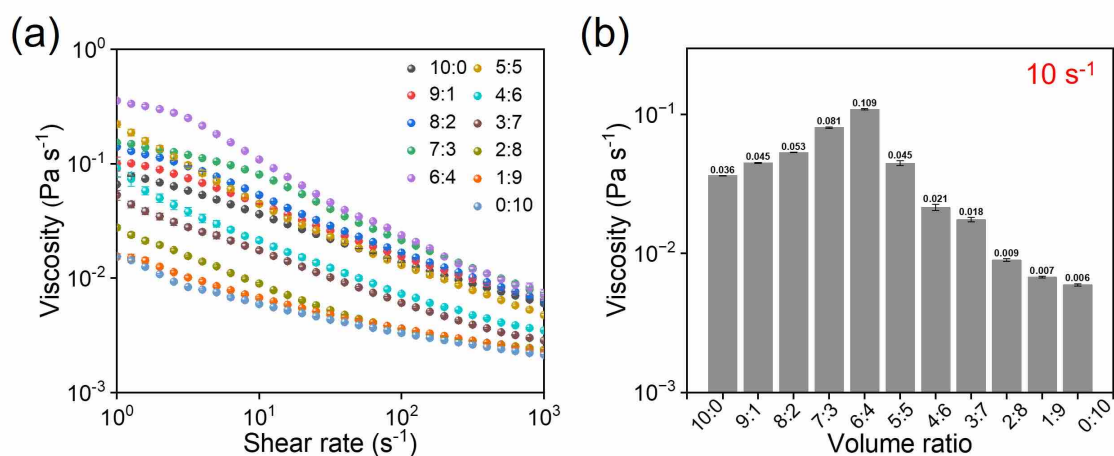
The effect of the heat-cool cycle on the viscosity of the pre-gelled solution was examined. The shear viscosity of the systems under investigation could be significantly modified by this simple treatment, especially for those rich in (L,D)-2NapFF components, where the viscosity at  $10 \text{ s}^{-1}$  increased by at least two times when compared with the original sample (refer to Figure 2-5 and Figure A2-19). This considerably extends the spectrum of sample properties. Hence, we stress the crucial need for precise control over the experimental temperature.



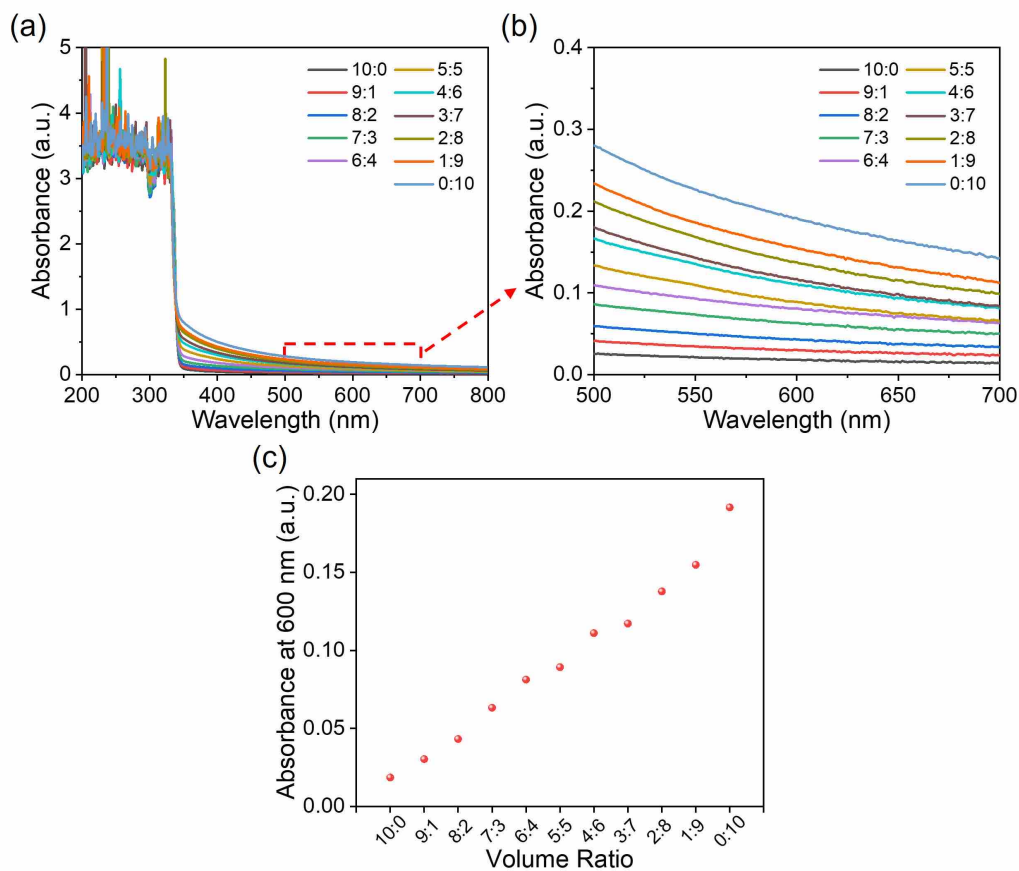
**Figure 2-3.** (a) Photographs of solutions of (L,L)-2NapFF and (L,D)-2NapFF at different ratios of an overall concentration at 10 mg/mL.



**Figure 2-4.** Normal-light and cross-polarized optical microscopy images ( $5\times$ magnification) of binary system solutions with various volume ratios of 10 mg/mL (L,L)-2NapFF:(L,D)-2NapFF stock solutions. Scale bars represent 500  $\mu\text{m}$  and the white crosses represent the polarizer directions.



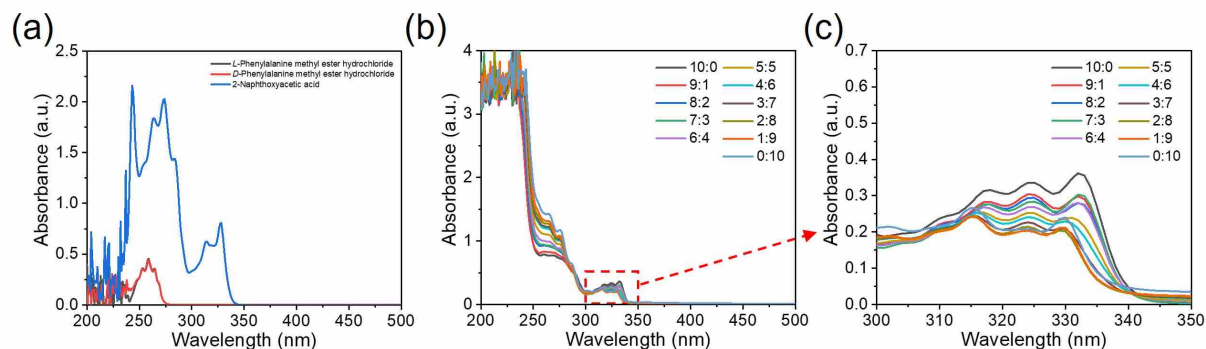
**Figure 2-5.** (a) The viscosity of binary system solutions with various volume ratios of 10 mg/mL (L,L)-2NapFF:(L,D)-2NapFF stock solutions. (b) Plot shows the viscosity data at a shear rate of 10 s<sup>-1</sup> against volume ratio.



**Figure 2-6.** (a) UV-Vis absorption spectra of solutions containing 10 mg/mL of (L,L)- and (L,D)-2NapFF at ratios ranging from 10:0 to 0:10 measured using a 2 mm path length quartz cuvette at 25 °C. (b) Spectra depicted the enlarged regions of the graph (a) at a wavelength range of 500-700 nm. (c) Change in turbidity over composition at 600 nm for binary solutions. The absorbance values above 3 should be disregarded, as they represent noise caused by low

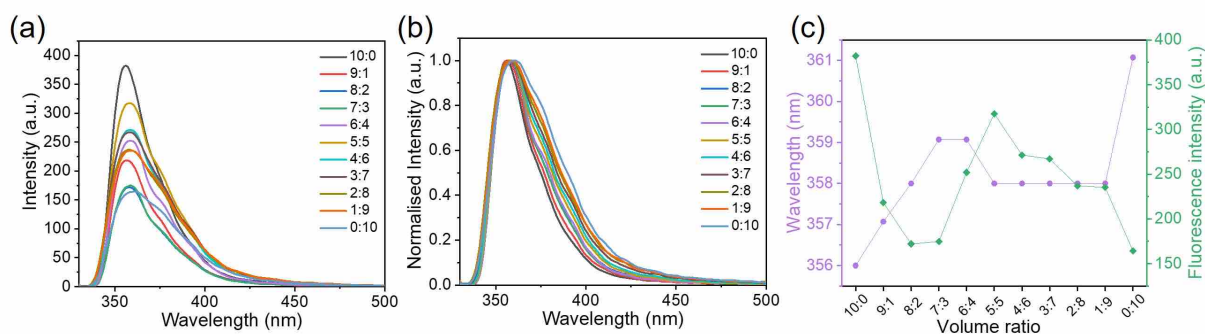
transmittance detected at high absorbance levels, rather than meaningful data.

UV-Vis absorption and fluorescence spectroscopic techniques were employed to gather insights into molecular-level interactions within the solution phase. To elucidate the specific roles of naphthalene and phenylalanine in the absorption spectrum of micellar solutions, we collected absorption data from compounds containing either of these chromophores. The observed noise between 200 and approximately 235 nm arose from DMSO absorbance. Naphthalene solution exhibits a maximum absorption peak at approximately 243 nm, a quadruple absorption peak at 250-300 nm, and multiple absorption peak at 300-350 nm. Phenylalanine demonstrates absorption peak within the 240-275 nm range (Figure 2-7a). In contrast, the multiple peaks that emerged within the 300-350 nm range in the 2NapFF binary system were tentatively attributed to the molecular packing of the naphthalene ring, which was preliminarily deduced from self-assembled aggregates (Figure 2-7b and c). As the volume fraction gradually rises, the absorption impact of (L,L)-2NapFF diminishes gradually, leading to a blue shift in the absorption spectrum. Concurrently, the influence of the second component becomes increasingly dominant, indicating a potential self-sorting assembly pattern of the two gelators within the solution phase. Besides, the absorption peak intensity here first decreased and then increased with increasing volume ratio, presumably due to the weak  $\pi$ - $\pi$  stacking between naphthalene and benzene rings.<sup>24</sup>



**Figure 2-7.** (a) UV-Vis spectroscopy of *L*-phenylalanine methyl ester hydrochloride, *D*-phenylalanine methyl ester hydrochloride, and 2-naphthoxyacetic acid with DMSO as solvent at concentrations of 0.1 g/mL, 0.1 g/mL, and 0.01 g/mL, respectively. (b) UV-Vis absorption spectra of solutions containing 10 mg/mL of (L,L)- and (L,D)-2NapFF at ratios ranging from 10:0 to 0:10 recorded with a 0.01 mm path length quartz demountable cuvette at 25 °C. (c) Spectra depicted the enlarged regions of the graph (b) at wavelengths of 300-350 nm. The absorbance values above 3 should be disregarded, as they represent noise caused by low transmittance detected at high absorbance levels, rather than meaningful data.

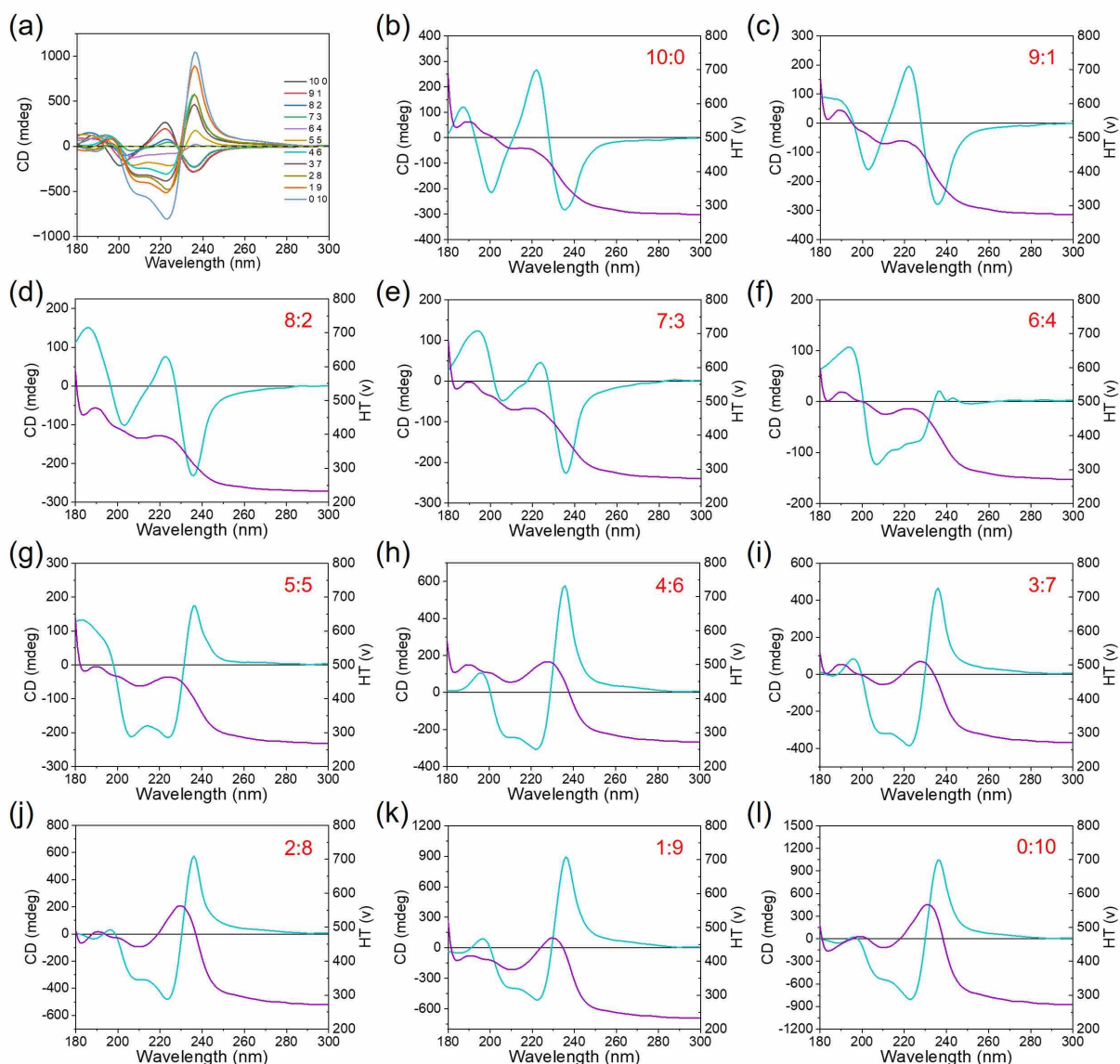
The observed intermolecular excimer emission  $\lambda_{em} = 355$  nm across all samples is attributed to the  $\pi$ - $\pi$  interactions of the naphthyl chromophores in the bicomponent assembly state (Figure 2-8a).<sup>25</sup> In Figure 2-8b, the normalized fluorescence spectra were plotted versus different ratios. The results confirmed that as the proportion of (L,L)-2NapFF component decreased, there was a slight redshift in the emission maximum from  $\lambda_{em} = 356$  nm to 361 nm. The plot of emission wavelength versus volume fraction illustrated a gradual increase in emission with wavelength, peaking at a 6:4 ratio before stabilizing at 358 nm within the range of 5:5 to 1:9 (Figure 2-8c). This suggests that alterations in the amount of a specific component can influence the stacking arrangement of naphthalene rings within supramolecular self-assembled structures in the liquid phase. Additionally, it is noteworthy that (L,D)-2NapFF exhibits the lowest emission intensity compared to other systems (Figure 2-8c).



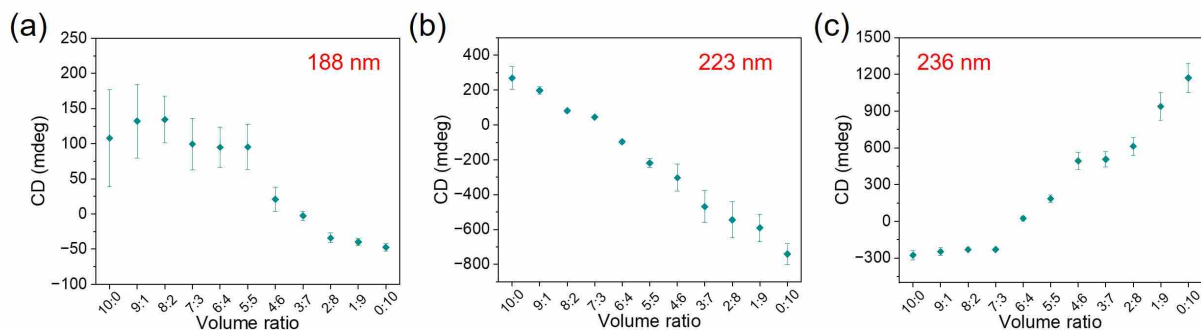
**Figure 2-8.** (a) Fluorescence emission spectrum, (b) normalized spectrum of solutions containing 10 mg/mL of (L,L)- and (L,D)-2NapFF at ratios ranging from 10:0 to 0:10. (c) Plots illustrating the evolution of wavelength and fluorescence intensity relative to the ratios of the peak at 356 nm.

### 2.2.1.2 Circular Dichroism

Circular dichroism (CD) spectra for solutions of (L,L)-2NapFF and (L,D)-2NapFF showed different signals. The CD spectra of (L,D)-2NapFF were much weaker than the (L,L)-2NapFF. In the mixtures, the CD signals became less intense as the ratio of (L,D)-2NapFF increased (Figures 2-9, 2-10 and Tables A2-1, A2-2, A2-3). In all cases, the spectra primarily featured the phenylalanine and naphthalene rings, showing signals between 200 and 230 nm with a maximum at 223 nm, and wavelengths ranging from 240 to 290 nm.<sup>26, 27</sup> The signal intensity at 223 nm declined almost linearly with the increasing addition of (L,D)-2NapFF (Figure 2-10b). More information on the CD will be discussed in Chapter 4.



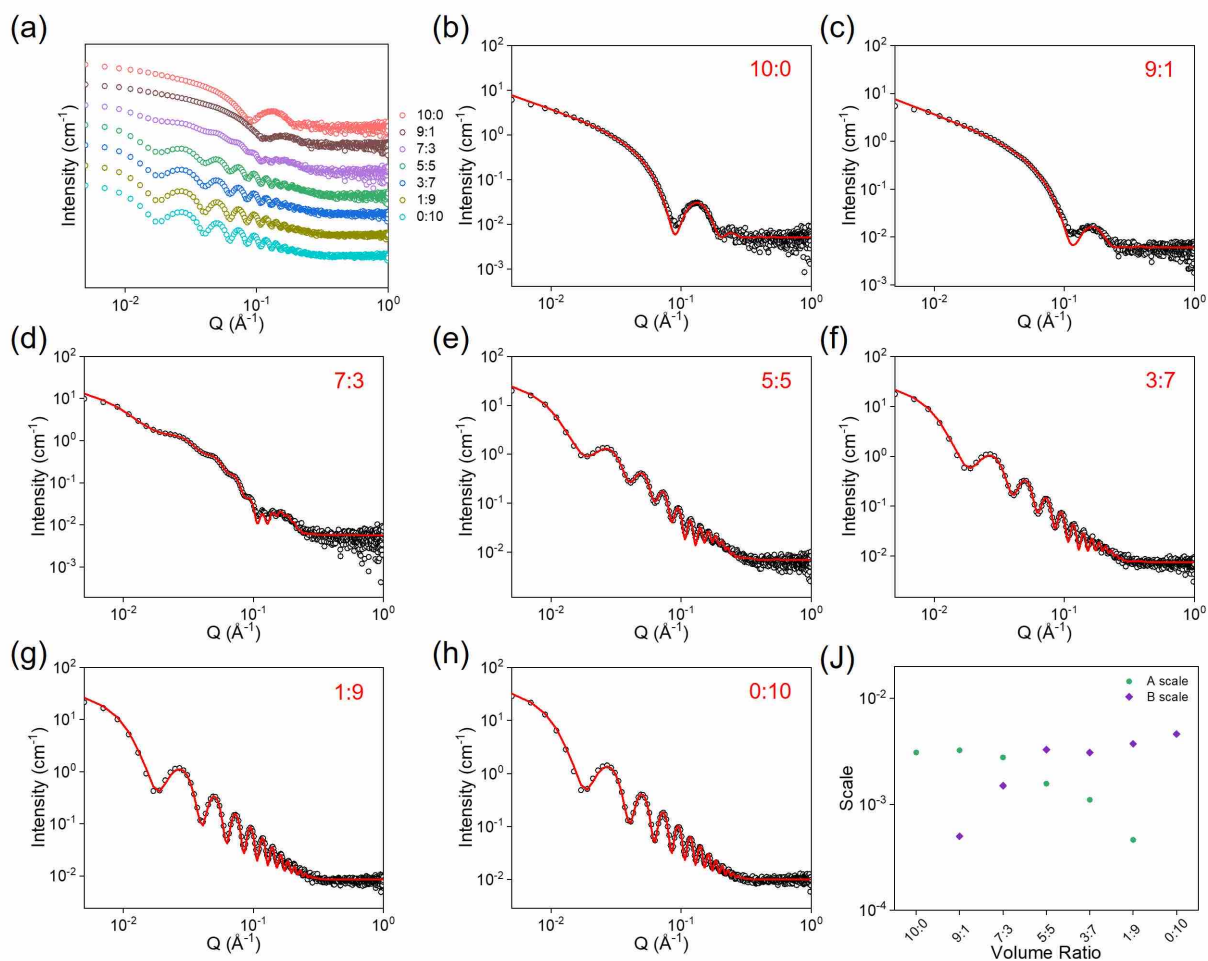
**Figure 2-9.** (a) CD profile, (b-l) HT and CD data for binary system solutions with volume ratios from 10:0 to 0:10 of 10 mg/mL (L,L)-2NapFF:(L,D)-2NapFF stock solutions.



**Figure 2-10.** Plot of CD signal intensity at (a) 188 nm, (b) 223 nm, and (c) 236 nm against ratio at for binary system solutions with various volume ratios of 10 mg/mL (L,L)-2NapFF:(L,D)-2NapFF stock solutions.

### 2.2.1.3 SANS and Cryo-TEM

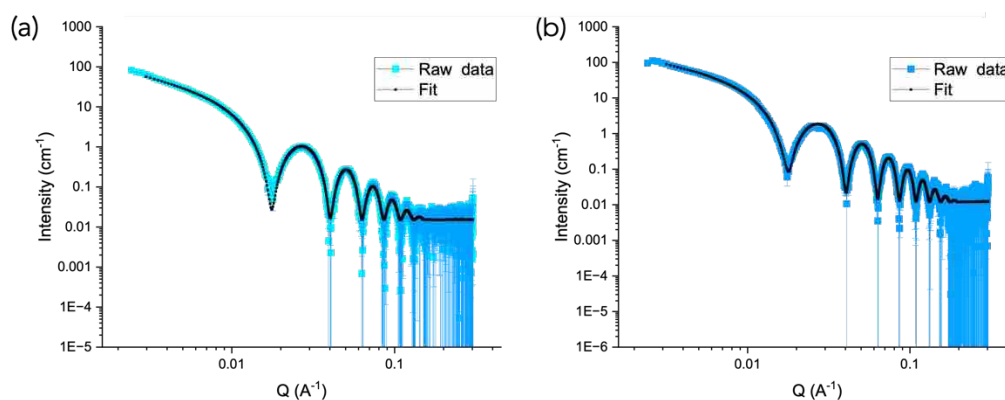
To understand these systems in more detail, we collected SANS data for mixtures of the (L,L)-2NapFF and (L,D)-2NapFF (Figure 2-11). The data for the single component systems fitted well to hollow cylinder models as previously described and summarized (Table 2-1).<sup>21</sup> The data for the mixtures were successfully fit to a combination of two hollow cylinders (Table 2-4). One of these has parameters which are identical to those of the (L,D)-2NapFF alone across this range of composition and concentration with a core radius of 13.4 nm and a wall thickness of 1.4 nm. The parameters for the second hollow cylinder depend on the exact composition and concentration (Table 2-4). It therefore appears that the (L,D)-2NapFF robustly forms the same structures (Figure 2-11) whilst the structures formed by (L,L)-2NapFF are affected by composition and concentration. We can rule out our changes in concentration leading to these changes by comparing to data for the (L,L)-2NapFF alone (see Figure 2-12). At lower concentrations, for example, 2 mg/mL, the SANS data fit best to a flexible cylinder model with a radius of around 3.1 nm (see Figure 2-13). Hence, in the presence of the second component, the micellar structures at low concentrations of (L,L)-2NapFF are different to those formed by (L,L)-2NapFF alone, again exemplifying the complexity of these systems. Cryo-TEM images corroborate the SANS data. Two populations of the structure are found in all mixtures examined (Figure 2-14 and Table 2-2). Hence, at high pH, we have a self-sorted micellar system with two co-existing populations. We highlight that this is not always the case; we have recently shown that two structurally dissimilar functionalized dipeptides form mixed micelles at high pH.<sup>28</sup> We also note that due to operational issues, the cryo-TEM data were collected around 1 year after sample formation, implying that there is no kinetic trapping occurring.



**Figure 2-11.** (a) Experimental SANS curves, (b-h) SANS data (black circle) with fits (red line) to a binary-cylinder model for two-component solutions with different volume ratios of 10 mg/mL (L,L)-2NapFF:(L,D)-2NapFF stock solutions. (i) Plots showing scales of the two models obtained from fits against volume ratio.

**Table 2-1.** Summary of SANS data fitting parameters of binary system solutions with volume ratios from 10:0 to 0:10 of 10 mg/mL (L,L)-2NapFF:(L,D)-2NapFF stock solutions.

	10:0	9:1	7:3	5:5	3:7	1:9	0:10
Scale		1	1	1	1	1	
Background (cm <sup>-1</sup> )	$5.22 \times 10^{-3} \pm 7.58 \times 10^{-5}$	$5.97 \times 10^{-3} \pm 7.10 \times 10^{-5}$	$5.60 \times 10^{-3} \pm 8.589 \times 10^{-5}$	$7.44 \times 10^{-3} \pm 8.45 \times 10^{-5}$	$7.83 \times 10^{-3} \pm 7.50 \times 10^{-5}$	$8.69 \times 10^{-3} \pm 8.75 \times 10^{-5}$	$1.02 \times 10^{-2} \pm 5.76 \times 10^{-5}$
A Scale	$3.09 \times 10^{-3} \pm 2.256 \times 10^{-5}$	$3.24 \times 10^{-3} \pm 2.25 \times 10^{-5}$	$2.77 \times 10^{-3} \pm 2.68 \times 10^{-5}$	$1.57 \times 10^{-3} \pm 5.04 \times 10^{-5}$	$1.10 \times 10^{-3} \pm 1.19 \times 10^{-4}$	$4.61 \times 10^{-4} \pm 7.40 \times 10^{-4}$	
A Radius (Å)	16.5±0.1	8.7±0.1	10.3±0.2	13.4±0.3	15.3±0.6	42.4±3.8	
A Thickness (Å)	19.3±0.2	21.9±0.2	19.9±0.2	14.1±0.5	9.2±1.0	4.5±7.3	
A Length (Å)	>1000	>1000	>1000	>1000	>1000	>1000	
B Scale		$5.00 \times 10^{-4} \pm$	$1.50 \times 10^{-3} \pm$	$3.28 \times 10^{-3} \pm 1.29 \times 10^{-5}$	$3.08 \times 10^{-3} \pm 1.18 \times 10^{-5}$	$3.73 \times 10^{-3} \pm 1.00 \times 10^{-5}$	$4.61 \times 10^{-3} \pm 2.25 \times 10^{-5}$
B Radius (Å)		131.4	131.4	131.4	131.4	131.4	131.4±0.1
B Thickness (Å)		17	17	17	17	17	17.0±0.1
B Length (Å)		491	491	491	491	491	491.1±4.8
$\chi^2$	2.09	3.03	2.91	4.93	5.71	9.80	8.00

**Figure 2-12.** SAXS data (black circle) and fit (red line) for a solution of (L,D)-2NapFF alone at (a) a concentration of 5 mg/mL and (b) a concentration of 10 mg/mL. The fits are to a hollow cylinder model. For (a), the fit implies the radius is 12.0 nm and the thickness 3.5 nm. For (b), the fit implies the radius is 12.3 nm and the thickness 2.8 nm.

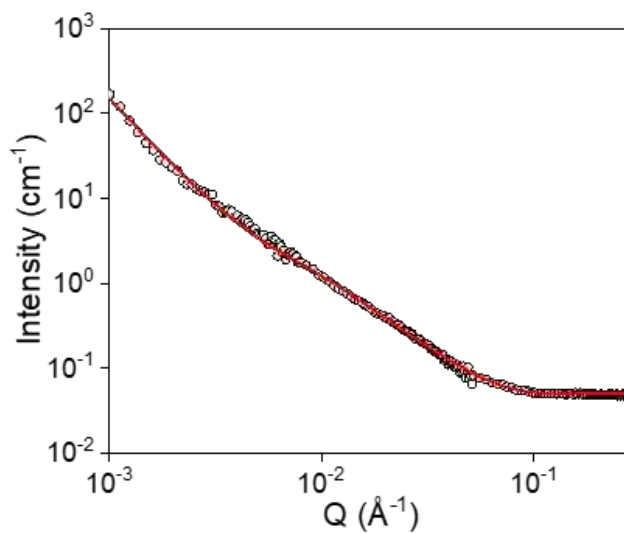


**Figure 2-13.** SANS data (black circle) and fit (red line) for a solution of (L,L)-2NapFF alone at a concentration of 2 mg/mL. The fit is to a flexible cylinder model with a radius of 3.2 nm combined with a power law.

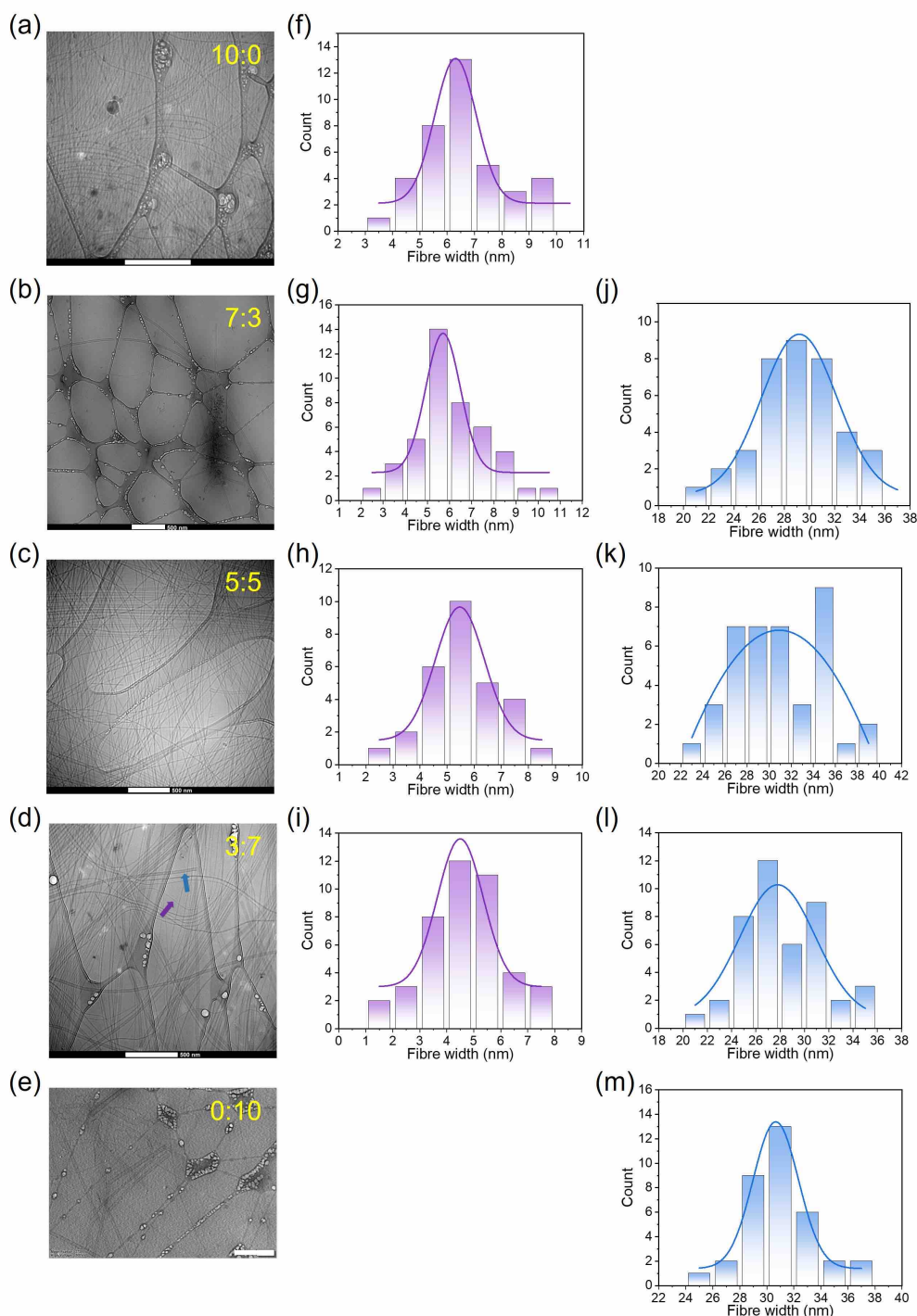


**Figure 2-14.** (a-e) Cryo-TEM images, histogram of width distribution of nanofibers derived from (f-i) (L,L)-2NapFF and (j-m) (L,D)-2NapFF component in binary system solutions with various volume ratios of 10 mg/mL (L,L)-2NapFF:(L,D)-2NapFF stock solutions. Plots in the histogram represent the nonlinear curve fits obtained from the Gaussian function. Image (d) shows a cryo-TEM image for the 3:7 mixture showing the co-existence of large nanotubes (one highlighted in a blue arrow) and thinner structures (one highlighted by a purple arrow). The scale bar represents 500 nm. The larger features observed on the hundreds of nanometer scale

are icing artifacts, not relevant to the actual sample structure, and should be considered as experimental artifacts rather than true features.

**Table 2-2.** Summary of average diameters of structures in binary system solutions with various volume ratios (10:0, 7:3, 5:5, 3:7, and 0:10) of 10 mg/mL (L,L)-2NapFF:(L,D)-2NapFF stock solutions through analysis of corresponding cryo-TEM images.

Volume ratio	Diameter of (L,L)-2NapFF component (nm)	Diameter of (L,D)-2NapFF component (nm)
10:0	6.60±1.57	
7:3	6.12±1.70	29.14±3.41
5:5	5.67±1.35	30.61±3.95
3:7	4.78±1.37	28.40±3.28
0:10		30.87±2.53

An interesting observation was made during the study of (L,D)-2NapFF, where the formation of nanotubes was seen to occur through the wrapping of a tape-like structure, likely originating from a bilayer, as seen in Figure 2-15. This suggests an early stage of the nanotube formation process, where ribbon-like structures begin to curl, a phenomenon previously discussed in the context of ribbon curling in similar systems.<sup>29, 30</sup> The formation of nanotubes through the chiral self-assembly of amphiphilic molecules, such as (L,D)-2NapFF, typically follows a multi-step process. Initially, amphiphiles self-assemble into tape-like structures, often formed by bilayers. These ribbons or tapes then curl into cylindrical shapes, transitioning into nanotubes. This curling process is a key feature of the early stage of nanotube formation, where the amphiphilic molecules' inherent chirality plays a crucial role in the alignment and stability of the assembled structures. The chirality influences the direction and degree of curling, leading to the final tubular form.

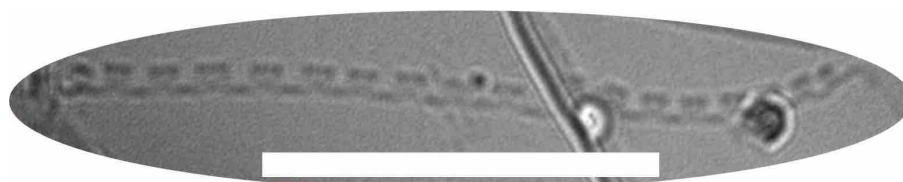


**Figure 2-15.** An expansion of a cryo-TEM image showing the formation of a nanotube. The scale bar represents 500 nm.

It is worth noting that Adams' group has worked with another example where co-assembly occurs<sup>20, 28</sup> – in this case, the molecules are very different, but the micellar structures are a wormlike micelle and a spherical micelle. Since very different molecules can co-assemble at high pH<sup>20, 28</sup> and (in some cases also at low pH<sup>20</sup>), the self-sorting here does not seem to be driven simply by the small differences in molecular structure, but rather in the fact that both of

these structures form robust nanotubes at high pH. However, further work is needed with other systems to understand this. It may be that mixing pre-formed micellar solutions as is done here also favors self-sorting and that it may be possible to drive more towards co-assembly by direct dissolution of a mixture of the two solids.<sup>31</sup>

## 2.2.2 Self-Sorting in Gels at Low pH

### 2.2.2.1 Rheology and Spectroscopy

Gels were then prepared from the solutions containing different ratios of (L,L)-, and (L,D)-2NapFF by lowering the pH slowly and controllably using the hydrolysis of GdL to gluconic acid to achieve reproducible and homogeneous kinetics of pH change and gelation.<sup>32, 33</sup> Vial inversion showed that all of the ratios formed self-supporting materials (Figure 2-14a). Consistent with the previous reports from the Adams' group, (L,L)-2NapFF started to gel earlier than (L,D)-2NapFF (Figure 2-16b) based on the higher  $pK_a$  of the terminal carboxylic acid.<sup>21</sup> Shifts in the apparent  $pK_a$  in the assembled structures, such as those observed in the gelation of (L,L)- and (L,D)-2NapFF, can occur due to the effects of self-assembly and the local environment around the amphiphiles. In the case of gelation, the  $pK_a$  values of the carboxylic acids at the terminal end of the molecules may be altered by interactions within the assembled structures (such as hydrogen bonding, hydrophobic effects, or electrostatic interactions). When the molecules self-assemble into ordered structures like fibrils or bilayers, the local environment becomes more constrained, which can influence the protonation state of the carboxylic groups. This can result in a shift in the apparent  $pK_a$ , making it either higher or lower compared to the  $pK_a$  observed for the isolated molecules in solution. The slower gelation observed for (L,D)-2NapFF, for example, could be attributed to a difference in the local electrostatic environment or hydrogen-bonding network within the assembled structure, which may delay the onset of gelation compared to (L,L)-2NapFF with its higher  $pK_a$  and faster gelation rate. Following the gelation by rheology with time, both the storage modulus ( $G'$ ) and loss modulus ( $G''$ ) gradually increased as the assembly progressed and became essentially constant after about 5 hours (Figure 2-17 and Table 2-3) except for ratios of 1:9 and 0:10 which took around 10 and 15 hours respectively. The gradual conversion of the viscous solutions to a gel was associated with the decrease in pH, with the resulting gels having a final pH of 3.1-3.4 (Table 2-2). A final gel was confirmed by the linear viscoelastic region in the strain sweep of the final gels (Figure 2-16c), and both  $G'$  and  $G''$  being frequency independent (Figure 2-16d). The final values of  $G'$  and  $G''$

varied slightly with the ratio of (L,L)-2NapFF and (L,D)-2NapFF. The turbidity of the gels increased as the concentration of (L,D)-2NapFF in the mixture increased (Figure 2-18).

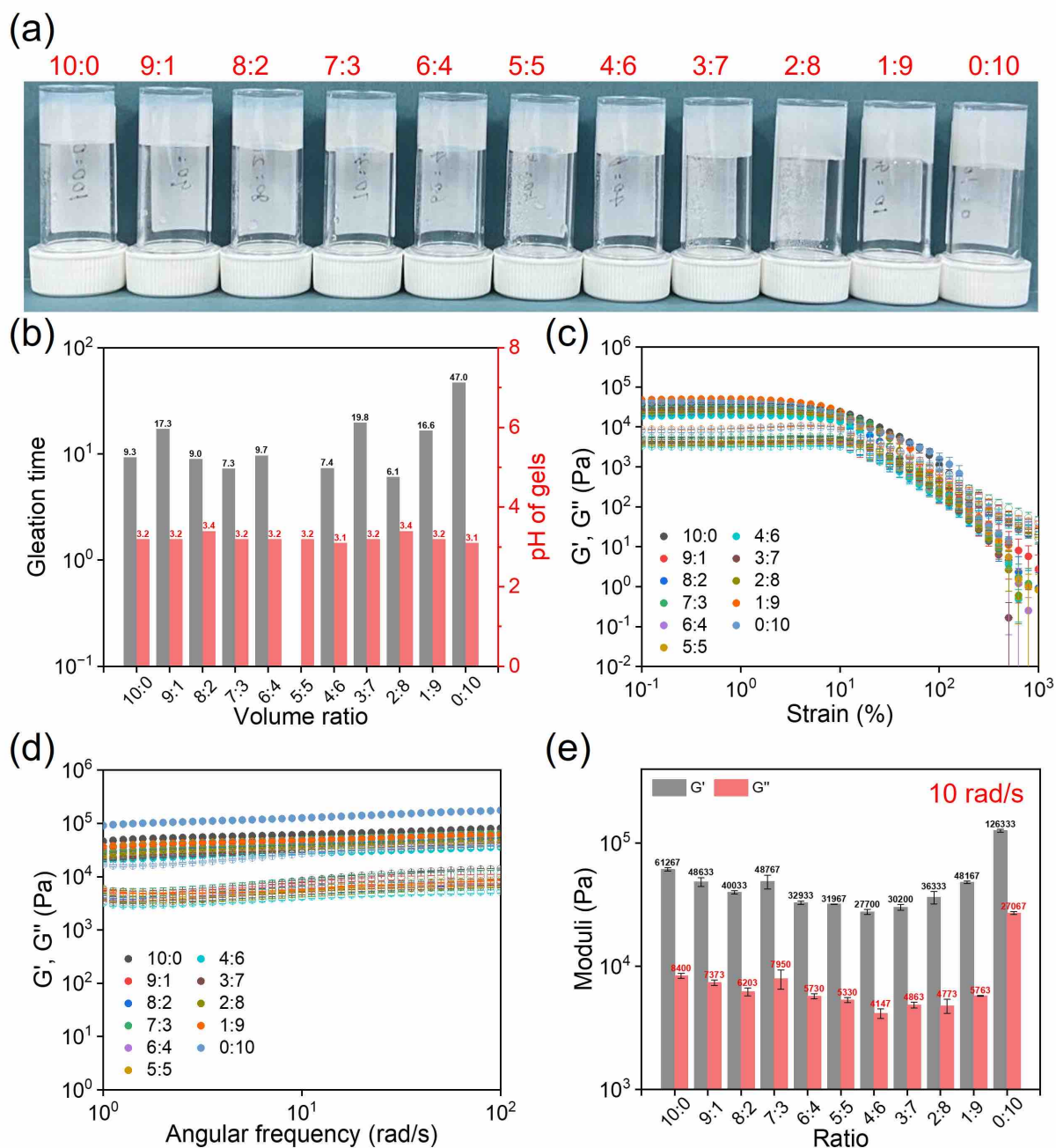


**Figure 2-16.** (a) Photographs, (b) plots of gelation time and pH of gel versus volume ratio, (c) strain, (d) frequency sweep, and (e) modulus at 10 rad/s of gels formed by solutions with various volume ratios of (L,L)-, and (L,D)-2NapFF. For (c) and (d), full symbols represent  $G'$  and open symbols represent  $G''$ . In all cases for (b)-(e), the data points represent the average value of the experimental data of the three samples, and the error bar represents their standard deviation.

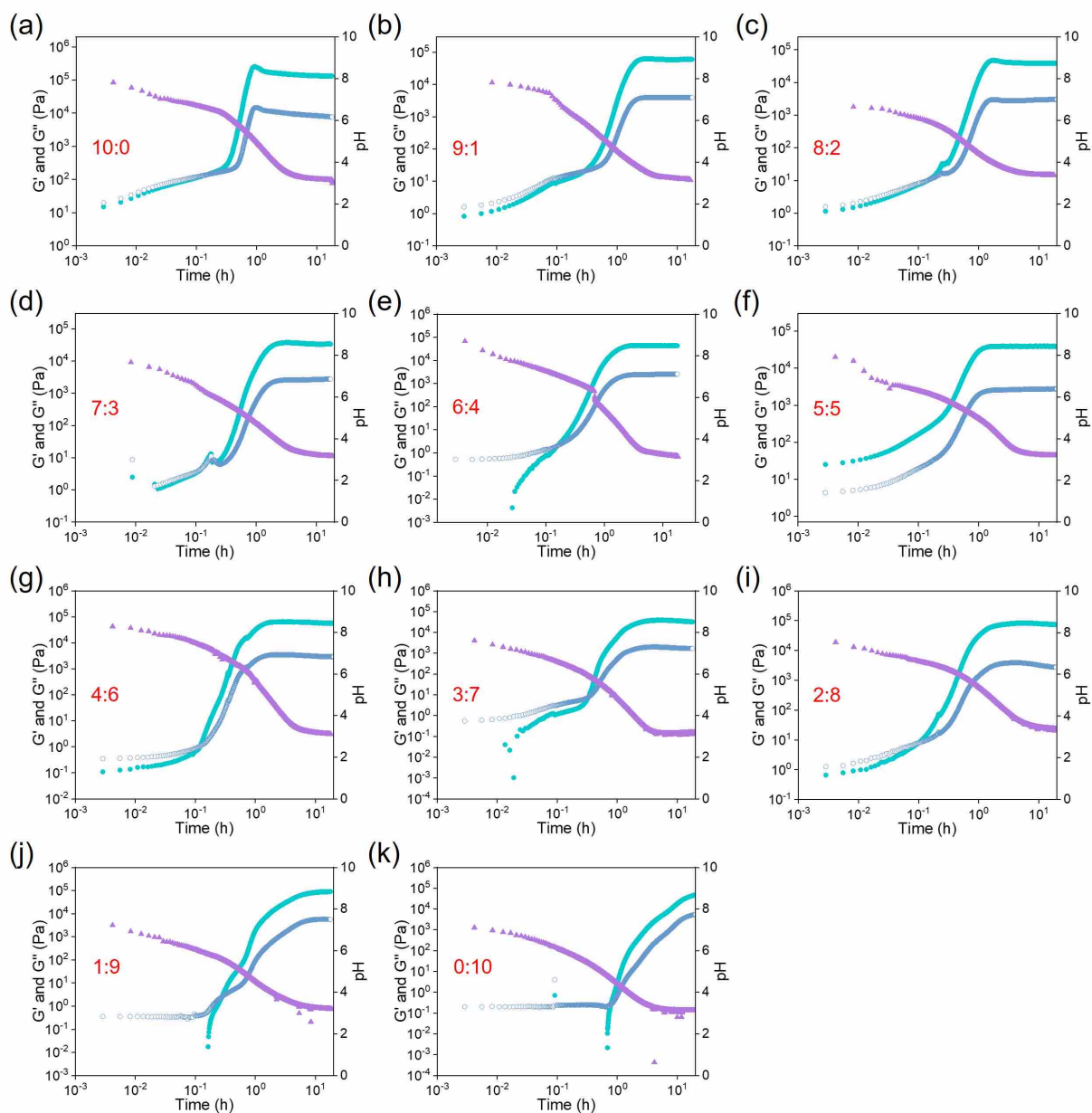


**Figure 2-17.** Time sweep (green closed circle and blue open circle represent  $G'$  and  $G''$ , respectively.) and pH monitoring (purple triangle) of binary system solutions with volume ratios from 10:0 to 0:10 of 10 mg/mL (L,L)-2NapFF:(L,D)-2NapFF stock solutions after the addition of GdL.

**Table 2-3.** Summary of gelation time and pH of gel of binary systems with volume ratios from 10:0 to 0:10 of 10 mg/mL (L,L)-2NapFF:(L,D)-2NapFF stock solutions after the addition of GdL.

Volume ratio	Gelation time (min)	pH of gel
10:0	9.3	3.2
9:1	17.3	3.2
8:2	9.0	3.4
7:3	7.3	3.2
6:4	9.7	3.2
5:5	0	3.2
4:6	7.4	3.1
3:7	19.8	3.2
2:8	6.1	3.4
1:9	16.6	3.2
0:10	47.0	3.1

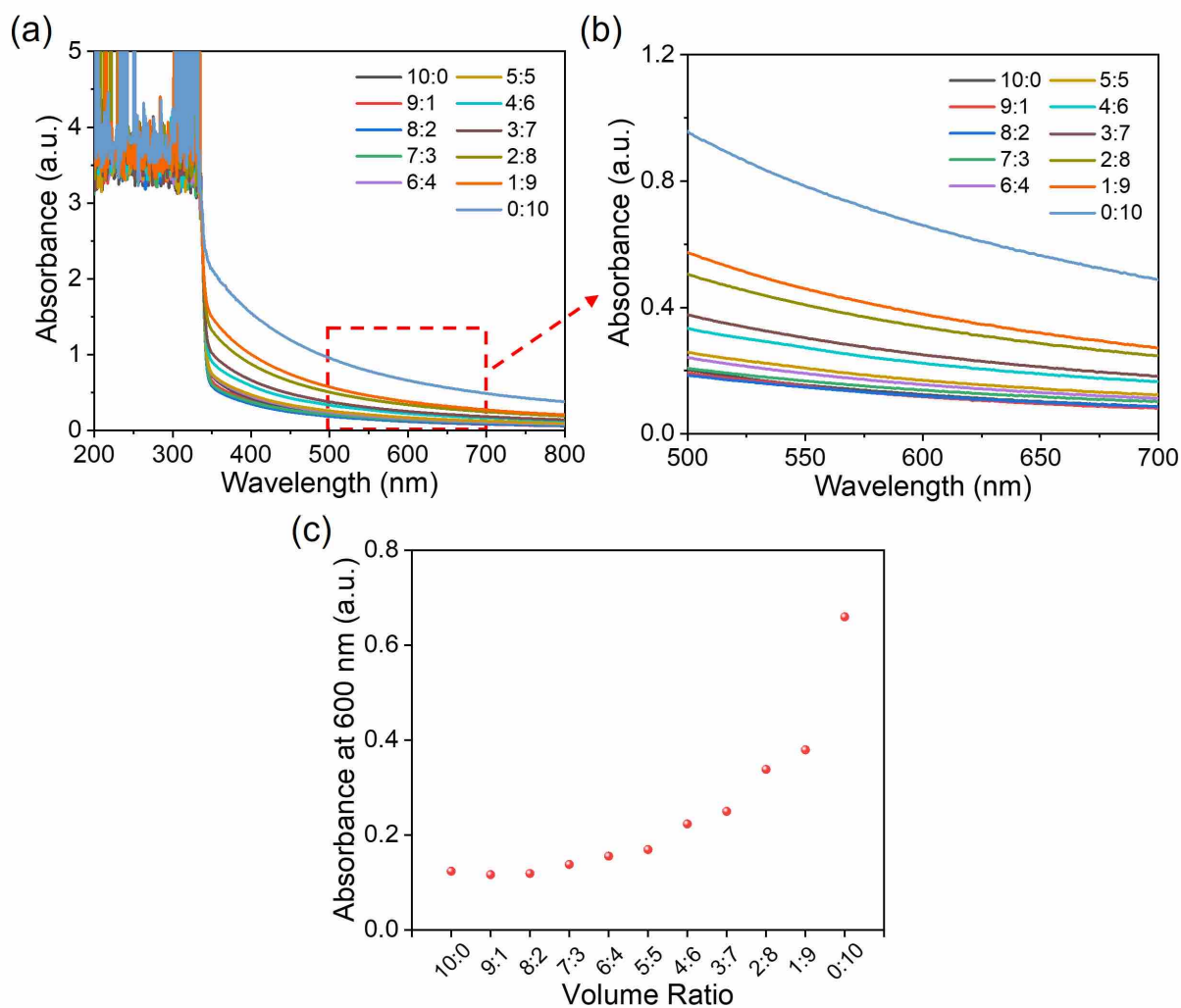


**Figure 2-18** (a) UV-Vis absorption spectra of gels containing 10 mg/mL of (L,L)- and (L,D)-2NapFF at ratios ranging from 10:0 to 0:10 collected using a 2 mm path length quartz cuvette at 25 °C. (b) Spectra depicted the enlarged regions of the graph (a) at wavelengths of 500-700 nm. (c) Change in turbidity over composition at 600 nm for gels.

Due to the significant increase in gel turbidity, we must acknowledge the impact of this factor on the UV-Vis absorption spectrum, particularly the enhanced absorption peak intensity observed in highly turbid gels with ratios of 2:8, 1:9, and 0:10, as depicted in Figure 2-19, in contrast to the solution state counterpart. Consequently, the data is too intricate for direct interpretation.

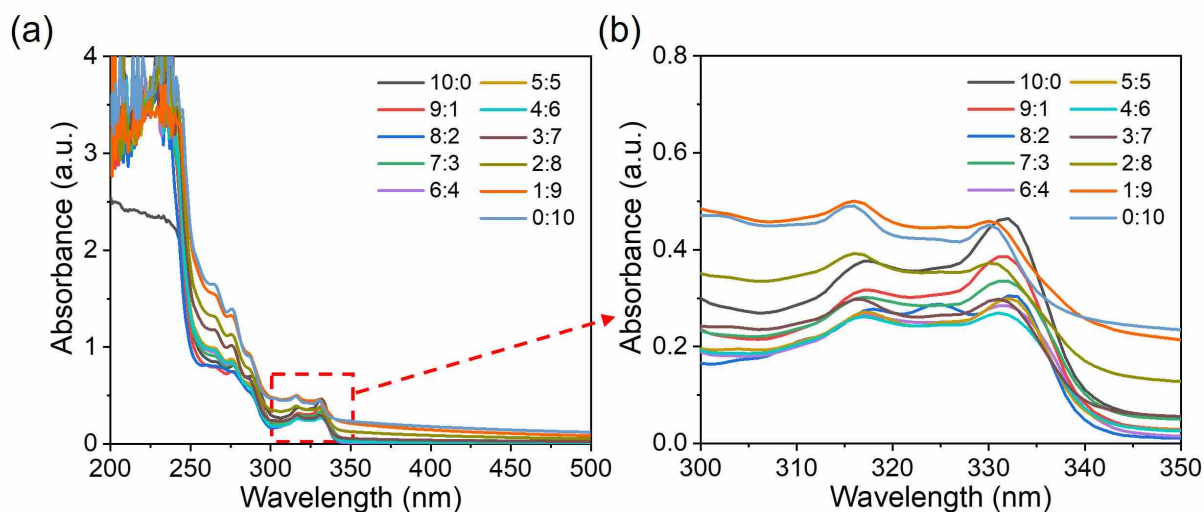


**Figure 2-19** (a) UV-Vis absorption spectra of gels containing 10 mg/mL of (L,L)- and (L,D)-2NapFF at ratios ranging from 10:0 to 0:10 recorded with a 0.01 mm path length quartz demountable cuvette at 25 °C. (b) Spectra depicted the enlarged regions of the graph (a) at wavelengths of 300-350 nm.

### 2.2.2.2 SAXS

To understand the gel phase, we used SAXS to probe the underlying structures (Figure 2-20 and Table 2-4). The data for the (L,L)-2NapFF alone agree with our previous data,<sup>22</sup> showing that the network is formed by structures that best fit to a flexible elliptical cylinder model. For (L,L)-2NapFF, as the pH decreases, the core first collapses, followed by the lateral association of the resulting cylinders.<sup>22</sup> For the (L,D)-2NapFF, the structures best fit to a hollow cylinder model,<sup>21</sup> showing that the micellar structures template the structures in the gel state. The SAXS data for the mixtures rich in (L,D)-2NapFF (5:5 and higher) can be fit to a mixture of a hollow cylinder and flexible elliptical cylinder models, with the parameters for the hollow cylinder being close to that for the pure (L,D)-2NapFF. At lower concentrations, the data best fit to a flexible elliptical cylinder model alone. We interpret this as there being self-sorting in these systems, but the scattering being dominated by the (L,L)-2NapFF as this becomes the highest concentration species.

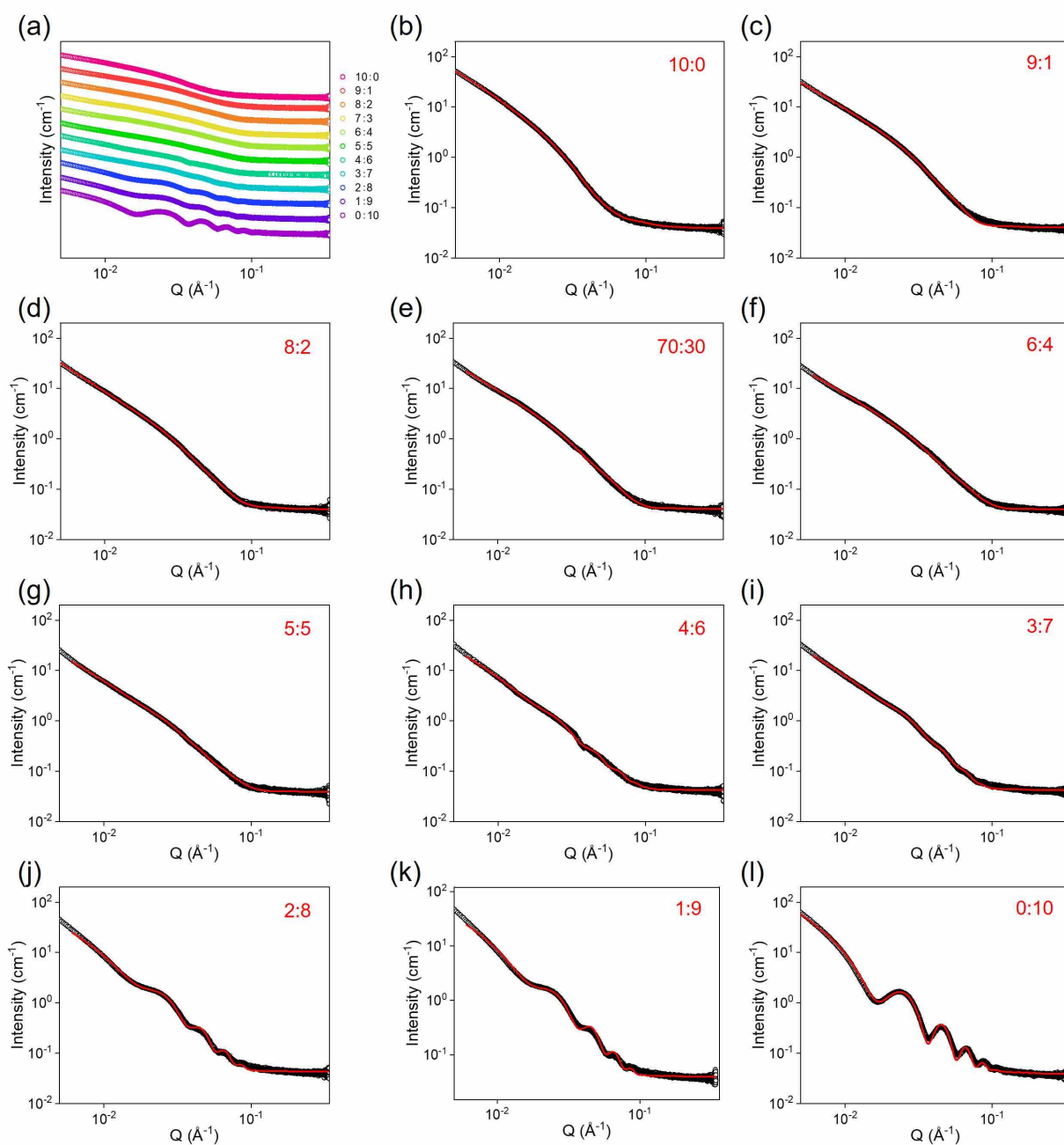


**Figure 2-20.** (a) Experimental SAXS curves, (b-l) SAXS data (black circle) and fits (red line) for binary system gels with volume ratios from 10:0 to 0:10 of 10 mg/mL (L,L)-2NapFF:(L,D)-2NapFF stock solutions.

**Table 2-4.** Summary of SAXS data fitting parameters for the binary system gels with volume ratios from 10:0 to 0:10 of 10 mg/mL (L,L)-2NapFF:(L,D)-2NapFF stock solutions. The abbreviations FEC, HC and PL represent flexible elliptical cylinder, hollow cylinder, and power law, respectively.

	10:0	9:1	8:2	7:3	6:4	5:5	4:6	3:7	2:8	1:9	0:10
Model	FEC+PL	FEC	FEC+PL	FEC	FEC+PL	FEC+H C	FEC+H C	FEC+H C	FEC+H C	FEC+H C	HC+PL
scale	1		1		1	1	1	1	1	1	1
Background (cm <sup>-1</sup> )	$3.85 \times 10^{-2} \pm 4.26 \times 10^{-5}$	$4.06 \times 10^{-2} \pm 3.36 \times 10^{-5}$	$4.05 \times 10^{-2}$	$4.03 \times 10^{-2} \pm 3.49 \times 10^{-5}$	$3.95 \times 10^{-2} \pm 3.29 \times 10^{-5}$	$3.89 \times 10^{-2} \pm 3.56 \times 10^{-5}$	$4.19 \times 10^{-2} \pm 3.94 \times 10^{-5}$	$4.20 \times 10^{-2} \pm 3.70 \times 10^{-5}$	$4.27 \times 10^{-2} \pm 3.77 \times 10^{-5}$	$3.95 \times 10^{-2} \pm 3.47 \times 10^{-5}$	$3.84 \times 10^{-2} \pm 3.43 \times 10^{-5}$
A scale	$2.35 \times 10^{-4} \pm 2.90 \times 10^{-6}$	$3.61 \times 10^{-4} \pm 0.61 \times 10^{-6}$	$3.22 \times 10^{-4} \pm 0.82 \times 10^{-6}$	$3.49 \times 10^{-4} \pm 0.67 \times 10^{-6}$	$4.26 \times 10^{-4} \pm 0.19 \times 10^{-6}$	$2.94 \times 10^{-4} \pm 0.81 \times 10^{-6}$	$2.02 \times 10^{-4} \pm 0.41 \times 10^{-6}$	$2.86 \times 10^{-4} \pm 6.83 \times 10^{-4}$	$2.31 \times 10^{-4} \pm 0.59 \times 10^{-6}$	$1.35 \times 10^{-4} \pm 0.44 \times 10^{-6}$	
A_length (Å)	5000	5000	5000	5000	5000	5000	5000	5000	5000	5000	
A_kuhn_length (Å)	87.4±1.6	224.6±1.1	250.6±2.3	209.0±1.3	90.2	172.8±1.3	147.7±2.2	196.6±1.4	141.1±3.0	500.0±8.1	
A_radius (Å)	49.9±0.12	35.3±0.0	31.7±0.06	28.9±0.0	25.0	24.9±0.0	26.3±0.0	31.5±0.0	30.2±0.1	30.5±0.0	
A_axis_ratio	1.9±0.01	2.7±0.01	2.8±0.01	3.2±0.01	2.3	3.0±0.01	3.5±0.01	2.7±0.01	2.7±0.02	4.8±0.02	
B scale						$0.22 \times 10^{-4} \pm 5.21 \times 10^{-7}$	$0.95 \times 10^{-4} \pm 6.16 \times 10^{-7}$	$6.51 \times 10^{-4} \pm 5.61 \times 10^{-4}$	$2.86 \times 10^{-4} \pm 6.35 \times 10^{-7}$	$3.38 \times 10^{-4} \pm 6.48 \times 10^{-7}$	$6.36 \times 10^{-4} \pm 7.87 \times 10^{-7}$
B_radius (Å)						124.8	124.8	124.8	124.8	124.8	$124.8 \pm 4.63 \times 10^{-2}$
B_thickness (Å)						51.45	51.45	51.45	51.45	51.45	$51.452 \pm 8.03 \times 10^{-2}$
B_length (Å)						5000	5000	5000	5000	5000	5000
scale	$2.43 \times 10^{-5} \pm 3.51 \times 10^{-7}$		$1.11 \times 10^{-5} \pm 4.40 \times 10^{-7}$		$2.79 \times 10^{-8} \pm 2.81 \times 10^{-10}$						$1.39 \times 10^{-5} \pm 9.28 \times 10^{-8}$
power	$2.5 \pm 4.26 \times 10^{-3}$		$2.6 \pm 7.11 \times 10^{-3}$		3.5						$2.7 \pm 1.54 \times 10^{-3}$
χ <sup>2</sup>	1.31	5.77	1.87	8.39	9.67	2.85	6.27	3.96	11.00	19.02	22.15

## 2.3 Conclusions

Previous work examining multicomponent systems similar to those described here in water tend to focus on the gel state, with little if any discussion of the importance (or not) of any structures present before gelation.<sup>7, 34-38</sup> There seems to often be an assumption that there is complete dissolution before gelation, which we and others have shown is often not the case for such hydrophobic molecules that are charged at high pH.<sup>31, 39</sup> This is an interesting point – in most organogel systems, gels are formed by heating to dissolve the gelator and then cooling to form the gels. Similarly, for gelators such as those used in this work, gelation can often also be achieved by dissolution in a good solvent such as DMSO followed by the addition of water.

Indeed, mixed assemblies have been prepared by such methods.<sup>40-42</sup> In this scenario there ought to be molecular dissolution before water addition and gelation.

Here, this pre-formation of a micellar dispersion at high pH before gelation at low pH provides different possibilities in self-sorting and co-assembly (and scenarios in between) compared to direct dissolution. We show that the structures formed at high pH can persist into the gel state and self-sorting can occur based on the chirality of one of the amino acids. Chirality has been examined previously in low molecular weight gelling systems,<sup>43, 44</sup> but generally as single components where the gelling efficiency of different enantiomers and diastereomers have been compared.<sup>45-47</sup> Xu's group has compared the L,L- and D,D- analogs of naphthalene dipeptides from the perspective of *in vivo* hydrolysis.<sup>48</sup> Here, we have shown that self-sorting can be driven by the chirality of a single amino acid in these functionalized dipeptide systems, with two distinct micellar structures being formed at high pH. The structures formed are affected to some degree by the relative concentrations of each component showing the complexity of such an approach. This aspect of relative concentration is rarely discussed as a possible means of tuning the system in multicomponent systems. On lowering the pH, a gel is formed in all cases, with self-sorting again occurring. Hence, the structures underpinning the gel network are predefined by the micellar structures at high pH, and a change in the chirality of a single amino acid can drive differences here. This work shows both the power and complexity of these systems.

## 2.4 Experimental Section

### 2.4.1 Sample Preparation Protocols

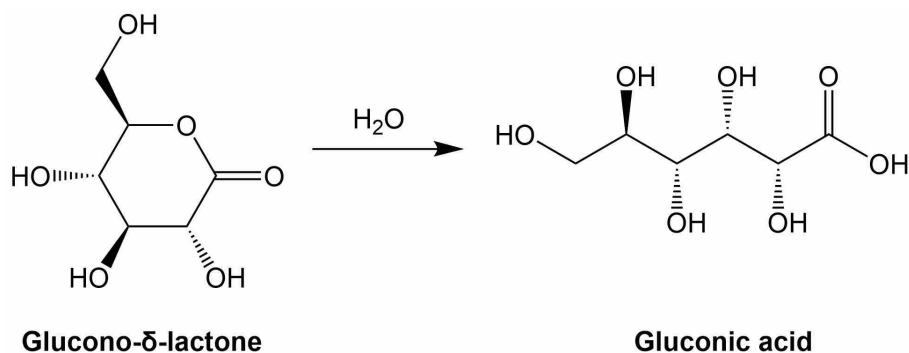
#### 2.4.1.1 Preparation of Micellar Solutions

Stock solutions with a concentration of 10 mg/mL were prepared in a Falcon Tube by suspending 200 mg of 2NapFF in deionized water (15.97 mL) and adding 0.1 M sodium hydroxide solution (1 eq., 4.03 mL) so that the molar ratio of sodium hydroxide and 2NapFF was kept as 1:1 and the total volume of the solution was 20 mL. Then, the solution was stirred at 1000 rpm overnight to ensure complete dissolution. Afterward, the pH of the solution was measured and adjusted to approximately 10.5 if needed with the addition of NaOH (2 M) or HCl (2 M) aqueous using a pipette with a full scale of 20  $\mu$ L. Multiple solutions were created by combining portions of the previously mentioned stock solutions of (L,L)-2NapFF and (L,D)-2NapFF in various volume ratios from 10:0 to 0:10, ensuring the total concentration of LMWGs

remains at 10 mg/mL. The resultant blend was subsequently agitated at 1000 rpm for an hour. Subsequently, the pH of the mixtures was measured and adjusted to 10.5 if needed with the addition of NaOH (2 M) or HCl (2 M) aqueous using a pipette with a maximum scale of 20  $\mu$ L.

### 2.4.1.2 Preparation of pH-Triggered Gels

pH-triggered gels were prepared using glucono- $\delta$ -lactone (GdL), which hydrolyses in water to produce gluconic acid (Scheme 2-1). This approach not only results in reproducible, homogeneous, and controllable gels, but it also allows for tracking pH changes and rheology during the gelation process. Gels were prepared in Sterilin vials (7 mL) by adding 2 mL of a stock solution prepared as above to GdL (16 mg/mL, 32 mg). The vials were gently rotated by hand to ensure the complete dissolution of GdL and left to stand overnight quiescently. Rheology data were collected 18 hours after the addition of GdL.



**Scheme 2-1.** Hydrolysis of GdL to gluconic acid.

## 2.4.2 Characterization

### 2.4.2.1 pH Measurement

An FC200 pH probe (HANNA instruments) with a 6 mm x 10 mm conical tip was employed for all pH measurements. The precision of the pH measurements is stated as  $\pm 0.1$ .

To keep track of pH fluctuations during the gelation process, 2 mL of gelator solution was introduced into Sterilin vials (7 mL) containing previously weighed GdL (16 mg/mL, 32 mg). The vial was then placed in a circulating water bath at 25°C. The pH was measured at 0.5-minute intervals. It is important to refrain from stirring the sample during this process.

### 2.4.2.2 Apparent $pK_a$ Titration

The titration process reaches equilibrium (horizontal region) where pH equals the  $pK_a$  of the weak acid, according to the Henderson-Hasselbalch equation (Equation 2-1). The titration was performed by measuring the pH of the solution (2 mL) after slowly lowering the pH by adding aliquots (2  $\mu$ L) of 0.1 HCl in water. After adding each portion of HCl, the mixture was stirred thoroughly for about 2 minutes to prevent gel formation and allow pH to equilibrate. A circulating water bath was used to maintain the temperature of the sample solution at 25°C during the titration process.

$$\text{pH} = \text{p}K_{\alpha} + \log_{10} \frac{[\text{A}^{-}]}{[\text{HA}]} \quad \text{Equation 2-1}$$

$K_{\alpha}$  is the acid dissociation constant,  $[\text{A}^{-}]$  represents the concentration of the conjugate base (deprotonated fraction), and  $[\text{HA}]$  refers to the concentration of the weak acid (protonated fraction). When  $[\text{A}^{-}] = [\text{HA}]$ , the pH of the solution is equal to the  $pK_a$  of the acid.

### 2.4.2.3 Nuclear Magnetic Resonance Spectroscopy

$^1\text{H}$  NMR spectra were recorded on a Bruker Avance III 400 MHz instrument. Spectra were referenced to the residual  $^1\text{H}$  signal from the DMSO- $d_6$  at 2.50 ppm for integration. The temperature of the samples was maintained at  $298 \pm 0.5$  K.

### 2.4.2.4 Optical Microscopy

Optical microscopy images (5 $\times$ magnification) of solutions were obtained using a Nikon Eclipse LV100 microscope with a Nikon Plan ELWD 50 $\times$ /0.60 lens attached to an Infinity2-1C camera. The images were acquired at 5x magnification and were captured with either no polarizers (NP) or cross-polarizers (CP). Scale bars were indicated to the images using the ImageJ.

For optical microscopic images of samples exposed to the magnetic field, 1 mL of micellar solution prepared as above was pipetted into a 5 mm NMR tube and exposed to a magnetic field for 30 minutes in the NMR spectrometer. Optical microscopy images were taken before and after the exposure to the magnetic field for comparison.

### 2.4.2.5 Ultraviolet-Visible Spectroscopy

An Agilent Cary 60 UV-Vis spectrophotometer (Agilent Technology, Selangor, Malaysia) was employed to record absorption spectra, using a 0.1 mm path length quartz demountable cuvette at 25 °C. For gels, 200  $\mu$ L of pre-gelation solution containing GdL was introduced into the

cuvette while in its liquid state. The cuvette was then sealed with Parafilm, and the sample was left to gel overnight before recording the spectrum.

#### 2.4.2.6 Turbidity Measurements

Using an Agilent Cary 60 UV-Vis spectrophotometer (Agilent Technology, Selangor, Malaysia), the turbidity of all samples was measured at a wavelength of 600 nm with a 2 mm path length quartz cuvette at 25 °C. For gels, 1 mL of a pre-gelation solution containing GdL was placed into the cuvette while still in its liquid form. The cuvette was then sealed with Parafilm, and the sample was left to gel overnight before the spectrum was recorded.

#### 2.4.2.7 Fluorescence Spectroscopy

Measurements were conducted using an Agilent Technologies Cary Eclipse fluorescence spectrometer. A 4-clear side PMMA cuvette with a path length of 1 cm was utilized to capture spectra within the 330–630 nm range. Throughout the experiments, the excitation wavelength remained fixed at 320 nm, with both excitation and emission slit widths set to 5 nm. For gel samples, 2 mL of pre-gelation solution containing GdL was added to the cuvette while remaining liquid. Following this, the cuvette was sealed with Parafilm, and the sample was allowed to gel overnight before spectral acquisition. Time-resolved data during the gelation process were recorded at 1 min, 2 min, 5 min, 10 min, 15 min, 30 min, 1 h, 1.5 h, 2 h, and subsequently at hourly intervals until 16 h.

#### 2.4.2.8 Shear Rheology

An Anton Paar Physica MCR301 rheometer was used for rheological performance measurement.

**Viscosity measurement:** The viscosity was collected using the cone (CP50-1 18237) and plate system at 25°C. The experiment gap distance between the cone and plate was fixed at 0.1 mm. Then the 5 mL pipette and tip were used to transfer 1.5 mL of the solution onto the rheometer plate to minimize the shearing effect. The viscosity of each solution with the rotational shear rate was recorded, varying from 1 to 1000 s<sup>-1</sup>.

To prepare the heat-cool viscosity samples, 3 mL of binary system solutions with varying volume ratios of 10 mg/mL (L,L)-2NapFF and (L,D)-2NapFF stock solutions were taken and transferred into 14 mL glass vials. The vials were then placed in a preheated oven set at 50°C

for 1 hour. After that, the solution was allowed to cool down to room temperature quiescently for 2 hours. Finally, viscosity data of these samples after heat-cool treatment were collected.

**Frequency and strain sweep:** A vane (ST10-4V-8.8/97.5-SN42404) and cup system were used to directly measure the gap in a 7 mL plastic Sterilin vial containing 2 mL of gel sample was set to 1.8 mm during the entire test. Frequency sweep was measured from  $1 \text{ rad s}^{-1}$  to  $100 \text{ rad s}^{-1}$  at a fixed strain of 0.5%; strain sweep was measured from 0.1% to 1000% at a constant frequency of  $10 \text{ rad s}^{-1}$  to guarantee that 0.5% strain was in the viscoelastic region required for the frequency sweep.

**Time sweep:** A cone (PP50/S 17154) and plate system were employed with the experiment gap at 0.8 mm. Then 2 mL of the solution was added into a Sterilin vial containing pre-weighed 32 mg of GdL, and the vial was gently rotated to ensure that the GdL was completely dissolved. Subsequently, a 5 mL pipette tip was used to transfer the mixed solution onto the plate. To prevent the sample from evaporating, the edge of the cone was sealed with a small amount of mineral oil while avoiding the mineral oil from contacting the upper surface of the cone after the measurement proceeded for 15 minutes. Time sweep was measured at a constant frequency of  $10 \text{ rad s}^{-1}$  and a strain of 0.5% at  $25 \text{ }^\circ\text{C}$  for 16 hours.

#### 2.4.2.9 Circular Dichroism

CD measurements were conducted using a detachable quartz cuvette (Hellma) with a path length of 0.01 mm and a Chirascan VX spectrometer (Applied Photophysical Limited, UK) outfitted with a Peltier temperature controller. The scanning parameters were configured as follows: a scanning step of 1.0 nm, a scanning speed of 240 nm/min, a wavelength ( $\lambda$ ) scanning range spanning from 180 to 300 nm, and a bandwidth of 1 nm. The recorded data are expressed in millidegrees (mdeg) of ellipticity. During the scanning process, CD, absorption, and HT (High Tension) data were simultaneously collected. To investigate the temperature-dependent behaviour, CD evolution was tracked within a temperature range of 25 to  $85 \text{ }^\circ\text{C}$  using  $10 \text{ }^\circ\text{C}$  intervals during a heating-cooling cycle. Except for the CD over temperature, the other data are the average of 3 scans at  $25 \text{ }^\circ\text{C}$ .

#### 2.4.2.10 Cryogenic Transmission Electron Microscopy

Cryo-TEM imaging was performed either using FEI Tecnai 12 TWIN Transmission Electron Microscope operated at 100kV or using FEI Talos 200SC FEG that was operated at 200 kV. In

general, a drop of the studied sample solution, approximately 7 microliters, was placed on a holey carbon film supported on a TEM copper grid (Electron Microscopy Services, Hatfield, PA). Before TEM sample preparation, all the TEM grids used for cryo-TEM imaging were treated with plasma air to render the lacey carbon film hydrophilic. A vitrified thin film of the sample solution, typically less than 200 nm, was produced using the Vitrobot with a controlled humidity chamber (FEI). The vitrified samples were then transferred to a cryo-holder and cryo-transfer stage, cooled by liquid nitrogen. The cryo-holder temperature was maintained below -170 °C during the imaging process to prevent the sublimation of vitreous water. All images were recorded by an EMSIS Megaview G III wide-angle CCD camera or Thermo Scientific Ceta (CMOS) camera.

#### **2.4.2.11 Image Analysis**

Cryo-TEM involved the assessment of fiber width through ImageJ. The scale bar served as a reference for width measurement. Histograms were generated based on approximately 30–50 fiber measurements. Multiple images of identical samples were analyzed to ensure accurate width measurements.

#### **2.4.2.12 Small-Angle Neutron Scattering**

SANS measurements of the gelator solutions and gel samples were performed at either ISIS or the ILL. At ISIS, measurements were carried out using the SANS2D time-of-flight diffractometer (STFC ISIS Pulsed Neutron Source, Oxfordshire, UK). A simultaneous Q-range of 0.005 to 1.0 Å<sup>-1</sup> was achieved using an incident wavelength ( $\lambda$ ) range of 1.75 to 16.5 Å and employing two 1 m<sup>2</sup> detectors. The small-angle detector was positioned 4 m from the sample and offset vertically 80 mm and sideways 100 mm. The wide-angle detector was positioned 2.4 m from the sample, offset sideways by 980 mm, and rotated to face the sample. The incident neutron beam was collimated to 8 mm diameter. Samples were housed in 2 mm pathlength quartz cuvettes and measured for 60 minutes each. The ‘raw’ scattering data were normalized to the incident neutron wavelength distribution, corrected for the linearity and efficiency of the detector response and the measured neutron transmission (i.e., absorbance) using the Mantid framework.<sup>49, 50</sup> They were then placed on an absolute scale by comparison with the expected scattering from a partially-deuterated polystyrene blend of known composition and molecular weights following established procedures. The background scattering from a quartz cell containing D<sub>2</sub>O was then subtracted.

Measurements using the small angle neutron scattering instrument D11 at the Institut Laue – Langevin (ILL; Grenoble, France) were performed using a neutron wavelength of 10 Å, and three samples to detector distances of 39 m, 8 m, and 1.2 m (with respective collimation distances of 40.5m, 8m, and 5.5m). A MWPC 3He detector consisting of 128 x 128 pixels of 7.5x7.5 mm<sup>2</sup> size was used. The employed neutron beam was 13mm in diameter. The thermostatic rack was kept at 20 °C. Data reduction was performed using the facility-provided software LAMP. Data have been put on an absolute scale by measuring the secondary calibration standard H<sub>2</sub>O (1mm thickness), cross-calibrated against h/d polymer blends, with the known differential scattering cross-section of 1.245 1/cm for 10 Å.

#### 2.4.2.13 Small-Angle X-Ray Scattering

SAXS measurements were performed at Diamond Light Source (Oxfordshire, UK) on the B21 beamline.<sup>51</sup> Samples were loaded into 1.5 mm diameter glass capillaries using a 1 mL syringe and a 19G needle immediately after GdL addition, allowing gelation in the capillary. The capillaries were sealed with parafilm, loaded into a 3D-printed cell, and then into the instrument via the multipurpose sample (MPS) cell.<sup>52</sup> 20 x 1 s frames were collected on the samples. The X-ray beam possessed a wavelength of 0.9537 Å and an energy of 13 keV. An EigerX 4M (Dectris) detector was used at a sample-to-detector distance of 3712.7 mm, resulting in a Q range of 0.0026-0.34 Å<sup>-1</sup>. The data were processed in Dawn Science (version 2.25, <https://dawnsci.org/>). The scattering from deionized water in a glass capillary was used as the background. The 2D images were azimuthally integrated to produce the 1D I vs Q plots.

The analysis of small scattering data was conducted using SasView (version 5.0.6)<sup>53</sup>, which entails fitting the data to an appropriate model. The NIST neutron activation and scattering calculator<sup>54</sup> was employed to compute the scattering length density (SLD) values. The derived SLD values are provided in Table 2-5.

**Table 2-5.** SLD values of compound and solvent used in the fitting process.

Compound	Density(g/cm <sup>3</sup> )	SAXS scattering length densities (10 <sup>-6</sup> /Å <sup>2</sup> )	SANS scattering length densities (10 <sup>-6</sup> /Å <sup>2</sup> )
H <sub>2</sub> O	1.00	9.469	-0.561
2NapFF	1.58	14.196	2.730

## 2.5 References

- (1) Terech, P.; Weiss, R. G. Low Molecular Mass Gelators of Organic Liquids and the Properties of Their Gels. *Chemical Reviews* **1997**, *97* (8), 3133-3160.
- (2) Estroff, L. A.; Hamilton, A. D. Water Gelation by Small Organic Molecules. *Chemical Reviews* **2004**, *104* (3), 1201-1218.
- (3) Du, X.; Zhou, J.; Shi, J.; Xu, B. Supramolecular hydrogelators and hydrogels: from soft matter to molecular biomaterials. *Chemical Reviews* **2015**, *115* (24), 13165-13307.
- (4) Buerkle, L. E.; Rowan, S. J. Supramolecular gels formed from multi-component low molecular weight species. *Chemical Society Reviews* **2012**, *41* (18), 6089-6102.
- (5) Raeburn, J.; Adams, D. J. Multicomponent low molecular weight gelators. *Chemical Communications* **2015**, *51* (25), 5170-5180.
- (6) Draper, E. R.; Adams, D. J. How should multicomponent supramolecular gels be characterised? *Chemical Society Reviews* **2018**, *47* (10), 3395-3405.
- (7) Zhou, M.; Smith, A. M.; Das, A. K.; Hodson, N. W.; Collins, R. F.; Ulijn, R. V.; Gough, J. E. Self-assembled peptide-based hydrogels as scaffolds for anchorage-dependent cells. *Biomaterials* **2009**, *30* (13), 2523-2530.
- (8) Alakpa, Enateri V.; Jayawarna, V.; Lampel, A.; Burgess, Karl V.; West, Christopher C.; Bakker, Sanne C. J.; Roy, S.; Javid, N.; Fleming, S.; Lamprou, Dimitris A.; et al. Tunable Supramolecular Hydrogels for Selection of Lineage-Guiding Metabolites in Stem Cell Cultures. *Chem* **2016**, *1* (2), 298-319.
- (9) Sugiyasu, K.; Kawano, S.-i.; Fujita, N.; Shinkai, S. Self-Sorting Organogels with p-n Heterojunction Points. *Chemistry of Materials* **2008**, *20* (9), 2863-2865.
- (10) Prasanthkumar, S.; Ghosh, S.; Nair, V. C.; Saeki, A.; Seki, S.; Ajayaghosh, A. Organic Donor-Acceptor Assemblies form Coaxial p-n Heterojunctions with High Photoconductivity. *Angewandte Chemie International Edition* **2015**, *54* (3), 946-950.
- (11) Cross, E. R.; Sproules, S.; Schweins, R.; Draper, E. R.; Adams, D. J. Controlled Tuning of the Properties in Optoelectronic Self-Sorted Gels. *Journal of the American Chemical Society* **2018**, *140* (28), 8667-8670.
- (12) Shigemitsu, H.; Fujisaku, T.; Tanaka, W.; Kubota, R.; Minami, S.; Urayama, K.; Hamachi, I. An adaptive supramolecular hydrogel comprising self-sorting double nanofibre networks. *Nature Nanotechnology* **2018**, *13* (2), 165-172.
- (13) Liu, X.; Li, M.; Liu, J.; Song, Y.; Hu, B.; Wu, C.; Liu, A.-A.; Zhou, H.; Long, J.; Shi, L.; Yu, Z. In Situ Self-Sorting Peptide Assemblies in Living Cells for Simultaneous Organelle Targeting. *Journal of the American Chemical Society* **2022**, *144* (21), 9312-9323.
- (14) Das, A.; Ghosh, S. A generalized supramolecular strategy for self-sorted assembly between donor and acceptor gelators. *Chemical Communications* **2011**, *47* (31), 8922-8924.
- (15) Loos, J. N.; D'Acerno, F.; Vijay Mody, U.; MacLachlan, M. J. Manipulating the Self-Assembly of Multicomponent Low Molecular Weight Gelators (LMWGs) through Molecular Design. *ChemPlusChem* **2022**, *87* (4), e202200026.
- (16) Nagy, K. J.; Giano, M. C.; Jin, A.; Pochan, D. J.; Schneider, J. P. Enhanced Mechanical Rigidity of Hydrogels Formed from Enantiomeric Peptide Assemblies. *Journal of the American Chemical Society* **2011**, *133* (38), 14975-14977.
- (17) Patterson, A. K.; El-Qarra, L. H.; Smith, D. K. Chirality-directed hydrogel assembly and interactions with enantiomers of an active pharmaceutical ingredient. *Chemical Communications* **2022**, *58* (24), 3941-3944.
- (18) Liao, R.; Wang, F.; Guo, Y.; Han, Y.; Wang, F. Chirality-controlled supramolecular donor-acceptor copolymerization with distinct energy transfer efficiency. *Journal of the American Chemical Society* **2022**, *144* (22), 9775-9784.

- (19) Morris, K. L.; Chen, L.; Raeburn, J.; Sellick, O. R.; Cotanda, P.; Paul, A.; Griffiths, P. C.; King, S. M.; O'Reilly, R. K.; Serpell, L. C.; Adams, D. J. Chemically programmed self-sorting of gelator networks. *Nature Communications* **2013**, *4* (1), 1480.
- (20) Draper, E. R.; Wallace, M.; Schweins, R.; Poole, R. J.; Adams, D. J. Nonlinear effects in multicomponent supramolecular hydrogels. *Langmuir* **2017**, *33* (9), 2387-2395.
- (21) McAulay, K.; Dietrich, B.; Su, H.; Scott, M. T.; Rogers, S.; Al-Hilaly, Y. K.; Cui, H.; Serpell, L. C.; Seddon, Annela M.; Draper, E. R.; Adams, D. J. Using chirality to influence supramolecular gelation. *Chemical Science* **2019**, *10* (33), 7801-7806.
- (22) Draper, E. R.; Dietrich, B.; McAulay, K.; Brasnett, C.; Abdizadeh, H.; Patmanidis, I.; Marrink, S. J.; Su, H.; Cui, H.; Schweins, R.; et al. Using small-angle scattering and contrast matching to understand molecular packing in low molecular weight gels. *Matter* **2020**, *2* (3), 764-778.
- (23) Sonani, R. R.; Bianco, S.; Dietrich, B.; Douth, J.; Draper, E. R.; Adams, D. J.; Egelman, E. H. Atomic structures of naphthalene dipeptide micelles unravel mechanisms of assembly and gelation. *Cell Reports Physical Science* **2024**, *5* (2), 101812.
- (24) Sun, H.; Jiang, J.; Xiao, Y.; Du, J. Efficient Removal of Polycyclic Aromatic Hydrocarbons, Dyes, and Heavy Metal Ions by a Homopolymer Vesicle. *ACS Applied Materials & Interfaces* **2018**, *10* (1), 713-722.
- (25) Belova, A. S.; Kononevich, Y. N.; Sazhnikov, V. A.; Safonov, A. A.; Ionov, D. S.; Anisimov, A. A.; Shchegolikhina, O. I.; Alfimov, M. V.; Muzafarov, A. M. Solvent-controlled intramolecular excimer emission from organosilicon derivatives of naphthalene. *Tetrahedron* **2021**, *93*, 132287.
- (26) Chen, Y.; Sun, K.; Sun, H.; Yang, Y.; Han, L.; Zheng, H.; Xing, B. Investigation on parameters optimization to produce hydrochar without carbohydrate carbon. *Science of The Total Environment* **2020**, *748*, 141354.
- (27) Ryzhkina, I. S.; Murtazina, L. I.; Sergeeva, S. Y.; Kostina, L. A.; Sharapova, D. A.; Shevelev, M. D.; Konovalov, A. I. Fluorescence characteristics of aqueous dispersed systems of succinic acid as potential markers of their self-organization and bioeffects in low concentration range. *Environmental Technology & Innovation* **2021**, *21*, 101215.
- (28) Marshall, L. J.; Wallace, M.; Mahmoudi, N.; Ciccone, G.; Wilson, C.; Vassalli, M.; Adams, D. J. Hierarchical Composite Self-Sorted Supramolecular Gel Noodles. *Advanced Materials* **2023**, *35* (n/a), 2211277.
- (29) Ziserman, L.; Lee, H.-Y.; Raghavan, S. R.; Mor, A.; Danino, D. Unraveling the Mechanism of Nanotube Formation by Chiral Self-Assembly of Amphiphiles. *Journal of the American Chemical Society* **2011**, *133* (8), 2511-2517.
- (30) Uesaka, A.; Ueda, M.; Makino, A.; Imai, T.; Sugiyama, J.; Kimura, S. Morphology control between twisted ribbon, helical ribbon, and nanotube self-assemblies with his-containing helical peptides in response to pH change. *Langmuir* **2014**, *30* (4), 1022-1028.
- (31) Randle, R. I.; Ginesi, R. E.; Matsarskaia, O.; Schweins, R.; Draper, E. R. Process dependent complexity in multicomponent gels. *Macromolecular Rapid Communications* **2023**, *44* (4), 2200709.
- (32) Adams, D. J.; Butler, M. F.; Frith, W. J.; Kirkland, M.; Mullen, L.; Sanderson, P. A new method for maintaining homogeneity during liquid-hydrogel transitions using low molecular weight hydrogelators. *Soft Matter* **2009**, *5* (9), 1856-1862.
- (33) Pocker, Y.; Green, E. Hydrolysis of D-glucono- $\delta$ -lactone. I. General acid-base catalysis, solvent deuterium isotope effects, and transition state characterization. *Journal of the American Chemical Society* **1973**, *95* (1), 113-119.

- (34) Jayawarna, V.; Ali, M.; Jowitt, T. A.; Miller, A. F.; Saiani, A.; Gough, J. E.; Ulijn, R. V. Nanostructured Hydrogels for Three-Dimensional Cell Culture Through Self-Assembly of Fluorenylmethoxycarbonyl–Dipeptides. *Advanced Materials* **2006**, *18* (5), 611-614.
- (35) Horgan, C. C.; Rodriguez, A. L.; Li, R.; Bruggeman, K. F.; Stupka, N.; Raynes, J. K.; Day, L.; White, J. W.; Williams, R. J.; Nisbet, D. R. Characterisation of minimalist co-assembled fluorenylmethoxycarbonyl self-assembling peptide systems for presentation of multiple bioactive peptides. *Acta Biomaterialia* **2016**, *38*, 11-22.
- (36) Hsu, S.-M.; Wu, F.-Y.; Lai, T.-S.; Lin, Y.-C.; Lin, H.-C. Self-assembly and hydrogelation from multicomponent coassembly of pentafluorobenzyl-phenylalanine and pentafluorobenzyl-diphenylalanine. *RSC Advances* **2015**, *5* (29), 22943-22946.
- (37) Fleming, S.; Debnath, S.; Frederix, P. W. J. M.; Hunt, N. T.; Ulijn, R. V. Insights into the Coassembly of Hydrogelators and Surfactants Based on Aromatic Peptide Amphiphiles. *Biomacromolecules* **2014**, *15* (4), 1171-1184.
- (38) Fleming, S.; Ulijn, R. V. Design of nanostructures based on aromatic peptide amphiphiles. *Chemical Society Reviews* **2014**, *43* (23), 8150-8177.
- (39) McAulay, K.; Ucha, P. A.; Wang, H.; Fuentes-Caparrós, A. M.; Thomson, L.; Maklad, O.; Khunti, N.; Cowieson, N.; Wallace, M.; Cui, H.; et al. Controlling the properties of the micellar and gel phase by varying the counterion in functionalised-dipeptide systems. *Chemical Communications* **2020**, *56* (29), 4094-4097.
- (40) Fichman, G.; Guterman, T.; Adler-Abramovich, L.; Gazit, E. Synergetic functional properties of two-component single amino acid-based hydrogels. *CrystEngComm* **2015**, *17* (42), 8105-8112.
- (41) Halperin-Sternfeld, M.; Ghosh, M.; Sevostianov, R.; Grigoriants, I.; Adler-Abramovich, L. Molecular co-assembly as a strategy for synergistic improvement of the mechanical properties of hydrogels. *Chemical Communications* **2017**, *53* (69), 9586-9589.
- (42) Liyanage, W.; Nilsson, B. L. Substituent Effects on the Self-Assembly/Coassembly and Hydrogelation of Phenylalanine Derivatives. *Langmuir* **2016**, *32* (3), 787-799.
- (43) Vujičić, N. Š.; Glasovac, Z.; Zweep, N.; van Esch, J. H.; Vinković, M.; Popović, J.; Žinić, M. Chiral Hexa- and Nonamethylene-Bridged Bis(L-Leu-oxalamide) Gelators: The First Oxalamide Gels Containing Aggregates with a Chiral Morphology. *Chemistry – A European Journal* **2013**, *19* (26), 8558-8572.
- (44) Liu, M.; Zhang, L.; Wang, T. Supramolecular chirality in self-assembled systems. *Chemical Reviews* **2015**, *115* (15), 7304-7397.
- (45) Marchesan, S.; Easton, C. D.; Kushkaki, F.; Waddington, L.; Hartley, P. G. Tripeptide self-assembled hydrogels: unexpected twists of chirality. *Chemical Communications* **2012**, *48* (16), 2195-2197.
- (46) Marchesan, S.; Easton, C. D.; Styan, K. E.; Waddington, L. J.; Kushkaki, F.; Goodall, L.; McLean, K. M.; Forsythe, J. S.; Hartley, P. G. Chirality effects at each amino acid position on tripeptide self-assembly into hydrogel biomaterials. *Nanoscale* **2014**, *6* (10), 5172-5180.
- (47) Yang, Z.; Liang, G.; Ma, M.; Gao, Y.; Xu, B. Conjugates of naphthalene and dipeptides produce molecular hydrogelators with high efficiency of hydrogelation and superhelical nanofibers. *Journal of Materials Chemistry* **2007**, *17* (9), 850-854.
- (48) Liang, G.; Yang, Z.; Zhang, R.; Li, L.; Fan, Y.; Kuang, Y.; Gao, Y.; Wang, T.; Lu, W. W.; Xu, B. Supramolecular Hydrogel of a d-Amino Acid Dipeptide for Controlled Drug Release in Vivo. *Langmuir* **2009**, *25* (15), 8419-8422.
- (49) Wignall, G. T.; Bates, F. Absolute calibration of small-angle neutron scattering data. *Journal of Applied Crystallography* **1987**, *20* (1), 28-40.
- (50) Mantid. <https://www.mantidproject.org/> (accessed 2023/04/15).

(51) Cowieson, N. P.; Edwards-Gayle, C. J. C.; Inoue, K.; Khunti, N. S.; Douth, J.; Williams, E.; Daniels, S.; Preece, G.; Krumpa, N. A.; Sutter, J. P.; et al. Beamline B21: high-throughput small-angle X-ray scattering at Diamond Light Source. *Journal of Synchrotron Radiation* **2020**, 27 (5), 1438-1446.

(52) Edwards-Gayle, C. J. C.; Khunti, N.; Hamley, I. W.; Inoue, K.; Cowieson, N.; Rambo, R. Design of a multipurpose sample cell holder for the Diamond Light Source high-throughput SAXS beamline B21. *Journal of Synchrotron Radiation* **2021**, 28 (1), 318-321.

(53) *SasView*. <https://www.sasview.org/> (accessed 2024/04/08).

(54) *NIST neutron activation and scattering calculator*. <https://www.ncnr.nist.gov/resources/activation/> (accessed 2024/04/15).

## **Chapter 3: A Comprehensive Study on Self-Sorting in a Library of Naphthyl Diphenylalanine Diastereomers**

---

Guan, Q. led the synthesis and characterization of the gelators under investigation, utilizing rheological experiments, microscopy, spectroscopy, and circular dichroism. Dr. Squires, A., Liu, W., Bianco, S., and Seddon, Professor A. M. assisted with the collection and analysis of SAXS data, while Xu, T., and Professor Cui, H. assisted in gathering and processing Cryo-TEM images.

### 3.1 Introduction

Low molecular weight gelators (LMWGs) are small molecules that spontaneously form three-dimensional networks within solvents, creating gels that respond to specific stimuli.<sup>1-4</sup> The ability of these gels to dynamically reverse non-covalent interactions gives them a unique responsiveness and broad functional diversity. This makes them particularly valuable in applications such as drug delivery, catalysis, and tissue regeneration.<sup>5-7</sup> Among these, dipeptides featuring a hydrophobic aromatic group and hydrophilic ends are notable for their efficiency and have been the focus of extensive research.<sup>8-10</sup> The main forces driving their self-assembly include  $\pi$ - $\pi$  stacking and hydrogen bonding, crucial for forming stable gel structures.<sup>11, 12</sup>

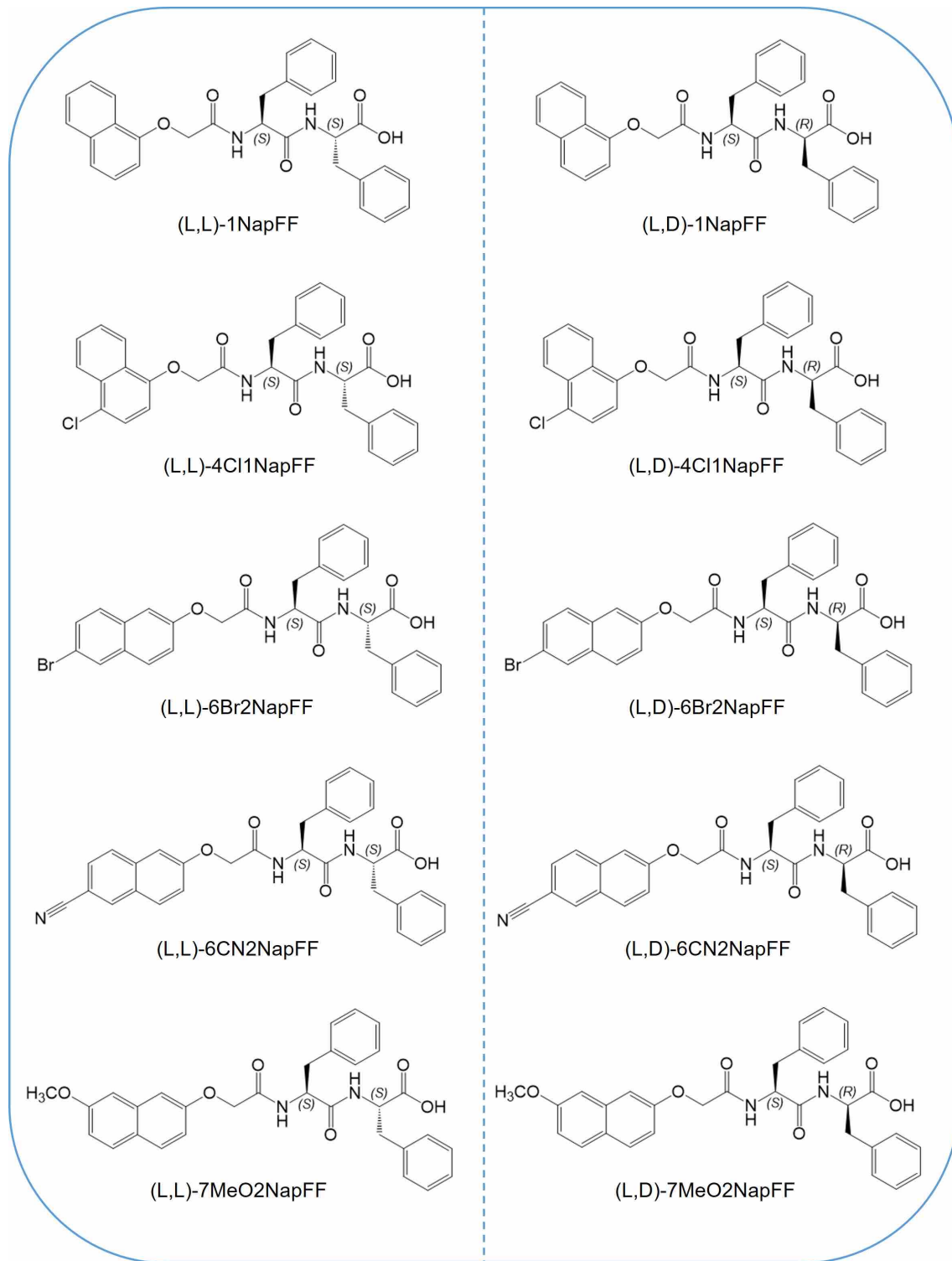
Multicomponent systems mark a significant advancement in material science, enabling the creation of novel materials by combining various gelators. These combinations can lead to either co-assembled structures, where all components merge, or self-sorted structures, where each component remains distinct.<sup>13, 14</sup> Such self-sorting is crucial for applications in optoelectronics and biomimetics.<sup>15, 16</sup> Self-sorting can be achieved through various methods, including differences in size, shape, chirality, and binding motifs, even if the components share similar basic properties, such as  $pK_a$ .<sup>1, 17</sup> However, differences in the apparent  $pK_a$  of two gelators do not always guarantee self-sorting.<sup>18</sup> In chiral self-sorting systems, pairs of enantiomers with opposite chirality, but identical size and shape, are typically used.<sup>14, 19-21</sup> In a detailed investigation covered in Chapter 2, we examined the gelling behavior and performance of binary systems composed of 2NapFF with opposite terminal amino acid chirality.<sup>22</sup> This study is particularly significant because the two gelator precursors differ only in the chirality of their terminal amino acid, highlighting the subtle yet impactful role of molecular symmetry in gel formation.

In this study, we explore a variety of naphthalene dipeptide diastereomers by introducing different substitutions on the naphthalene ring. This strategy allows us to tailor the molecules' structure, thereby altering their physical and chemical properties as well as their ability to form gels. We assessed the rheological and structural properties of multi-component systems based on the concentration ratio of the components. Furthermore, we observed that individual components within two-component systems formed self-assembled nanostructures, demonstrating self-sorting behavior at various scales. This behavior was verified through detailed molecular, microscopic, and bulk-level analyses. Our findings enhance the

understanding of self-sorting phenomena and pave the way for innovative designs of LMWGs, opening new avenues for creating functional and more complex material systems.

## 3.2 Results and Discussion

Here, we investigated a library of naphthyl diphenylalanine (FF) dipeptides with reversed chirality of the terminal amino acids, where the naphthalene rings were functionalized with different groups (Scheme 3-1). Table 3-1 lists the properties of the one-component systems formed by 5 pairs of diastereomers. All gelators except (L,D)-1NapFF formed self-supporting gels at 10 mg/mL concentrations. We investigated the rheological properties, supramolecular assembly patterns, and gelation behavior of binary mixtures containing naphthalene dipeptide diastereomers across various length scales. We aimed to develop a controllable, reproducible, and adaptable methodology for designing self-sorting, multicomponent LMWG systems. Viscosity at  $10 \text{ s}^{-1}$  is chosen because it represents a balanced shear rate, reflecting typical flow behavior during processes like mixing or pumping. Low shear rates can overestimate viscosity, while high shear rates can cause shear thinning. A shear rate of  $10 \text{ s}^{-1}$  avoids these extremes, providing a more accurate measure for real-world applications. Storage Modulus at  $10 \text{ rad s}^{-1}$  is selected to assess a gel's viscoelasticity under moderate oscillatory shear. At low frequencies, gels may appear too solid, while at high frequencies, they may behave like liquids. The  $10 \text{ rad s}^{-1}$  frequency offers a balanced measure of structural integrity, relevant for dynamic or cyclic conditions commonly encountered in mechanical or biological settings.



**Scheme 3-1.** The chemical structures of dipeptides investigated in this research.

**Table 3-1.** Characteristics for solutions and gels formed from the gelators discussed in this chapter as single components at 10 mg/mL concentrations. The symbol \* indicates that the compound cannot form a gel under the investigated experimental conditions.

Gelator	Appearance of solution at pH 10.5	Viscosity at 10 s <sup>-1</sup> (Pa s <sup>-1</sup> )	Appearance of gel at pH 3-4	Storage modulus at 10 rad s <sup>-1</sup> (kPa)	tanδ=G''/G'	pK <sub>a</sub>
(L,L)-7MeO2NapFF	Transparent	0.057	Opaque	45.7	0.17	7.6
(L,D)-7MeO2NapFF	Opaque	0.007	Turbid	17.1	0.14	6.7
(L,L)-6Br2NapFF	Slightly turbid	0.041	Slightly turbid	27.9	0.14	7.8
(L,D)-6Br2NapFF	Turbid	0.025	Turbid	29.6	0.12	7.1
(L,L)-6CN2NapFF	Slightly turbid	0.0054	Slightly turbid	88.8	0.14	7.3
(L,D)-6CN2NapFF	Turbid	0.056	Turbid	31.6	0.12	8.5
(L,L)-1NapFF	Opaque	0.085	Opaque	61.8	0.14	8.8
(L,D)-1NapFF	Turbid	0.0026	Turbid slurry*	1.1	0.12	7.7
(L,L)-4Cl1NapFF	Opaque	0.019	Opaque	38.9	0.22	8.2
(L,D)-4Cl1NapFF	Turbid	0.0084	Turbid	33.0	0.08	7.6

### 3.2.1 7MeO2NapFF

#### 3.2.1.1 Self-Sorting in Multicomponent Solutions at Alkaline pH

Pure (L,L)-7MeO2NapFF and pure (L,D)-7MeO2NapFF formed transparent and turbid solutions at pH 10.5 respectively. In comparison, the solution of (L,L)-7MeO2NapFF gradually shifted from a translucent to a turbid state when diluted by (L,D)-7MeO2NapFF (Figure 3-1a). Changes in absorption intensity at 600 nm are attributed to transmittance caused by scattering rather than dipeptide absorption, providing an approach to assess variations in turbidity.<sup>23, 24</sup> Figure 3-2 illustrates a progressive increase in absorbance at 600 nm with the increase in the (L,D)-7MeO2NapFF component, reaching a peak at a 6:4 ratio before small fluctuations.

Polarized optical microscopy showed highly ordered and aligned birefringent arrangements in samples, with enlarged domain sizes as the ratio of (L,D)-7MeO2NapFF increases. This suggests the presence of anisotropic hierarchical structures within the system (Figure 3-1(b-l)). Shear viscosity data indicated that (L,L)-7MeO2NapFF solution at pH 10.5 was more viscous than the (L,D)-7MeO2NapFF. All solutions showed shear-thinning (or pseudoplastic flow) non-Newtonian fluid behavior as shear rates increased (Figure 3-1m). This phenomenon arises as

applied shear rates align long, anisotropic worm-like micelles/particles along the shear flow direction, diminishing intermolecular interactions and increasing free space.<sup>25, 26</sup> At low shear rates, the viscosity of the (L,D)-7MeO2NapFF solution remained stable, referred to as zero-shear viscosity or Newtonian plateau, until the critical shear rate ( $0.02 \text{ s}^{-1}$ ) is reached, signalling the onset of the shear-thinning region. These findings indicate the existence of highly anisotropic worm-like micelles in these high-viscosity systems. The viscosity at a shear rate of  $10 \text{ s}^{-1}$  exhibited a slight increase with rising ratios, reaching its peak value of  $0.068 \text{ Pa s}^{-1}$  at 8:2, before sharply declining with further increases in the ratio (Figure 3-1n).

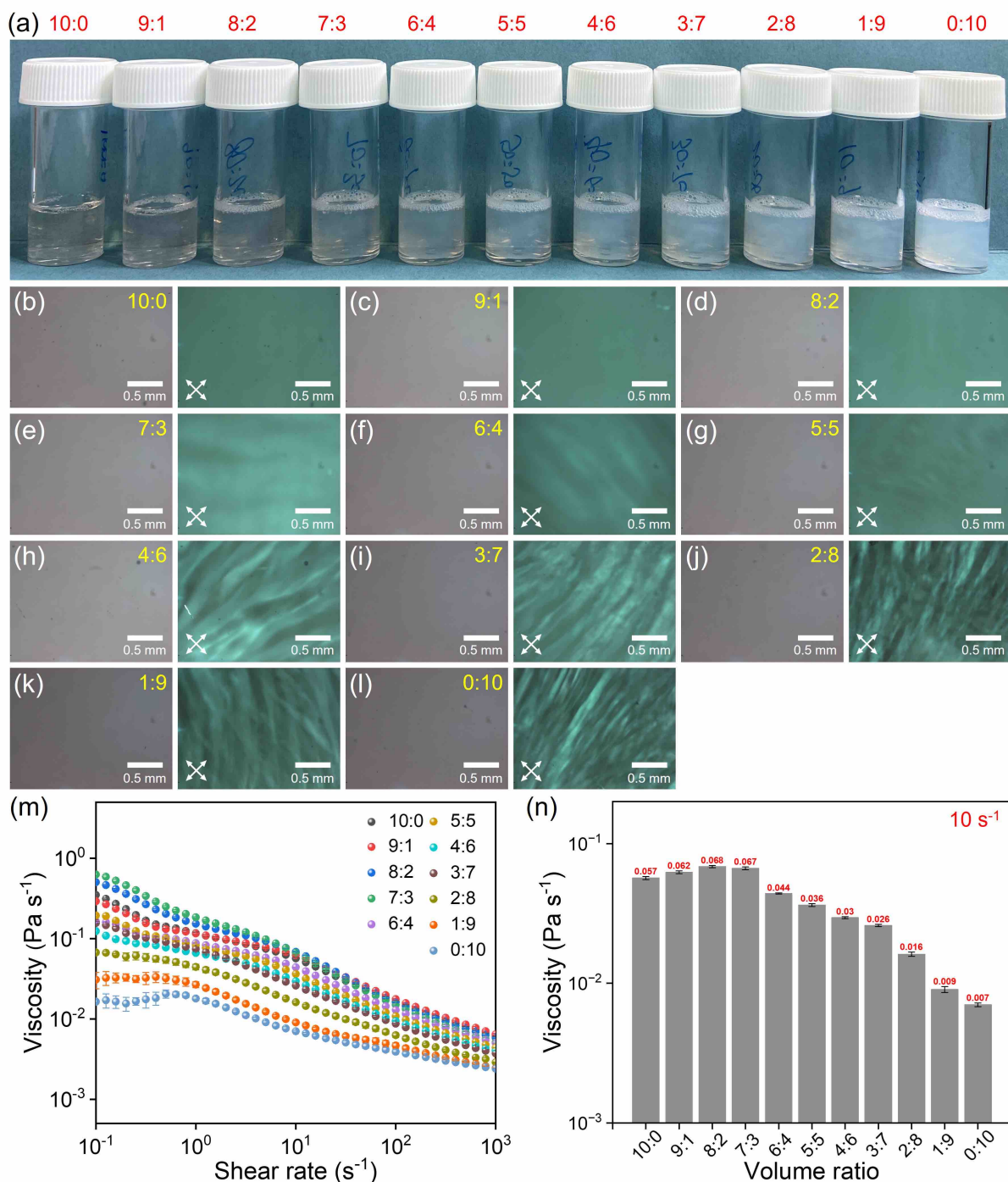


**Figure 3-1.** (a) Photographs of solutions at different ratios of (L,L)-7MeO<sub>2</sub>NapFF:(L,D)-7MeO<sub>2</sub>NapFF, (b-l) optical microscopy images taken under normal light and cross-polarized conditions (magnified at 5×; scale bars represent 500 μm, with white crosses denoting polariser orientations), (m) viscosity measurements of binary solutions at different volume ratios of 10 mg/mL (L,L)-7MeO<sub>2</sub>NapFF:(L,D)-7MeO<sub>2</sub>NapFF stock solutions. (n) A plot illustrating viscosity data at a shear rate of 10 s<sup>-1</sup> plotted against volume ratios. The data points on the graphs

represent the average value of the experimental data of the three samples, and the error bar represents their standard deviation.

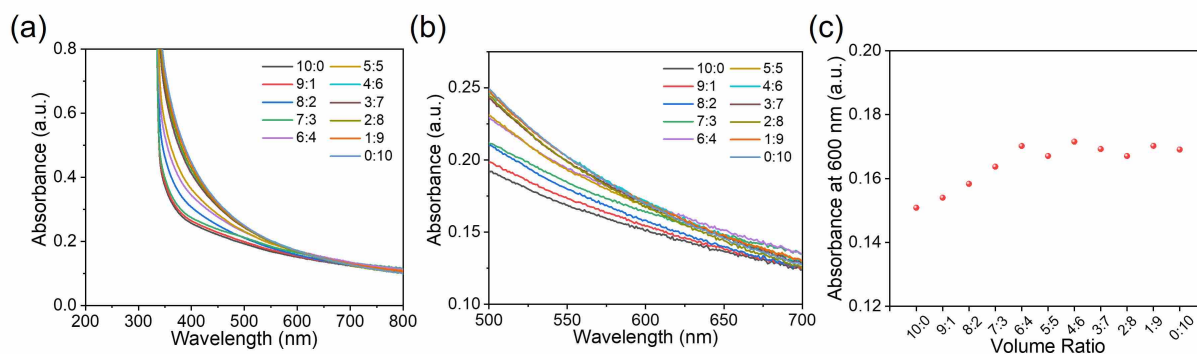


**Figure 3-2.** (a) UV-Vis absorption spectra of solutions containing 10 mg/mL of (L,L)-7MeO<sub>2</sub>NapFF:(L,D)-7MeO<sub>2</sub>NapFF at ratios ranging from 10:0 to 0:10 measured using a 2 mm path length quartz cuvette at 25 °C. (b) Spectra depicted the enlarged regions of the graph (a) at the wavelength range of 500-700 nm. (c) Change in turbidity over composition at 600 nm for binary solutions.

The CD spectrum of 5 mg/mL (L,L)-7MeO<sub>2</sub>NapFF was notably distinct from that of (L,D)-7MeO<sub>2</sub>NapFF, producing a unique and consistent signal for each system (Figure 3-3a). The CD pattern of the combined system resembled the sum of the expected spectral characteristics of individual components, suggesting self-sorting is occurring (Figure 3-3b). The changes in band intensity indicated an overall change in the left- and right-handed structures. The naphthalene chromophore exhibited absorbance in the ranges of 200–230 nm and 240–290 nm. The  $\pi$ - $\pi^*$  transitions of the peptide chromophores are primarily around 195 nm, with a less intense n- $\pi^*$  transition at 220 nm, where substituents typically cause transitions to shift towards longer wavelengths.<sup>27</sup> The signal from the peptide peak partially overlapped with the naphthalene peak, and due to the weaker amplitude of peptide transition compared to the coupling transition of the naphthalene moiety, the spectrum was predominantly dominated by exciton couplets (200–230 nm) originating from the naphthalene group (Figure 3-3c). The induced helicity of naphthalene resulted from dipeptide stacking, potentially causing variations in the direction of the naphthalene signal.<sup>28</sup> Moreover, the existent anisotropy (i.e., fibril arrangement) in the self-assembly system may result in LD artifacts. These factors increase the complexity of CD spectral interpretation. Further elaboration on the explanation of these CD data will be provided in Chapter 4.

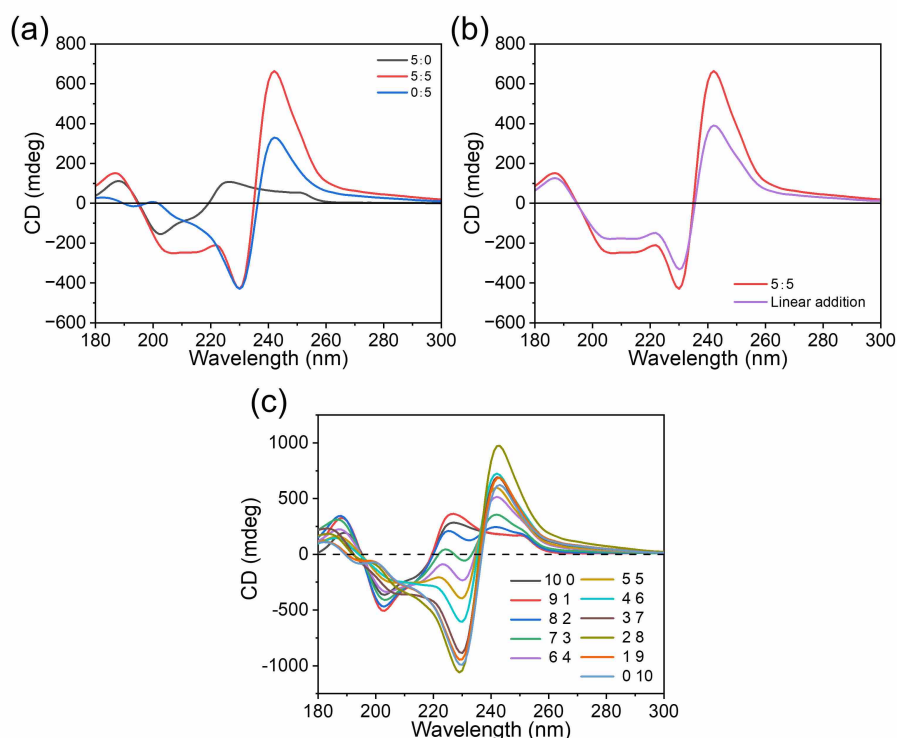


**Figure 3-3.** (a) CD spectra of 5 mg/mL of (L,L)-7MeO<sub>2</sub>NapFF (labelled as 5:0), a mixture with 5:5 ratio of 10 mg/mL (L,L)-7MeO<sub>2</sub>NapFF:(L,D)-7MeO<sub>2</sub>NapFF stock solutions, and 5 mg/mL (L,D)-7MeO<sub>2</sub>NapFF (labelled as 0:5) solutions at pH 10.5. (b) The spectra illustrate a comparison between the 5:5 ratio of 10 mg/mL (L,L)-7MeO<sub>2</sub>NapFF:(L,D)-7MeO<sub>2</sub>NapFF stock solutions and the calculated theoretical self-sorted combination of the 5:0 and 0:5 spectra. (c) CD spectra of solutions containing 10 mg/mL of (L,L)-7MeO<sub>2</sub>NapFF:(L,D)-7MeO<sub>2</sub>NapFF at ratios ranging from 10:0 to 0:10.

Temperature-sensitive CD studies are instrumental in understanding the thermodynamic properties and structural stability of supramolecular assemblies. Such analyses are pivotal for elucidating how variations in peptide stereochemistry influence the self-assembly process and the stability of the structures formed, thereby providing insights critical to the design and application of peptide-based materials. The evolution in the CD data with temperature was recorded to explore the self-sorting behavior in hybrid systems. Within the specified experimental temperature range, the high tension (HT) voltage was lower than 600 V and the total absorbance signal was below the non-linear threshold of the photomultiplier (usually  $\ll 2$  AU) with the HT voltage being proportional to absorbance (Figure 3-4(c-f), Figure 3-5(c-f), and Figure 3-6(c-f)). These show the reliability of the CD data obtained within these conditions. The temperature-dependent CD data obtained from the (L,L)-7MeO<sub>2</sub>NapFF solution revealed a significant alteration in signal intensity and spectral shape following a heat-cooling cycle

ranging from 25 to 85 to 25°C (Figure 3-4(a-b)). This divergence from the initial peak strongly suggested that the self-assembled nanostructures formed by this compound could not withstand elevated temperatures, with the observed change being irreversible. Conversely, the CD data associated with (L,D)-7MeO2NapFF exhibited a similarity to the initial state (Figure 3-5(a-b)), indicating structural integrity despite temperature changes.

Further investigation into binary mixtures with a 5:5 ratio demonstrated that the CD data post-heat-cool cycle was very similar to that of pure (L,D)-7MeO2NapFF (Figure 3-6(a-b)), implying the preservation of the self-assembled nanostructure generated by this component within the two-component system. In the event of co-assembly, it is expected that the structures of individual components would either disintegrate or give rise to novel, distinct architectures. We thus propose that self-sorting prevails in these two-component systems, as evidenced by the retention of structural integrity observed in the temperature-dependent CD spectra.

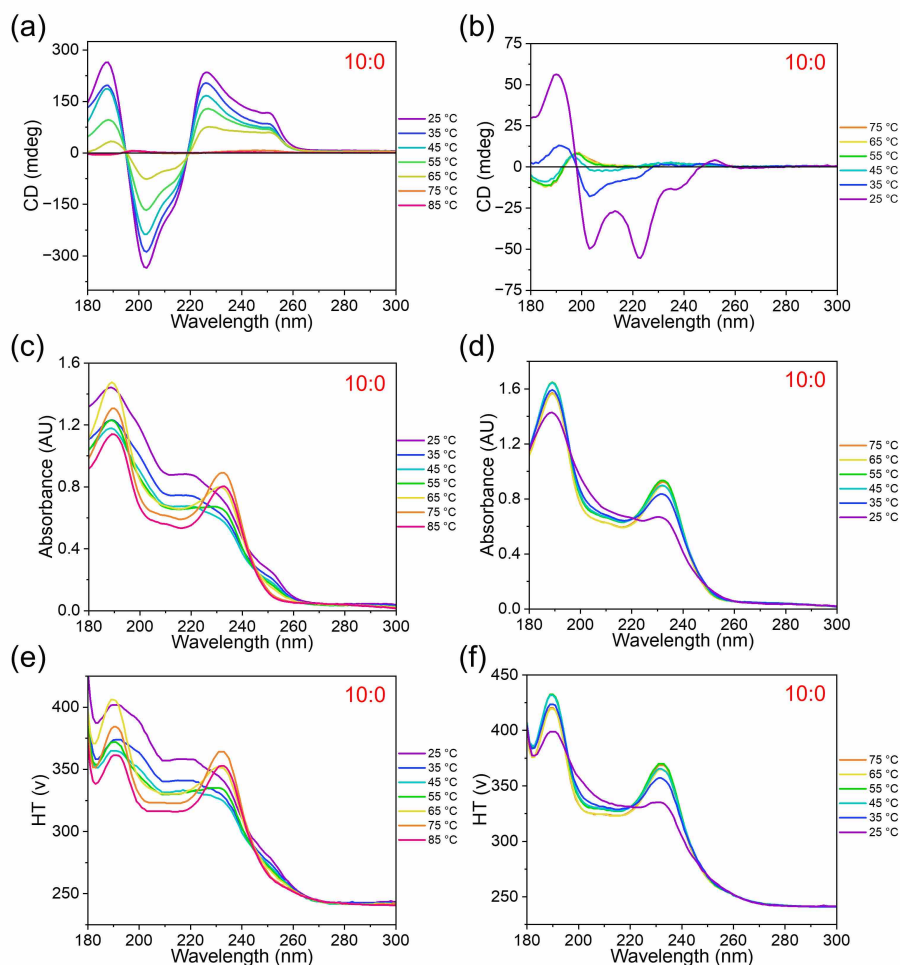


**Figure 3-4.** Temperature-dependent (a-b) CD, (c-d) absorbance, and (e-f) HT data for 10 mg/mL (L,L)-7MeO2NapFF solutions at pH 10.5. (a), (c), and (e) represent the heating process, while (b), (d), and (f) correspond to the cooling process.

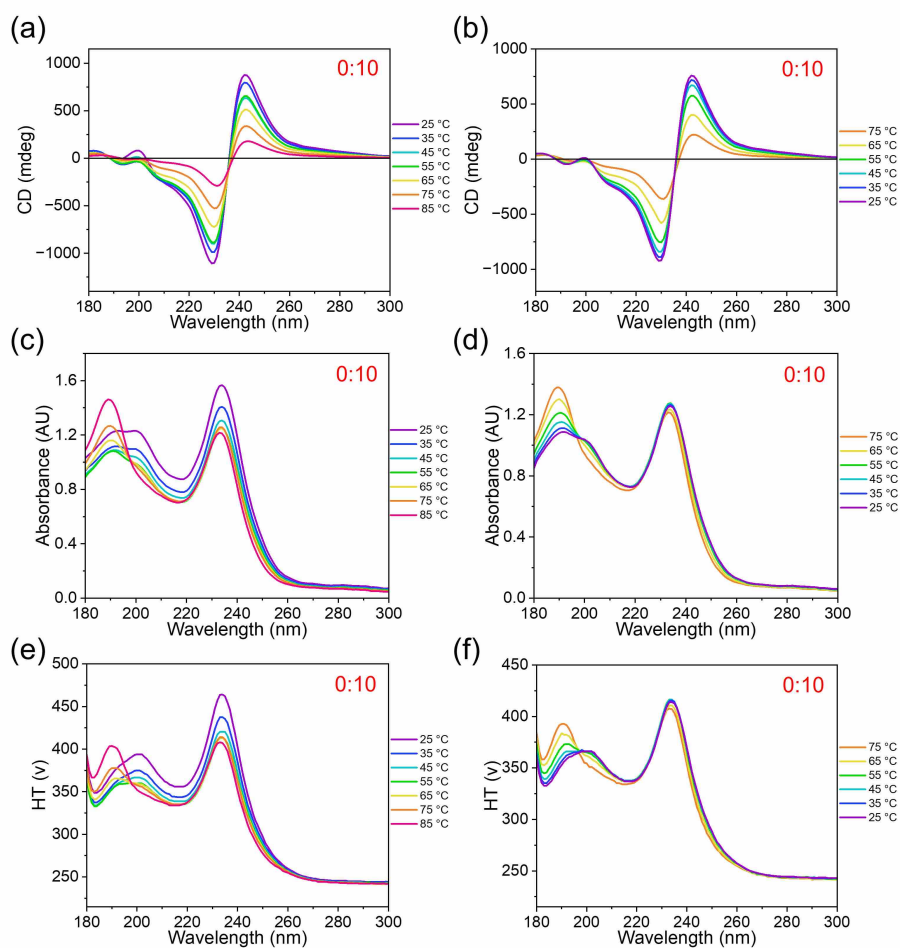


**Figure 3-5.** Temperature-dependent (a-b) CD, (c-d) absorbance, and (e-f) HT data for 10 mg/mL (L,D)-7MeO<sub>2</sub>NapFF solutions at pH 10.5. (a), (c), and (e) represent the heating process, while (b), (d), and (f) correspond to the cooling process.

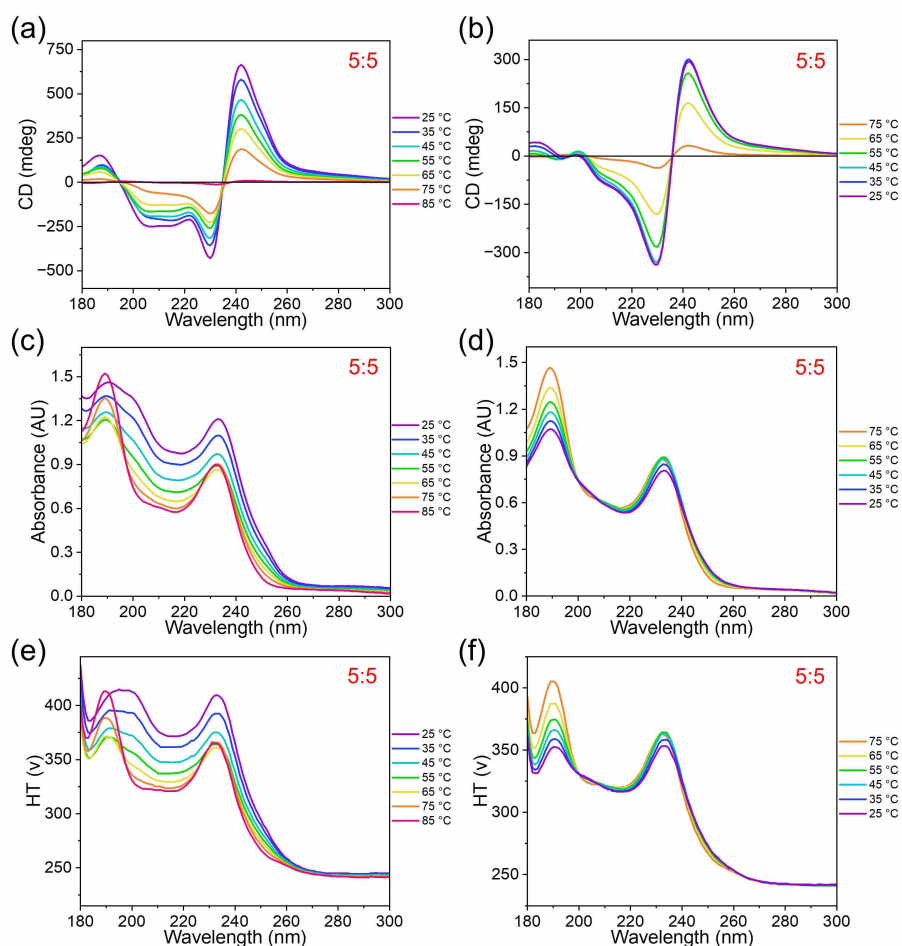


**Figure 3-6.** Temperature-dependent (a-b) CD, (c-d) absorbance, and (e-f) HT data for a mixture with 5:5 ratio of 10 mg/mL (L,L)-7MeO<sub>2</sub>NapFF:(L,D)-7MeO<sub>2</sub>NapFF stock solutions at pH 10.5. (a), (c), and (e) represent the heating process, while (b), (d), and (f) correspond to the cooling process.

Fluorescence spectroscopy was used to investigate molecular interactions within the solutions. The asymmetry detected in the emission spectrum was linked to the existence of oligomeric species (see Figure 3-7a).<sup>29</sup> Notably, the individual solutions emitted strongly at 365 and 356 nm respectively indicating distinct molecular arrangements in each system (see Figure 3-7c). The maximum emission peak was associated with the  $\pi$ - $\pi$  stacking of the naphthalene ring, with the wavelength gradually shifting towards shorter wavelengths and fluorescence intensity increasing as the ratio rose. The normalized spectra show that the solutions with ratios between 10:0 and 4:6 displayed a broad shoulder around 435 nm, with intensity diminishing gradually as the ratio increased (refer to Figure 3-7b). These findings suggest minimal alteration in the local packing of the gelator within the mixed system, indicating that co-assembly is improbable.

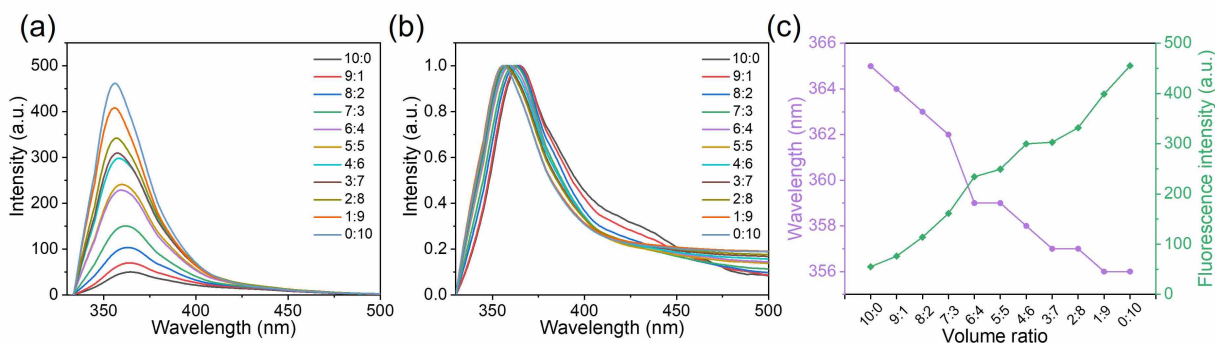


**Figure 3-7.** (a) Fluorescence emission spectrum, (b) normalized spectrum for solutions comprising 10 mg/mL of (L,L)-7MeO<sub>2</sub>NapFF:(L,D)-7MeO<sub>2</sub>NapFF at ratios spanning from 10:0 to 0:10. (c) The plot depicts ratio-dependent wavelength and fluorescence intensity of the maximum emission peak.

Small-angle X-ray Scattering (SAXS) was employed to extract information regarding the supramolecular configuration. As shown in Figure 3-8 and Table 3-2, the fits to the scattering data for (L,L)-7MeO<sub>2</sub>NapFF show that this dipeptide self-assembled into a cylinder with a diameter of  $35.4 \pm 0.1$  Å and a length of  $381 \pm 10$  Å at pH 10.5, while (L,D)-7MeO<sub>2</sub>NapFF formed a more ordered hollow cylindrical structure with a core radius of  $221.6 \pm 0.2$  Å, a wall thickness of  $26.3 \pm 0.3$  Å, and a length of  $892 \pm 10$  Å.

Molecular self-sorting represents the thermodynamically most favorable arrangement of a supramolecular system consisting of two or more molecules.<sup>30</sup> Due to differences in the self-assembled nanostructure, the two micelles do not match during the self-assembly process between chains. The fitting results of the SAXS data corresponding to the binary mixtures support this inference (Figure 3-8 and Table 3-2). SAXS data of two-component solutions at all ratios could be fitted by combining the two models derived from single components with small variations in corresponding parameters except for the 8:2 and 7:3 binary systems. The core radii of the hollow cylinders formed in the 8:2 and 7:3 systems expanded by 20.2 Å and 17.2 Å respectively. Additionally, the wall thickness of the 8:2 binary system diminished by 12.1 Å. The cylinder radius of (L,L)-7MeO<sub>2</sub>NapFF self-assembly gradually reduced as the (L,D) component increased, ultimately reaching 28.4 nm for the 1:9 complex system. This could be ascribed to the altered fiber packing arrangement influenced by the presence of the second compound. To ascertain whether these alterations resulted solely from dilution, the self-assembled nanostructures of the lower-concentration counterparts were examined (Figure 3-11, Figure 3-12, and Table 3-4). In contrast to the 5:5 binary system, the 5 mg/mL single-component solution exhibited distinct parameters. Specifically, the cylinder radius was 0.9 Å greater than

the 5:5 two-component mixture and the thickness of the hollow cylinder wall was 19.3 Å greater. This implied that the micellar structure of each compound was delicately influenced by the other components, rather than simply by dilution.

The self-assembled structures formed by (L,D)-7MeO2NapFF are expected to align due to their aspect ratio, resulting in increased sample rigidity as the proportion of (L,D)-7MeO2NapFF increases. The 2D-SAXS patterns of all collected data are depicted in Figure 3-9. As the amount of (L,D)-7MeO2NapFF increased, the samples exhibited alignment parallel to the long axis of the capillary during 2D-SAXS measurements, leading to enhanced anisotropy.

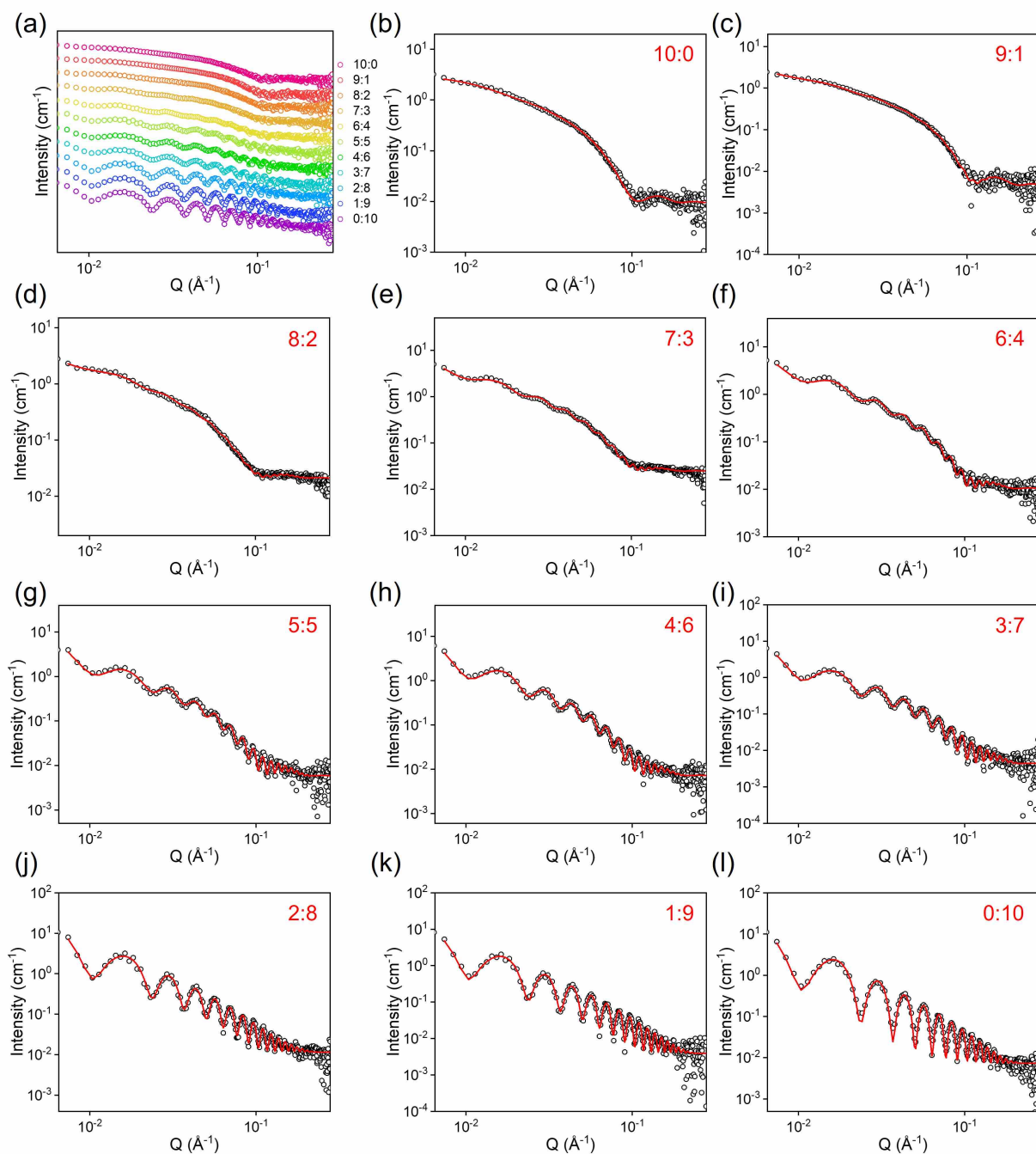


**Figure 3-8.** (a) Experimental SAXS curves (The data were arranged vertically by volume ratio for clear comparison); (b-l) Experimental SAXS profiles (black circle) and corresponding fits (red line) for pre-gelation binary solutions with volume ratios from 10:0 to 0:10 of 10 mg/mL (L,L)-7MeO<sub>2</sub>NapFF:(L,D)-7MeO<sub>2</sub>NapFF stock solutions.

**Table 3-2.** Summary of parameters employed for fitting SAXS data of binary solutions, spanning volume ratios from 10:0 to 0:10, derived from 10 mg/mL stock solutions of (L,L)-7MeO2NapFF:(L,D)-7MeO2NapFF. The abbreviations "C" and "HC" denote the cylinder and hollow cylinder models, respectively.

Ratio	10:0	9:1	8:2	7:3	6:4	5:5	4:6	3:7	2:8	1:9	0:10
Model	C	C+HC	HC								
Scale		1	1	1	1	1	1	1	1	1	
Background	0.009	0.005	0.02	0.02	0.01	0.006	0.007	0.004	0.01	0.004	0.007
Background error	0.0002	0.0002	0.0002	0.0002	0.0002	0.0002	0.0002	0.0002	0.0002	0.0002	0.0002
A scale		$2.9 \times 10^{-5}$	$9.6 \times 10^{-5}$	0.0002	0.0003	0.0003	0.0004	0.0004	0.001	0.001	0.001
A scale error		$8.8 \times 10^{-6}$	$3.4 \times 10^{-5}$	$9.9 \times 10^{-6}$	$1.0 \times 10^{-5}$	$1.2 \times 10^{-5}$	$1.3 \times 10^{-5}$	$1.0 \times 10^{-5}$	$1.6 \times 10^{-5}$	$1.3 \times 10^{-5}$	$1.0 \times 10^{-5}$
A radius (Å)		223.4	241.8	238.8	222.9	223.7	222.5	222.5	223.3	223.4	221.6
A radius error (Å)		5.2	2.9	0.9	0.7	0.7	0.4	0.4	0.2	0.2	0.2
A thickness (Å)		27.4	14.2	27.0	28.5	24.1	25.8	25.6	24.2	23.5	26.3
A thickness error (Å)		9.1	5.6	1.4	1.2	1.0	0.8	0.7	0.4	0.4	0.3
A length (Å)		>1000	>1000	>1000	>1000	723.4	756.2	767.3	799.4	824.6	891.8
A length error (Å)						24.6	19.2	12.9	9.7	9.9	9.9
B scale	0.001	0.0008	0.0009	0.001	0.0008	0.0005	0.0005	0.0003	0.0003	0.0001	
B scale error	$4.8 \times 10^{-6}$	$5.2 \times 10^{-6}$	$5.5 \times 10^{-6}$	$6.8 \times 10^{-6}$	$6.4 \times 10^{-6}$	$5.3 \times 10^{-6}$	$6.0 \times 10^{-6}$	$4.4 \times 10^{-6}$	$6.8 \times 10^{-6}$	$5.0 \times 10^{-6}$	
B radius (Å)	35.4	34.5	34.0	34.1	34.3	33.3	33.3	33.3	30.1	28.4	
B radius error (Å)	0.1	0.1	0.1	0.1	0.1	0.2	0.3	0.2	0.5	0.8	
B length (Å)	380.5	386.9	348.1	505.9	>1000	468.7	479.2	>1000	418.9	>1000	
B length error (Å)	10.2	11.3	8.0	35.5		70.5	69.4		78.3		
$\chi^2$	1.81	1.47	3.15	3.94	2.83	4.23	3.11	2.60	6.13	4.34	4.32

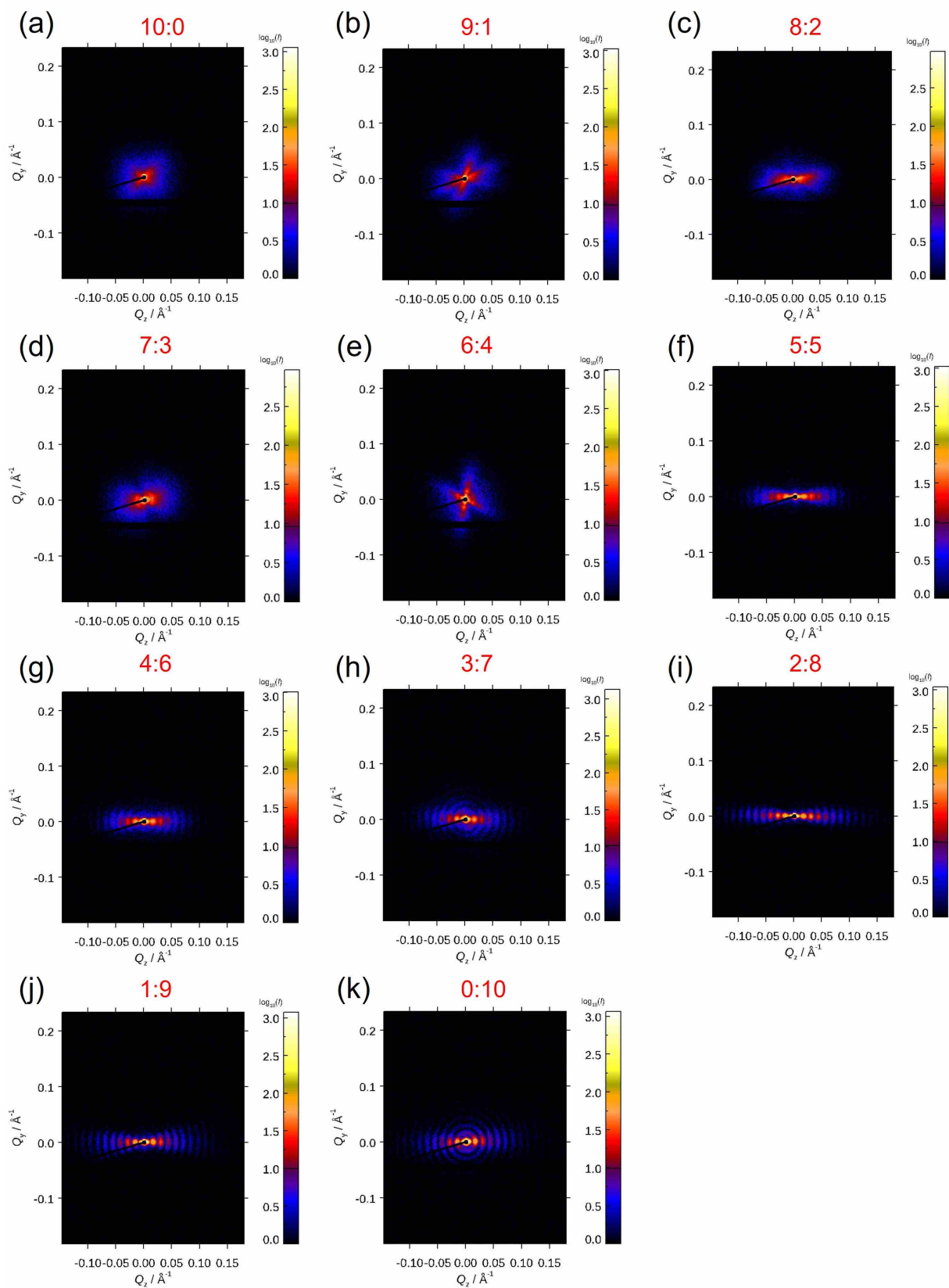


**Figure 3-9.** 2D-SAXS profiles for pre-gelation binary solutions with volume ratios from 10:0 to 0:10 of 10 mg/mL (L,L)-7MeO2NapFF:(L,D)-7MeO2NapFF stock solutions.

Cryo-TEM, collected by Dr. Ravi Sonani (Virginia Tech, USA) corroborated the findings from the SAXS data, indicating the coexistence of thinner structures and larger thin-walled nanotubes within the hybrid systems (Figure 3-10 and Table 3-3). The mixtures were composed of self-sorting micelles at all volume ratios as proved by the combination of SAXS and cryo-TEM. The aggregate length derived from cryo-TEM images was much longer than that from SAXS fits. A possible reason is that the entire  $q$  range of SAXS measurements tends to underestimate larger micelle sizes, and shear-induced elongation may occur during the preparation of cryo-TEM samples, indicating the existence of larger micelles in a medium state.<sup>31</sup> Another possibility might be the absence of a Kuhn length parameter in the hollow cylinder model. However, it is important to note that this inference stems from the fitting process rather than representing an absolute length. Thus, the length derived from the fits is probably a Kuhn length rather than an absolute length and the  $q$  range used in SAXS measurements might not accurately capture larger micelle sizes.

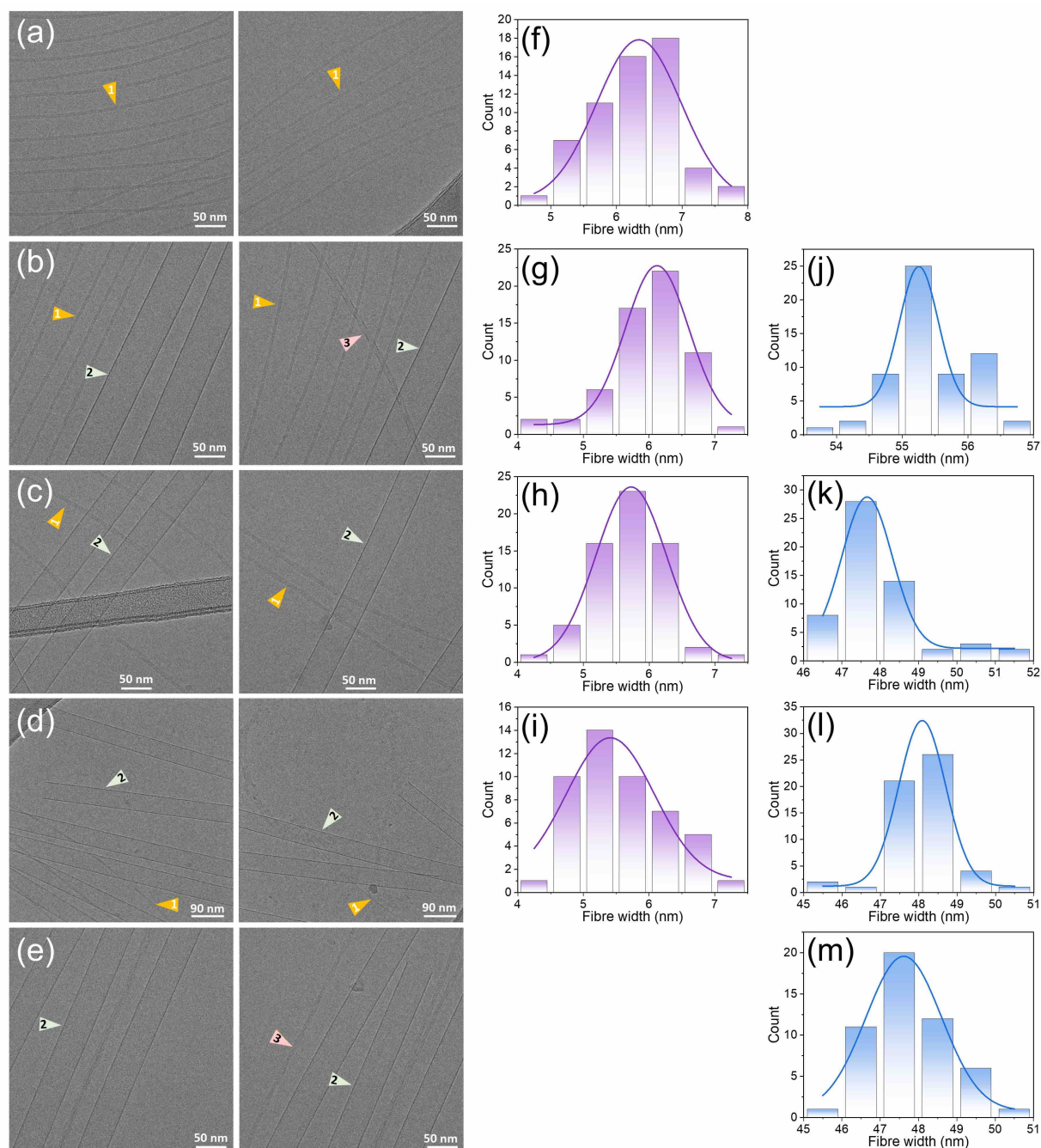


**Figure 3-10.** (a-e) Cryo-TEM images, histogram of width distribution for nanotubes derived from (f-i) (L,L)-7MeO<sub>2</sub>NapFF and (j-m) (L,D)-7MeO<sub>2</sub>NapFF component in pre-gelation binary solutions, covering diverse volume ratios (10:0, 7:3, 5:5, 3:7, and 0:10) of 10 mg/mL (L,L)-7MeO<sub>2</sub>NapFF:(L,D)-7MeO<sub>2</sub>NapFF stock solutions. The coexistence of multi-component and multi-morphological aggregates was highlighted by triangles within the images. The image features triangles that illustrate the coexistence of multi-morph aggregate morphologies. Specifically, the yellow triangle labeled "1" identifies the self-assembled nanofibers of (L,L)-7MeO<sub>2</sub>NapFF, while the light green triangle labeled "2" corresponds to the

self-assembled nanofibers of (L,D)-7MeO2NapFF. Plots in the histogram represent the nonlinear curve fits obtained from the Gaussian function.

**Table 3-3.** An overview of the average diameters of structures present in binary solutions with different volume ratios (10:0, 7:3, 5:5, 3:7, and 0:10) of 10 mg/mL (L,L)-7MeO2NapFF:(L,D)-7MeO2NapFF stock solutions, derived from an analysis of corresponding cryo-TEM images.

Volume ratio	Nanotube width of (L,L)-7MeO2NapFF component	Nanotube width of (L,D)-7MeO2NapFF component
10:0	6.2±0.6 nm	
7:3	6.0±0.6 nm	55.5±0.6 nm
5:5	5.7±0.5 nm	48.0±1.1 nm
3:7	5.6±0.7 nm	48.0±0.8 nm
0:10		47.8±1.1 nm

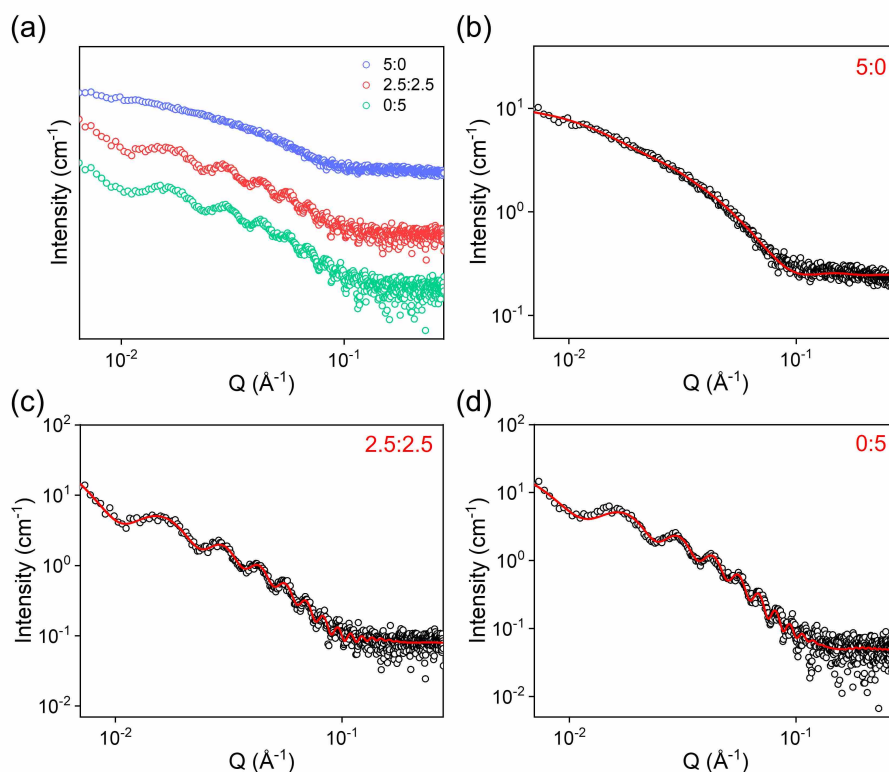


**Figure 3-11.** (a) Experimental SAXS curves (The data were arranged vertically by volume ratio for clear comparison), (b-d) SAXS data (black circle) and fits (red line) for pre-gelation binary solutions with varying volume ratios (5:5, 2.5:2.5, and 0:5) of 5 mg/mL (L,L)-7MeO2NapFF:(L,D)-7MeO2NapFF stock solutions.

**Table 3-4.** Overview of parameters used to fit SAXS data for pre-gelation binary solutions with varying volume ratios (5:5, 2.5:2.5, and 0:5) of 5 mg/mL (L,L)-7MeO2NapFF:(L,D)-7MeO2NapFF stock solutions. The abbreviations C and HC correspond to the cylinder and hollow cylinder respectively.

Ratio	5:0	2.5:2.5	0:5
Model	C	C+HC	HC
Scale		1.00E+00	

Background	0.2	0.08	0.05
Background error	0.0009	0.001	0.0008
A scale		0.0009	0.003
A scale error		$5.8 \times 10^{-5}$	$3.0 \times 10^{-5}$
A radius (Å)		223.7	223.3
A radius error (Å)		1.0	0.5
A thickness (Å)		26.9	43.4
A thickness error (Å)		1.8	0.6
A length (Å)		679.2	80.9
A length error (Å)		31.2	1.0
B scale	0.004	0.002	
B scale error	$2.6 \times 10^{-5}$	$2.6 \times 10^{-5}$	
B radius (Å)	34.2	34.5	
B radius error (Å)	0.2	0.3	
B length (Å)	373.0	433.2	
B length error (Å)	11.4	47.5	
$\chi^2$	1.52	1.36	1.70

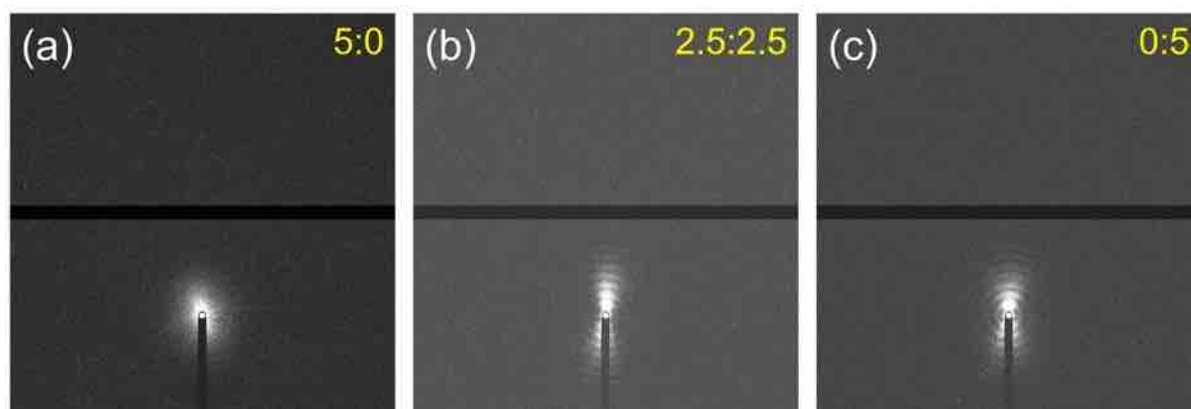


**Figure 3-12.** 2D-SAXS profiles for pre-gelation binary solutions with volume ratios from 5:0, 2.5:2.5 0:5 of 5 mg/mL (L,L)-7MeO2NapFF:(L,D)-7MeO2NapFF stock solutions.

### 3.2.1.2 Self-Sorting in Multicomponent Gels at Acidic pH

Glucono- $\delta$ -lactone (GdL) was used to slowly decrease the pH in the systems described above and trigger gelation which resulted in uniform and reproducible gels while allowing kinetic monitoring such as rheology and pH variations over time.<sup>28, 32</sup> Time-dependent rheology revealed a progressive increase in moduli during gelation, reaching stability around 13 hours (Figure A3-82). In certain cases, the initial storage modulus ( $G'$ ) value surpassed the loss modulus ( $G''$ ), suggesting gel formation before measurement.  $\text{Tan}\delta$  ( $G''/G'$ ) values confirmed the rise in gel stiffness with pH reduction.

Figure 3-13a demonstrates solutions with varying proportions that transformed into self-supporting gels upon mixing with GdL. The turbidity of gels consistently increased with higher portions of (L,D)-7MeO2NapFF components (Figure 3-14). Confocal microscopy (Figure 3-13(b-f)) illustrated the presence of uniformly distributed long and high-density fibers in the gels,

the microstructures commonly observed in gels triggered by pH changes.<sup>33-35</sup> The findings reveal that the worm-like micelle structures, first noted in the solution phase, have now formed into large bundles of dense nanofibers through a hierarchical packing process.<sup>36</sup> A strain sweep was conducted to determine the linear viscoelastic region (LVE region) where testing could occur without disrupting the sample structure.<sup>37</sup> The data in Figure 3-13g show a plateau with constant moduli, with  $G'$  continuously around one order of magnitude higher than  $G''$ , indicating a gel-like or viscoelastic solid behavior. (L,L)-7MeO2NapFF formed a stiffer yet less robust gel at low pH, as evidenced by the higher  $G'$  and a narrower LVE region compared to (L,D)-7MeO2NapFF.  $G'$  exhibited a steady decline post-LVE region, indicating uniform 3D-network breakdown. This implies that the network originated from rigid fibers associated laterally, capable of enduring a degree of strain before sustaining damage. The absence of robust cross-links between these fibers led to the irreversible destruction of the network when subjected to significant strains.

Subsequent oscillatory frequency measurements, performed at a 0.5% strain located at the LVE region, demonstrated frequency-independent properties across all gels (Figure 3-13h). Figure 3-13i highlights the superior mechanical characteristics of hybrid systems compared to (L,D)-7MeO2NapFF, with gels ranging from 4:6 to 2:8 exhibiting even greater stiffness than that of (L,L)-7MeO2NapFF. The enhanced strength of the two-component hydrogels is likely attributed to the extensive and interpenetrating double network formed between the components, which strengthens the overall structure.<sup>38, 39</sup> This interpenetration significantly influences the hydrogel's mechanical properties, confirming possible self-sorting behavior within the system.

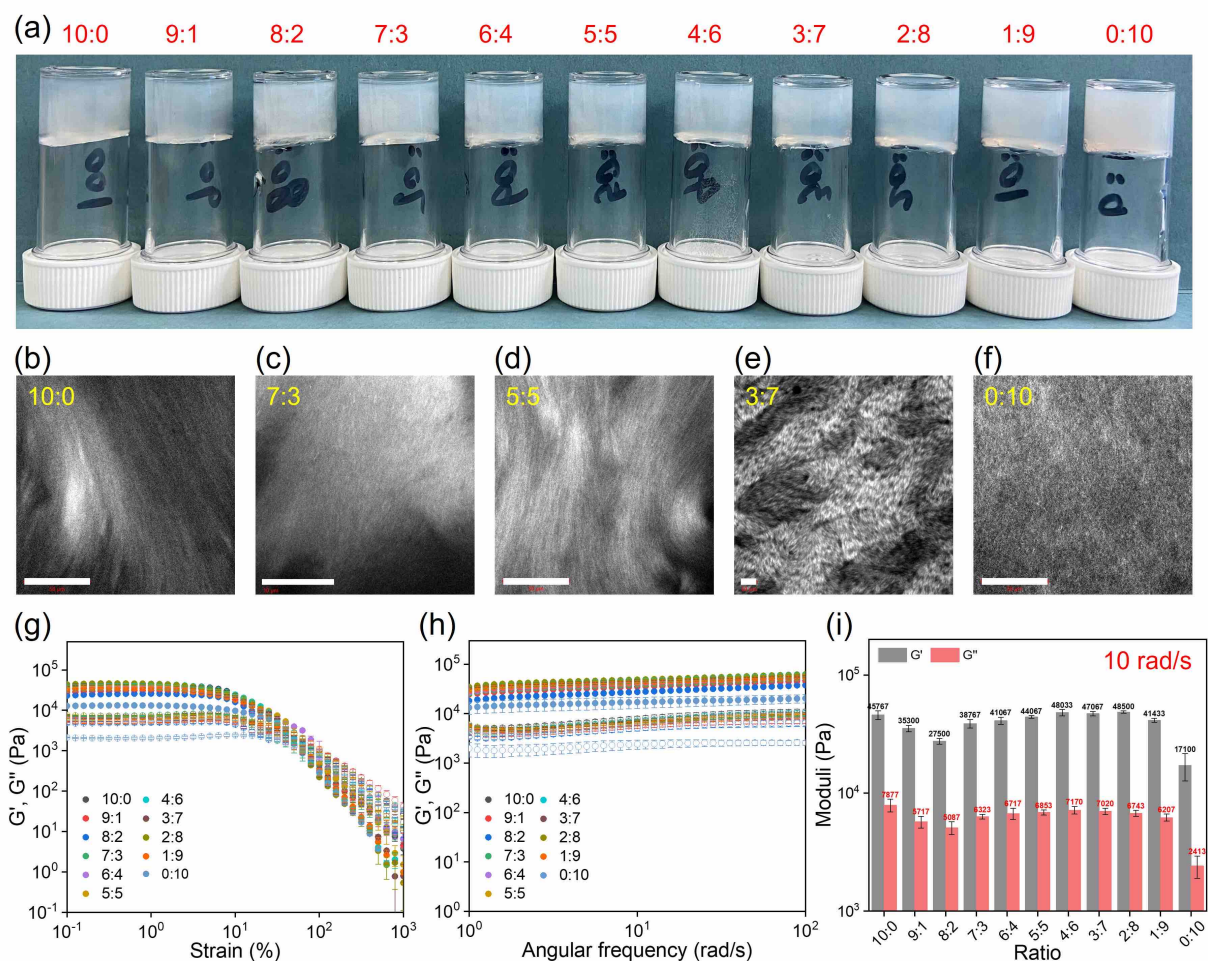


**Figure 3-13.** (a) Photographs, (b-f) confocal fluorescent microscopy images (scale bars indicate 50  $\mu\text{m}$ ), (g) strain sweep, (h) frequency sweep of binary gels at different volume ratios of 10 mg/mL (L,L)-7MeO<sub>2</sub>NapFF:(L,D)-7MeO<sub>2</sub>NapFF stock solutions. (i) A plot illustrating moduli at an angular frequency of 10 rad/s plotted against volume ratios. The data points on the graphs represent the average value of the experimental data of the three samples, and the error bar represents their standard deviation.

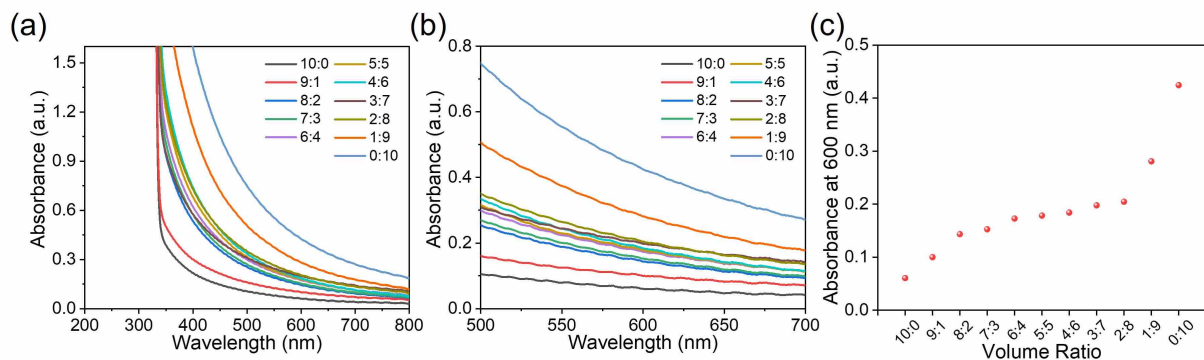


**Figure 3-14.** (a) UV-Vis absorption spectra of gels containing 10 mg/mL of (L,L)-7MeO<sub>2</sub>NapFF:(L,D)-7MeO<sub>2</sub>NapFF at ratios ranging from 10:0 to 0:10 measured using a 2 mm

path length quartz cuvette at 25 °C. (b) Spectra depicted the enlarged regions of the graph (a) at the wavelength range of 500-700 nm. (c) Change in turbidity over composition at 600 nm for binary gels.

The SAXS data of pH-induced individual component gels of (L,L)- and (L,D)-7MeO<sub>2</sub>NapFF could be fitted well by a combined flexible elliptical cylinder plus power law model, with ellipse minor radii of 19.0 Å and 39.8 Å, axial ratios (major radius/minor radius) of 2.3 and 2.4, and Kuhn lengths of 57.3 Å and 116.1 Å, respectively (Figure 3-15 and Table 3-5). The transition from cylindrical structures at pH 10.5 to elliptical structures at acidic pH is presumed to result from the lateral association of cylindrical structures. We speculate that the disparity in apparent  $pK_a$  values between the interior and exterior of (L,D)-7MeO<sub>2</sub>NapFF nanotubes resulted in the collapse of the hollow core during gelation as described for a related system.<sup>40</sup> This collapse disrupted the molecular packing to form cylindrical structures that subsequently associated laterally to form elliptical cylinders. The Kuhn lengths derived from these global fits indicated that the (L,L)-7MeO<sub>2</sub>NapFF exhibited greater flexibility than the (L,D)-7MeO<sub>2</sub>NapF, correlating with the anisotropic profile illustrated by 2D-SAXS images (Figure 3-16). For the two-component gels, the scattering data exhibited good agreement with a combined model comprising two distinct flexible elliptical cylinders derived from individual components (Figure 3-15 and Table 3-5). Notably, these cylinders shared identical parameters with those obtained in the one-component gels, indicating the self-sorting in two gelling components across all investigated compositions. Applying the same combined model to the SAXS data of the 9:1 gel yielded a negative scale associated with (L,D)-7MeO<sub>2</sub>NapFF, despite the best fit being achieved with parameters resembling those of (L,L)-7MeO<sub>2</sub>NapFF. This inconsistency may stem from the minimal proportion of one component in the mixture, which might not have been detectable, hence represented by a single model.

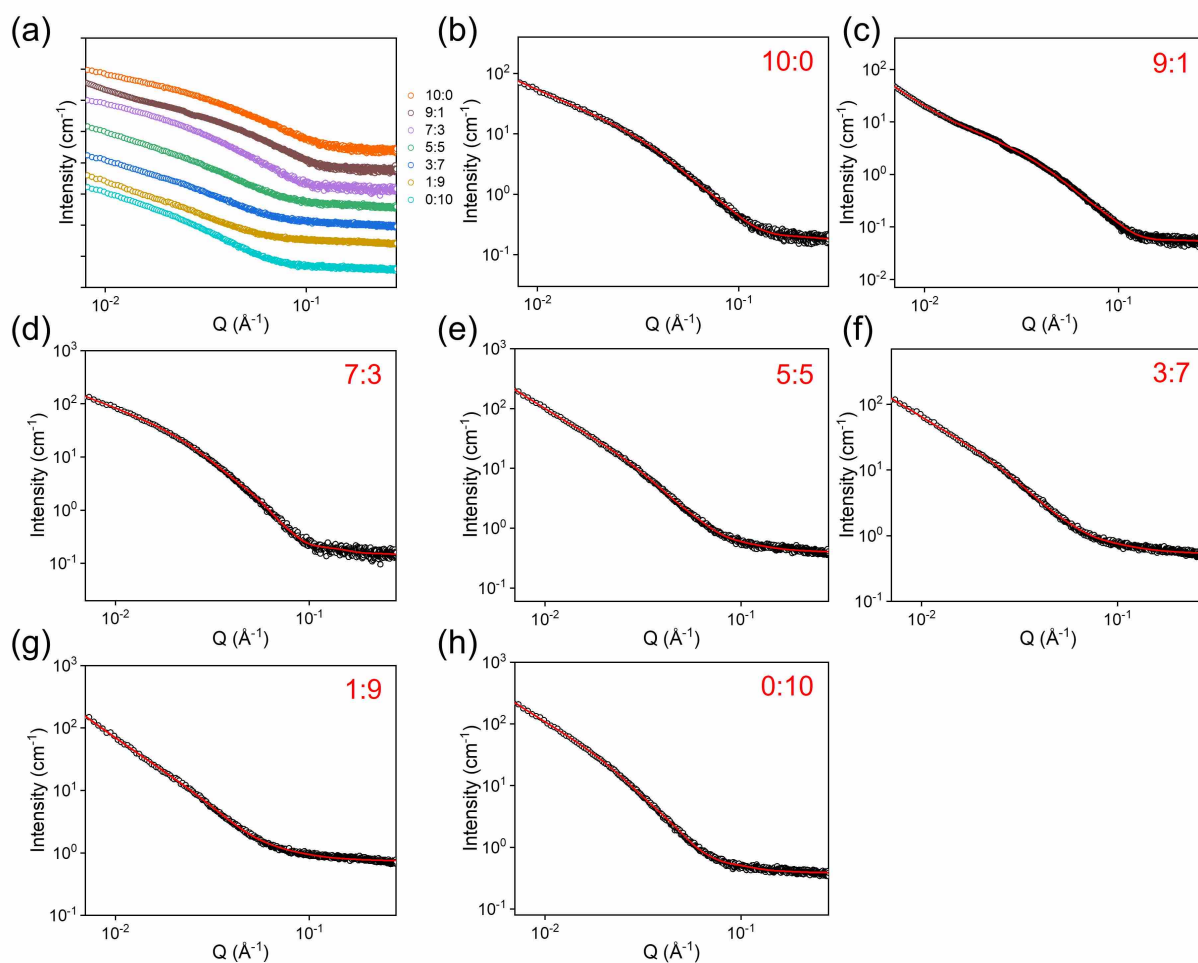


**Figure 3-15.** (a) Experimental SAXS curves (The data were arranged vertically by volume ratio for clear comparison); (b-l) SAXS data (depicted by black circles) and their respective fits (illustrated by red lines) for binary gels with varying volume ratios, ranging from 10:0, 9:1, 7:3, 5:5, 3:7, 1:9, to 0:10, prepared from 10 mg/mL stock solutions of (L,L)-7MeO<sub>2</sub>NapFF:(L,D)-7MeO<sub>2</sub>NapFF.

**Table 3-5.** Summary of parameters used to fit SAXS data for binary gels, encompassing different volume ratios (10:0, 9:1, 7:3, 5:5, 3:7, 1:9, and 0:10) derived from 10 mg/mL stock solutions of (L,L)-7MeO2NapFF:(L,D)-7MeO2NapFF. The abbreviations "FEC" and "PL" represent the flexible elliptical cylinder and power law models.

Ratio	10:0	9:1	7:3	5:5	3:7	1:9	0:10
Model	FEC+PL	FEC	FEC+FEC	FEC+FEC	FEC+FEC	FEC+FEC	FEC+PL
Scale	1	1	1	1	1	1	1
Background	0.2	0.05	0.1	0.4	0.6	0.8	0.4
Background error	0.003	0.0003	0.001	0.001	0.001	0.001	0.001
Power law scale	0.0003						0.0004
Power law scale error	$8.6 \times 10^{-5}$						$3.1 \times 10^{-5}$
Power	2.5						2.4
Power error	0.06						0.03
A scale	0.004	0.001	0.002	0.003	0.002	0.001	
A scale error	$2.6 \times 10^{-4}$	$2.6 \times 10^{-6}$	$3.1 \times 10^{-5}$	$2.1 \times 10^{-5}$	$2.0 \times 10^{-5}$	$1.9 \times 10^{-5}$	
A radius (Å)	19.0	19.0	19.0	19.0	19.0	19.0	
A radius error (Å)	0.7	0.7	0.7	0.7	0.7	0.7	
A kuhn length (Å)	57.3	57.3	57.3	57.3	57.3	57.3	
A_kuhn_length_err (Å)							
A axis ratio	10.9	10.9	10.9	10.9	10.9	10.9	
A axis ratio error	2.3	2.3	2.3	2.3	2.3	2.3	
A length (Å)	0.08	0.08	0.08	0.08	0.08	0.08	
A length error (Å)	572.4	>1000	>1000	>1000	>1000	>1000	>1000
B scale	76.0						
B scale error			0.002	0.002	0.001	0.001	0.002
B radius (Å)			$2.9 \times 10^{-5}$	$1.3 \times 10^{-5}$	$1.1 \times 10^{-5}$	$1.1 \times 10^{-5}$	$6.4 \times 10^{-5}$
B radius error (Å)			39.8	39.8	39.8	39.8	39.8
B kuhn length (Å)			0.6	0.6	0.6	0.6	0.6
B_kuhn_length_err (Å)			116.1	116.1	116.1	116.1	116.1
B axis ratio			8.3	8.3	8.3	8.3	8.3
B axis ratio error			2.4	2.4	2.4	2.4	2.4
B length (Å)			0.04	0.04	0.04	0.04	0.04
B length error (Å)			>1000	>1000	>1000	>1000	>1000
$\chi^2$	1.09	1.64	2.41	2.86	3.58	6.63	1.29

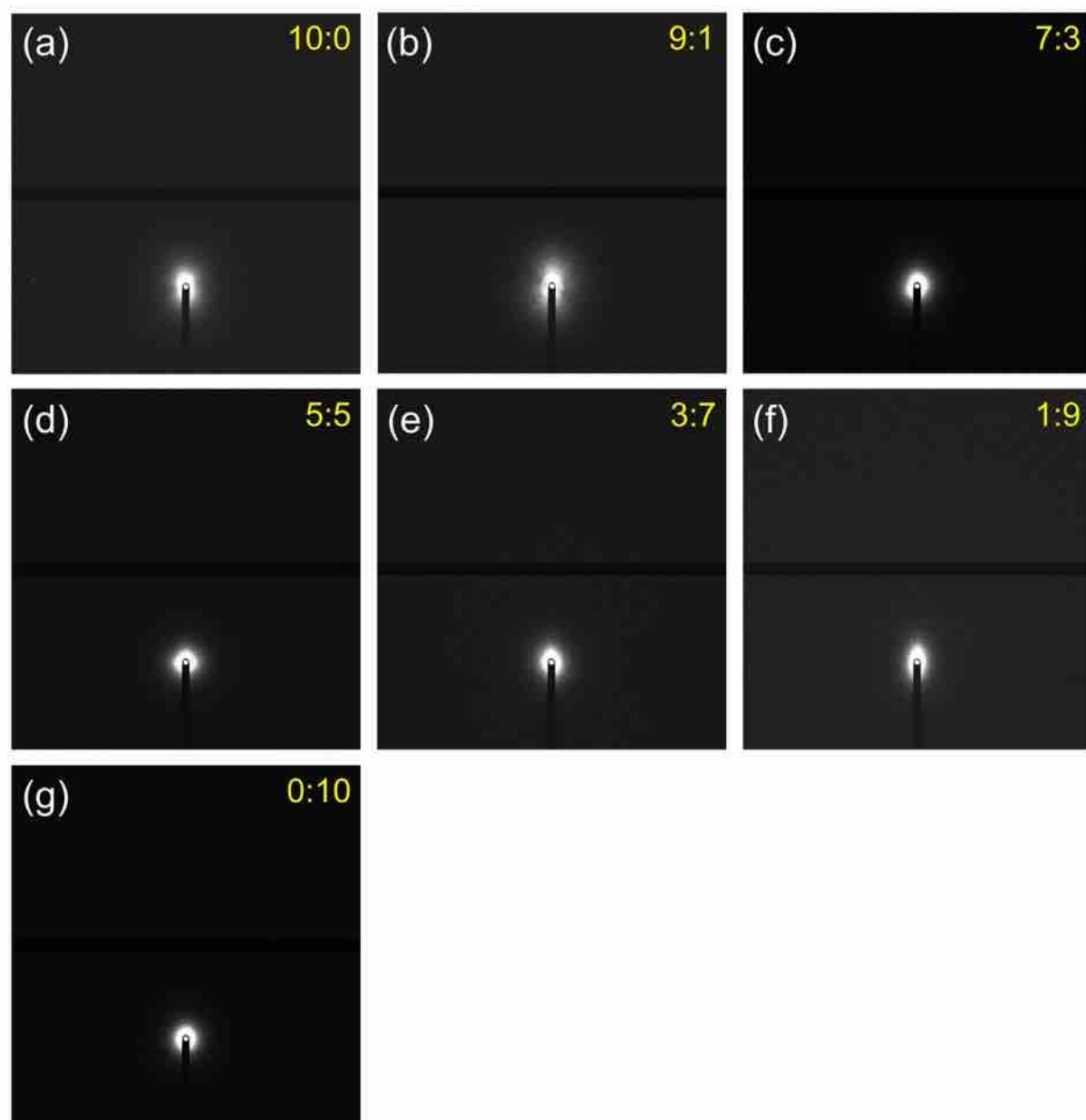


**Figure 3-16.** (a) 2D-SAXS profiles for binary gels with varying volume ratios, ranging from 10:0, 9:1, 7:3, 5:5, 3:7, 1:9, to 0:10, prepared from 10 mg/mL stock solutions of (L,L)-7MeO<sub>2</sub>NapFF:(L,D)-7MeO<sub>2</sub>NapFF.

The fluorescence emission peak of the single-component gels exhibited distinct shifts from the solutions (365 to 356 nm for (L,L)-7MeO<sub>2</sub>NapFF and 356 to 358 nm for (L,L)-7MeO<sub>2</sub>NapFF), suggesting alterations in molecular interactions during gelation, which was consistent with the SAXS data (Figure 3-17a and b). An increase in the fluorescence intensity of the maximum emission peak correlated with the ratio, suggesting co-assembly was impossible among the mixed components (Figure 3-17c). Moreover, the maximum emission peak of the resulting gels

fluctuated between 355 and 358 nm, suggesting the potential absence of a specific order within the aggregates forming the gel network.

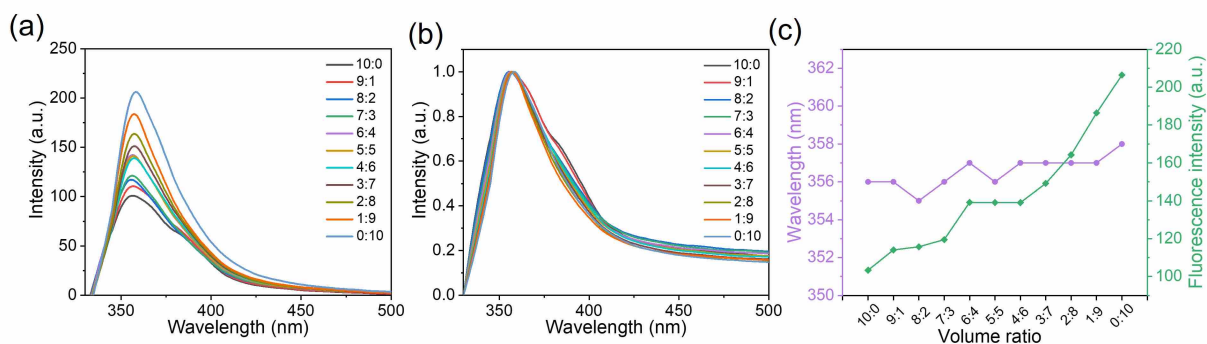


**Figure 3-17.** (a) Fluorescence emission spectrum, (b) normalized spectrum for gels comprising 10 mg/mL of (L,L)-7MeO<sub>2</sub>NapFF:(L,D)-7MeO<sub>2</sub>NapFF at ratios spanning from 10:0 to 0:10. (c) Spectra depicted the expanded regions of the graph (b) at the wavelength range of 340-385 nm.

### 3.2.2 6Br2NapFF

At a concentration of 10 mg/mL and a pH of 10.5, (L,L)-6Br<sub>2</sub>NapFF and (L,D)-6Br<sub>2</sub>NapFF formed a turbid, viscous solution (Figure 3-18a). The turbidity of the binary solutions increased almost linearly upon dilution with (L,D)-6Br<sub>2</sub>NapFF (Figure A3-84). Optical microscopy images reveal highly aligned birefringent domains in all solutions, with the ordered area gradually diminishing as the portion of (L,D)-6Br<sub>2</sub>NapFF increases (Figures 3-18(b-l)), indicating the presence of aligned fibres or worm-like micelles. Additionally, flow sweep analysis demonstrated that a shear rate of 2.5 s<sup>-1</sup> was necessary to induce flow for (L,L)-6Br<sub>2</sub>NapFF solutions (Figure 3-18m). All the solutions exhibited shear-thinning behavior. The combination of (L,L)-6Br<sub>2</sub>NapFF and (L,D)-6Br<sub>2</sub>NapFF resulted in more viscous two-component solutions across all ratios compared to the individual counterparts, as evidenced by a slight increase in viscosity at a shear rate of 10 s<sup>-1</sup> (Figure 3-18n). Moreover, the similar viscosity observed in binary solutions suggests comparable underlying structures.

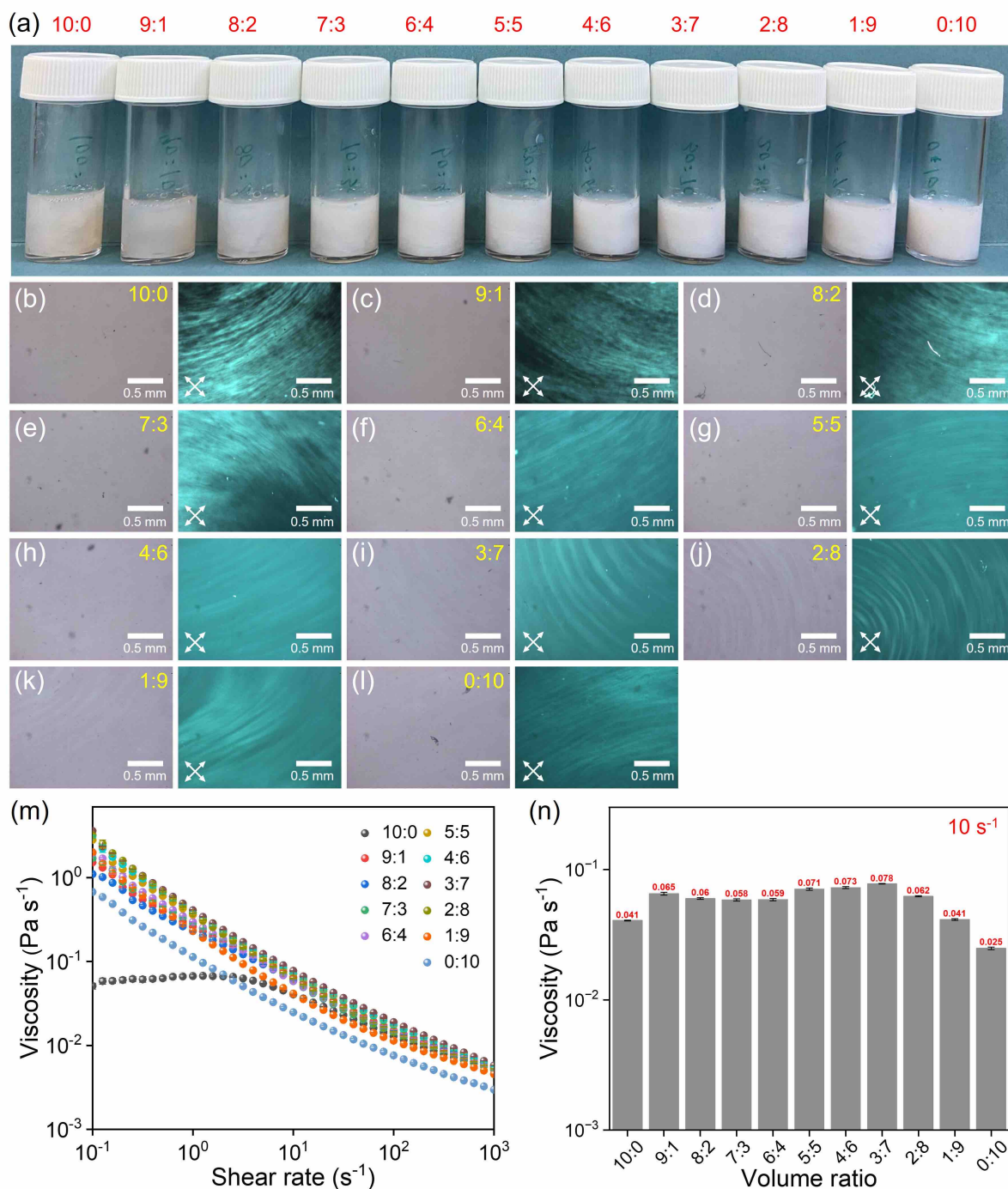


**Figure 3-18.** (a) Photographs of solutions, (b-l) optical microscopy images taken under normal light and cross-polarized conditions (magnified at 5 $\times$ ; scale bars indicated 500  $\mu\text{m}$ , with white crosses denoting polariser orientations), (m) viscosity measurements of binary solutions at different volume ratios of 10 mg/mL (L,L)-6Br2NapFF:(L,D)-6Br2NapFF stock solutions. (n) A plot illustrating viscosity data at a shear rate of 10 s<sup>-1</sup> plotted against volume ratios. The data points on the graphs represent the average value of the experimental data of the three samples, and the error bar represents their standard deviation.

CD data were collected to evaluate how combining the diastereomers impacts the secondary structure of the self-assembled aggregates. The CD spectra obtained from the 5:5 mixed solution revealed absorbance signals at approximately 188 nm, 230 nm, and 242 nm, consistent with theoretical calculations derived from two single components (refer to Figure 3-19b). The notable distinction was observed in the 200-220 nm region: the 5:0 solution exhibited a single negative absorption peak at 208 nm, whereas the 5:5 mixture displayed a double peak at 205 nm and 218 nm, resembling the characteristics seen in the 10:0 solution (see Figure 3-19c). This indicates that a single component within the mixed system is not fully diluted by the other component, instead tending to retain its self-assembled structure at higher concentrations. Furthermore, Figure 3-19c demonstrates that the CD signal representing the chiral self-assembled aggregates decreases with higher proportions of (L,D)-6Br2NapFF across all ratios. This strongly suggests the occurrence of self-sorting in this binary system.

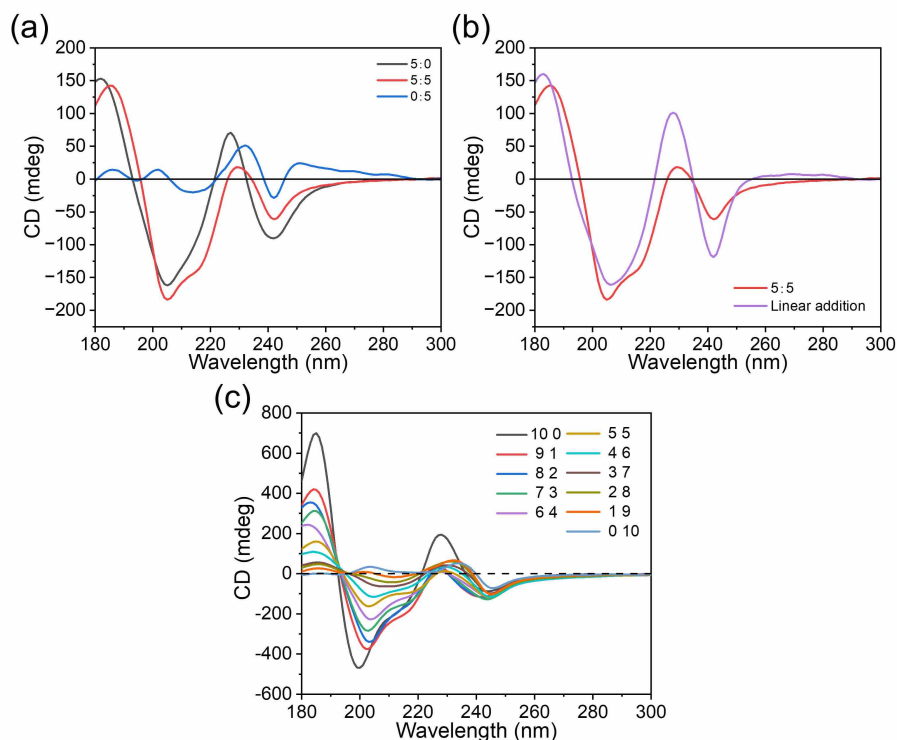


**Figure 3-19.** (a) CD spectra of 5 mg/mL of (L,L)-6Br2NapFF (labeled as 5:0), a mixture with 5:5 ratio of 10 mg/mL (L,L)-6Br2NapFF:(L,D)-6Br2NapFF stock solutions, and 5 mg/mL (L,D)-6Br2NapFF (labeled as 0:5) solutions at pH 10.5. (b) The spectra illustrate a comparison between the 5:5 ratio of 10 mg/mL (L,L)-6Br2NapFF:(L,D)-6Br2NapFF stock solutions and the calculated theoretical self-sorted combination of the 5:0 and 0:5 spectra. (c) CD spectra of solutions containing 10 mg/mL of (L,L)-6Br2NapFF:(L,D)-6Br2NapFF at ratios ranging from 10:0 to 0:10.

The temperature-dependent CD data for the (L,L)-6Br2NapFF solution were similar to the initial state (Figure 3-20(a-b)), suggesting that its self-assembled structure remains stable at elevated temperatures. In contrast, the CD data of the (L,D)-6Br2NapFF solution changed between 180–220 nm during heating (Figure 3-21(a-b)), with no recovery observed upon cooling. These results indicate that the self-assembled structures formed by this compound undergo irreversible alterations at high temperatures. Regarding the 5:5 binary mixture, the CD characteristics throughout the heat-cooling cycle consistently matched those of the initial state (Figure 3-22(a-b)). This finding implies that the presence of the second component enhances the thermal stability of the supramolecular structure formed by another component the mixed system.

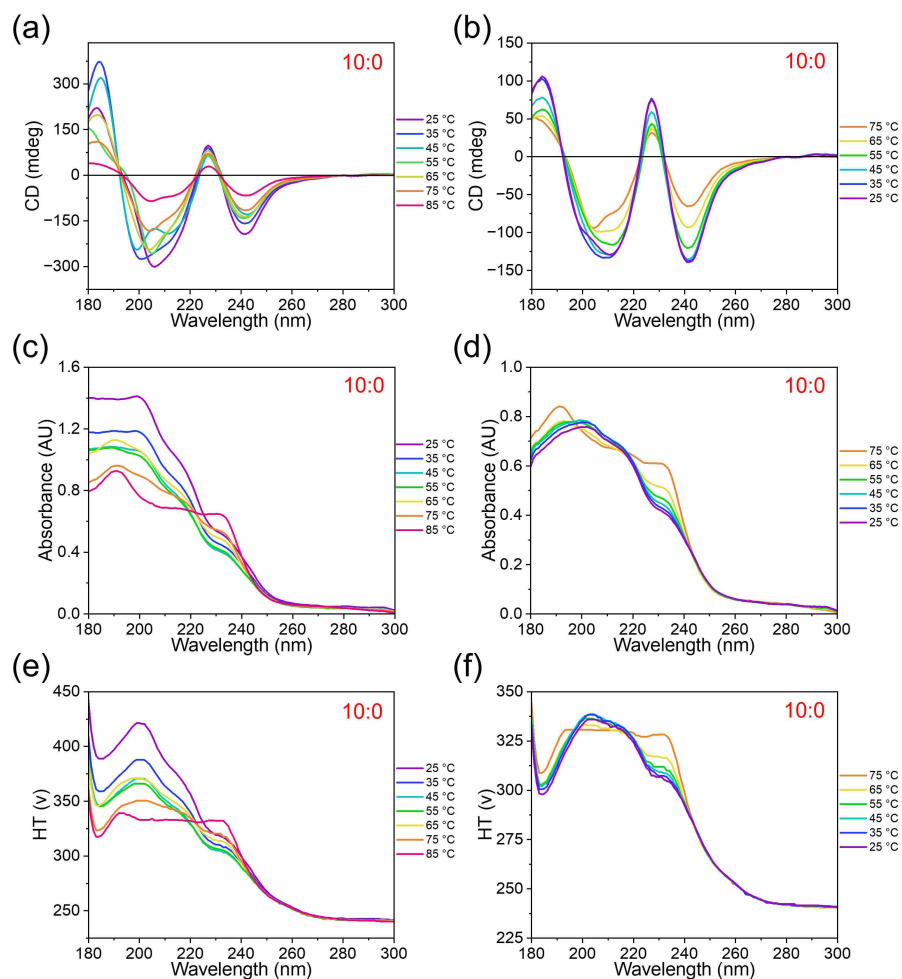


**Figure 3-20.** Temperature-dependent (a-b) CD, (c-d) absorbance, and (e-f) HT data for 10 mg/mL (L,L)-6Br2NapFF solutions at pH 10.5. (a), (c), and (e) represent the heating process, while (b), (d), and (f) correspond to the cooling process.

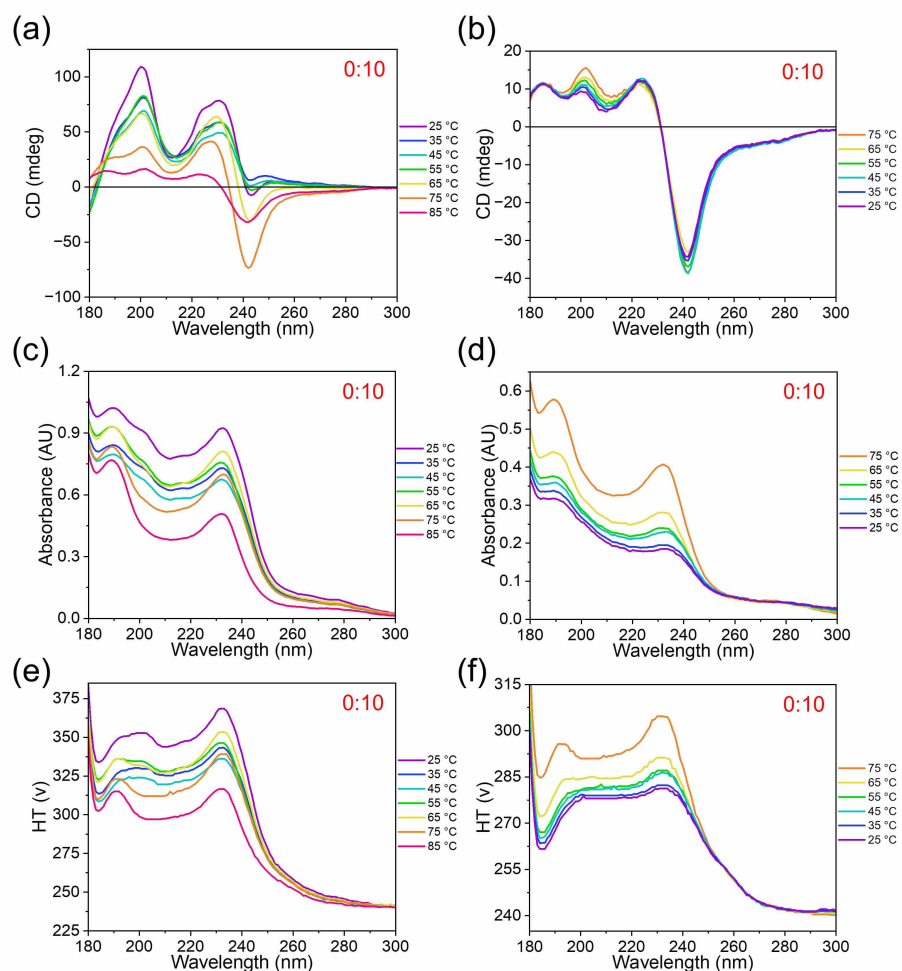


**Figure 3-21.** Temperature-dependent (a-b) CD, (c-d) absorbance, and (e-f) HT data for 10 mg/mL (L,D)-6Br<sub>2</sub>NapFF solutions at pH 10.5. (a), (c), and (e) represent the heating process, while (b), (d), and (f) correspond to the cooling process.

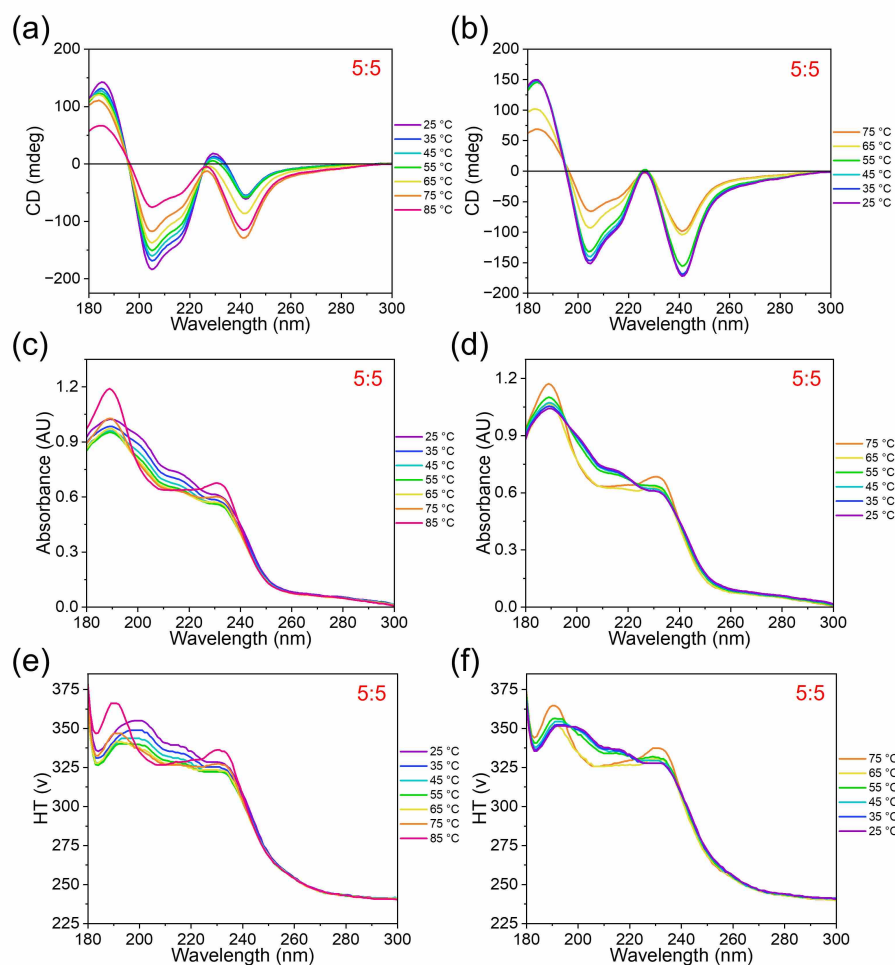


**Figure 3-22.** Temperature-dependent (a-b) CD, (c-d) absorbance, and (e-f) HT data for a mixture with a 5:5 ratio of 10 mg/mL (L,L)-6Br2NapFF:(L,D)-6Br2NapFF stock solutions at high pH. (a), (c), and (e) represent the heating process, while (b), (d), and (f) correspond to the cooling process.

SAXS was again used to study nanofiber structures. The SAXS data for (L,D)-6Br2NapFF at pH 10.5 reveals a prominent Bragg peak at  $Q = 0.189 \text{ \AA}^{-1}$  ( $d = 33.2 \text{ \AA}$ ), suggesting the formation of large crystalline-like aggregates with extended molecular order, that is, the accumulation of individual self-assembled fibers into larger bundles with crystalline-like ordering and periodic arrangement (Figure 3-23a).<sup>41, 42</sup> (L,L)-6Br2NapFF formed cylindrical nanofibers (diameter:  $35.2 \pm 0.1 \text{ \AA}$ , length:  $385.7 \pm 7.8 \text{ \AA}$ ) under alkaline pH, while (L,D)-6Br2NapFF self-assembled into elliptical cylinders (minor radius:  $141.6 \pm 0.3 \text{ \AA}$ , axis ratio:  $2.1 \pm 0.01$ , length:  $203.2 \pm 0.3 \text{ \AA}$ ) (Figure 3-23 and Table 3-6). The scattering at low  $Q$  was well-fitted by a power law model. Analysis of the SAXS data for the binary mixture revealed that the assembly mode of the two components is self-sorting, as evidenced by the combination of two models derived from the individual components, consistent with the CD data. 2D-SAXS patterns revealed intensity

modulations denoting higher anisotropy in (L,L)-6Br2NapFF fibers compared to (L,D)-6Br2NapFF. Decreasing (L,L)-6Br2NapFF content resulted in reduced orientation, suggesting increased isotropy (Figure 3-24).

The SAXS data of half-concentration counterparts were examined (Figure 3-25, Figure 3-26, and Table 3-7). Compared to the 5:5 binary system, the cylinder radius in the 5:0 ratio solution increased by 5.0 Å, and the ellipse cylinder radius and axis ratio in the 0:5 ratio solution decreased by 5.7 Å and 1.8, respectively. This suggests mutual influence between components, beyond simple dilution.

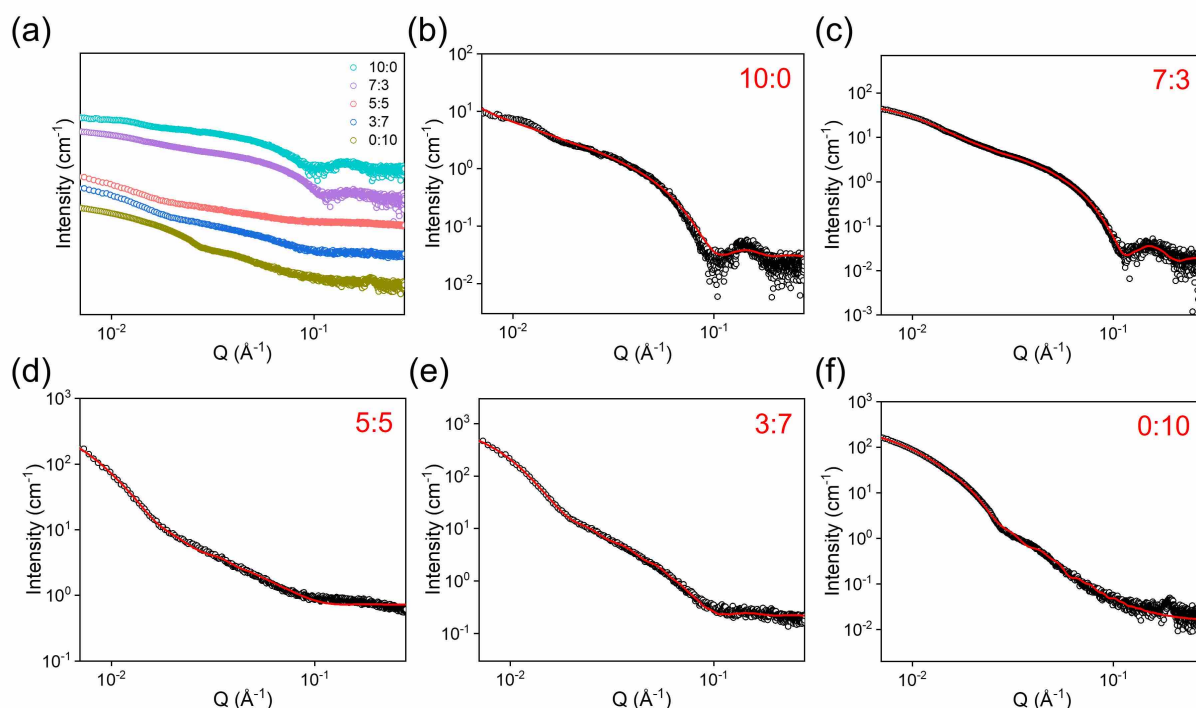


**Figure 3-23.** (a) Experimental SAXS curves (The data were arranged vertically by volume ratio for clear comparison); (b-f) SAXS data (depicted by black circles) and their respective fits (illustrated by red lines) for pre-gelation binary solutions with varying volume ratios, ranging from 10:0, 7:3, 5:5, 3:7, to 0:10, prepared from 10 mg/mL stock solutions of (L,L)-6Br2NapFF:(L,D)-6Br2NapFF.

**Table 3-6.** Summary of parameters used to fit SAXS data for binary solutions, encompassing different volume ratios (10:0, 7:3, 5:5, 3:7, and 0:10) derived from 10 mg/mL stock solutions of (L,L)-6Br2NapFF:(L,D)-6Br2NapFF before gelation. The abbreviations "C", "EC", and "PL" represent the cylinder, elliptical cylinder, and power law models, respectively.

Ratio	10:0	7:3	5:5	3:7	0:10
Model	C+PL	C+EC	C+EC	C+EC	EC+PL
Scale	1	1	1	1	1
Background	0.03	0.02	0.7	0.2	0.02
Background error		0.0004	0.002	0.001	0.0004

Chapter 3: A Comprehensive Study on Self-Sorting in a Library of Naphthyl Diphenylalanine Diastereomers

Power law scale	$1.5 \times 10^{-8}$				$1.4 \times 10^{-5}$
Power law scale error	$3.0 \times 10^{-9}$				$3.2 \times 10^{-7}$
Power	3.9				3.1
Power error	0.04				0.006
A scale		0.001	0.003	0.008	0.003
A scale error		$3.5 \times 10^{-6}$	$2.1 \times 10^{-5}$	$2.3 \times 10^{-5}$	$8.9 \times 10^{-6}$
A radius (Å)		132.6	148.8	151.9	141.6
A radius error (Å)		0.7	0.8	0.4	0.3
A axis ratio		1.4	3.0	2.4	2.1
A axis ratio error		0.02	0.1	0.03	0.01
A length (Å)		471.3	456.0	417.5	203.2
A length error (Å)		2.4	3.3	1.4	0.3
B scale	0.003	0.008	0.008	0.009	
B scale error	$8.0 \times 10^{-6}$	$9.5 \times 10^{-6}$	$6.6 \times 10^{-5}$	$4.3 \times 10^{-5}$	
B radius (Å)	35.2	33.3	27.7	34.4	
B radius error (Å)	0.07	0.03	0.2	0.1	
B length (Å)	385.7	238.7	414.4	380.8	
B length error (Å)	7.8	2.2	36.2	21.6	
$\chi^2$	2.73	<1	6.43	2.57	2.84

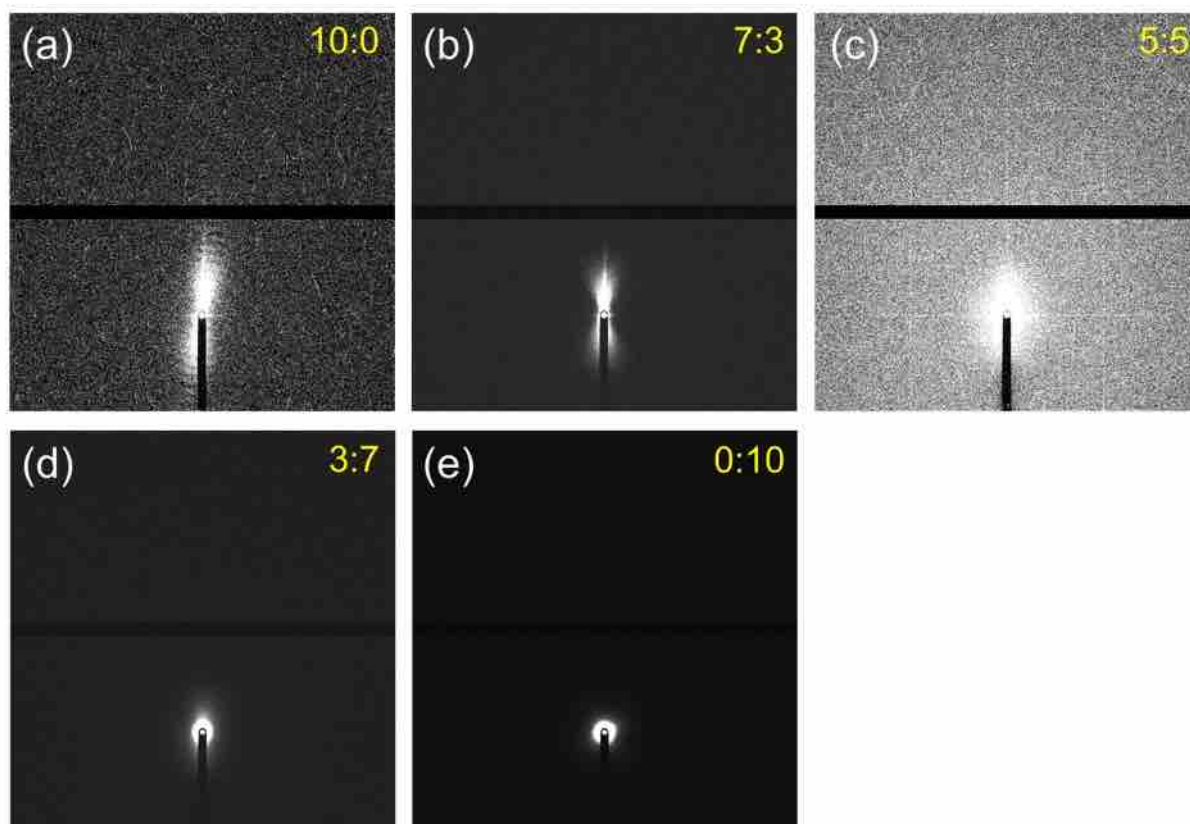


**Figure 3-24.** 2D-SAXS profiles for pre-gelation binary solutions with volume ratios from 10:0, 7:3, 5:5, 3:7, to 0:10 of 10 mg/mL (L,L)-6Br2NapFF:(L,D)-6Br2NapFF stock solutions.

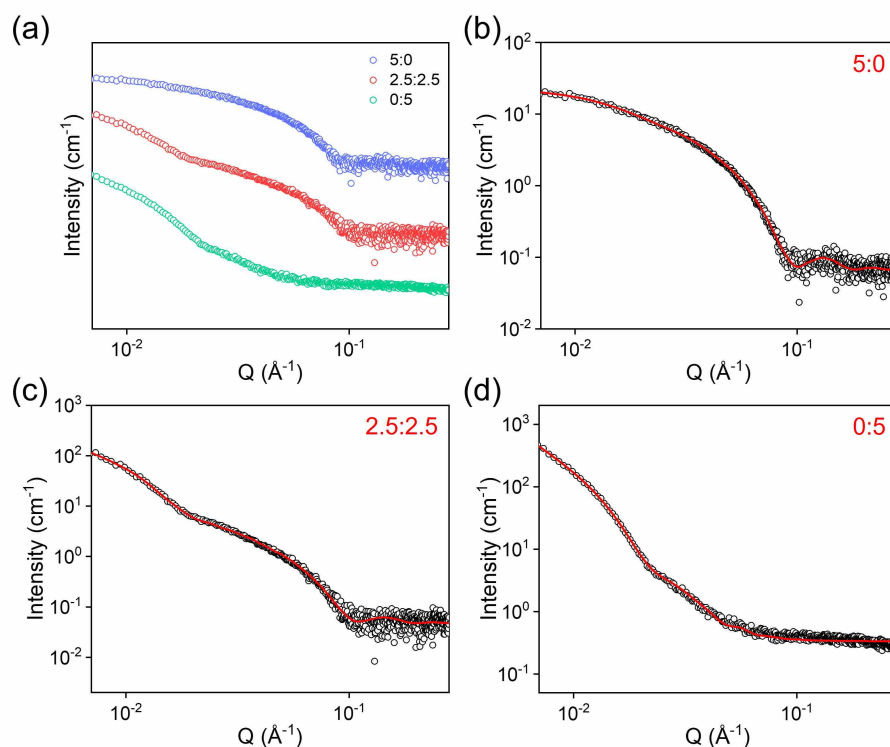


**Figure 3-25.** (a) Experimental SAXS curves (The data were arranged vertically by volume ratio for clear comparison); (b-d) SAXS data (depicted by black circles) and their respective fits (illustrated by red lines) for pre-gelation binary solutions with varying volume ratios including 5:0, 2.5:2.5 and 0:5 prepared from 5 mg/mL stock solutions of (L,L)-6Br2NapFF and (L,D)-6Br2NapFF.

**Table 3-7.** Summary of parameters used to fit SAXS data for binary solutions, encompassing different volume ratios (5:0, 2.5:2.5, and 0:5) derived from 5 mg/mL stock solutions of (L,L)-6Br2NapFF and (L,D)-6Br2NapFF before gelation. The abbreviations "C", "EC", and "PL" represent the cylinder, elliptical cylinder, and power law models, respectively.

Ratio	5:0	2.5:2.5	0:5
Model	C	C+EC	EC+PL
Scale		1	1
Background	0.07	0.05	0.3
Background error	0.0007	0.0007	0.001
Power law scale			$4.2 \times 10^{-6}$
Power law scale error			$2.4 \times 10^{-7}$
Power			3.6
Power error			0.02
A scale		0.002	0.005
A scale error		$1.2 \times 10^{-5}$	$7.2 \times 10^{-5}$
A radius (Å)		<b>151.0</b>	<b>143.1</b>
A radius error (Å)		1.2	0.5
A axis ratio		1.5	1.5
A axis ratio error		0.03	0.01
A length (Å)		962.3	>1000
A length error (Å)		16.1	
B scale	0.008	0.005	

B scale error	$3.0 \times 10^{-5}$	$2.8 \times 10^{-5}$	
B radius (Å)	<b>38.7</b>	<b>35.1</b>	
B radius error (Å)	0.1	0.2	
B length (Å)	326.6	491.7	
B length error (Å)	4.9	39.0	
$\chi^2$	1.21	1.46	2.50

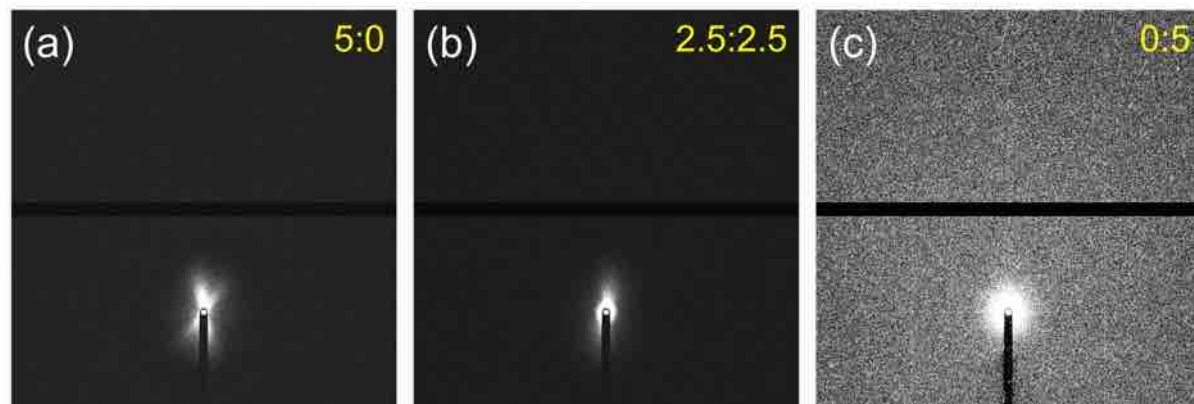


**Figure 3-26.** 2D-SAXS profiles for pre-gelation binary solutions with volume ratios from 5:0, 2.5:2.5 0:5 of 5 mg/mL (L,L)-6Br2NapFF:(L,D)-6Br2NapFF stock solutions.

Turning to hydrogels at acidic pH, both (L,L)- and (L,D)-6Br2NapFF can form self-supporting gels with comparable moduli (see Figure 3-27a and Figure 3-27(g-i)). Consequently, the resulting hybrid systems are classified as two-gelator systems. As the content of the (L,D)-6Br2NapFF component increased, the turbidity of the gel continued to rise (see Figure A3-86). Confocal microscopy (see Figure 3-27(b-f)) revealed the presence of densely and evenly distributed long fibers within the gel. Figure 3-27g exhibits a plateau where  $G'$  is approximately an order of magnitude higher than  $G''$ , indicating a gel state across all ratios. Beyond the yield point, the modulus steadily decreased with increasing strain, signifying uniform destruction of the gel network. Oscillation frequency measurements confirmed the frequency-independent characteristics of all gels (Figure 3-27h). Figure 3-27i shows that the stiffness of two-component gels initially declined slightly and then increased after a 2:8 ratio as the percentage of (L,D)-6Br2NapFF increased, compared to single-component gels at a frequency of 10 rad/s.

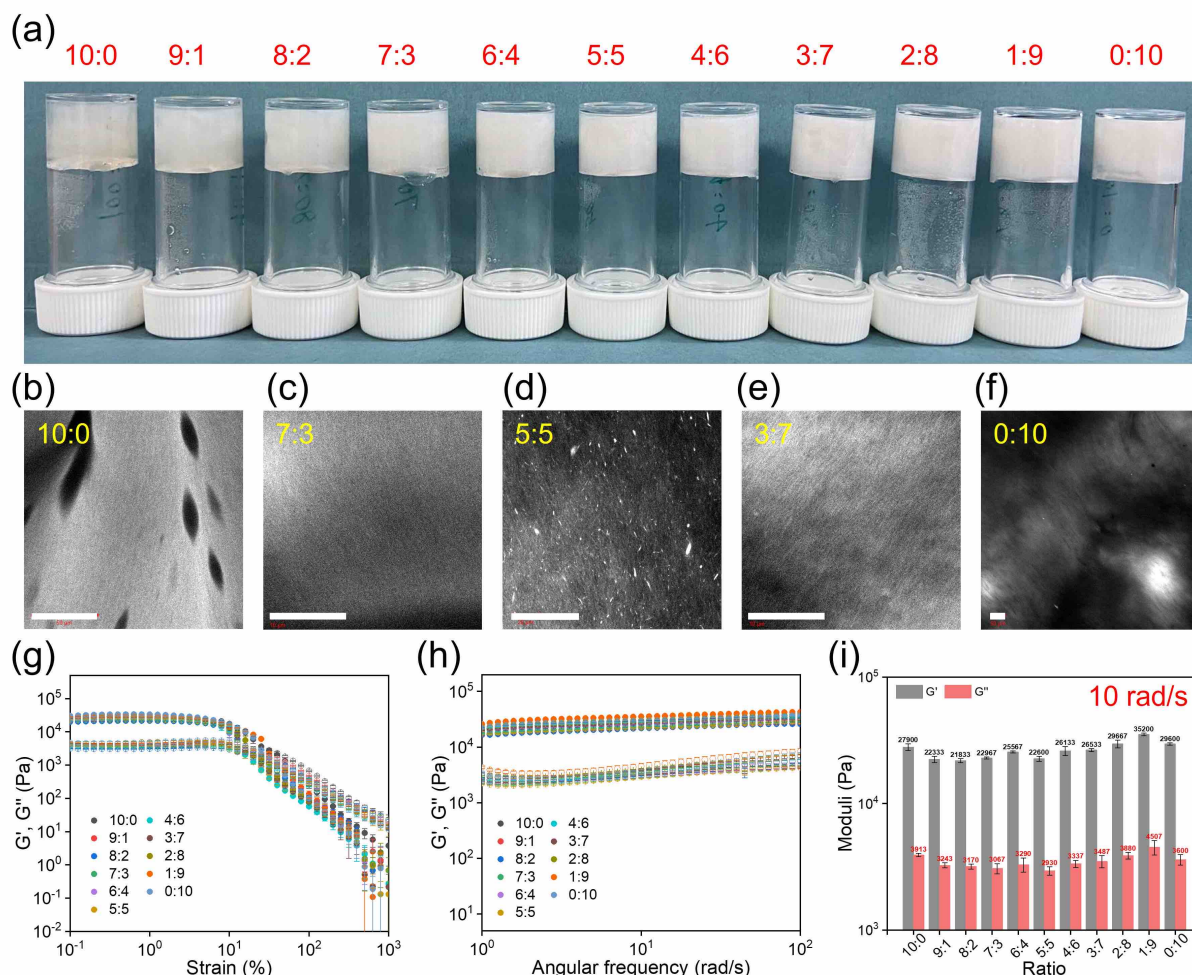


**Figure 3-27.** (a) Photographs, (b-f) confocal fluorescent microscopy images (scale bars indicate 50  $\mu\text{m}$ ), (g) strain sweep, (h) frequency sweep of binary gels at different volume ratios of 10 mg/mL (L,L)-6Br2NapFF:(L,D)-6Br2NapFF stock solutions. (i) A plot illustrating moduli at an angular frequency of 10 rad/s plotted against volume ratios. The data points on the graphs represent the average value of the experimental data of the three samples, and the error bar represents their standard deviation.

The SAXS data of the gel with a 5:5 ratio showed a Bragg peak at  $Q = 0.194 \text{ \AA}^{-1}$  ( $d = 32.4 \text{ \AA}$ ), indicating the presence of crystalline-like ordering within the fibrillar networks of the gel state (Figure 3-28a). As the proportion of (L,D)-6Br2NapFF increased, the Bragg peak sharpened, suggesting a higher fraction of ordered and periodically arranged bundles of individual fibers. The SAXS data of the pH-triggered (L,L)-6Br2NapFF hydrogel can be fitted to a flexible cylinder model with a radius of  $30.2 \pm 0.2 \text{ \AA}$  and a Kuhn length of  $43.8 \pm 2.9 \text{ \AA}$ . In contrast, the (L,D)-6Br2NapFF gel can be well described by an elliptical cylinder plus power law model, where the ellipse minor radius is  $176.5 \pm 0.4 \text{ \AA}$ , the axis ratio is  $2.0 \pm 0.02$ , and the length is  $431.6 \pm 1.0 \text{ \AA}$  (see Figure 3-28 and Table 3-8). For two-component gels, the scattering data can

be modeled by a combined model of two different cylinders derived from a single-component gel with consistent parameters, indicating the self-sorting of the two gelators across all compositions studied (Figure 3-28 and Table 3-8). 2D-SAXS patterns showed greater directional alignment in (L,L)-6Br2NapFF fibers compared to (L,D)-6Br2NapFF. As the amount of (L,L)-6Br2NapFF was decreased, the alignment decreased, indicating the shift towards a more random orientation (refer to Figure 3-29).

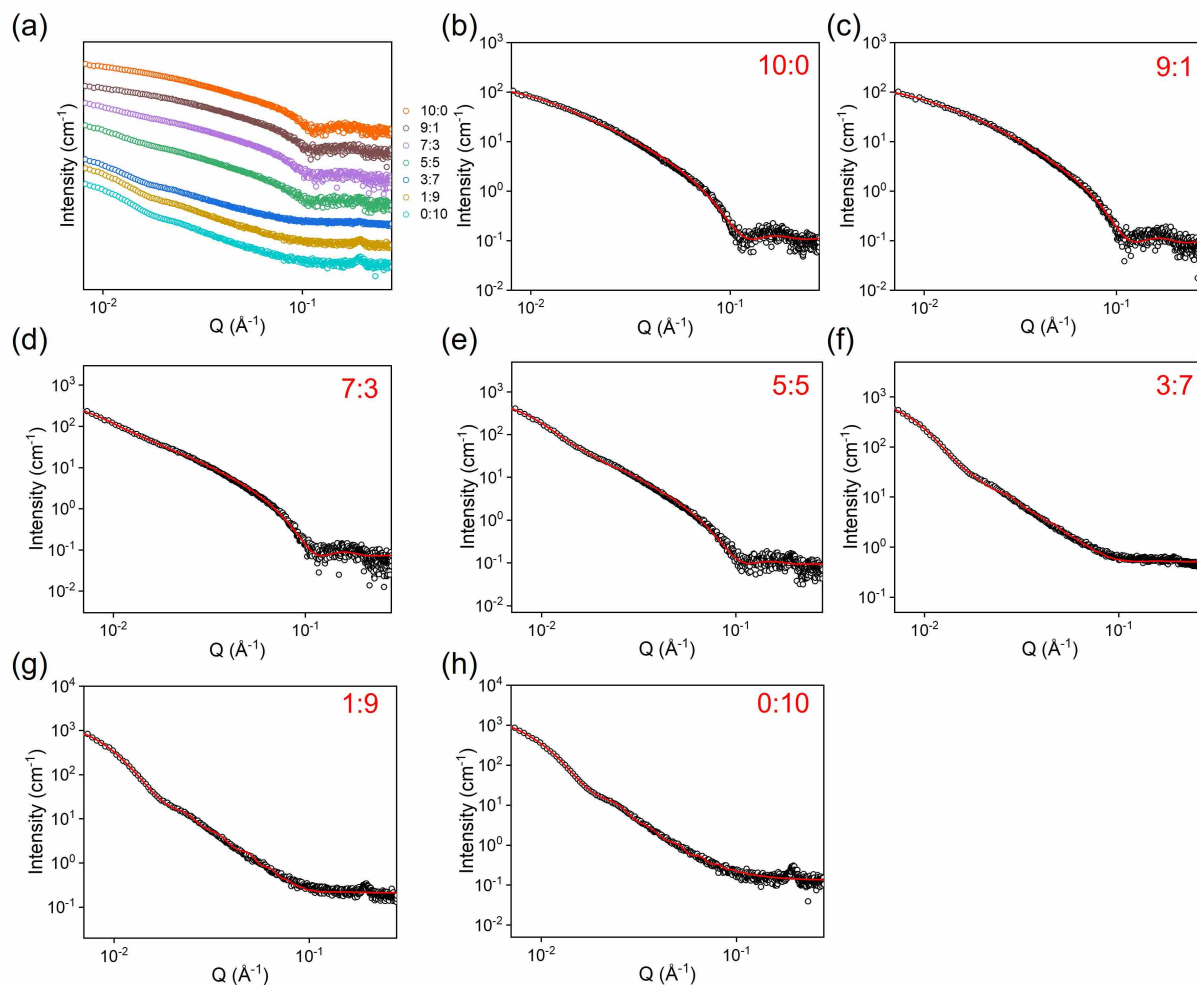


**Figure 3-28.** (a) Experimental SAXS curves (The data were arranged vertically by volume ratio for clear comparison); (b-f) SAXS data (depicted by black circles) and their respective fits (illustrated by red lines) for binary gels with varying volume ratios, ranging from 10:0, 9:1, 7:3, 5:5, 3:7, 1:9, to 0:10, prepared from 10 mg/mL stock solutions of (L,L)-6Br2NapFF and (L,D)-6Br2NapFF.

**Table 3-8.** Summary of parameters used to fit SAXS data for binary gels, encompassing different volume ratios (10:0, 9:1, 7:3, 5:5, 3:7, 1:9, and 0:10) derived from 10 mg/mL stock solutions of (L,L)-6Br2NapFF and (L,D)-6Br2NapFF. The abbreviations "FC", "EC", and "PL" represent the flexible cylinder, elliptical cylinder, and power law models, respectively.

Ratio	10:0	9:1	7:3	5:5	3:7	1:9	0:10
Model	FC	FC	FC+EC	FC+EC	FC+EC	FC+EC	EC+PL
Scale			1	1	1	1	1
Background	0.2	0.1	0.06	0.08	0.5	0.2	0.1
Background error	0.001	0.001	0.001	0.001	0.001	0.001	0.001
Power law scale							$9.3 \times 10^{-5}$
Power law scale error							$6.1 \times 10^{-6}$
Power							2.9
Power error							0.02
A scale	0.01	0.01	0.01	0.01	0.006	0.004	
A scale error	0.0005	$1.9 \times 10^{-5}$	$2.5 \times 10^{-5}$	$2.4 \times 10^{-5}$	$2.2 \times 10^{-5}$	$2.0 \times 10^{-5}$	
A kuhn length (Å)	43.8	43.8	43.8	43.8	43.8	43.8	
A_kuhn_length_error (Å)	2.9						
A length (Å)	>1000	>1000	>1000	>1000	>1000	>1000	
A length error (Å)							
A radius (Å)	30.2	30.2	30.2	30.2	30.2	30.2	
A radius error (Å)	0.2						
B scale			0.002	0.005	0.008	0.01	0.01
B scale error			$1.5 \times 10^{-5}$	$1.6 \times 10^{-5}$	$1.8 \times 10^{-5}$	$2.0 \times 10^{-5}$	$9.4 \times 10^{-5}$
B radius (Å)			176.5	176.5	176.5	176.5	176.5
B radius error (Å)							0.4
B axis ratio			2.0	2.0	2.0	2.0	2.0
B axis ratio error							0.02
B length (Å)			431.6	431.6	431.6	431.6	431.6
B length error (Å)							1.0
$\chi^2$	3.43	3.14	3.65	6.98	5.58	4.93	3.04

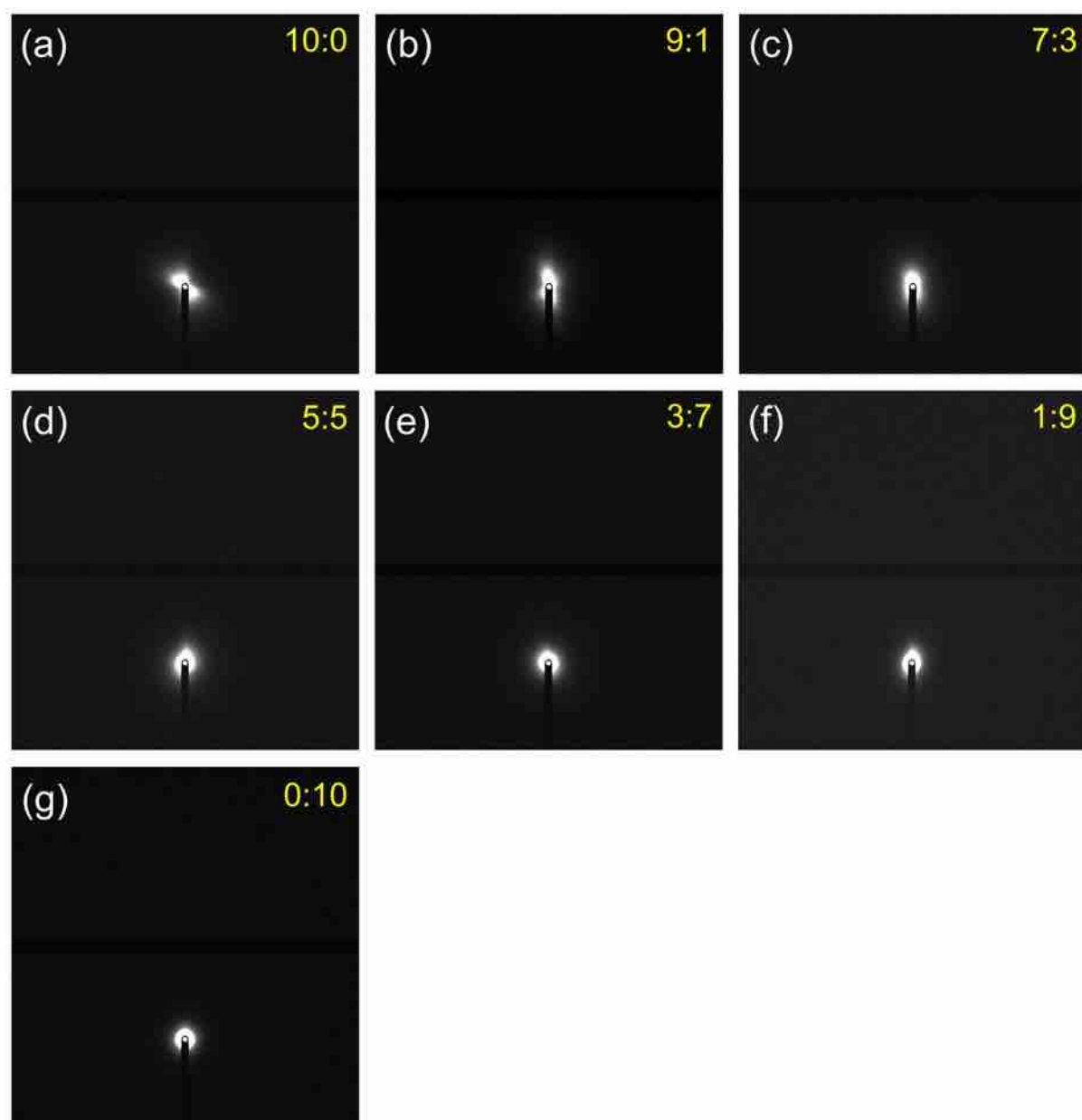


**Figure 3-29.** (a) 2D-SAXS profiles for binary gels with varying volume ratios, ranging from 10:0, 9:1, 7:3, 5:5, 3:7, 1:9, to 0:10, prepared from 10 mg/mL stock solutions of (L,L)-6Br2NapFF:(L,D)-6Br2NapFF.

### 3.2.3 1NapFF

Figure 3-30a shows the pre-gelled solutions of 1NapFF at an alkaline pH of 10.5. The 10:0 and 0:10 systems appeared translucent and turbid, respectively. The turbidity increased progressively with more (L,D)-1NapFF, peaking at a 4:6 ratio before stabilizing (Figure A3-88). Polarized optical microscopy revealed highly ordered birefringent arrangements in samples, except at the 0:10 ratio, with smaller domains at higher ratios, suggesting the presence of

anisotropic hierarchical structures (Figure 3-30(b-l)). Shear viscosity data illustrated highly viscous solutions from 10:0 to 3:7 ratios at pH 10.5, indicating the presence of worm-like micelles. The rest of the solutions behaved like free-flowing liquids, signifying fewer assembled aggregates. The significant difference in viscosity between (L,L)-1NapFF and (L,D)-1NapFF implied disparate nanostructures in their solutions at pH 10.5.<sup>43</sup> Overall, the supramolecular fluids displayed shear-thinning behavior as shear rates increased (see Figure 3-30m). The viscosity at a shear rate of  $10\text{ s}^{-1}$  generally declined with increasing ratio, stabilizing around the 2:8 system, signalling minimal further viscosity alterations (Figure 3-30n).

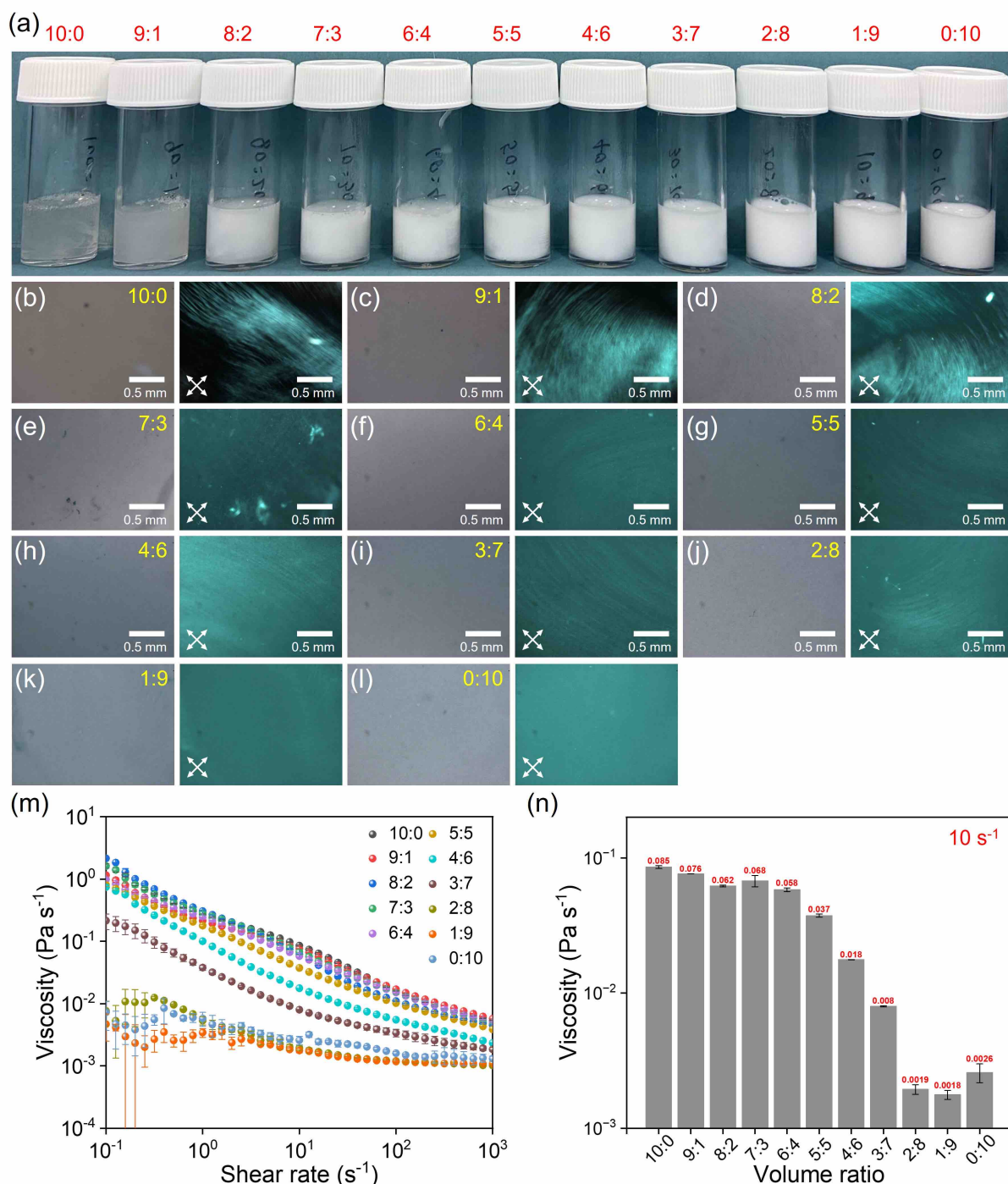


**Figure 3-30.** (a) Photographs of solutions, (b-l) optical microscopy images taken under normal light and cross-polarized conditions (magnified at 5 $\times$ ; scale bars indicated 500  $\mu\text{m}$ , with white crosses denoting polariser orientations), (m) viscosity measurements of binary solutions at different volume ratios of 10 mg/mL (L,L)-1NapFF:(L,D)-1NapFF stock solutions. (n) A plot illustrating viscosity data at a shear rate of 10  $\text{s}^{-1}$  plotted against volume ratios. The data points on the graphs represent the average value of the experimental data of the three samples, and the error bar represents their standard deviation.

To further examine the chiral characteristics of the two-component solution system, CD spectra were collected. The CD signal intensity of (L,D)-1NapFF located at the monomer transition range of naphthalene was significantly smaller, indicating that the naphthalene chromophore was not efficiently stacked in the self-assembled structure (Figure 3-31a). The CD spectrum from the 5:5 mixed solution exhibited absorbance signals at approximately 190 nm, 225 nm, and 242 nm, separately, consistent with a linear combination of signals collected from (L,L)-1NapFF or (L,D)-1NapFF alone (Figure 3-31b). The broad shoulder observed at 222 nm indicated the presence of disorder in the binary system. Figure 3-31c shows that in most binary scenarios, the CD signal denoting the chiral self-assembled aggregates diminished with higher proportions of (L,D)-1NapFF, except for the 9:1 and 8:2 systems where chirality amplifications occurred. This behavior reflects the majority rules effect,<sup>44, 45</sup> where an abundance of one component can dictate the dominant organization.

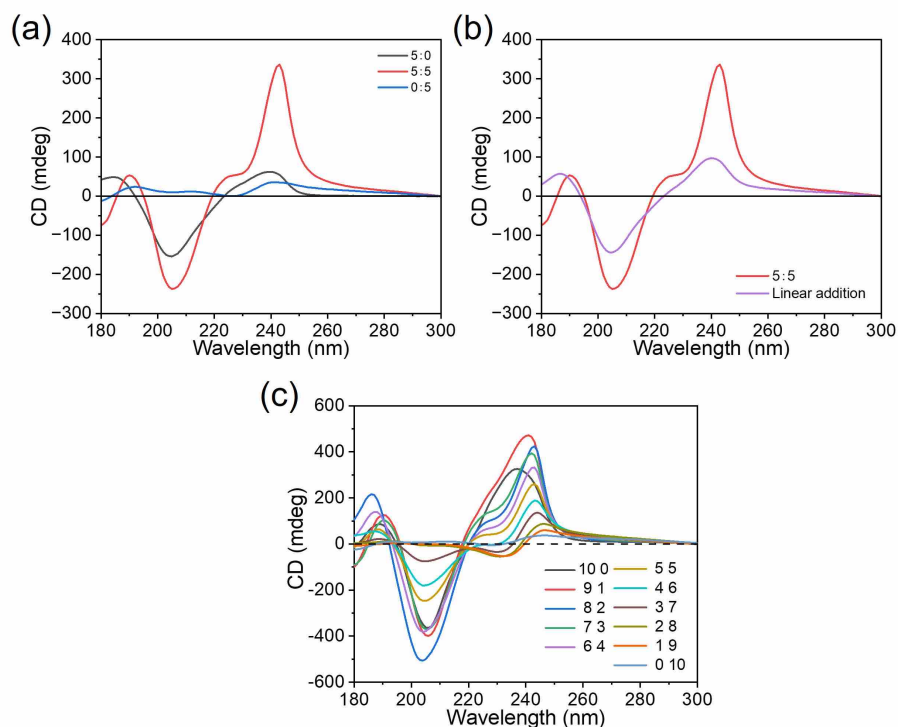


**Figure 3-31.** (a) CD spectra of 5 mg/mL of (L,L)-1NapFF (labelled as 5:0), a mixture with a 5:5 ratio of 10 mg/mL (L,L)-1NapFF:(L,D)-1NapFF stock solutions, and 5 mg/mL (L,D)-1NapFF (labelled as 0:5) solutions at pH 10.5. (b) The spectra illustrate a comparison between the 5:5 ratio of 10 mg/mL (L,L)-1NapFF:(L,D)-1NapFF stock solutions and the calculated theoretical self-sorted combination of the 5:0 and 0:5 spectra. (c) CD spectra of solutions containing 10 mg/mL of (L,L)-1NapFF:(L,D)-1NapFF at ratios ranging from 10:0 to 0:10.

After heating to 55°C, the spectral shape of an individual (L,L)-1NapFF differed significantly from its initial state (see Figure 3-32(a-b)). The signal recovered following heat-cooling cycles between 25°C and 85°C, indicating that high temperatures lead to changes in the self-assembled nanostructure formed by (L,L)-1NapFF, with this alteration being reversible. In contrast, no notable variation in the CD spectra for (L,L)-1NapFF was observed after exposure to temperature fluctuations (Figure 3-33(a-b)), indicating that its structural integrity remained unaffected. In the case of the 5:5 ratio mixture, the CD data also exhibited changes after heating to 55°C, suggesting a likelihood of self-sorting between these two components in the mixture (Figure 3-34(a-b)). Notably, during cooling, the signals at 205 nm and 222 nm vanished, while a negative peak around 230 nm appeared. This is attributed to the (L,L)-1NapFF self-assembled aggregate in the binary system.

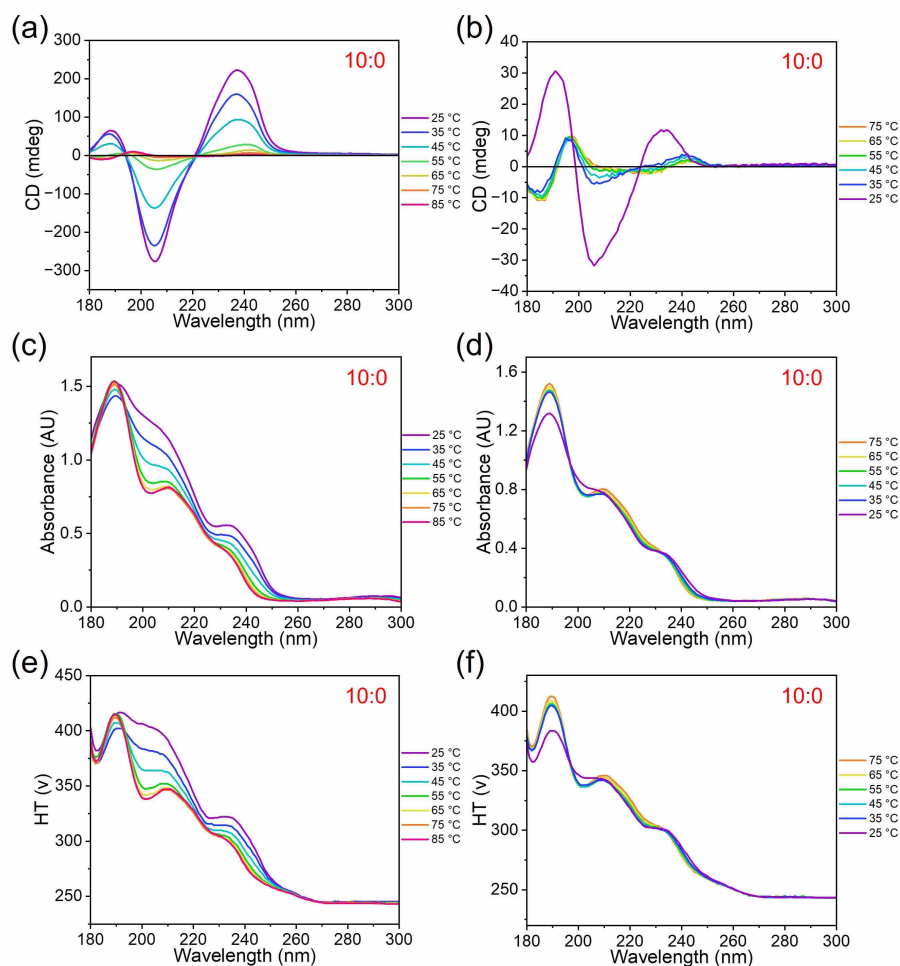


**Figure 3-32.** Temperature-dependent (a-b) CD, (c-d) absorbance, and (e-f) HT data for 10 mg/mL (L,L)-1NapFF solutions at pH 10.5. (a), (c), and (e) represent the heating process, while (b), (d), and (f) correspond to the cooling process.

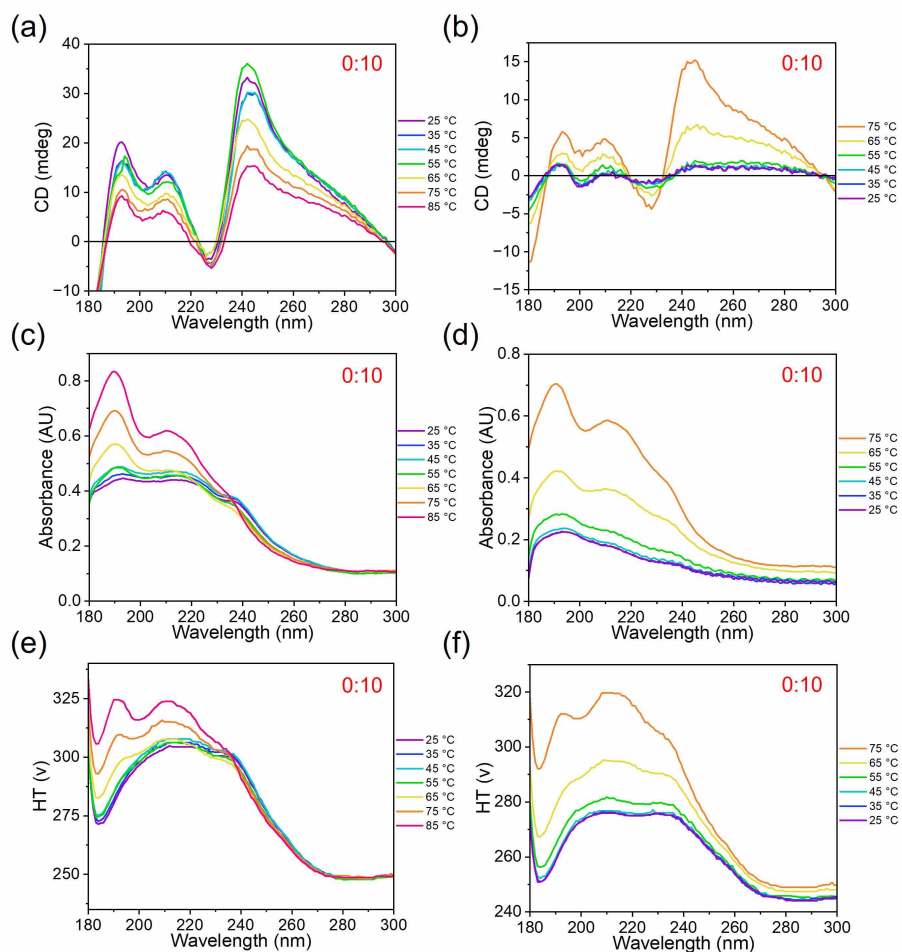


**Figure 3-33.** Temperature-dependent (a-b) CD, (c-d) absorbance, and (e-f) HT data for 10 mg/mL (L,D)-1NapFF solutions at pH 10.5. (a), (c), and (e) represent the heating process, while (b), (d), and (f) correspond to the cooling process.

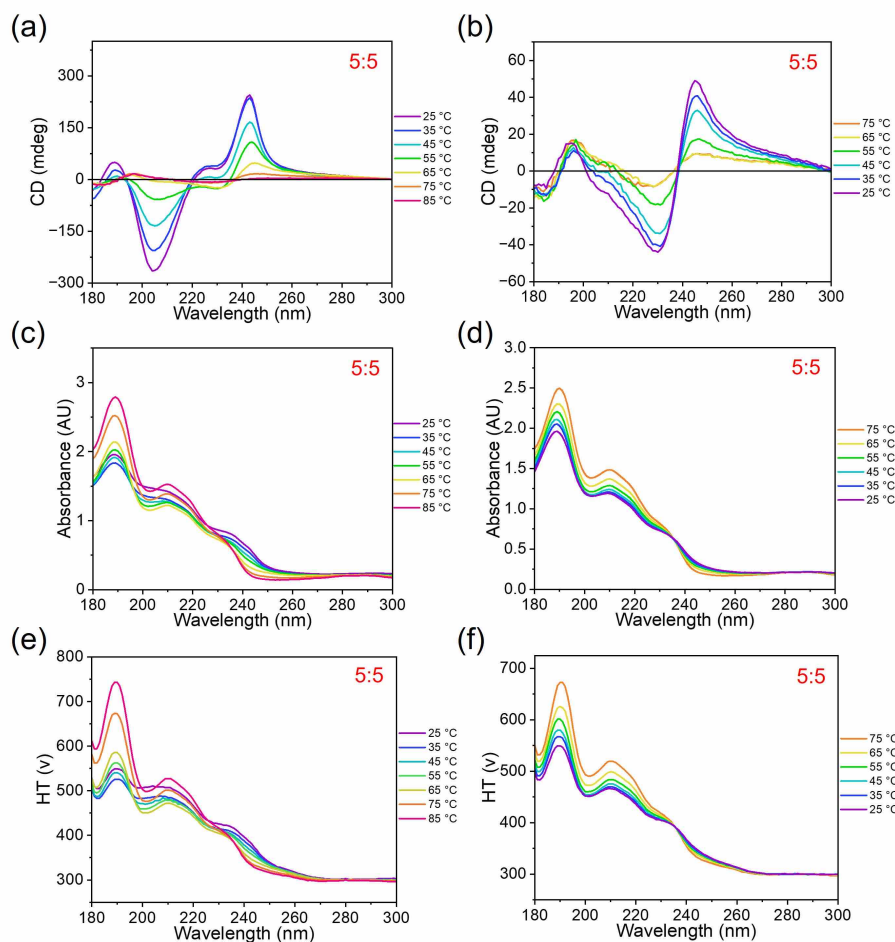


**Figure 3-34.** Temperature-dependent (a-b) CD, (c-d) absorbance, and (e-f) HT data for a mixture with a 5:5 ratio of 10 mg/mL (L,L)-1NapFF:(L,D)-1NapFF stock solutions at high pH. (a), (c), and (e) represent the heating process, while (b), (d), and (f) correspond to the cooling process.

The SAXS data of (L,L)-1NapFF solutions were best fitted to a cylinder model with a radius of  $28.6 \pm 0.1$  Å and a length of  $223.9 \pm 2.6$  Å (refer to Figure 3-35, Table 3-9). In contrast, (L,D)-1NapFF data were best described by a power law model, suggesting a deficiency in effective self-assembly and the presence of heterogeneities. For multicomponent solutions, the scattering patterns were modelled by cylinder plus power law, with a comparable radius ranging from 29.2 to 36.6 Å and a power law exponent of 4.3–4.5. This suggests that the primary self-assembled structures consist of individual components self-sorted from others. Furthermore, the fading orientation in the 2D-scattering patterns indicated the improved isotropy of the binary systems following the enlarged portion of (L,D)-1NapFF (Figure 3-36). The SAXS data of diluted (L,L)-1NapFF solution (5:0) could also be modelled by a cylinder, but with a radius approximately

9.3 Å smaller than the counterpart (5:5) in the mixture, indicating subtle interactions between the two components rather than simple dilution (Figure 3-37, Figure 3-38, and Table 3-10).

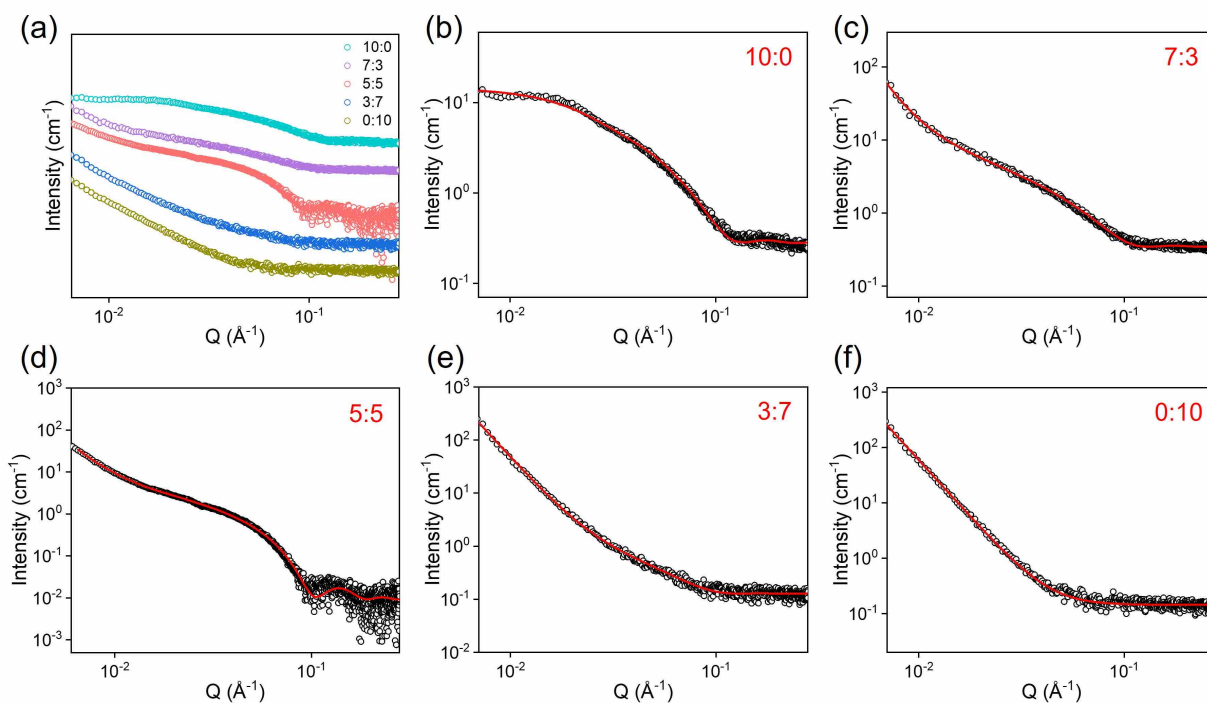


**Figure 3-35.** (a) Experimental SAXS curves (The data were arranged vertically by volume ratio for clear comparison); (b-f) SAXS data (depicted by black circles) and their respective fits (illustrated by red lines) for pre-gelation binary solutions with varying volume ratios, ranging from 10:0, 7:3, 5:5, 3:7, to 0:10, prepared from 10 mg/mL stock solutions of (L,L)-1NapFF:(L,D)-1NapFF.

**Table 3-9.** Summary of parameters used to fit SAXS data for binary solutions, encompassing different volume ratios (10:0, 7:3, 5:5, 3:7, and 0:10) derived from 10 mg/mL stock solutions of (L,L)-1NapFF:(L,D)-1NapFF before gelation. The abbreviations "C" and "PL" represent the cylinder and power law models, respectively.

Ratio	10:0	7:3	5:5	3:7	0:10
Model	C	C+PL	C+PL	C+PL	PL
Scale		1	1	1	
Background	0.3	0.3	0.01	0.1	0.1
Background error	0.001	0.0008	0.0004	0.0008	0.0008
A scale		$7.2 \times 10^{-9}$	$9.1 \times 10^{-9}$	$1.4 \times 10^{-7}$	$4.1 \times 10^{-7}$
A scale error		$2.3 \times 10^{-9}$	$1.3 \times 10^{-9}$	$1.1 \times 10^{-8}$	$1.5 \times 10^{-8}$
A power		4.5	4.3	4.3	4.1
A power error		0.07	0.03	0.02	0.01
B scale	0.01	0.006	0.002	0.001	
B scale error	$4.6 \times 10^{-5}$	$3.3 \times 10^{-5}$	$5.9 \times 10^{-6}$	$2.5 \times 10^{-5}$	
B radius (Å)	28.6	29.2	36.6	30.6	
B radius error (Å)	0.1	0.1	0.1	0.6	
B length (Å)	223.9	>1000	506.6	766.5	
B length error (Å)	2.6		13.0	364.9	

$\chi^2$	2.18	2.12	<1	2.13	1.89
----------	------	------	----	------	------

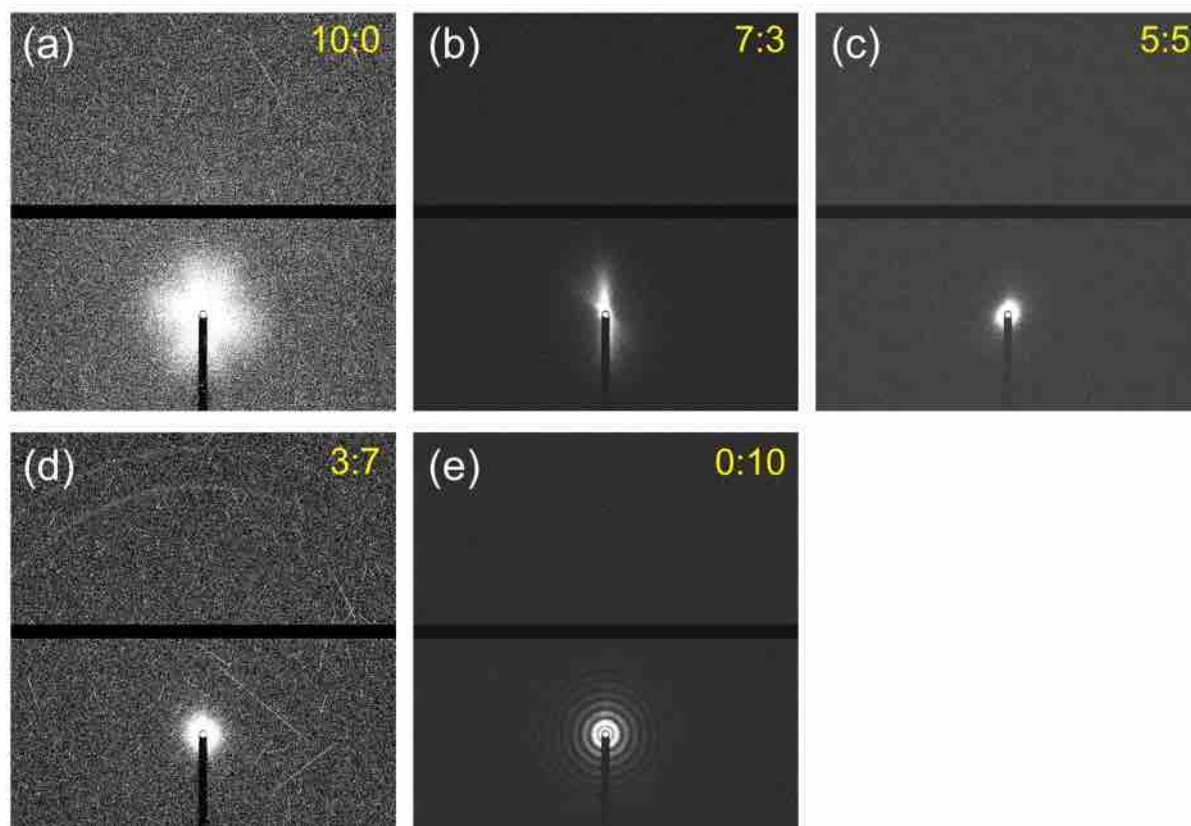


**Figure 3-36.** 2D-SAXS profiles for pre-gelation binary solutions with volume ratios from 10:0, 7:3, 5:5, 3:7, to 0:10 of 10 mg/mL (L,L)-1NapFF:(L,D)-1NapFF stock solutions.

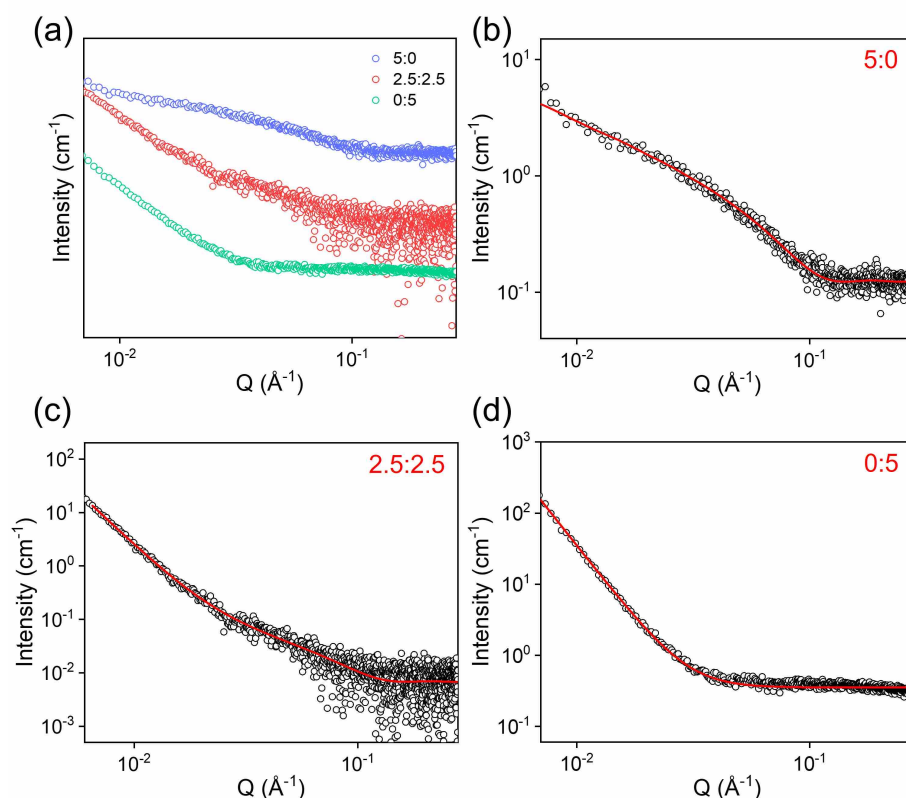


**Figure 3-37.** (a) Experimental SAXS curves (The data were arranged vertically by volume ratio for clear comparison); (b-d) SAXS data (depicted by black circles) and their respective fits (illustrated by red lines) for pre-gelation binary solutions with varying volume ratios including 5:0, 2.5:2.5 and 0:5 prepared from 5 mg/mL stock solutions of (L,L)-1NapFF and (L,D)-1NapFF.

**Table 3-10.** Summary of parameters used to fit SAXS data for binary solutions, encompassing different volume ratios (5:0, 2.5:2.5, and 0:5) derived from 5 mg/mL stock solutions of (L,L)-1NapFF and (L,D)-1NapFF before gelation. The abbreviations "C" and "PL" represent the cylinder and power law models, respectively.

Ratio	5:0	2.5:2.5	0:5
Model	C	C+PL	PL
scale		1	
Background	0.1	0.007	0.4
Background error	0.0009	0.0004	0.001
A scale		$2.7 \times 10^{-8}$	$1.7 \times 10^{-7}$
A scale error		$5.1 \times 10^{-9}$	$8.8 \times 10^{-9}$
A power		4.0	4.2
A power error		0.04	0.01
B scale	0.002	0.0001	
B scale error	$3.1 \times 10^{-5}$	$1.5 \times 10^{-5}$	
B radius (Å)	27.3	23.9	
B radius error (Å)	0.3	1.6	
B length (Å)	682.4	512.4	
B length error (Å)	118.6	367.1	
$\chi^2$	1.16	<1	2.58

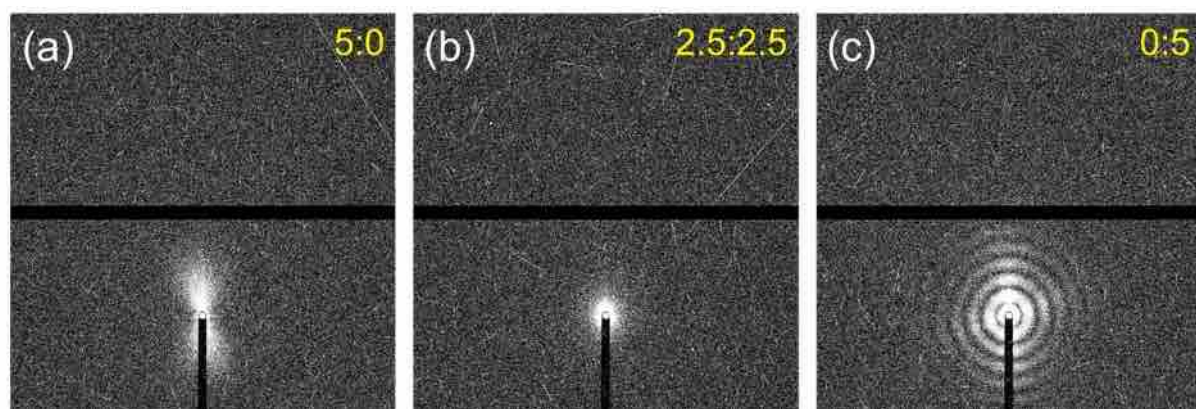


**Figure 3-38.** 2D-SAXS profiles for pre-gelation binary solutions with volume ratios from 5:0, 2.5:2.5 0:5 of 5 mg/mL (L,L)-1NapFF:(L,D)-1NapFF stock solutions.

(L,L)-1NapFF can form self-supported gels, but (L,D)-1NapFF cannot. When these two components are combined, (L,L)-1NapFF acts as the gelator, and (L,D)-1NapFF serves as a non-gelling additive (Figure 3-39a). Self-supporting gels were observed in all two-component systems except at the 1:9 ratio. Interestingly, the gels with 8:2 and 7:3 ratios were notably more transparent than those with only (L,L)-1NapFF or in the 9:1 mixture. Further increasing the percentage of (L,D)-1NapFF increased the turbidity (Figure A3-92). Confocal microscopy demonstrated prominent differences in the microstructure of (L,L)-1NapFF and (L,D)-1NapFF under acidic conditions (Figure 3-39b and f). The (L,L)-1NapFF gel displayed a uniform arrangement of fibers, whereas (L,D)-1NapFF exhibited randomly dispersed domains resembling spherical aggregates. However, the image resolution was inadequate to fully characterize these structures. The coexistence of spherulites and fibrous structures in the binary systems suggested the potential self-sorting behavior between the two components (Figure 3-39(c-e)). Rheological experiments were utilized to investigate the mechanical stability of the gels. A strain-softening behavior for all gels was observed, manifested by a drop in  $G'$  above a certain strain amplitude, which was ascribed to the shear-induced disruption of the supramolecular gelation network (Figure 3-39g). In all cases, the modulus was largely independent of frequency (Figure 3-39h). The relatively large  $G'$  values confirmed (L,L)-1NapFF formed the stiffest hydrogel (Figure 3-39i). Binary systems with ratios from 9:1 to 6:4 possessed comparable moduli with pure (L,L)-1NapFF at 10 rad/s, and expanding the (L,D)-1NapFF portion resulted in a sharp decrease in moduli. Thus, the gelator plus non-gelator two-component system composed of (L,L)-, and (L,D)-1NapFF contributed to the weakened rheological properties.

The storage modulus ( $G'$ ) increases with concentration ( $C$ ) according to power laws of  $G' \propto C^{2.43}$ ,  $G' \propto C^{2.27}$ , and  $G' \propto C^{2.83}$  for pH-triggered hydrogels composed of (L,L)-1NapFF, a 1:1 volume ratio mixture of (L,L)-1NapFF:(L,D)-1NapFF, and (L,D)-1NapFF (Figure A3-91), suggesting a semi-flexible polymer network.<sup>46-48</sup> The  $G'$  values were obtained from the plateau moduli observed in the linear viscoelastic region during strain sweeps.

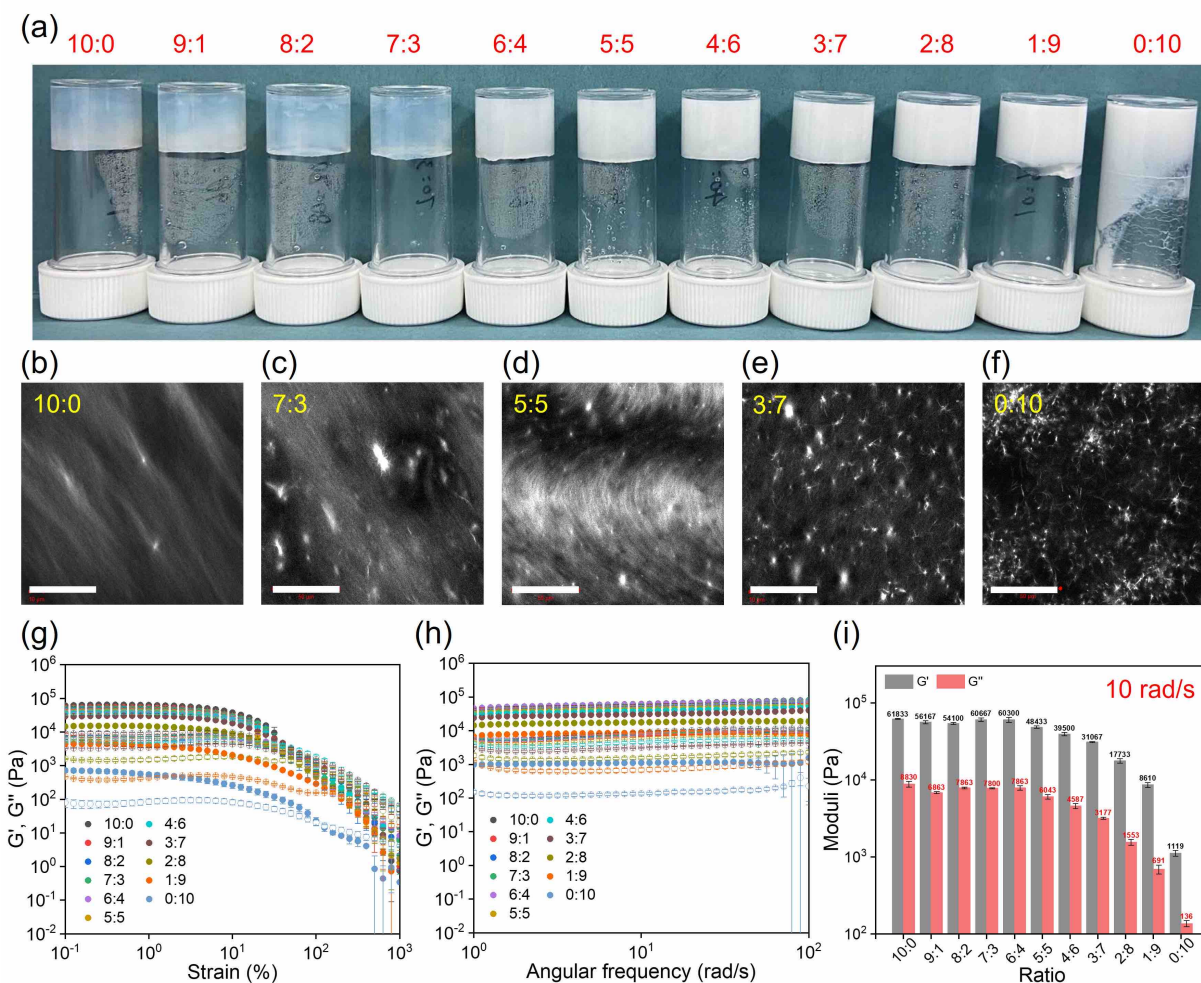


**Figure 3-39.** (a) Photographs, (b-f) confocal fluorescent microscopy images (scale bars indicate 50  $\mu\text{m}$ ), (g) strain sweep, (h) frequency sweep of binary gels at different volume ratios of 10 mg/mL (L,L)-1NapFF:(L,D)-1NapFF stock solutions. (i) A plot illustrating moduli at an angular frequency of 10 rad/s plotted against volume ratios. The data points on the graphs represent the average value of the experimental data of the three samples, and the error bar represents their standard deviation.

SAXS was performed to investigate self-sorting at the nanoscale in hydrogels. The data analysis revealed that the best fit for the (L,L)-1NapFF hydrogel was an elliptical cylinder characterized by an ellipse minor radius of  $31.7 \pm 0.2 \text{ \AA}$  and an axis ratio of  $2.5 \pm 0.02$  (Figure 3-40 and Table 3-11). In contrast, (L,L)-1NapFF alone exhibited markedly different scattering patterns, fitting

best to a power law model with a power law exponent of  $4.1 \pm 0.01$ , suggesting a limited degree of anisotropic self-assemblies, as the uniform intensities along concentric circles around the incident exhibited in the 2D scattering pattern (Figure 3-41). The multicomponent gels were effectively modelled by a combination of an elliptical cylinder and a power law, with adjustments to specific parameters. These findings demonstrate that in gels containing both (L,L)-1NapFF and (L,D)-1NapFF, fiber formation primarily resulted from self-sorting of (L,L)-1NapFF, while (L,D)-1NapFF acted as non-gelling additives.

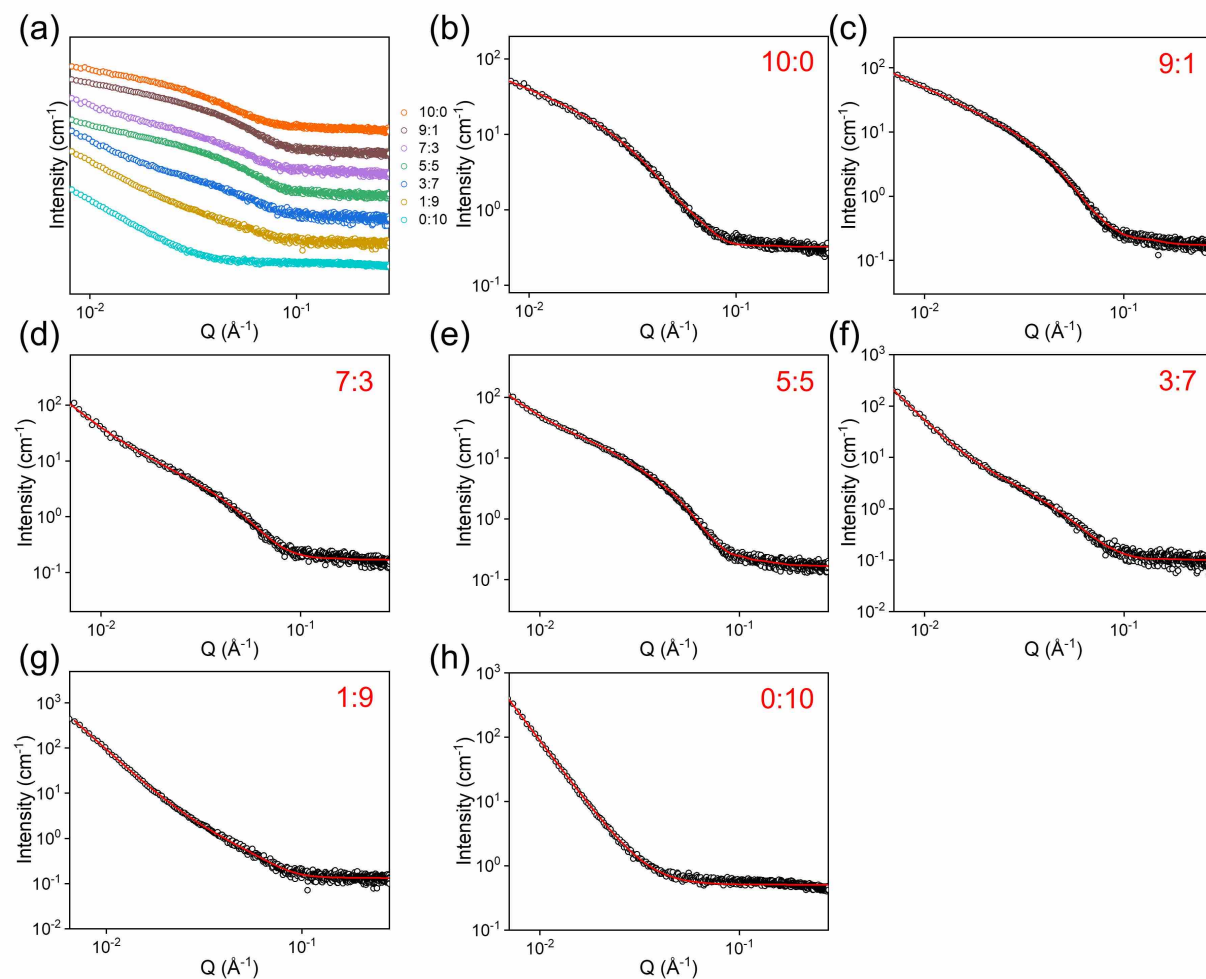


**Figure 3-40.** (a) Experimental SAXS curves (The data were arranged vertically by volume ratio for clear comparison); (b-f) SAXS data (depicted by black circles) and their respective fits (illustrated by red lines) for binary gels with varying volume ratios, ranging from 10:0, 9:1, 7:3, 5:5, 3:7, 1:9, to 0:10, prepared from 10 mg/mL stock solutions of (L,L)-1NapFF and (L,D)-1NapFF.

**Table 3-11.** Summary of parameters used to fit SAXS data for binary gels, encompassing different volume ratios (10:0, 9:1, 7:3, 5:5, 3:7, 1:9, and 0:10) derived from 10 mg/mL stock solutions of (L,L)-1NapFF and (L,D)-1NapFF. The abbreviations "EC" and "PL" represent the elliptical cylinder and power law models, respectively.

Ratio	10:0	9:1	7:3	5:5	3:7	1:9	0:10
Model	EC	EC+PL	EC+PL	EC+PL	EC+PL	EC+PL	PL
Scale		1	1	1	1	1	
Background	0.3	0.2	0.2	0.2	0.1	0.1	0.5
Background error	0.001	0.001	0.001	0.001	0.001	0.001	0.001
A scale		0.0001	$9.1 \times 10^{-6}$	$4.7 \times 10^{-5}$	$3.4 \times 10^{-7}$	$1.0 \times 10^{-6}$	$5.2 \times 10^{-7}$
A scale error		$2.0 \times 10^{-5}$	$1.9 \times 10^{-6}$	$7.5 \times 10^{-6}$	$4.0 \times 10^{-8}$	$6.0 \times 10^{-8}$	$1.6 \times 10^{-8}$
A power		2.6	3.2	2.9	4.1	4.0	4.1
A power error		0.03	0.04	0.03	0.02	0.01	0.01
B scale	0.01	0.01	0.004	0.007	0.003	0.001	
B scale error	$3.0 \times 10^{-5}$	$9.5 \times 10^{-5}$	$8.4 \times 10^{-5}$	0.00	$4.1 \times 10^{-5}$	$4.6 \times 10^{-5}$	
B radius (Å)	31.7	33.9	30.3	35.0	26.5	24.7	
B radius error (Å)	0.2	0.3	0.4	0.4	0.4	1.2	
B axis ratio	2.5	1.9	1.8	1.6	2.1	1.7	
B axis ratio error	0.02	0.03	0.06	0.03	0.07	0.2	
B length (Å)	>1000	391.6	622.1	220.6	398.3	456.7	
B length error (Å)		9.0	46.2	3.6	28.4	99.1	
$\chi^2$	2.86	1.21	2.42	1.18	1.66	1.32	3.61

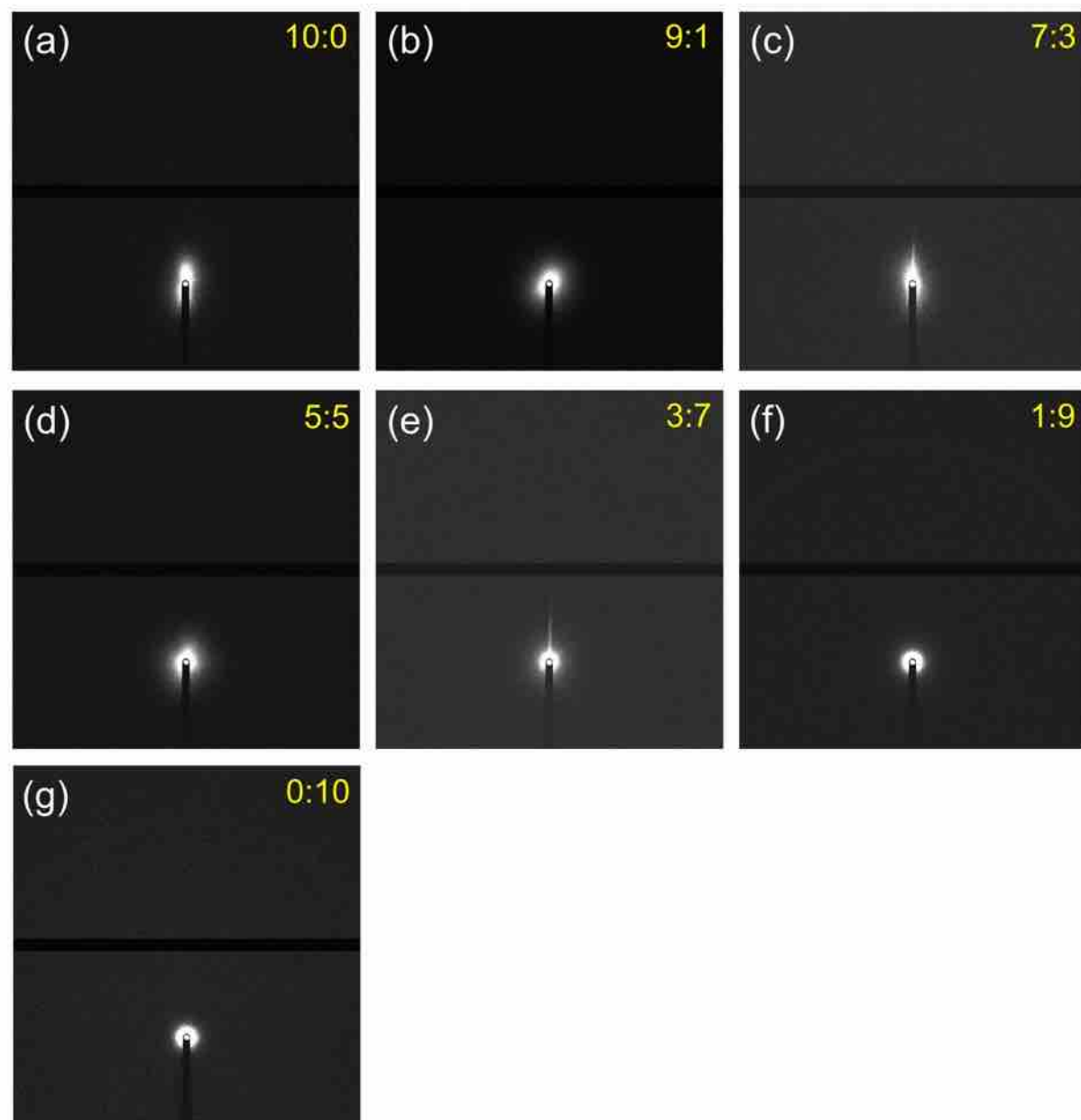


**Figure 3-41.** (a) 2D-SAXS profiles for binary gels with varying volume ratios, ranging from 10:0, 9:1, 7:3, 5:5, 3:7, 1:9, to 0:10, prepared from 10 mg/mL stock solutions of (L,L)-1NapFF:(L,D)-1NapFF.

The self-sorting assembly behavior of 1NapFF and 2NapFF systems shows both similarities and differences, particularly influenced by chirality and pH. At high pH, 2NapFF forms stable, distinct nanotube structures for (L,L)-2NapFF and (L,D)-2NapFF, leading to a robust self-sorted system with two co-existing populations, while 1NapFF forms less rigid worm-like micelles, with (L,D)-1NapFF acting as a non-gelator. At low pH, both systems form gels, but 2NapFF maintains a strong self-sorted gel network driven by chirality, whereas 1NapFF relies on (L,L)-1NapFF to form the gel network, with (L,D)-1NapFF altering the gel structure. Spectroscopic

and structural data support the self-sorting behavior, with 2NapFF showing distinct molecular stacking and CD shifts, while 1NapFF exhibits less pronounced sorting, influenced by concentration ratios. Overall, 2NapFF demonstrates a more robust self-sorting mechanism, while 1NapFF shows a more subtle behavior, where the non-gelating (L,D)-1NapFF impacts the system without contributing to gel formation.

### 3.2.4 6CN2NapFF

Both (L,L)-6CN2NapFF and (L,D)-6CN2NapFF form cloudy solutions under alkaline pH conditions (refer to Figure 3-42a). When diluted with the (L,D)-6CN2NapFF component, the turbidity of the mixed solution increased (refer to Figure A3-94). Analysis using polarized light microscopy revealed the presence of worm-like micelles in the samples, with highly organized and aligned birefringent patterns observed in solutions with ratios ranging from 3:7 to 0:10, indicating an anisotropic hierarchical structure within the system (refer to Figure 3-42(b-l)). Shear viscosity measurements showed that (L,D)-6CN2NapFF solutions were more viscous than (L,L)-6CN2NapFF solutions under alkaline pH conditions (refer to Figure 3-42m). Additionally, all solutions displayed shear-thinning non-Newtonian behavior as the shear rate increased. The viscosity at a shear rate of  $10 \text{ s}^{-1}$  gradually increased with higher ratios, reaching a range of  $0.053$  to  $0.065 \text{ Pa}\cdot\text{s}^{-1}$  after a ratio of 5:5 (refer to Figure 3-42n).

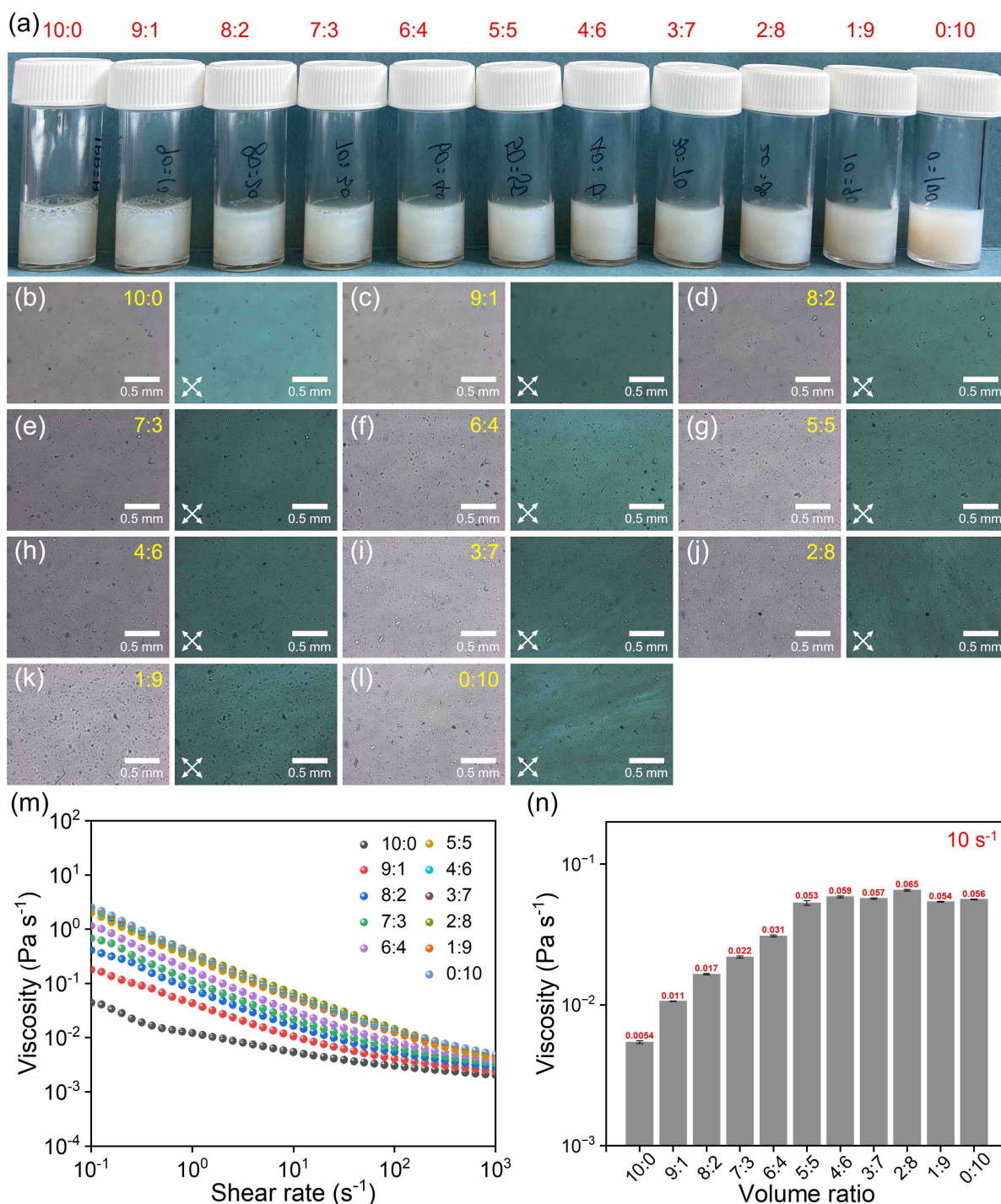


**Figure 3-42.** (a) Photographs of solutions, (b-l) optical microscopy images taken under normal light and cross-polarized conditions (magnified at 5 $\times$ ; scale bars indicated 500  $\mu$ m, with white crosses denoting polariser orientations), (m) viscosity measurements of binary solutions at different volume ratios of 10 mg/mL (L,L)-6CN2NapFF:(L,D)-6CN2NapFF stock solutions. (n) A plot illustrating viscosity data at a shear rate of 10 s<sup>-1</sup> plotted against volume ratios. The data points on the graphs represent the average value of the experimental data of the three samples, and the error bar represents their standard deviation.

The CD was used to explore supramolecular chirality. The CD spectrum obtained from the 5:5 mixed solution showed absorbance peaks around 188 nm and 250 nm, consistent with theoretical calculations based on the two individual components (see Figure 3-43b). A distinct difference was observed in the 200-240 nm region: the 5:5 mixture exhibited a negative broad shoulder around 223 nm, resembling that of the 10:0 solution (see Figure 3-43c). In contrast, the linear combination of CD spectra from 5:0 and 0:5 solutions displayed negative absorption peaks at approximately 210 nm and 230 nm. This indicates that the (L,L)-6CN2NapFF component in the hybrid system maintains its self-assembled aggregates at higher concentrations rather than being completely diluted by the other component. Figure 3-43c illustrates that the CD signal representing chiral self-assembled aggregates progressively resembles that of the 0:10 solution as the proportion of (L,D)-6CN2NapFF increases across all ratios, suggesting the occurrence of self-sorting within this binary system.

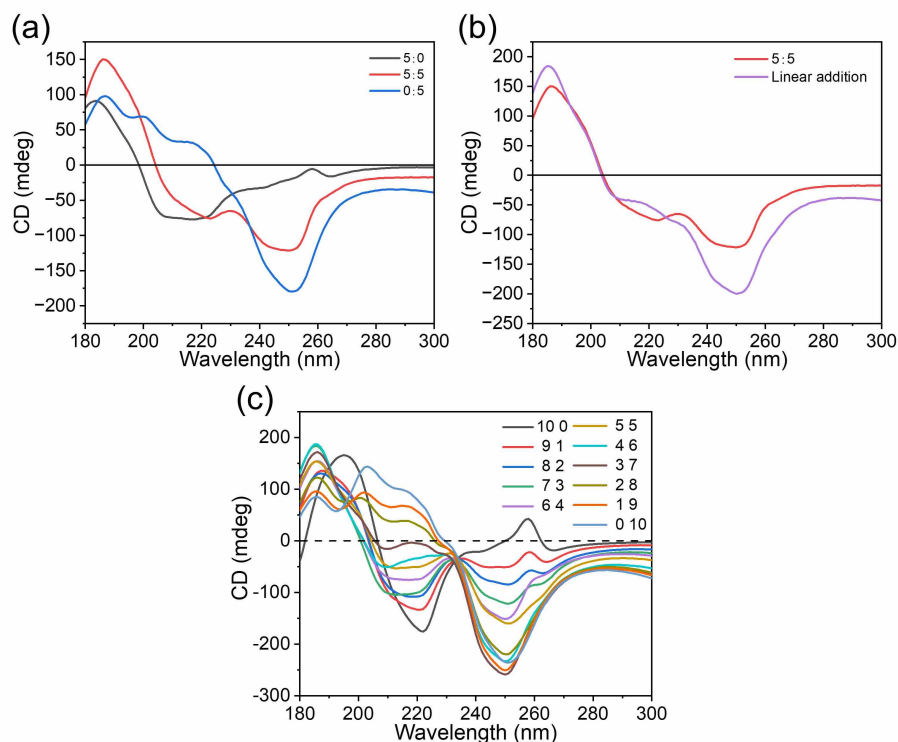


**Figure 3-43.** (a) CD spectra of 5 mg/mL of (L,L)-6CN2NapFF (labeled as 5:0), a mixture with 5:5 ratio of 10 mg/mL (L,L)-6CN2NapFF:(L,D)-6CN2NapFF stock solutions, and 5 mg/mL (L,D)-6CN2NapFF (labeled as 0:5) solutions at pH 10.5. (b) The spectra illustrate a comparison between the 5:5 ratio of 10 mg/mL (L,L)-6CN2NapFF:(L,D)-6CN2NapFF stock solutions and the calculated theoretical self-sorted combination of the 5:0 and 0:5 spectra. (c) CD spectra of solutions containing 10 mg/mL of (L,L)-6CN2NapFF:(L,D)-6CN2NapFF at ratios ranging from 10:0 to 0:10.

The temperature-dependent CD data of (L,L)-6CN2NapFF exhibited significant similarity to the initial state (refer to Figure 3-44(a-b)), indicating that its structural integrity was maintained despite temperature changes. In contrast, the corresponding CD data obtained from (L,D)-6CN2NapFF solutions showed irreversible and substantial changes in spectral shape in the 180-230 nm range after the heat-cooling cycle from 25°C to 85°C and back to 25°C (refer to Figure 3-45(a-b)), suggesting a change in the self-assembled nanostructure. For the 5:5 binary mixture, the temperature-dependent CD data closely resembled those of pure (L,D)-6CN2NapFF (refer to Figure 3-46(a-b)), indicating the preservation of the self-assembled nanostructures formed by this component within the two-component system. Self-sorting thus occurred in these two-component systems.

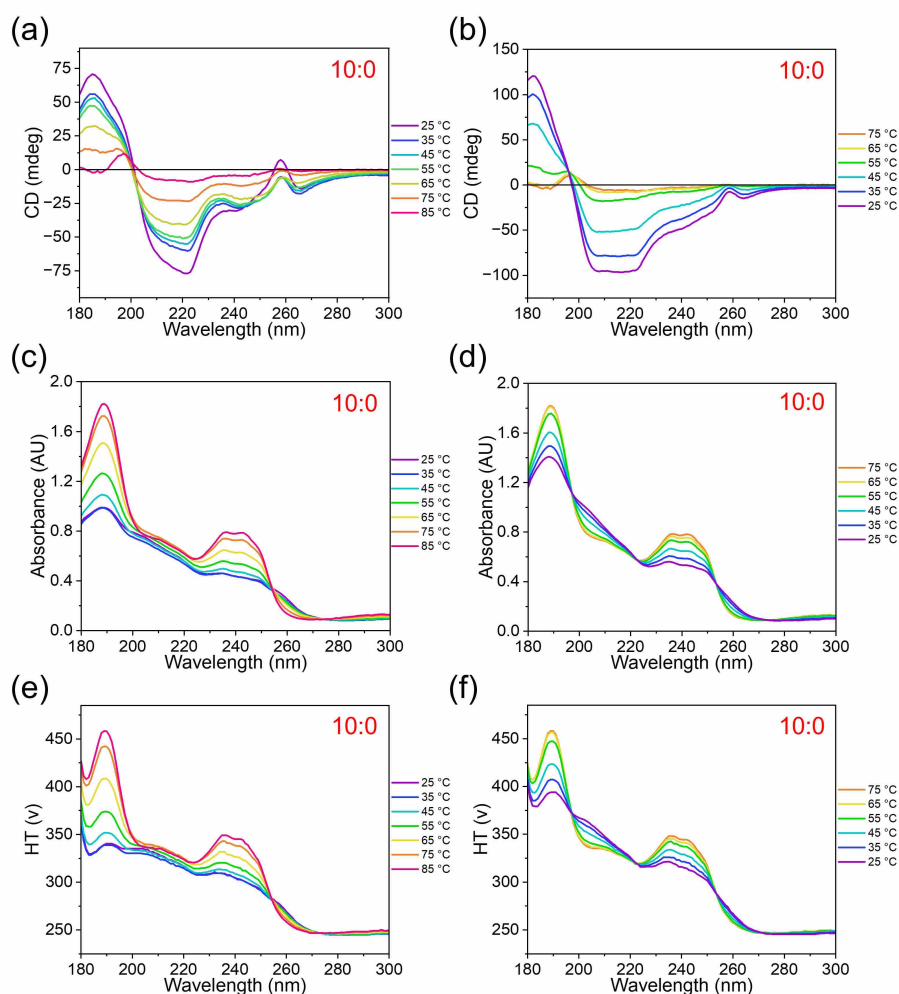


**Figure 3-44.** Temperature-dependent (a-b) CD, (c-d) absorbance, and (e-f) HT data for 10 mg/mL (L,L)-6CN2NapFF solutions at pH 10.5. (a), (c), and (e) represent the heating process, while (b), (d), and (f) correspond to the cooling process.

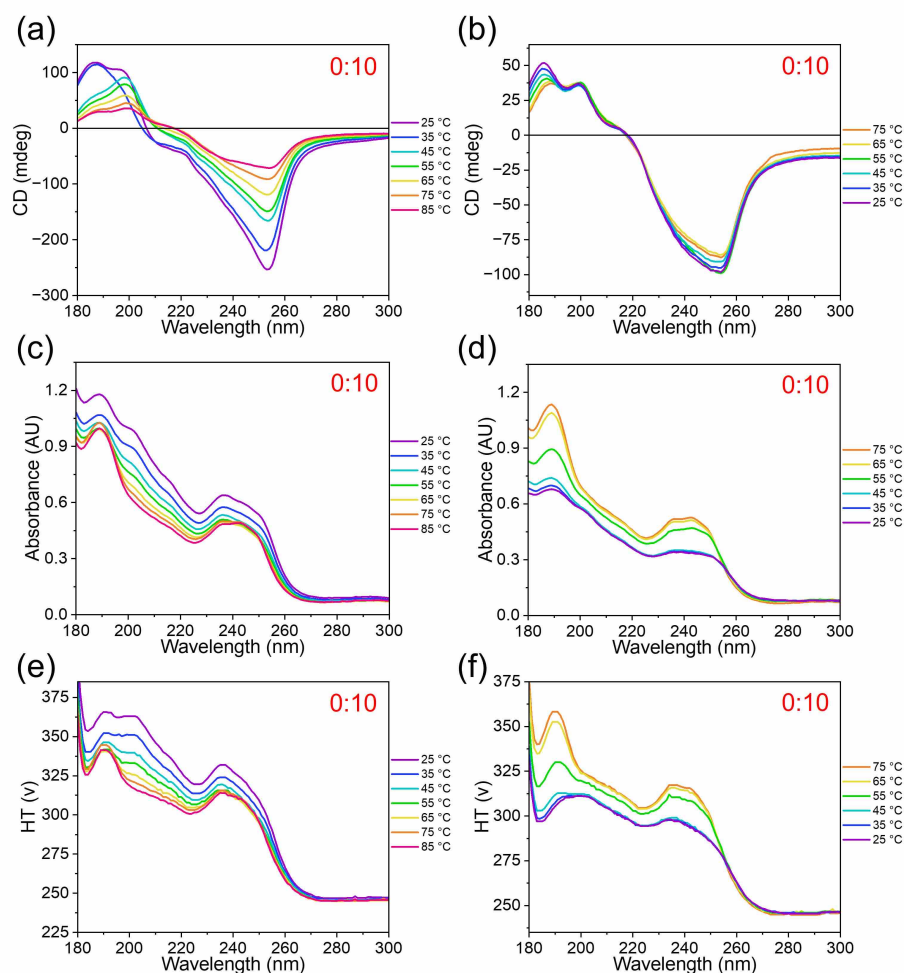


**Figure 3-45.** Temperature-dependent (a-b) CD, (c-d) absorbance, and (e-f) HT data for 10 mg/mL (L,D)-6CN2NapFF solutions at pH 10.5. (a), (c), and (e) represent the heating process, while (b), (d), and (f) correspond to the cooling process.

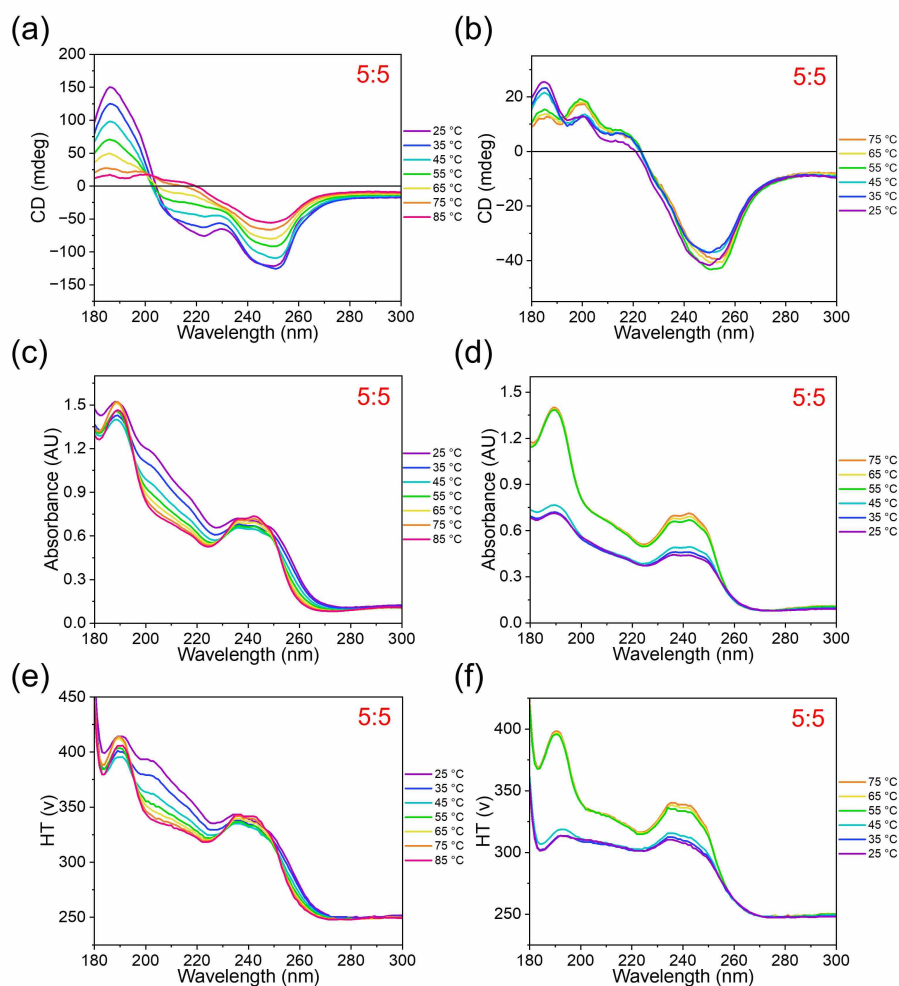


**Figure 3-46.** Temperature-dependent (a-b) CD, (c-d) absorbance, and (e-f) HT data for a mixture with a 5:5 ratio of 10 mg/mL (L,L)-6CN2NapFF:(L,D)-6CN2NapFF stock solutions at high pH. (a), (c), and (e) represent the heating process, while (b), (d), and (f) correspond to the cooling process.

The SAXS data of the (L,L)-6CN2NapFF solution were fitted using a power law model with an elliptical cylinder having a minor radius of  $114.5 \pm 0.2$  Å and an axis ratio of  $2.2 \pm 0.01$ , along with an elliptical cylinder of length  $624.1 \pm 2.2$  Å and a power law exponent of  $2.6 \pm 0.01$  (see Figure 3-47, Table 3-12). In contrast, the (L,D)-6CN2NapFF data were best modeled by a combination of a cylinder with a radius of  $32.0 \pm 0.1$  Å and a length of  $543.6 \pm 13.5$  Å, along with a power law model having a power law exponent of  $3.1 \pm 0.01$ . For multicomponent solutions, the scattering pattern was modeled using a combination of elliptical cylinders with an ellipse minor radius ranging from 100.8 to 104.9 Å and a cylinder radius ranging from 38.1 to 38.3 Å. This suggests that the primary self-assembled structure consists of individual components that exhibit self-sorting behavior from other components. Furthermore, the loss of directionality in the two-dimensional scattering pattern indicate increased isotropy of the two-component system

after the addition of (L,D)-6CN2NapFF (refer to Figure 3-48). Fits the SAXS data for dilute (L,L)-6CN2NapFF and (L,D)-6CN2NapFF solutions (5:0 and 0:5 ratios) were comparable to their higher concentration counterparts (10:0 and 0:10 ratios) but not as similar as the 5:5 binary mixture. The minor radius of the ellipse was 12.7 Å larger, and the cylinder radius was 5.9 Å smaller compared to the model parameters corresponding to each component in the 5:5 solution fits, indicating a subtle interaction between the two components in the mixture. (refer to Figure 3-49, Figure 3-50, and Table 3-13).

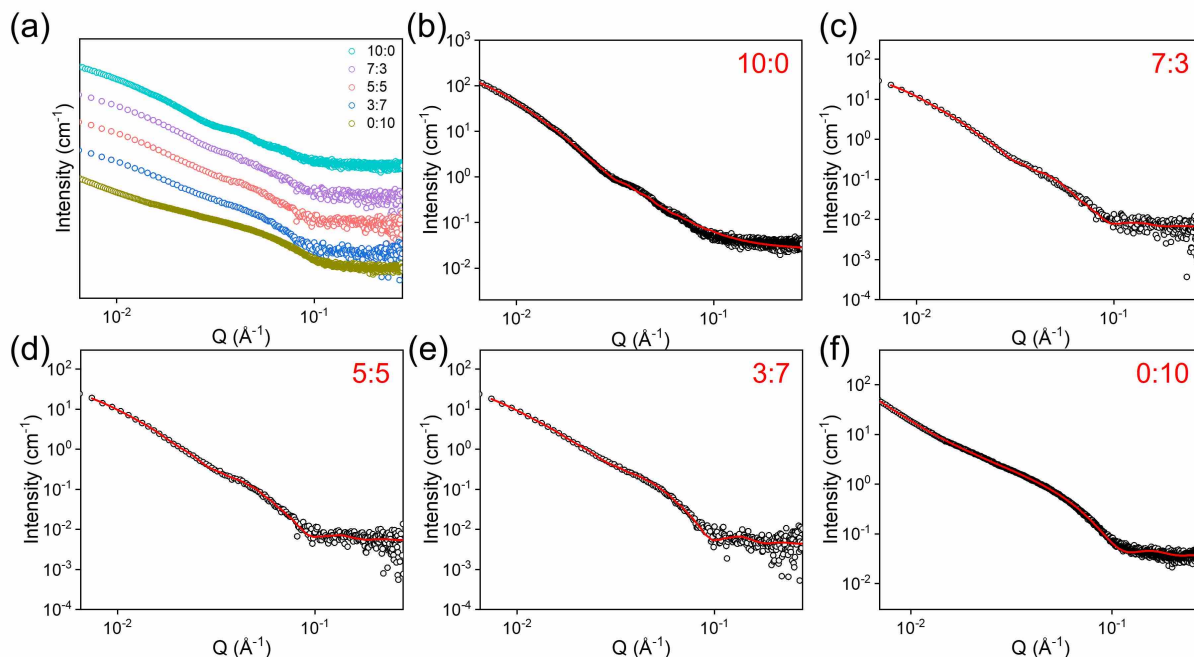


**Figure 3-47.** (a) Experimental SAXS curves (The data were arranged vertically by volume ratio for clear comparison); (b-f) SAXS data (depicted by black circles) and their respective fits (illustrated by red lines) for pre-gelation binary solutions with varying volume ratios, ranging from 10:0, 7:3, 5:5, 3:7, to 0:10, prepared from 10 mg/mL stock solutions of (L,L)-6CN2NapFF:(L,D)-6CN2NapFF.

**Table 3-12.** Summary of parameters used to fit SAXS data for binary solutions, encompassing different volume ratios (10:0, 7:3, 5:5, 3:7, and 0:10) derived from 10 mg/mL stock solutions of (L,L)-6CN2NapFF:(L,D)-6CN2NapFF before gelation. The abbreviations "C", "EC", and "PL" represent the cylinder, elliptical cylinder, and power law models, respectively.

Ratio	10:0	7:3	5:5	3:7	0:10
Model	EC+PL	EC+C	EC+C	EC+C	C+PL
Scale	1	1	1	1	1
Background	0.03	0.01	0.005	0.004	0.04
Background error	0.0004	0.0001	0.0001	0.0001	0.0004
Power law scale	$7.6 \times 10^{-5}$				$9.7 \times 10^{-6}$
Power law scale error	$2.5 \times 10^{-6}$				$3.9 \times 10^{-7}$
Power	2.6				3.1

Chapter 3: A Comprehensive Study on Self-Sorting in a Library of Naphthyl Diphenylalanine Diastereomers

Power error	0.01				0.01
A scale	0.001	0.0005	0.0004	0.0004	
A scale error	$1.1 \times 10^{-5}$	$2.6 \times 10^{-6}$	$2.3 \times 10^{-6}$	$2.4 \times 10^{-6}$	
A radius (Å)	<b>114.5</b>	<b>100.8</b>	<b>104.9</b>	<b>103.1</b>	
A radius error (Å)	0.2	0.6	0.7	0.7	
A axis ratio	2.2	2.5	2.4	2.6	
A axis ratio error	0.01	0.03	0.04	0.04	
A length (Å)	624.1	655.6	698.6	708.1	
A length error (Å)	2.2	7.0	9.0	9.8	
B scale		0.0003	0.0003	0.0005	0.003
B scale error		$3.6 \times 10^{-6}$	$3.4 \times 10^{-6}$	$3.6 \times 10^{-6}$	$9.7 \times 10^{-6}$
B radius (Å)		<b>38.3</b>	<b>38.2</b>	<b>38.1</b>	<b>32.0</b>
B radius error (Å)		0.3	0.3	0.2	0.1
B length (Å)		564.0	605.5	601.5	543.6
B length error (Å)		90.3	91.8	64.8	13.5
$\chi^2$	2.10	1.96	1.51	1.56	<1

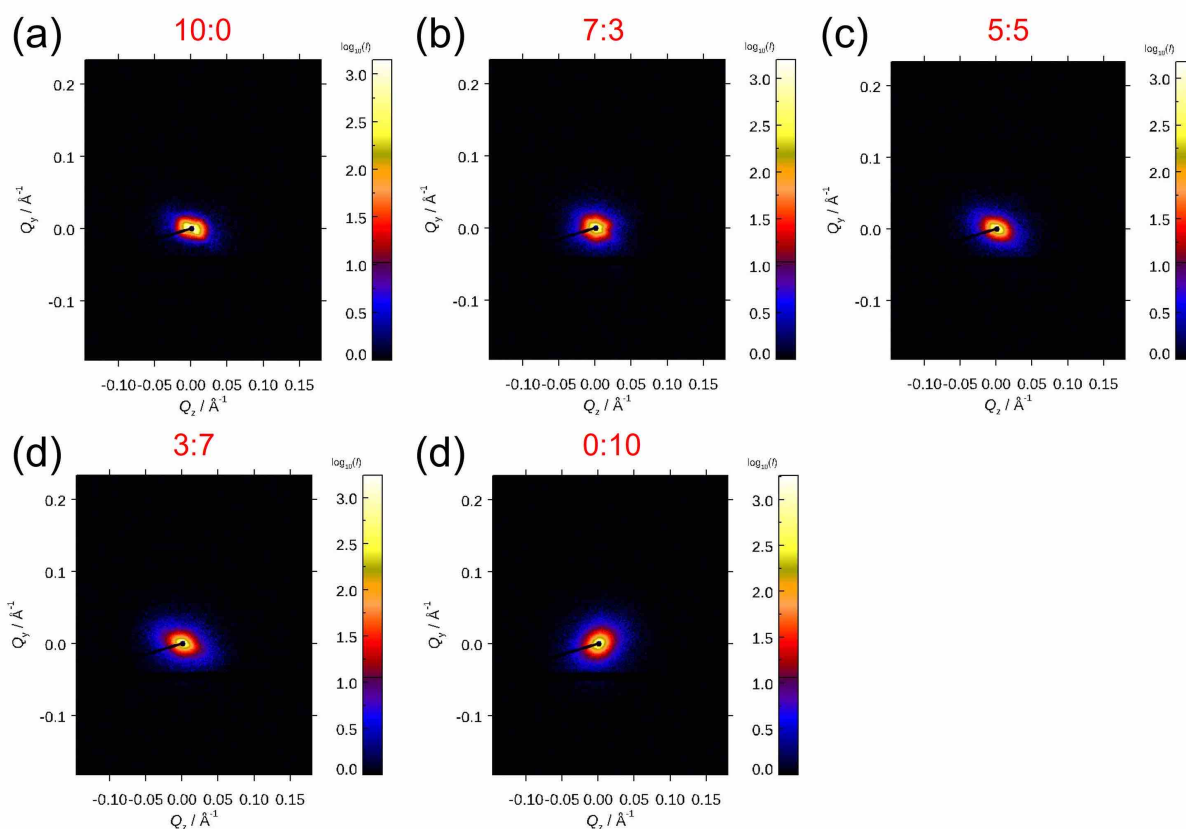


**Figure 3-48.** 2D-SAXS profiles for pre-gelation binary solutions with volume ratios from 10:0, 7:3, 5:5, 3:7, to 0:10 of 10 mg/mL (L,L)-6CN2NapFF:(L,D)-6CN2NapFF stock solutions.

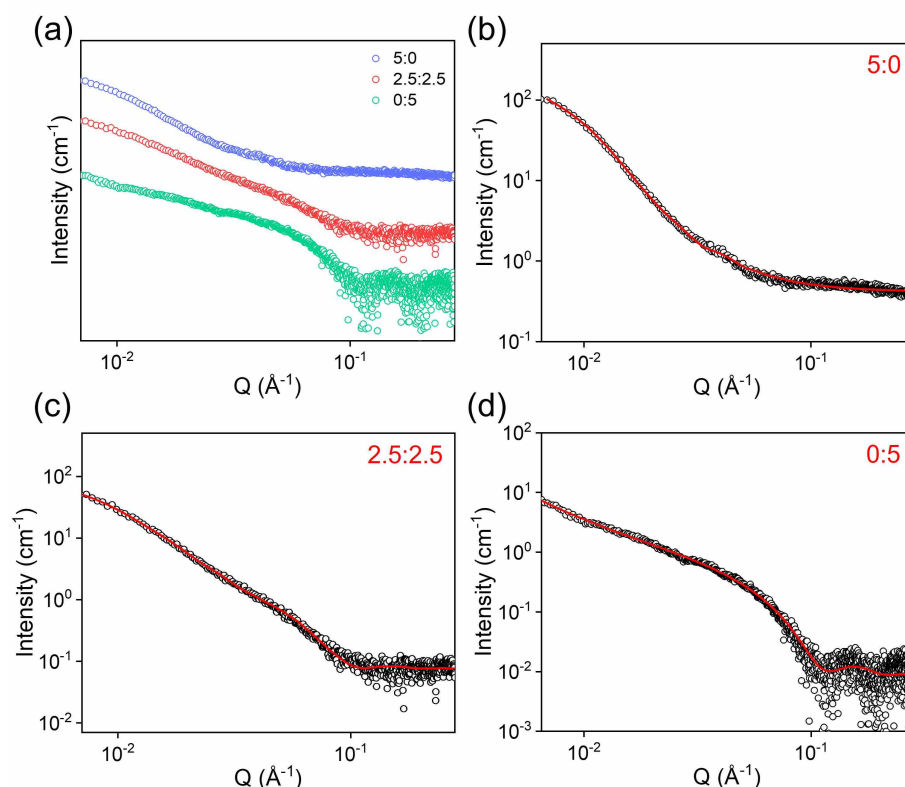


**Figure 3-49.** (a) Experimental SAXS curves (The data were arranged vertically by volume ratio for clear comparison); (b-d) SAXS data (depicted by black circles) and their respective fits (illustrated by red lines) for pre-gelation binary solutions with varying volume ratios including 5:0, 2.5:2.5 and 0:5 prepared from 5 mg/mL stock solutions of (L,L)-6CN2NapFF and (L,D)-6CN2NapFF.

**Table 3-13.** Summary of parameters used to fit SAXS data for binary solutions, encompassing different volume ratios (5:0, 2.5:2.5, and 0:5) derived from 5 mg/mL stock solutions of (L,L)-6CN2NapFF and (L,D)-6CN2NapFF before gelation. The abbreviations "C", "EC", and "PL" represent the cylinder, elliptical cylinder, and power law models, respectively.

Ratio	5:0	2.5:2.5	0:5
Model	EC+PL	EC+C	C+PL
Scale	1	1	1
Background	0.4	0.08	0.009
Background error	0.002	0.0007	0.0004
Power law scale	0.0007		$4.9 \times 10^{-6}$
Power law scale error	$8.5 \times 10^{-5}$		$2.6 \times 10^{-6}$
Power	2.1		2.7
Power error	0.04		0.1
A scale	0.001	0.002	
A scale error	$3.7 \times 10^{-5}$	$3.8 \times 10^{-5}$	
A radius (Å)	117.6	110.72	
A radius error (Å)	1.2	1.3	
A axis ratio	2.8	1.6	
A axis ratio error	0.1	0.06	
A length (Å)	382.2	546.6	
A length error (Å)	4.3	15.4	

B scale		0.003	0.001
B scale error		$2.5 \times 10^{-5}$	$1.7 \times 10^{-5}$
B radius (Å)		35.8	32.3
B radius error (Å)		0.3	0.2
B length (Å)		>1000	>1000
B length error (Å)			
$\chi^2$	2.00	1.24	<1

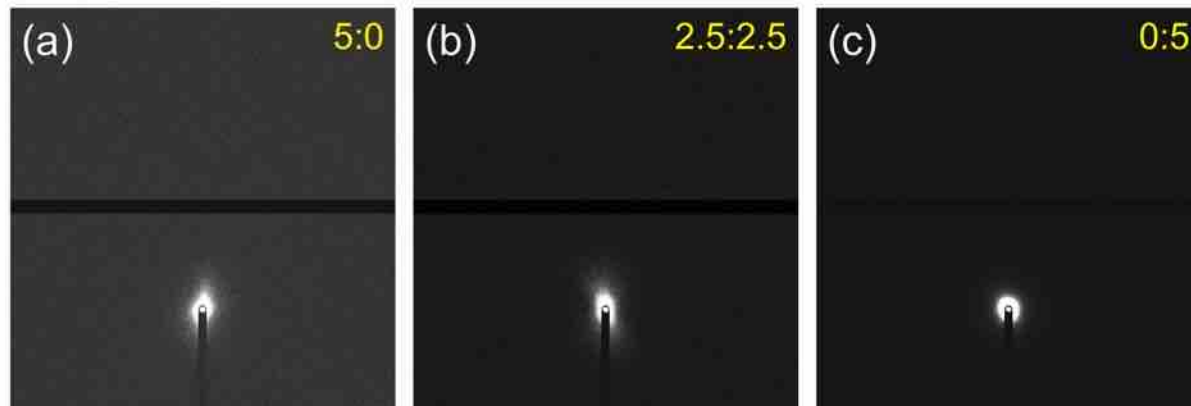


**Figure 3-50.** 2D-SAXS profiles for pre-gelation binary solutions with volume ratios from 5:0, 2.5:2.5 0:5 of 5 mg/mL (L,L)-6CN2NapFF:(L,D)-6CN2NapFF stock solutions.

(L,L)- and (L,D)-6CN2NapFF can both form self-supporting gels under acidic pH (see Figure 3-51a). The turbidity of the binary gel increased with a higher percentage of (L,D)-6CN2NapFF (see Figure A3-96). Confocal microscopy revealed a densely distributed fiber network within the acidic gels (see Figure 3-51(b-f)). During strain sweep tests, a plateau with  $G'$  approximately one order of magnitude higher than  $G''$  was observed in all gels, indicating a gel state across all ratios. The steady strain-softening behavior was observed for all gels after exceeding the yield point, suggesting the uniform distribution of the supramolecular gel network within the gel (see Figure 3-51g). The moduli were found to be independent of frequency in all cases (see Figure 3-51h). (L,L)-6CN2NapFF formed the stiffest hydrogel (see Figure 3-51i). Generally, the moduli of the binary gels exhibited a decreasing trend with increasing (L,D)-6CN2NapFF fraction, suggesting that the fibrous structures composed of the individual components self-sort within the two-component system.

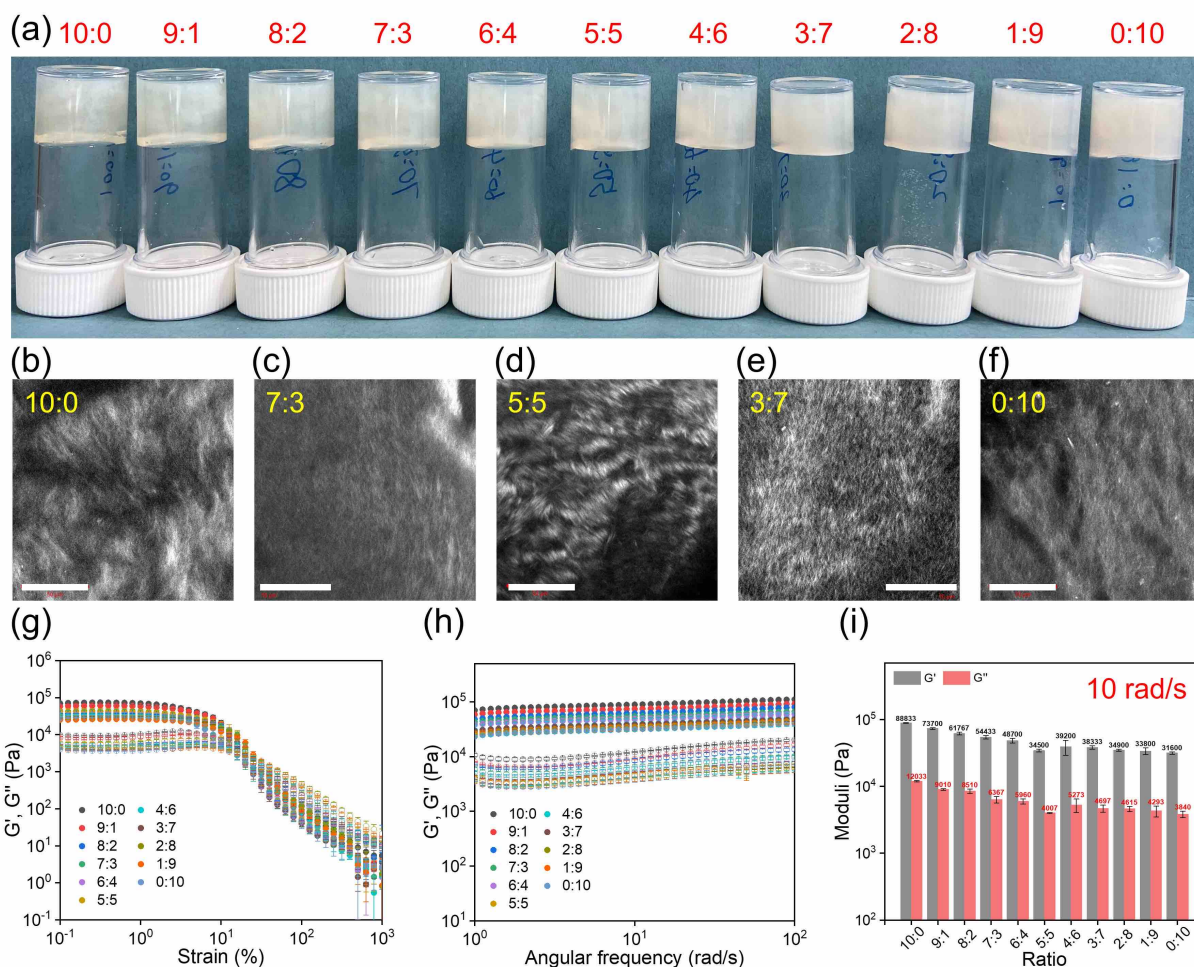


**Figure 3-51.** (a) Photographs, (b-f) confocal fluorescent microscopy images (scale bars indicate 50  $\mu\text{m}$ ), (g) strain sweep, (h) frequency sweep of binary gels at different volume ratios of 10 mg/mL (L,L)-6CN2NapFF:(L,D)-6CN2NapFF stock solutions. (i) A plot illustrating moduli at an angular frequency of 10 rad/s plotted against volume ratios. The data points on the graphs represent the average value of the experimental data of the three samples, and the error bar represents their standard deviation.

The SAXS analysis of (L,L)- and (L,D)-6CN2NapFF gels was conducted using an elliptical cylinder plus a power law model, yielding ellipse minor radii of 110.3  $\text{\AA}$  and 116.0  $\text{\AA}$ , axial ratios of 1.6 and 1.8, and lengths of 393.3  $\text{\AA}$  and 986.5  $\text{\AA}$ , respectively (refer to Figure 3-52 and Table 3-14). In the case of multicomponent gels, the scattering patterns closely resembled and were well-fitted by a combination of elliptical cylinder and power law models, with the ellipse minor radii progressively increasing from 101.6  $\text{\AA}$  in a 9:1 ratio to 120.9  $\text{\AA}$  in a 1:9 ratio as the proportion of (L,D)-6CN2NapFF increased. Attempts to use a combined model involving identical elliptical cylinders with parameters consistent with those obtained in the one-component gels resulted in a negative scale (scale factor or volume fraction of sample),

indicating that SAXS cannot distinguish fibers with Angstrom-level differences in the mixed system. The 2D-SAXS profile also exhibited similar intensity modulations (Figure 3-53).

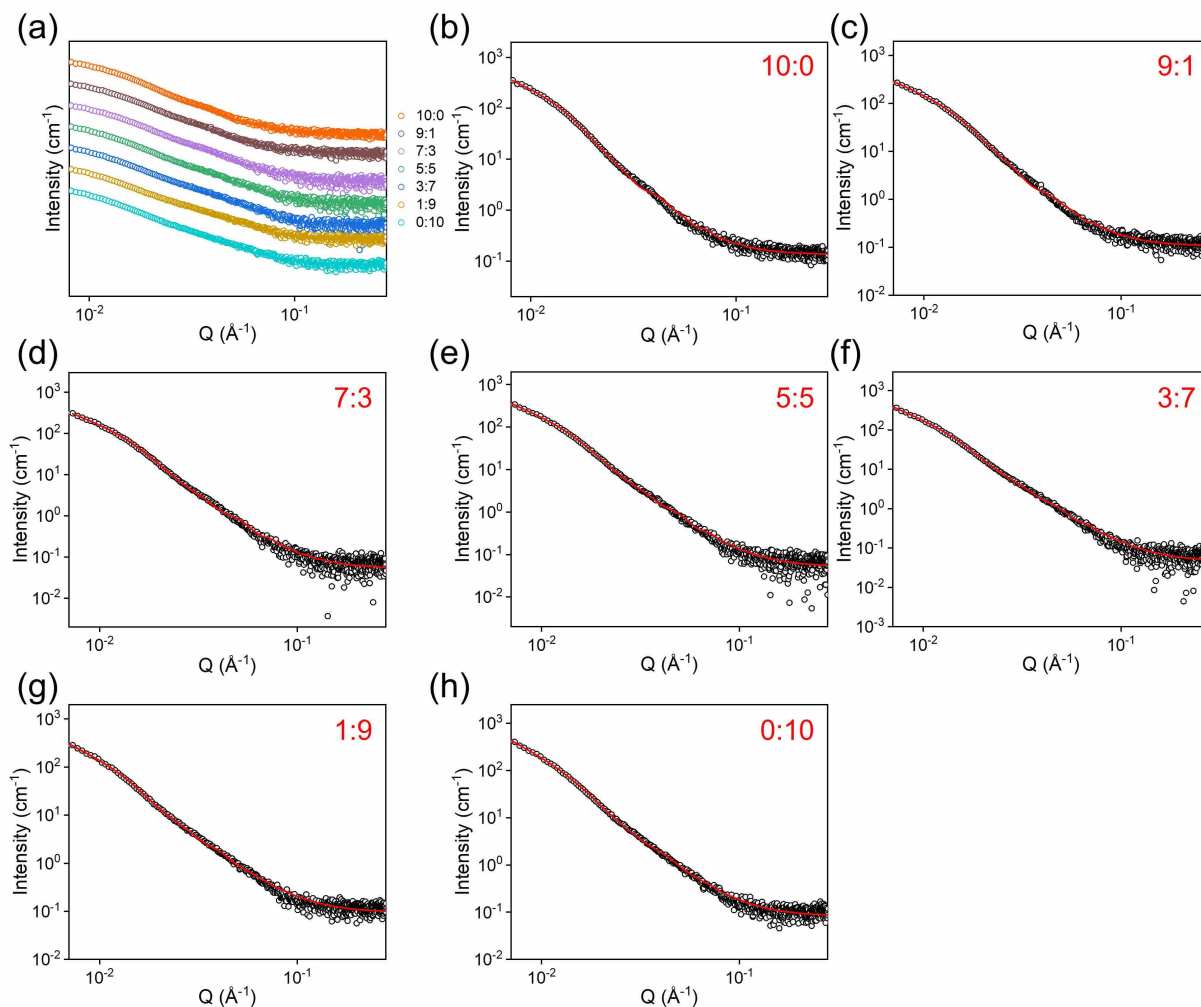


**Figure 3-52.** (a) Experimental SAXS curves (The data were arranged vertically by volume ratio for clear comparison); (b-f) SAXS data (depicted by black circles) and their respective fits (illustrated by red lines) for binary gels with varying volume ratios, ranging from 10:0, 9:1, 7:3, 5:5, 3:7, 1:9, to 0:10, prepared from 10 mg/mL stock solutions of (L,L)-6CN2NapFF and (L,D)-6CN2NapFF.

**Table 3-14.** Summary of parameters used to fit SAXS data for binary gels, encompassing different volume ratios (10:0, 9:1, 7:3, 5:5, 3:7, 1:9, and 0:10) derived from 10 mg/mL stock solutions of (L,L)-6CN2NapFF and (L,D)-6CN2NapFF. The abbreviations "EC" and "PL" represent the elliptical cylinder and power law models, respectively.

Ratio	10:0	9:1	7:3	5:5	3:7	1:9	0:10
Model	EC+PL						
Scale	1	1	1	1	1	1	1
Background	0.1	0.1	0.05	0.05	0.05	0.09	0.08
Background error	0.001	0.001	0.001	0.001	0.001	0.001	0.001
A scale	$5.8 \times 10^{-5}$	$7.6 \times 10^{-5}$	$7.2 \times 10^{-5}$	$7.6 \times 10^{-5}$	$9.6 \times 10^{-5}$	$1.6 \times 10^{-4}$	$9.8 \times 10^{-5}$

Chapter 3: A Comprehensive Study on Self-Sorting in a Library of Naphthyl Diphenylalanine Diastereomers

A scale error	$2.0 \times 10^{-6}$	$3.0 \times 10^{-6}$	$3.0 \times 10^{-6}$	$3.1 \times 10^{-6}$	$3.3 \times 10^{-6}$	$6.4 \times 10^{-6}$	$3.5 \times 10^{-6}$
A power	3.1	2.9	3.0	3.0	3.0	2.8	3.0
A power error	0.01	0.01	0.01	0.01	0.01	0.01	0.01
B scale	0.006	0.004	0.004	0.004	0.003	0.003	0.004
B scale error	$5.2 \times 10^{-5}$	$4.6 \times 10^{-5}$	$6.8 \times 10^{-5}$	$7.4 \times 10^{-5}$	$7.5 \times 10^{-5}$	$6.8 \times 10^{-5}$	$7.5 \times 10^{-5}$
B radius (Å)	<b>110.3</b>	<b>101.6</b>	<b>103.4</b>	<b>109.3</b>	<b>112.7</b>	<b>120.9</b>	<b>116.0</b>
B radius error (Å)	0.4	0.6	0.6	0.6	0.7	0.9	0.6
B axis ratio	1.6	1.8	2.4	2.4	2.3	2.1	1.8
B axis ratio error	0.01	0.02	0.06	0.06	0.06	0.06	0.03
B length (Å)	393.3	390.1	305.2	312.2	326.5	353.1	986.5
B length error (Å)	2.2	3.3	2.0	2.1	2.6	3.7	13.2
$\chi^2$	2.68	2.52	2.14	1.93	2.19	2.22	2.01

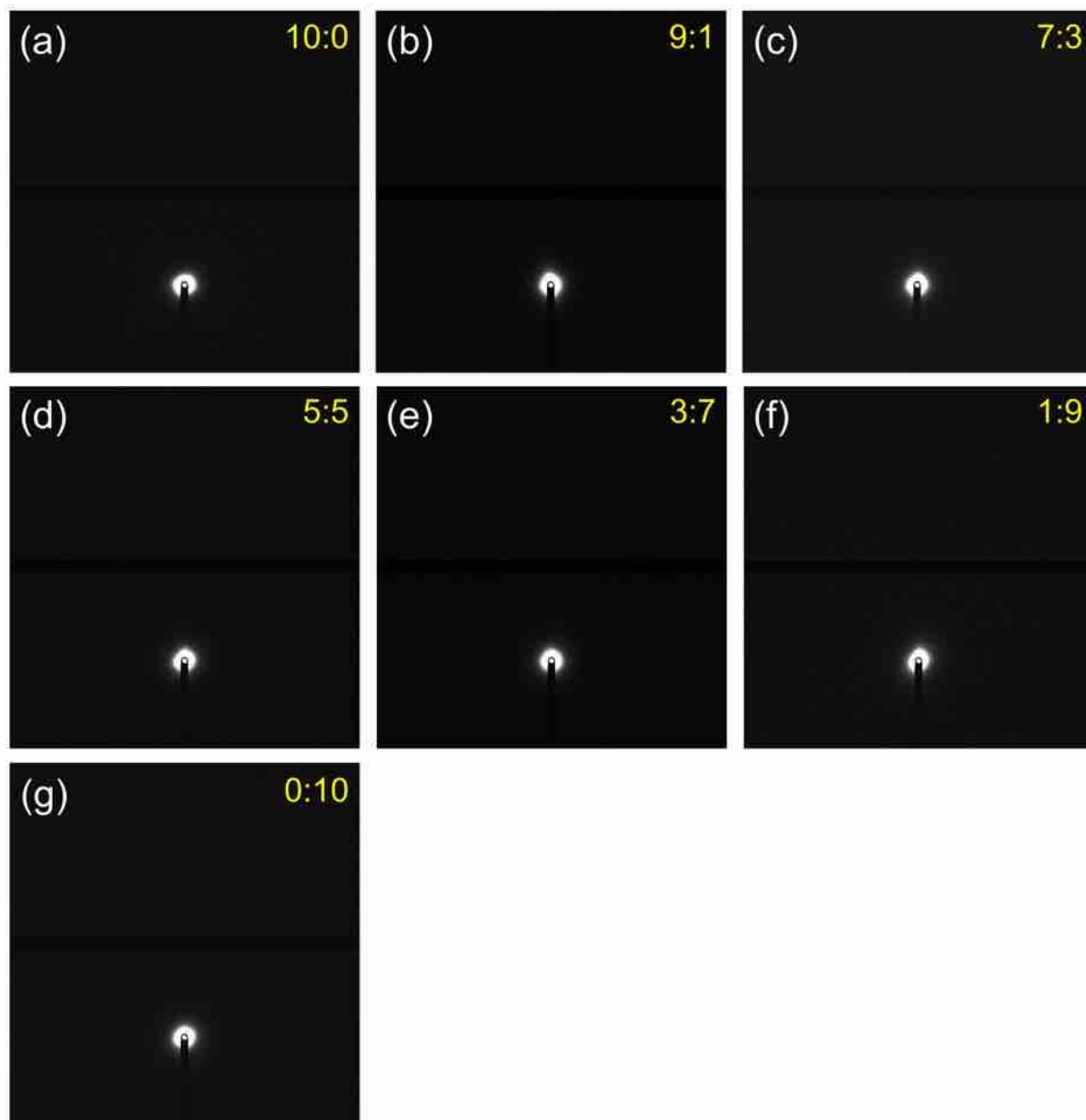


**Figure 3-53.** (a) 2D-SAXS profiles for binary gels with varying volume ratios, ranging from 10:0, 9:1, 7:3, 5:5, 3:7, 1:9, to 0:10, prepared from 10 mg/mL stock solutions of (L,L)-6CN2NapFF:(L,D)-6CN2NapFF.

### 3.2.5 4C11NapFF

(L,L)-4C11NapFF and (L,D)-4C11NapFF form opaque and turbid solutions, respectively, under alkaline pH conditions (refer to Figure 3-54a). Upon dilution with the (L,D)-4C11NapFF component, the turbidity of the mixed solution gradually increased (Figure A3-98). Examination under cross-polarized optical microscopy revealed the presence of worm-like micelles in the samples (Figure 3-54(b-1)). Aligned fibrous structures with birefringent areas were observed in solutions with ratios ranging from 6:4 to 0:10, indicating various levels of anisotropy hierarchies. Shear viscosity measurements demonstrated that all solutions exhibited shear-thinning non-Newtonian behavior with increasing shear rate (Figure 3-54m). Solutions ranging from 10:0 to 4:6 required a specific shear rate to induce fluid flow. At low shear rates, the (L,L)-4C11NapFF solution exhibited a zero-shear viscosity plateau until reaching the critical shear rate ( $63.1 \text{ s}^{-1}$ ). The viscosity at a shear rate of  $10 \text{ s}^{-1}$  gradually increased with the enlarged ratio, peaking at  $0.037 \text{ Pa s}^{-1}$  at 6:4, and then sharply decreased with further increases in the ratio (refer to Figure 3-54n).

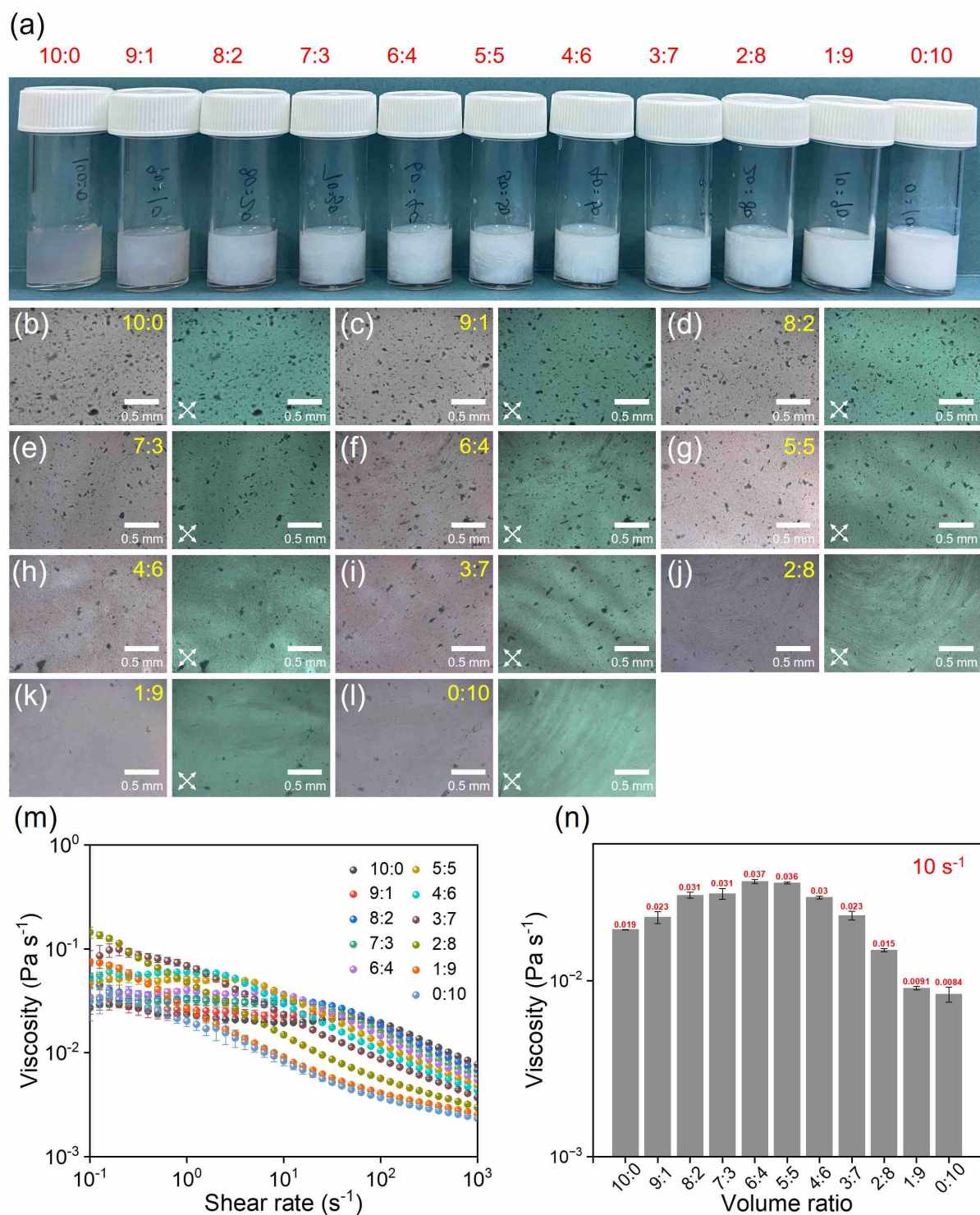


**Figure 3-54.** (a) Photographs of solutions, (b-l) optical microscopy images taken under normal light and cross-polarized conditions (magnified at 5 $\times$ ; scale bars indicated 500  $\mu\text{m}$ , with white crosses denoting polariser orientations), (m) viscosity measurements of binary solutions at different volume ratios of 10 mg/mL (L,L)-4C11NapFF:(L,D)-4C11NapFF stock solutions. (n) A plot illustrating viscosity data at a shear rate of 10 s<sup>-1</sup> plotted against volume ratios. The data

points on the graphs represent the average value of the experimental data of the three samples, and the error bar represents their standard deviation.

The CD data obtained from a concentration of 5 mg/mL of (L,L)-4C11NapFF showed a notably distinct profile compared to that of (L,D)-4C11NapFF, indicating unique and consistent signals for each system (see Figure 3-55a). The CD pattern of 5:5 binary solutions resembled the sum of the CD spectra of individual components, suggesting the presence of self-sorting (see Figure 3-55b). Furthermore, Figure 3-55c demonstrates that the CD signal representing the chiral self-assembled aggregates diminished with higher proportions of (L,D)-4C11NapFF across all ratios, strongly indicating the existence of self-sorting in this binary system.

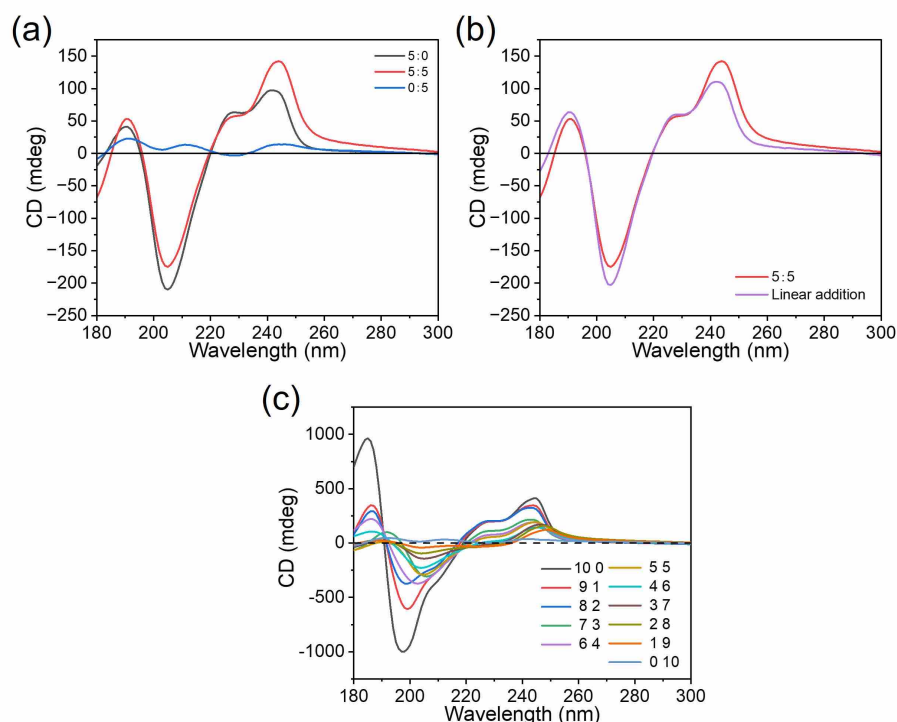


**Figure 3-55.** (a) CD spectra of 5 mg/mL of (L,L)-4C11NapFF (labeled as 5:0), a mixture with 5:5 ratio of 10 mg/mL (L,L)-4C11NapFF:(L,D)-4C11NapFF stock solutions, and 5 mg/mL (L,D)-4C11NapFF (labeled as 0:5) solutions at pH 10.5. (b) The spectra illustrate a comparison between the 5:5 ratio of 10 mg/mL (L,L)-4C11NapFF:(L,D)-4C11NapFF stock solutions and the calculated theoretical self-sorted combination of the 5:0 and 0:5 spectra. (c) CD spectra of solutions containing 10 mg/mL of (L,L)-4C11NapFF:(L,D)-4C11NapFF at ratios ranging from 10:0 to 0:10.

The temperature-dependent CD data of the (L,L)-4C11NapFF solution remained comparable to the initial state even at high temperatures, as shown in Figure 3-56(a-b), indicating that its self-assembled structure was stable under elevated temperatures. The absorption peak intensity

gradually recovered during the cooling process without reaching the initial level. In contrast, for the (L,D)-4C11NapFF solution (Figure 3-57(a-b)), the spectrum did not change significantly during the heating cycle and the signal intensity dropped sharply and was unable to recover during the cooling process. Regarding the 5:5 binary mixture, as depicted in Figure 3-58(a-b), the CD signal at 228 nm gradually weakened during heating and recovered during cooling.

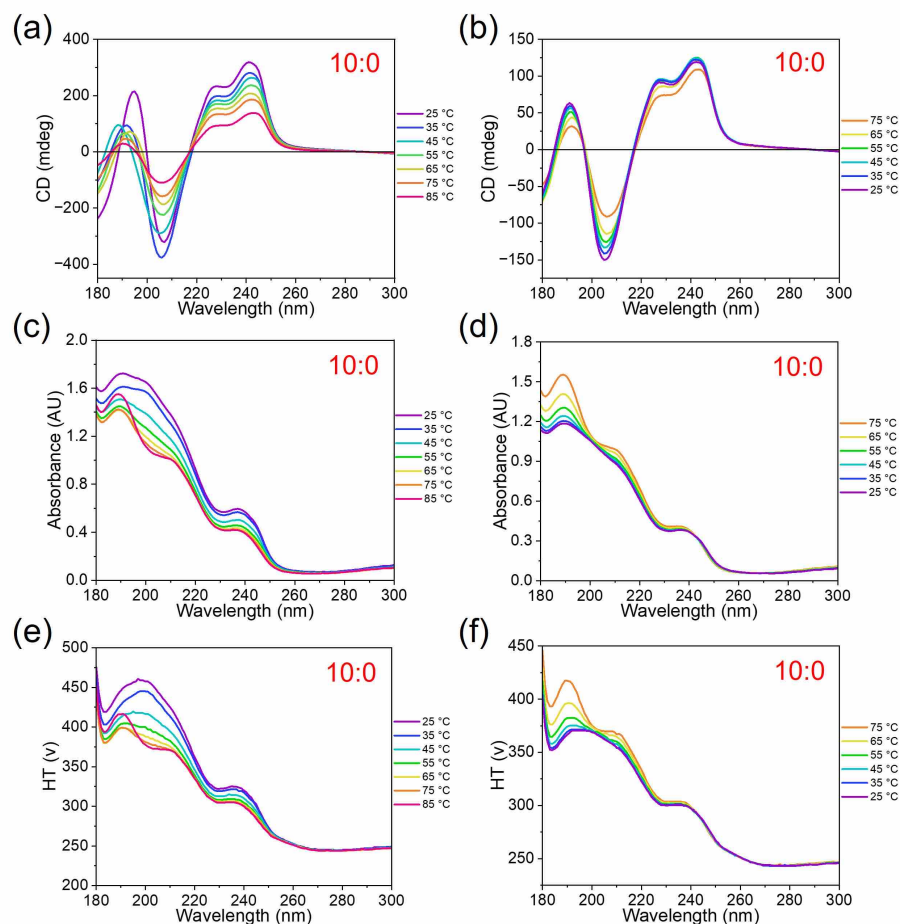


**Figure 3-56.** Temperature-dependent (a-b) CD, (c-d) absorbance, and (e-f) HT data for 10 mg/mL (L,L)-4C11NapFF solutions at pH 10.5. (a), (c), and (e) represent the heating process, while (b), (d), and (f) correspond to the cooling process.

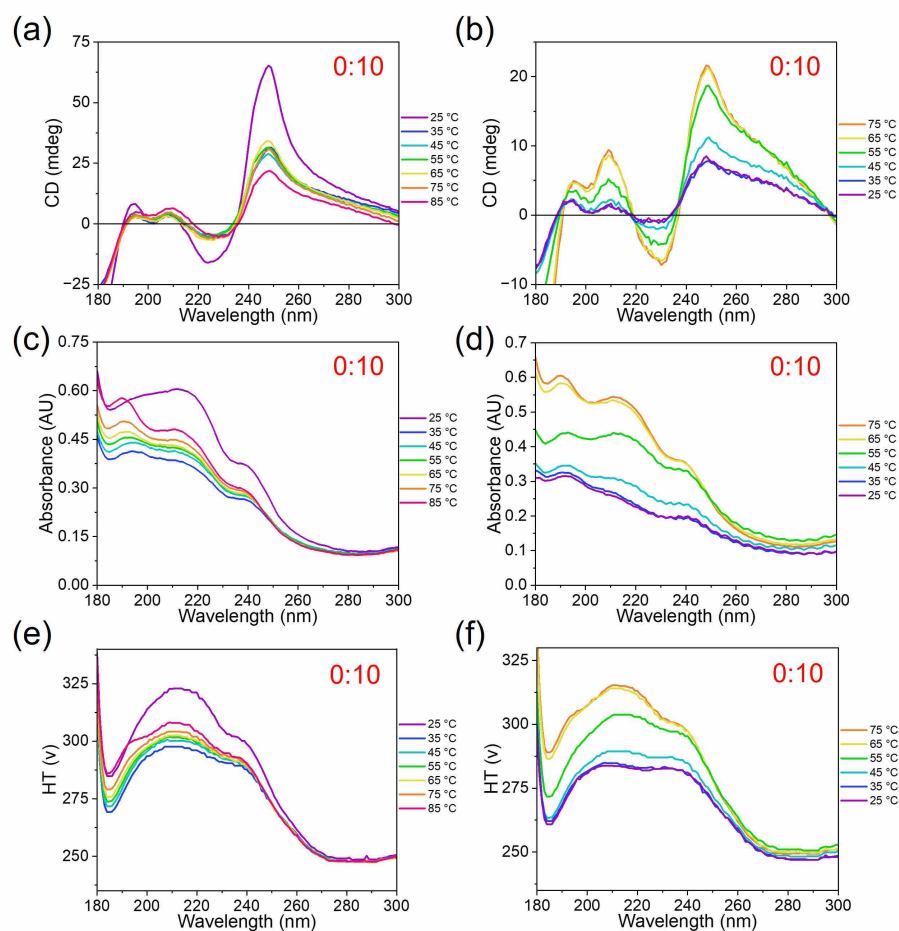


**Figure 3-57.** Temperature-dependent (a-b) CD, (c-d) absorbance, and (e-f) HT data for 10 mg/mL (L,D)-4C11NapFF solutions at pH 10.5. (a), (c), and (e) represent the heating process, while (b), (d), and (f) correspond to the cooling process.

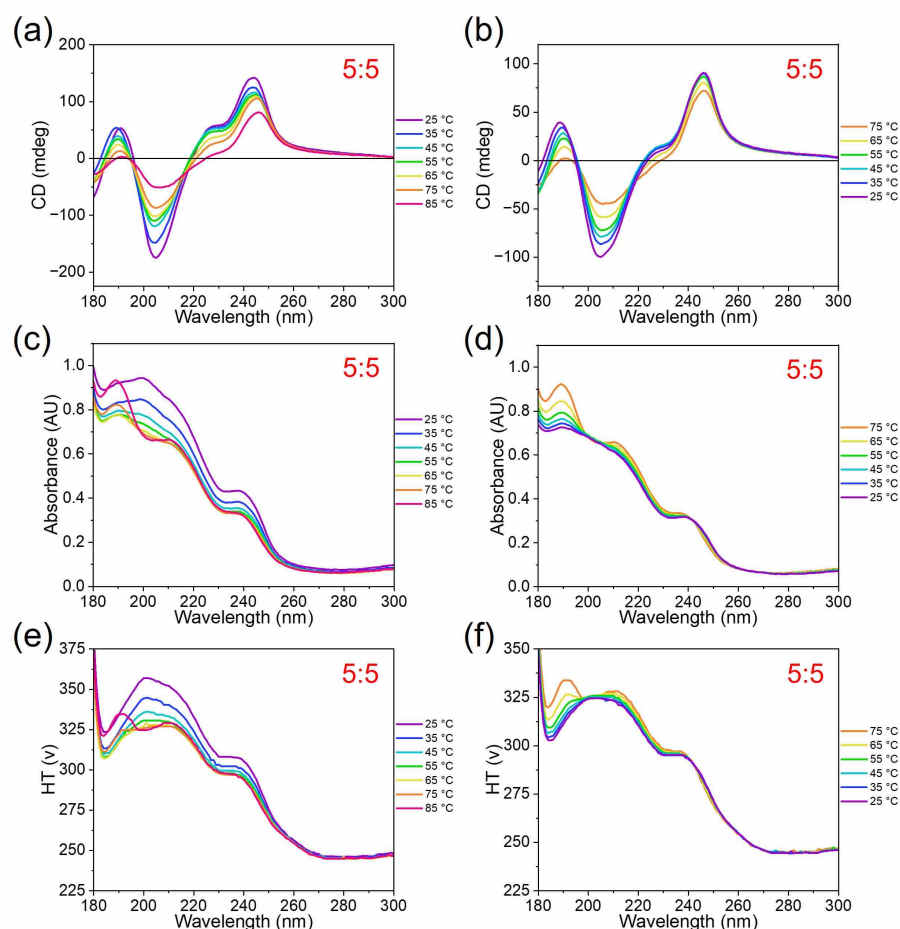


**Figure 3-58.** Temperature-dependent (a-b) CD, (c-d) absorbance, and (e-f) HT data for a mixture with a 5:5 ratio of 10 mg/mL (L,L)-4C11NapFF:(L,D)-4C11NapFF stock solutions at high pH. (a), (c), and (e) represent the heating process, while (b), (d), and (f) correspond to the cooling process.

SAXS was employed to probe the self-assembled structure in solutions. As shown in Figure 3-59 and Table 3-15, (L,L)-4C11NapFF self-assembles into a flexible cylinder with a diameter of  $28.0 \pm 0.1 \text{ \AA}$ , a Kuhn length of  $83.9 \pm 4.4 \text{ \AA}$ , and a length of  $335.7 \pm 7.6 \text{ \AA}$ ; (L,D)-4C11NapFF formed a flexible cylinder with a diameter of  $29.7 \pm 0.1 \text{ \AA}$ , a Kuhn length of  $352.0 \pm 30.9 \text{ \AA}$ , and a length exceeding  $1000 \text{ \AA}$ . The scattering at low  $Q$  was well-fitted by a power law model. The Kuhn length ( $b$ ) is proportional to the persistence length ( $l_p$ ), which represents the length of segments that are locally stiff ( $b = 2 * l_p$ ). Therefore, (L,D)-4C11NapFF self-assemblies have a persistence length 4.2 times that of (L,L)-4C11NapFF, indicating higher stiffness in the fibers of the former. Since the radii of the fibrous structures consisting of the diastereomers are too close to be differentiated by SAXS, the hybrid system cannot be fitted by combining two-cylinder models derived from individual components. The SAXS data of the binary solutions was modelled by a flexible cylinder with a power law, where the radius and Kuhn length of the

cylindrical micelles are between 29.9-30.9 Å and 319.5-428.2 Å, respectively. The diminishing orientation in the 2D scattering pattern shows that the anisotropic structure in the binary system decreases with increasing (L,D)-4C11NapFF fraction (see Figure 3-60).

The SAXS data of the dilute (L,L)-4C11NapFF solution (5:0) were modeled by a cylinder with a radius of  $31.0 \pm 0.1$  Å and a length of  $364.5 \pm 8.3$  Å, whereas the dilute (L,D)-4C11NapFF solution (0:5) fitted well by cylinder plus power law, with a cylinder radius and length of  $147.4 \pm 4.3$  Å and  $733.7 \pm 100.5$  Å, respectively. These parameters differ significantly from the corresponding parameters in the 5:5 ratio mixture, indicating interactions between individual components in the two-component systems (see Figure 3-61, Figure 3-62, and Table 3-16)

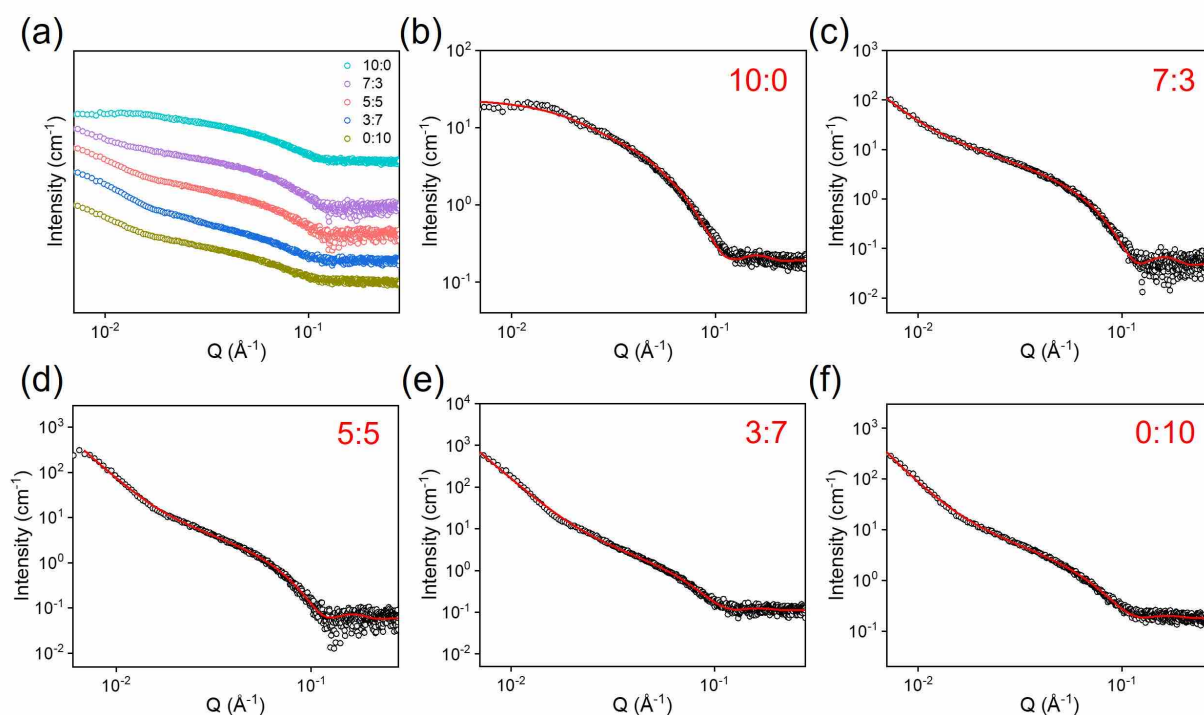


**Figure 3-59.** (a) Experimental SAXS curves (The data were arranged vertically by volume ratio for clear comparison); (b-f) SAXS data (depicted by black circles) and their respective fits (illustrated by red lines) for pre-gelation binary solutions with varying volume ratios, ranging from 10:0, 7:3, 5:5, 3:7, to 0:10, prepared from 10 mg/mL stock solutions of (L,L)-4C11NapFF:(L,D)-4C11NapFF.

**Table 3-15.** Summary of parameters used to fit SAXS data for binary solutions, encompassing different volume ratios (10:0, 7:3, 5:5, 3:7, and 0:10) derived from 10 mg/mL stock solutions of (L,L)-4C11NapFF:(L,D)-4C11NapFF before gelation. The abbreviations "FC" and "PL" represent the flexible cylinder and power law models, respectively.

Ratio	10:0	7:3	5:5	3:7	0:10
Model	FC	FC+PL	FC+PL	FC+PL	FC+PL

Chapter 3: A Comprehensive Study on Self-Sorting in a Library of Naphthyl Diphenylalanine Diastereomers

Scale		1	1	1	1
Background	0.2	0.05	0.06	0.1	0.1
Background error	0.001	0.0007	0.0007	0.001	0.001
A scale		$1.4 \times 10^{-7}$	$3.5 \times 10^{-7}$	$4.5 \times 10^{-7}$	$3.5 \times 10^{-7}$
A scale error		$1.3 \times 10^{-9}$	$2.8 \times 10^{-9}$	$1.7 \times 10^{-9}$	$1.1 \times 10^{-9}$
A power		4.0	4.1	4.3	4.1
A power error		1.3	0.01	0.01	0.01
B scale	0.01	0.009	0.007	0.005	0.01
B scale error	$1.6 \times 10^{-4}$	$9.2 \times 10^{-5}$	$2.6 \times 10^{-5}$	$2.8 \times 10^{-5}$	$4.2 \times 10^{-5}$
B radius (Å)	<b>28.0</b>	<b>30.9</b>	<b>30.4</b>	<b>29.9</b>	<b>29.7</b>
B radius error (Å)	0.1	0.1	0.1	0.1	0.1
B kuhn length (Å)	<b>83.9</b>	<b>428.2</b>	<b>345.1</b>	<b>319.5</b>	<b>352.0</b>
B kuhn length error (Å)	4.4	25.8	31.2	36.1	30.9
B length (Å)	335.7	>1000	>1000	>1000	>1000
B length error (Å)	7.6				
$\chi^2$	2.50	1.68	3.63	9.40	3.45

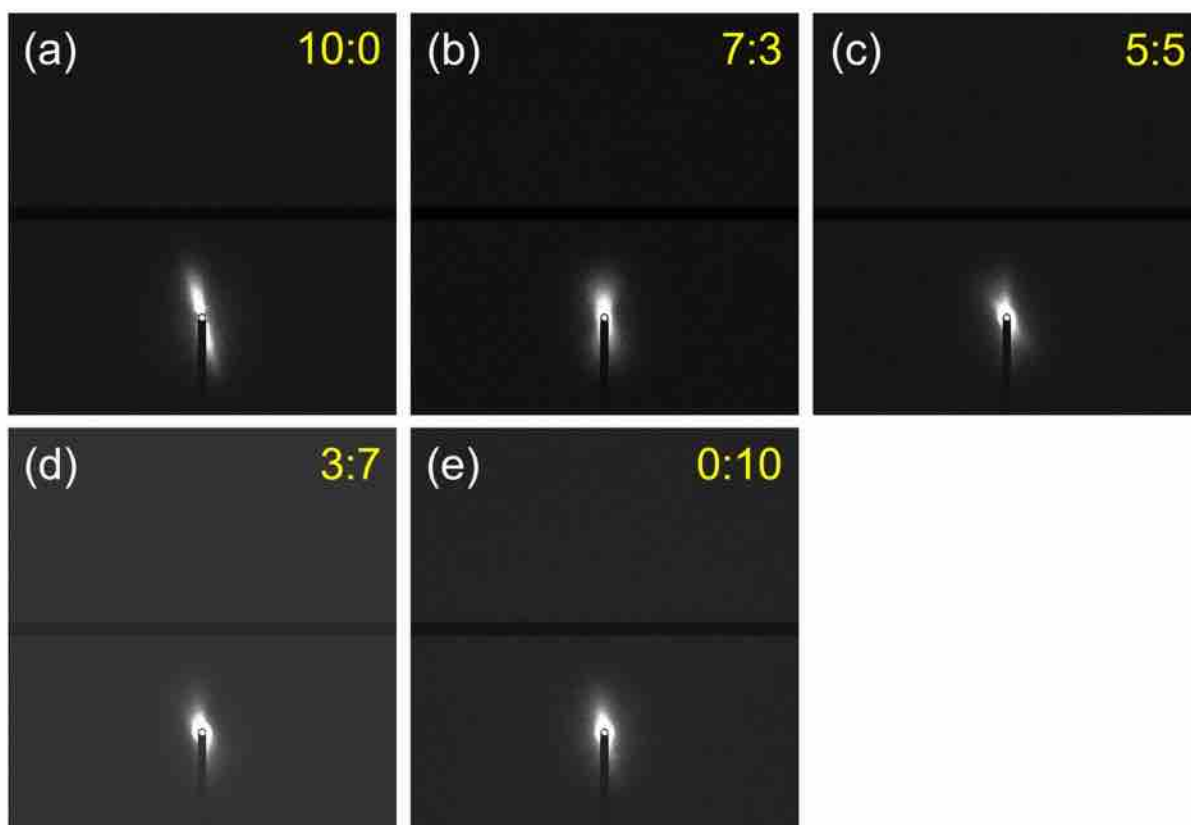


**Figure 3-60.** 2D-SAXS profiles for pre-gelation binary solutions with volume ratios from 10:0, 7:3, 5:5, 3:7, to 0:10 of 10 mg/mL (L,L)-4C11NapFF:(L,D)-4C11NapFF stock solutions.

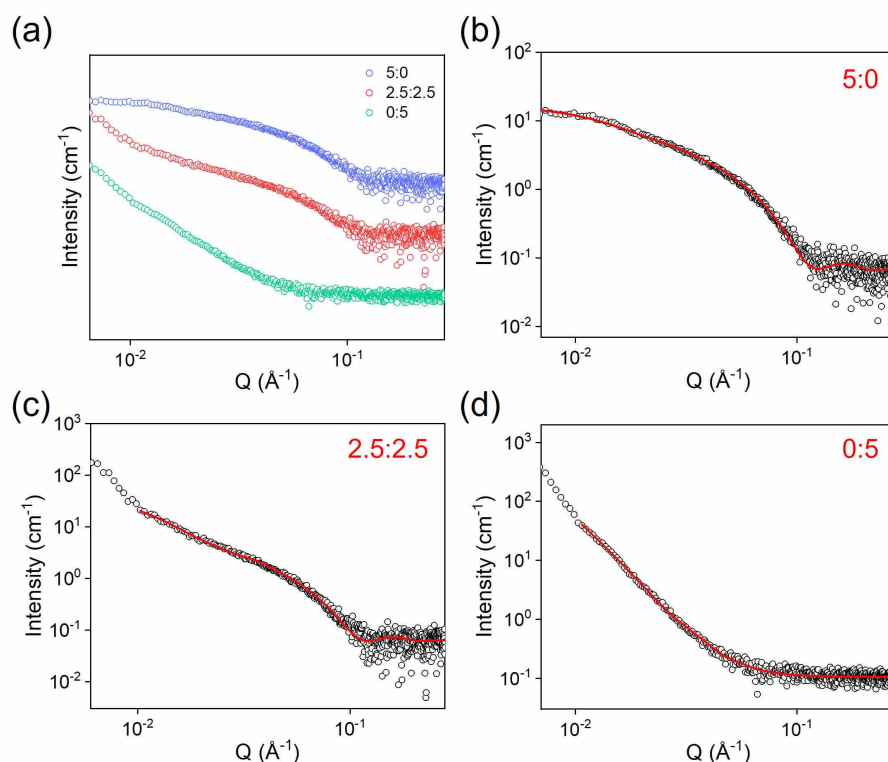


**Figure 3-61.** (a) Experimental SAXS curves (The data were arranged vertically by volume ratio for clear comparison); (b-d) SAXS data (depicted by black circles) and their respective fits (illustrated by red lines) for pre-gelation binary solutions with varying volume ratios including 5:0, 2.5:2.5 and 0:5 prepared from 5 mg/mL stock solutions of (L,L)-4C11NapFF and (L,D)-4C11NapFF.

**Table 3-16.** Summary of parameters used to fit SAXS data for binary solutions, encompassing different volume ratios (5:0, 2.5:2.5, and 0:5) derived from 5 mg/mL stock solutions of (L,L)-4C11NapFF and (L,D)-4C11NapFF before gelation. The abbreviations "C" and "PL" represent the cylinder and power law models, respectively.

Ratio	5:0	2.5:2.5	0:5
Model	C	C+C	C+PL
scale		1	1
Background	0.07	0.06	0.2
Background error	0.001	0.001	0.001
Power law scale			$1.2 \times 10^{-6}$
Power law scale error			$9.2 \times 10^{-8}$
Power			3.8
Power error			0.02
A scale		0.0004	0.0002
A scale error		$9.1 \times 10^{-6}$	$3.4 \times 10^{-5}$
A radius (Å)		144.5	147.4
A radius error (Å)		1.9	4.3
A length (Å)		436.6	733.7
A length error (Å)		24.6	100.5
B scale	0.007	0.001	
B scale error	$3.8 \times 10^{-5}$	$1.0 \times 10^{-5}$	

B radius (Å)	31.0	31.6	
B radius error (Å)	0.1	0.2	
B length (Å)	364.5	>1000	
B length error (Å)	8.3		
$\chi^2$	1.40	1.49	1.10

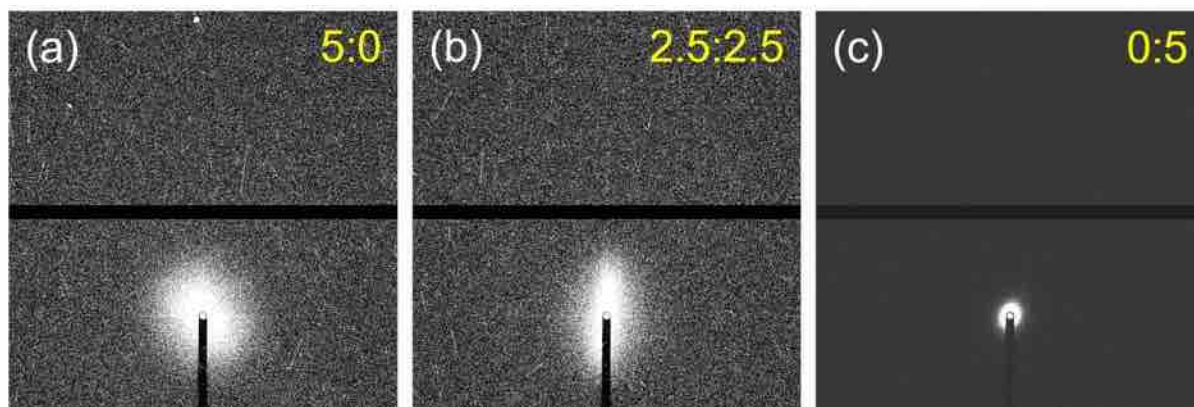


**Figure 3-62.** 2D-SAXS profiles for pre-gelation binary solutions with volume ratios from 5:0, 2.5:2.5 0:5 of 5 mg/mL (L,L)-4C11NapFF:(L,D)-4C11NapFF stock solutions.

The vial inversion test demonstrated the formation of self-supporting supramolecular gels at all ratios under acidic pH (refer to Figure 3-63a). Binary hydrogels underwent syneresis, involving volume contraction and expulsion of entrapped solvent due to fibre-fibre interactions. Syneresis is particularly driven by changes in gelator hydrophobicity triggered by pH, leading to increased hydrophobicity of self-assembled fibers and water expulsion from the gel network.<sup>49, 50</sup> The turbidity of the binary gel increased with the increasing percentage of (L,D)-4C11NapFF, remaining stable after the 2:8 ratio (refer to Figure A3-100). Confocal microscopy reveals an evenly distributed fiber network in the acidic gels and syneresis leads to a denser network in the mixed system (refer to Figure 3-63 (b-f)).

Strain sweep data for all gels exhibit a plateau with  $G'$  approximately one order of magnitude higher than  $G''$ , indicating gel-like behavior across all ratios under acidic conditions (refer to Figure 3-63g). Smooth strain-softening behavior was observed for all gels after exceeding the yield point, suggesting the uniform distribution of the supramolecular fiber network within the gels. In all cases, the modulus was largely independent of frequency (see Figure 3-63h). (L,L)-4C11NapFF formed a stiffer hydrogel than (L,D)-4C11NapFF (refer to Figure 3-63i). Generally, the moduli of binary gels show a decreasing trend with decreasing (L,L)-4C11NapFF fractions, indicating that the self-assembled fibers consisting of single components are likely to self-sort within the two-component system.

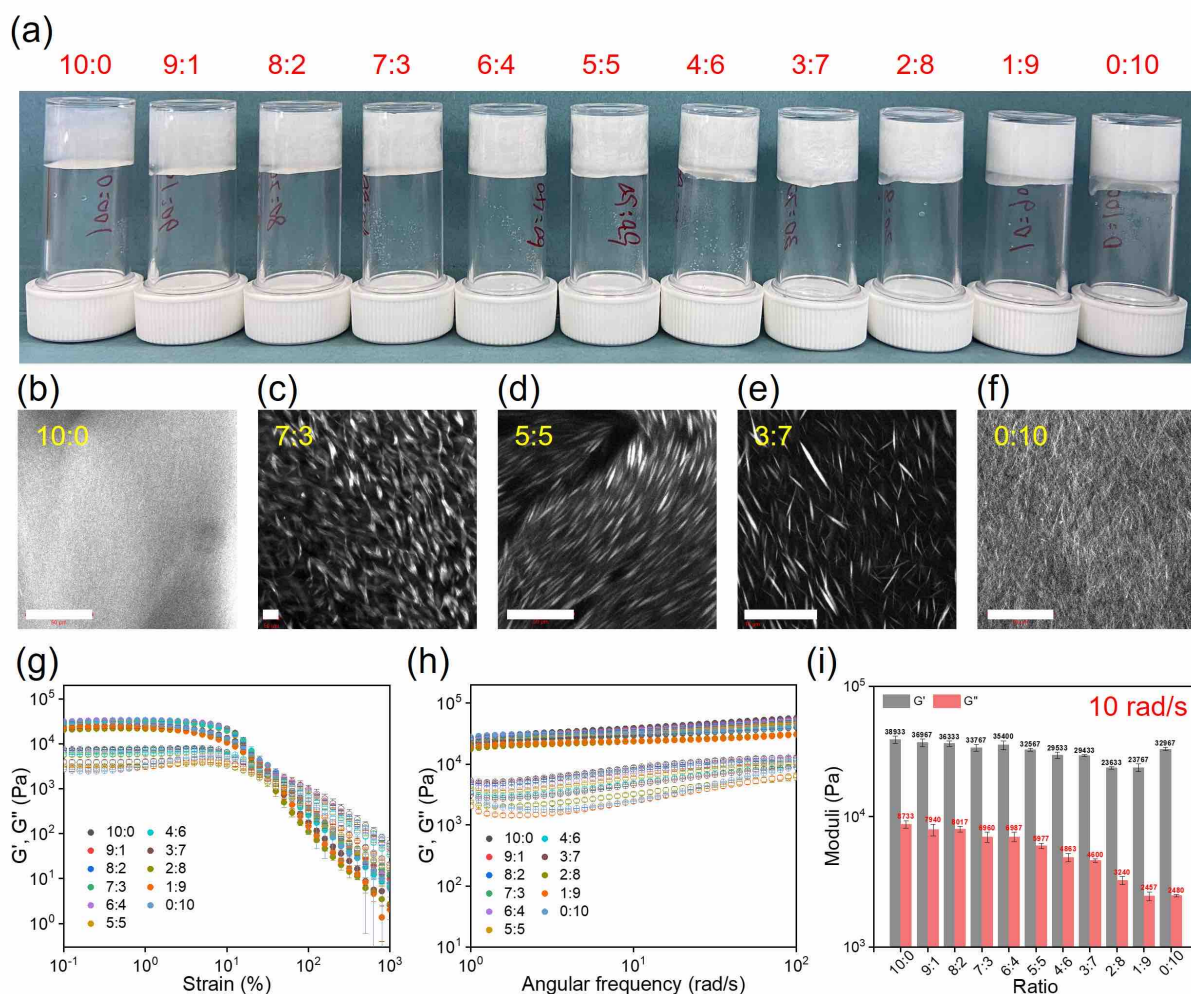


**Figure 3-63.** (a) Photographs, (b-f) confocal fluorescent microscopy images (scale bars indicate 50  $\mu\text{m}$ ), (g) strain sweep, (h) frequency sweep of binary gels at different volume ratios of 10 mg/mL (L,L)-4C11NapFF:(L,D)-4C11NapFF stock solutions. (i) A plot illustrating moduli at an angular frequency of 10 rad/s plotted against volume ratios. The data points on the graphs represent the average value of the experimental data of the three samples, and the error bar represents their standard deviation.

The experimental SAXS data for hydrogels with ratios ranging from 5:5 to 0:10 exhibited a Bragg peak at  $Q = 0.199 \text{ \AA}^{-1}$  ( $d = 31.6 \text{ \AA}$ ), indicating the presence of crystal-like order and periodic arrangement within the fibrous network in the gel (Figure 3-64a). The SAXS data of pH-triggered (L,L)-4C11NapFF and (L,D)-4C11NapFF hydrogels could be fitted to ellipse minor radii of 27.3  $\text{\AA}$  and 19.1  $\text{\AA}$ , axis ratios of 4.0 and 2.6, and lengths of 549.4  $\text{\AA}$  and  $>1000 \text{ \AA}$  for elliptical cylinders (see Figure 3-64 and Table 3-17). The low-Q region could be described by a power law model. For multicomponent gels, the scattering pattern was modelled as a combination of elliptical cylinder and power law. As the ratio of (L,D)-4C11NapFF increased, the ellipse minor radii gradually increased from 42.5  $\text{\AA}$  at the 9:1 ratio to 12.2  $\text{\AA}$  at the 1:9 ratio.

The SAXS data are unable to distinguish fibers with Angstrom-scale differences in the mixture. Attempting to use a combined model containing identical elliptical cylinders with parameters consistent with those obtained in single-component gels resulted in a negative scale (scale factor or the volume fraction of the sample). The orientation of the 2D-SAXS pattern revealed that (L,L)-4C11NapFF fibers exhibited higher anisotropy compared to (L,D)-4C11NapFF. Decreasing the (L,L)-4C11NapFF content led to a decrease in orientation, indicating increased isotropy (see Figure 3-65).

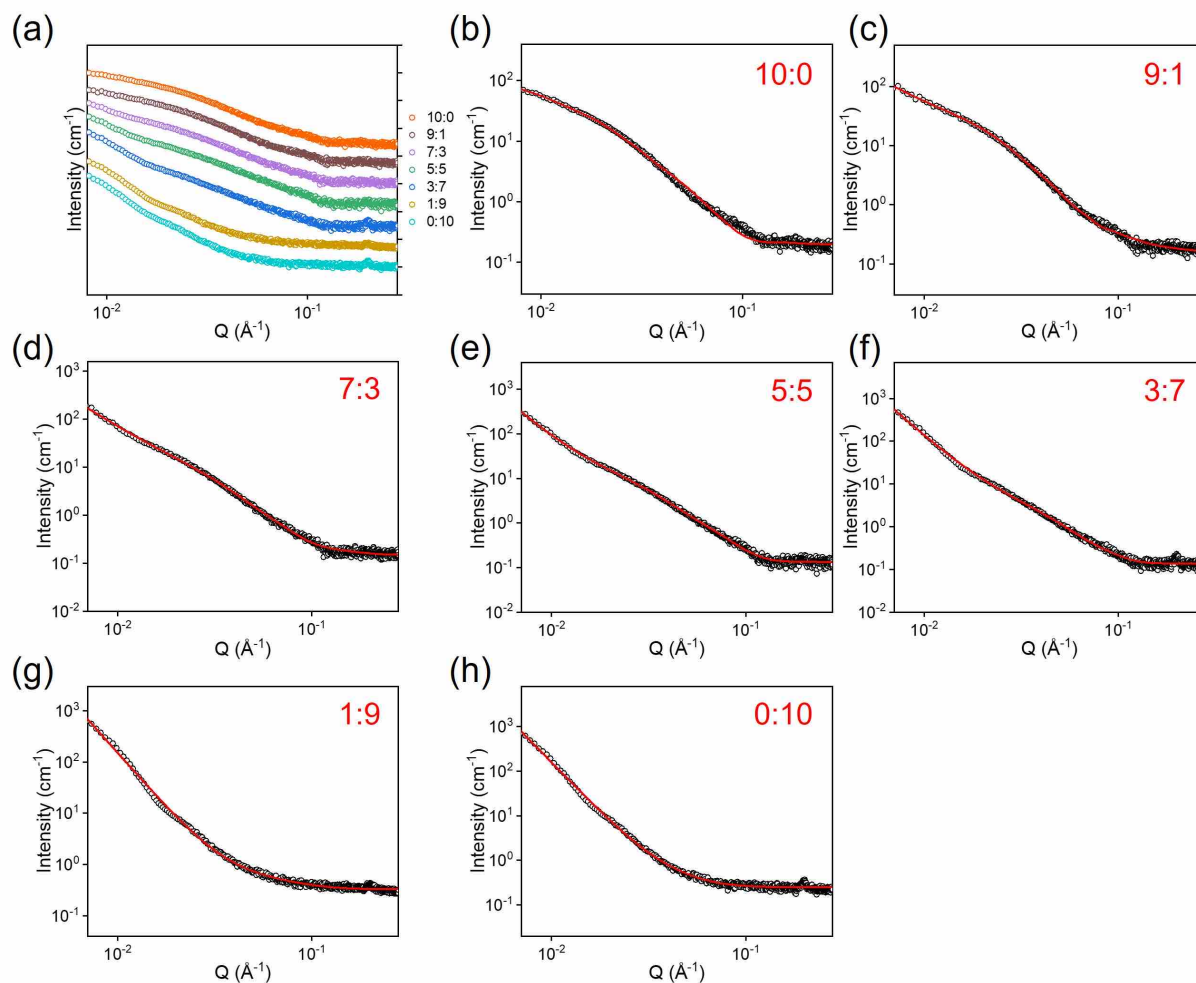


**Figure 3-64.** (a) Experimental SAXS curves (The data were arranged vertically by volume ratio for clear comparison); (b-f) SAXS data (depicted by black circles) and their respective fits (illustrated by red lines) for binary gels with varying volume ratios, ranging from 10:0, 9:1, 7:3, 5:5, 3:7, 1:9, to 0:10, prepared from 10 mg/mL stock solutions of (L,L)-4C11NapFF and (L,D)-4C11NapFF.

**Table 3-17.** Summary of parameters used to fit SAXS data for binary gels, encompassing different volume ratios (10:0, 9:1, 7:3, 5:5, 3:7, 1:9, and 0:10) derived from 10 mg/mL stock solutions of (L,L)-4Cl1NapFF and (L,D)-4Cl1NapFF. The abbreviations "EC" and "PL" represent the elliptical cylinder and power law models, respectively.

Ratio	10:0	9:1	7:3	5:5	3:7	1:9	0:10
Model	EC	EC+PL	EC+PL	EC+PL	EC+PL	EC+PL	EC+PL
Scale		1	1	1	1	1	1
Background	0.2	0.2	0.1	0.1	0.1	0.3	0.2
Background error	0.001	0.001	0.001	0.001	0.001	0.002	
A scale		0.0007	0.0002	$1.3 \times 10^{-6}$	$1.3 \times 10^{-6}$	$4.4 \times 10^{-7}$	$1.8 \times 10^{-7}$
A scale error		$2.8 \times 10^{-5}$	$1.7 \times 10^{-5}$	$2.0 \times 10^{-7}$	$8.0 \times 10^{-8}$	$1.4 \times 10^{-8}$	$3.3 \times 10^{-10}$
A power		2.3	2.7	3.9	4.0	4.3	4.5
A power error		0.01	0.02	0.03	0.01	0.01	
B scale	0.01	0.005	0.005	0.008	0.005	0.003	0.0008
B scale error	$3.9 \times 10^{-5}$	$5.9 \times 10^{-5}$	0.0002	$8.6 \times 10^{-5}$	$6.4 \times 10^{-5}$	$2.9 \times 10^{-4}$	$2.1 \times 10^{-5}$
B radius (Å)	<b>27.3</b>	<b>42.5</b>	<b>28.4</b>	<b>22.3</b>	<b>22.0</b>	<b>12.2</b>	<b>19.1</b>
B_radius_error (Å)	0.1	0.4	0.5	0.2	0.3	2.0	
B axis ratio	4.0	2.2	2.7	3.4	2.6	2.1	2.6
B axis ratio error	0.03	0.04	0.09	0.06	0.08	0.5	
B length (Å)	549.4	234.5	573.4	518.5	481.6	441.2	>1000
B_length_error (Å)	9.7	3.5	34.7	20.6	37.8	206.7	
$\chi^2$	3.59	2.23	2.66	2.38	5.26	8.79	7.23

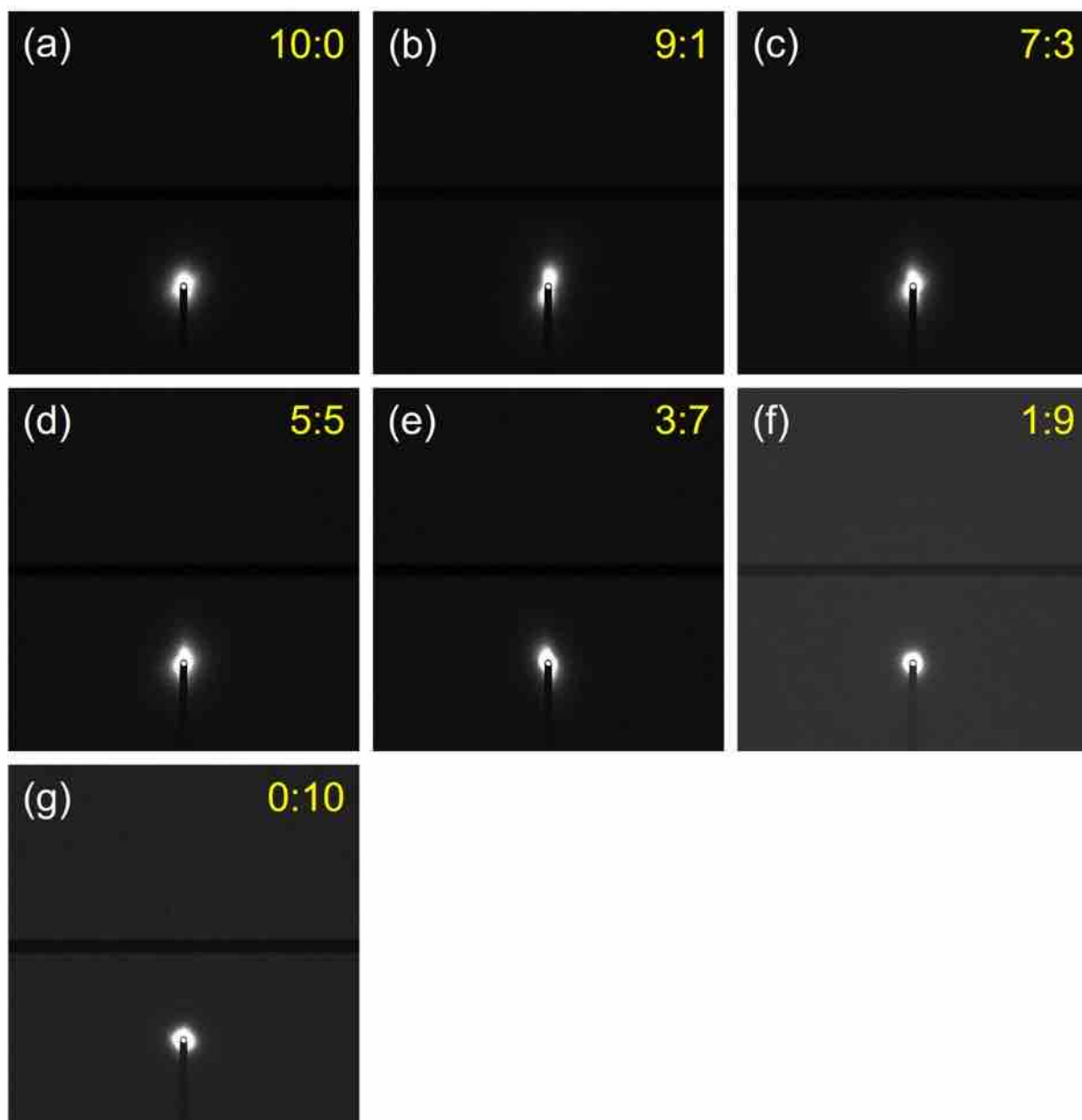


**Figure 3-65.** (a) 2D-SAXS profiles for binary gels with varying volume ratios, ranging from 10:0, 9:1, 7:3, 5:5, 3:7, 1:9, to 0:10, prepared from 10 mg/mL stock solutions of (L,L)-4Cl1NapFF:(L,D)-4Cl1NapFF.

### 3.3 Impact of the Mixing Approach on Multicomponent Systems

Different methods of combining water-soluble components can affect the resulting structures, with solution mixing potentially locking in larger-scale structures before gelation, compared to starting from powders, which could lead to co-assembly or different structures. Preparation methods could even induce self-sorting or co-assembly in fibers of the gel network.<sup>51</sup> We further explored the effect of mixing methods on the resulting two-component systems.

Liquid-phase mixing involves combining prepared gelator micellar solutions in specific volume ratios to create two-component systems. In contrast, solid-phase mixing entails blending gelator powders in defined mass ratios to form a micellar solution. The viscosity of the two-component solutions obtained by solid-state mixing differed somewhat from their liquid-phase mixing counterparts, especially for the 6Br2NapFF system (see Figure 3-66). This difference might be caused by the discrepancy in the supramolecular aggregates and/or the assembly mode of diastereomers in the binary system. SAXS was employed to confirm this conjecture. Figure 3-67 illustrates that the SAXS profiles of the solutions at pH 10.5 obtained by the two methods were somewhat different from the other. All these two-component solutions were best fit to combined models, with variations in specific parameters and/or types of models for individual components compared to the liquid-phase mixing counterparts (see Figure 3-68, Table 3-18, and Table 3-19). This evidence suggested that self-sorting occurred in these systems despite modifications to the self-assembled nanostructures formed by each component. Besides, solid-phase mixed hydrogels were less stiff than those prepared by liquid-phase mixing (see Figure 3-69). This may be due to reduced structural order within the gel network in the system, i.e., a lack of organization or random arrangement of molecules resulting in a weaker gel structure.

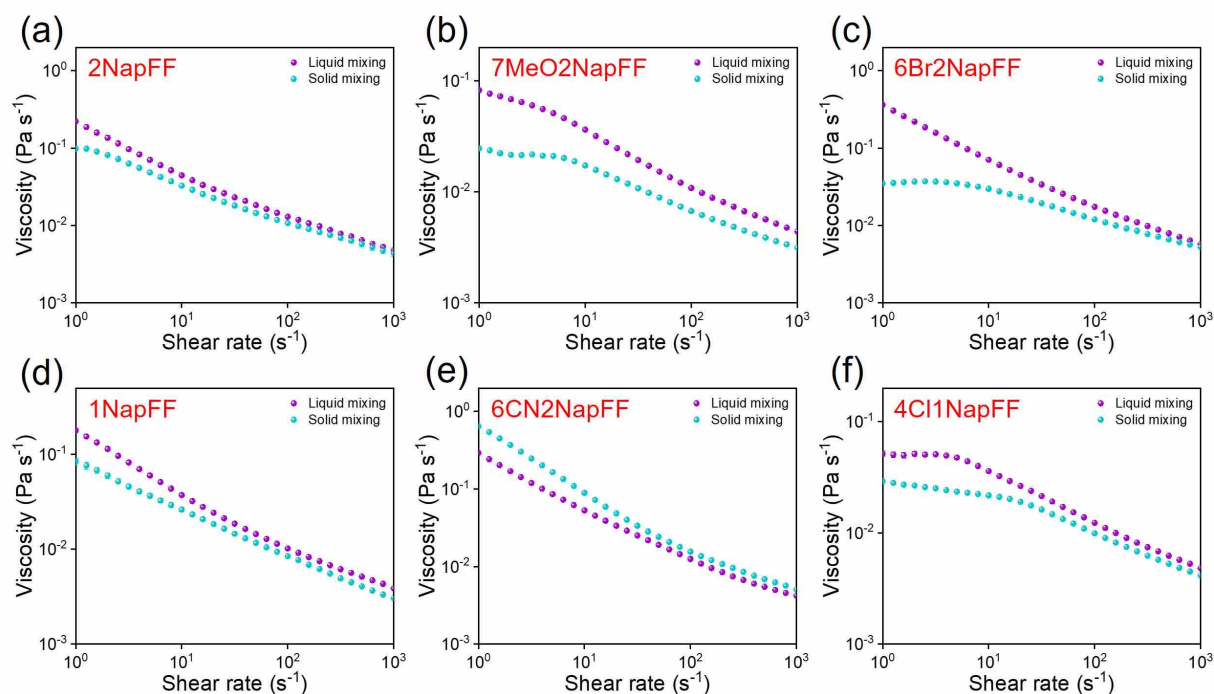


**Figure 3-66.** Dynamic viscosity for two-component solutions prepared through solid mixing approaches under equal percentages of diastereomers with a total concentration of 10 mg /mL, pH of 10.5, and temperature of 25 °C.

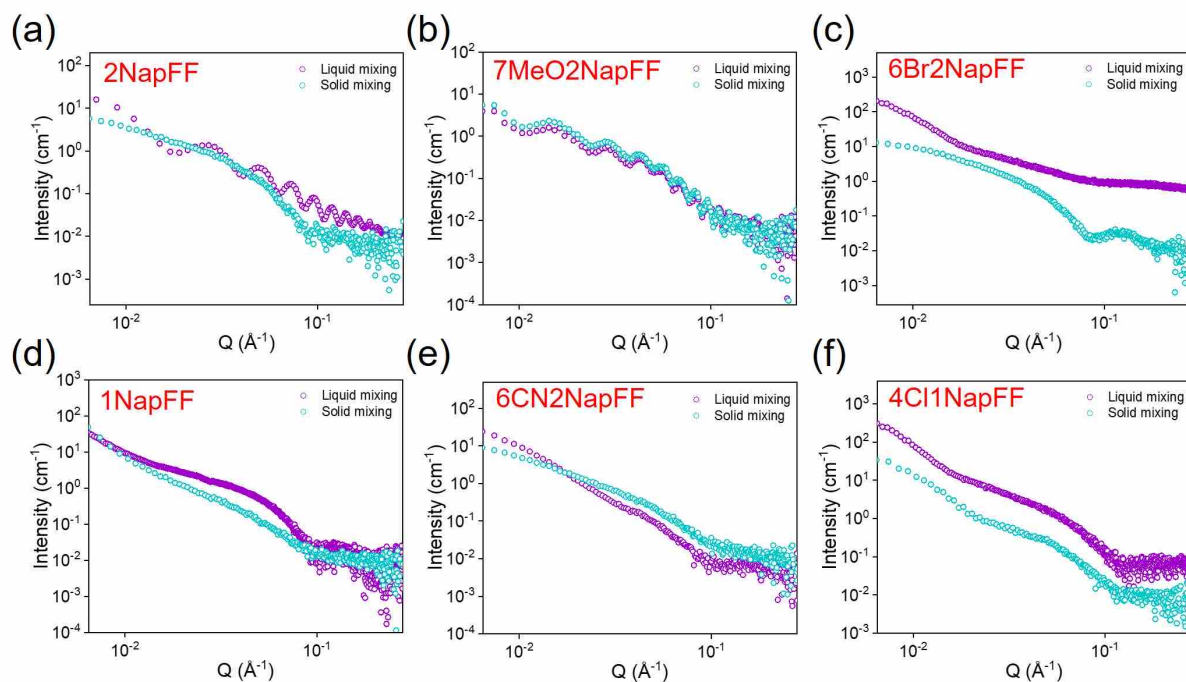


**Figure 3-67.** Combination of experimental SAXS curves for binary solutions prepared through liquid and solid mixing approaches under a 1:1 proportion of diastereomers with a total gelator concentration of 10 mg/mL, pH of 10.5, and temperature of 25 °C.

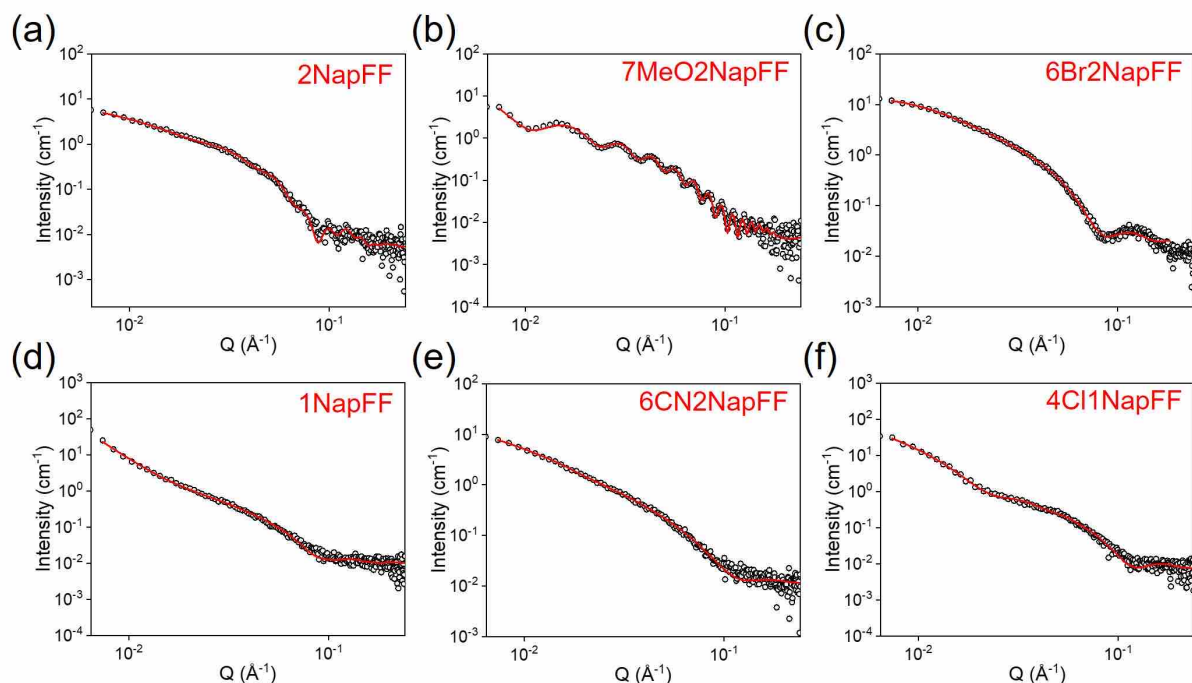


**Figure 3-68.** SAXS profiles (black circle) and fits (red line) for two-component solutions prepared through solid mixing approaches under a 1:1 proportion of diastereomers with a total gelator concentration of 10 mg/mL, pH of 10.5, and temperature of 25 °C.

**Table 3-18.** Summary of parameters employed for fitting SAXS data of binary solutions prepared through solid mixing approaches under a 1:1 proportion of diastereomers with a total gelator concentration of 10 mg/mL, pH of 10.5, and temperature of 25 °C. The abbreviations "C", "HC", "FC", "EC", and "PL" denote the cylinder, hollow cylinder, flexible cylinder, elliptical cylinder, and power law models, respectively.

Gelator	2NapFF	7MeO2NapFF	6Br2NapFF	1NapFF	6CN2NapFF	4Cl1NapFF
Model	C+HC	C+HC	C+EC	C+PL	C+EC	C+FC
Scale	1	1	1	1	1	1
Background	0.005	0.004	0.02	0.01	0.01	0.008
Background error	0.0003	0.0003	0.0003	0.0002	0.0003	0.0002
Power law scale				$1.8 \times 10^{-7}$		
Power law scale error				$3.6 \times 10^{-8}$		
Power				3.8		
Power error				0.04		
A scale	$1.7 \times 10^{-4}$	$4.0 \times 10^{-4}$	$6.9 \times 10^{-4}$		$4.0 \times 10^{-4}$	$1.7 \times 10^{-4}$
A scale error	$1.9 \times 10^{-5}$	$1.5 \times 10^{-5}$	$2.8 \times 10^{-4}$		$7.1 \times 10^{-5}$	$5.0 \times 10^{-5}$
A radius (Å)	123.8	223.9	42.7		39.7	153.0
A radius error (Å)	1.9	0.6	12.6		5.3	0.7
A kuhn length (Å)						87.3
A_kuhn_length_error (Å)						37.6
A thickness (Å)	23.7	26.4				
A thickness error (Å)	3.8	1.1				
A axis ratio			3.2		4.4	
A axis ratio error			0.9		0.5	
A length (Å)	197.0	694.6	445.8		706.6	>1000
A length error (Å)	19.5	19.8	17.1		52.5	
B scale	$7.6 \times 10^{-4}$	$6.5 \times 10^{-4}$	$1.4 \times 10^{-3}$	$4.6 \times 10^{-4}$	$7.5 \times 10^{-4}$	$1.0 \times 10^{-3}$
B scale error	$1.0 \times 10^{-5}$	$7.8 \times 10^{-6}$	$2.8 \times 10^{-4}$	$9.1 \times 10^{-6}$	$7.0 \times 10^{-5}$	$9.9 \times 10^{-6}$
B radius (Å)	42.4	34.0	43.9	40.1	30.0	30.8
B radius error (Å)	0.2	0.2	1.6	0.4	0.6	0.2
B length	>1000	>1000	366.9	172.9	490.6	>1000
B length error (Å)			15.4	9.4	84.3	
$\chi^2$	1.80	2.23	1.98	1.98	2.64	3.36

**Table 3-19.** Summary of parameters employed for fitting SAS data of binary solutions prepared through liquid mixing approaches under a 1:1 proportion of diastereomers with a total gelator concentration of 10 mg/mL, pH of 10.5, and temperature of 25 °C. The abbreviations "C", "HC", "FC", "EC", and "PL" denote the cylinder, hollow cylinder, flexible cylinder, elliptical cylinder, and power law models, respectively.

Gelator	2NapFF	7MeO2NapFF	6Br2NapFF	1NapFF	6CN2NapFF	4Cl1NapFF
SAS	SANS	SAXS	SAXS	SAXS	SAXS	SAXS
Model	HC+HC	C+HC	C+EC	C+PL	C+EC	FC+PL
Scale	1	1	1	1	1	1
Background	0.007	0.006	0.7	0.01	0.005	0.06
Background error	0.0001	0.0002	0.002	0.0004	0.0001	0.0007
Power law scale				$1.8 \times 10^{-7}$		$3.5 \times 10^{-7}$
Power law scale error				$3.6 \times 10^{-8}$		$2.8 \times 10^{-9}$
Power				3.8		4.1
Power error				0.04		0.01
A scale	0.003	0.0003	0.003	$9.1 \times 10^{-9}$	0.0004	0.007
A scale error	$1.3 \times 10^{-5}$	$1.2 \times 10^{-5}$	$2.1 \times 10^{-5}$	$1.3 \times 10^{-9}$	$2.3 \times 10^{-6}$	$2.6 \times 10^{-5}$

A radius (Å)	131.4	223.7	148.8	4.3	104.9	30.4
A radius error (Å)		0.7	0.8	0.03	0.7	0.1
A kuhn length (Å)						345.1
A kuhn length error (Å)						31.2
A thickness (Å)	17.0	24.1				
A thickness error (Å)		1.0				
A axis ratio			3.0		2.4	
A axis ratio error			0.1		0.04	
A length (Å)	491.0	723.4	456		698.6	>1000
A length error (Å)		24.6	3.3		9.0	
B scale	0.002	0.0005	0.008	0.002	0.0003	
B scale error	$5.0 \times 10^{-5}$	$5.3 \times 10^{-6}$	$6.6 \times 10^{-5}$	$5.9 \times 10^{-6}$	$3.4 \times 10^{-6}$	
B radius (Å)	13.4	33.3	27.7	36.6	38.2	
B radius error (Å)	0.3	0.2	0.2	0.1	0.3	
B thickness (Å)	14.1					
B thickness error (Å)	0.5					
B length	>1000	468.7	414.4	506.6	605.5	
B length error (Å)		70.5	36.2	13	91.8	
$\chi^2$	4.93	4.23	6.43	<1	1.51	3.63

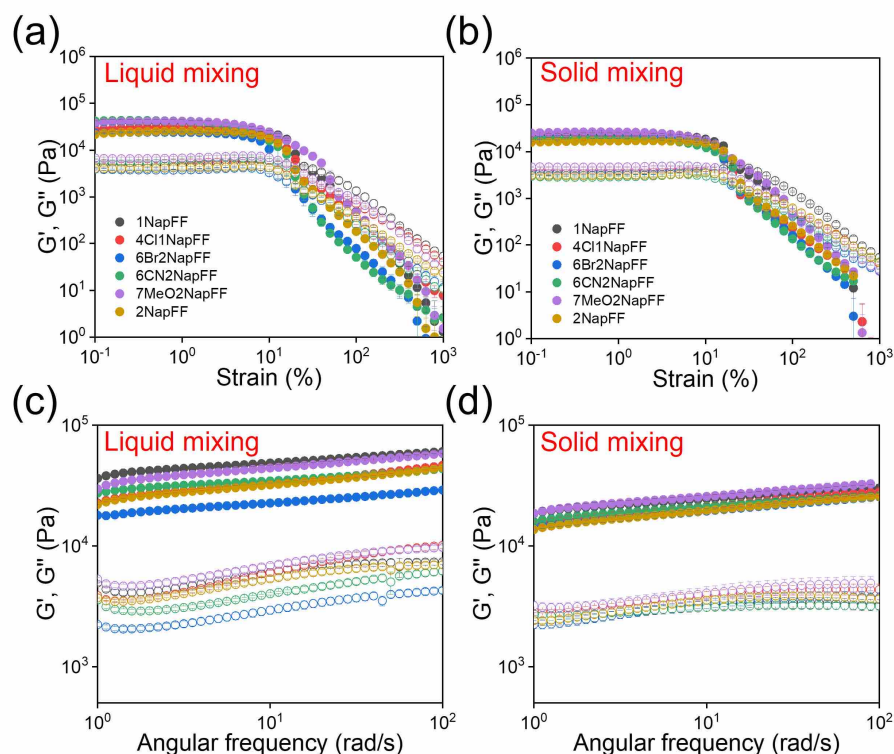


**Figure 3-69.** (a-b) Strain and (c-d) frequency sweep for binary gels prepared through liquid and solid mixing approaches under 1:1 proportion of diastereomers with a total gelator concentration of 10 mg/mL, pH of 10.5, and temperature of 25 °C.

### 3.4 Conclusions

This study examines the self-assembly behaviors of six diastereomer pairs (2NapFF, 1NapFF, 6Br2NapFF, 6CN2NapFF, 7MeO2NapFF, and 4Cl1NapFF), each of which exhibits unique and shared properties linked to their molecular structures and the substituents on the naphthalene

core. All six systems form organized micellar structures under acidic or alkaline conditions, showing anisotropic properties and birefringence, indicating well-ordered assemblies. These systems also demonstrate shear-thinning behavior, which is typical of supramolecular assemblies that reorganize under applied stress. CD spectra confirm partial self-sorting in binary mixtures, while SANS/AXS reveal that the self-assembled structures remain largely intact, with minimal interaction between components in the mixtures. Additionally, the systems show temperature-dependent behavior, with (L,L)-components forming more stable assemblies at higher temperatures compared to the more thermally sensitive (L,D)-components.

Despite these common features, the systems differ in key aspects such as viscosity, gel formation, and SAXS patterns. For instance, 2NapFF, 1NapFF, and 6Br2NapFF exhibit moderate viscosity, which increases slightly as the proportion of (L,D)-components rises, suggesting flexible but moderately strong self-assembled structures. In contrast, 6CN2NapFF, 7MeO2NapFF, and 4Cl1NapFF show more pronounced viscosity changes, with 6CN2NapFF displaying the highest viscosity due to stronger intermolecular interactions from the CN group. Gel formation varies: 2NapFF and 1NapFF form stable gels with resilient networks, while 6Br2NapFF and 7MeO2NapFF form weaker gels prone to syneresis. 6CN2NapFF and 4Cl1NapFF exhibit a decrease in gel modulus with increasing (L,D)-component fractions, resulting in weaker gels and more pronounced syneresis. SAXS analysis shows that 2NapFF, 1NapFF, and 6Br2NapFF form more uniform, flexible cylindrical micelles, while 6CN2NapFF, 7MeO2NapFF, and 4Cl1NapFF display more variability in fiber size and shape, with the Cl and MeO substituents contributing to stiffer, more rigid assemblies.

The observed differences in self-assembly behavior are primarily driven by the nature of the substituents on the naphthalene core. Electron-withdrawing groups like CN and Cl increase rigidity and intermolecular interactions, leading to stronger, more stable networks and gels. In contrast, electron-donating groups like MeO reduce intermolecular interactions, resulting in more flexible assemblies and weaker gels. Bulky substituents like Br and Cl can hinder close packing, leading to irregular fiber dimensions and less stable gels. Simpler derivatives such as 2NapFF and 1NapFF, with fewer or less bulky substituents, form more flexible and stable assemblies, while more substituted derivatives, like 6Br2NapFF and 6CN2NapFF, tend to form stiffer, more rigid structures.

In conclusion, while all six diastereomer pairs share the ability to form self-assembled micellar structures, their varying behaviors in terms of viscosity, gelation, and structural integrity are

influenced by a combination of electrostatic interactions, steric effects, and molecular flexibility. The substituents on the naphthalene core play a key role in dictating these interactions, which ultimately determine the stability and characteristics of the self-assembled structures. Our study demonstrates that binary systems of naphthyl diphenylalanine diastereoisomers exhibit self-sorting behaviors in both solution and gel phases, regardless of the mixing method. By adjusting the component ratios, we can fine-tune the rheological properties and microstructure of the material, paving the way for the development of tailored gels for specific applications.

This innovative approach using diastereoisomers instead of racemic mixtures provides distinct structures, offering new possibilities for chiral recognition in complex systems. However, a deeper understanding of the interactions between the self-sorting fibers is needed to fully improve and optimize these systems. Furthermore, while our current research focuses on naphthyl dipeptide derivatives, expanding this work to other diastereoisomers and peptides may introduce new complexities and open exciting avenues for future research.

## **3.5 Experimental Section**

### **3.5.1 Sample Preparation Protocols**

Unless otherwise specified, the sample preparation and characterization techniques employed in this chapter adhere to those detailed in Chapter 2.

#### **3.5.1.1 Preparation of w/w=1/1 Micellar Solutions**

Stock solutions with a gelator concentration of 10 mg/mL were prepared in a Falcon Tube by suspending 100 mg each of (L,L)-1NapFF and (L,D)-1NapFF in deionized water (15.97 mL) and adding 0.1 M sodium hydroxide solution (1 equivalent, 4.03 mL) so that the molar ratio of sodium hydroxide to 1NapFF was maintained at 1:1, resulting in a total volume of 20 mL. The solution was then stirred at 1000 rpm overnight to ensure complete dissolution. Subsequently, the pH of the solution was measured and adjusted to 10.5 if necessary, using a pipette calibrated to 20  $\mu$ L with either 2 M NaOH or HCl aqueous solutions.

#### **3.5.1.2 Preparation of pH-Triggered Gels from w/w=1/1 Micellar Solutions**

pH-triggered gels were prepared using glucono- $\delta$ -lactone (GdL), which hydrolysed in water to produce gluconic acid. This method not only yields reproducible, homogeneous, and

controllable gels but also facilitates monitoring of pH changes and rheological properties during gelation. Gels were prepared in Sterilin vials (7 mL) by adding 2 mL of the stock solution to GdL (16 mg/mL, 32 mg). The vials were gently rotated by hand to ensure complete dissolution of GdL and left to stand overnight. Rheology data were collected 18 hours after the addition of GdL.

Other w/w=1/1 two-component solutions and gels were prepared in the same manner.

## 3.5.2 Characterization

### 3.5.2.1 Circular Dichroism Spectroscopy

Circular Dichroism (CD) measurements were conducted using a detachable quartz cuvette (Hellma) with a path length of 0.01 mm and a Chirascan VX spectrometer (Applied Photophysical Limited, UK) outfitted with a Peltier temperature controller. The scanning parameters were set as follows: a scanning step of 1.0 nm, a scanning speed of 240 nm/min, a wavelength ( $\lambda$ ) scanning range spanning from 180 to 300 nm, and a bandwidth of 1 nm. The recorded data were expressed in millidegree (mdeg) of ellipticity. CD, absorption, and High Tension (HT) data were simultaneously collected throughout the scanning process. To investigate the temperature-dependent behaviour, CD evolution was monitored over a temperature range of 25 to 85 to 25 °C using 10 °C intervals during the heat-cooling cycle. Apart from the CD over temperature, the other data represented the average of 3 scans at 25 °C.

### 3.5.2.2 Confocal Fluorescence Microscopy

A Zeiss LSM710 confocal microscope (Zeiss, Göttingen, Germany) equipped with an LD EC Epiplan NEUFLUAR 50X, 0.55 DIC (Carl Zeiss, White Plains, NY, USA) objective and a Zeiss N-Achroplan 10 $\times$  was employed for imaging. Initially, 2  $\mu$ L of aqueous Nile Blue A dye (0.1 wt%) was directly added to 1 mL of the alkaline pH aqueous solution before introducing 16 mg GdL for pH-triggered gel. Subsequently, 400  $\mu$ L of the pre-gelation solution containing Nile Blue and GdL was introduced into CELLview culture dishes (35 mm diameter) while in its liquid state. These dishes were then sealed with Parafilm, and the sample was allowed to gel overnight before imaging. Excitation of all samples was achieved at 633 nm using a He-Ne laser, with emission detection occurring between 650 and 710 nm. Image acquisition was performed using Zeiss ZEN software (Zeiss, Jena, Germany).

### 3.5.2.3 Small-Angle X-Ray Scattering

Small-angle X-ray scattering (SAXS) experiments were conducted using an Anton Paar SAXS Point 2.0 instrument at the University of Bath. This beamline operates consistently at a fixed energy of 8.04 keV. Wide- and small-angle X-ray scattering patterns were obtained with sample-detector distances of 113 mm and 575 mm, respectively, employing Cu as the radiation source with a wavelength of  $K_{\alpha} = 1.54\text{\AA}$ . Data were acquired in the  $Q$  range of 0.07– 3.3  $\text{nm}^{-1}$ . Each sample underwent a single frame acquisition, lasting 10 minutes. The resulting 2D-scattering patterns were captured using a Dectris Eiger detector and then processed through azimuthal integration to generate 1D radial intensity profiles against the scattering vector ( $I$  vs.  $Q$ ) using the Anton Paar SAX Analysis software. Samples were introduced into borosilicate glass capillary tubes with a diameter of 1.5 mm from Capillary Tube Supplies Ltd.

For solution systems with alkaline pH based on 7MeO2NapFF and 6CN2NapFF, SAXS data were collected using a SAXSLAB Ganesha 300XL instrument (Xenocs) at the University of Bristol. Following the prescribed preparation protocol, solutions were transferred into 1.5 mm borosilicate glass capillaries (Capillary Tube Supplies Ltd.). The loading of samples into the capillaries was facilitated using a wide-bore glass Pasteur pipette. Subsequently, capillaries were sealed with UV curable epoxy for 30 minutes (Norland) before being measured for 3600 seconds within a  $Q$  range of 0.007–0.25  $\text{\AA}^{-1}$  for SAXS measurements.

The scattering intensity ( $I(Q)$ ) is typically presented as a function of the magnitude of the scattering vector,  $Q$ , which is given by Equation 3-1:

$$Q = \frac{4\pi}{\lambda} \cdot \sin\left(\frac{2\theta}{2}\right) \quad \text{Equation 3-1}$$

Here,  $\lambda$  represents the wavelength of the incident radiation, and  $2\theta$  corresponds to the scattering angle.

The distance between crystalline lattice planes (known as d-spacing) can be calculated using Bragg's law (Equation 3-2):

$$d = \frac{n\lambda}{2\sin\theta} \quad \text{Equation 3-2}$$

Where  $\lambda$  is the wavelength of the incident X-rays,  $2\theta$  is the scattering angle, and  $n$  is the diffraction order, typically assumed to be 1 (first order).

Substituting Equation 3-1 into Equation 3-2, the simplified Equation 3-3 was obtained:

$$d = 2\pi/Q \quad \text{Equation 3-3}$$

In all cases, the acquired data underwent correction for capillary and solvent (deionized water) backgrounds and were analyzed for fitting using SasView software (Version 5.0.6).<sup>52</sup> When experimental data exhibits a Bragg's peak, it is excluded from the fitting process. Instead, the relevant parameters are calculated using Equation 3-1 to 3-3. It's important to highlight that the error estimation is derived solely from the fitting software and does not encompass other potential sources of error. The NIST neutron activation and scattering calculator<sup>53</sup> was employed to compute the scattering length density (SLD) values. The derived SLD values are provided in Table 3-20.

**Table 3-20.** SLD values of compound and solvent used in the fitting process.

Compound	Density(g/cm <sup>3</sup> )	SAXS scattering length densities (10 <sup>-6</sup> /Å <sup>2</sup> )	SANS scattering length densities (10 <sup>-6</sup> /Å <sup>2</sup> )
H <sub>2</sub> O	1.00	9.469	-0.561
D <sub>2</sub> O	1.11	9.455	6.393
1NapFF	1.58	14.196	2.730
4Cl1NapFF	1.58	14.102	2.791
6CN2NapFF	1.58	14.135	2.959
6Br2NapFF	1.58	13.803	2.530
7MeO2NapFF	1.58	14.205	2.664

### 3.6 References

- (1) Li, L.; Sun, R.; Zheng, R. Tunable morphology and functionality of multicomponent self-assembly: A review. *Materials & Design* **2021**, *197*, 109209.
- (2) Vega-Granados, K.; Ramírez-Rodríguez, G. B.; Contreras-Montoya, R.; Ramírez, F. J.; Palomo, L.; Parra, A.; Delgado-López, J. M.; Lopez-Lopez, M. T.; de Cienfuegos, L. Á. Atmospheric water triggers supramolecular gel formation of novel low molecular weight maslinic and oleanolic triterpenic derivatives. *Materials Chemistry Frontiers* **2019**, *3* (12), 2637-2646.
- (3) Smith, D. K. Molecular Gels – Nanostructured Soft Materials. In *Organic Nanostructures*, 2008; pp 111-154.
- (4) Yu, X.; Chen, L.; Zhang, M.; Yi, T. Low-molecular-mass gels responding to ultrasound and mechanical stress: towards self-healing materials. *Chemical Society Reviews* **2014**, *43* (15), 5346-5371.
- (5) Feliciano, A. J.; van Blitterswijk, C.; Moroni, L.; Baker, M. B. Realizing tissue integration with supramolecular hydrogels. *Acta Biomaterialia* **2021**, *124*, 1-14.
- (6) Valls, A.; Burguete, M. I.; Kuret, L.; Altava, B.; Luis, S. V. Open chain pseudopeptides as hydrogelators with reversible and dynamic responsiveness to pH, temperature and sonication as vehicles for controlled drug delivery. *Journal of Molecular Liquids* **2022**, *348*, 118051.
- (7) Patterson, A.; Piras, C. C.; Smith, D. K. Hybrid Self-Assembled Gel Beads for Tunable pH-Controlled Rosuvastatin Delivery. *Chemistry: A European Journal* **2021**.
- (8) McDougall, L.; Draper, E. R.; Beadle, J. D.; Shipman, M.; Raubo, P.; Jamieson, A. G.; Adams, D. J. Enzymatically-stable oxetane-based dipeptide hydrogels. *Chemical Communications* **2018**, *54* (14), 1793-1796.

- (9) Chakraborty, P.; Tang, Y.; Yamamoto, T.; Yao, Y.; Guterman, T.; Zilberzwige-Tal, S.; Adadi, N.; Ji, W.; Dvir, T.; Ramamoorthy, A.; et al. Unusual two-step assembly of a minimalistic dipeptide-based functional hypergelator. *Advanced Materials* **2020**, *32* (9), 1906043.
- (10) Li, Y.; Männel, M. J.; Hauck, N.; Patel, H. P.; Auernhammer, G. K.; Chae, S.; Fery, A.; Li, J.; Thiele, J. Embedment of quantum dots and biomolecules in a dipeptide hydrogel formed in situ using microfluidics. *Angewandte Chemie International Edition* **2021**, *60* (12), 6724-6732.
- (11) Tomasini, C.; Castellucci, N. Peptides and peptidomimetics that behave as low molecular weight gelators. *Chemical Society Reviews* **2013**, *42* (1), 156-172.
- (12) Xian, S.; Webber, M. J. Temperature-responsive supramolecular hydrogels. *Journal of Materials Chemistry B* **2020**, *8* (40), 9197-9211.
- (13) Buerkle, L. E.; Rowan, S. J. Supramolecular gels formed from multi-component low molecular weight species. *Chemical Society Reviews* **2012**, *41* (18), 6089-6102.
- (14) Kulkarni, C.; Berrocal, J. A.; Lutz, M.; Palmans, A. R. A.; Meijer, E. W. Directing the solid-state organization of racemates via structural mutation and solution-state assembly processes. *Journal of the American Chemical Society* **2019**, *141* (15), 6302-6309.
- (15) Boekhoven, J.; Brizard, A. M.; Stuart, M. C. A.; Florusse, L.; Raffy, G.; Del Guerso, A.; van Esch, J. H. Bio-inspired supramolecular materials by orthogonal self-assembly of hydrogelators and phospholipids. *Chemical Science* **2016**, *7* (9), 6021-6031.
- (16) Draper, E. R.; Lee, J. R.; Wallace, M.; Jäckel, F.; Cowan, A. J.; Adams, D. J. Self-sorted photoconductive xerogels. *Chemical Science* **2016**, *7* (10), 6499-6505.
- (17) Chakraborty, R.; Mukherjee, P. S.; Stang, P. J. Supramolecular coordination: self-assembly of finite two- and three-dimensional ensembles. *Chemical reviews* **2011**, *111* (11), 6810-6918.
- (18) Colquhoun, C.; Draper, E. R.; Eden, E. G.; Cattoz, B. N.; Morris, K. L.; Chen, L.; McDonald, T. O.; Terry, A. E.; Griffiths, P. C.; Serpell, L. C.; Adams, D. J. The effect of self-sorting and co-assembly on the mechanical properties of low molecular weight hydrogels. *Nanoscale* **2014**, *6* (22), 13719-13725.
- (19) Basak, S.; Singh, I.; Ferranco, A.; Syed, J.; Kraatz, H.-B. On the role of chirality in guiding the self-assembly of peptides. *Angewandte Chemie International Edition* **2017**, *56* (43), 13288-13292.
- (20) Smith, D. K. Lost in translation? Chirality effects in the self-assembly of nanostructured gel-phase materials. *Chemical Society Reviews* **2009**, *38* (3), 684-694.
- (21) Edwards, W.; Smith, D. K. Chiral assembly preferences and directing effects in supramolecular two-component organogels. *Gels* **2018**, *4* (2), 31.
- (22) Guan, Q.; McAulay, K.; Xu, T.; Rogers, S. E.; Edwards-Gayle, C.; Schweins, R.; Cui, H.; Seddon, A. M.; Adams, D. J. Self-sorting in diastereomeric mixtures of functionalized dipeptides. *Biomacromolecules* **2023**, *24* (6), 2847-2855.
- (23) Loos, J. N.; Boott, C. E.; Hayward, D. W.; Hum, G.; MacLachlan, M. J. Exploring the tunable optical and mechanical properties of multicomponent low-molecular-weight gelators. *Langmuir* **2021**, *37* (1), 105-114.
- (24) Wu, S.; Zhang, Q.; Deng, Y.; Li, X.; Luo, Z.; Zheng, B.; Dong, S. Assembly pattern of supramolecular hydrogel induced by lower critical solution temperature behavior of low-molecular-weight gelator. *Journal of the American Chemical Society* **2020**, *142* (1), 448-455.
- (25) Draper, E. R.; Mykhaylyk, O. O.; Adams, D. J. Aligning self-assembled gelators by drying under shear. *Chemical Communications* **2016**, *52* (42), 6934-6937.
- (26) Eelkema, R.; Pich, A. Pros and cons: supramolecular or macromolecular: what is best for functional hydrogels with advanced properties? *Advanced Materials* **2020**, *32* (20), 1906012.
- (27) Morris, K. L.; Chen, L.; Rodger, A.; Adams, D. J.; Serpell, L. C. Structural determinants in a library of low molecular weight gelators. *Soft Matter* **2015**, *11* (6), 1174-1181.

- (28) McAulay, K.; Dietrich, B.; Su, H.; Scott, M. T.; Rogers, S.; Al-Hilaly, Y. K.; Cui, H.; Serpell, L. C.; Seddon, A. M.; Draper, E. R.; Adams, D. J. Using chirality to influence supramolecular gelation. *Chemical Science* **2019**, *10* (33), 7801-7806.
- (29) Adams, D. J.; Butler, M. F.; Frith, W. J.; Kirkland, M.; Mullen, L.; Sanderson, P. A new method for maintaining homogeneity during liquid-hydrogel transitions using low molecular weight hydrogelators. *Soft Matter* **2009**, *5* (9), 1856-1862.
- (30) Görl, D.; Zhang, X.; Stepanenko, V.; Würthner, F. Supramolecular block copolymers by kinetically controlled co-self-assembly of planar and core-twisted perylene bisimides. *Nature Communications* **2015**, *6* (1), 7009.
- (31) Chen, Z.; Penfold, J.; Li, P.; Douth, J.; Fan, Y.; Wang, Y. Effects of length and hydrophilicity/hydrophobicity of diamines on self-assembly of diamine/SDS gemini-like surfactants. *Soft Matter* **2017**, *13* (47), 8980-8989.
- (32) Draper, E. R.; Dietrich, B.; McAulay, K.; Brasnett, C.; Abdizadeh, H.; Patmanidis, I.; Marrink, S. J.; Su, H.; Cui, H.; Schweins, R. Using small-angle scattering and contrast matching to understand molecular packing in low molecular weight gels. *Matter* **2020**, *2* (3), 764-778.
- (33) Adams, D. J. Personal perspective on understanding low molecular weight gels. *Journal of the American Chemical Society* **2022**, *144* (25), 11047-11053.
- (34) Hill, M. J. S.; Fuentes-Caparrós, A. M.; Adams, D. J. Effect of imposing spatial constraints on low molecular weight gels. *Biomacromolecules* **2023**, *24* (9), 4253-4262.
- (35) Panja, S.; Fuentes-Caparrós, A. M.; Cross, E. R.; Cavalcanti, L.; Adams, D. J. Annealing Supramolecular Gels by a Reaction Relay. *Chemistry of Materials* **2020**, *32* (12), 5264-5271.
- (36) Cardoso, A. Z.; Mears, L. L. E.; Cattoz, B. N.; Griffiths, P. C.; Schweins, R.; Adams, D. J. Linking micellar structures to hydrogelation for salt-triggered dipeptide gelators. *Soft Matter* **2016**, *12* (15), 3612-3621.
- (37) McAulay, K.; Thomson, L.; Porcar, L.; Schweins, R.; Mahmoudi, N.; Adams, D. J.; Draper, E. R. Using rheo-small-angle neutron scattering to understand how functionalised dipeptides form gels. *Organic Materials* **2020**, *02* (02), 108-115.
- (38) Liu, G.; Zhou, C.; Teo, W. L.; Qian, C.; Zhao, Y. Self-sorting double-network hydrogels with tunable supramolecular handedness and mechanical properties. *Angewandte Chemie International Edition* **2019**, *58* (28), 9366-9372.
- (39) Gong, J. P. Materials both tough and soft. *Science* **2014**, *344* (6180), 161-162.
- (40) Draper, E. R.; Dietrich, B.; McAulay, K.; Brasnett, C.; Abdizadeh, H.; Patmanidis, I.; Marrink, S. J.; Su, H.; Cui, H.; Schweins, R.; et al. Using small-angle scattering and contrast matching to understand molecular packing in low molecular weight gels. *Matter* **2020**, *2* (3), 764-778.
- (41) Terech, P.; Clavier, G.; Bouas-Laurent, H.; Desvergne, J.-P.; Demé, B.; Pozzo, J.-L. Structural variations in a family of orthodialkoxyarenes organogelators. *Journal of Colloid and Interface Science* **2006**, *302* (2), 633-642.
- (42) Sangeetha, N. M.; Bhat, S.; Raffy, G.; Belin, C.; Loppinet-Serani, A.; Aymonier, C.; Terech, P.; Maitra, U.; Desvergne, J.-P.; Del Guerzo, A. Hybrid Materials Combining Photoactive 2,3-DidecyloxyAnthracene Physical Gels and Gold Nanoparticles. *Chemistry of Materials* **2009**, *21* (14), 3424-3432.
- (43) Draper, E. R.; Su, H.; Brasnett, C.; Poole, R. J.; Rogers, S.; Cui, H.; Seddon, A.; Adams, D. J. Opening a can of worm (-like micelle)s: the effect of temperature of solutions of functionalized dipeptides. *Angewandte Chemie* **2017**, *129* (35), 10603-10606.
- (44) Palmans, A. R. A.; Vekemans, J. A. J. M.; Havinga, E. E.; Meijer, E. W. Sergeants-and-soldiers principle in chiral columnar stacks of disc-shaped molecules with C<sub>3</sub> symmetry. *Angewandte Chemie International Edition* **1997**, *36* (23), 2648-2651.

- (45) Green, M. M.; Garetz, B. A.; Munoz, B.; Chang, H.; Hoke, S.; Cooks, R. G. Majority rules in the copolymerization of mirror image isomers. *Journal of the American Chemical Society* **1995**, *117* (14), 4181-4182.
- (46) Gao, J.; Tang, C.; Elsayy, M. A.; Smith, A. M.; Miller, A. F.; Saiani, A. Controlling self-assembling peptide hydrogel properties through network topology. *Biomacromolecules* **2017**, *18* (3), 826-834.
- (47) Ozbas, B.; Rajagopal, K.; Schneider, J. P.; Pochan, D. J. Semiflexible chain networks formed via self-assembly of  $\beta$ -hairpin molecules. *Physical Review Letters* **2004**, *93* (26), 268106.
- (48) MacKintosh, F. C.; Käs, J.; Janmey, P. A. Elasticity of semiflexible biopolymer networks. *Physical Review Letters* **1995**, *75* (24), 4425-4428.
- (49) Panja, S.; Dietrich, B.; Adams, D. J. Controlling syneresis of hydrogels using organic salts. *Angewandte Chemie* **2022**, *134* (4), e202115021.
- (50) Shi, N.; Dong, H.; Yin, G.; Xu, Z.; Li, S. A smart supramolecular hydrogel exhibiting pH - modulated viscoelastic properties. *Advanced Functional Materials* **2007**, *17* (11), 1837-1843.
- (51) Randle, R. I.; Ginesi, R. E.; Matsarskaia, O.; Schweins, R.; Draper, E. R. Process dependent complexity in multicomponent gels. *Macromolecular Rapid Communications* **2023**, *44* (4), 2200709.
- (52) *SasView*. <https://www.sasview.org/> (accessed 2024/04/08).
- (53) *NIST neutron activation and scattering calculator*. <https://www.ncnr.nist.gov/resources/activation/> (accessed 2024/04/15).

## **Chapter 4: Mueller Matrix Polarimetry Study in Diastereomeric Mixtures of Functionalized Dipeptides**

---

Guan, Q. performed the preparation and characterization of the samples under investigation. Marshall, L. J., Guan, Q., Ghosh, D., and Stewart, F. H. contributed to the data collection and processing. Siligardi, G. and Gianga, T. M. provided essential guidance and advice on data collection, processing, and analysis.

## 4.1 Introduction

Optical activity is a fundamental concept in stereochemistry that provides essential insights into the behavior of chiral molecules. Recent advances in spectroscopic techniques have significantly improved our ability to study these properties. For example, Synchrotron Radiation Circular Dichroism (SRCDD) has proven to be superior to traditional circular dichroism (CD) spectroscopy. It enhances our understanding by efficiently managing data at low wavelengths, enriching information content, and delivering better signal-to-noise ratios, thus becoming increasingly important in structural and functional genomics.<sup>1-3</sup> However, as light travels through materials, it undergoes continuous changes in polarization due to effects such as linear retardation, diattenuation, and depolarization.<sup>4, 5</sup> These changes can lead to misinterpretations when analyzing anisotropic media. Moreover, issues like circular birefringence, linear dichroism, and linear birefringence can mask the actual optical activities. The Partially Modulated Polarization (PMP) method provides an alternative way to measure CD with minimal interference from other polarizations. Nonetheless, it does not account for additional polarization effects and may simplify data too much, ignoring the complex interactions between various polarization phenomena. This can limit its effectiveness in providing a comprehensive understanding of molecular dynamics.<sup>6, 7</sup>

To effectively tackle these challenges, the use of the differential Mueller matrix method through Mueller Matrix Polarimetry (MMP) is essential. MMP provides a detailed analysis of complex media by quantitatively evaluating potential polarization effects such as circular dichroism, circular birefringence, linear dichroism, and linear birefringence.<sup>8-10</sup> This technique assesses all 16 elements of the Mueller matrix, allowing for accurate identification of various optical phenomena and offering a complete overview of a sample's optical characteristics. MMP proves especially useful in studying large, structured molecules like anisotropic supramolecular aggregates, polymers, and thin films, where the configuration of chiral centers greatly influences molecular interactions and functionality.<sup>11-14</sup>

Furthermore, combining MMP with established spectroscopic methods deepens our understanding of stereochemistry, thereby expanding its utility in fields such as drug design and biomolecular engineering. Technological improvements at facilities like the Diamond Light Source B23 beamline have significantly enhanced these measurements. The B23 SRCDD setup provides an outstanding photon flux and a highly collimated microbeam, making it ideal for precise investigations in the vacuum ultraviolet (VUV) and far-ultraviolet (FUV) regions. These

features surpass the capabilities of traditional benchtop circular dichroism instruments and other SRCD beamlines, enabling more refined and accurate measurements.<sup>10, 15-18</sup>

In this study, we analyzed the optical properties of functionalized dipeptide pre-gel systems, focusing on (L,L)-2NapFF, (L,D)-2NapFF, and their equimolar mixtures, using the B23 Mueller Matrix Polarimetry (MMP). The MMP results revealed the presence of all polarization effects in these systems, showing significant differences in molecular orientation and electronic interactions between homochiral (same-handedness) and heterochiral (different-handedness) systems. These differences suggest distinct assembly mechanisms and structural orientations, which are influenced by the stereochemical composition of the dipeptides. The analysis highlighted the profound impact of chiral interactions on the optical birefringence of the systems, a phenomenon that significantly influences the optical and mechanical properties of the resulting bulk gels. These insights demonstrate how chirality affects the self-assembly process and the orientation behaviors of molecules, providing valuable guidance for the development of materials with specific optical functionalities tailored to advanced applications.

## **4.2 Results and Discussion**

### **4.2.1 SRCD Studies for 2NapFF Pre-Gel Solutions**

The highly collimated microbeam of the B23 beamline is instrumental for detailed assessments of chiral supramolecular structures via SRCD. This study explores the chiral properties of three distinct systems: a 10 mg/mL (L,L)-2NapFF pre-gel solution (10:0), a 10 mg/mL (L,D)-2NapFF pre-gel solution (0:10), and a binary mixture of (L,L)-2NapFF and (L,D)-2NapFF at 10 mg/mL with a 1:1 volume ratio (5:5). The SRCD responses observed were consistent with those recorded using a conventional benchtop spectrophotometer, as illustrated in Figures 4-1 and 2-9. Notably, the SRCD profile of the pure (L,L)-2NapFF exhibits an inverse response compared to that of (L,D)-2NapFF in the 235-220 nm range, with the binary mixture displaying spectral characteristics similar to those of the latter in this region (Figure 4-1).

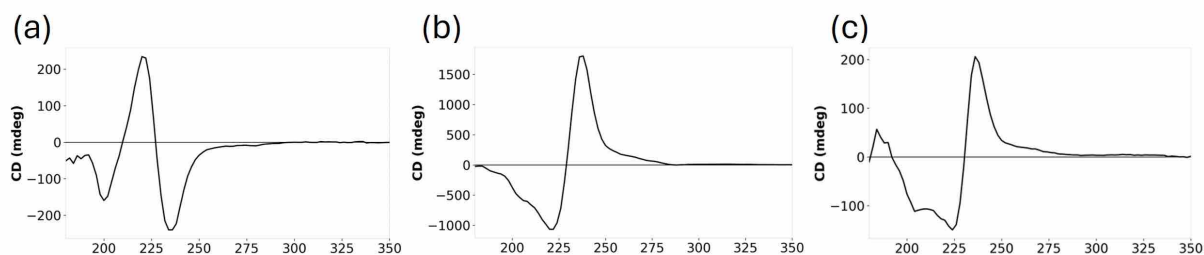


**Figure 4-1.** SRCD spectra of (a) 10 mg/mL (L,L)-2NapFF pre-gel solution, (b) 10 mg/mL (L,D)-2NapFF pre-gel solution, and (c) binary solution of (L,L)-2NapFF and (L,D)-2NapFF each at 10 mg/mL with a 1:1 volume ratio (5:5) at pH 10.5, 25 °C.

The SRCD signal observed on a spectrometer does not represent a "pure" differential absorbance of left- and right-handed circularly polarized light (apparent CD), as 2NapFF spontaneously self-assembles into anisotropic cylindrical nanostructures at high pH.<sup>19-21</sup> As light traverses these structures, its polarization may alter or even vanish due to phenomena such as linear retardation. The Mueller matrix offers a comprehensive framework for analyzing the polarization characteristics of a light wave interacting with an object. This matrix, consisting of 16 elements, encapsulates all polarization information of the sample. The B23 MMP beamline was used to thoroughly evaluate the contributions of various chiroptical phenomena.

#### 4.2.2 MMP Studies for 2NapFF Pre-Gel Solutions

The MMP facility, equipped with four photoelastic modulators (PEMs), enables simultaneous measurements of all Mueller matrix elements,<sup>10, 22</sup> facilitating the decomposition of the apparent CD signal into LD, LB, CB, and true CD, and sample absorption.

The preliminary differential Mueller matrix of the 10 mg/mL (L,L)-2NapFF pre-gel solution at pH 10.5, 25 °C, conducted using the B23 MMP tower, is presented in Figure 4-2. This analysis confirms the presence of essential polarization components: LD, LB, CD, and CB. Despite the similarities in shape and peaks between the two diagonal elements representing CD in the differential Mueller matrix, depolarization causes discrepancies in their intensity magnitudes.<sup>23</sup> The average of these two CD elements provides a more accurate representation of the sample's circular dichroism properties. This approach helps mitigate the impact of depolarization on the measured CD signal, allowing for a more reliable analysis of the sample's chiral characteristics. Moreover, such discrepancies underline the complexity of depolarization effects within anisotropic systems and highlight the need for precise polarimetric analysis to discern subtle differences in optical behavior.

In a homogeneous reciprocal medium wherein the emerging polarization state remains consistent irrespective of which side of the differential sample is first encountered, due to the uniform optical properties of the medium, reciprocal symmetry requires that the differential Mueller matrix be symmetric.<sup>24, 25</sup> However, the presence of depolarization within the system under study introduces asymmetries into the matrix. Notably, the elements M02 and M20, both representing  $-LD'$ , exhibit discrepancy (Figure 4-2).

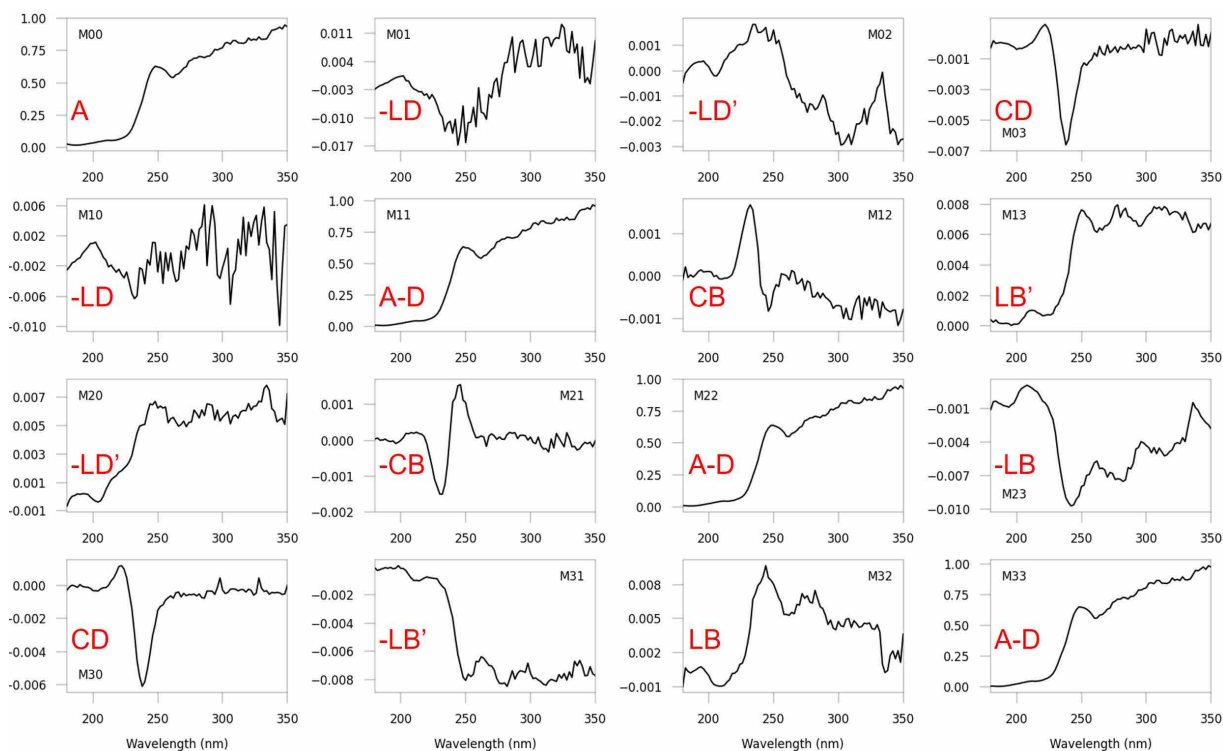


**Figure 4-2.** Preliminary differential Mueller matrix plots of 10 mg/mL (L,L)-2NapFF pre-gel solution at pH 10.5, 25 °C. The physical interpretations of elements are circular dichroism (CD), circular birefringence (CB), horizontal linear dichroism (LD), horizontal linear birefringence (LB), 45° linear dichroism (LD'), 45° linear birefringence (LB'), absorbance (A), and depolarization (D, which is equal to zero for materials that exhibit no depolarization).

#### 4.2.2.1 Analysis of True CD Spectra in MMP Data

The custom-developed processing software at B23 for the analysis of MMP data<sup>10, 26</sup> efficiently extracts 9 critical polarimetric elements from the MMP data: circular dichroism (CD), circular birefringence (CB), horizontal linear dichroism (LD), horizontal linear birefringence (LB), 45° linear dichroism (LD'), 45° linear birefringence (LB'), absorbance (A), G-factor, and transmittance. These measurements are essential for a detailed analysis of the sample's optical

properties. Table 1 summarizes various optical effects, their definitions, and physical implications as derived from the differential Mueller matrix analysis.

**Table 4-1** Summary of basic optical properties involved in this study.

Symbol	Effect	Definition	Physical implication
CD	Circular dichroism	The differential absorption of left- and right-handed circularly polarized light as it passes through optically active chiral materials.	The different refractive indices and absorptions of chiral molecules for left- and right-handed circularly polarized light cause the linearly polarized light passing through these molecules to differ in phase and amplitude, resulting in elliptically polarized light.; indicates chirality, molecular structure, and conformations.
CB	Circular birefringence	Or optical rotatory dispersion (ORD), the differential refractive indices for left-handed and right-handed circularly polarized light in chiral material.	The rotation of the orientation of the plane of polarization around the optical axis of linearly polarized light as it passes through chiral materials.
LD	Horizontal linear dichroism	Or diattenuation, the differential absorption of light linearly polarized parallel and perpendicular to an orientation axis in an anisotropic material.	Influencing transmittance based on the orientation of incident linearly polarized light; reveals molecular orientation and material anisotropy.
LB	Horizontal linear birefringence	The differential refractive indices of linearly polarized light with orthogonal planes of polarization in an anisotropic material.	Affecting the phase of two orthogonal polarization components of light; Indicates structural anisotropy.
LD'	45° linear dichroism	The differential absorption of linearly polarized light oriented at 45° and -45° to an orientation axis in an anisotropic material.	How light polarized at 45° and 135° is absorbed differently compared to light polarized at other angles; study molecular orientation and anisotropy in materials with specific alignment.
LB'	45° linear birefringence	The differential refractive indices of linearly polarized light oriented at 45° and -45° to an orientation axis in an anisotropic material.	How the propagation speed of light varies along 45° and 135° within the medium; Indicates directional dependence of optical properties.
A	Isotropic absorption	The uniform absorption of light in all directions within a material, regardless of the polarization or direction of the incident light; correlates to	How much light is absorbed by a sample at different wavelengths; study molecular structure and concentration.

		electronic transition within a material.	
D	Depolarization	The reduction in the degree of polarization of the light as it passes through a material.	The coupling of polarized light into unpolarized light; Indicates molecular interactions, scattering information, and structural heterogeneity.
G-factor	Anisotropy/dissymmetry factor	Quantifies the degree of asymmetry of circular polarization in light scattering function in a material; equals the ratio of CD to absorption.	How light is directionally scattered by particles within a medium; reveals electronic transition and chiral environment of material.
N/A	Transmittance	The proportion of light that passes through a sample without being absorbed or reflected compared to the incident light.	Indicates material transparency and thickness.

The transmittance plots, illustrated in Figure 4-3, aggregate results from four separate runs to examine any potential diattenuation or depolarization effects that could obscure data interpretation. The subtle discrepancy observed across these measurements confirms their presence, thereby validating the reliability and reproducibility of the data. Such analysis highlights MMP's capability to identify tiny variations in the sample's polarimetric properties, providing deep insights into the system's molecular interactions and structural dynamics.

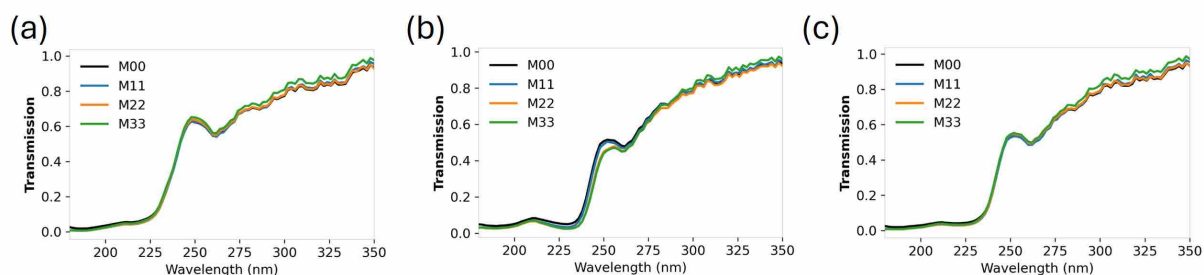


**Figure 4-3.** Transmission spectra derived from MMP data of (a) 10 mg/mL (L,L)-2NapFF pre-gel solution, (b) 10 mg/mL (L,D)-2NapFF pre-gel solution, and (c) (L,L)-2NapFF and (L,D)-2NapFF each at 10 mg/mL with a 1:1 volume ratio at pH 10.5, 25 °C. The transmission graph displays all four runs (M00, M11, M22, and M33) to check for deattenuation or depolarization in the dataset, and the subtle discrepancy of the data for each sample indicates the existence of these effects.

The comparison between the apparent and true CD spectra of (L,L)-2NapFF, (L,D)-2NapFF, and their 1:1 mixture reveals notable differences in spectral patterns and peak intensities. The true CD spectra (Figures 4-4) exhibit complex and nuanced profiles, with (L,L)-2NapFF

showing multiple peaks, (L,D)-2NapFF showing a dominant peak, and the 1:1 mixture displaying blended features from both diastereoisomers. These spectra suggest a more detailed representation of the system's chiral interactions and self-assembly behaviors. In contrast, the apparent CD spectra (Figures 2-9) display simpler and more exaggerated peaks. For example, the (L,D)-2NapFF spectrum in the apparent CD shows a more pronounced peak, indicating an amplification of chiral properties compared to the true CD spectra. The 1:1 mixture in the apparent CD also shows combined features, but with differences in peak intensity and positions, reflecting an altered representation of the self-sorting behavior. These discrepancies suggest that the apparent CD spectra may overstate certain chiral properties or interactions due to limitations in the measurement technique. The true CD spectra, on the other hand, provide a more accurate and detailed picture of the molecular interactions and assembly behaviors, especially in complex mixtures. The differences in peak intensities and spectral clarity highlight the importance of using MMP for a more nuanced understanding of these systems. Overall, the apparent CD spectra, while useful for preliminary analysis, may not fully capture the complexities of molecular interactions and structural behavior. True CD spectra are essential for more precise characterization.

The true CD spectrum (Figure 4-4a) of the 10 mg/mL (L,L)-2NapFF pre-gel solution at pH 10.5, 25 °C, exhibits pronounced peaks centred around 225–230 nm, attributed to the  $\pi$ - $\pi$  stacking of the aromatic naphthalene chromophore.<sup>27</sup> Additional spectral features likely arise from interactions among aromatic N-terminal capping groups as they self-assemble into chiral structures.<sup>28</sup> These patterns reflect the distinctive electronic environment and spatial arrangement of the naphthalene ring in this homochiral dipeptide, indicating that molecular interactions or orientations may stabilize these transitions, potentially suggesting a specific stacking pattern influenced by homochirality.<sup>29, 30</sup>

Conversely, the true CD spectrum of 10 mg/mL (L,D)-2NapFF pre-gel solution at pH 10.5, 25 °C (Figure 4-4b) significantly diverges from its (L,L) counterpart, showcasing sharply defined peaks between 220-235 nm. This variation suggests an alternate chromophore arrangement that enhances electron transitions, with increased peak intensity denoting a more structured or ordered molecular conformation in (L,D)-2NapFF, which influences its molecular interactions and self-assembly dynamics. This organized arrangement optimally engages chromophores with polarized light, amplifying the circular dichroism signal.

In comparison, the true CD spectra of the 5:5 binary mixture (Figure 4-4c) exhibit substantial spectral variations from the homochiral samples, marked by a noticeable decrease in peak amplitude and intensity. Dominated by the chirality of (L,D)-2NapFF, the CD profiles closely resemble those of the pure (L,D) samples in the 220-235 nm region. No new absorption peaks were observed in the binary complex compared to the individual components, indicating that the interactions between the chromophores and the chiral environment remained unchanged. This observation demonstrates that the structural arrangement and ordering within the complex were preserved. The stability of these spectral features emphasizes the robustness of chiral and chromophoric interactions, even in the presence of mixed diastereomeric components. This confirms the maintenance of molecular structure in the binary complex, as extensively discussed in Chapter 2.

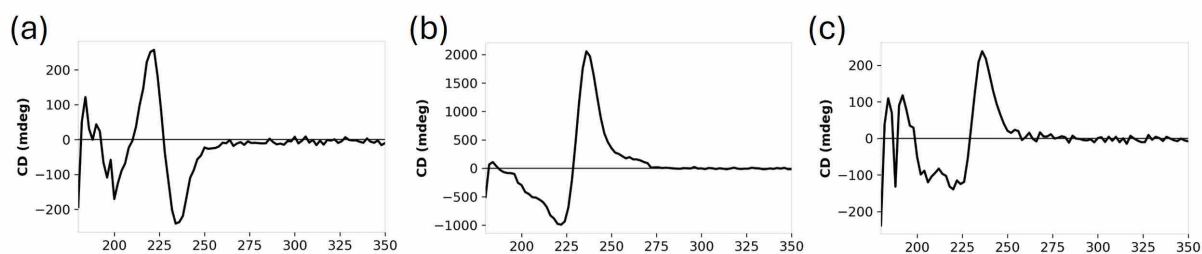


**Figure 4-4.** CD spectra derived from MMP data of (a) 10 mg/mL (L,L)-2NapFF pre-gel solution, (b) 10 mg/mL (L,D)-2NapFF pre-gel solution, and (c) (L,L)-2NapFF and (L,D)-2NapFF each at 10 mg/mL with a 1:1 volume ratio at pH 10.5, 25 °C.

#### 4.2.2.2 Analysis of CB in MMP Data

Circular birefringence (CB) and circular dichroism (CD) are fundamental manifestations of optical activity. The analysis of CB spectra reveals that optical activity varies with molecular structure and chirality. Positive signals represent right-handed chirality due to clockwise rotational polarization, while negative signals denote left-handed chirality with counterclockwise rotation. The (L,L)-2NapFF spectra exhibit pronounced peaks at 213 nm and 230 nm, indicative of strong circular birefringence arising from specific intermolecular interactions within ordered supramolecular structures. This pattern, similar to that observed in homochiral peptides that form ordered helical aggregates,<sup>29, 31</sup> is illustrated in Figure 4-5a. Conversely, the (L,D)-2NapFF spectra, with peaks at 230 nm and a more intense peak at 245 nm, suggest a greater degree of chiral ordering and stronger molecular interactions,

characteristic of a unique supramolecular assembly different from systems with homochiral amino acids, as shown in Figure 4-5b.<sup>32-34</sup>

Both dipeptide types display foundational stacking facilitated by aromatic rings bonded via hydrogen bonds; however, their higher-order structural organization diverges.<sup>20</sup> In (L,L) configurations, two outer chains align with an inner chain to form eight protofilaments that twist right-handedly, creating narrow, hollow structures. In contrast, (L,D) configurations consist of 32 protofilaments, each initiated by an outer chain's alignment with an inner chain, twisting left-handedly to form larger hollow structures. This demonstrates how molecular orientation significantly influences the structural properties of peptide assemblies.<sup>35</sup>

CB analysis of the binary mixtures revealed a decreased intensity compared to the pure isomers, with distinct peaks observed at 230 nm and 245 nm (Figure 4-5c). This reduction suggests that the coexistence of two diastereoisomers may diminish overall chiral differentiation within the system. The likely explanation is that the chiral contributions of each isomer may interfere with each other, resulting in a reduced CB signal. Additionally, concentration effects may also play a role; the concentration of overall chiral self-assembled aggregates in the mixed system might be lower than in the 10 mg/mL solutions of individual isomers, even though the total concentration of the gelators remained consistent across the systems.

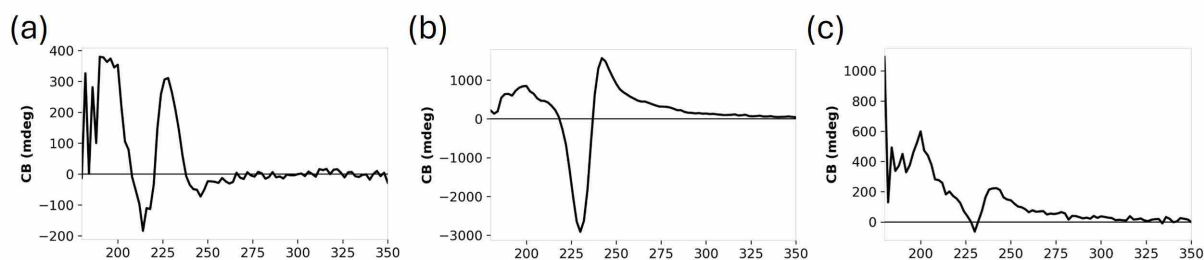


**Figure 4-5.** CB spectra derived from MMP data of (a) 10 mg/mL (L,L)-2NapFF pre-gel solution, (b) 10 mg/mL (L,D)-2NapFF pre-gel solution, and (c) (L,L)-2NapFF and (L,D)-2NapFF each at 10 mg/mL with a 1:1 volume ratio at pH 10.5, 25 °C.

#### 4.2.2.3 Analysis of LD in MMP Data

The linear dichroism (LD) spectra of the self-assembled systems at a concentration of 10 mg/mL indicated some degree of preliminary molecular orientation, suggesting that smaller aggregates begin aligning and assembling before forming the final macroscopic gel network. This

observation aligns with the hierarchical self-assembly processes observed in LMWGs, where pre-organized structures are evident before the establishment of a 3D gel network.<sup>19, 36, 37</sup>

For the homochiral (L,L)-2NapFF, the LD spectrum displays a distinct peak at approximately 190 nm, corresponding to the  $\pi$ - $\pi^*$  transitions of the peptide chromophore (see Figure 4-6a). The decreasing trend in LD intensity across the spectrum suggests a reduction in structural order within the solution. In contrast, the (L,D)-2NapFF spectrum exhibits robust signals within the aromatic absorption range of 200-300 nm, particularly around 200 nm and 235 nm, consistent with  $\pi$ - $\pi$  stacking interactions of the naphthalene groups (see Figure 4-6b). These pronounced LD signals indicate more highly oriented structures in (L,D)-2NapFF, potentially due to distinct intermolecular interactions or molecular packing influenced by chirality.

In the 1:1 binary mixture of (L,L) and (L,D) isomers, the LD spectra reveal features characteristic of the peptide bond at 190 nm alongside weaker signals in the naphthalene chromophore region (200-250 nm), suggesting intricate interactions between the heterochiral molecules (see Figure 4-6c). This complex interaction landscape results in a more heterogeneous molecular environment compared to the uniformity seen in homochiral solutions, possibly leading to the attenuation of LD signals. Moreover, the presence of LD characteristics corresponding to both gelators within the mixture suggests that the diastereomers undergo a process of self-sorting, retaining structural features typical of their respective pure forms.

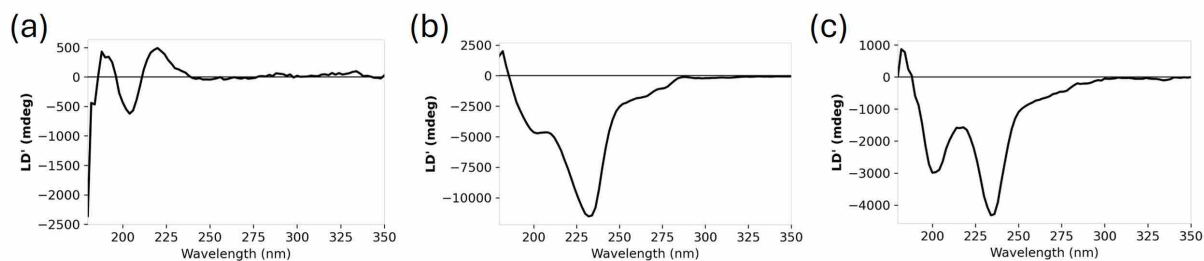


**Figure 4-6.** LD spectra derived from MMP data of (a) 10 mg/mL (L,L)-2NapFF pre-gel solution, (b) 10 mg/mL (L,D)-2NapFF pre-gel solution, and (c) (L,L)-2NapFF and (L,D)-2NapFF each at 10 mg/mL with a 1:1 volume ratio at pH 10.5, 25 °C.

#### 4.2.2.4 Analysis of LB in MMP Data

Linear birefringence (LB) is an essential optical property that elucidates the impact of molecular chirality on supramolecular self-assemblies, offering deep insights into molecular ordering and structural anisotropy. In this study, all three samples demonstrated LB signals, indicative of the presence of ordered structures within the pre-gel solutions. An upward trend in LB typically

signifies increased anisotropy due to enhanced molecular alignment, whereas a downward trend may suggest reduced anisotropy, likely arising from disordered molecular arrangements.

The (L,L)-2NapFF spectrum exhibited marked fluctuations in LB intensity with distinct peaks at 195 nm, 207 nm, and 235 nm, indicative of a structured, directional molecular orientation contributing to pronounced LB (see Figure 4-7a). Conversely, the LB signal for (L,D)-2NapFF appeared more uniform and intense, reflecting a highly ordered supramolecular morphology, corroborated by polarization microscopy (see Figure 2-4). The LB spectrum for (L,D)-2NapFF showed a significant peak at approximately 243 nm and two troughs at 193 nm and 218 nm, suggesting complex molecular orientations or interactions, potentially indicative of a unique supramolecular assembly mechanism or enhanced birefringence effects (see Figure 4-7b).

Compared to the individual isomer samples, the binary mixtures exhibited diminished birefringence, with notable peaks around 210 nm and 243 nm (see Figure 4-7c). This attenuation implies that interactions between different chiral forms may disrupt or alter molecular ordering, leading to reduced structural anisotropy and birefringence.

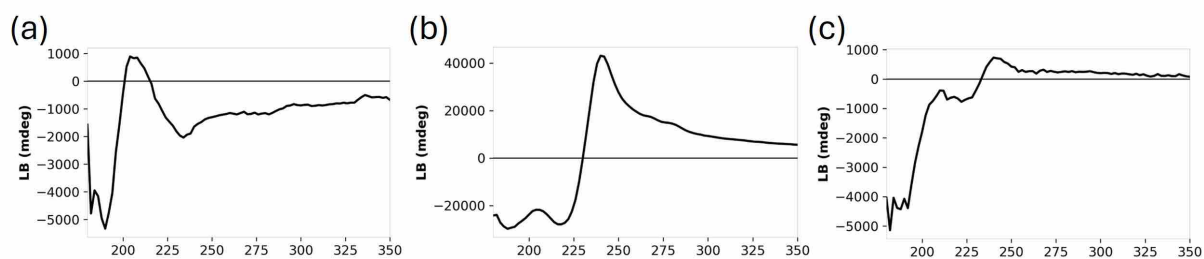


**Figure 4-7.** LB spectra derived from MMP data of (a) 10 mg/mL (L,L)-2NapFF pre-gel solution, (b) 10 mg/mL (L,D)-2NapFF pre-gel solution, and (c) (L,L)-2NapFF and (L,D)-2NapFF each at 10 mg/mL with a 1:1 volume ratio at pH 10.5, 25 °C.

#### 4.2.2.5 Analysis of LD' in MMP Data

The LD' spectrum of the 10 mg/mL (L,L)-2NapFF solution exhibits positive peaks at 190 nm and 220 nm and a negative peak at 205 nm (Figure 4-8a). This pattern indicates the formation of anisotropically oriented structures within the solution, likely fibers or elongated aggregates aligned by the flow field during measurement. In contrast, the LD' spectrum of 10 mg/mL (L,D)-2NapFF is characterized by greater variability, displaying a positive peak around 185 nm and negative peaks at 200 nm and 235 nm (Figure 4-8b). This suggests a more uniform or stronger molecular alignment, with the predominant orientation of aromatic groups more effectively aligned with the direction of polarized light. The differences in signal intensity and spectral

features between the (L,L)- and (L,D)-2NapFF samples indicate that stereochemistry-influenced variations in the assembly process lead to structures that are more oriented and mechanically robust, as corroborated by SANS data (Figure 2-11) and cryo-TEM images (Figure 2-14).

The LD' spectrum of the binary mixture closely mirrors that of the (L,D)-2NapFF, suggesting the dominance of the (L,D) isomer in the mixture (Figure 4-8c). Chapter 2 outlines that both components form distinct structures, with the fiber widths of the (L,D) component remaining consistent, whereas those of the (L,L) component vary with proportion.<sup>38</sup> This interaction between the diastereoisomers likely results in less uniform orientation within the mixed molecules, potentially leading to both constructive and destructive interference in polarized light absorption. Such interactions can significantly influence the material's structural attributes (e.g., orientation, rigidity, and overall structure of the aggregates) and functional properties, such as the rheology of the bulk gel.

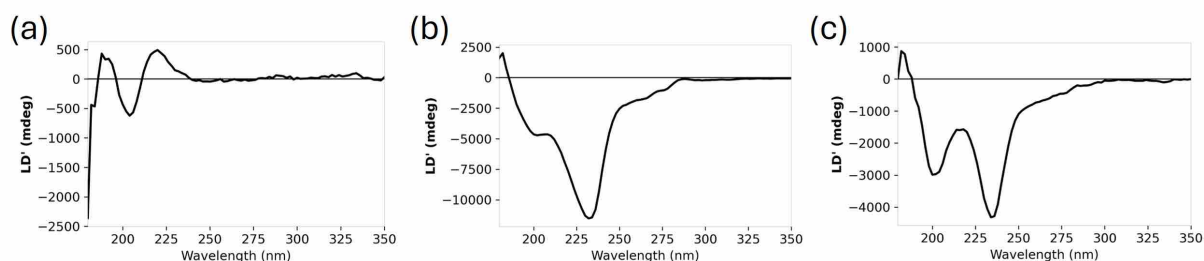


**Figure 4-8.** LD' spectra derived from MMP data of (a) 10 mg/mL (L,L)-2NapFF pre-gel solution, (b) 10 mg/mL (L,D)-2NapFF pre-gel solution, and (c) (L,L)-2NapFF and (L,D)-2NapFF each at 10 mg/mL with a 1:1 volume ratio at pH 10.5, 25 °C.

#### 4.2.2.6 Analysis of LB' in MMP Data

LB' quantifies the phase delay differences in light polarized at +45° and -45° as it traverses a material. In the data, peaks indicate areas of pronounced linear birefringence, suggesting highly ordered molecular structures. An upward trend in LB' data signals increasing molecular order and enhanced material anisotropy, whereas a downward trend implies a transition towards isotropic or disordered states.

The LB' spectra of the three dipeptide samples ((L,L)-2NapFF, (L,D)-2NapFF, and their binary mixture) exhibit a consistent trend with LD', with (L,L)-2NapFF showing the weakest signal and (L,D)-2NapFF the strongest (Figure 4-9). The binary mixture displays intermediate intensity. This pattern indicates a direct correlation between molecular configuration and spectral intensity, suggesting that different molecular configurations contribute distinctly to the linear

birefringence observed. Additionally, the spectral patterns and peak positions in the binary system closely mirror those in the (L,D) configuration, suggesting similar molecular orientations and interactions. This resemblance implies that the (L,D) configuration potentially exerts a dominant influence over the spectral characteristics of the mixed system, even when combined with the (L,L) configuration.

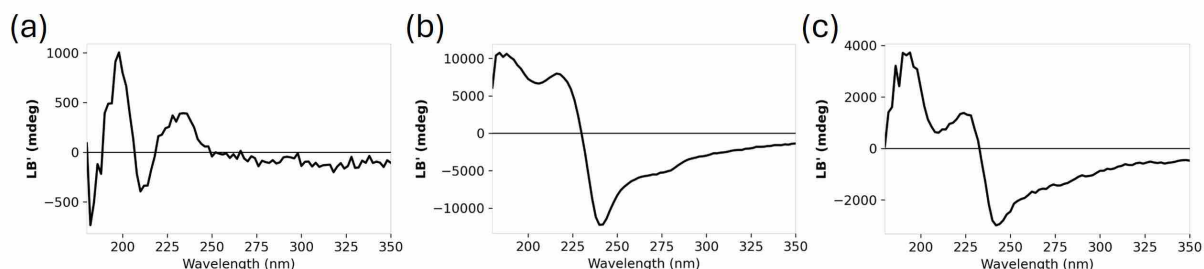


**Figure 4-9.** LB' spectra derived from MMP data of (a) 10 mg/mL (L,L)-2NapFF pre-gel solution, (b) 10 mg/mL (L,D)-2NapFF pre-gel solution, and (c) (L,L)-2NapFF and (L,D)-2NapFF each at 10 mg/mL with a 1:1 volume ratio at pH 10.5, 25 °C.

#### 4.2.2.7 Analysis of Absorption in MMP Data

The analysis of the absorption spectra for (L,L)-2NapFF, (L,D)-2NapFF, and their 1:1 diastereomeric mixtures reveals distinctive electronic interactions and environments. The absorption spectrum of 10 mg/mL (L,L)-2NapFF features a pronounced peak at approximately 220 nm, indicative of the  $\pi$ - $\pi^*$  transitions associated with the aromatic naphthalene ring (Figure 4-10a). This peak reflects a robust and stable electronic environment, conducive to effective  $\pi$ -electron conjugation and delocalization.

In contrast, the absorption spectrum of (L,D)-2NapFF shows significant deviation from its (L,L) counterpart, with an intensified and shifted peak around 230 nm (Figure 4-10b). This variation suggests modifications in molecular arrangement and an elevated level of electron conjugation, likely resulting from changes in chromophore orientation or denser molecular stacking, which enhance electronic transitions.

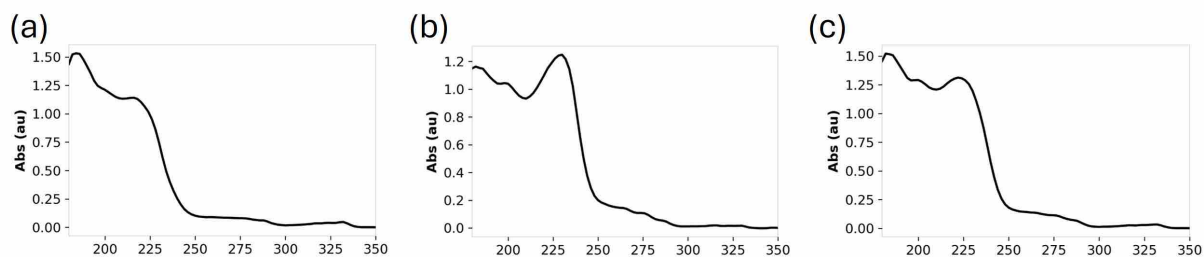


**Figure 4-10.** Absorption spectra derived from MMP data of (a) 10 mg/mL (L,L)-2NapFF pre-gel solution, (b) 10 mg/mL (L,D)-2NapFF pre-gel solution, and (c) (L,L)-2NapFF and (L,D)-2NapFF each at 10 mg/mL with a 1:1 volume ratio at pH 10.5, 25 °C.

The spectrum of the equimolar multicomponent mixture exhibits peaks at 185 nm and 225 nm with comparable intensity derived from the pure (L,L) and (L,D) form sample (Figure 4-10c), reflecting no obvious interactive effects between the (L,L) and (L,D) forms. These findings underline the complex dynamics between molecular structure and chromophore interactions within diastereomeric systems.

#### 4.2.2.8 Analysis of G-factor in MMP Data

The G-factor, or dissymmetry factor, is instrumental in quantifying the circular polarization of light within a sample and sheds light on the relative contributions of magnetic and electric dipole transitions in chiral molecules.<sup>39-41</sup> The G-factor values are pivotal in classifying electronic transitions: values exceeding  $10^{-2}$  suggest magnetic allowance with electrical prohibition, values around  $10^{-2}$  indicate both are permissible, and values below  $10^{-2}$  generally imply electrical allowance and magnetic prohibition.<sup>40</sup> Consistently low G-factor values across a spectrum suggest minimal magnetic dipole activity, whereas pronounced peaks may indicate specific molecular interactions or anomalous dispersion at particular wavelengths. Both positive and negative G-factor values typically represent contrasting molecular conformations or configurations.<sup>42, 43</sup> In regions lacking significant light scattering, the G-factor consistently indicates transitions that are both electrically and magnetically permissible, with values reaching up to orders of  $10^{-2}$  (Figure 4-11).

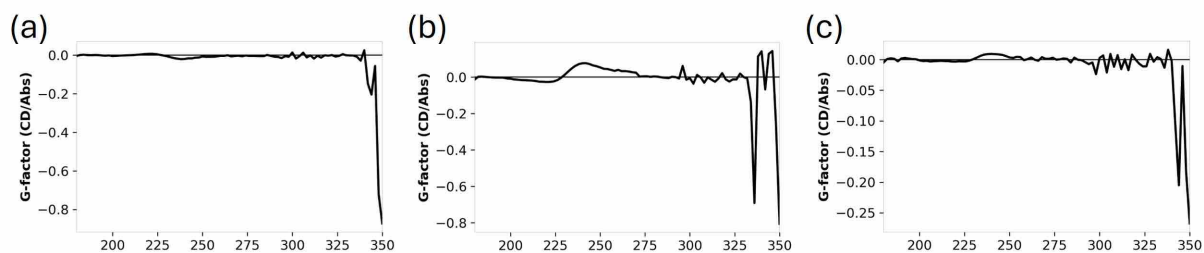


**Figure 4-11.** G-factor spectra derived from MMP data of (a) 10 mg/mL (L,L)-2NapFF pre-gel solution, (b) 10 mg/mL (L,D)-2NapFF pre-gel solution, and (c) (L,L)-2NapFF and (L,D)-2NapFF each at 10 mg/mL with a 1:1 volume ratio at pH 10.5, 25 °C.

### 4.2.3 MMP Analysis of Other Diastereomeric Dipeptide Solutions

The transmission results from four experimental runs showed slight variations across each sample, suggesting the presence of light deattenuation or depolarization effects, as depicted in Figures 4-12i to 4-26i. Analysis of the pre-gel solutions for both (L,L) and (L,D) diastereoisomers, as well as their binary mixtures with five naphthyl diphenylalanine derivatives, confirmed the presence of inherent optical activity, as demonstrated in Figures 4-12a to 4-26a. These findings underscore the significant impact of optical phenomena such as CB, LD, and LB in these systems. It is crucial to consider the significant influence of linearly polarized light when studying supramolecular aggregates, as it plays a pivotal role in LB measurements.

The CD spectra of most dipeptide amphiphiles showed distinct peaks between 225-230 nm, aligning with  $\pi$ - $\pi$  interactions among the aromatic phenylalanine residues. Notably, compounds like (L,D)-1NapFF, 6CN2NapFF, and (L,D)-4Cl1NapFF did not exhibit these characteristics, as indicated in Figures 4-19a, 4-21a, 4-22a, and 4-25a. A broad signal from 260-320 nm in (L,L)-7MeO2NapFF (Figure 4-12a) suggested limited mobility of aromatic amino acid side chains within the chiral environment of the supramolecular assemblies.<sup>44-46</sup> Furthermore, a comprehensive MMP analysis of a 10 mg/mL (L,D)-1NapFF solution showed minimal CD, revealing that many molecules remained unassembled in the monomer state within the absorption spectrum. (Figure 4-19).

The CD spectrum of (L,L)-7MeO2NapFF exhibited a distinctive negative peak near 200 nm followed by a double positive peak around 225-250 nm (Figure 4-12a), indicative of specific chiral molecular environments. This pattern suggests that the L-configuration amino acids in the peptide backbone help form well-defined assemblies that exhibit supramolecular chirality, affecting the differential absorption of left- and right-handedly polarized light. Conversely, the

CD spectrum of (L,D)-7MeO2NapFF showed a pronounced sharp positive peak near 235 nm and a deeper negative valley around 225 nm (Figure 4-13a), indicating stronger or distinct chiral interactions compared to the (L,L) form. The intensity and profile of these peaks likely reflect a more structured chiral molecular arrangement.

The CD spectra of the binary mixtures presented features intermediate between the individual components, indicating that interactions between the (L,L) and (L,D) forms moderate the CD signal (Figure 4-14a). The presence of both positive and negative peaks at lower intensities than those seen in the pure (L,D) samples suggests that chiral interactions and molecular orientations are influenced by the stereoisomer mixture. The observed spectrum, which closely approximates the average of the two individual spectra, implies minimal significant interaction between the (L,L) and (L,D) species.

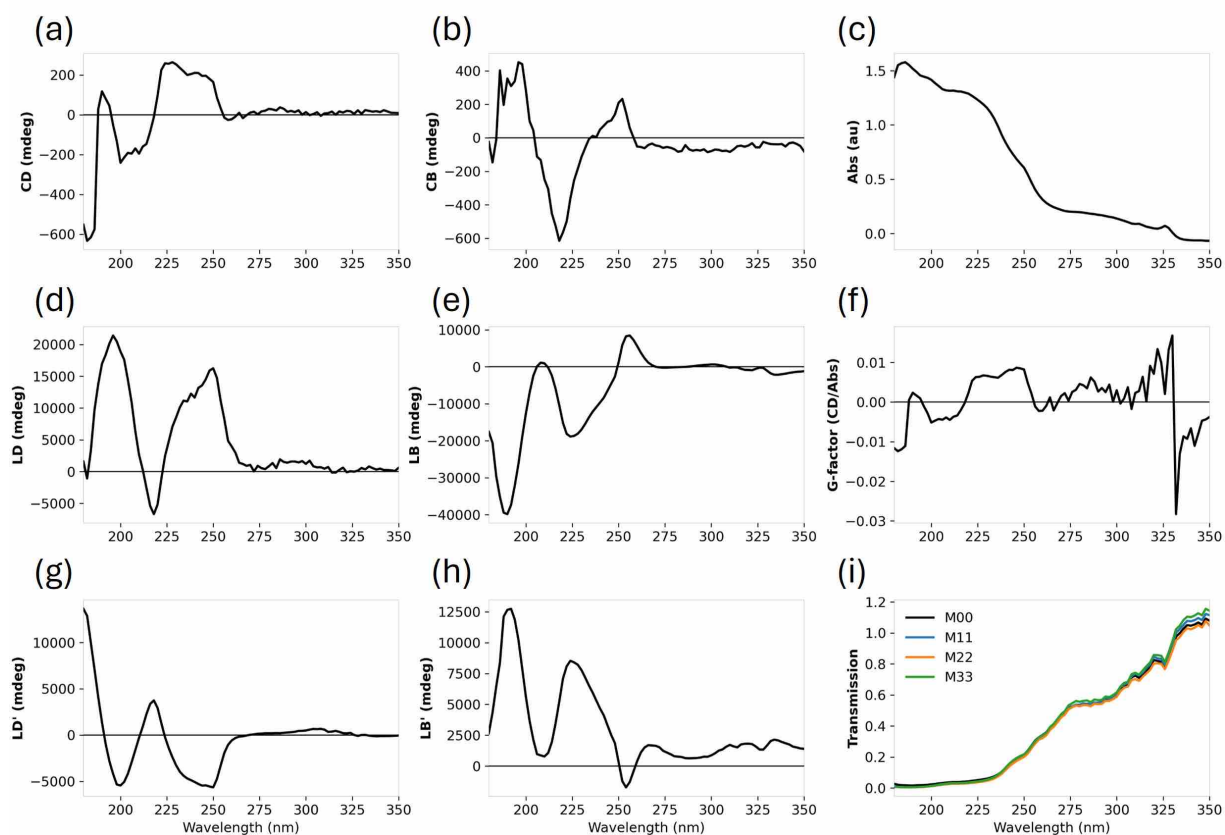


**Figure 4-12.** MMP data of 10 mg/mL (L,L)-7MeO2NapFF pre-gel solution at pH 10.5, 25 °C. (a) circular dichroism, (b) circular birefringence, (c) absorption, (d) linear dichroism, (e) linear birefringence, (f) G-factor, (g) 45° linear dichroism, (h) 45° linear birefringence, (i) transmission. The data presented are averages of four scans. The transmission graph displays all four runs (M00, M11, M22, and M33) to check for deattenuation or depolarization in the dataset, and the subtle discrepancy of the data for each sample indicates the existence of these effects.

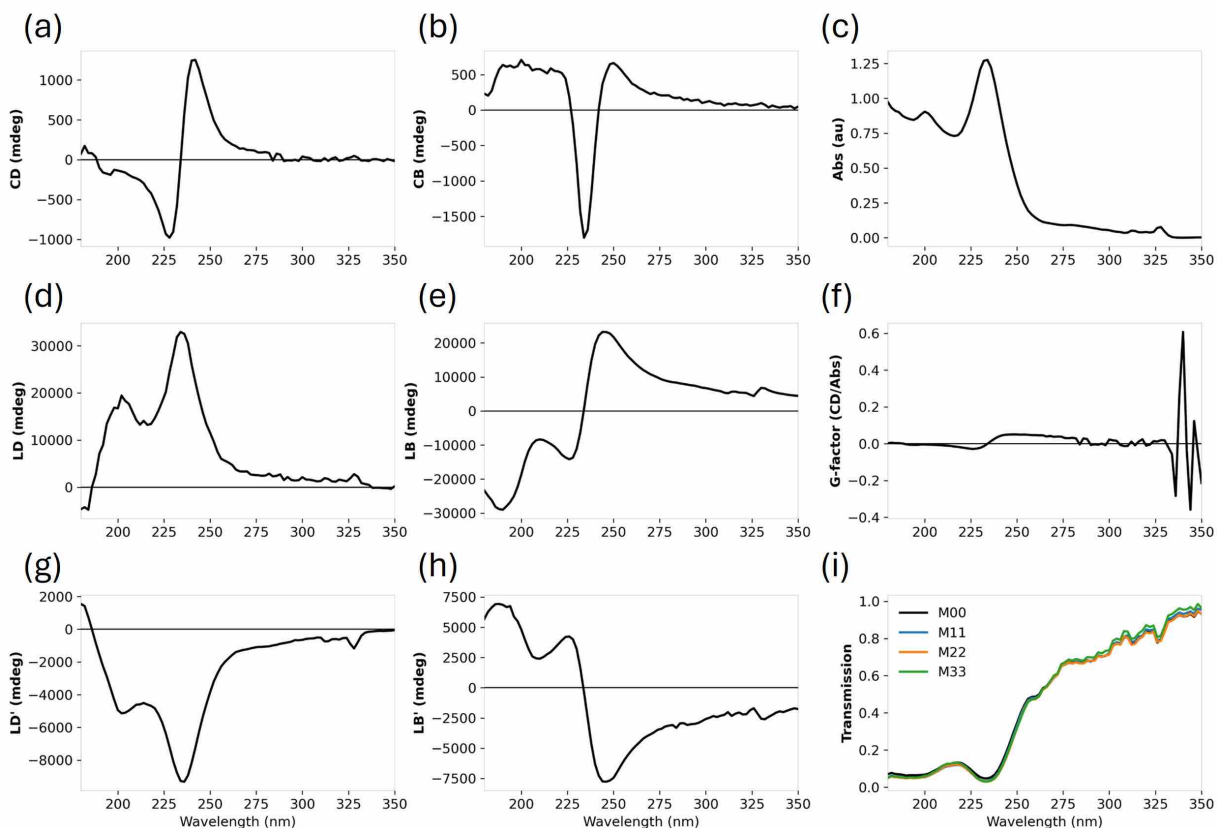


**Figure 4-13.** MMP data of 10 mg/mL (L,D)-7MeO<sub>2</sub>NapFF pre-gel solution at pH 10.5, 25 °C. (a) circular dichroism, (b) circular birefringence, (c) absorption, (d) linear dichroism, (e) linear birefringence, (f) G-factor, (g) 45° linear dichroism, (h) 45° linear birefringence, (i) transmission. The data presented are averages of four scans. The transmission graph displays all four runs (M00, M11, M22, and M33) to check for deattenuation or depolarization in the dataset, and the subtle discrepancy of the data for each sample indicates the existence of these effects.

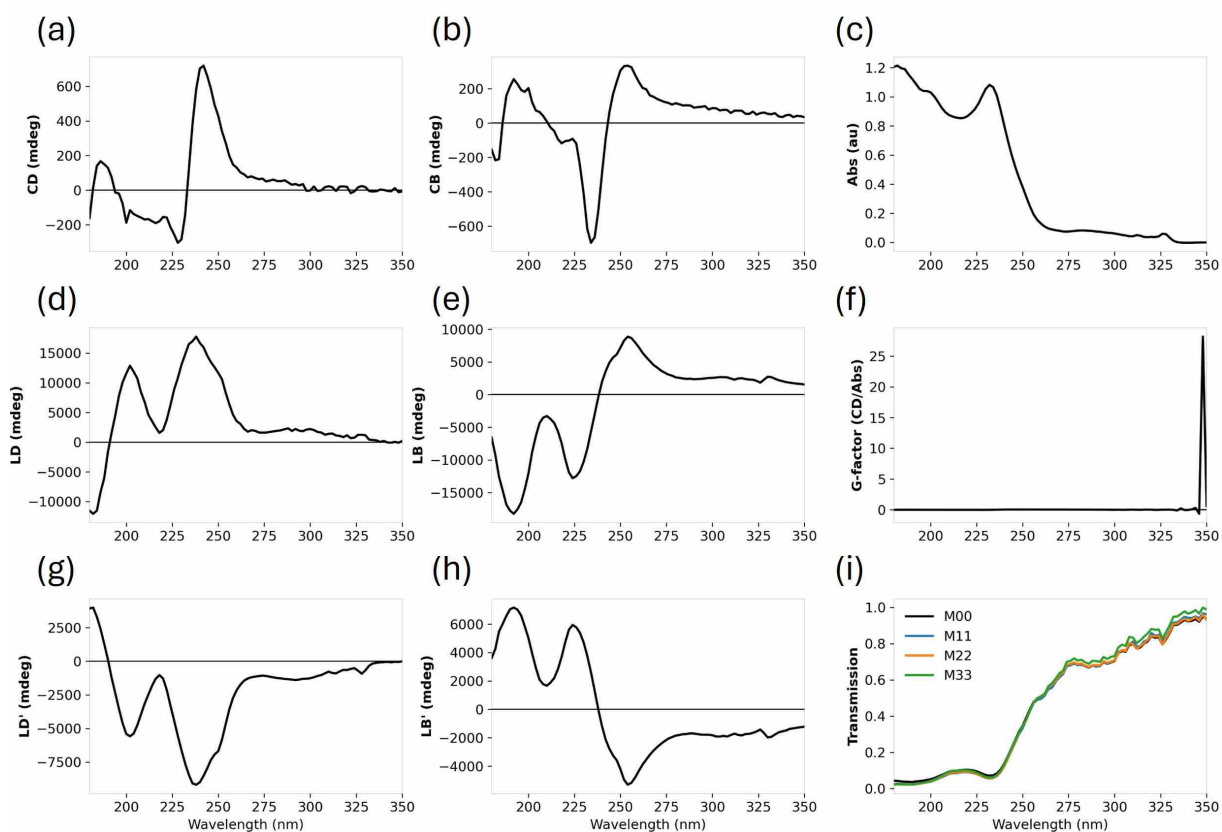


**Figure 4-14.** MMP data of binary solution composed of (L,L)-7MeO<sub>2</sub>NapFF and (L,D)-7MeO<sub>2</sub>NapFF each at 10 mg/mL with a 1:1 volume ratio (5:5) at pH 10.5, 25 °C. (a) circular dichroism, (b) circular birefringence, (c) absorption, (d) linear dichroism, (e) linear birefringence, (f) G-factor, (g) 45° linear dichroism, (h) 45° linear birefringence, (i) transmission. The data presented are averages of four scans. The transmission graph displays all four runs (M00, M11, M22, and M33) to check for deattenuation or depolarization in the dataset, and the subtle discrepancy of the data for each sample indicates the existence of these effects.

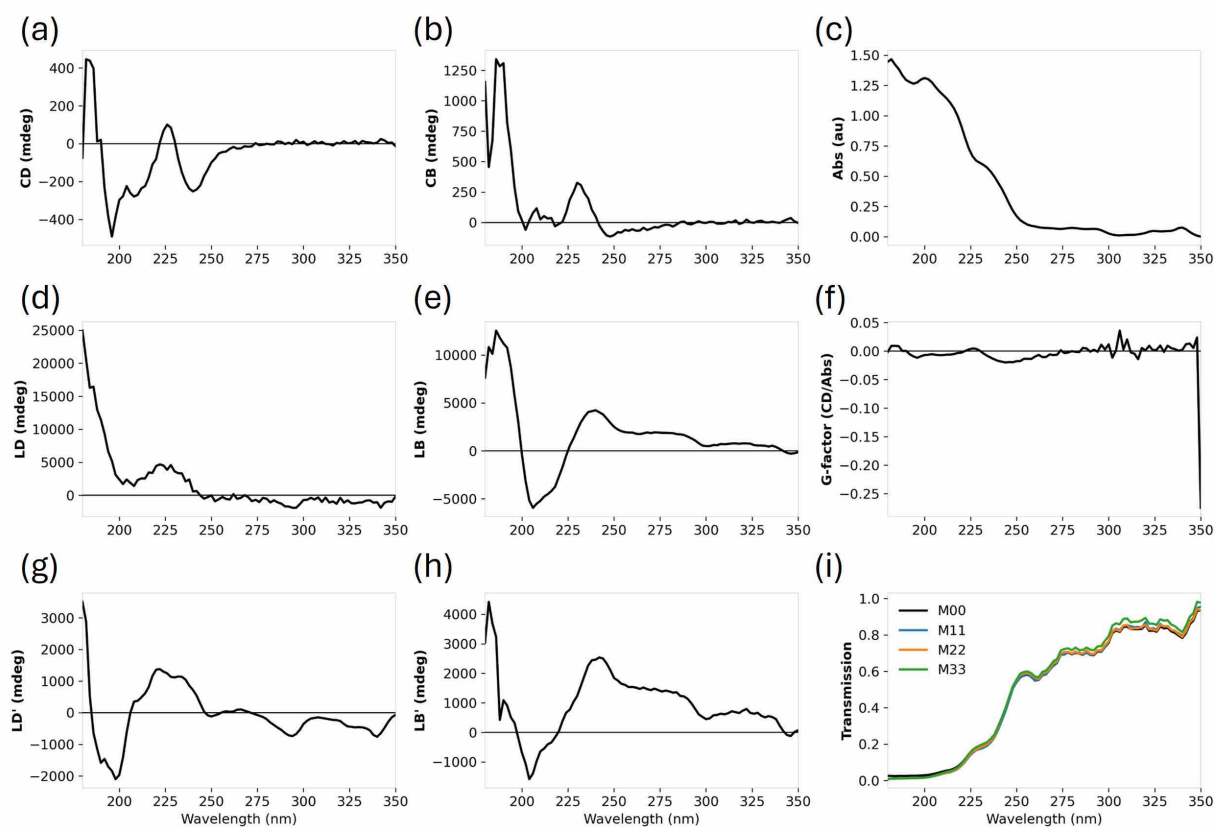


**Figure 4-15.** MMP data of 10 mg/mL (L,L)-6Br<sub>2</sub>NapFF pre-gel solution at pH 10.5, 25 °C. (a) circular dichroism, (b) circular birefringence, (c) absorption, (d) linear dichroism, (e) linear birefringence, (f) G-factor, (g) 45° linear dichroism, (h) 45° linear birefringence, (i) transmission. The data presented are averages of four scans. The transmission graph displays all four runs (M00, M11, M22, and M33) to check for deattenuation or depolarization in the dataset, and the subtle discrepancy of the data for each sample indicates the existence of these effects.

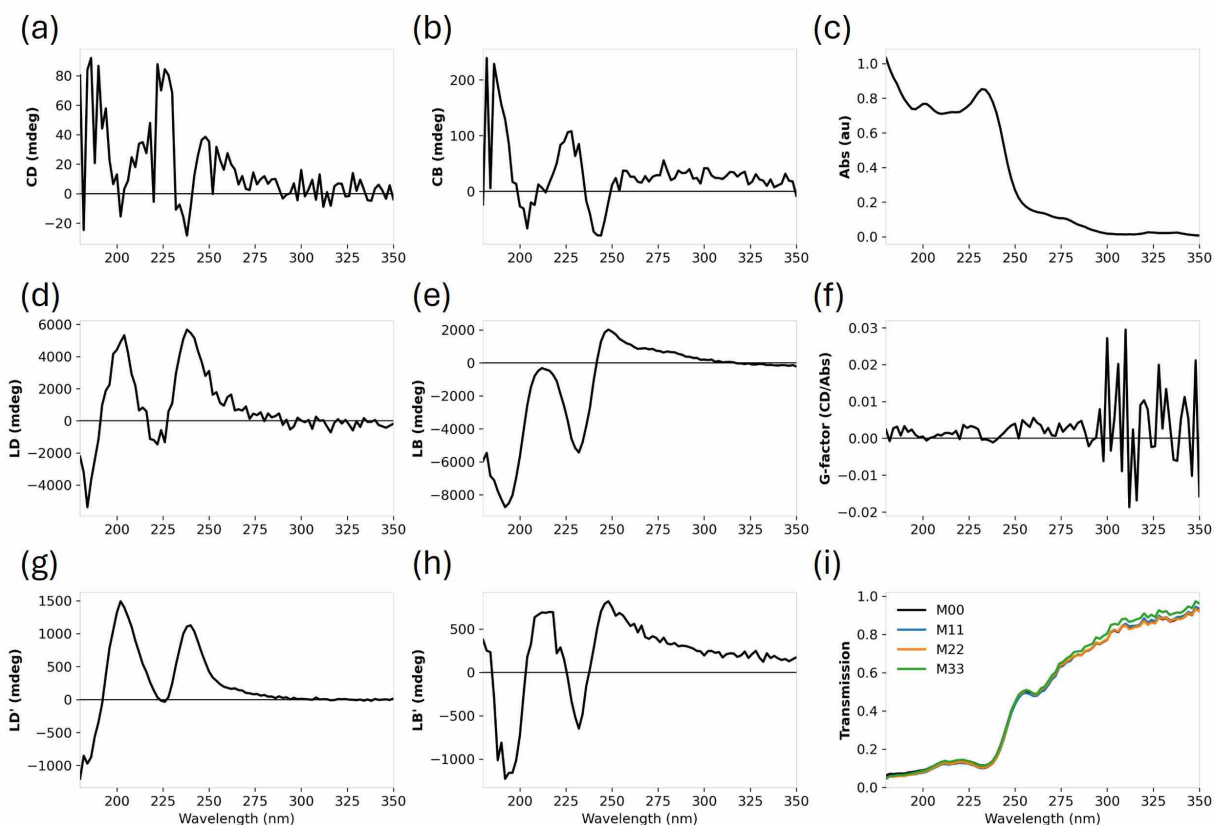


**Figure 4-16.** MMP data of 10 mg/mL (L,D)-6Br2NapFF pre-gel solution at pH 10.5, 25 °C. (a) circular dichroism, (b) circular birefringence, (c) absorption, (d) linear dichroism, (e) linear birefringence, (f) G-factor, (g) 45° linear dichroism, (h) 45° linear birefringence, (i) transmission. The data presented are averages of four scans. The transmission graph displays all four runs (M00, M11, M22, and M33) to check for deattenuation or depolarization in the dataset, and the subtle discrepancy of the data for each sample indicates the existence of these effects.

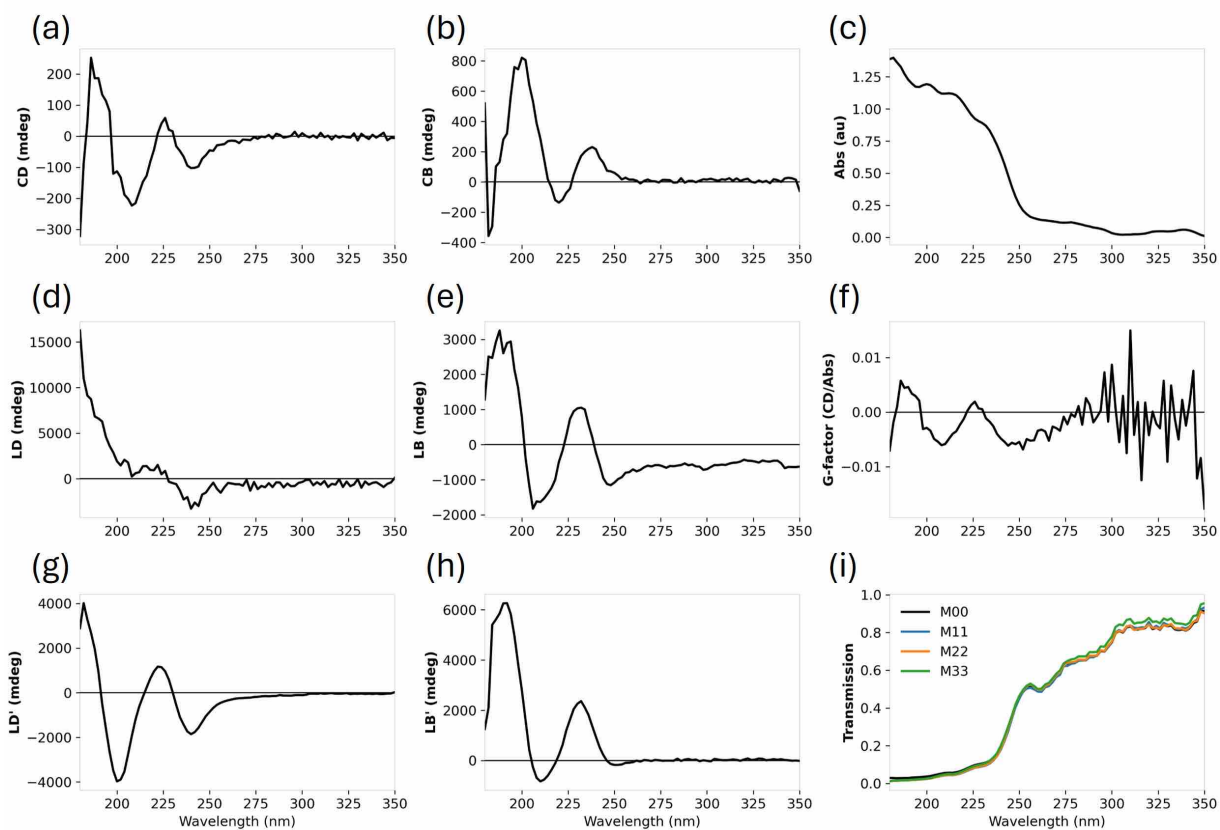


**Figure 4-17.** MMP data of binary solution composed of (L,L)-6Br2NapFF and (L,D)-6Br2NapFF each at 10 mg/mL with a 1:1 volume ratio (5:5) at pH 10.5, 25 °C. (a) circular dichroism, (b) circular birefringence, (c) absorption, (d) linear dichroism, (e) linear birefringence, (f) G-factor, (g) 45° linear dichroism, (h) 45° linear birefringence, (i) transmission. The data presented are averages of four scans. The transmission graph displays all four runs (M00, M11, M22, and M33) to check for deattenuation or depolarization in the dataset, and the subtle discrepancy of the data for each sample indicates the existence of these effects.

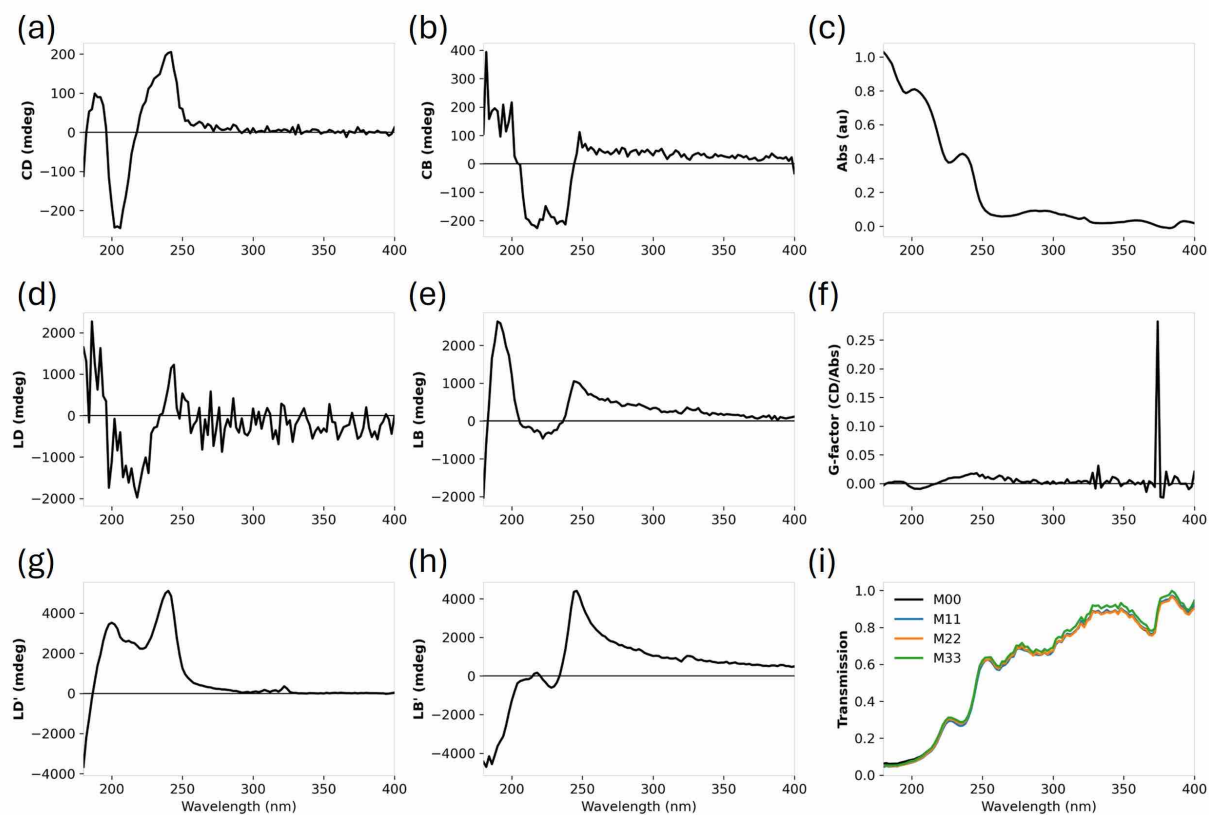


**Figure 4-18.** MMP data of 10 mg/mL (L,L)-1NapFF pre-gel solution at pH 10.5, 25 °C. (a) circular dichroism, (b) circular birefringence, (c) absorption, (d) linear dichroism, (e) linear birefringence, (f) G-factor, (g) 45° linear dichroism, (h) 45° linear birefringence, (i) transmission. The data presented are averages of four scans. The transmission graph displays all four runs (M00, M11, M22, and M33) to check for deattenuation or depolarization in the dataset, and the subtle discrepancy of the data for each sample indicates the existence of these effects.

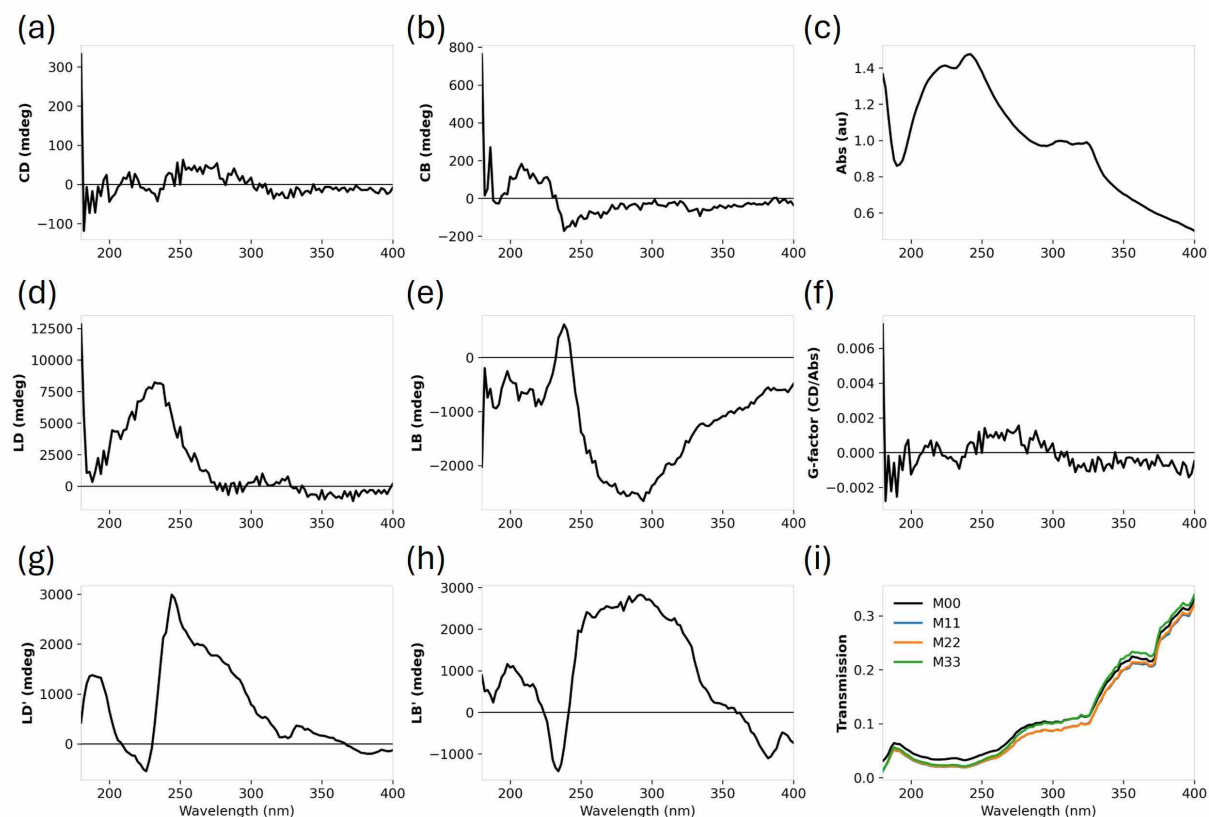


**Figure 4-19.** MMP data of 10 mg/mL (L,D)-1NapFF pre-gel solution at pH 10.5, 25 °C. (a) circular dichroism, (b) circular birefringence, (c) absorption, (d) linear dichroism, (e) linear birefringence, (f) G-factor, (g) 45° linear dichroism, (h) 45° linear birefringence, (i) transmission. The data presented are averages of four scans. The transmission graph displays all four runs (M00, M11, M22, and M33) to check for deattenuation or depolarization in the dataset, and the subtle discrepancy of the data for each sample indicates the existence of these effects.

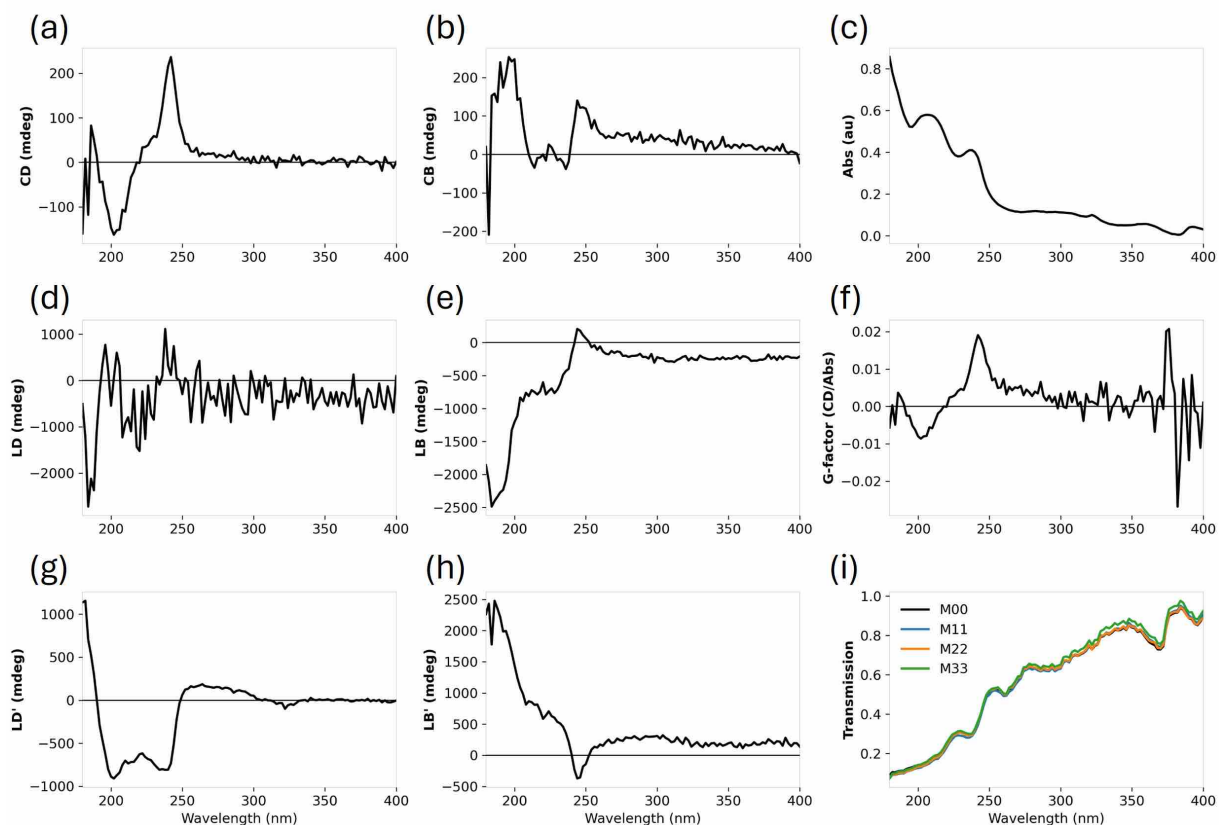


**Figure 4-20.** MMP data of binary solution composed of (L,L)-1NapFF and (L,D)-1NapFF each at 10 mg/mL with a 1:1 volume ratio (5:5) at pH 10.5, 25 °C. (a) circular dichroism, (b) circular birefringence, (c) absorption, (d) linear dichroism, (e) linear birefringence, (f) G-factor, (g) 45° linear dichroism, (h) 45° linear birefringence, (i) transmission. The data presented are averages of four scans. The transmission graph displays all four runs (M00, M11, M22, and M33) to check for deattenuation or depolarization in the dataset, and the subtle discrepancy of the data for each sample indicates the existence of these effects.

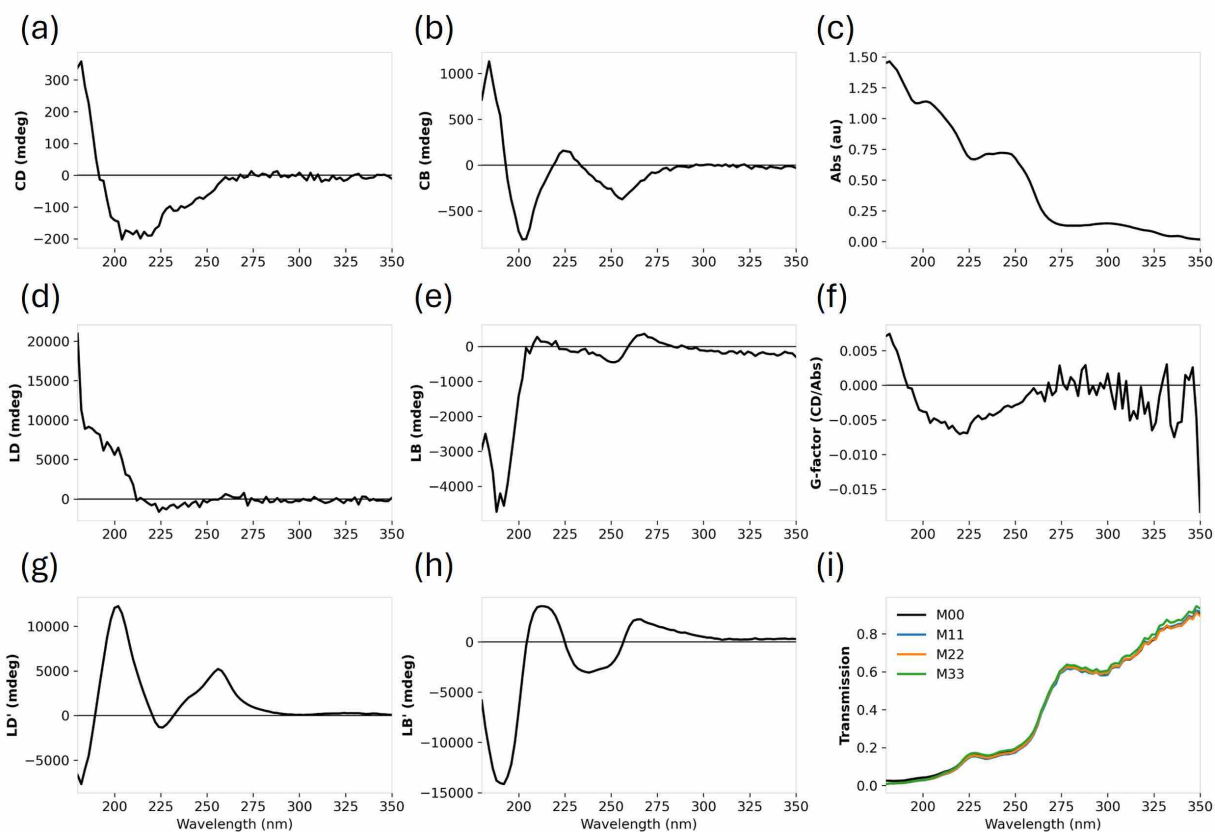


**Figure 4-21.** MMP data of 10 mg/mL (L,L)-6CN2NapFF pre-gel solution at pH 10.5, 25 °C. (a) circular dichroism, (b) circular birefringence, (c) absorption, (d) linear dichroism, (e) linear birefringence, (f) G-factor, (g) 45° linear dichroism, (h) 45° linear birefringence, (i) transmission. The data presented are averages of four scans. The transmission graph displays all four runs (M00, M11, M22, and M33) to check for deattenuation or depolarization in the dataset, and the subtle discrepancy of the data for each sample indicates the existence of these effects.

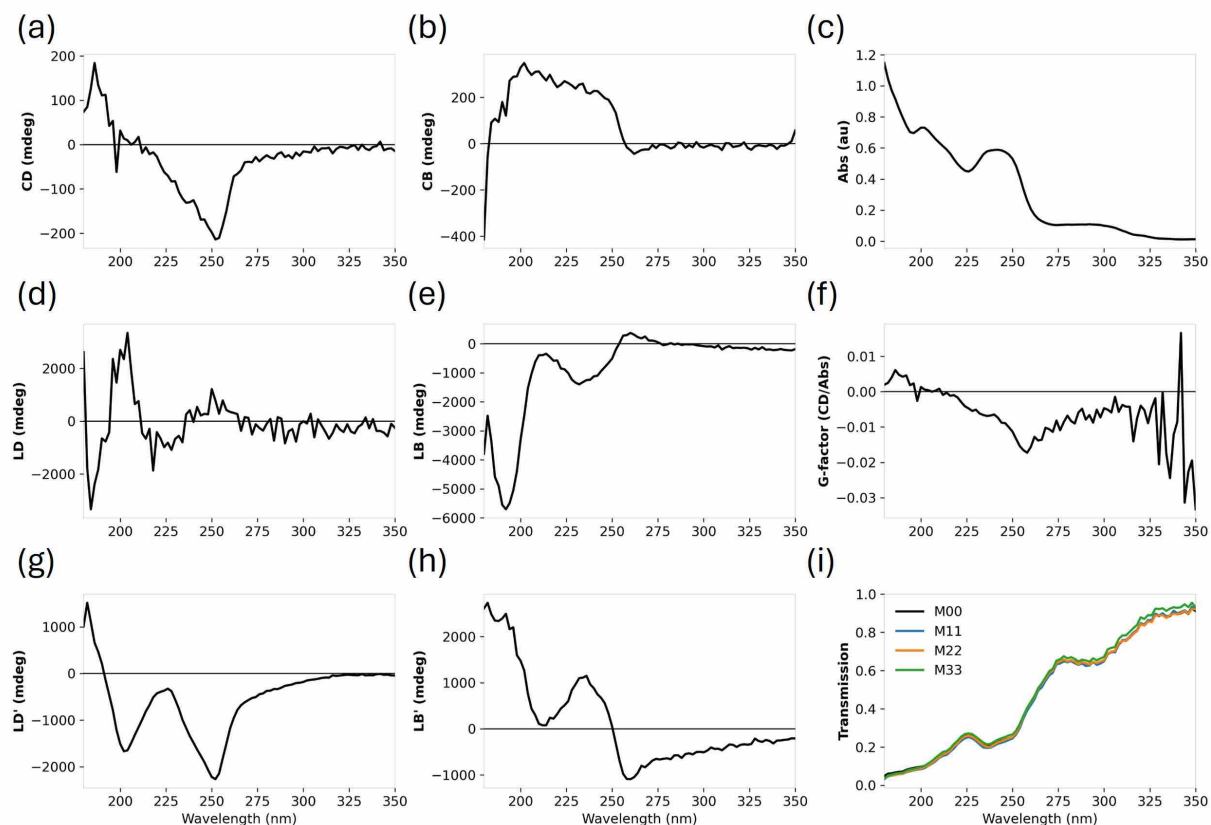


**Figure 4-22.** MMP data of 10 mg/mL (L,D)-6CN2NapFF pre-gel solution at pH 10.5, 25 °C. (a) circular dichroism, (b) circular birefringence, (c) absorption, (d) linear dichroism, (e) linear birefringence, (f) G-factor, (g) 45° linear dichroism, (h) 45° linear birefringence, (i) transmission. The data presented are averages of four scans. The transmission graph displays all four runs (M00, M11, M22, and M33) to check for deattenuation or depolarization in the dataset, and the subtle discrepancy of the data for each sample indicates the existence of these effects.

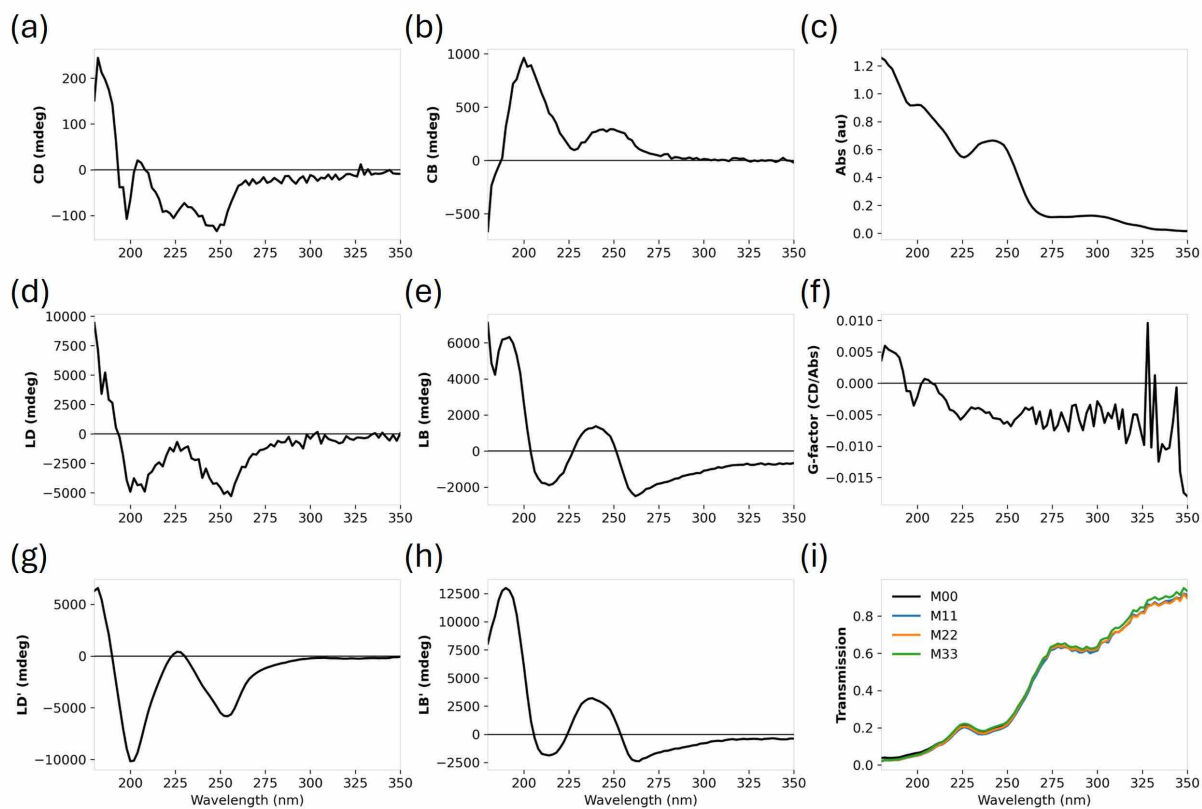


**Figure 4-23.** MMP data of binary solution composed of (L,L)-6CN2NapFF and (L,D)-6CN2NapFF each at 10 mg/mL with a 1:1 volume ratio (5:5) at pH 10.5, 25 °C. (a) circular dichroism, (b) circular birefringence, (c) absorption, (d) linear dichroism, (e) linear birefringence, (f) G-factor, (g) 45° linear dichroism, (h) 45° linear birefringence, (i) transmission. The data presented are averages of four scans. The transmission graph displays all four runs (M00, M11, M22, and M33) to check for deattenuation or depolarization in the dataset, and the subtle discrepancy of the data for each sample indicates the existence of these effects.

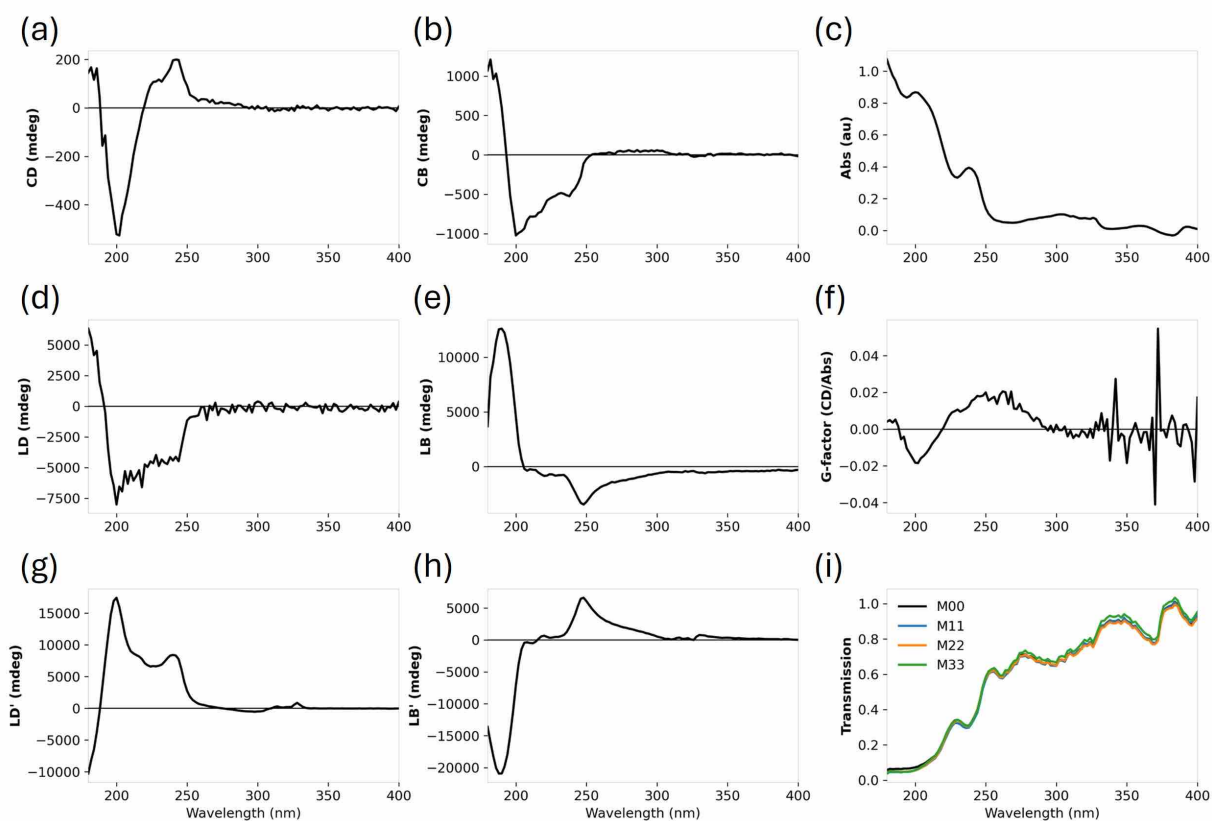


**Figure 4-24.** MMP data of 10 mg/mL (L,L)-4C11NapFF pre-gel solution at pH 10.5, 25 °C. (a) circular dichroism, (b) circular birefringence, (c) absorption, (d) linear dichroism, (e) linear birefringence, (f) G-factor, (g) 45° linear dichroism, (h) 45° linear birefringence, (i) transmission. The data presented are averages of four scans. The transmission graph displays all four runs (M00, M11, M22, and M33) to check for deattenuation or depolarization in the dataset, and the subtle discrepancy of the data for each sample indicates the existence of these effects.

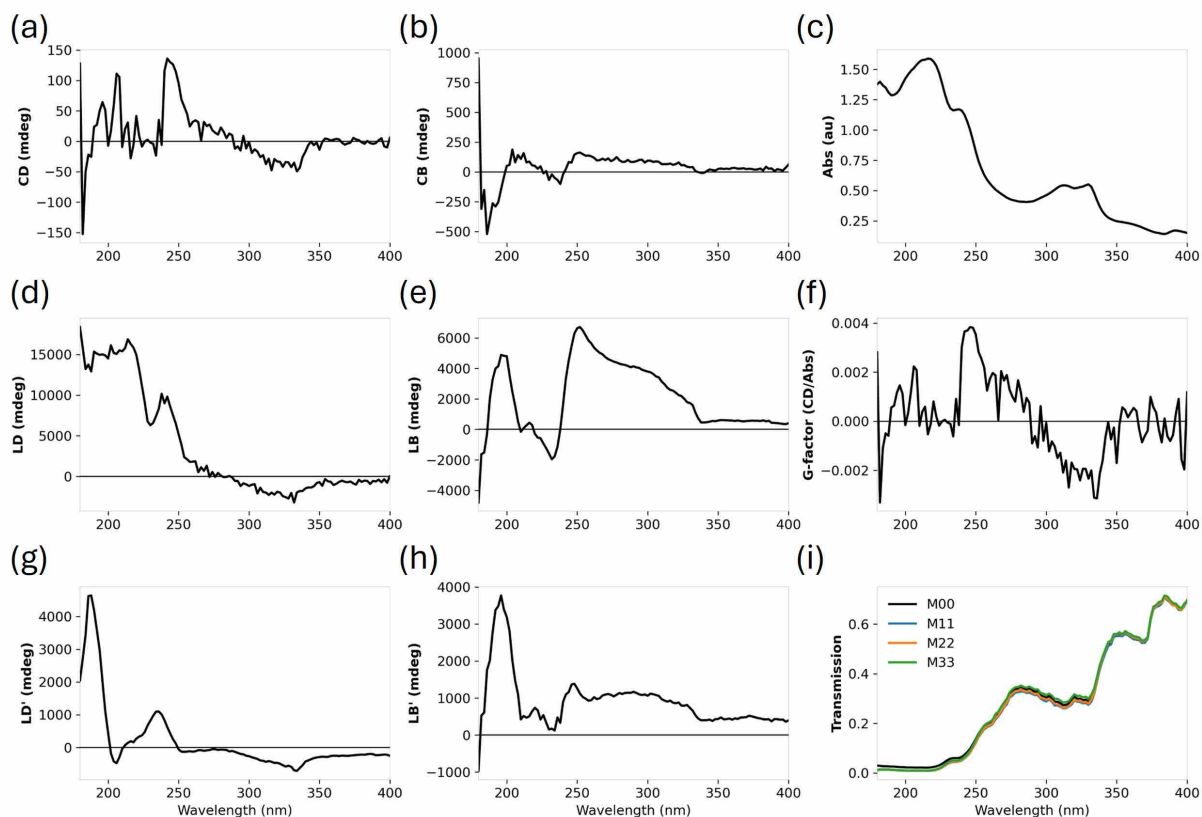


**Figure 4-25.** MMP data of 10 mg/mL (L,D)-4Cl1NapFF pre-gel solution at pH 10.5, 25 °C. (a) circular dichroism, (b) circular birefringence, (c) absorption, (d) linear dichroism, (e) linear birefringence, (f) G-factor, (g) 45° linear dichroism, (h) 45° linear birefringence, (i) transmission. The data presented are averages of four scans. The transmission graph displays all four runs (M00, M11, M22, and M33) to check for deattenuation or depolarization in the dataset, and the subtle discrepancy of the data for each sample indicates the existence of these effects.

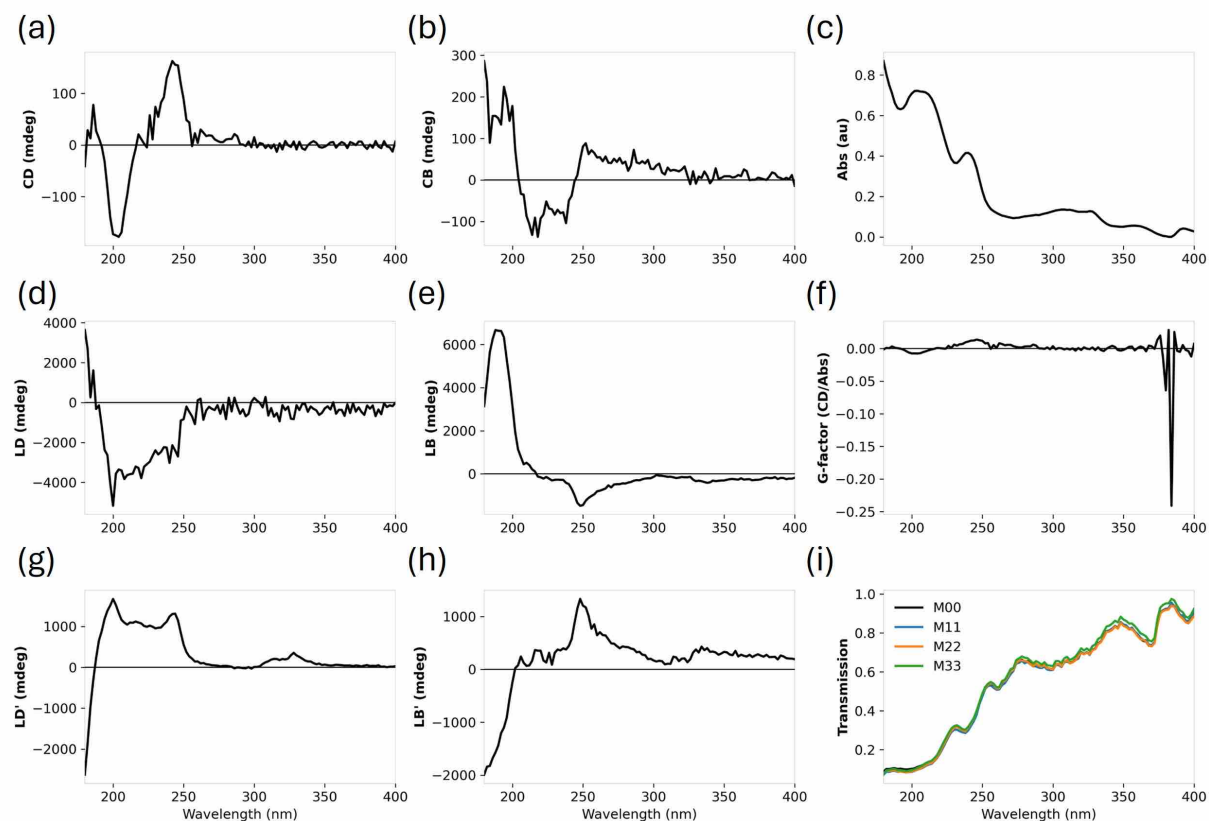


**Figure 4-26.** MMP data of binary solution composed of (L,L)-4Cl1NapFF and (L,D)-4Cl1NapFF each at 10 mg/mL with a 1:1 volume ratio (5:5) at pH 10.5, 25 °C. (a) circular dichroism, (b) circular birefringence, (c) absorption, (d) linear dichroism, (e) linear birefringence, (f) G-factor, (g) 45° linear dichroism, (h) 45° linear birefringence, (i) transmission. The data presented are averages of four scans. The transmission graph displays all four runs (M00, M11, M22, and M33) to check for deattenuation or depolarization in the dataset, and the subtle discrepancy of the data for each sample indicates the existence of these effects.

### 4.3 Conclusions

This study demonstrates the effectiveness of MMP in investigating molecular interactions within diastereomeric mixtures of functionalized dipeptide-based pre-gel systems. The results show that altering component ratios significantly impacts the optical properties of these systems, enhancing our understanding of their self-assembly and behavior in various environments. By adjusting molecular composition and chirality, researchers can precisely control molecular order and orientation, thereby improving the functional properties of the materials. These insights are crucial for understanding the complex interactions that govern self-assembly and functionality in such materials, advancing the design of dynamic supramolecular systems that adapt to

environmental changes. Ultimately, this work aims to refine these systems for applications in biomaterials science and innovative therapeutic strategies based on diastereomer-specific activities.

MMP offers significant advantages for characterizing complex, anisotropic, or chiral systems, providing detailed insights into the optical behavior of self-assembled structures like dipeptide hydrogels and supramolecular assemblies. MMP excels in analyzing systems with ordered structures, where molecular alignment and chirality play a crucial role in optical properties. By measuring multiple polarization states, MMP can capture features such as CD, LD, and birefringence (LB), which conventional techniques like SRCD might overlook. This makes MMP particularly useful for studying self-assembly processes, molecular interactions, and depolarization effects, especially in systems with mixed components or structural heterogeneity. MMP is also invaluable for studying highly structured assemblies, such as LMWGs, where understanding molecular orientation and ordering is key to characterizing mechanical properties and rheology. Additionally, MMP can detect subtle depolarization effects that may complicate data interpretation in anisotropic or disordered systems. For binary mixtures, MMP helps identify interactions between components and reveals structural heterogeneity that simpler methods may not capture.

However, MMP is not always necessary. For isotropic systems or those lacking significant chirality or anisotropy, traditional techniques like UV-vis or SRCD are often sufficient. MMP is most beneficial for systems where polarization effects and structural order are critical to understanding the sample. In cases where depolarization effects are minimal or when dealing with simpler systems without complex molecular interactions, conventional methods may be more efficient and less complex.

In summary, MMP is particularly well-suited for characterizing systems with high structural order and complex chirality, especially at high concentrations where molecular self-assembly leads to more pronounced polarization effects. The decision to use MMP should be based on the specific research objectives and the level of detail needed to understand the sample's optical properties and structure.

## **4.4 Experimental Section**

### **4.4.1 Preparation of Solutions**

Sample preparation for the pH 10.5 pre-gel solutions investigated in this chapter follows the methodology outlined in Chapter 2 and Chapter 3.

#### 4.4.2 Basics of Mueller Matrix Analysis

Maxwell's electromagnetic theory identifies light waves as electromagnetic and transverse with distinct polarization properties. When polarized light interacts with surfaces, it reflects and scatters, conveying data about the surface's roughness, dielectric constant, and structural characteristics.<sup>47-49</sup> The Stokes vector, as represented in Equation 4-1, quantifies the total and the differential intensities of polarized light components.

$$S = \begin{bmatrix} I \\ Q \\ U \\ V \end{bmatrix} = \begin{bmatrix} I_0 + I_{90} \\ I_0 - I_{90} \\ I_{45^\circ} - I_{135^\circ} \\ I_R - I_L \end{bmatrix} \quad \text{Equation 4-1}$$

where  $I$  represents the total light intensity, defined as the sum of the horizontally and vertically polarized components;  $Q$  quantifies the difference between horizontally and vertically polarized components;  $U$  denotes the difference between the  $45^\circ$  and  $135^\circ$  polarized components; and  $V$  measures the differential between right-handed and left-handed circularly polarized components.

The Stokes vector was correlated with a  $4 \times 4$  matrix to assess an optical system's effect on incident light polarization.<sup>50</sup> Mueller expanded this concept by introducing the Mueller matrix  $\mathbf{M}$  and the Stokes-Mueller (SM) system,<sup>51</sup> which facilitates comprehensive polarization handling and quantitative analysis (Equation 4-2).

$$S_o = \mathbf{M}S_i \Leftrightarrow \begin{bmatrix} I_o \\ Q_o \\ U_o \\ V_o \end{bmatrix} = \begin{bmatrix} M_{00} & M_{01} & M_{02} & M_{03} \\ M_{10} & M_{11} & M_{12} & M_{13} \\ M_{20} & M_{21} & M_{22} & M_{23} \\ M_{30} & M_{31} & M_{32} & M_{33} \end{bmatrix} \begin{bmatrix} I_i \\ Q_i \\ U_i \\ V_i \end{bmatrix} \quad \text{Equation 4-2}$$

Here,  $S_o$  represents the Stokes vector of the outgoing light;  $S_i$  indicates the Stokes vector of the incident light; and  $\mathbf{M}$  denotes the Mueller matrix, which describes the transformation between these two states.

For anisotropic and homogeneous media with light propagating along  $z$ , the Mueller matrix  $\mathbf{M}$  can be expressed exponentially in terms of the differential Mueller matrix  $\mathbf{m}$  ( $\mathbf{m}$  is independent of  $z$ ), and the optical path length  $l$ , providing a foundational equation<sup>25, 52, 53</sup>

$$\mathbf{L} = \ln \mathbf{M} = \mathbf{m}l \quad \text{Equation 4-3}$$

The differential Mueller matrix  $\mathbf{m}$  is effectively utilized to characterize anisotropic, depolarizing, homogeneous media and is defined as follows<sup>25, 52</sup>

$$\mathbf{m} = \begin{bmatrix} \alpha & \beta & \gamma & \delta \\ \beta' & \alpha_1 & \mu & \nu \\ \gamma' & -\mu' & \alpha_2 & \eta \\ \delta' & -\nu' & -\eta' & \alpha_3 \end{bmatrix} \quad \text{Equation 4-4}$$

Here, the parameters  $\alpha$  and  $\alpha_1, \alpha_2, \alpha_3$  represent absorption, horizontal linear, 45° linear, and circular depolarization, respectively;  $\beta, \gamma, \delta$  denote horizontal linear, 45° linear, and circular dichroism, correspondingly;  $\eta, \nu, \mu$  describe horizontal linear, 45° linear, and circular retardance, respectively. In homogeneous reciprocal media, the matrix must satisfy the following reciprocal conditions:  $\beta = \beta', \gamma = \gamma', \delta = \delta', \mu = \mu', \nu = \nu',$  and  $\eta = \eta'$ .

To correlate the parameters of the differential Mueller matrix with various physical effects in polarimetric analysis, the parametrization outlined below satisfies six critical conditions previously established:<sup>25, 53, 54</sup>

$$\mathbf{L} = \begin{bmatrix} A & -LD & -LD' & CD \\ -LD & A - LDP & CB & LB' \\ -LD' & -CB & A - LDP' & -LB \\ CD & -LB' & LB & A - CDP \end{bmatrix} \quad \text{Equation 4-5}$$

Where LDP, LDP', and CDP denote the horizontal linear, 45° linear, and circular depolarization, respectively. Notably, for a non-depolarising sample, the values of LDP, LDP', and CDP are all equal to zero, indicating no depolarization effects.

## 4.4.3 SRCD and MMP Measurement

### 4.4.3.1 Instrumentation

Experiments involving SRCD, absorption spectroscopy, and MMP were conducted at the B23 beamline of Diamond Light Source Ltd. in Didcot, UK. These studies utilized a Mueller matrix polarimeter tower, situated on module B of the B23 beamline, and incorporated an MMP system from Hinds Instruments (USA), integrated with the Diamond B23 light source and a dual grating subtractive monochromator from Olis Instruments (USA).<sup>9, 10, 22, 42</sup> This configuration exploited the highly collimated micro-beam produced by the B23 beamline, facilitating precise light manipulation through an array of optical components and finally channelling the light through the sample to a Photomultiplier Tube (PMT) detector.

The optical pathway within the B23 MMP vertical chamber<sup>10, 22</sup> is intricately designed, starting from the bottom with a dual grating subtractive monochromator covering 190-650 nm, followed by a 45° MgF<sub>2</sub> coated aluminium planar mirror (M1), a linear polarizer prism (P1), and dual

photoelastic modulators (PEM1 and PEM2) designed for generating polarization states. This assembly continues with a UV-transparent 10× objective which directs the beam toward the PMT detector, an X-Y electrically operated, temperature-controlled sample stage (Linkam MDS600), and a motorized mirror (M2) for the UV camera. The polarization analysis system includes additional photoelastic modulators (PEM3 and PEM4), and a linear polariser analyzer prism (A1) positioned at the PMT detector. These four photoelastic modulators operate simultaneously at various frequencies to enable comprehensive polarization analysis.

#### **4.4.3.2 Sample Loading**

For the SRCD and MMP experiments, 20  $\mu$ L of pre-gel solutions were precisely pipetted into a custom 14.6- $\mu$ m-pathlength CaF<sub>2</sub> demountable disc cuvette cell (Model 124.036, Hellma, Müllheim, Germany) and carefully placed within the cell holder. It is crucial to prevent air bubbles during loading to maintain the validity of the results. Consistent sample loading and uniform application of procedures across all samples are essential to ensure data reliability and reproducibility, and that variations in data are due to sample differences rather than experimental inconsistencies.

The cell holder with cuvette was then centrally placed in the B23 MMP sample stage and scanned using both CD and MMP modes at 25 °C, without needing to remove the sample, ensuring consistent positioning throughout the experiment. SRCD spectra were initially recorded, followed by MMP data collection for each sample using the same parameters for both modes. MMP results were then averaged from four separate runs to maintain consistency in the experimental data.

#### **4.4.3.3 SRCD and Absorption Measurements**

For robust MMP analysis, an SRCD signal of at least 50 millidegrees (mdeg) was necessary to achieve a satisfactory signal-to-noise ratio for comprehensive deconvolution. The absorbance intensity was required to be no more than 1.6 to ensure sufficient light reached the detector. Measurements across the full spectrum for both SRCD and absorption involved the following settings: the scanning range covered 180 to 350 nm, with 2 nm intervals; the integration time was set at 0.03 seconds with 16 cycles of integration; single scan repeats were conducted; the pathlength of cuvette cell was 14.6  $\mu$ m; the operating current was 200 mA; and the temperature was controlled at 25°C.

#### 4.4.3.4 MMP Measurement

In the full deconvolution MMP analyses, the setup included a 4×4 matrix for point measurements in MMP mode under conditions identical to those in the SRCD and absorption spectroscopy measurements.

#### 4.4.3.5 Data Processing

MMP output data processing utilized the Matrix logarithm method of the differential Mueller matrix measurements.<sup>26</sup> The CD elements of the differential Mueller matrix were analyzed according to the established methodology.<sup>8, 55</sup> Both SRCD and MMP datasets underwent analysis using an MMP converter and OriginPro® 2021b, employing scripts developed by Gianga, T. M. to analyze individual matrix data.

### 4.5 References

- (1) Miles, A. J.; Wallace, B. A. Synchrotron radiation circular dichroism spectroscopy of proteins and applications in structural and functional genomics. *Chemical Society Reviews* **2006**, 35 (1), 39-51.
- (2) Wallace, B. A.; Janes, R. W. Synchrotron radiation circular dichroism spectroscopy of proteins: secondary structure, fold recognition and structural genomics. *Current Opinion in Chemical Biology* **2001**, 5 (5), 567-571.
- (3) Wallace, B. A. Protein characterisation by synchrotron radiation circular dichroism spectroscopy. *Quarterly Reviews of Biophysics* **2009**, 42 (4), 317-370.
- (4) Chue-Sang, J.; Gonzalez, M.; Pierre, A.; Laughrey, M.; Saytashev, I.; Novikova, T.; Ramella-Roman, J. C. Optical phantoms for biomedical polarimetry: a review. *Journal of biomedical optics* **2019**, 24 (3), 030901-030901.
- (5) Le Roy-Brehonnet, F.; Le Jeune, B. Utilization of Mueller matrix formalism to obtain optical targets depolarization and polarization properties. *Progress in Quantum Electronics* **1997**, 21 (2), 109-151.
- (6) Szustakiewicz, P.; Kowalska, N.; Grzelak, D.; Narushima, T.; Góra, M.; Bagiński, M.; Pocięcha, D.; Okamoto, H.; Liz-Marzán, L. M.; Lewandowski, W. Supramolecular chirality synchronization in thin films of plasmonic nanocomposites. *ACS nano* **2020**, 14 (10), 12918-12928.
- (7) Narushima, T.; Okamoto, H. Circular dichroism microscopy free from commingling linear dichroism via discretely modulated circular polarization. *Scientific Reports* **2016**, 6 (1), 35731.
- (8) Arteaga, O.; Freudenthal, J.; Wang, B.; Kahr, B. Mueller matrix polarimetry with four photoelastic modulators: theory and calibration. *Applied Optics* **2012**, 51 (28), 6805-6817.
- (9) Clowes, S. R.; Rășădean, D. M.; Gianga, T.-M.; Jávorfı, T.; Hussain, R.; Siligardi, G.; Pantoş, G. D. Mueller Matrix Polarimetry on cyanine dye J-aggregates. *Molecules* **2023**, 28 (4), 1523.
- (10) Hussain, R.; Javorfi, T.; Siligardi, G. CD imaging at high spatial resolution at diamond B23 beamline: Evolution and applications. *Frontiers in Chemistry* **2021**, 9, 616928.
- (11) Albano, G.; Pescitelli, G.; Di Bari, L. Chiroptical properties in thin Films of  $\pi$ -conjugated systems. *Chemical Reviews* **2020**, 120 (18), 10145-10243.

- (12) Shyla, N.; Nizar, S. Characterization of chiral supramolecular assemblies using Mueller polarimetry. Université de Strasbourg, 2023.
- (13) Albano, G.; Taddeucci, A.; Pescitelli, G.; Di Bari, L. Spatially resolved chiroptical spectroscopies emphasizing recent applications to thin films of chiral organic dyes. *Chemistry – A European Journal* **2023**, *29* (62), e202301982.
- (14) Ribo, J. M.; El-Hachemi, Z.; Arteaga, O.; Canillas, A.; Crusats, J. Hydrodynamic effects in soft-matter self-assembly: the case of J-aggregates of amphiphilic porphyrins. *The Chemical Record* **2017**, *17* (7), 713-724.
- (15) Zinna, F.; Resta, C.; Górecki, M.; Pescitelli, G.; Di Bari, L.; Jávorfí, T.; Hussain, R.; Siligardi, G. Circular dichroism imaging: mapping the local supramolecular order in thin films of chiral functional polymers. *Macromolecules* **2017**, *50* (5), 2054-2060.
- (16) Borisenko, K. B.; Shanmugam, J.; Williams, B. A. O.; Ewart, P.; Gholipour, B.; Hewak, D. W.; Hussain, R.; Jávorfí, T.; Siligardi, G.; Kirkland, A. I. Photo-induced optical activity in phase-change memory materials. *Scientific Reports* **2015**, *5* (1), 8770.
- (17) Dressel, C.; Liu, F.; Prehm, M.; Zeng, X.; Ungar, G.; Tschierske, C. Dynamic mirror - symmetry breaking in bicontinuous cubic phases. *Angewandte Chemie International Edition* **2014**, *53* (48), 13115-13120.
- (18) Cseh, L.; Mang, X.; Zeng, X.; Liu, F.; Mehl, G. H.; Ungar, G.; Siligardi, G. Helically twisted chiral arrays of gold nanoparticles coated with a cholesterol mesogen. *Journal of the American Chemical Society* **2015**, *137* (40), 12736-12739.
- (19) Thomson, L.; McDowall, D.; Marshall, L.; Marshall, O.; Ng, H.; Homer, W. J. A.; Ghosh, D.; Liu, W.; Squires, A. M.; Theodosiou, E.; et al. Transferring micellar changes to bulk properties via tunable self-assembly and hierarchical ordering. *ACS Nano* **2022**, *16* (12), 20497-20509.
- (20) Draper, E. R.; Dietrich, B.; McAulay, K.; Brasnett, C.; Abdizadeh, H.; Patmanidis, I.; Marrink, S. J.; Su, H.; Cui, H.; Schweins, R.; et al. Using small-angle scattering and contrast matching to understand molecular packing in low molecular weight gels. *Matter* **2020**, *2* (3), 764-778.
- (21) McAulay, K.; Dietrich, B.; Su, H.; Scott, M. T.; Rogers, S.; Al-Hilaly, Y. K.; Cui, H.; Serpell, L. C.; Seddon, A. M.; Draper, E. R.; Adams, D. J. Using chirality to influence supramolecular gelation. *Chemical Science* **2019**, *10* (33), 7801-7806.
- (22) Hussain, R.; Jávorfí, T.; Hughes, C. S.; Sriram, H.; Lashminarayanan, R.; Siligardi, G. Diamond B23 CD imaging of thin films of chiral materials or achiral polymers coated with chiral molecules. *Symmetry* **2020**, *12* (11), 1847.
- (23) Azzam, R. M. A. Propagation of partially polarized light through anisotropic media with or without depolarization: A differential  $4 \times 4$  matrix calculus. *Journal of the Optical Society of America* **1978**, *68* (12), 1756-1767.
- (24) Schönhofer, A.; Kuball, H.-G. Symmetry properties of the Mueller matrix. *Chemical Physics* **1987**, *115* (2), 159-167.
- (25) Arteaga, O. Number of independent parameters in the Mueller matrix representation of homogeneous depolarizing media. *Opt. Lett.* **2013**, *38* (7), 1131-1133.
- (26) Schellman, J.; Jensen, H. P. Optical spectroscopy of oriented molecules. *Chemical Reviews* **1987**, *87* (6), 1359-1399.
- (27) Marchesan, S.; Easton, C. D.; Kushkaki, F.; Waddington, L.; Hartley, P. G. Tripeptide self-assembled hydrogels: unexpected twists of chirality. *Chemical Communications* **2012**, *48* (16), 2195-2197.
- (28) Marshall, L. J.; Bianco, S.; Ginesi, R. E.; Douth, J.; Draper, E. R.; Adams, D. J. Investigating multigelator systems across multiple length scales. *Soft Matter* **2023**, *19* (26), 4972-4981.

- (29) Liu, M.; Zhang, L.; Wang, T. Supramolecular chirality in self-assembled systems. *Chemical Reviews* **2015**, *115* (15), 7304-7397.
- (30) Le, K. V.; Takezoe, H.; Araoka, F. Chiral superstructure mesophases of achiral bent-shaped molecules – hierarchical chirality amplification and physical properties. *Advanced Materials* **2017**, *29* (25), 1602737.
- (31) Wang, M.; Zhou, P.; Wang, J.; Zhao, Y.; Ma, H.; Lu, J. R.; Xu, H. Left or right: how does amino acid chirality affect the handedness of nanostructures self-assembled from short amphiphilic peptides? *Journal of the American Chemical Society* **2017**, *139* (11), 4185-4194.
- (32) Kralj, S.; Bellotto, O.; Parisi, E.; Garcia, A. M.; Iglesias, D.; Semeraro, S.; Deganutti, C.; D'Andrea, P.; Vargiu, A. V.; Geremia, S.; et al. Heterochirality and halogenation control Phe-Phe hierarchical assembly. *ACS Nano* **2020**, *14* (12), 16951-16961.
- (33) Xie, Y.-Y.; Qin, X.-T.; Zhang, J.; Sun, M.-Y.; Wang, F.-P.; Huang, M.; Jia, S.-R.; Qi, W.; Wang, Y.; Zhong, C. Self-assembly of peptide nanofibers with chirality-encoded antimicrobial activity. *Journal of Colloid and Interface Science* **2022**, *622*, 135-146.
- (34) Bellotto, O.; Kralj, S.; Melchionna, M.; Pengo, P.; Kisovec, M.; Podobnik, M.; De Zorzi, R.; Marchesan, S. Self-assembly of unprotected dipeptides into hydrogels: water-channels make the difference. *Chembiochem* **2022**, *23* (2), e202100518.
- (35) Sonani, R. R.; Bianco, S.; Dietrich, B.; Douth, J.; Draper, E. R.; Adams, D. J.; Egelman, E. H. Atomic structures of naphthalene dipeptide micelles unravel mechanisms of assembly and gelation. *Cell Reports Physical Science* **2024**, *5* (2), 101812.
- (36) Cardoso, A. Z.; Mears, L. L. E.; Cattoz, B. N.; Griffiths, P. C.; Schweins, R.; Adams, D. J. Linking micellar structures to hydrogelation for salt-triggered dipeptide gelators. *Soft Matter* **2016**, *12* (15), 3612-3621.
- (37) Smith, D. K. Supramolecular gels – a panorama of low-molecular-weight gelators from ancient origins to next-generation technologies. *Soft Matter* **2024**, *20* (1), 10-70.
- (38) Guan, Q.; McAulay, K.; Xu, T.; Rogers, S. E.; Edwards-Gayle, C.; Schweins, R.; Cui, H.; Seddon, A. M.; Adams, D. J. Self-sorting in diastereomeric mixtures of functionalized dipeptides. *Biomacromolecules* **2023**, *24* (6), 2847-2855.
- (39) Mori, T. Chiroptical properties of symmetric double, triple, and multiple helices. *Chemical Reviews* **2021**, *121* (4), 2373-2412.
- (40) Sznatke, G. Circular dichroism and optical rotatory dispersion — principles and application to the investigation of the stereochemistry of natural products. *Angewandte Chemie International Edition in English* **1968**, *7* (1), 14-25.
- (41) Li, C.; Jin, X.; Han, J.; Zhao, T.; Duan, P. Toward large dissymmetry factor of circularly polarized luminescence in donor-acceptor hybrid systems. *The Journal of Physical Chemistry Letters* **2021**, *12* (35), 8566-8574.
- (42) Albano, G.; Górecki, M.; Pescitelli, G.; Di Bari, L.; Jávorfí, T.; Hussain, R.; Siligardi, G. Electronic circular dichroism imaging (CDi) maps local aggregation modes in thin films of chiral oligothiophenes. *New Journal of Chemistry* **2019**, *43* (36), 14584-14593.
- (43) Riva, S. Laccases: blue enzymes for green chemistry. *Trends in Biotechnology* **2006**, *24* (5), 219-226.
- (44) Kelly, S. M.; Jess, T. J.; Price, N. C. How to study proteins by circular dichroism. *Biochimica et Biophysica Acta (BBA) - Proteins and Proteomics* **2005**, *1751* (2), 119-139.
- (45) Andersson, D.; Carlsson, U.; Freskgård, P. O. Contribution of tryptophan residues to the CD spectrum of the extracellular domain of human tissue factor: application in folding studies and prediction of secondary structure. *European Journal of Biochemistry* **2001**, *268* (4), 1118-1128.

- (46) Sarkar, D.; Khan, A. H.; Polepalli, S.; Sarkar, R.; Das, P. K.; Dutta, S.; Sahoo, N.; Bhunia, A. Multiscale materials engineering via self - assembly of pentapeptide derivatives from SARS CoV E protein. *Small* **2024**, 2404373.
- (47) Kravets, V. G.; Kabashin, A. V.; Barnes, W. L.; Grigorenko, A. N. Plasmonic surface lattice resonances: A review of properties and applications. *Chemical Reviews* **2018**, 118 (12), 5912-5951.
- (48) Huynh, C. P.; Robles-Kelly, A.; Hancock, E. R. Shape and refractive index from single-view spectro-polarimetric images. *International Journal of Computer Vision* **2013**, 101 (1), 64-94.
- (49) Kahr, B.; Freudenthal, J.; Gunn, E. Crystals in Light. *Accounts of Chemical Research* **2010**, 43 (5), 684-692.
- (50) Soleillet, P. Sur les paramètres caractérisant la polarisation partielle de la lumière dans les phénomènes de fluorescence. *Annales de physique* **1929**, 10 (12), 23-97.
- (51) Mueller, H. The foundation of optics. *Journal of the Optical Society of America* **1948**, 661 (38), 10-35.
- (52) Iqbal, M.; Khan, S.; Gul, B.; Ahmad, M.; Ahmad, I. Comparison of Mueller matrix differential decomposition and transformation. *Biomedical Signal Processing and Control* **2021**, 69, 102815.
- (53) Schulz, M.; Zablocki, J.; Abdullaeva, O. S.; Brück, S.; Balzer, F.; Lützen, A.; Arteaga, O.; Schiek, M. Giant intrinsic circular dichroism of prolinol-derived squaraine thin films. *Nature Communications* **2018**, 9 (1), 2413.
- (54) Arteaga, O.; Kahr, B. Mueller matrix polarimetry of bianisotropic materials. *J. Opt. Soc. Am. B* **2019**, 36 (8), F72-F83.
- (55) Arwin, H.; Mendoza-Galván, A.; Magnusson, R.; Andersson, A.; Landin, J.; Järrendahl, K.; Garcia-Caurel, E.; Ossikovski, R. Structural circular birefringence and dichroism quantified by differential decomposition of spectroscopic transmission Mueller matrices from *Cetonia aurata*. *Opt. Lett.* **2016**, 41 (14), 3293-3296.

## Chapter 5: Conclusions and Outlooks

---

### 5.1 Conclusions

In this thesis, we conducted a comprehensive study of the assembly behaviors and gel properties of a library of naphthyl diphenylalanine derivatives and their diastereoisomeric mixtures. A key observation was that the chirality of the terminal amino acids primarily distinguishes these gel precursors. Regardless of the mixing method, these isomers consistently self-sort in both solution and gel phases. By adjusting the ratios of these components, we gained precise control over the rheological characteristics and microstructure.

We applied a variety of spectroscopic methods, including small-angle scattering, cryogenic transmission electron microscopy, and rheological assessments, along with UV-Vis, fluorescence, and circular dichroism spectroscopy. Our results demonstrated that changes in the component ratios significantly affect the material's physical and optical properties. This highlights how minor alterations in molecular composition can significantly influence material self-assembly and characteristics.

Additionally, we engineered multi-component systems that allow for the modification of self-assembled nanostructures or gelation properties by selectively replacing hydrogen atoms on the naphthalene rings. Systematic evaluation of these components' concentration ratios revealed diverse self-assembled nanostructures and ordering behaviors, enriching our understanding of self-sorting phenomena and paving the way for innovative supramolecular multicomponent system designs.

We also discovered that the specific method used to combine these components affects the final structure of the gels. For example, gels formed from solution mixing exhibited different properties than those from powder mixing. Advanced optical characterization techniques, such as synchrotron-based circular dichroism and Mueller matrix polarimetry, enabled us to detect significant differences in molecular orientation and electronic interactions among systems with the same or differing chirality. These observations provide deeper insights into how chiral order and molecular interactions shape the self-assembly process and material properties.

In summary, this research not only emphasizes the critical role of chirality and molecular symmetry in the self-assembly and gelation processes but also demonstrates the potential for molecular designs to create hydrogels with tailored functionalities. These findings furnish

essential design principles and scientific insights for developing more adaptable and functionally supramolecular systems.

## 5.2 Outlooks

Describing the complexity of multicomponent supramolecular gel systems presents significant challenges. In these systems, components can self-assemble in the presence of other molecules, where differences in assembly can be influenced not only by the self-assembled network itself but also by additives. For example, a new network might expand upon an existing one through epitaxial growth or intensive entanglement, or the networks might develop completely independently. Additionally, it is crucial to consider the spatial distribution of these networks at the microscopic scale, specifically whether fibers are uniformly distributed or localized. Present characterization techniques struggle to fully resolve these complex structures and interactions. To conduct in-depth studies of supramolecular gels, a careful selection and integration of multiple experimental techniques is necessary to address various gelation mechanisms and influencing factors. Furthermore, developing new and more efficient characterization methods is essential to enhance their practical applications.

Although systematic design is generally advocated, most discoveries of self-assembling gels have historically depended on modifying existing gelators or have been made by chance. Even minor structural changes can result in significant behavioral differences, implying the complexity of these materials and the challenges in controlling them. The current research capable of accurately predicting gel properties is limited, presenting significant opportunities for future studies. With advancements in understanding peptide design and functionalities, leveraging artificial intelligence to predict gel capabilities and properties represents a crucial technological breakthrough.

## Appendices

### A2 Appendix for Chapter 2

#### A2.1 Materials

*N*-(tert-Butoxycarbonyl)-L-phenylalanine, L-phenylalanine methyl ester hydrochloride, D-phenylalanine methyl ester hydrochloride, 2-(naphthalen-2-yloxy)acetic acid, deuterium oxide, sodium deuterioxide 40% in D<sub>2</sub>O, deuterium chloride 35% in D<sub>2</sub>O were obtained from Sigma-Aldrich; glucono- $\delta$ -lactone, 1,4-dioxane, lithium hydroxide were purchased from Alfa Aesar; diethyl ether, *N*-methylnmorpholine, sodium hydroxide, hydrochloric acid were received from Honeywell; acetonitrile, chloroform, tetrahydrofuran, sodium chloride were acquired from Fisher Scientific; hydrogen chloride (ca. 4 mol/L in 1,4-dioxane) was obtained from Tokyo Chemical Industry; magnesium sulfate, dichloromethane, trifluoroacetic acid, isobutyl chloroformate were purchased from VWR International, Fluorochem, and Thermo Scientific, respectively. All chemicals were used directly without further treatment. Deionized water was used throughout this research. Table A2-1 details the specific hazards associated with each reagent to guide safe handling practices in the laboratory

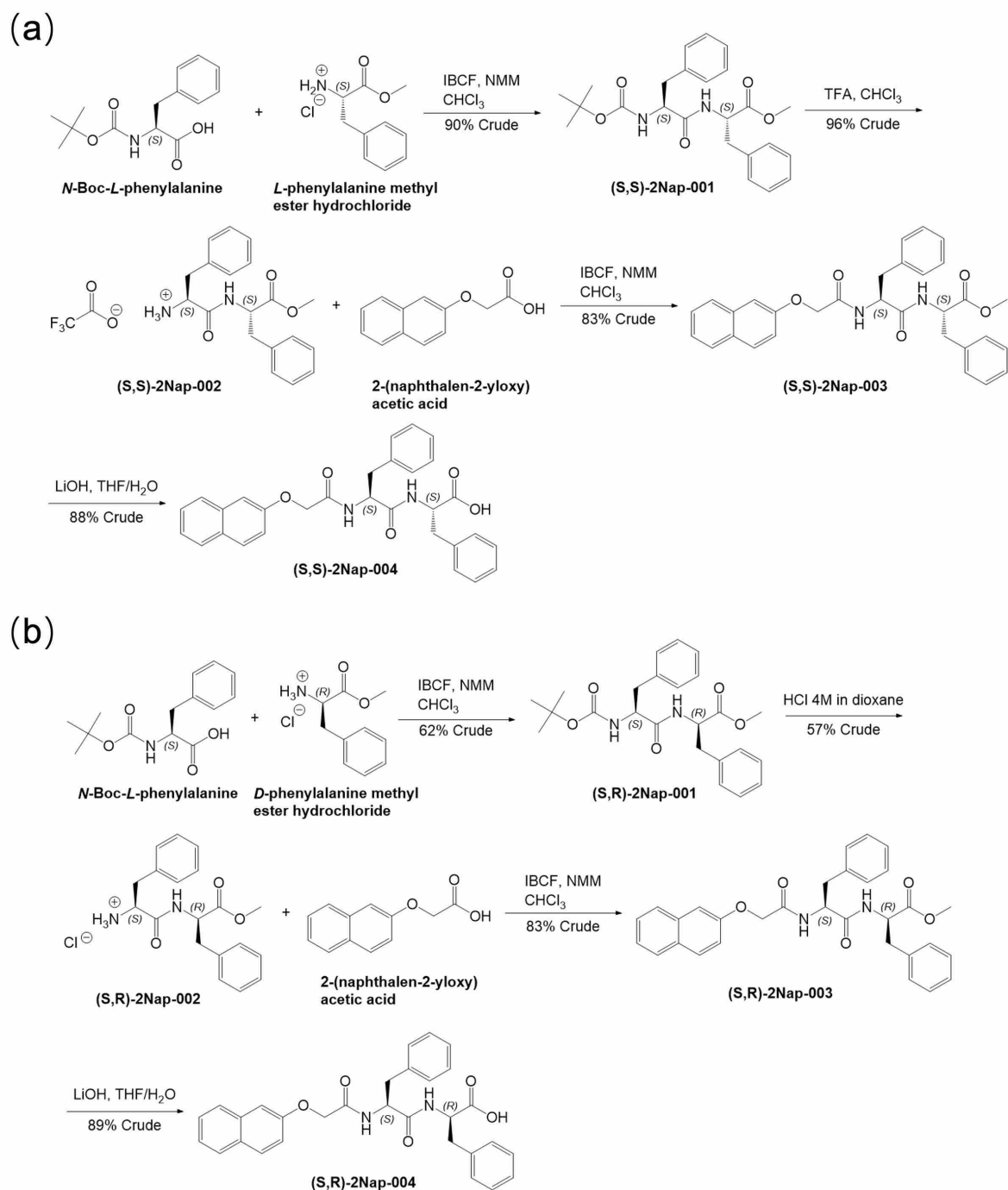
**Table A2-1.** Overview of primary health and safety risks associated with reagents used in synthesis protocols.

Full Name	Acronym	Primary Risks
<i>N</i> -(tert-Butoxycarbonyl)-L-phenylalanine	Boc-L-Phe	Irritant; can cause skin and eye irritation
L-phenylalanine methyl ester hydrochloride		Irritant; harmful if swallowed or in contact with skin
D-phenylalanine methyl ester hydrochloride		Irritant; harmful if swallowed or in contact with skin
2-(naphthalen-2-yloxy)acetic acid		Corrosive; causes skin corrosion and serious eye damage
Deuterium oxide	D <sub>2</sub> O	Primarily non-toxic but can moderate chemical reactions differently due to isotopic effects
Sodium deuterioxide 40% in D <sub>2</sub> O		Highly corrosive; can cause severe burns and eye damage
Deuterium chloride 35% in D <sub>2</sub> O		Corrosive; can cause respiratory irritation and damage to respiratory tract
Glucono- $\delta$ -lactone	GdL	Generally recognized as safe but can be mildly irritating to skin and eyes
1,4-dioxane		Carcinogenic; suspected of causing genetic defects and damaging fertility or the unborn child
Lithium hydroxide	LiOH	Corrosive; causes severe skin burns and eye damage; reacts violently with water

## Appendices

Diethyl ether		Highly flammable; may form explosive peroxides
N-Methylmorpholine	NMM	Corrosive; harmful if swallowed, inhaled, or in contact with skin
Sodium hydroxide	NaOH	Corrosive; causes severe skin burns and eye damage
Hydrochloric acid	HCl	Corrosive; causes severe skin burns and eye damage
Acetonitrile		Toxic if inhaled or absorbed through skin; suspected of causing genetic defects
Chloroform	CHCl <sub>3</sub>	Carcinogenic; central nervous system depressant; potential liver and kidney damage
Tetrahydrofuran	THF	Highly flammable; forms explosive peroxides; inhalation hazard
Sodium chloride	NaCl	Generally safe but can irritate eyes and respiratory tract in high concentrations
Hydrogen chloride 4M in 1,4-dioxane		Corrosive; causes severe respiratory and mucous membrane irritation
Magnesium sulfate	MgSO <sub>4</sub>	Generally safe; used as a laxative and to treat magnesium deficiency
Dichloromethane	DCM	Potential carcinogen; may cause organ damage through prolonged or repeated exposure
Trifluoroacetic acid	TFA	Corrosive; can cause severe burns and is a respiratory irritant, inhalation hazard
Isobutyl chloroformate	IBCF	Highly reactive and toxic; can cause severe skin burns and eye damage; respiratory irritant

## A2.2 Synthesis of Dipeptides



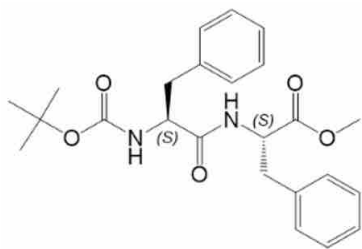
Scheme A2-1. Synthetic route of (a) (L,L)-2NapFF and (b) (L,D)-2NapFF.

Chemical structures were named using MarvinSketch (Version 23.11, <https://chemaxon.com/>) from ChemAxon. Mass spectra were recorded on a Bruker micrOTOFQ at the University of Glasgow.  $^1\text{H}$  NMR spectra were recorded on a Bruker Avance III 400 MHz instrument at the

University of Glasgow. Spectra were referenced to the residual  $^1\text{H}$  signal from the  $\text{DMSO-}d_6$  at 2.50 ppm for integration. The temperature of the samples was maintained at  $298 \pm 0.5$  K.

### A2.2.1 (L,L)-2NapFF

#### Methyl (2S)-2-[(2S)-2-[(tert-butoxy)carbonyl]amino]-3-phenylpropanamido]-3-phenylpropanoate ((S,S)-2Nap-001)



To a solution of *N*-Boc-*L*-phenylalanine (2.65 g, 10 mmol) in chloroform (30 mL) was added *N*-methylmorpholine (2 eq., 2.20 mL) and isobutylchloroformate (1.1 eq., 1.43 mL), and the mixture was stirred on ice for 10 min. Meanwhile, to a suspension of *L*-phenylalanine methyl ester hydrochloride (2.92 g, 10 mmol) in chloroform (30 mL) was added *N*-methylmorpholine (2 eq., 2.20 mL), and the mixture was stirred at room temperature for 10 minutes. Subsequently, the latter mixture was added to the former and kept stirring overnight on ice. The resulting clear solution was diluted with chloroform and washed in turn with 100 mL of 1M hydrochloric acid, water, and brine (saturated), before being dried (magnesium sulfate), and the solvent was removed under vacuum. (S,S)-2Nap-001 (3.85 g, 90%) was obtained as a white powder (Scheme 2-1a)

$\delta_{\text{H}}$  (400 MHz,  $\text{DMSO-}d_6$ , 25 °C) 8.38 (0.2H, d,  $J$  6.68, Rot-1  $\text{NHCH}^*\text{CO}_2\text{Me}$ ), 8.31 (0.8H, d,  $J$  7.59, Rot-2  $\text{NHCH}^*\text{CO}_2\text{Me}$ ), 7.30-7.16 (10.2H, m,  $\text{H}_{\text{Ar}}$ ), 6.83 (0.8H, d,  $J$  8.76, Rot-2  $\text{NH}^*\text{Boc}$ ), 6.39 (0.2H, d,  $J$  7.89, Rot-1  $\text{NH}^*\text{Boc}$ ), 4.51 (1H, dd,  $J$  13.88, 7.92,  $\text{CH}^*\text{NHBoc}$ ), 4.20 (0.8H, td,  $J$  10.06, 4.23, Rot-2  $\text{CH}^*\text{CO}_2\text{Me}$ ), 4.08-4.02 (0.2H, Rot-1  $\text{CH}^*\text{CO}_2\text{Me}$ ), 3.58 (3H, s,  $\text{OCH}_3$ ), 3.32 (2.9H, br s,  $\text{H}_2\text{O}$ ), 3.08-2.94 (2.1H, m,  $\text{PhC}_a\text{H}_2$ ), 2.89 (1H, dd,  $J$  13.76, 4.12,  $\text{PhC}_b\text{H}_a\text{H}_b$ ), 2.67 (1H, dd,  $J$  13.71, 10.49,  $\text{PhC}_b\text{H}_a\text{H}_b$ ), 2.50 (1.4H, quintet, residual  $\text{DMSO-}d_5$ ), 1.28 (7.6H, s, Rot-2  $\text{C}(\text{CH}_3)_3$ ), 1.15 (1.5H, s, Rot-1  $\text{C}(\text{CH}_3)_3$ ).  $\delta_{\text{C}}$  (100 MHz,  $\text{DMSO-}d_6$ , 25 °C) 171.87, 171.83, and 155.12 ( $\text{C}=\text{O}$ ), 138.03, 137.02, 129.18, 129.14, 128.28, 128.00, 126.60 and 126.18 ( $\text{C}_{\text{Ar}}$ ), 78.05 ( $\text{C}(\text{CH}_3)_3$ ), 55.53 ( $\text{CH}^*\text{NHBoc}$ ), 53.53 ( $\text{CH}^*\text{CO}_2\text{Me}$ ), 51.86 ( $\text{CO}_2\text{CH}_3$ ), 39.52 (septet,  $\text{DMSO-}d_6$ ), 37.45 ( $\text{PhC}_b\text{H}_2$ ), 36.74 ( $\text{PhC}_a\text{H}_2$ ), 28.13 (Rot-2  $\text{C}(\text{CH}_3)_3$ ), 27.76 (Rot-1  $\text{C}(\text{CH}_3)_3$ ).

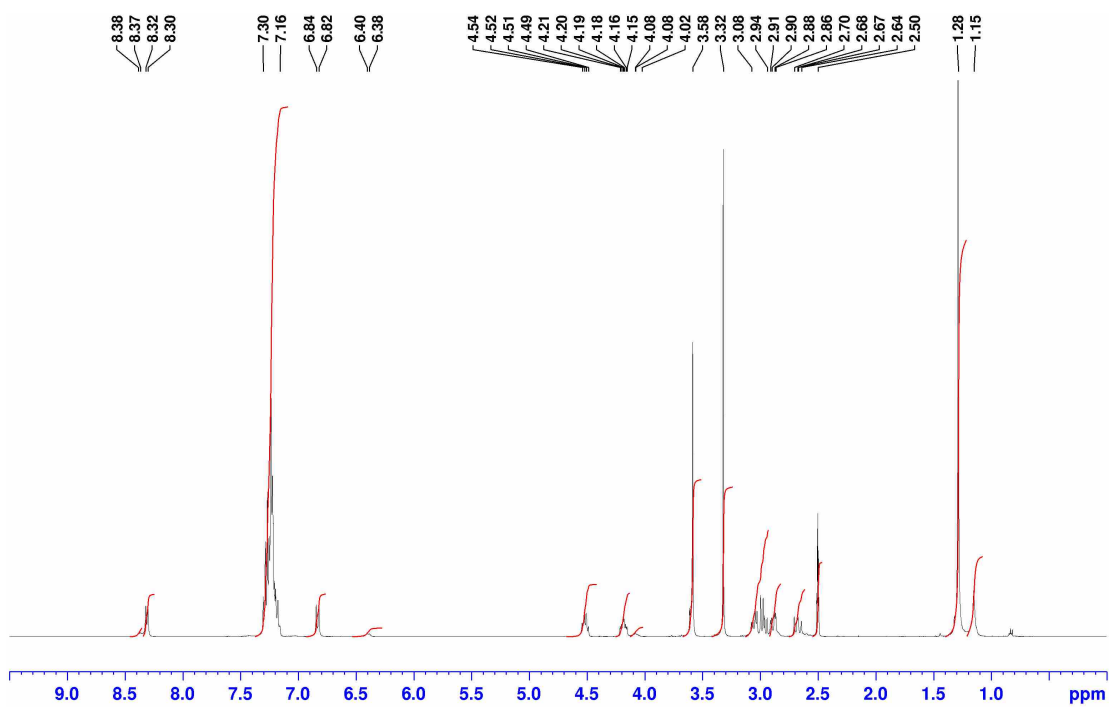


Figure A2-1.  $^1\text{H}$  NMR spectrum of (S,S)-2Nap-001 in  $\text{d}_6$ -DMSO at 25 °C.

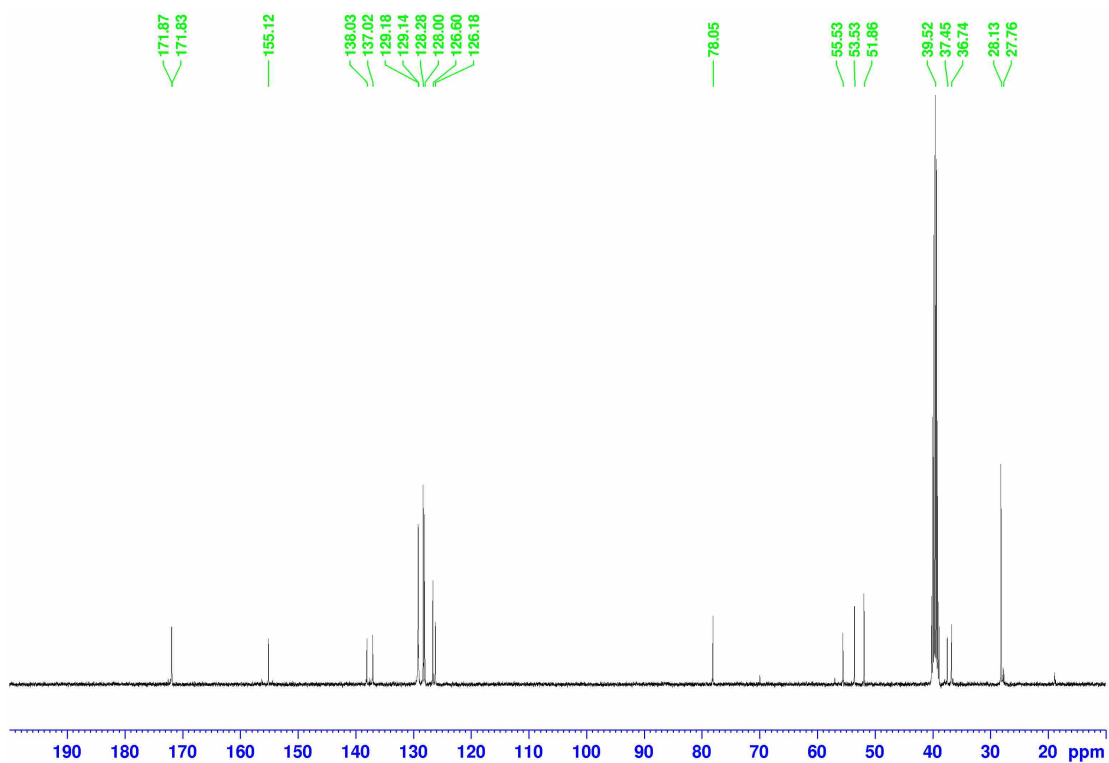
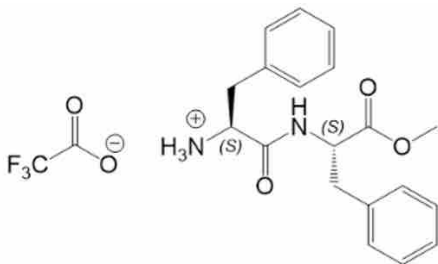


Figure A2-2.  $^{13}\text{C}$  NMR spectrum of (S,S)-2Nap-001 in  $\text{d}_6$ -DMSO at 25 °C.

**Methyl (2S)-2-[(2S)-2-amino-3-phenylpropanamido]-3-phenylpropanoate trifluoroacetate salt ((S,S)-2Nap-002)**



To a solution of (S,S)-2Nap-001 (3.85 g, 9.02 mmol) in chloroform (10 mL) was added trifluoroacetic acid (5 mL), and the mixture was stirred at room temperature overnight. The mixture was subsequently concentrated under reduced pressure to remove most of the excess TFA, and the resulting viscous oil was then dissolved in ~30 mL of chloroform, transferred to ~200 mL of diethyl ether and stirred for 2 h to allow complete precipitation. The white solid was collected by filtration. The solid was washed with a small amount of diethyl ether (~10 mL) and dried under vacuum. (S,S)-2Nap-002 (3.81 g, 96%) was collected as a white powder (Scheme 2-1a).

$\delta_{\text{H}}$  (400 MHz, DMSO- $d_6$ , 25 °C) 9.07 (1H, d,  $J$  7.48, NH), 8.23 (2.8H, br s,  $\text{NH}_3^+$ ), 7.34-7.22 (9.8H, m,  $\text{H}_{\text{Ar}}$ ), 4.56 (1H, dd,  $J$  14.15, 7.44,  $\text{CH}^*\text{NH}_3^+$ ), 4.09-4.06 (1H, m,  $\text{CH}^*\text{CO}_2\text{Me}$ ), 3.60 (3H, s,  $\text{OCH}_3$ ), 3.40 (5.7H, br s,  $\text{H}_2\text{O}$ ), 3.14-3.04 (2.0H, m,  $\text{PhC}_a\text{H}_2$ ), 3.00-2.93 (1.9H, m,  $\text{PhC}_b\text{H}_2$ ), 2.50 (0.7H, quintet, residual DMSO- $d_5$ ).  $\delta_{\text{C}}$  (100 MHz, DMSO- $d_6$ , 25 °C) 171.21 and 168.31 ( $\text{CH}-\text{C}=\text{O}$ ), 158.26 (q,  $J$  31.01,  $\text{CF}_3-\text{C}=\text{O}$ ), 136.76, 134.77, 129.61, 129.12, 128.55, 128.45, 127.20, and 126.80 ( $\text{C}_{\text{Ar}}$ ), 117.80 (d,  $J$  300.36,  $\text{CF}_3$ ), 53.92 ( $\text{CH}^*\text{CO}_2\text{Me}$ ), 53.18 ( $\text{OCH}_3$ ), 52.07 ( $\text{CH}^*\text{NH}_3^+$ ), 39.52 (septet, DMSO- $d_6$ ), 36.92 ( $\text{PhC}_a\text{H}_2$ ), 36.70 ( $\text{PhC}_b\text{H}_2$ ).

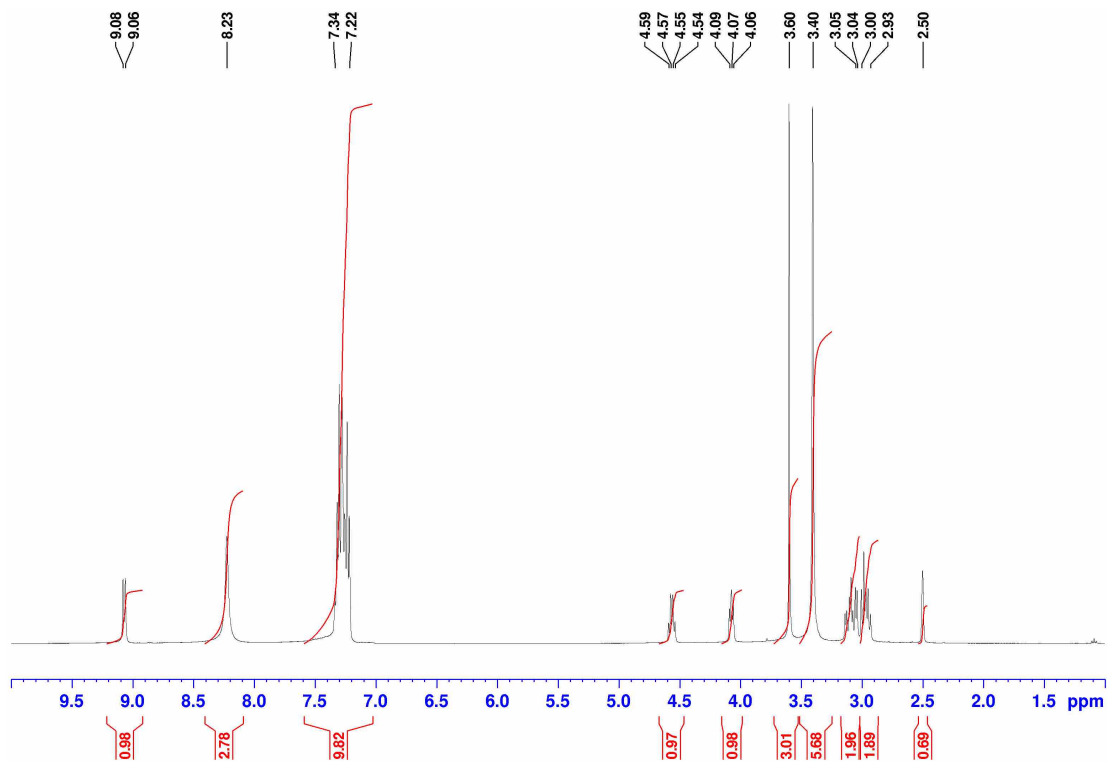


Figure A2-3.  $^1\text{H}$  NMR spectrum of (S,S)-2Nap-002 in  $\text{d}_6$ -DMSO at 25 °C.

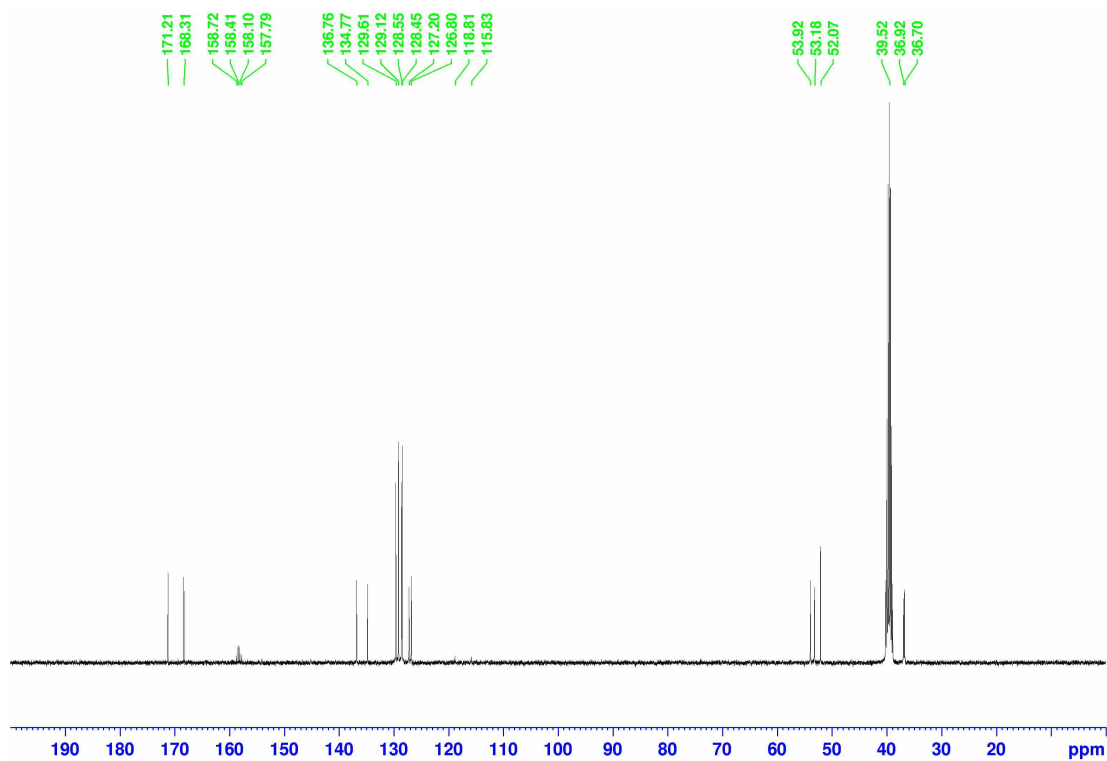
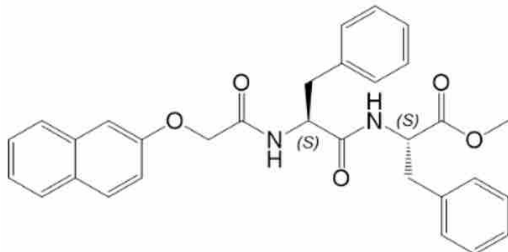


Figure A2-4.  $^{13}\text{C}$  NMR spectrum of (S,S)-2Nap-002 in  $\text{d}_6$ -DMSO at 25 °C.

**Methyl (2S)-2-[(2S)-2-[2-(naphthalen-2-yloxy)acetamidol]-3-phenylpropanamidol]-3-phenylpropanoate ((S,S)-2Nap-003)**



To a solution of (S,S)-2Nap-002 (3.81 g, 8.64 mmol) in chloroform (30 mL) was added *N*-methylmorpholine (2 eq., 1.90 mL) and the mixture was stirred at room temperature for 10 min. Meanwhile, to a solution of 2-(naphthalene-2- acyloxy) acetic acid (1.75 g, 8.64 mmol) in chloroform (30 mL) was added *N*-methylmorpholine (2 eq., 1.90 mL) and isobutylchloroformate (1.1 eq., 1.24 mL) and the mixture was stirred on ice for 10 min. Subsequently, the former mixture was slowly added into the latter and kept stirring overnight on ice. The resulting clear solution was diluted with chloroform and washed in turn with 100 mL of 1M hydrochloric acid, water, and brine (saturated), before being dried (magnesium sulfate), and the solvent removed under vacuum. (S,S)-2Nap-003 (3.65 g, 83%) was obtained as a light brown solid (Scheme 2-1a).

$\delta_{\text{H}}$  (400 MHz, DMSO- $d_6$ , 25 °C) 8.61 (1H, d,  $J$  7.55, NH), 8.31 (0.7H, s, CH in chloroform), 8.14 (1H, d,  $J$  8.56, NH), 7.85-7.82 (2H, m,  $\underline{\text{H}}_{\text{Ar}}$ ), 7.73 (1H, d,  $J$  7.74,  $\underline{\text{H}}_{\text{Ar}}$ ), 7.48-7.44 (1H, m,  $\underline{\text{H}}_{\text{Ar}}$ ), 7.38-7.34 (1.1H, m,  $\underline{\text{H}}_{\text{Ar}}$ ), 7.28-7.12 (12.2H, m,  $\underline{\text{H}}_{\text{Ar}}$ ), 4.67 (1H, td,  $J$  9.16, 4.42,  $\underline{\text{C}}\underline{\text{H}}^*$ ), 4.55 (1.8H, s,  $\underline{\text{O}}\underline{\text{C}}\underline{\text{H}}_2$ ), 4.54-4.50 (1.1H, m,  $\underline{\text{C}}\underline{\text{H}}^*$ ), 3.59 (3.1H, s,  $\underline{\text{O}}\underline{\text{C}}\underline{\text{H}}_3$ ), 3.34 (4.9H, br s,  $\underline{\text{H}}_2\text{O}$ ), 3.08-2.93 (3.2H, m,  $\text{PhC}_a\underline{\text{H}}_2$  and  $\text{PhC}_b\underline{\text{H}}_a\underline{\text{H}}_b$ ), 2.86 (1H, dd,  $J$  13.83, 9.43,  $\text{PhC}_b\underline{\text{H}}_a\underline{\text{H}}_b$ ), 2.50 (1.3H, quintet, residual DMSO- $d_5$ ).  $\delta_{\text{C}}$  (100 MHz, DMSO- $d_6$ , 25 °C) 171.75, 171.01, and 167.30 ( $\underline{\text{C}}=\underline{\text{O}}$ ), 155.52, 137.46, 136.98, 134.06, 129.39, 129.24, 129.09, 128.78, 128.30, 128.04, 127.54, 126.82, 126.62, 126.46, 126.33, 123.90, 118.49, and 107.34 ( $\underline{\text{C}}_{\text{Ar}}$ ), 66.69 ( $\underline{\text{O}}\underline{\text{C}}\underline{\text{H}}_2$ ), 53.69 ( $\underline{\text{C}}\underline{\text{H}}^*$ ), 53.23 ( $\underline{\text{C}}\underline{\text{H}}^*$ ), 51.90 ( $\underline{\text{O}}\underline{\text{C}}\underline{\text{H}}_3$ ), 39.52 (septet, DMSO- $d_6$ ), 37.46 ( $\text{PhC}_b\underline{\text{H}}_2$ ), 36.65 ( $\text{PhC}_a\underline{\text{H}}_2$ ).

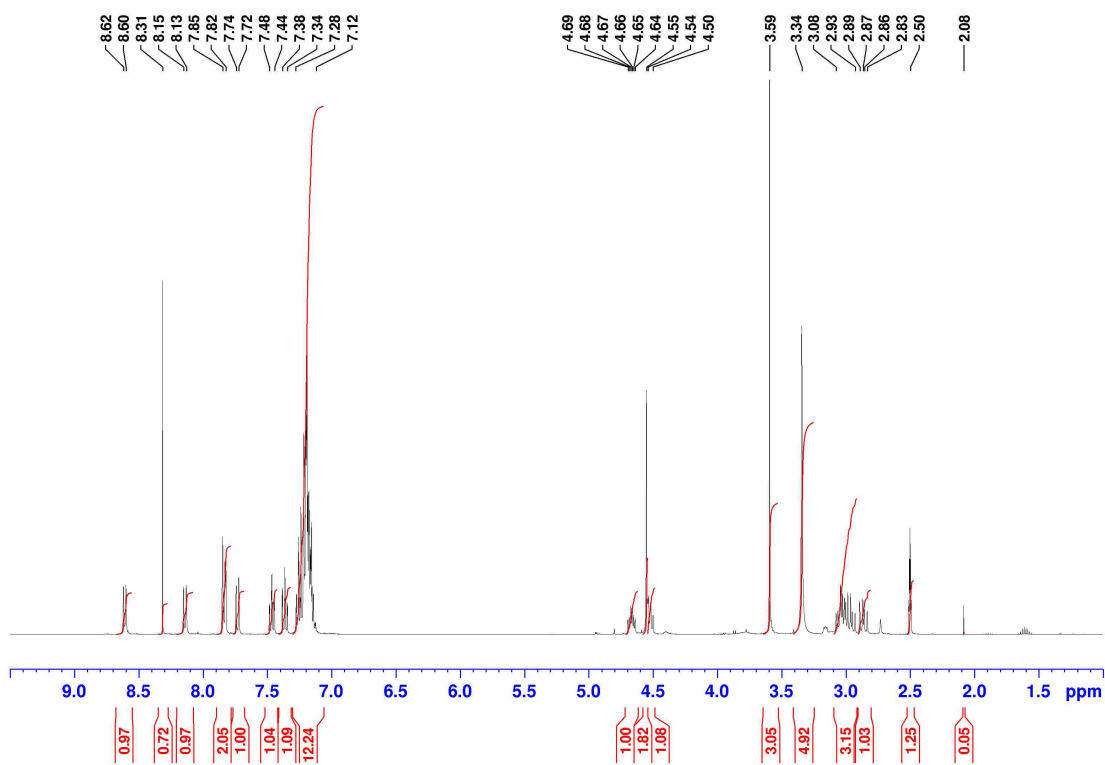


Figure A2-5.  $^1\text{H}$  NMR spectrum of (S,S)-2Nap-003 in  $\text{d}_6$ -DMSO at 25 °C.

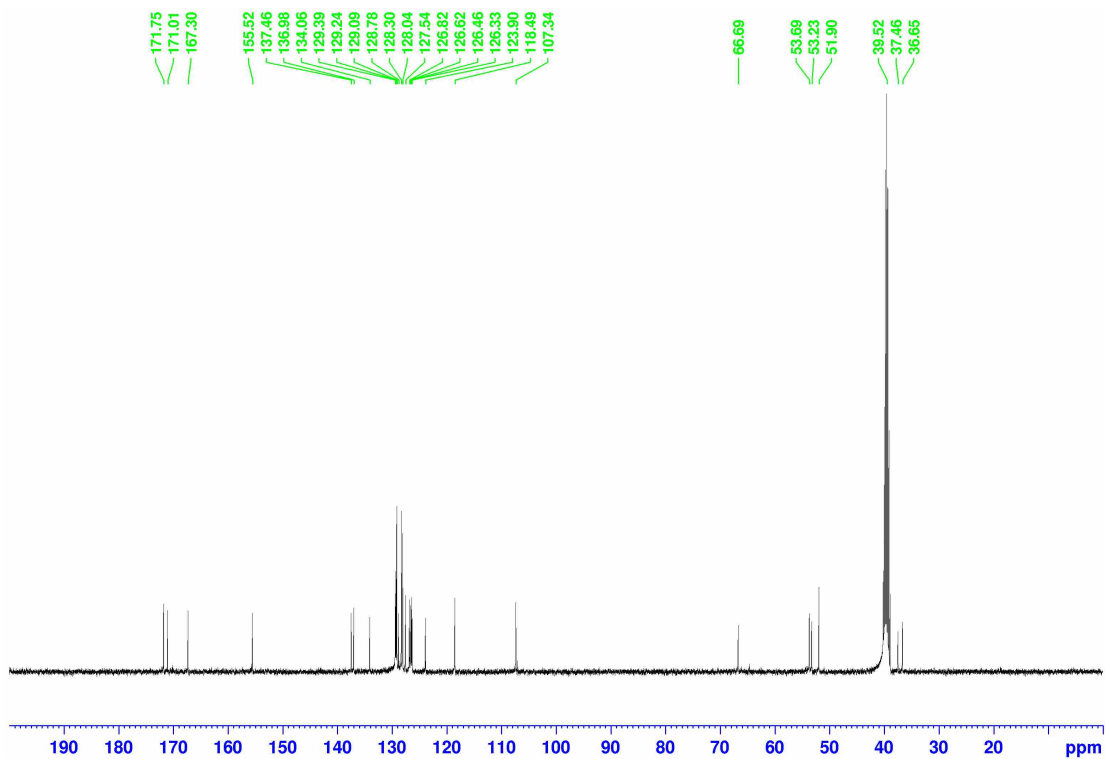
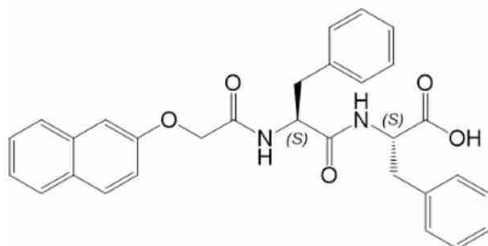


Figure A2-6.  $^{13}\text{C}$  NMR spectrum of (S,S)-2Nap-003 in  $\text{d}_6$ -DMSO at 25 °C.

**(2S)-2-[(2S)-2-[2-(naphthalen-2-yloxy)acetamido]-3-phenylpropanamido]-3-phenylpropanoic acid ((S,S)-2Nap-004)**



A solution of (S,S)-2Nap-003 (3.65 g, 7.15 mmol) in tetrahydrofuran (30 mL) was stirred at room temperature for 10 min. Meanwhile, a solution of lithium hydroxide (685 mg, 28.59 mmol) in water (30 mL) was prepared. The latter was slowly added to the former and the mixture stirred at room temperature for 1.5 h. TLC confirmed the absence of starting materials. The clear solution was poured into 200 mL 1 M hydrochloric acid and stirred overnight. The suspension was collected by filtration, followed by washing with 200 mL of deionized water and a small amount of acetonitrile to remove the brown color. After that, 30 mL of acetonitrile was added, and the mixture stirred for 1 hour before the solvent was removed under vacuum. 30 mL of diethyl ether was then added into the flask and then stirred overnight to help the bulk solids break up into small fragments. Finally, (S,S)-2Nap-004 (3.14 g, 88%) was obtained as a white powder by filtration (Scheme 2-1a).

$\delta_{\text{H}}$  (400 MHz, DMSO- $d_6$ , 25 °C) 12.58 (0.4H, br s, COOH), 8.46 (1.0H, d,  $J$  7.82, NH), 8.14 (1.0H, d,  $J$  8.52, NH), 7.85-7.82 (1.9H, m,  $\text{H}_{\text{Ar}}$ ), 7.73 (1.0H, d,  $J$  8.20,  $\text{H}_{\text{Ar}}$ ), 7.48-7.45 (1.0H, m,  $\text{H}_{\text{Ar}}$ ), 7.38-7.34 (1.1H, m,  $\text{H}_{\text{Ar}}$ ), 7.27-7.12 (11.8H, m,  $\text{H}_{\text{Ar}}$ ), 4.67 (1.0H, td,  $J$  8.94, 3.72,  $\text{CH}^*$ ), 4.55 (1.8H, s,  $\text{OCH}_2$ ), 4.52-4.47 (1.1H, m,  $\text{CH}^*$ ), 3.43 (8.5H, br s,  $\text{H}_2\text{O}$ ), 3.11-3.02 (2.4H, m,  $\text{PhCH}_2$ ), 2.97-2.84 (2.3H, m,  $\text{PhCH}_2$ ), 2.50 (0.9H, quintet, residual DMSO- $d_5$ ).  $\delta_{\text{C}}$  (100 MHz, DMSO- $d_6$ , 25 °C) 172.79, 170.92, and 167.30 ( $\text{C}=\text{O}$ ), 155.54, 137.55, 137.40, 134.08, 129.42, 129.31, 129.18, 128.81, 128.25, 128.04, 127.56, 126.85, 126.51, 126.49, 126.32, 123.92, 118.51, and 107.38 ( $\text{C}_{\text{Ar}}$ ), 66.74 ( $\text{OCH}_2$ ), 53.57 ( $\text{CH}^*$ ), 53.30 ( $\text{CH}^*$ ), 39.52 (septet, DMSO- $d_6$ ), 37.49 ( $\text{PhCH}_2$ ), 36.75 ( $\text{PhCH}_2$ ).

**HRMS (ESI)  $m/z$ :**  $[\text{M}+\text{H}]^+$  accurate mass calculated for  $\text{C}_{30}\text{H}_{28}\text{N}_2\text{HO}_5$ : 497.1998; Found: 497.2076.

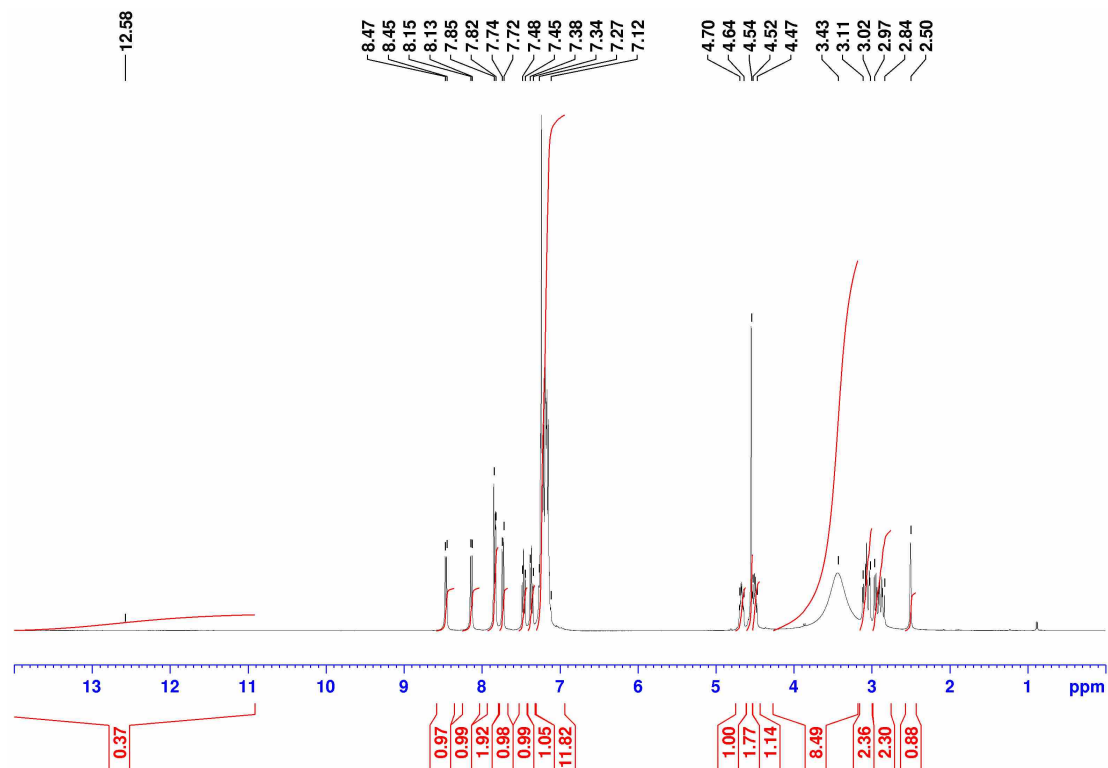


Figure A2-7.  $^1\text{H}$  NMR spectrum of (S,S)-2Nap-004 in  $\text{d}_6$ -DMSO at 25 °C.

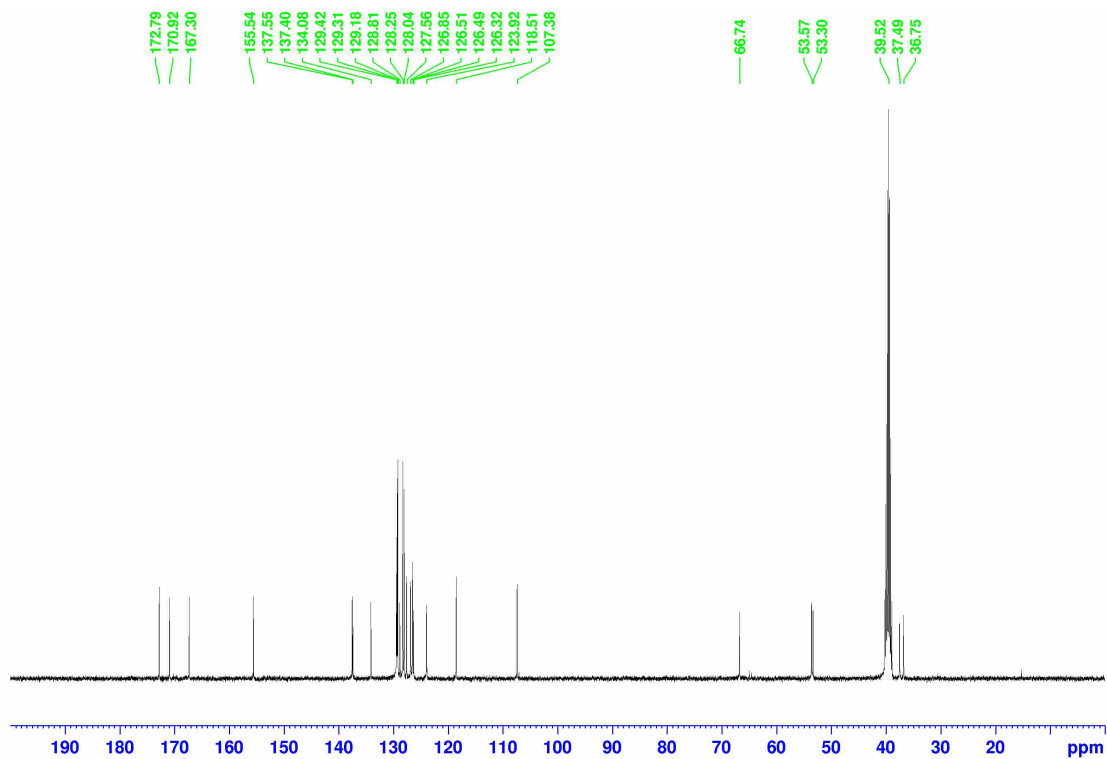
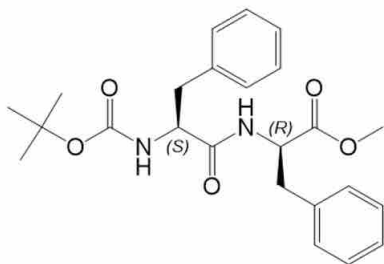


Figure A2-8.  $^{13}\text{C}$  NMR spectrum of (S,S)-2Nap-004 in  $\text{d}_6$ -DMSO at 25 °C.

## A2.2.2 (L,D)-2NapFF

**Methyl (2R)-2-[(2S)-2-[(tert-butoxy)carbonyl]amino-3-phenylpropanamido]-3-phenylpropanoate ((S,R)-2Nap-001)**

To a solution of *N*-Boc-*L*-phenylalanine (2.65 g, 10 mmol) in chloroform (30 mL) was added *N*-methylmorpholine (2 eq., 2.20 mL) and isobutylchloroformate (1.1 eq., 1.43 mL) and the mixture was stirred on ice for 10 min. Meanwhile, to a solution of *D*-phenylalanine methyl ester hydrochloride (2.92 g, 10 mmol) in chloroform (30 mL) was added *N*-methylmorpholine (5 eq., 5.50 mL) and the mixture was stirred at room temperature for 10 min. The latter mixture was added to the former and stirred overnight on ice. The resulting clear solution was diluted with chloroform and washed in turn with 100 mL of 1M hydrochloric acid, water, and brine (saturated), before being dried (magnesium sulfate), and then the solvent was removed under vacuum. Afterwards, the yellowish powder was purified using column chromatography ((1:9 ethyl acetate/dichloromethane, ca. 50×4 cm, wet-loaded) and (S,R)-2Nap-001 (2.64 g, 62%) was obtained as a white solid (Scheme 2-1b).

$\delta_{\text{H}}$  (400 MHz, DMSO- $d_6$ , 25 °C) 8.49 (0.2H, d,  $J$  7.30, Rot-1  $\text{NHCH}^*\text{CO}_2\text{Me}$ ), 8.43 (0.8H, d,  $J$  8.08, Rot-2  $\text{NHCH}^*\text{CO}_2\text{Me}$ ), 7.29-7.13 (9.8H, m,  $\text{H}_{\text{Ar}}$ ), 6.73 (0.8H, d,  $J$  8.81, Rot-2  $\text{NHBoc}$ ), 6.31 (0.2H, d,  $J$  8.16, Rot-1  $\text{NHBoc}$ ), 4.55-4.50 (1H, m,  $\text{CH}^*\text{CO}_2\text{Me}$ ), 4.18 (0.8H, td,  $J$  9.82, 4.00, Rot-2  $\text{CH}^*\text{NHBoc}$ ), approx. 4.07-4.02 (0.2H, m, Rot-1  $\text{CH}^*\text{NHBoc}$ ), 3.63 (2.9H, s,  $\text{OCH}_3$ ), 3.33 (8.3H, br s,  $\text{H}_2\text{O}$ ), 3.06 (1H, dd,  $J$  13.68, 5.13,  $\text{PhCH}_a\text{H}_b\text{CH}^*\text{CO}_2\text{Me}$ ), 2.88 (1H, dd,  $J$  13.67, 9.48,  $\text{PhCH}_a\text{H}_b\text{CH}^*\text{CO}_2\text{Me}$ ), 2.69 (0.8H, dd,  $J$  13.76, 3.88,  $\text{PhCH}_a\text{H}_b\text{CH}^*\text{NHBoc}$ ), 2.61-2.39 (0.9H, m,  $\text{PhCH}_a\text{H}_b\text{CH}^*\text{NHBoc}$  overlapped by residual DMSO- $d_5$  peak), 1.28 (7.1H, s, Rot-2  $\text{C}(\text{CH}_3)_3$ ), 1.21 (1.6H, s, Rot-1  $\text{C}(\text{CH}_3)_3$ ).  $\delta_{\text{C}}$  (100 MHz, DMSO- $d_6$ , 25 °C) 171.86, 171.62, and 155.07 ( $\text{C}=\text{O}$ ), 138.01, 137.05, 129.19, 129.15, 128.21, 127.90, 126.58, and 126.10 ( $\text{C}_{\text{Ar}}$ ), 77.93 ( $\text{C}(\text{CH}_3)_3$ ), 55.30 ( $\text{CH}^*\text{NHBoc}$ ), 53.36 ( $\text{CH}^*\text{CO}_2\text{Me}$ ), 51.92 ( $\text{OCH}_3$ ), 39.52 (septet, DMSO- $d_6$ ), 37.52 ( $\text{PhCH}_2\text{CH}^*\text{NHBoc}$ ), 36.96 ( $\text{PhCH}_2\text{CH}^*\text{CO}_2\text{Me}$ ), 28.11 (Rot-2  $\text{C}(\text{CH}_3)_3$ ), 27.73 (Rot-1  $\text{C}(\text{CH}_3)_3$ ).

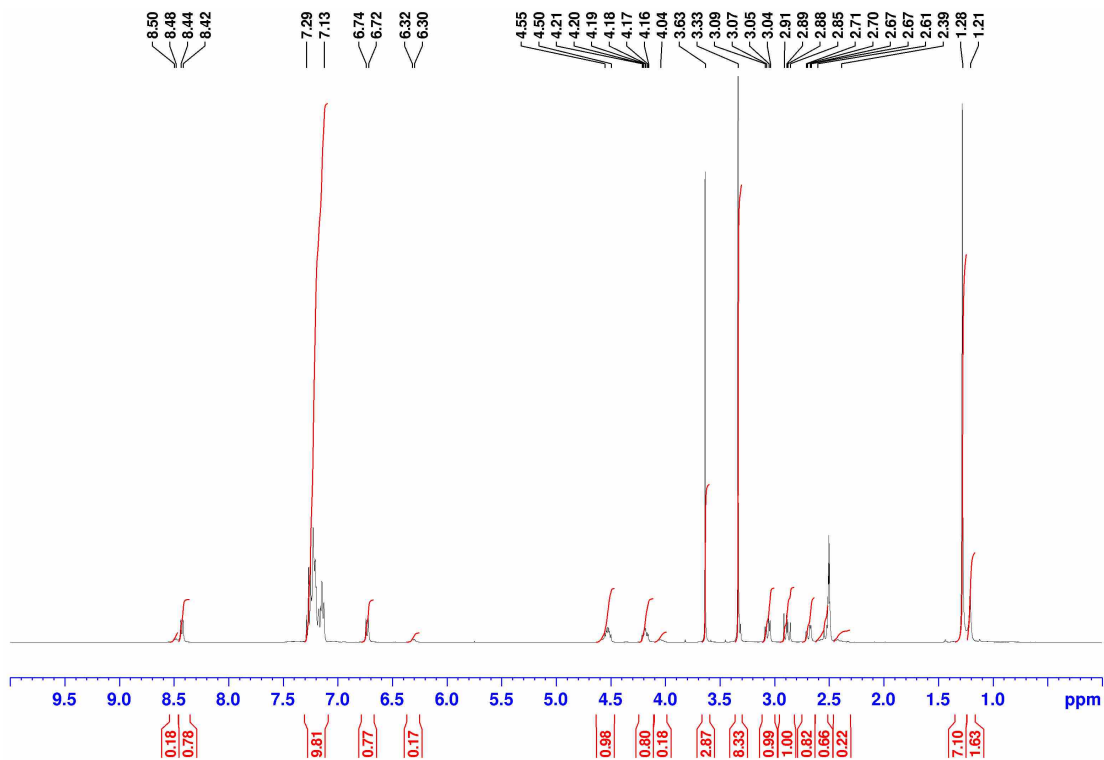


Figure A2-9.  $^1\text{H}$  NMR spectrum of (S,R)-2Nap-001 in  $\text{d}_6\text{-DMSO}$  at  $25\text{ }^\circ\text{C}$ .

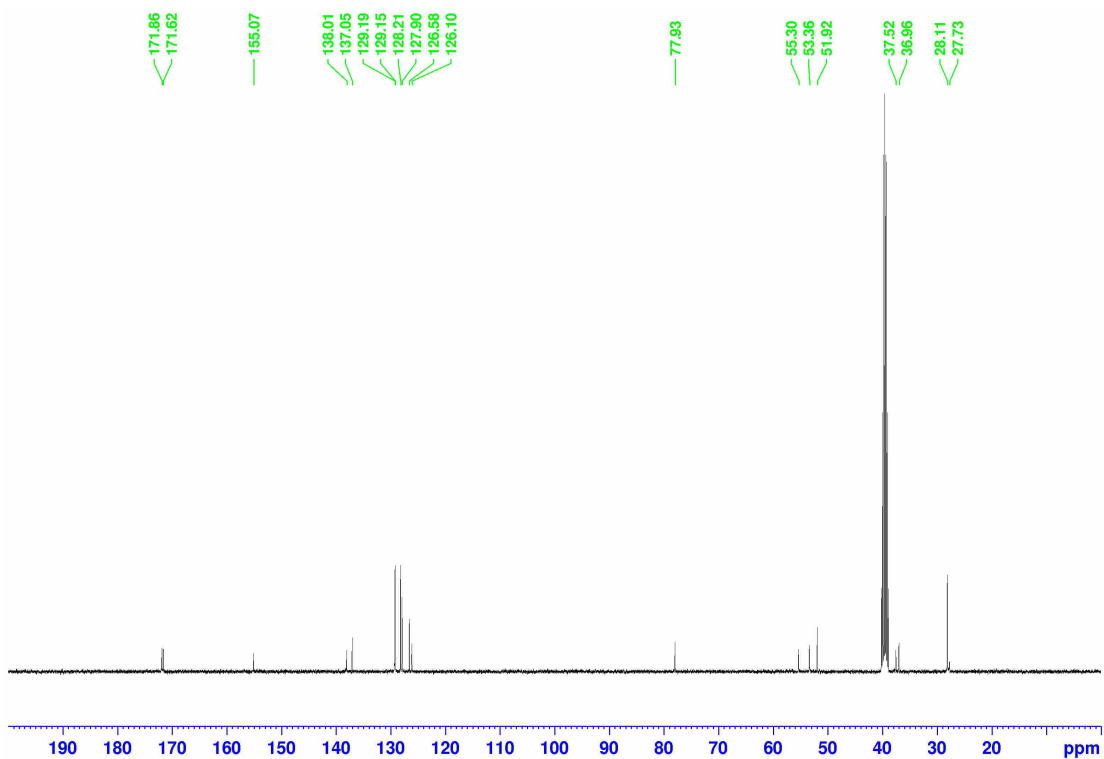
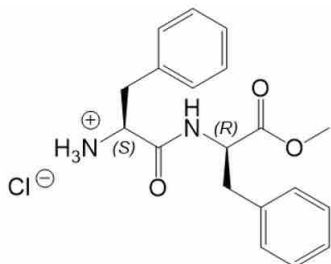


Figure A2-10.  $^{13}\text{C}$  NMR spectrum of (S,R)-2Nap-001 in  $\text{d}_6\text{-DMSO}$  at  $25\text{ }^\circ\text{C}$ .

**Methyl (2R)-2-[(2S)-2-azaniumyl-3-phenylpropanamido]-3-phenylpropanoate hydrochloride ((S,R)-2Nap-002)**



To a solution of (S,R)-2Nap-001 (2.64 g, 6.19 mmol) in 1,4-dioxane (15 mL) was added hydrogen chloride 4M in 1,4-dioxane (30.96 mL, ca. 20 eq.) and the mixture stirred overnight at room temperature. TLC confirmed the absence of starting materials. The resulted mixture was evaporated in vacuo, redissolved in 30 mL acetonitrile, well-stirred and then the solvent removed under vacuum. (S,R)-2Nap-002 (1.27 g, 57%) was collected as a white foam (Scheme 2-1b).

$\delta_{\text{H}}$  (400 MHz, DMSO- $d_6$ , 25 °C) 9.30 (0.9H, d,  $J$  8.07, Rot-2 NH), 9.11 (0.1H, d,  $J$  8.08, Rot-1 NH), 8.27 (2.9H, br s,  $\text{NH}_3^+$ ), 7.30-7.21 (8.0H, m,  $\text{H}_{\text{Ar}}$ ), 7.03-6.97 (2.0H, m,  $\text{H}_{\text{Ar}}$ ), 4.56-4.50 (1H, m,  $\text{NHCH}^*$ ), 4.10 (1H, t,  $J$  6.38,  $\text{CH}^*\text{NH}_3^+$ ), 3.63 (2.7H, s,  $\text{OCH}_3$ ), 3.56 (0.3H, s,  $\text{CH}_2$  in 1,4-dioxane), 3.38 (6.5H, br s,  $\text{H}_2\text{O}$ ), 3.09-2.93 (2.0H, m,  $\text{PhCH}_2$ ), 2.88-2.72 (2H, m,  $\text{PhCH}_2$ ), 2.50 (1.0H, quintet, residual DMSO- $d_5$ ), 2.07 (0.3H, s,  $\text{CH}_3$  in acetonitrile).  $\delta_{\text{C}}$  (100 MHz, DMSO- $d_6$ , 25 °C), not all carbons resolved) 171.42 and 167.98 ( $\text{C}=\text{O}$ ), 136.86, 134.60, 129.62, 129.25, 128.35, 127.02, and 126.78 ( $\text{C}_{\text{Ar}}$ ), 53.79 ( $\text{NHCH}^*$ ), 53.10 ( $\text{CH}^*\text{NH}_3^+$ ), 52.08 ( $\text{OCH}_3$ ), 39.52 (septet, DMSO- $d_6$ ), 36.88 and 36.66 ( $\text{PhCH}_2$ ).

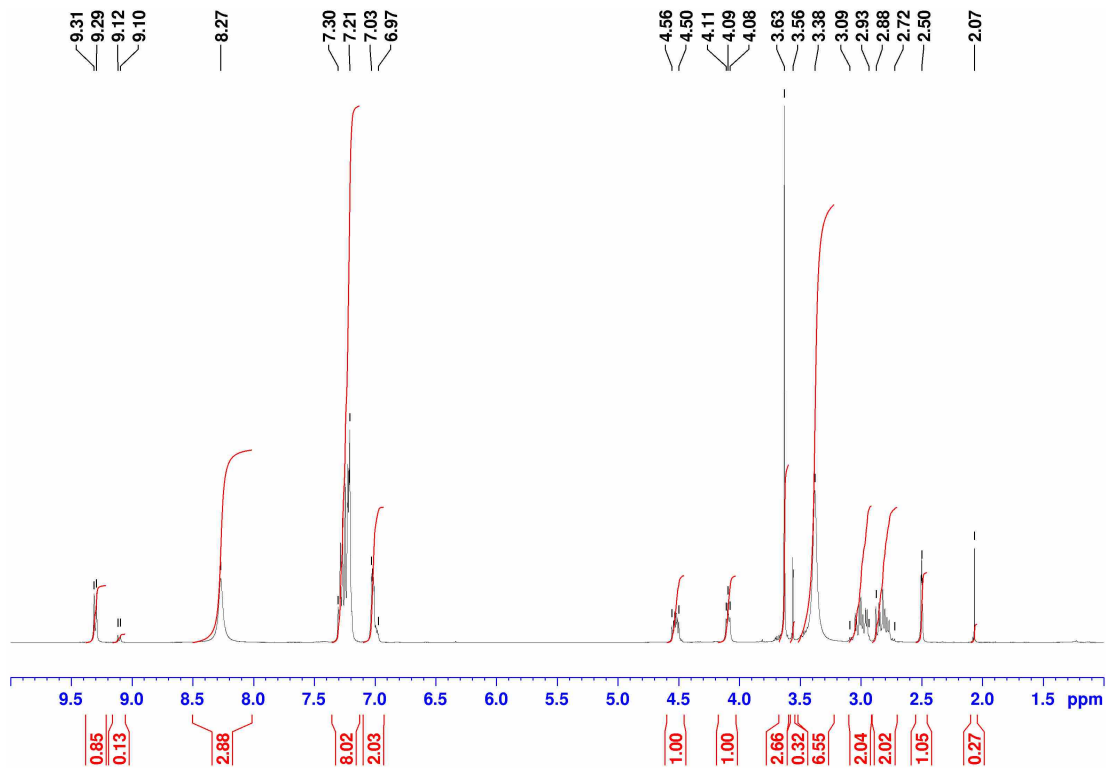


Figure A2-11.  $^1\text{H}$  NMR spectrum of (S,R)-2Nap-002 in  $\text{d}_6$ -DMSO at 25 °C.

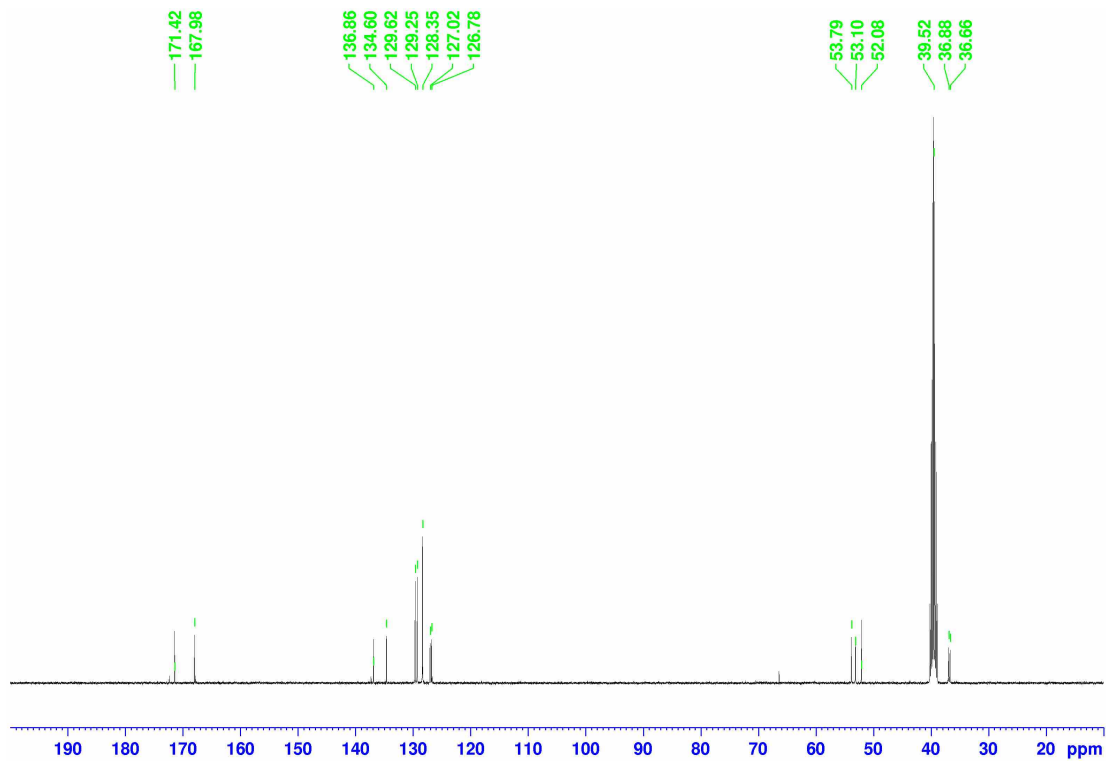
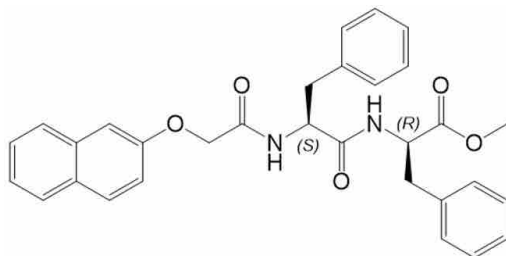


Figure A2-12.  $^{13}\text{C}$  NMR spectrum of (S,R)-2Nap-002 in  $\text{d}_6$ -DMSO at 25 °C.

**Methyl (2R)-2-[(2S)-2-[2-(naphthalen-2-yloxy)acetamido]-3-phenylpropanamido]-3-phenylpropanoate ((S,R)-2Nap-003)**



To a solution of (S,R)-2Nap-002 (1.27 g, 4.61 mmol) in chloroform (30 mL) was added *N*-methylmorpholine (2 eq., 1.90 mL) and the mixture was stirred at room temperature for 10 min. To a solution of 2-(naphthalene-2-acyloxy) acetic acid (0.93 g, 4.61 mmol) in chloroform (30 mL) was added *N*-methylmorpholine (2 eq., 1.90 mL) and isobutylchloroformate (1.1 eq., 1.24 mL), and the mixture was stirred on ice for 10 min. Subsequently, the former mixture was slowly added into the latter and stirred overnight on ice. The resulting clear solution was diluted with chloroform and washed in turn with 100 mL of 1M hydrochloric acid, water, and brine (saturated), dried (magnesium sulfate), and the solvent removed under vacuum. The resulting yellowish powder was purified using column chromatography ((1:9 ethyl acetate/dichloromethane, ca. 50×4 cm, wet-loaded) and (S,R)-2Nap-003 (1.94 g, 83%) was obtained as a white powder (Scheme 2-1b).

$\delta_{\text{H}}$  (400 MHz, DMSO- $d_6$ ) 8.74 (0.9H, d,  $J$  8.14, NH), 8.11 (0.9H, d,  $J$  8.59, NH), 7.83 (1.8H, d,  $J$  8.83,  $\text{H}_{\text{Ar}}$ ), 7.73 (1.0H, d,  $J$  8.19,  $\text{H}_{\text{Ar}}$ ), 7.47 (0.9H, t,  $J$  7.64,  $\text{H}_{\text{Ar}}$ ), 7.37 (1.0H, t,  $J$  7.92,  $\text{H}_{\text{Ar}}$ ), 7.30-7.00 (12.1H, m,  $\text{H}_{\text{Ar}}$ ), 4.66 (1H, td,  $J$  8.91, 4.43,  $\text{CH}^*$ ), 4.56 (1.8H, s,  $\text{OCH}_2$ ), 4.54-4.51 (0.9H, m,  $\text{CH}^*$ ), 3.62 (2.8H, s,  $\text{OCH}_3$ ), 3.41 (9.7H, br s,  $\text{H}_2\text{O}$ ), 3.09 (1.1H, dd,  $J$  13.59, 4.88,  $\text{PhCH}_2$ ), 2.87 (1H, dd,  $J$  13.52, 10.14,  $\text{PhCH}_2$ ), 2.76 (0.9H, dd,  $J$  13.56, 3.99,  $\text{PhCH}_2$ ), 2.66 (1.0H, dd,  $J$  13.50, 9.33,  $\text{PhCH}_2$ ), 2.50 (0.9H, quintet, residual DMSO- $d_5$ ).  $\delta_{\text{C}}$  (100 MHz, DMSO- $d_6$ , 25 °C) 171.95, 170.85, and 167.27 ( $\text{C}=\text{O}$ ), 155.52, 137.33, 137.14, 134.08, 129.42, 129.30, 129.21, 128.79, 128.31, 128.00, 127.56, 126.83, 126.71, 126.49, 126.31, 123.92, 118.50, and 107.33 ( $\text{C}_{\text{Ar}}$ ), 66.68 ( $\text{OCH}_2$ ), 53.59 ( $\text{CH}^*$ ), 53.30 ( $\text{CH}^*$ ), 52.05 ( $\text{OCH}_3$ ), 39.52 (septet, DMSO- $d_6$ ), 37.73 ( $\text{PhCH}_2$ ), 36.96 ( $\text{PhCH}_2$ ).

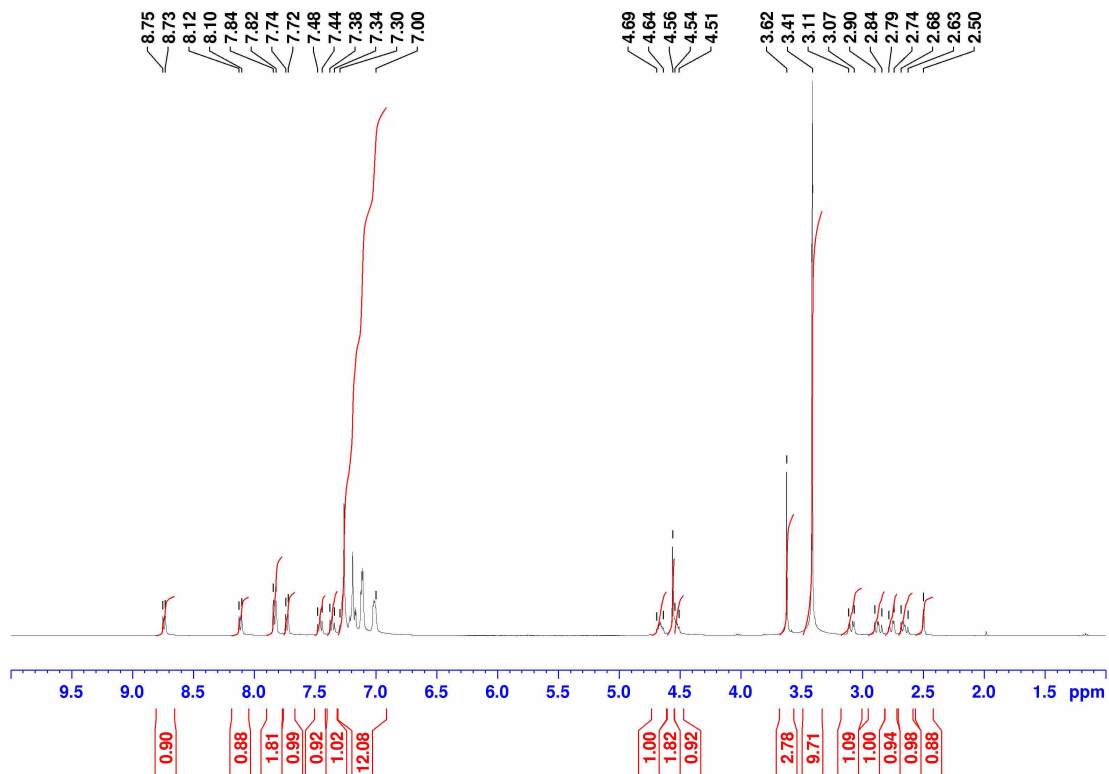


Figure A2-13.  $^1\text{H}$  NMR spectrum of (S,R)-2Nap-003 in  $d_6$ -DMSO at 25 °C.

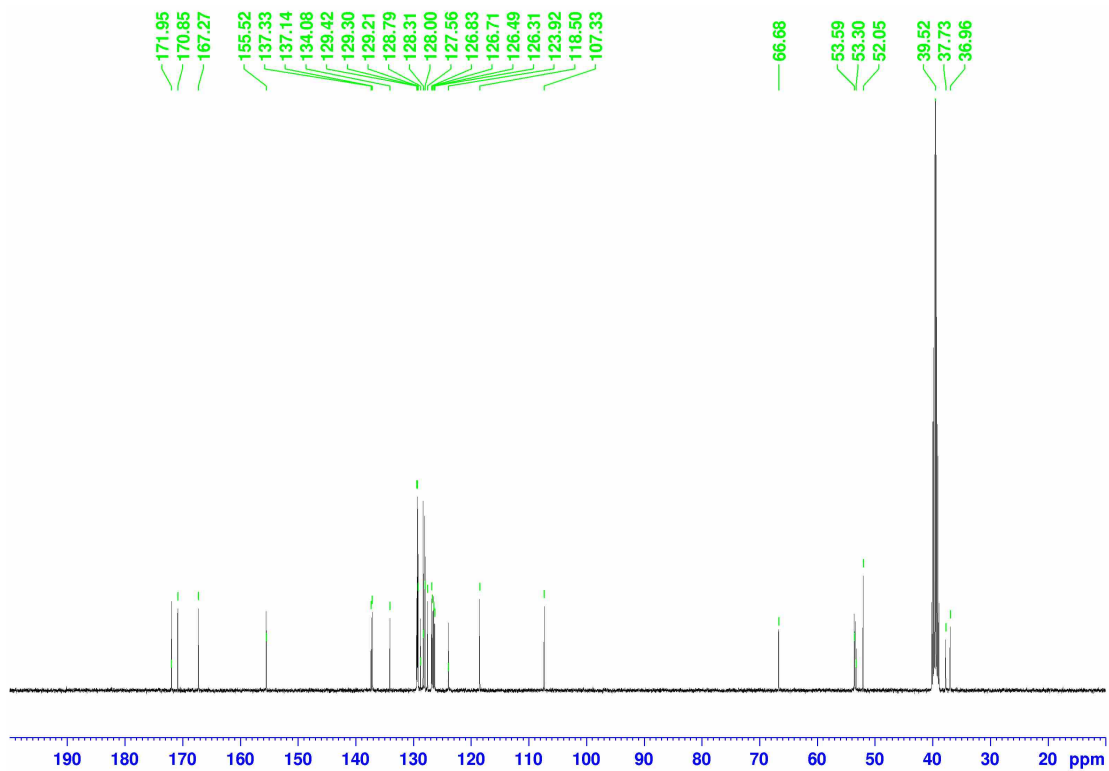
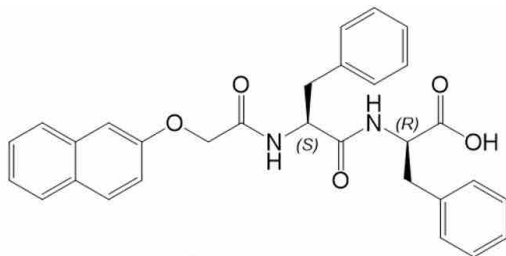


Figure A2-14.  $^{13}\text{C}$  NMR spectrum of (S,R)-2Nap-003 in  $d_6$ -DMSO at 25 °C.

**(2R)-2-[(2S)-2-[2-(naphthalen-2-yloxy)acetamido]-3-phenylpropanamido]-3-phenylpropanoic acid ((S,R)-2Nap-004)**



A solution of (S,R)-2Nap-003 (1.94 g, 3.81 mmol) in tetrahydrofuran (30 mL) was stirred at room temperature for 10 minutes. A solution of lithium hydroxide (374 mg, 20 eq.) in water (30 mL) was slowly added into the former solution and kept stirring at room temperature for 1 h. TLC confirmed the absence of starting materials. The resulting clear solution was poured into 200 mL of 1 M hydrochloric acid and stirred overnight to allow total precipitate. Then the suspension was collected by filtration using a Buchner funnel, washed with 200 mL deionized water and then a small amount of acetonitrile to remove the brown colour. The obtained solid was further dried under vacuum. (S,R)-2Nap-004 (1.69 g, 89 %) was collected as a white solid (Scheme 2-1b).

$\delta_{\text{H}}$  (400 MHz, DMSO- $d_6$ ) 12.90 (0.8H, br s, COOH), 8.63 (1.0H, d,  $J$  8.32, NH), 8.10 (1.0H, d,  $J$  8.56, NH), 7.83 (2.0H, d,  $J$  8.72,  $\text{H}_{\text{Ar}}$ ), 7.74 (1.0H, d,  $J$  8.20,  $\text{H}_{\text{Ar}}$ ), 7.46 (1.1H, t,  $J$  7.20,  $\text{H}_{\text{Ar}}$ ), 7.36 (1.1H, t,  $J$  7.28,  $\text{H}_{\text{Ar}}$ ), 7.29-6.99 (11.8H, m,  $\text{H}_{\text{Ar}}$ ), 4.69 (1H, td,  $J$  8.88, 4.28,  $\text{CH}^*$ ), 4.57 (1.8H, s,  $\text{OCH}_2$ ), 4.54-4.49 (1.0H, m,  $\text{CH}^*$ ), 3.43 (1.4H, br s,  $\text{H}_2\text{O}$ ), 3.14 (1.1H, dd,  $J$  13.62, 4.41,  $\text{Ph}_a\text{CH}_a\text{H}_b$ ), 2.87 (1.0H, dd,  $J$  13.56, 10.19,  $\text{Ph}_a\text{CH}_a\text{H}_b$ ), 2.78 (1.0H, dd,  $J$  13.60, 3.94,  $\text{Ph}_b\text{CH}_b\text{H}_b$ ), 2.65 (1.0H, dd,  $J$  13.57, 9.24,  $\text{Ph}_b\text{CH}_b\text{H}_b$ ), 2.50 (0.9H, quintet, residual DMSO- $d_5$ ).  $\delta_{\text{C}}$  (100 MHz, DMSO- $d_6$ , 25 °C) 172.92, 170.65, and 167.18 ( $\text{C}=\text{O}$ ), 155.52, 137.54, 137.35, 134.07, 129.41, 129.32, 129.22, 128.79, 128.23, 127.95, 127.54, 126.83, 126.57, 126.47, 126.24, 123.90, 118.47, and 107.36 ( $\text{C}_{\text{Ar}}$ ), 66.72 ( $\text{OCH}_2$ ), 53.55 ( $\text{CH}^*$ ), 53.30 ( $\text{CH}^*$ ), 39.52 (septet, DMSO- $d_6$ ), 37.81 ( $\text{Ph}_b\text{CH}_2$ ), 37.07 ( $\text{Ph}_a\text{CH}_2$ ).

**HRMS (ESI) m/z:**  $[\text{M}+\text{H}]^+$  accurate mass calculated for  $\text{C}_{30}\text{H}_{28}\text{N}_2\text{HO}_5$ : 497.1998; Found: 497.2074.

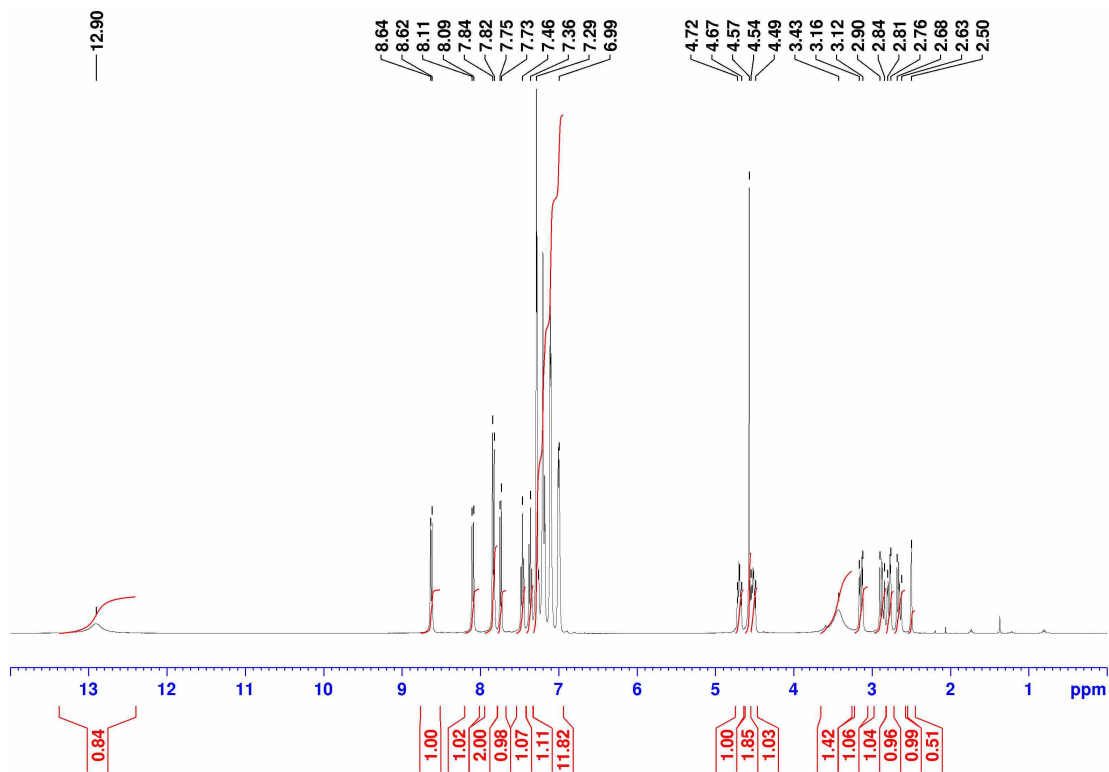


Figure A2-15. <sup>1</sup>H NMR spectrum of (S,R)-2Nap-004 in d<sub>6</sub>-DMSO at 25 °C.

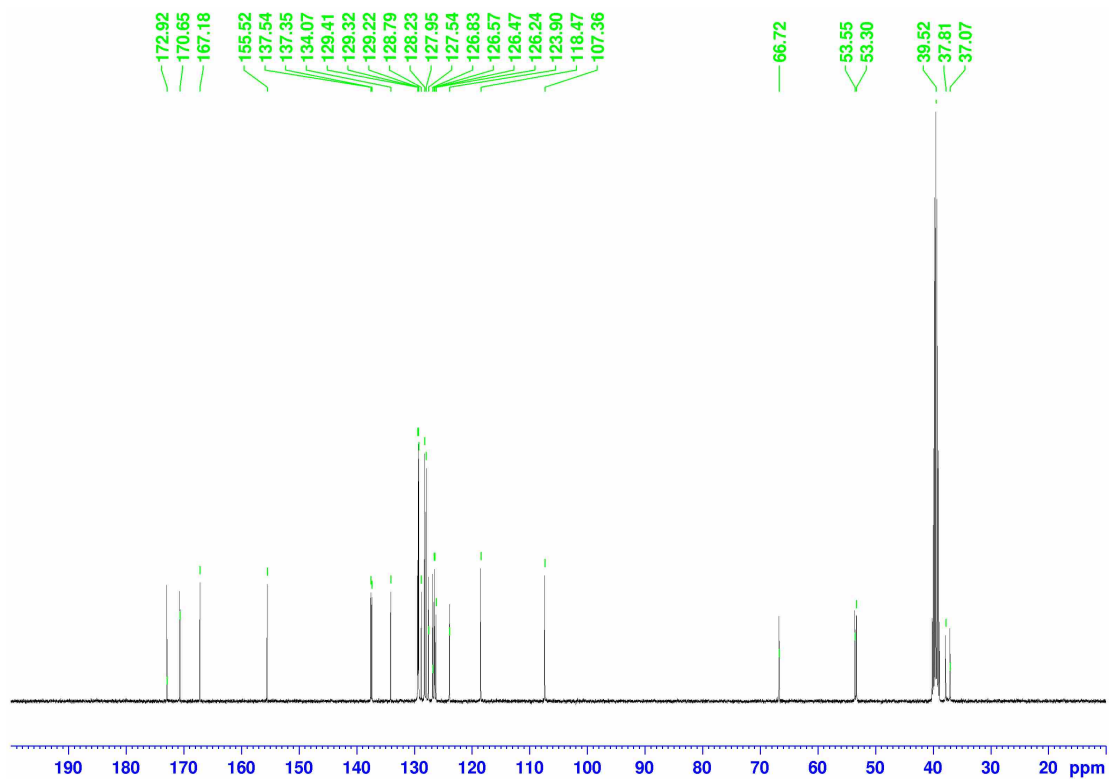


Figure A2-16. <sup>13</sup>C NMR spectrum of (S,R)-2Nap-004 in d<sub>6</sub>-DMSO at 25 °C.

### A2.3 Additional Figures and Tables

**Table A2-2.** CD data at 188 nm for binary system solutions with volume ratios from 10:0 to 0:10 of 10 mg/mL (L,L)-2NapFF:(L,D)-2NapFF stock solutions.

Volume Ratio	1	2	3	4	5	6	7	8	Average	Error bar
10:0	77.5	66.2	102.2	59.6	23.7	261.0	153.2	119.2	107.8	68.7
9:1	163.7	162.2	49.0	91.5	206.5	82.5	189.7	111.8	132.1	52.7
8:2	175.9	178.8	153.9	111.1	90.6	143.7	87.7	131.5	134.2	33.2
7:3	85.3	69.6	108.9	86.9	97.1	192.2	74.7	81.3	99.5	36.9
6:4	89.5	133.0	87.0	72.3	121.4	92.0	124.6	40.7	95.1	28.7
5:5	52.3	66.1	147.1	113.6	88.2	132.6	62.3	101.0	95.4	32.2
4:6	54.0	5.3	1.9	8.6	21.4	9.1	27.0	39.6	20.9	17.3
3:7	-6.7	-2.4	3.6	-2.5	11.6	-9.3	-5.7	-8.5	-2.5	6.6
2:8	-25.2	-29.9	-45.6	-34.7	-32.2	-39.5	-24.7	-41.0	-34.1	7.0
1:9	-34.3	-37.8	-41.2	-43.8	-32.6	-46.6	-40.2	-42.3	-39.9	4.4
0:10	-38.8	-43.2	-43.8	-47.6	-54.2	-45.9	-49.1	-56.0	-47.3	5.4

**Table A2-3.** CD data at 223 nm of binary system solutions with volume ratios from 10:0 to 0:10 of 10 mg/mL (L,L)-2NapFF:(L,D)-2NapFF stock solutions.

Volume Ratio	1	2	3	4	5	6	7	8	Average	Error bar
10:0	188.2	278.3	271.8	279.2	177.2	394.5	312.2	257.0	269.8	64.1
9:1	195.4	179.8	164.2	200.2	195.2	188.4	239.4	222.6	198.1	22.1
8:2	111.0	77.7	82.6	80.2	74.1	75.9	75.8	78.5	82.0	11.3
7:3	41.3	43.2	42.9	46.7	44.3	46.0	43.5	48.9	44.6	2.3
6:4	-81.5	-115.9	-91.2	-99.4	-99.9	-100.2	-105.9	-79.5	-96.7	11.4
5:5	-194.8	-188.7	-223.7	-213.0	-195.1	-258.2	-212.4	-260.1	-218.3	26.0
4:6	-313.3	-225.2	-232.1	-231.5	-306.0	-264.8	-433.1	-419.5	-303.2	77.7
3:7	-518.7	-383.1	-310.5	-469.1	-575.2	-477.6	-603.0	-414.5	-469.0	91.7
2:8	-507.9	-446.1	-661.6	-480.6	-578.8	-666.9	-366.6	-648.2	-544.6	104.5
1:9	-645.2	-573.6	-512.0	-664.3	-458.7	-611.9	-544.2	-717.0	-590.9	79.7
0:10	-731.2	-732.7	-830.1	-779.9	-638.4	-672.5	-737.0	-807.2	-741.1	60.4

**Table A2-4.** CD data at 226 nm of binary system solutions with volume ratios from 10:0 to 0:10 of 10 mg/mL (L,L)-2NapFF:(L,D)-2NapFF stock solutions.

Volume Ratio	1	2	3	4	5	6	7	8	Average	Error bar
10:0	-224.6	-277.4	-237.2	-248.7	-291.2	-351.4	-303.7	-281.5	-277.0	38.1
9:1	-220.3	-223.4	-222.4	-232.4	-222.3	-278.8	-296.1	-286.2	-247.8	30.9
8:2	-262.5	-213.8	-234.9	-231.5	-215.3	-231.7	-219.4	-233.1	-230.3	14.5
7:3	-210.5	-235.0	-233.4	-216.7	-226.9	-240.3	-237.2	-239.9	-230.0	10.4
6:4	20.2	59.1	55.1	6.2	17.8	8.3	8.7	11.4	23.4	20.0
5:5	172.2	148.7	179.7	174.2	142.7	214.9	238.4	205.6	184.5	30.8
4:6	333.2	567.8	464.2	517.4	577.1	493.7	524.7	471.4	493.7	71.7
3:7	578.5	465.6	389.7	467.4	536.4	497.2	586.7	529.3	506.4	61.2
2:8	521.2	530.0	557.0	574.3	745.6	680.2	651.3	641.4	612.6	74.4

1:9	1086.9	727.5	894.5	1009.0	1068.1	891.7	974.2	858.4	938.8	111.9
0:10	1149.5	1121.9	1370.6	1360.9	1197.9	1058.0	1068.7	1045.9	1171.7	121.6

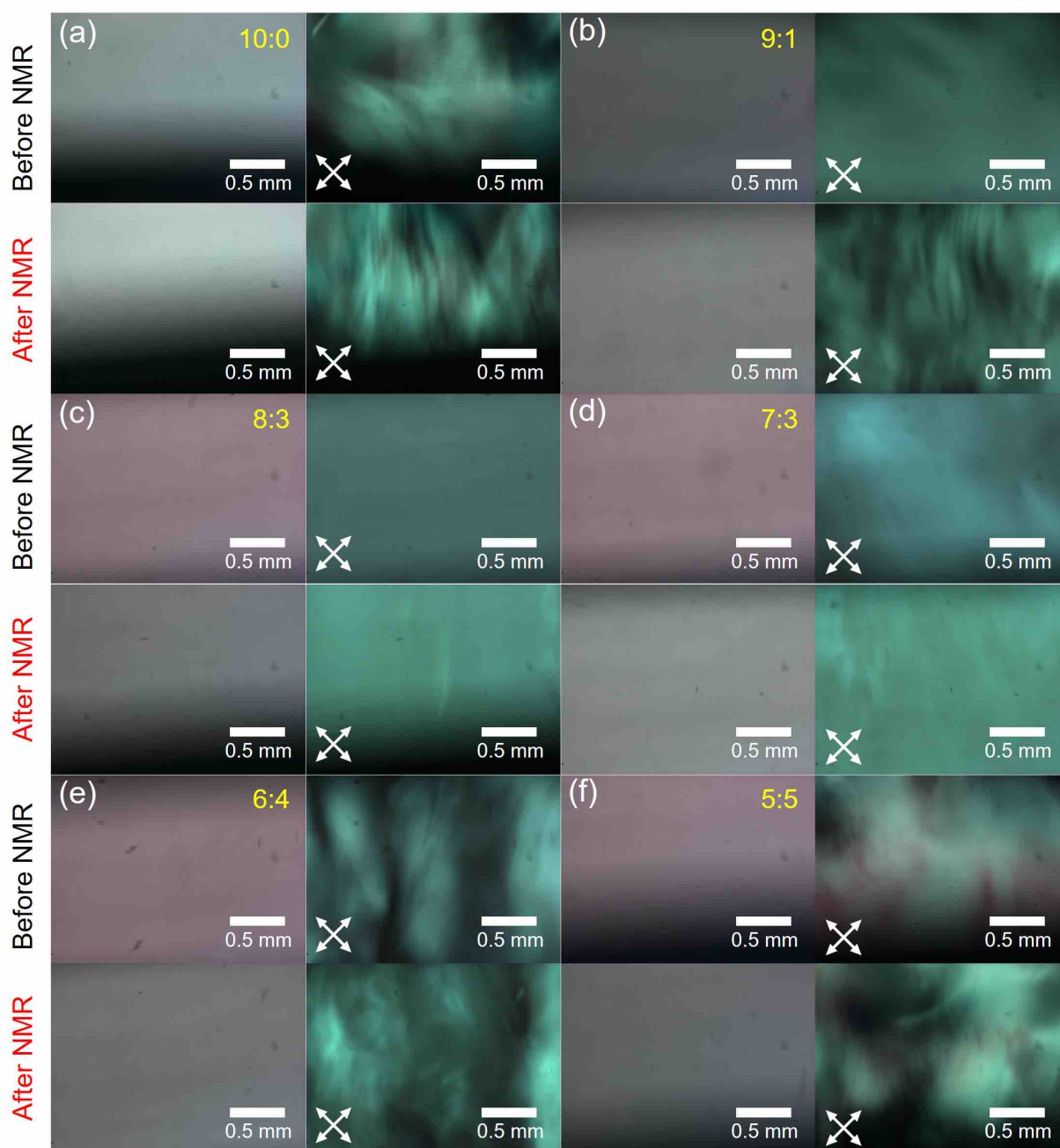


**Figure A2-17.** Normal-light and cross-polarized optical microscopy images (5×magnification) of binary system solutions with various volume ratios (10:0, 9:1, 8:2, 7:3, 6:4, 5:5) of 10 mg/mL (L,L)-2NapFF:(L,D)-2NapFF stock solutions before and after inserting into the NMR spectrometer. Scale bars represent 500  $\mu\text{m}$  and the white crosses represent the polariser directions.

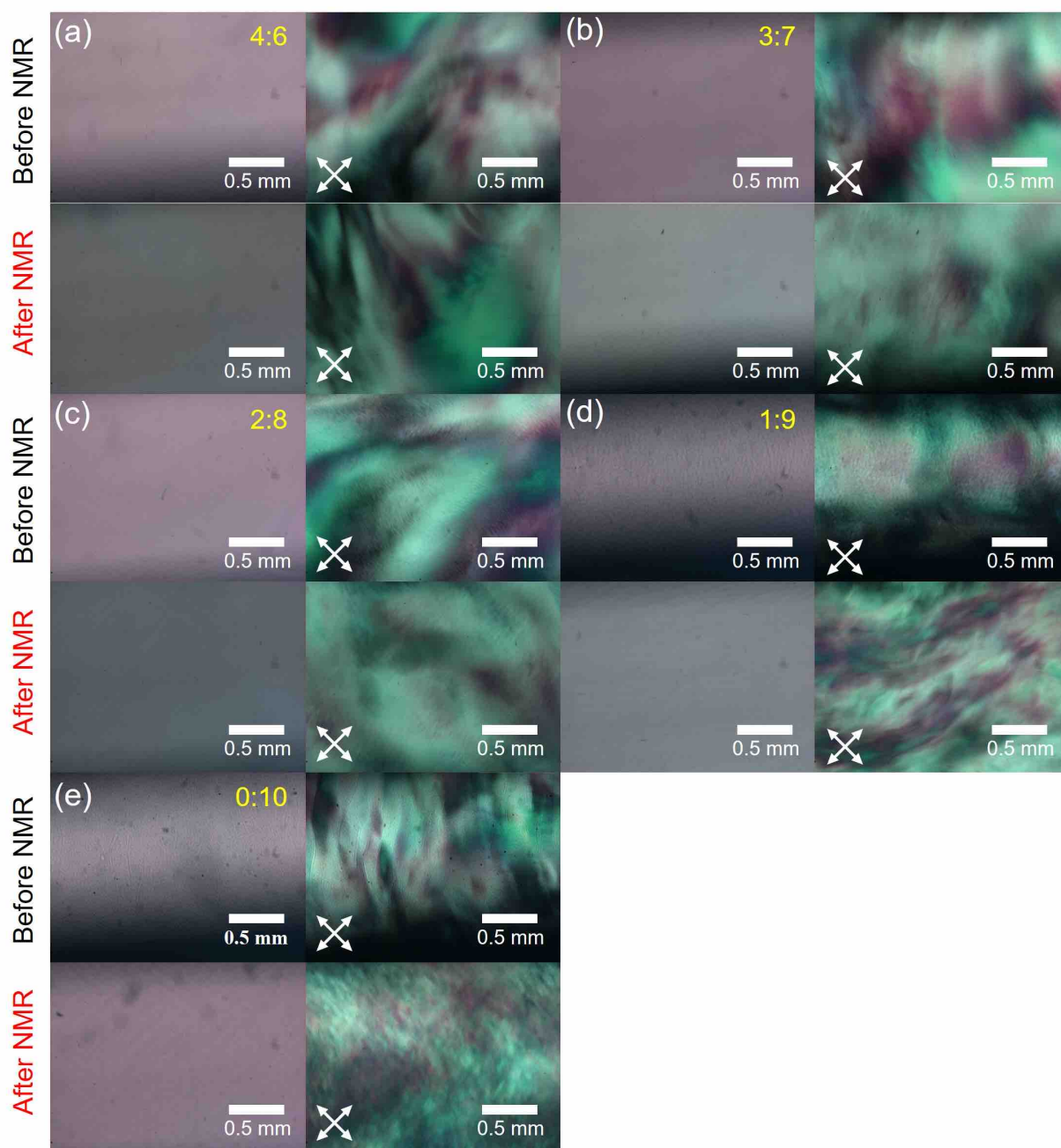


**Figure A2-18.** Normal-light and cross-polarized optical microscopy images ( $5\times$ magnification) of binary system solutions with various volume ratios (4:6, 3:7, 2:8, 1:9, 0:10) of 10 mg/mL (L,L)-2NapFF:(L,D)-2NapFF stock solutions before and after inserting into the NMR spectrometer. Scale bars represent 500  $\mu\text{m}$  and the white crosses represent the polarizer directions.

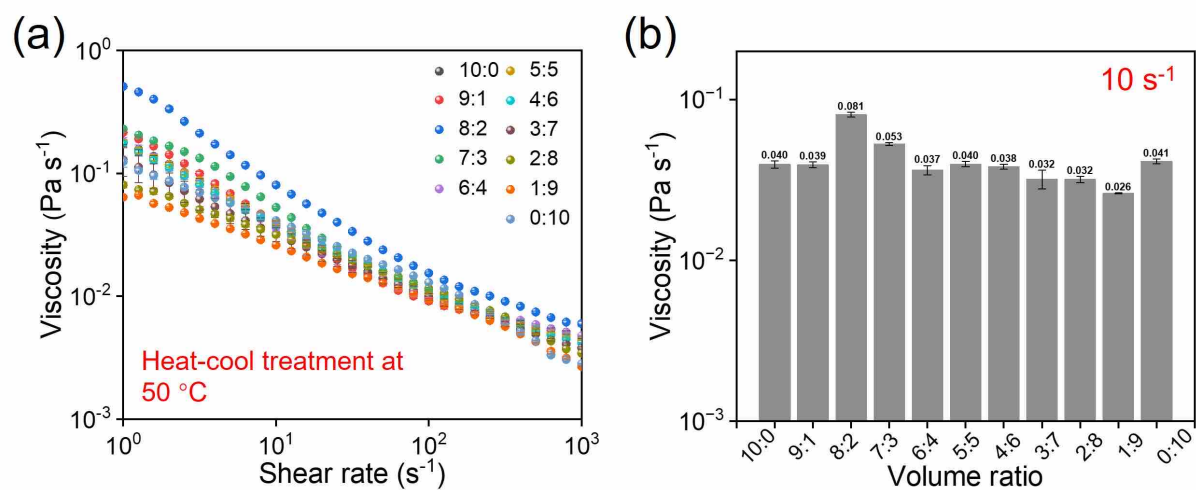


**Figure A2-19.** (a) The viscosity of binary system solutions after heat-cool cycle at 50 °C with various volume ratios of 10 mg/mL (L,L)-2NapFF:(L,D)-2NapFF stock solutions. (b) Plot shows the viscosity data at a shear rate of 10 s<sup>-1</sup> against volume ratio.

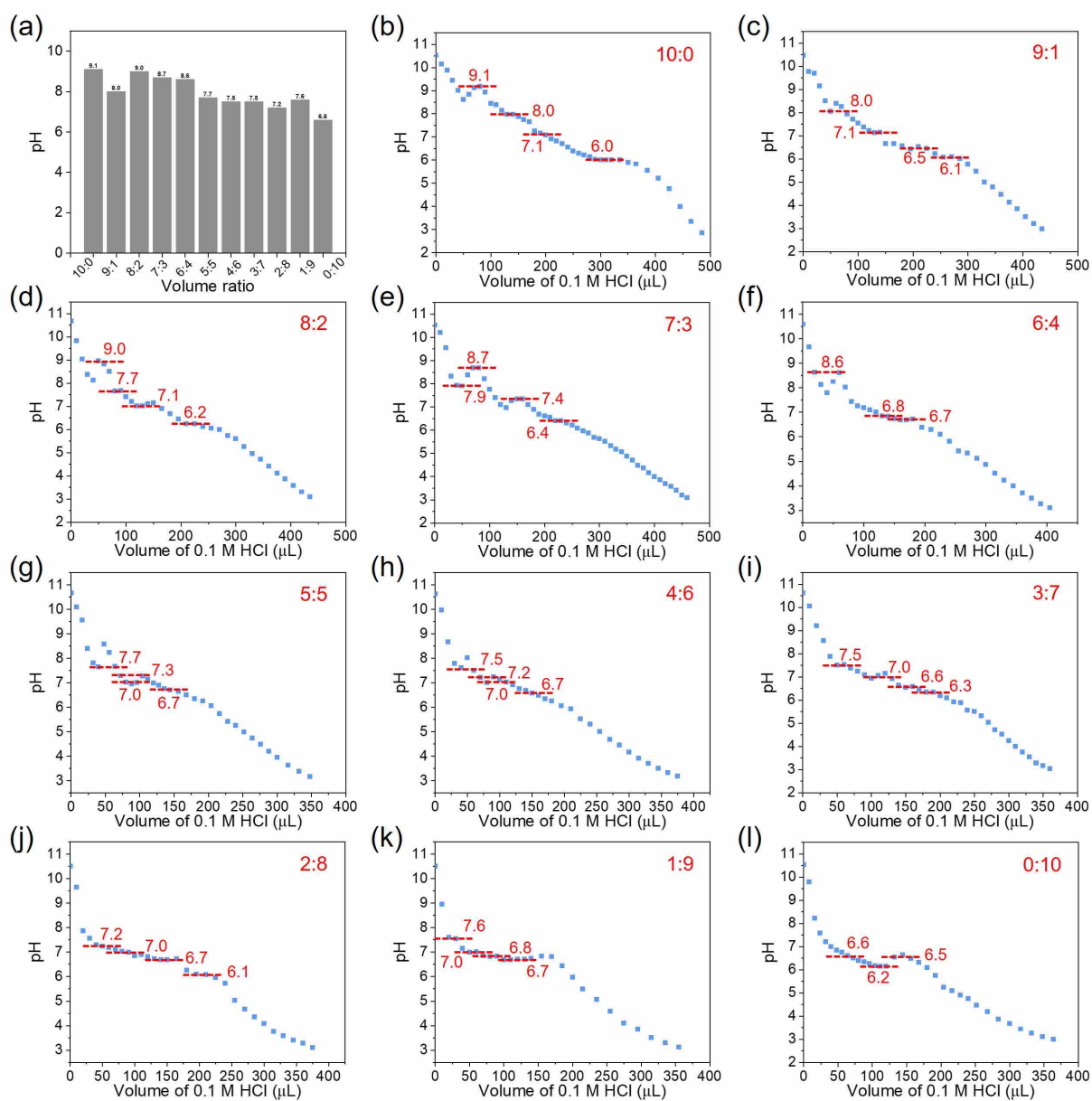


**Figure A2-20.** (a) Histogram exhibiting the first  $pK_a$  and (b-l) apparent  $pK_a$  titration results of micellar solutions with varying volume ratios of 10 mg/mL (L,L)-2NapFF: (L,L)-2NapFF.

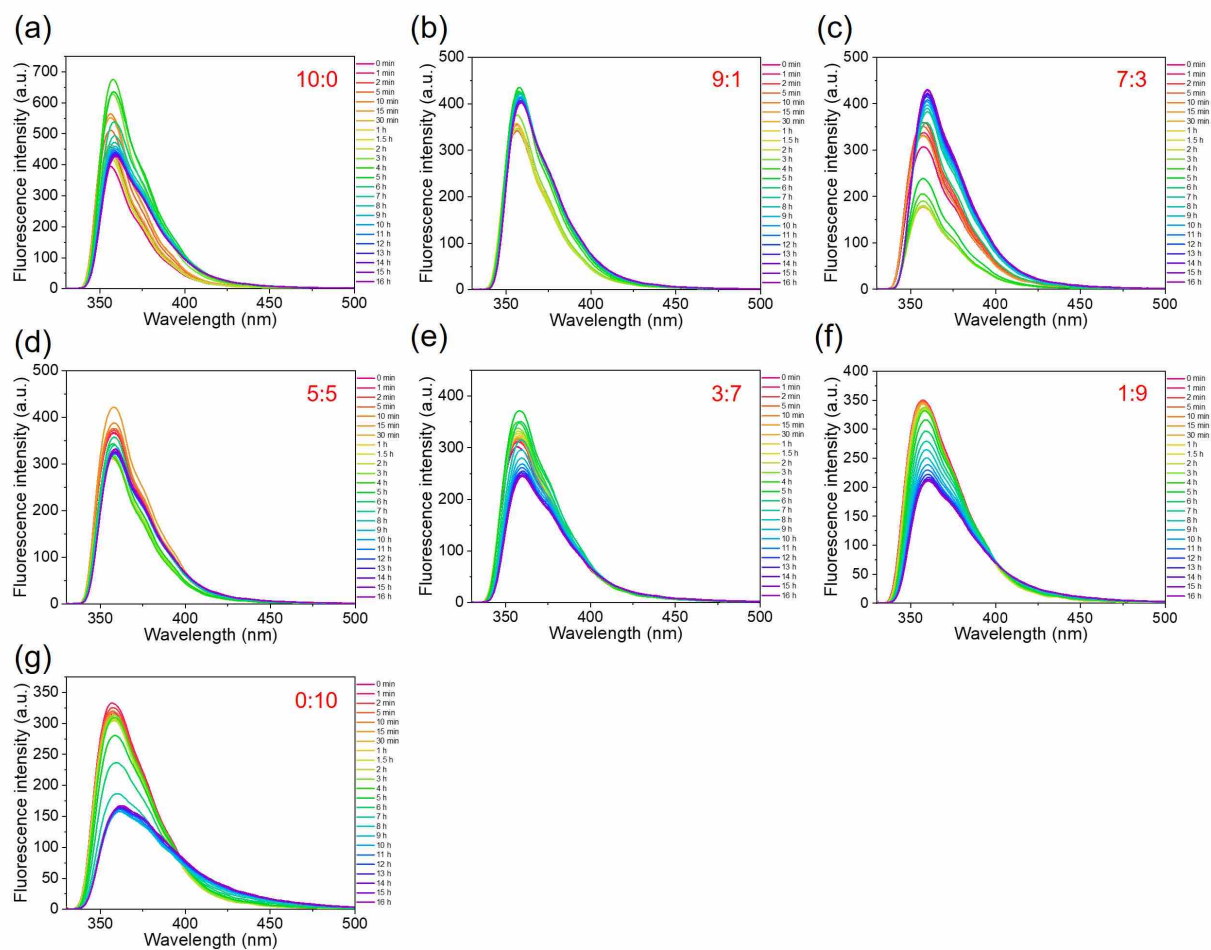


**Figure A2-21.** (a-g) Evolution of fluorescence spectra over time of micellar solutions containing 10 mg/mL of (L,L)- and (L,D)-2NapFF at ratios of 10:0, 9:1, 7:3, 5:5, 3:7, 1:9, and 0:10.

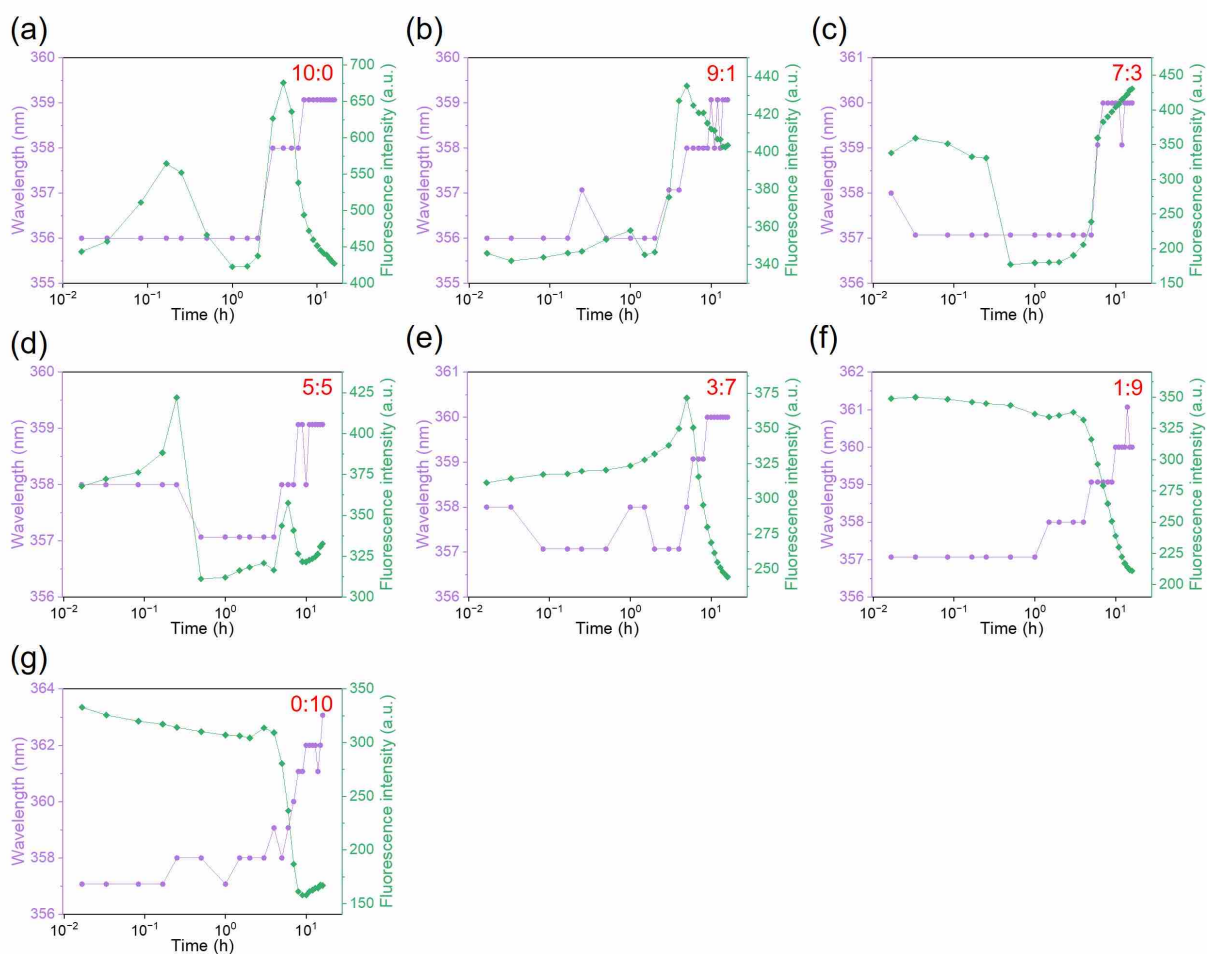


**Figure A2-22.** (a-g) Plots illustrating the evolution of wavelength and fluorescence intensity relative to time of the peak at 356 nm for micellar solutions containing 10 mg/mL of (L,L)- and (L,D)-2NapFF at ratios of 10:0, 9:1, 7:3, 5:5, 3:7, 1:9, and 0:10.

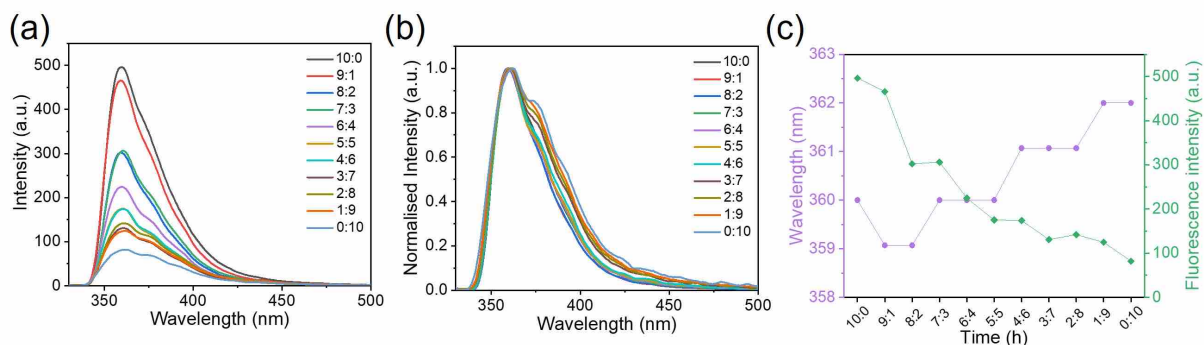


**Figure 2-23.** (a) Fluorescence emission spectrum, (b) normalized spectrum of gels containing 10 mg/mL of (L,L)- and (L,D)-2NapFF at ratios ranging from 10:0 to 0:10. (c) Plots illustrating the evolution of wavelength and fluorescence intensity relative to the ratios of the peak at 356 nm.

## A3 Appendix for Chapter 3

### A3.1 Materials

1-Naphthol, 4-chloro-1-naphthol, 6-bromo-2-naphthol, 6-cyano-2-naphthol, and 7-methoxy-2-naphthol were purchased from Sigma-Aldrich. *tert*-butyl chloroacetate, *L*-phenylalanine methyl ester hydrochloride, *D*-phenylalanine methyl ester hydrochloride, and trifluoroacetic acid were purchased from Fluorochem Ltd. Potassium carbonate (anhydrous, 99.5%), acetone (AR,  $\geq 99.8\%$ ), chloroform (AR,  $\geq 99.8\%$ ), hexanes (AR,  $\geq 95\%$ ), and tetrahydrofuran (AR,  $\geq 99.8\%$ ) were obtained from Fisher Scientific International, Inc. Magnesium sulfate (anhydrous, 99.5% min), *N*-methylmorpholine (99%), isobutyl chloroformate (98%), and lithium hydroxide (anhydrous, 98%) were acquired from Thermo Fisher Scientific Inc. Diethyl ether ( $\geq 99.8\%$ ), sodium hydroxide (98-100.5%), and hydrochloric acid (36.5-38%), were obtained from Honeywell International, Inc. All chemicals were used in their original form without any additional processing. Deionized water was used consistently. Table A3-1 provides an overview of the chemicals and their associated risks to assist with safe handling and usage.

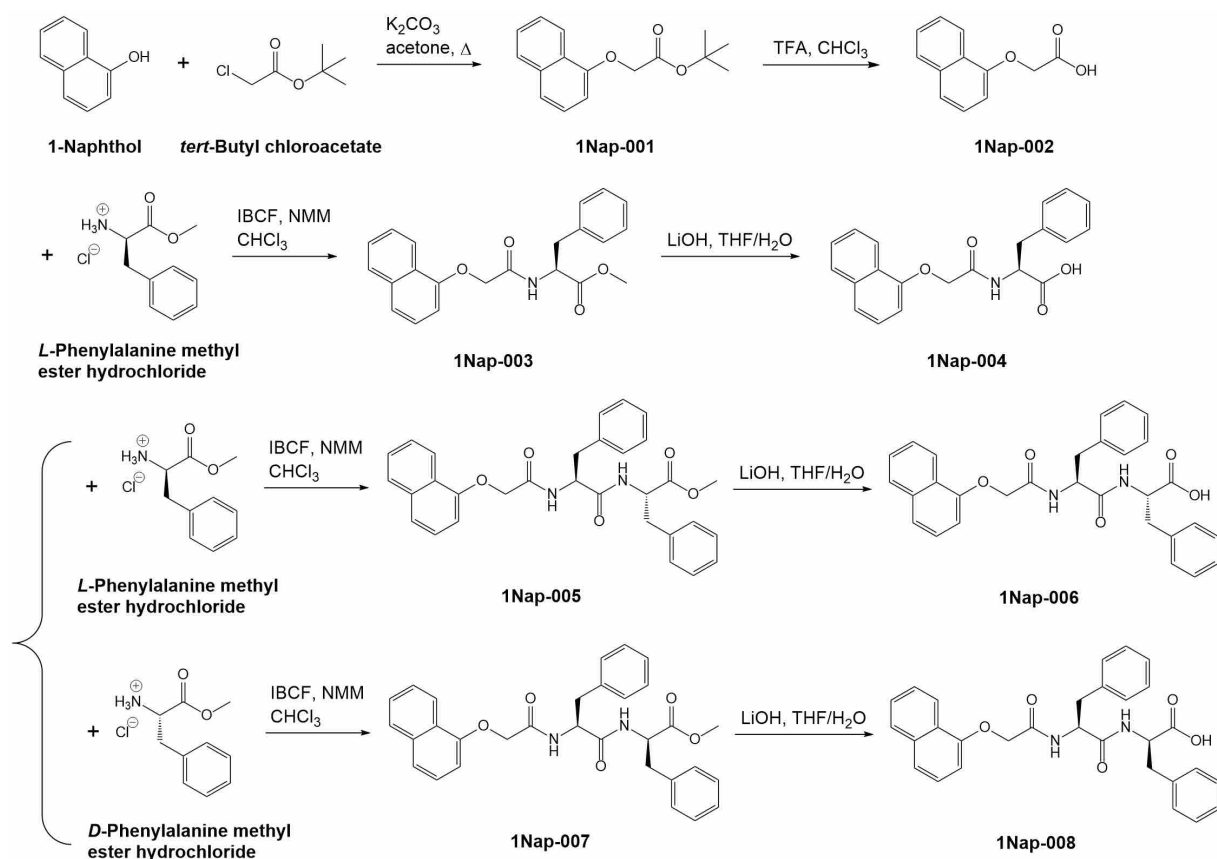
**Table A3-1.** Overview of Primary Health and Safety Risks Associated with Reagents Used in Synthesis Protocols.

Full Name	Acronym	Primary Risks
1-Naphthol		Irritant; harmful if swallowed, causes skin and eye irritation
4-chloro-1-naphthol		Toxic; harmful if swallowed, in contact with skin, or if inhaled
6-bromo-2-naphthol		Irritant; harmful if swallowed, causes severe skin and eye irritation
6-cyano-2-naphthol		Toxic; harmful if swallowed, inhaled, or in contact with skin
7-methoxy-2-naphthol		Irritant; harmful if swallowed, causes skin and eye irritation
<i>tert</i> -butyl chloroacetate		Highly reactive; causes severe skin burns and eye damage
<i>L</i> -phenylalanine methyl ester hydrochloride		Irritant; harmful if swallowed or in contact with skin
<i>D</i> -phenylalanine methyl ester hydrochloride		Irritant; harmful if swallowed or in contact with skin
Trifluoroacetic acid	THF	Corrosive; can cause severe burns and is a respiratory irritant
Potassium carbonate	K <sub>2</sub> CO <sub>3</sub>	Irritant; causes eye, skin, and respiratory tract irritation
Acetone		Highly flammable; irritant, may cause eye irritation and dizziness
Chloroform	CHCl <sub>3</sub>	Carcinogenic; central nervous system depressant
Hexanes		Highly flammable; neurotoxin that can cause nerve damage from inhalation
Tetrahydrofuran	THF	Highly flammable; forms explosive peroxides
Magnesium sulfate	MgSO <sub>4</sub>	Generally safe; used as a laxative and to treat magnesium deficiency

N-Methylmorpholine	NMM	Corrosive; harmful if swallowed, inhaled, or in contact with skin
Isobutyl chloroformate	IBCF	Highly reactive and toxic; can cause severe skin burns and eye damage
Lithium hydroxide	LiOH	Corrosive; causes severe skin burns and eye damage
Diethyl ether		Highly flammable; may form explosive peroxides
Sodium hydroxide	NaOH	Corrosive; causes severe skin burns and eye damage
Hydrochloric acid (36.5-38%)	HCl	Corrosive; causes severe skin burns and eye damage

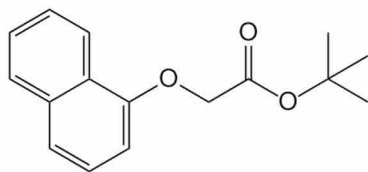
## A3.2 Synthesis of Dipeptides

### A3.2.1 1NapFF



**Scheme A3-1.** Synthetic route of 1NapFF.

Chemical structures were named using MarvinSketch (Version 23.11, <https://chemaxon.com/>) from ChemAxon. Mass spectra were recorded on a Bruker micrOTOFQ at the University of Glasgow.<sup>1</sup>H NMR spectra were recorded on a Bruker Avance III 400 MHz instrument at the University of Glasgow. Spectra were referenced to the residual <sup>1</sup>H signal from the DMSO-*d*<sub>6</sub> at 2.50 ppm for integration. The temperature of the samples was maintained at 298 ± 0.5 K.

**Tert-butyl 2-(naphthalen-1-yloxy)acetate (1Nap-001)**

*Tert*-butyl chloroacetate (5.5 mL, 1.1 eq., 38.1 mmol) was added to a stirred solution of 1-Naphthol (5.0 g, 34.7 mmol) and potassium carbonate (24.0 g, 5 eq., 173.4 mmol) in acetone (130 mL). After heating the solution to reflux at 70°C overnight, chloroform (200 mL) was added, and the solution was washed with deionized water (2 × 200 mL). The organic phase was dried over magnesium sulfate, and the solvent was removed in vacuo to obtain 1Nap-001 as an off-white solid in 71 yield (Scheme A3-1).

$\delta_{\text{H}}$  (400 MHz, DMSO- $d_6$ , 25 °C) 8.33 (0.01H, s,  $\underline{\text{CH}}$  in chloroform), 8.25-8.22 (1.0H, m,  $\underline{\text{H}}_{\text{Ar}}$ ), 7.90-7.85 (1.0H, m,  $\underline{\text{H}}_{\text{Ar}}$ ), 7.56-7.49 (3.1H, m,  $\underline{\text{H}}_{\text{Ar}}$ ), 7.41-7.40 (1.0H, m,  $\underline{\text{H}}_{\text{Ar}}$ ), 6.87 (1.0H, d,  $J$  7.28 Hz,  $\underline{\text{H}}_{\text{Ar}}$ ), 4.86 (2.0H, s,  $\underline{\text{OCH}}_2$ ), 3.37 (0.8H, br s,  $\underline{\text{H}}_2\text{O}$ ), 2.50 (0.3H, quintet, residual DMSO- $d_5$ ), 1.44 (8.3H, s, Rot-2  $\text{C}(\underline{\text{CH}}_3)_3$ ), 1.43 (0.7H, s, Rot-1  $\text{C}(\underline{\text{CH}}_3)_3$ ).  $\delta_{\text{C}}$  (100 MHz, DMSO- $d_6$ , 25 °C) 167.67 ( $\underline{\text{C}}=\text{O}$ ), 153.14, 134.06, 127.42, 126.49, 125.93, 125.37, 124.89, 121.57, 120.55, 105.41 ( $\underline{\text{C}}_{\text{Ar}}$ ), 81.42 ( $\underline{\text{C}}(\underline{\text{CH}}_3)_3$ ), 65.40 ( $\underline{\text{OCH}}_2$ ), 39.52 (septet, DMSO- $d_6$ ), 27.68 (Rot-2  $\text{C}(\underline{\text{CH}}_3)_3$ ), 27.52 (Rot-1  $\text{C}(\underline{\text{CH}}_3)_3$ ).

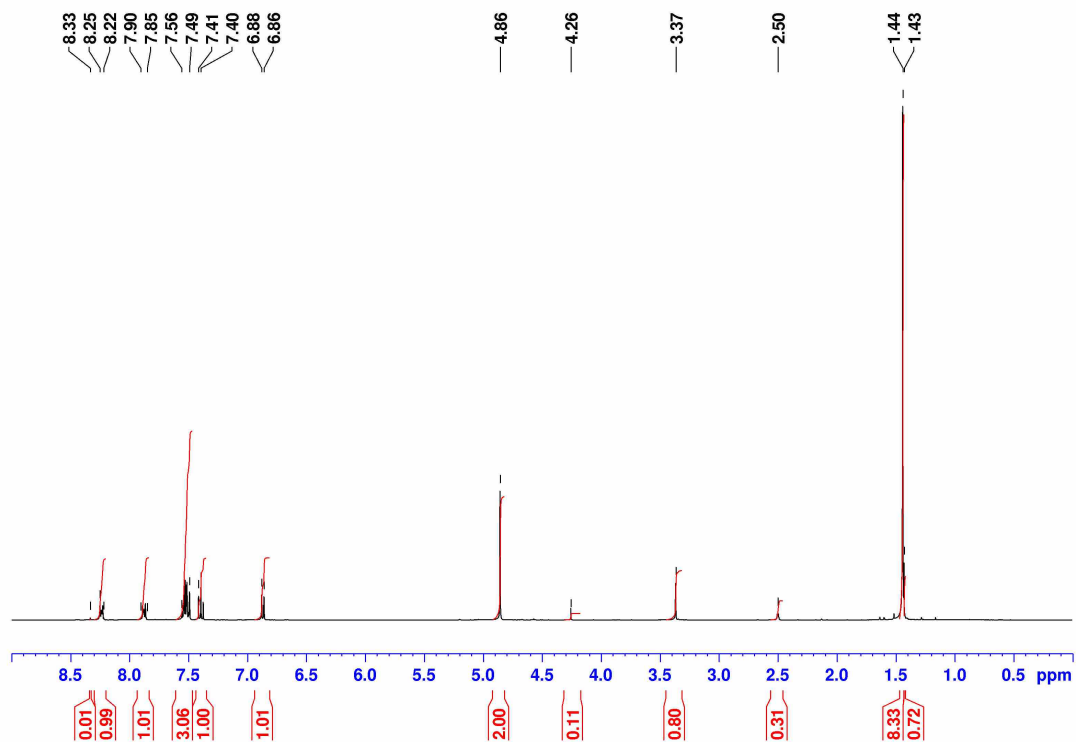


Figure A3-1.  $^1\text{H}$  NMR spectrum of 1Nap-001 in  $\text{d}_6$ -DMSO at 25 °C.

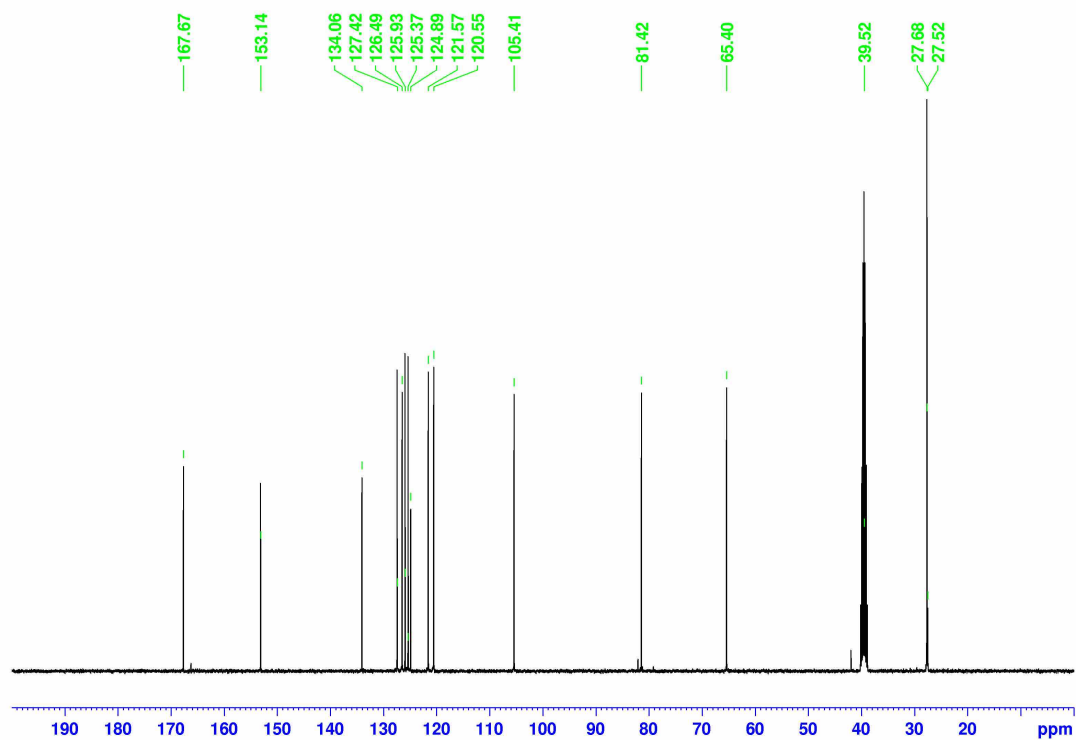
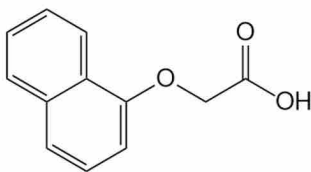
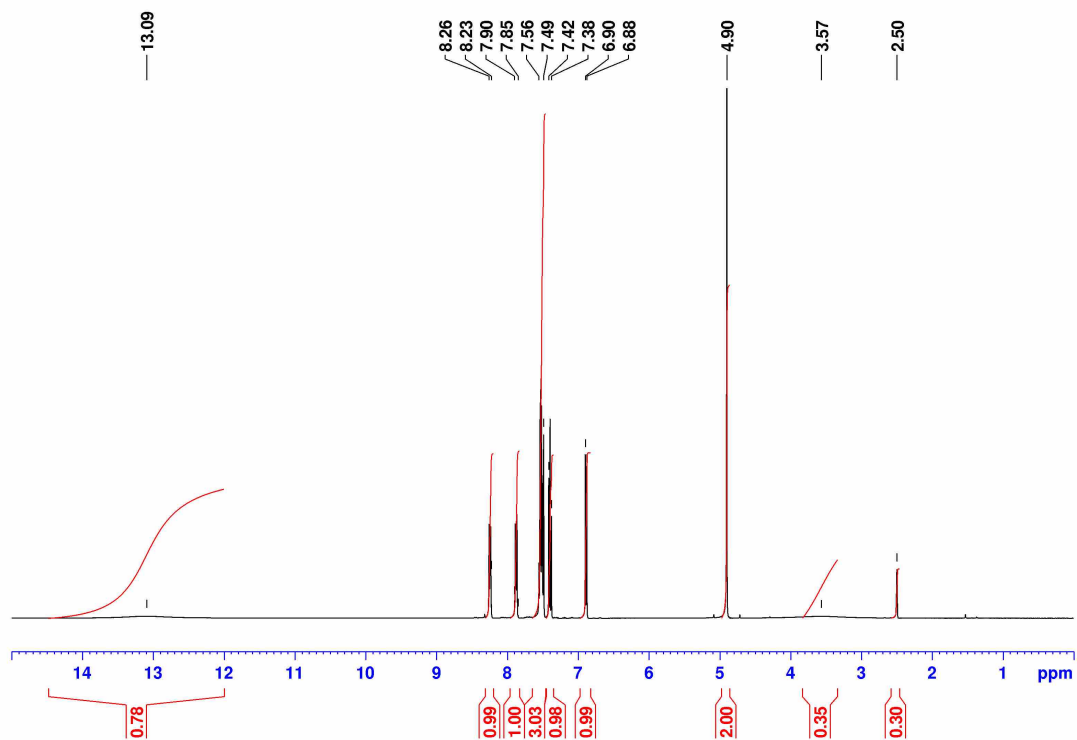


Figure A3-2.  $^{13}\text{C}$  NMR spectrum of 1Nap-001 in  $\text{d}_6$ -DMSO at 25 °C.

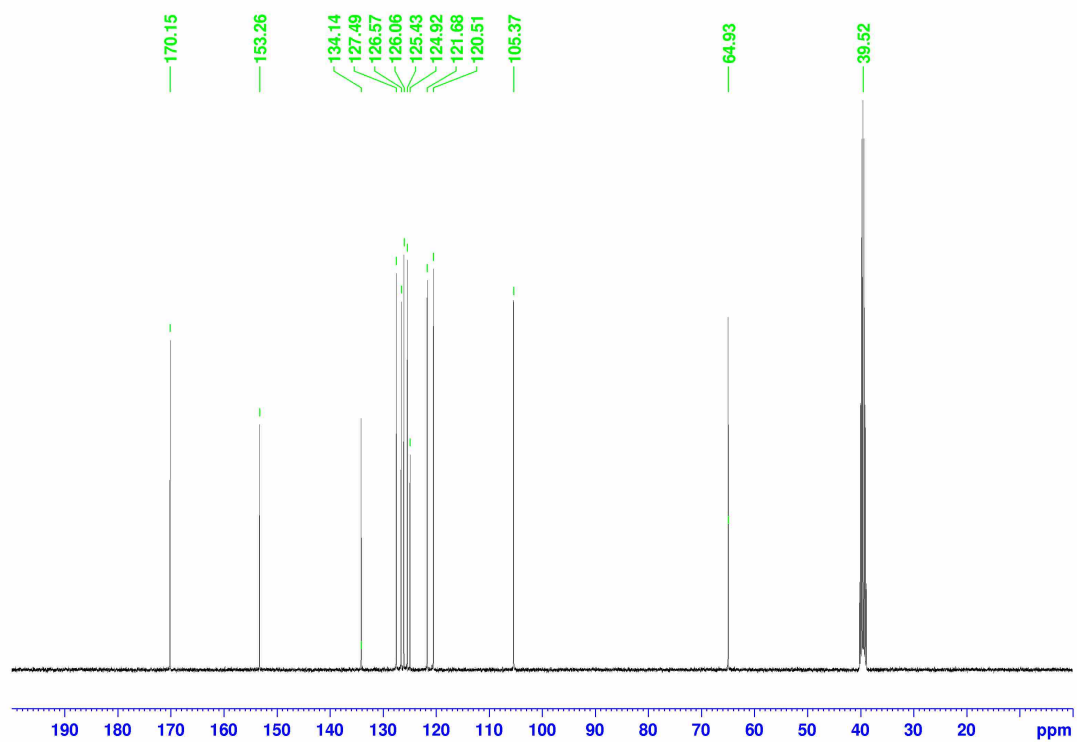
**2-(Naphthalen-1-yloxy)acetic acid (1Nap-002)**

To remove the *tert*-butyl protecting group, trifluoroacetic acid (11.2 mL, 6.1 eq., 151.0 mmol) was added to a mixture of 1Nap-001 (6.4 g, 24.7 mmol) in chloroform (30 mL), and the solution was stirred for 24 h. Subsequent evaporation under reduced pressure was performed to remove the solvent and most of the excess trifluoroacetic acid from the reactants. Then, hexane (200 mL) was added and stirred for 1 h to allow complete precipitation. The resulting white precipitate was collected by filtration, washed with hexane (10 mL), and vacuum dried to give 1Nap-002 in 86% yield (Scheme A3-1).

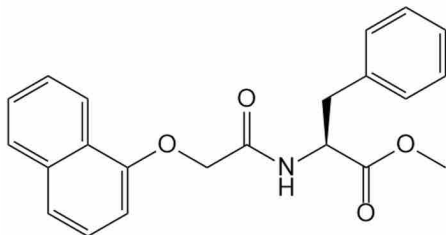
$\delta_{\text{H}}$  (400 MHz, DMSO- $d_6$ , 25 °C) 13.09 (0.8H, br s, COOH), 8.26-8.23 (1.0H, m,  $\underline{\text{H}}_{\text{Ar}}$ ), 7.90-7.85 (1.0H, m,  $\underline{\text{H}}_{\text{Ar}}$ ), 7.56-7.49 (3.0H, m,  $\underline{\text{H}}_{\text{Ar}}$ ), 7.42-7.38 (1.0H, m,  $\underline{\text{H}}_{\text{Ar}}$ ), 6.89 (1.0H, d,  $J$  7.56 Hz,  $\underline{\text{H}}_{\text{Ar}}$ ), 4.90 (2.0H, s, OCH $\underline{\text{H}}_2$ ), 3.57 (0.4H, br s,  $\underline{\text{H}}_2\text{O}$ ), 2.50 (0.3H, quintet, residual DMSO- $d_5$ ).  $\delta_{\text{C}}$  (100 MHz, DMSO- $d_6$ , 25 °C) 170.15 ( $\underline{\text{C}}=\text{O}$ ), 153.26, 134.14, 127.49, 126.57, 126.06, 125.43, 124.92, 121.68, 120.51, 105.37 ( $\underline{\text{C}}_{\text{Ar}}$ ), 64.93 (OCH $\underline{\text{H}}_2$ ), 39.52 (septet, DMSO- $d_6$ ).



**Figure A3-3.**  $^1\text{H}$  NMR spectrum of 1Nap-002 in  $\text{d}_6$ -DMSO at 25 °C.



**Figure A3-4.**  $^{13}\text{C}$  NMR spectrum of 1Nap-002 in  $\text{d}_6$ -DMSO at 25 °C.

**Methyl (2S)-2-[2-(naphthalen-1-yloxy)acetamido]-3-phenylpropanoate (1Nap-003)**

A standard coupling method to combine methyl ester-protected phenylalanine with 1NapOH was employed. *N*-Methylmorpholine (4.7 mL, 2 eq., 42.6 mmol) and isobutyl chloroformate (3.0 mL, 1.1 eq., 23.4 mmol) were added to a stirred solution of 1Nap-002 (4.3 g, 21.3 mmol) in chloroform (70 mL) in an ice bath and stirred for 5 min. A solution of *L*-phenylalanine methyl ester hydrochloride (4.6 g, 1 eq., 21.3 mmol) and *N*-Methylmorpholine (4.7 mL, 2 eq., 42.6 mmol) in chloroform (70 mL) was added. The mixture was kept in an ice bath and stirred overnight. The obtained solution was washed with deionized water (2 × 200 mL), hydrochloric acid (2 × 200 mL, 1 M), aqueous potassium carbonate (200 mL, 0.1 M), deionized water (2 × 200 mL), dried using magnesium sulfate, and the solvent was removed in vacuo to give 1Nap-003 in 97% yield (Scheme A3-1).

$\delta_{\text{H}}$  (400 MHz, DMSO- $d_6$ , 25 °C) 8.52 (1.1H, d,  $J$  7.99 Hz, NH), 8.32 (0.02H, s, CH in chloroform), 8.24-8.21 (1.1H, m,  $\text{H}_{\text{Ar}}$ ), 7.89-7.87 (1.1H, m,  $\text{H}_{\text{Ar}}$ ), 7.57-7.50 (3.2H, m,  $\text{H}_{\text{Ar}}$ ), 7.38-7.36 (1.1H, m,  $\text{H}_{\text{Ar}}$ ), 7.30-7.15 (6.0H, m,  $\text{H}_{\text{Ar}}$ ), 6.78 (1.0H, d,  $J$  7.59 Hz,  $\text{H}_{\text{Ar}}$ ), 4.74-4.63 (3.0H, m,  $\text{OCH}_2$  and  $\text{CH}^*$ ), 3.66 (3.0H, s,  $\text{OCH}_3$ ), 3.37 (3.4H, br s,  $\text{H}_2\text{O}$ ), 3.16 (1.0H, dd,  $J$  13.80, 5.10 Hz,  $\text{PhCH}_a\text{H}_b$ ), 3.06 (1.1H, q,  $J$  9.37 Hz,  $\text{PhCH}_a\text{H}_b$ ), 2.50 (0.7H, quintet, residual DMSO- $d_5$ ).  $\delta_{\text{C}}$  (100 MHz, DMSO- $d_6$ , 25 °C) 171.68, 167.71 ( $\text{C}=\text{O}$ ), 153.15, 137.15, 134.05, 129.16, 128.31, 127.43, 126.62, 126.56, 126.01, 125.35, 124.77, 121.88, 120.70 and 105.69 ( $\text{C}_{\text{Ar}}$ ), 67.07 ( $\text{OCH}_2$ ), 53.14 ( $\text{CH}^*$ ), 52.06 ( $\text{OCH}_3$ ), 39.52 (septet, DMSO- $d_6$ ), 36.33 ( $\text{PhCH}_2$ ).

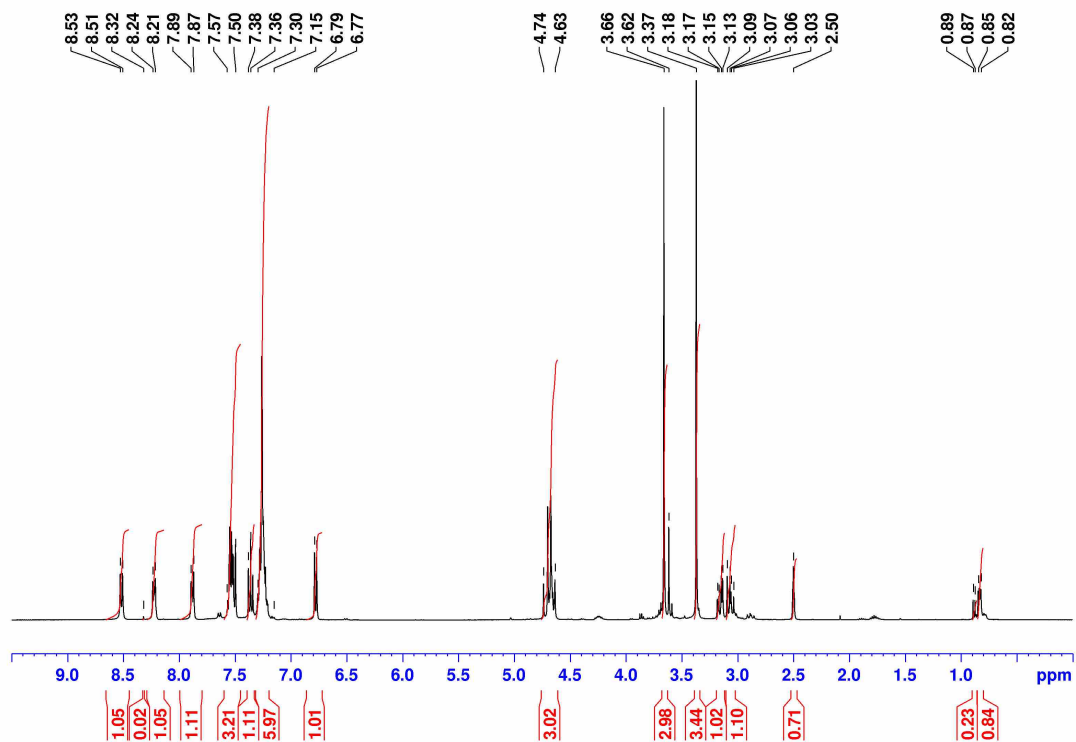


Figure A3-5.  $^1\text{H}$  NMR spectrum of 1Nap-003 in  $\text{d}_6$ -DMSO at 25 °C.

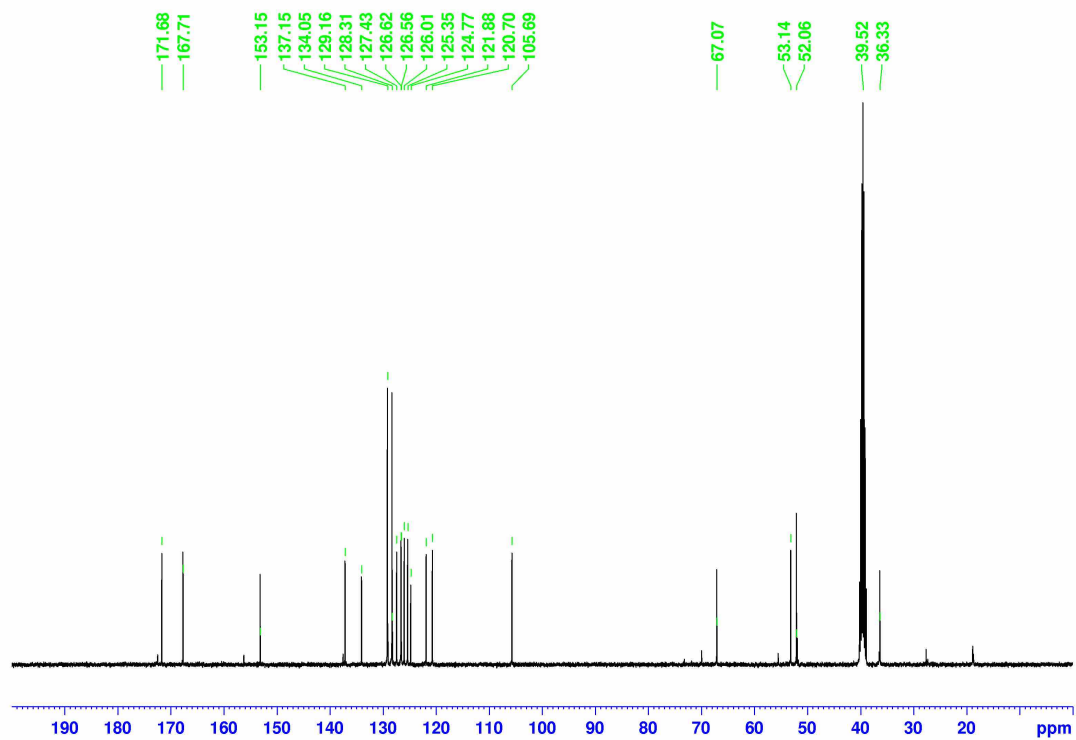
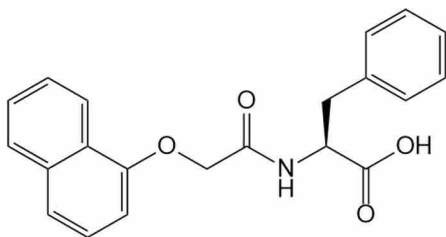


Figure A3-6.  $^{13}\text{C}$  NMR spectrum of 1Nap-003 in  $\text{d}_6$ -DMSO at 25 °C.

**(2S)-2-[2-(Naphthalen-1-yloxy)acetamidol]-3-phenylpropanoic acid (1Nap-004)**

To deprotect the C-terminus, an aqueous solution of lithium hydroxide (2.0 g, 4 eq., 82.9 mmol) in deionized water (20 mL) was added to 1Nap-003 (7.5 g, 20.7 mmol) in tetrahydrofuran (60 mL), and the mixture was stirred for 18 h. Subsequently, the resulting solution was transferred to hydrochloric acid (200 mL, 1.0 M) and stirred for 1 h to ensure complete precipitation. The resulting white precipitate was collected by filtration, washed thoroughly with deionized water (200 mL) and diethyl ether (10 mL) and dried in vacuo to yield 1Nap-004 as a white powder with a yield of 73% (Scheme A3-1).

$\delta_{\text{H}}$  (400 MHz, DMSO- $d_6$ , 25 °C) 12.96 (0.8H, br s, COOH), 8.33 (1.0H, d,  $J$  8.20 Hz, NH), 8.22-8.19 (1.0H, m,  $\text{H}_{\text{Ar}}$ ), 7.90-7.86 (1.1H, m,  $\text{H}_{\text{Ar}}$ ), 7.57-7.49 (3.2H, m,  $\text{H}_{\text{Ar}}$ ), 7.35 (1.1H, t,  $J$  7.87 Hz,  $\text{H}_{\text{Ar}}$ ), 7.29-7.20 (5.3H, m,  $\text{H}_{\text{Ar}}$ ), 6.79 (1.0H, d,  $J$  7.36 Hz,  $\text{H}_{\text{Ar}}$ ), 4.72 (2.0H, q,  $J$  14.68 Hz, OCH<sub>2</sub>), 4.65-4.60 (1.2H, m, CH\*), 3.41 (1.5H, br s, H<sub>2</sub>O), 3.18 (1.2H, dd,  $J$  13.82, 4.72 Hz, PhCH<sub>2</sub>H<sub>b</sub>), 3.06 (1.1H, q,  $J$  9.25 Hz, PhCH<sub>2</sub>H<sub>b</sub>), 2.50 (0.6H, quintet, residual DMSO- $d_5$ ).  $\delta_{\text{C}}$  (100 MHz, DMSO- $d_6$ , 25 °C) 172.69, 167.55 (C=O), 153.14, 137.47, 134.07, 129.22, 128.28, 127.46, 126.58, 126.55, 126.04, 125.38, 124.77, 121.84, 120.70 and 105.75 (C<sub>Ar</sub>), 67.13 (OCH<sub>2</sub>), 53.07 (CH\*), 39.52 (septet, DMSO- $d_6$ ), 36.43 (PhCH<sub>2</sub>).

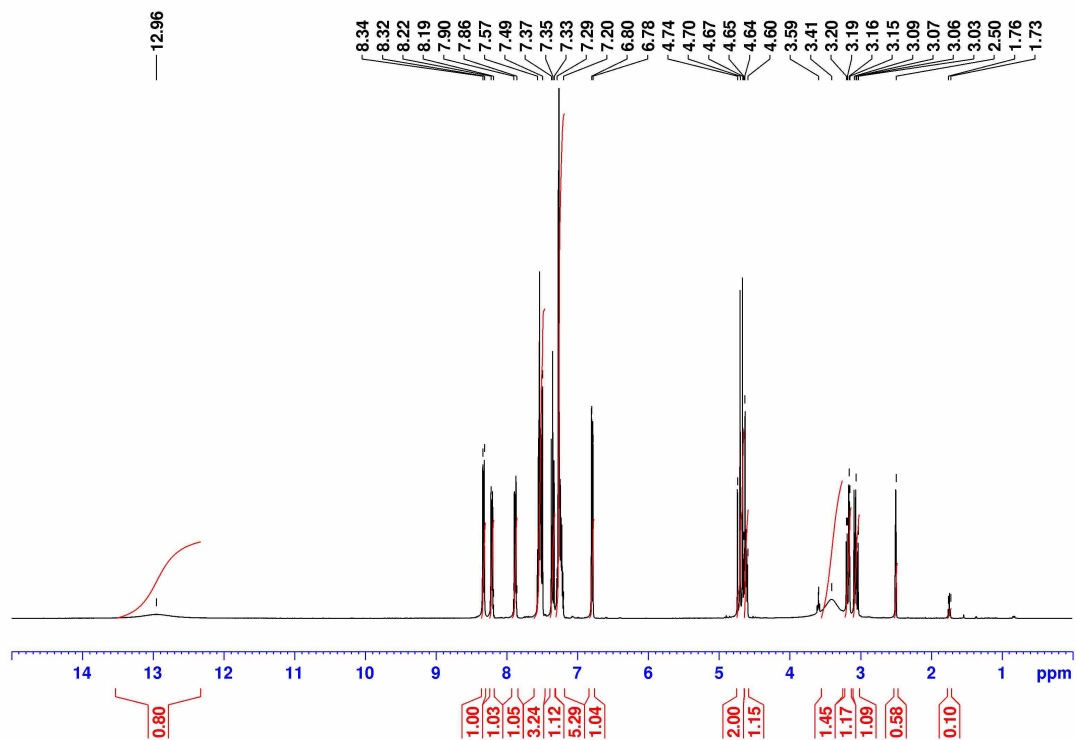


Figure A3-7.  $^1\text{H}$  NMR spectrum of 1Nap-004 in  $\text{d}_6\text{-DMSO}$  at  $25\text{ }^\circ\text{C}$ .

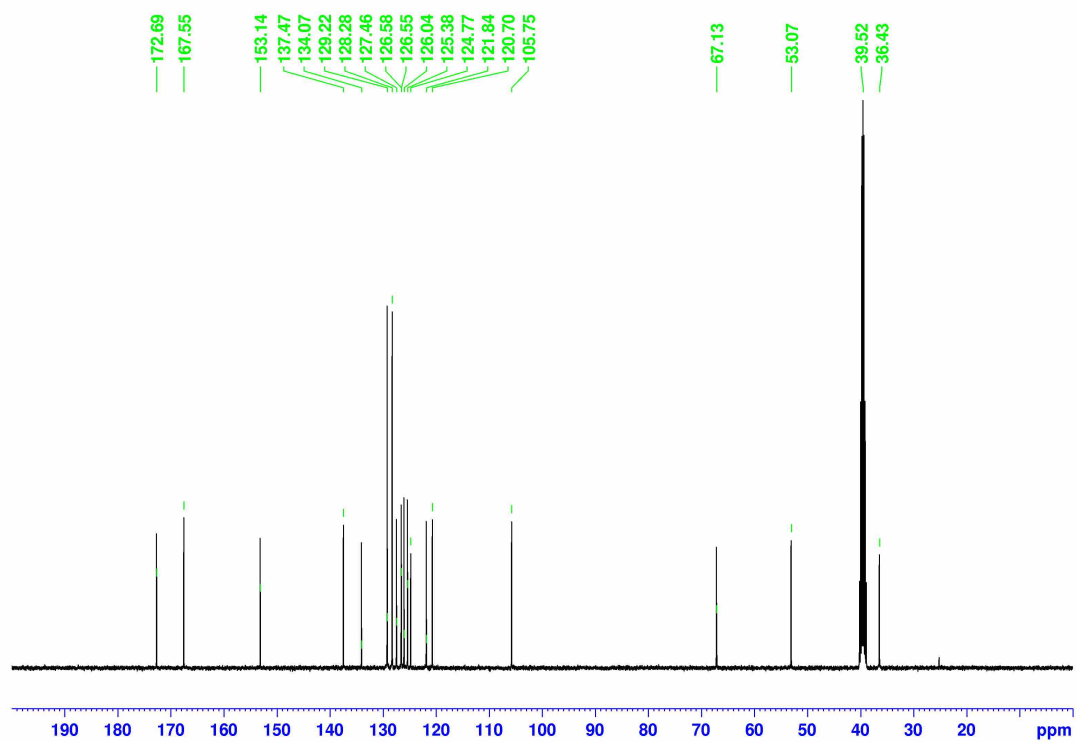
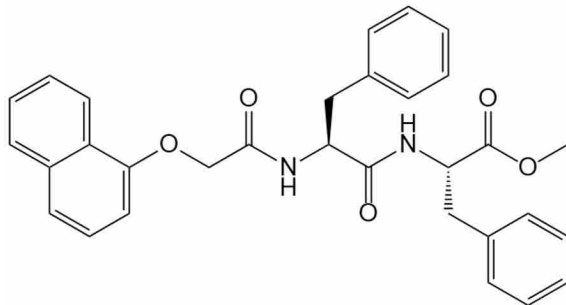


Figure A3-8.  $^{13}\text{C}$  NMR spectrum of 1Nap-004 in  $\text{d}_6\text{-DMSO}$  at  $25\text{ }^\circ\text{C}$ .

**Methyl (2s)-2-[(2s)-2-[2-(naphthalen-1-yloxy)acetamido]-3-phenylpropanamido]-3-phenylpropanoate (1Nap-005)**



The methyl ester-protected phenylalanine was coupled to 1Nap-004 using standard coupling methods. *N*-Methylmorpholine (3.3 mL, 2 eq., 30.4 mmol) and isobutyl chloroformate (2.2 mL, 1.1 eq., 16.7 mmol) were added to a stirred solution of 1NapFOH (5.3 g, 15.2 mmol) in chloroform (70 mL) in an ice bath. The mixture was stirred for 5 min. Subsequently, a solution of *L*-phenylalanine methyl ester hydrochloride (3.3 g, 1 eq., 15.2 mmol) and *N*-Methylmorpholine (3.3 mL, 2 eq., 30.4 mmol) in chloroform (70 mL) was added. The mixture was kept in an ice bath and stirred overnight. The obtained solution was washed with deionized water (2 × 200 mL), hydrochloric acid (2 × 200 mL, 1 M), aqueous potassium carbonate (200 mL, 0.1 M), deionized water (2 × 200 mL), dried using magnesium sulfate, and the solvent was removed in vacuo to produce 1Nap-005 in 92% yield (Scheme A3-1).

$\delta_{\text{H}}$  (400 MHz, DMSO- $d_6$ , 25 °C) 8.66 (0.7H, d,  $J$  7.55 Hz, NH), 8.32 (0.2H, s, CH in chloroform), 8.18-8.13 (1.9H, m, NH and  $\text{H}_{\text{Ar}}$ ), 7.89-7.86 (1.0H, m,  $\text{H}_{\text{Ar}}$ ), 7.56-7.49 (3.2H, m,  $\text{H}_{\text{Ar}}$ ), 7.35-7.20 (10.9H, m,  $\text{H}_{\text{Ar}}$ ), 6.72 (0.8H, d,  $J$  7.67 Hz,  $\text{H}_{\text{Ar}}$ ), 4.77-4.70 (1.0H, m,  $\text{CH}^*$ ), 4.68-4.62 (1.5H, m,  $\text{OCH}_2$ ), 4.60-4.55 (1.0H, m,  $\text{CH}^*$ ), 3.62 (3.3H, s,  $\text{OCH}_3$ ), 3.41 (4.2H, br s,  $\text{H}_2\text{O}$ ), 3.11-2.87 (4.1H, m,  $\text{PhCH}_2$ ), 2.50 (0.6H, quintet, residual DMSO- $d_5$ ), 2.08 (0.4H, s,  $\text{CH}_3$  in acetonitrile).  $\delta_{\text{C}}$  (100 MHz, DMSO- $d_6$ , 25 °C) 172.46, 170.91, and 167.70 ( $\text{C}=\text{O}$ ), 156.23, 137.50, 136.92, 134.05, 129.30, 129.18, 129.06, 128.27, 128.21, 128.07, 126.61, 126.56, 126.49, 126.02, 125.37, 121.86, 121.69, 120.69, 120.63, 105.69 and 105.64 ( $\text{C}_{\text{Ar}}$ ), 69.92 ( $\text{OCH}_2$ ), 55.47 ( $\text{CH}^*$ ), 54.00 ( $\text{CH}^*$ ), 51.86 ( $\text{OCH}_3$ ), 39.52 (septet, DMSO- $d_6$ ), 37.44 ( $\text{PhC}_b\text{H}_2$ ), 36.47 ( $\text{PhC}_a\text{H}_2$ ).

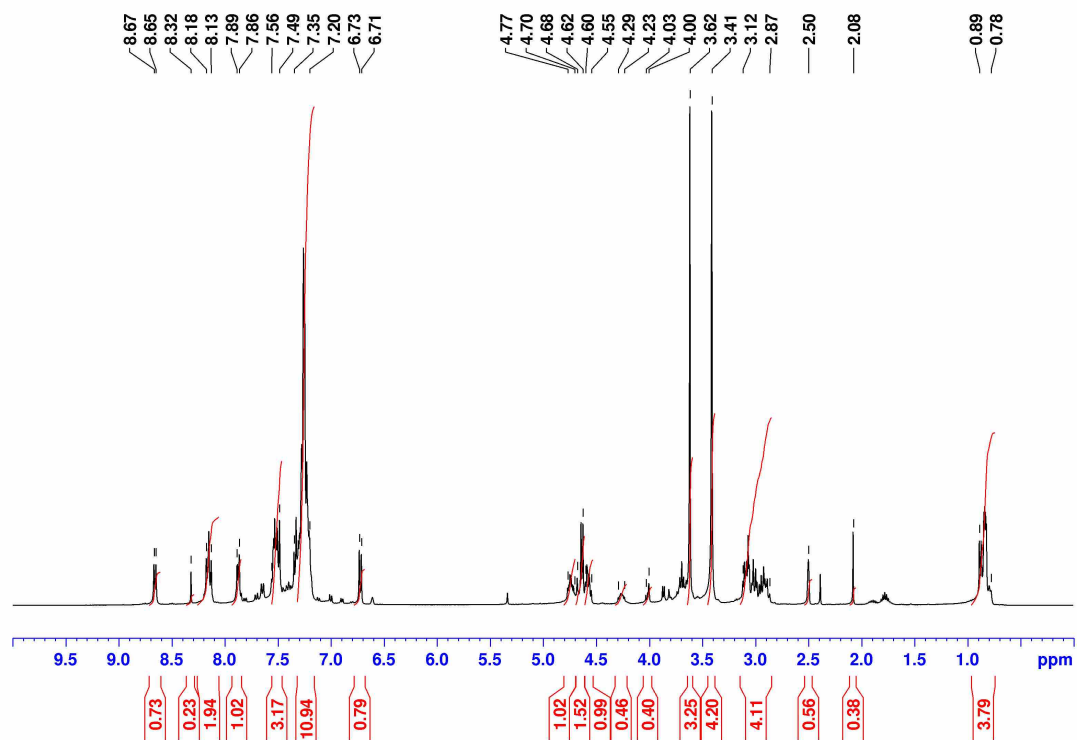


Figure A3-9.  $^1\text{H}$  NMR spectrum of 1Nap-005 in  $\text{d}_6$ -DMSO at 25 °C.

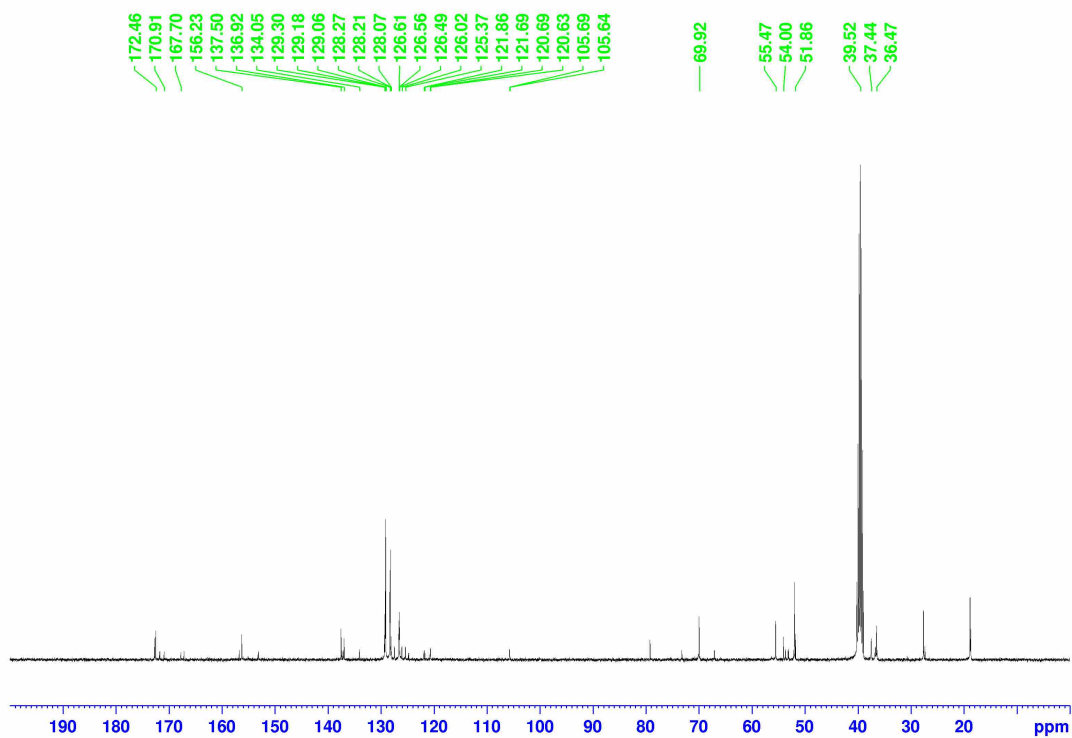
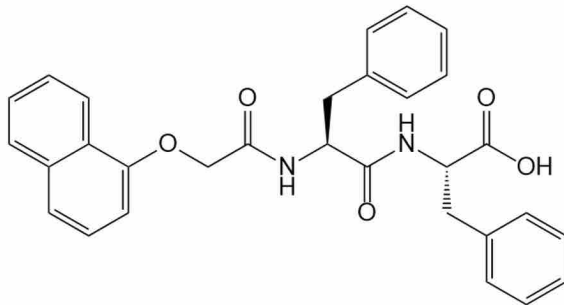


Figure A3-10.  $^{13}\text{C}$  NMR spectrum of 1Nap-005 in  $\text{d}_6$ -DMSO at 25 °C.

**(2S)-2-[(2S)-2-[2-(Naphthalen-1-yloxy)acetamido]-3-phenylpropanamido]-3-phenylpropanoic acid (1Nap-006)**



To deprotect the C-terminus, an aqueous solution of lithium hydroxide (1.4 g, 4 eq., 56.4 mmol) in deionized water (20 mL) was added to 1Nap-005 (7.2 g, 14.1 mmol) in tetrahydrofuran (60 mL), and the mixture was stirred for 18 h. Subsequently, the obtained solution was transferred to hydrochloric acid (200 mL, 1.0 M) and stirred for 1 h to allow complete precipitation. The resulting white precipitate was collected by filtration, washed thoroughly using deionized water (200 mL) and diethyl ether (10 mL), and dried in vacuo to give 1Nap-006 as a white powder in a yield of 83% (Scheme A3-1).

$\delta_{\text{H}}$  (400 MHz, DMSO- $d_6$ , 25 °C) 12.86 (0.9H, br s, COOH), 8.49 (0.9H, d,  $J$  7.90 Hz, NH), 8.16-8.11 (1.9H, m,  $\text{H}_{\text{Ar}}$ ), 7.89-7.86 (1.0H, m, NH), 7.56-7.48 (3.0H, m,  $\text{H}_{\text{Ar}}$ ), 7.35-7.17 (11.1H, m,  $\text{H}_{\text{Ar}}$ ), 6.71 (1.0H, d,  $J$  7.44 Hz, NH), 4.73 (1.0H, td,  $J$  9.04, 4.24 Hz,  $\text{CH}^*$ ), 4.62 (2.0H, dd,  $J$  22.60, 14.68 Hz,  $\text{OCH}_2$ ), 4.55-4.50 (1.0H, m,  $\text{CH}^*$ ), 3.39 (1.0H, br s,  $\text{H}_2\text{O}$ ), 3.15-3.06 (2.0H, m,  $\text{PhCH}_2$ ), 2.99-2.88 (2.0H, m,  $\text{PhCH}_2$ ), 2.50 (0.6H, quintet, residual DMSO- $d_5$ ), 2.07 (0.02H, s,  $\text{CH}_3$  in acetone).  $\delta_{\text{C}}$  (100 MHz, DMSO- $d_6$ , 25 °C) 172.75, 170.78, and 167.10 ( $\text{C}=\text{O}$ ), 153.07, 137.41, 137.39, 134.03, 129.35, 129.16, 128.21, 128.05, 127.44, 126.54, 126.49, 126.34, 126.03, 125.38, 124.72, 121.69, 120.64 and 105.65 ( $\text{C}_{\text{Ar}}$ ), 67.07 ( $\text{OCH}_2$ ), 53.52 ( $\text{CH}^*$ ), 53.09 ( $\text{CH}^*$ ), 39.52 (septet, DMSO- $d_6$ ), 37.50 ( $\text{PhCH}_2$ ), 36.74 ( $\text{PhCH}_2$ ).

**HRMS (ESI)  $m/z$ :**  $[\text{M}+\text{H}]^+$  accurate mass calculated for  $\text{C}_{30}\text{H}_{28}\text{N}_2\text{HO}_5$ : 497.1998; Found: 497.2071.

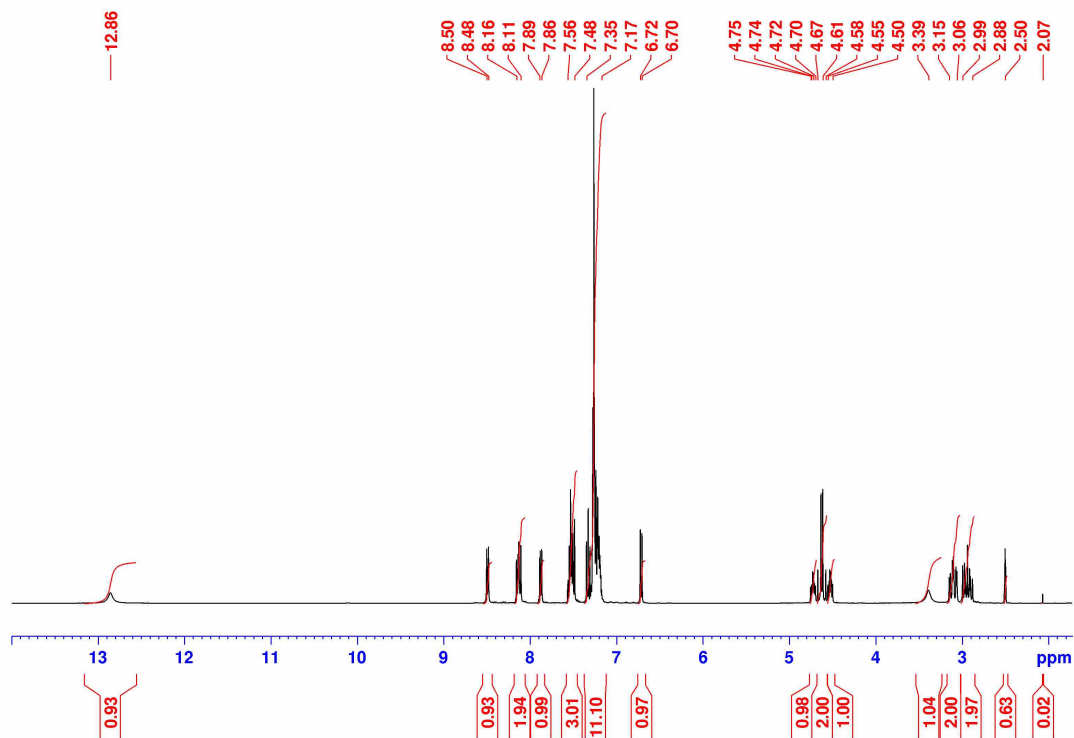


Figure A3-11.  $^1\text{H}$  NMR spectrum of 1Nap-006 in  $d_6$ -DMSO at 25 °C.

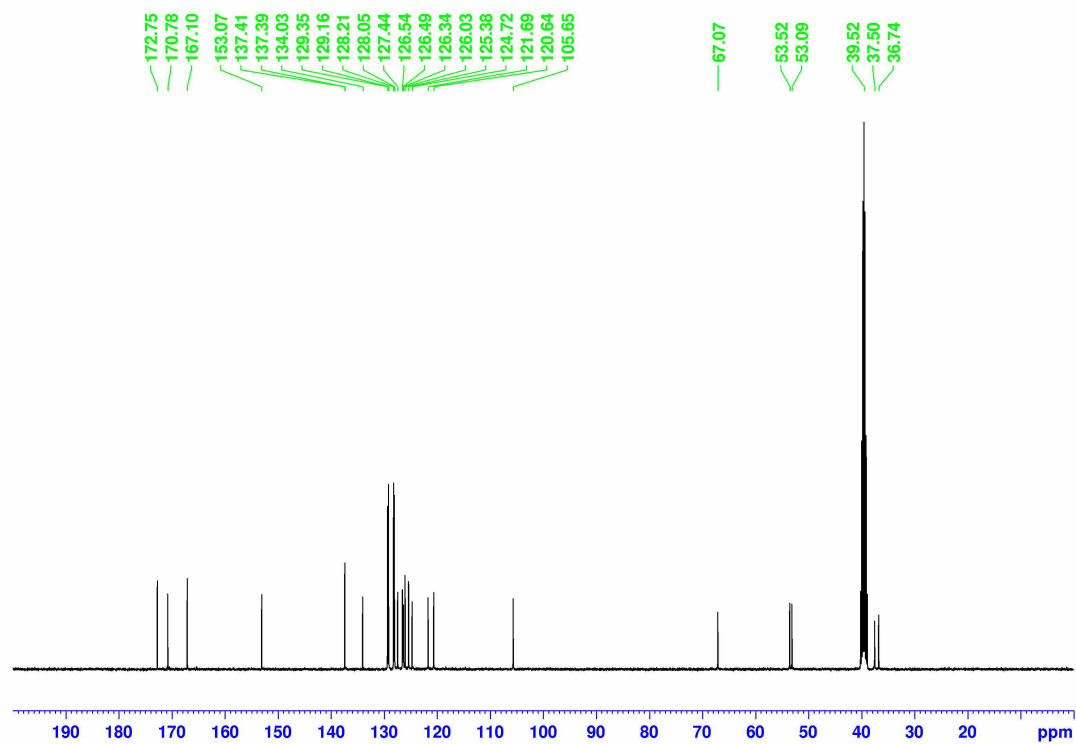
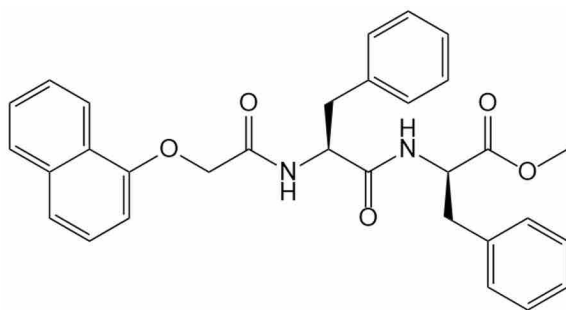


Figure A3-12.  $^{13}\text{C}$  NMR spectrum of 1Nap-006 in  $d_6$ -DMSO at 25 °C.

An identical synthesis approach was adopted to synthesize other target dipeptides from 1-naphthol, 4-chloro-1-naphthol, 6-bromo-2-naphthol, 6-cyano-2-naphthol, and 7-methoxy-2-naphthol. For the (S,R) dipeptide, a similar standard coupling method was followed, except that the second amino acid was substituted to *D*-phenylalanine methyl ester hydrochloride. The NMR spectra and corresponding interpretation of the products obtained in each step during the synthesis procedure are as follows.

**Methyl (2R)-2-[(2S)-2-[2-(naphthalen-1-yloxy)acetamido]-3-phenylpropanamido]-3-phenylpropanoate (1Nap-007)**



$\delta_{\text{H}}$  (400 MHz, DMSO- $d_6$ , 25 °C) 8.75 (0.9H, d,  $J$  8.14 Hz, NH), 8.13 (0.9H, d,  $J$  8.09, NH), 8.07 (0.9H, d,  $J$  8.58 Hz,  $\underline{\text{H}}_{\text{Ar}}$ ), 7.87 (1.0H, d,  $J$  7.68 Hz,  $\underline{\text{H}}_{\text{Ar}}$ ), 7.55-7.48 (3.0H, m,  $\underline{\text{H}}_{\text{Ar}}$ ), 7.35-7.01 (11.2H, m,  $\underline{\text{H}}_{\text{Ar}}$ ), 6.73 (1.0H, d,  $J$  7.68 Hz,  $\underline{\text{H}}_{\text{Ar}}$ ), 4.74-4.68 (1.2H, m,  $\underline{\text{CH}}^*$ ), 4.64 (1.5H, d,  $J$  7.21 Hz,  $\underline{\text{OCH}}_2$ ), 4.59-4.52 (1.1H, m,  $\underline{\text{CH}}^*$ ), 3.65 (3.1H, s,  $\underline{\text{OCH}}_3$ ), 3.38 (5.7H, br s,  $\underline{\text{H}}_2\text{O}$ ), 3.11 (0.9H, dd,  $J$  13.66, 4.90 Hz,  $\text{PhC}_b\underline{\text{H}}_a\underline{\text{H}}_b$ ), 2.91 (1.0H, q,  $J$  10.12 Hz,  $\text{PhC}_b\underline{\text{H}}_a\underline{\text{H}}_b$ ), 2.81 (0.9H, dd,  $J$  13.70, 4.22 Hz,  $\text{PhC}_a\underline{\text{H}}_a\underline{\text{H}}_b$ ), 2.70 (0.9H, q,  $J$  8.96 Hz,  $\text{PhC}_a\underline{\text{H}}_a\underline{\text{H}}_b$ ), 2.50 (0.8H, quintet, residual DMSO- $d_5$ ).  $\delta_{\text{C}}$  (100 MHz, DMSO- $d_6$ , 25 °C) 171.94, 170.75, and 167.09 ( $\underline{\text{C}}=\text{O}$ ), 153.06, 137.16, 137.14, 134.04, 129.28, 129.25, 128.31, 128.02, 127.46, 126.70, 126.56, 126.33, 126.04, 125.39, 124.70, 121.66, 120.64, and 105.61 ( $\underline{\text{C}}_{\text{Ar}}$ ), 67.01 ( $\underline{\text{OCH}}_2$ ), 53.59 ( $\underline{\text{CH}}^*$ ), 53.07 ( $\underline{\text{CH}}^*$ ), 52.04 ( $\underline{\text{OCH}}_3$ ), 39.52 (septet, DMSO- $d_6$ ), 37.76 ( $\text{Ph}\underline{\text{C}}_b\underline{\text{H}}_2$ ), 36.93 ( $\text{Ph}\underline{\text{C}}_a\underline{\text{H}}_2$ ).

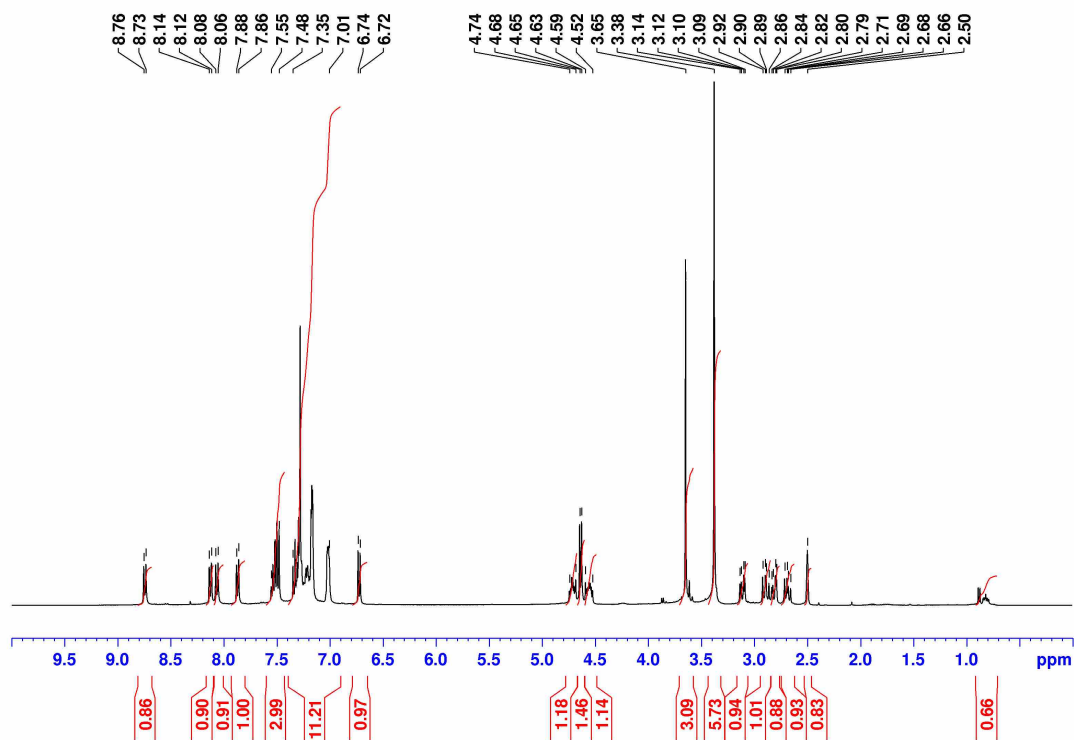


Figure A3-13.  $^1\text{H}$  NMR spectrum of 1Nap-007 in  $\text{d}_6\text{-DMSO}$  at  $25\text{ }^\circ\text{C}$ .

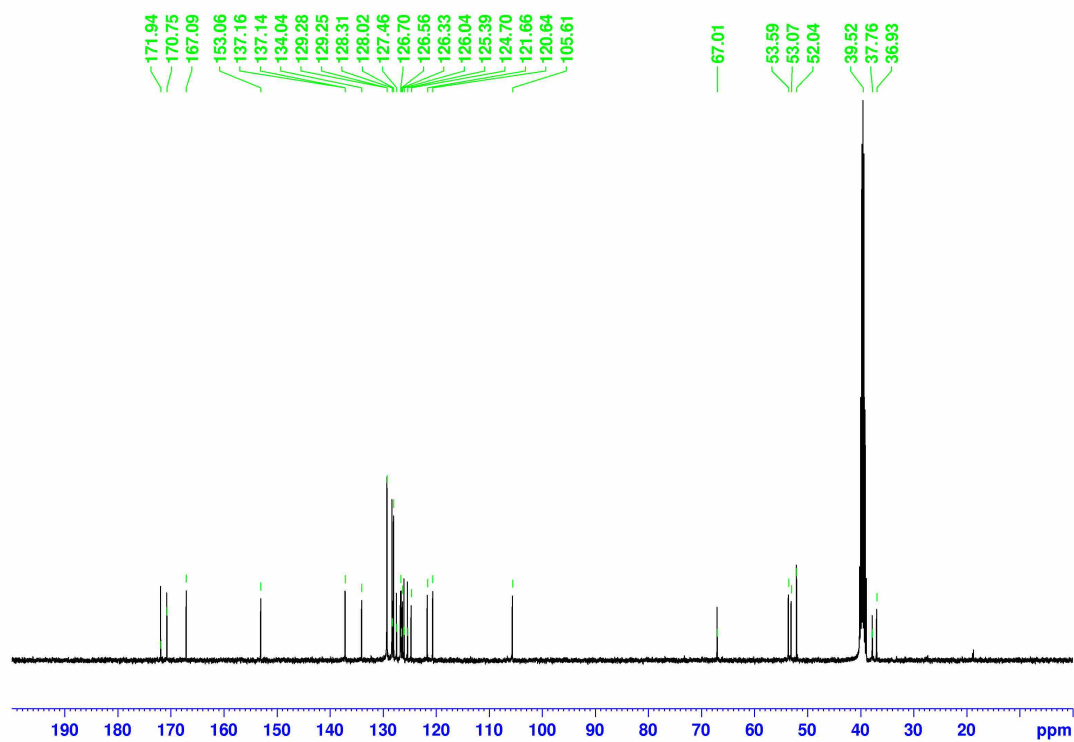
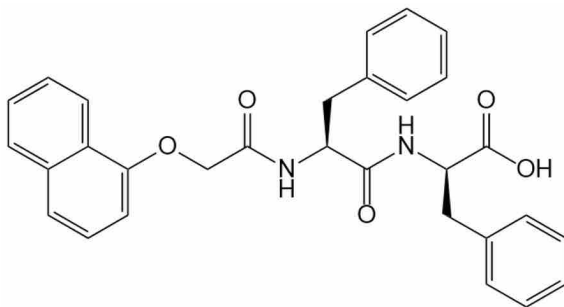


Figure A3-14.  $^{13}\text{C}$  NMR spectrum of 1Nap-007 in  $\text{d}_6\text{-DMSO}$  at  $25\text{ }^\circ\text{C}$ .

**(2R)-2-[(2S)-2-[2-(Naphthalen-1-yloxy)acetamido]-3-phenylpropanamido]-3-phenylpropanoic acid (1Nap-008)**



$\delta_{\text{H}}$  (400 MHz, DMSO- $d_6$ , 25 °C) 12.83 (0.2H, br s, COOH), 8.63 (1.1H, d,  $J$  8.36 Hz, NH), 8.13 (1.1H, d,  $J$  8.48 Hz, NH), 8.05 (1.0H, d,  $J$  8.60 Hz,  $\text{H}_{\text{Ar}}$ ), 7.87 (1.1H, d,  $J$  7.64 Hz,  $\text{H}_{\text{Ar}}$ ), 7.55-7.48 (3.4H, m,  $\text{H}_{\text{Ar}}$ ), 7.35-7.15 (8.8H, m,  $\text{H}_{\text{Ar}}$ ), 7.00-6.98 (1.8H, m,  $\text{H}_{\text{Ar}}$ ), 6.73 (0.9H, d,  $J$  7.68 Hz,  $\text{H}_{\text{Ar}}$ ), 4.74 (1.0H, td,  $J$  8.68, 4.18 Hz,  $\text{CH}^*$ ), 4.64 (1.9H, q,  $J$  14.74 Hz,  $\text{OCH}_2$ ), 4.55-4.49 (1.0H, m,  $\text{CH}^*$ ), 3.48 (2.9H, br s,  $\text{H}_2\text{O}$ ), 3.15 (1.1H, dd,  $J$  13.67, 4.41 Hz,  $\text{Ph}_a\text{CH}_a\text{H}_b$ ), 2.91-2.88 (0.8H, m,  $\text{Ph}_a\text{CH}_a\text{H}_b$ ), 2.85-2.81 (1.1H, m,  $\text{Ph}_b\text{CH}_a\text{H}_b$ ), 2.68 (1.0H, q,  $J$  8.89 Hz,  $\text{Ph}_b\text{CH}_a\text{H}_b$ ), 2.50 (0.6H, quintet, residual DMSO- $d_5$ ).  $\delta_{\text{C}}$  (100 MHz, DMSO- $d_6$ , 25 °C) 172.96, 170.62, and 167.07 ( $\text{C}=\text{O}$ ), 153.08, 137.58, 137.21, 134.07, 129.35, 129.31, 128.28, 128.02, 127.49, 126.62, 126.59, 126.32, 126.07, 125.43, 124.73, 121.68, 120.68, and 105.65 ( $\text{C}_{\text{Ar}}$ ), 67.06 ( $\text{OCH}_2$ ), 53.62 ( $\text{CH}^*$ ), 53.10 ( $\text{CH}^*$ ), 39.52 (septet, DMSO- $d_6$ ), 37.87 ( $\text{Ph}_b\text{CH}_2$ ), 37.05 ( $\text{Ph}_a\text{CH}_2$ ).

**HRMS (ESI)  $m/z$ :**  $[\text{M}+\text{H}]^+$  accurate mass calculated for  $\text{C}_{30}\text{H}_{28}\text{N}_2\text{HO}_5$ : 497.1998; Found: 497.2073.

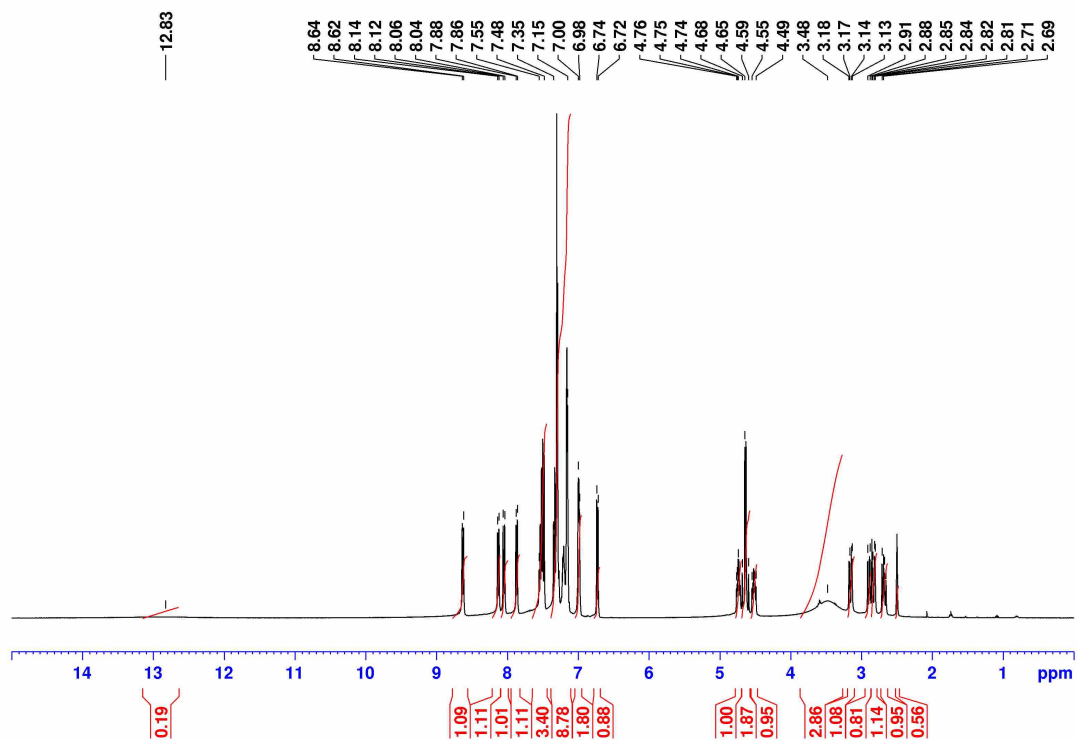


Figure A3-15.  $^1\text{H}$  NMR spectrum of 1Nap-008 in  $d_6$ -DMSO at 25 °C.

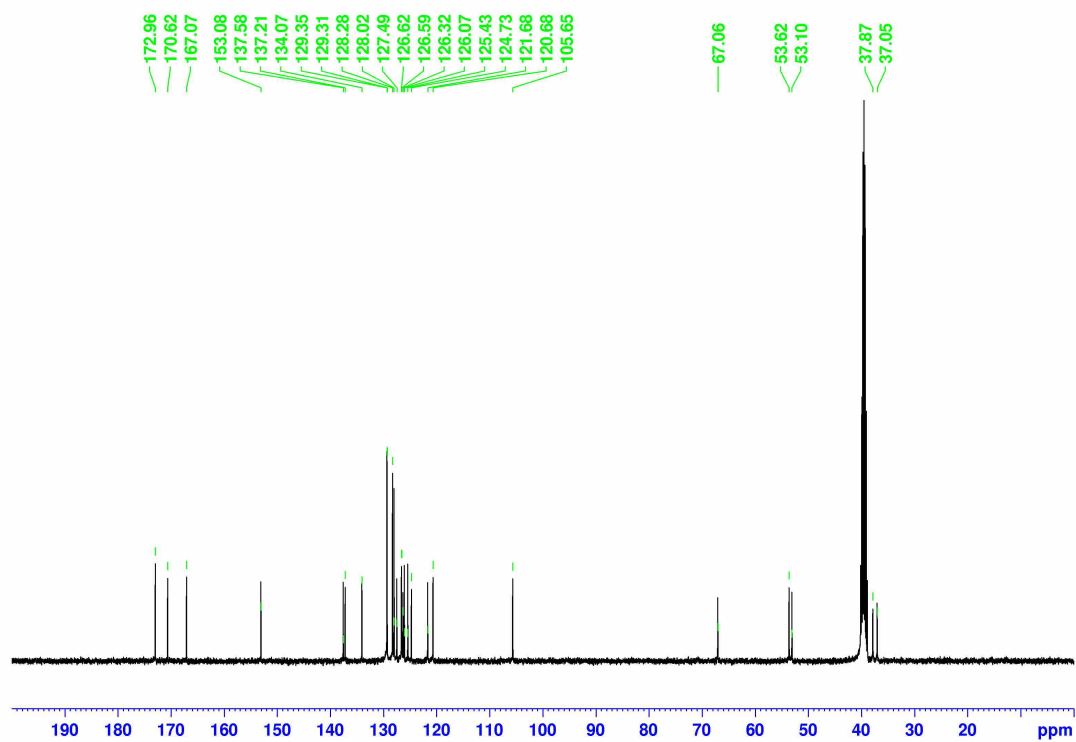
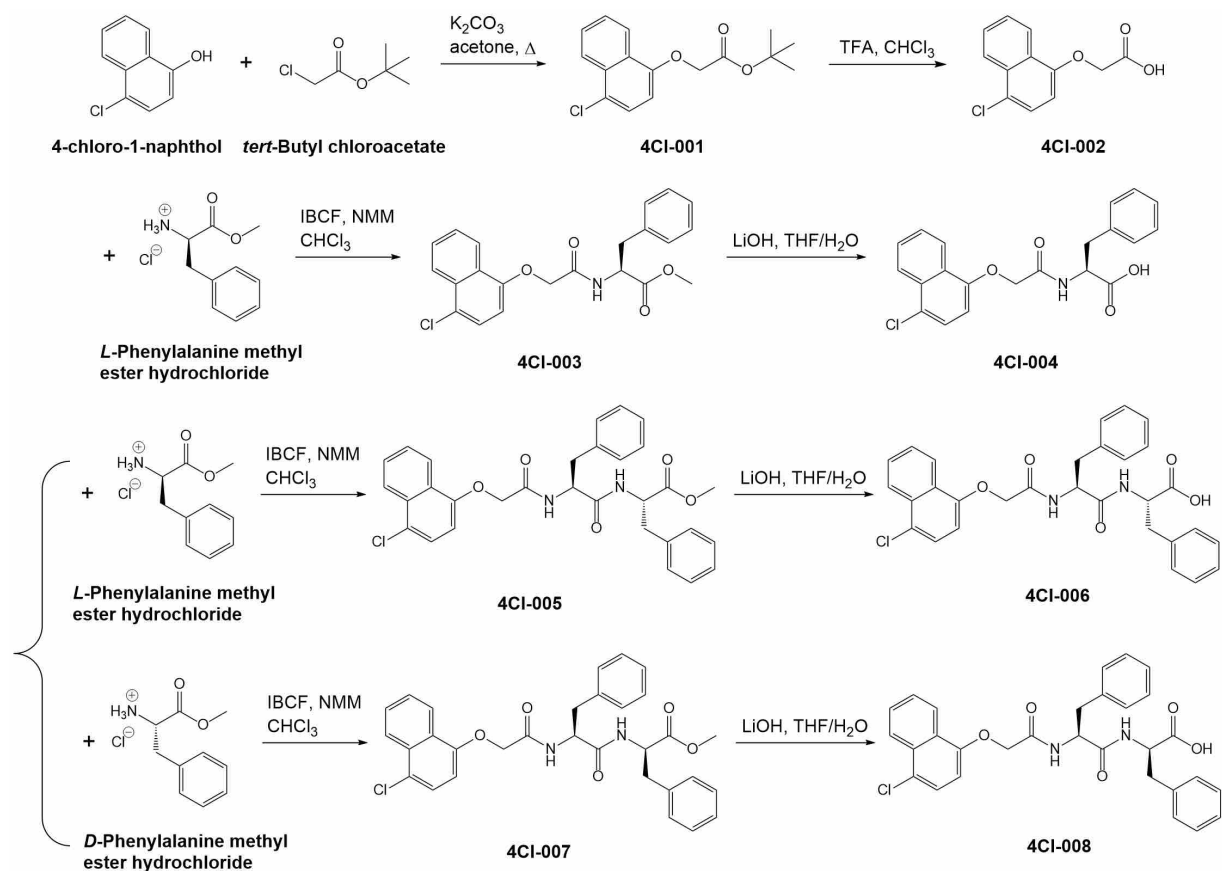


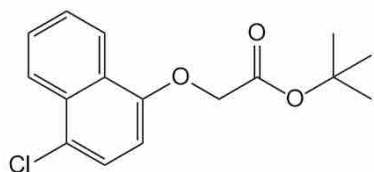
Figure A3-16.  $^{13}\text{C}$  NMR spectrum of 1Nap-008 in  $d_6$ -DMSO at 25 °C.

### A3.2.2 4Cl1NapFF



Scheme A3-2. Synthetic route of 4Cl1NapFF.

#### Tert-butyl 2-[(4-chloronaphthalen-1-yl)oxy]acetate (4CI-001)



$\delta_{\text{H}}$  (400 MHz, DMSO- $d_6$ ) 8.32 (0.1H, s,  $\underline{\text{CH}}$  in chloroform), 8.30 (1.0H, d,  $J$  8.40 Hz,  $\underline{\text{NH}}$ ), 8.11 (1.0H, d,  $J$  8.32 Hz,  $\underline{\text{NH}}$ ), 7.72-7.68 (1.0H, m,  $\underline{\text{H}}_{\text{Ar}}$ ), 7.65-7.61 (1.0H, m,  $\underline{\text{H}}_{\text{Ar}}$ ), 7.56 (1.0H, d,  $J$  8.28 Hz,  $\underline{\text{H}}_{\text{Ar}}$ ), 6.88 (1.0H, d,  $J$  8.36 Hz,  $\underline{\text{H}}_{\text{Ar}}$ ), 4.87 (2.0H, s,  $\underline{\text{CH}}^*$ ), 3.39 (1.8H, br s,  $\underline{\text{H}}_2\text{O}$ ), 2.50 (0.3H, quintet, residual DMSO- $d_5$ ), 1.43 (7.3H, s, Rot-2  $\text{C}(\underline{\text{CH}}_3)_3$ ), 1.42 (2.3H, s, Rot-1  $\text{C}(\underline{\text{CH}}_3)_3$ ).  $\delta_{\text{C}}$  (100 MHz, DMSO- $d_6$ , 25 °C) 167.39 ( $\underline{\text{C}}=\text{O}$ ), 152.51, 130.47, 128.02, 126.40, 126.03, 125.98, 123.57, 122.33, and 105.89 ( $\underline{\text{C}}_{\text{Ar}}$ ), 81.58 ( $\underline{\text{C}}(\underline{\text{CH}}_3)_3$ ), 79.18 ( $\underline{\text{CH}}$  in chloroform), 65.57 ( $\underline{\text{OCH}}_2$ ), 39.52 (septet, DMSO- $d_6$ ), 27.67 (Rot-2  $\text{C}(\underline{\text{CH}}_3)_3$ ), 27.51 (Rot-1  $\text{C}(\underline{\text{CH}}_3)_3$ ).

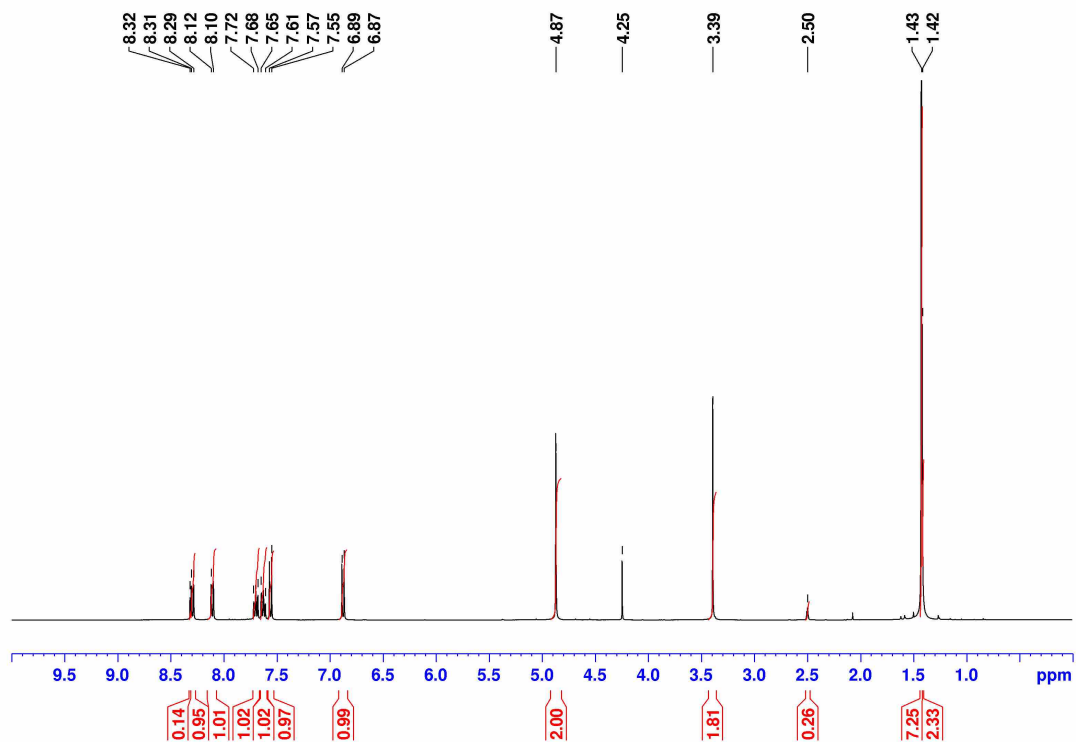


Figure A3-17.  $^1\text{H}$  NMR spectrum of 4Cl-001 in  $\text{d}_6$ -DMSO at 25 °C.

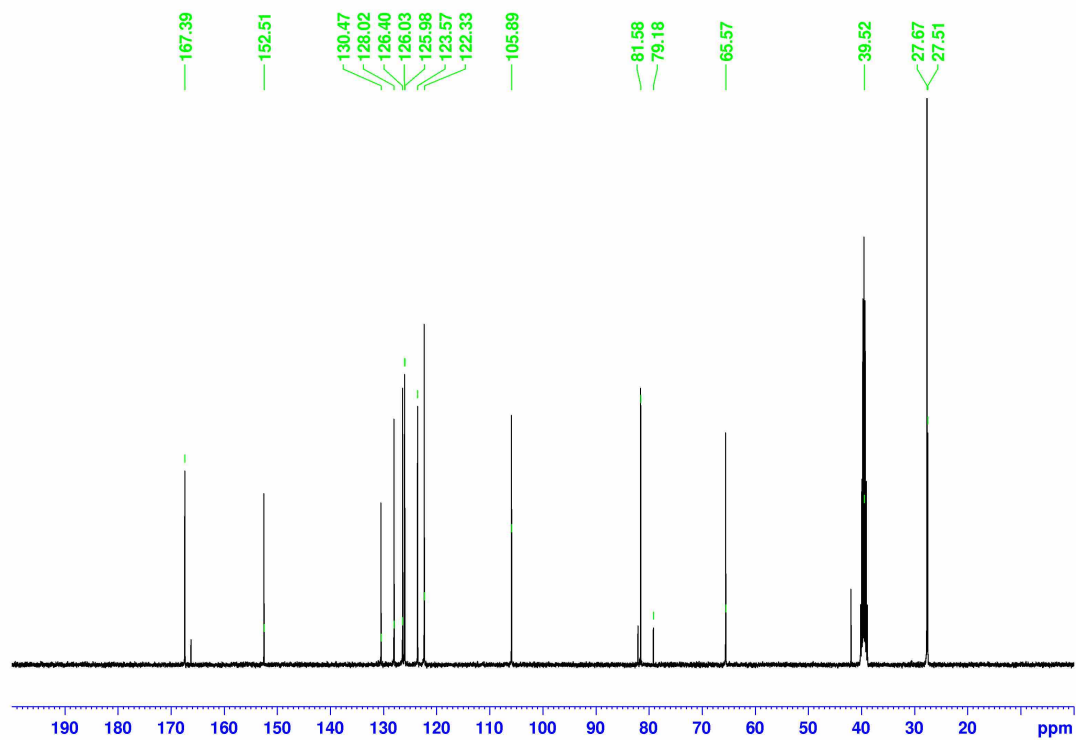
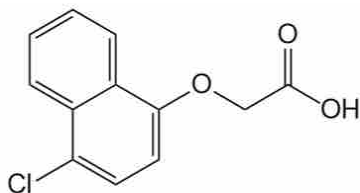
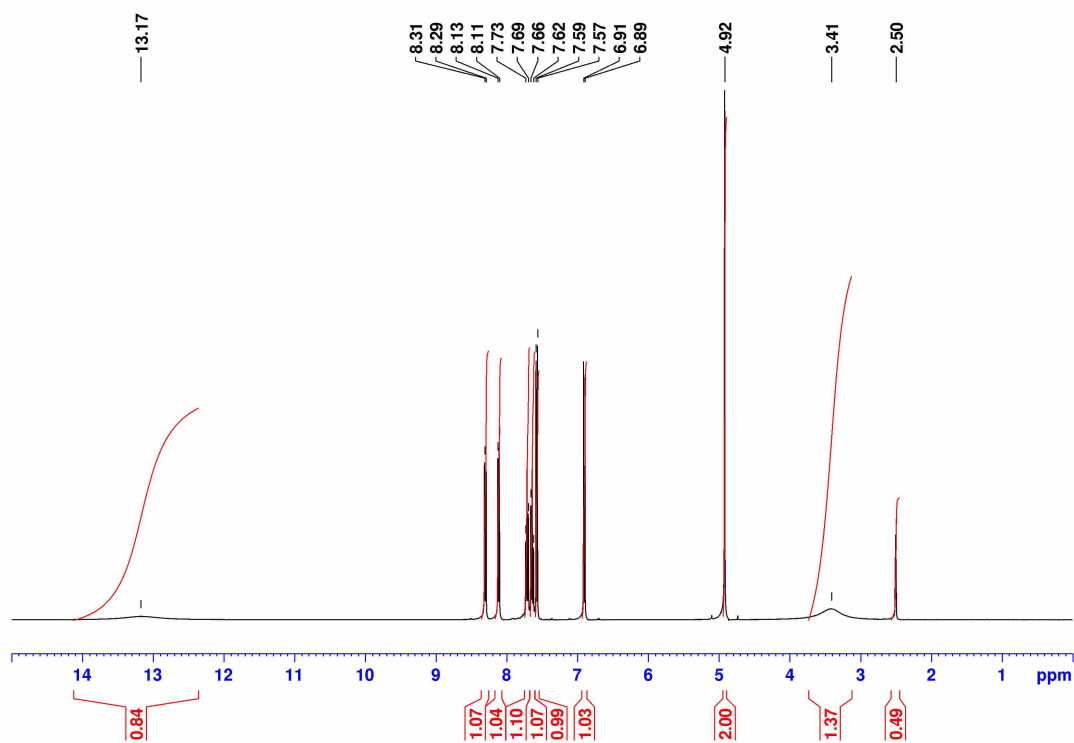


Figure A3-18.  $^{13}\text{C}$  NMR spectrum of 4Cl-001 in  $\text{d}_6$ -DMSO at 25 °C.

2-[(4-Chloronaphthalen-1-yl)oxy]acetic acid (**4Cl-002**)

$\delta_{\text{H}}$  (400 MHz, DMSO- $d_6$ ) 13.17 (0.8H, br s, COOH), 8.30 (1.1H, d,  $J$  8.36 Hz,  $\text{H}_{\text{Ar}}$ ), 8,12 (1.0H, d,  $J$  8.40 Hz,  $\text{H}_{\text{Ar}}$ ), 7.73-7.69 (1.1H, m,  $\text{H}_{\text{Ar}}$ ), 7.66-7.62 (1.1H, m,  $\text{H}_{\text{Ar}}$ ), 7.58 (1.0H, d,  $J$  8.32 Hz,  $\text{H}_{\text{Ar}}$ ), 6.90 (1.0H, d,  $J$  8.36 Hz,  $\text{H}_{\text{Ar}}$ ), 4.92 (2.0H, s,  $\text{OCH}_2$ ), 3.41 (1.4H, br s,  $\text{H}_2\text{O}$ ), 2.50 (0.5H, quintet, residual DMSO- $d_5$ ).  $\delta_{\text{C}}$  (100 MHz, DMSO- $d_6$ , 25 °C) 169.85 ( $\text{C}=\text{O}$ ), 152.62, 130.50, 128.08, 126.44, 126.12, 125.99, 123.61, 122.40, 122.25, 105.87 ( $\text{C}_{\text{Ar}}$ ), 65.12 ( $\text{OCH}_2$ ), 39.52 (septet, DMSO- $d_6$ ).



**Figure A3-19.**  $^1\text{H}$  NMR spectrum of 4Cl-002 in  $d_6$ -DMSO at 25 °C.

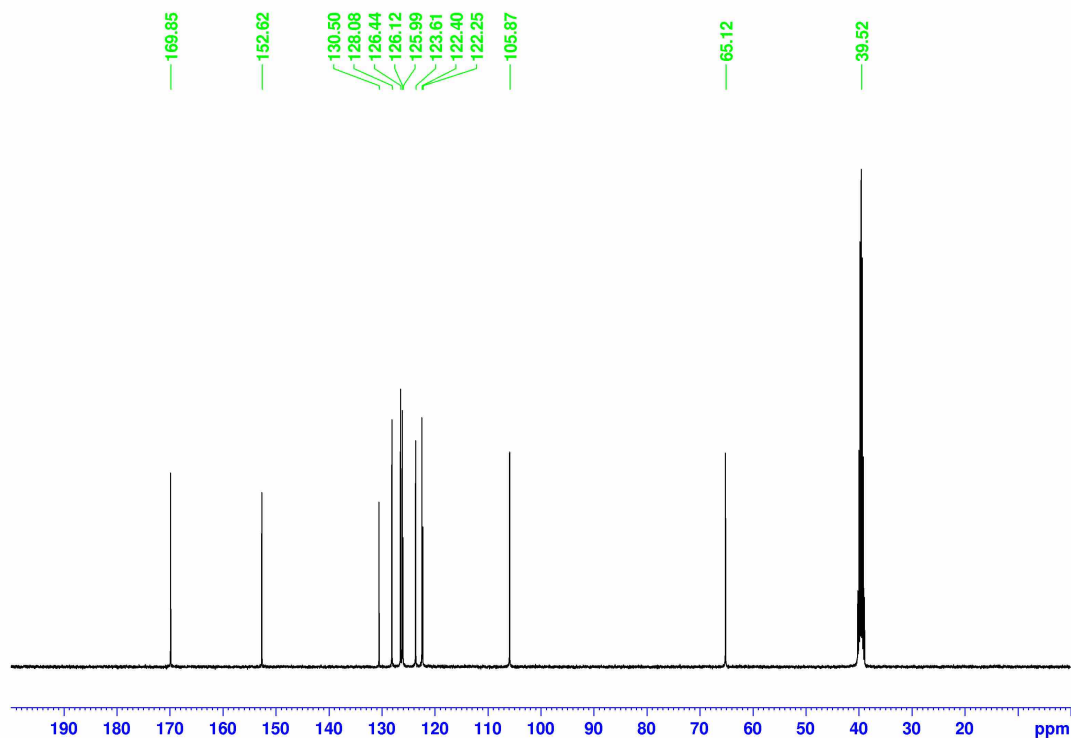
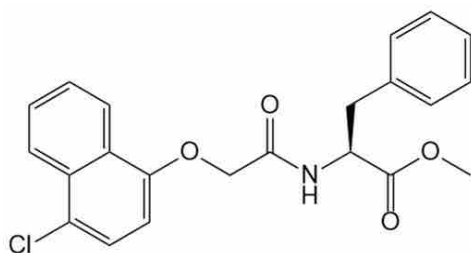


**Figure A3-20.**  $^{13}\text{C}$  NMR spectrum of 4Cl-002 in  $\text{d}_6$ -DMSO at 25 °C.

**Methyl (2S)-2-{2-[(4-chloronaphthalen-1-yl)oxy]acetamido}-3-phenylpropanoate (4Cl-003)**



$\delta_{\text{H}}$  (400 MHz,  $\text{DMSO-d}_6$ ) 8.56 (1.0H, d,  $J$  8.00 Hz,  $\text{NH}$ ), 8.30 (1.5H, d,  $J$  7.28 Hz,  $\text{NH}$ , overlapped by CH in chloroform), 8.12 (1.0H, d,  $J$  8.36 Hz,  $\text{H}_{\text{Ar}}$ ), 7.75-7.71 (1.0H, m,  $\text{H}_{\text{Ar}}$ ), 7.67-7.63 (1.0H, m,  $\text{H}_{\text{Ar}}$ ), 7.52 (0.9H, d,  $J$  8.31 Hz,  $\text{H}_{\text{Ar}}$ ), 7.28-7.19 (4.9H, m,  $\text{H}_{\text{Ar}}$ ), 6.75 (1.0H, d,  $J$  8.37 Hz,  $\text{H}_{\text{Ar}}$ ), 4.76-4.72 (1.0H, m,  $\text{CH}^*$ ), 4.69-4.62 (1.9H, m,  $\text{OCH}_2$ ), 3.66 (2.9H, s,  $\text{OCH}_3$ ), 3.37 (3.9H, br s,  $\text{H}_2\text{O}$ ), 3.15 (1.0H, dd,  $J$  13.80, 5.08 Hz,  $\text{PhCH}_a\text{H}_b$ ), 3.04 (1.0H, dd,  $J$  13.80, 9.52 Hz,  $\text{PhCH}_a\text{H}_b$ ), 2.50 (0.7H, quintet, residual  $\text{DMSO-d}_5$ ).  $\delta_{\text{C}}$  (100 MHz,  $\text{DMSO-d}_6$ , 25 °C) 171.66, 167.43 ( $\text{C}=\text{O}$ ), 152.54, 137.15, 130.44, 129.13, 128.28, 128.10, 126.57, 126.36, 126.05, 125.86, 123.54, 122.67, 122.41 and 106.02 ( $\text{C}_{\text{Ar}}$ ), 79.19 ( $\text{CH}$  in chloroform), 67.24 ( $\text{OCH}_2$ ), 53.18 ( $\text{CH}^*$ ), 52.06 ( $\text{OCH}_3$ ), 39.52 (septet,  $\text{DMSO-d}_6$ ), 36.31 ( $\text{PhCH}_2$ ).

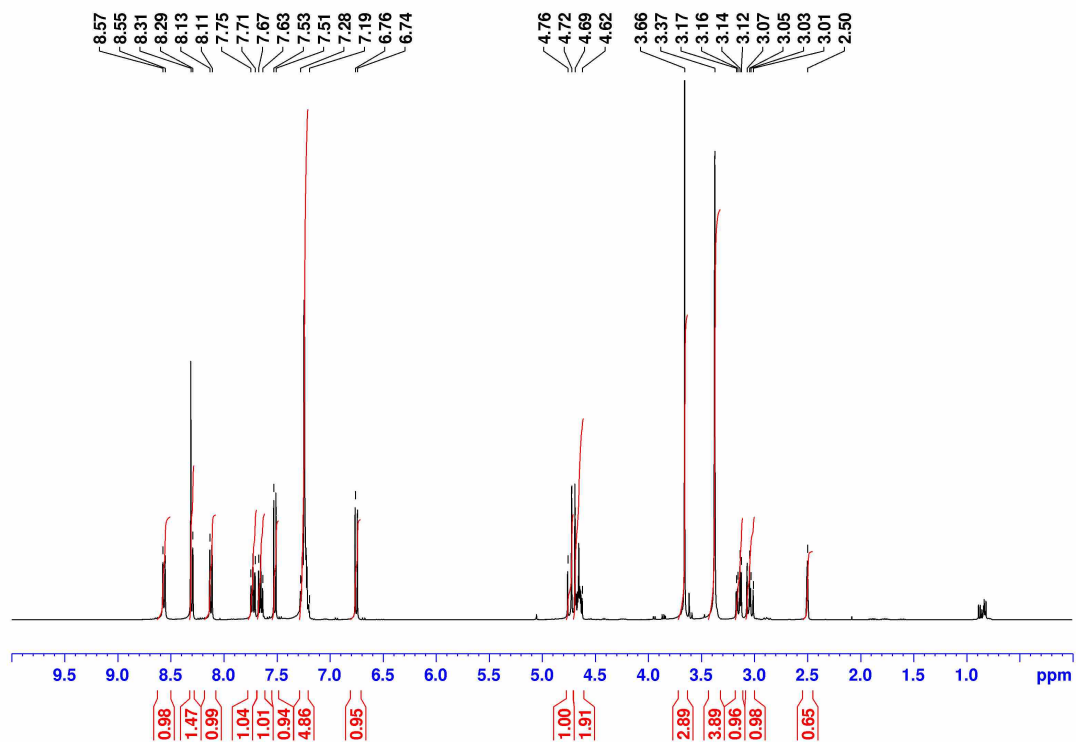


Figure A3-21.  $^1\text{H}$  NMR spectrum of 4Cl-003 in  $d_6$ -DMSO at 25 °C.

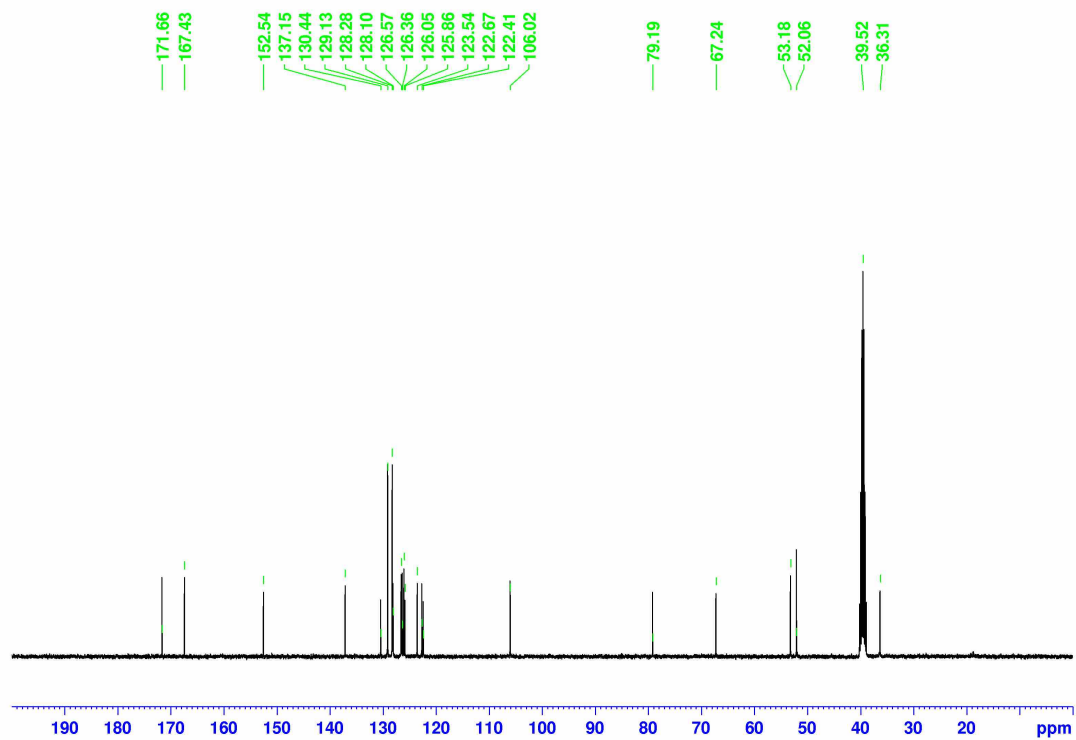
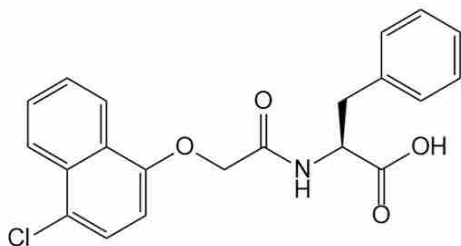
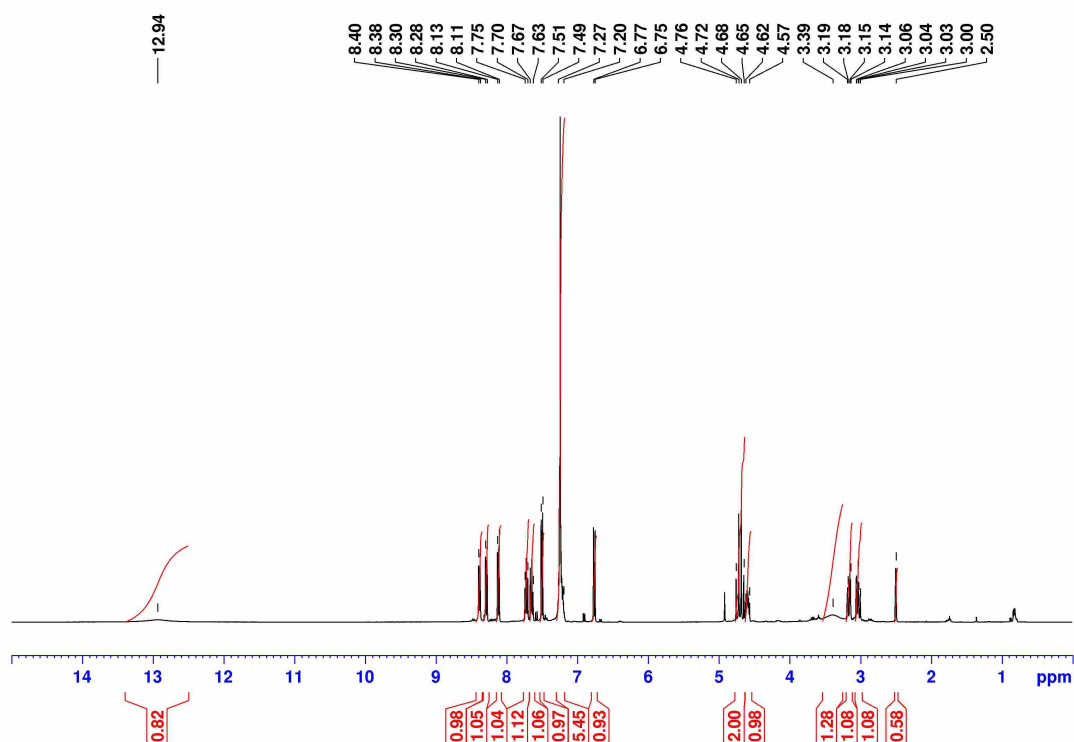


Figure A3-22.  $^{13}\text{C}$  NMR spectrum of 4Cl-003 in  $d_6$ -DMSO at 25 °C.

**(2S)-2-{2-[(4-Chloronaphthalen-1-yl)oxy]acetamido}-3-phenylpropanoic acid (4Cl-004)**

$\delta_{\text{H}}$  (400 MHz, DMSO- $d_6$ ) 12.94 (0.8H, br s, COOH), 8.39 (1.0H, d,  $J$  8.16 Hz, NH), 8.29 (1.1H, d,  $J$  8.20 Hz,  $\text{H}_{\text{Ar}}$ ), 8.12 (1.0H, d,  $J$  8.28 Hz,  $\text{H}_{\text{Ar}}$ ), 7.75-7.70 (1.1H, m,  $\text{H}_{\text{Ar}}$ ), 7.67-7.63 (1.1H, m,  $\text{H}_{\text{Ar}}$ ), 7.50 (1.0H, d,  $J$  8.31 Hz,  $\text{H}_{\text{Ar}}$ ), 7.27-7.20 (5.5H, m,  $\text{H}_{\text{Ar}}$ ), 6.76 (0.9H, d,  $J$  8.38 Hz,  $\text{H}_{\text{Ar}}$ ), 4.70 (2.0H, q,  $J$  14.67 Hz,  $\text{OCH}_2$ ), 4.62-4.57 (1.0H, m,  $\text{CH}^*$ ), 3.39 (1.3H, br s,  $\text{H}_2\text{O}$ ), 3.16 (1.1H, dd,  $J$  13.82, 4.65 Hz,  $\text{PhCH}_a\text{H}_b$ ), 3.03 (1.1H, q,  $J$  9.48 Hz,  $\text{PhCH}_a\text{H}_b$ ), 2.50 (0.6H, quintet, residual DMSO- $d_5$ ).  $\delta_{\text{C}}$  (100 MHz, DMSO- $d_6$ , 25 °C) 172.67, 167.27 (C=O), 152.53, 137.50, 130.44, 129.18, 128.24, 128.12, 126.49, 126.39, 126.09, 125.87, 123.57, 123.57, 122.64, 122.39 and 106.08 ( $\text{C}_{\text{Ar}}$ ), 67.30 ( $\text{OCH}_2$ ), 53.13 ( $\text{CH}^*$ ), 39.52 (septet, DMSO- $d_6$ ), 36.39 ( $\text{PhCH}_2$ ).



**Figure A3-23.**  $^1\text{H}$  NMR spectrum of 4Cl-004 in  $d_6$ -DMSO at 25 °C.

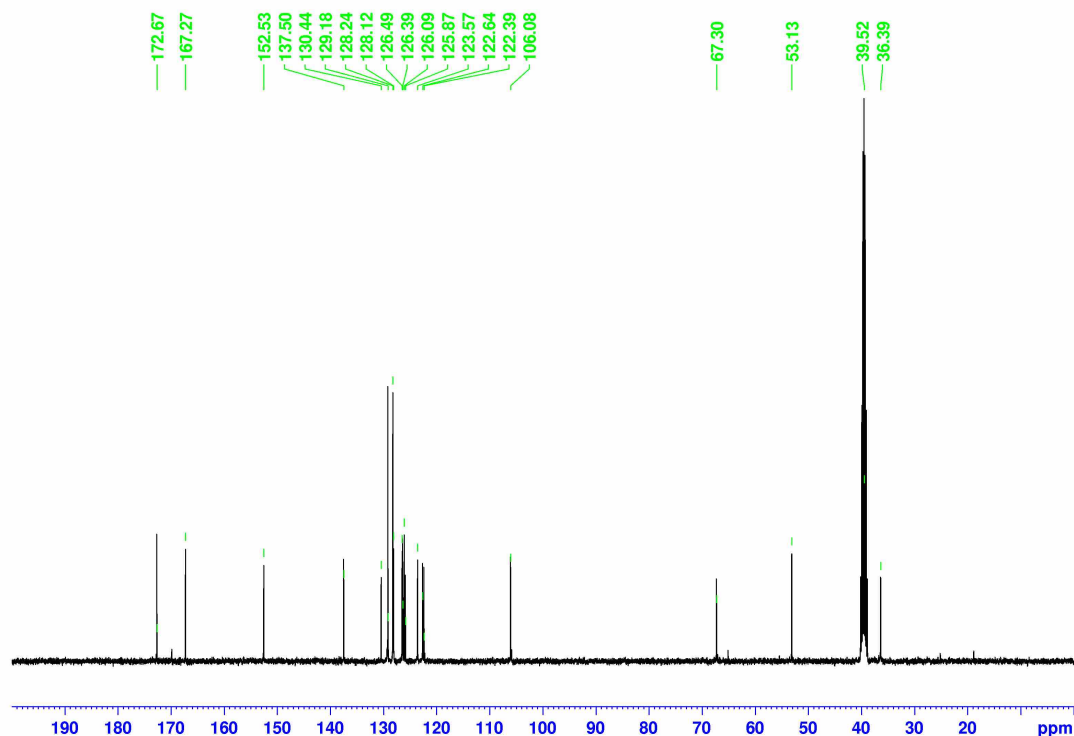
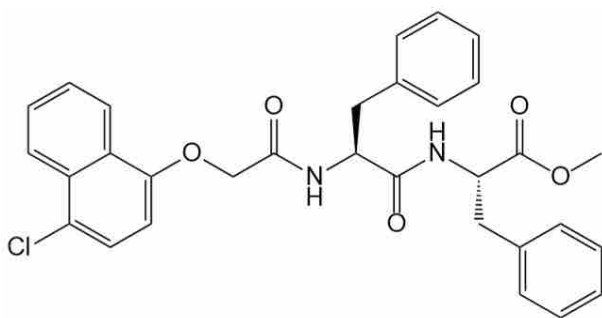


**Figure A3-24.**  $^{13}\text{C}$  NMR spectrum of 4Cl-004 in  $\text{d}_6\text{-DMSO}$  at  $25\text{ }^\circ\text{C}$ .

**Methyl (2S)-2-[(2S)-2-{2-[(4-chloronaphthalen-1-yl)oxy]acetamido}-3-phenylpropanamido]-3-phenylpropanoate (4Cl-005)**



$\delta_{\text{H}}$  (400 MHz,  $\text{DMSO-d}_6$ ,  $25\text{ }^\circ\text{C}$ ) 8.63 (0.9H, d,  $J$  7.56 Hz,  $\text{NH}$ ), 8.23 (0.9H, d,  $J$  8.35 Hz,  $\text{NH}$ ), 8.19 (1.0H, d,  $J$  8.53 Hz,  $\text{H}_{\text{Ar}}$ ), 8.12 (1.0H, d,  $J$  8.40 Hz,  $\text{H}_{\text{Ar}}$ ), 7.74-7.70 (1.0H, m,  $\text{H}_{\text{Ar}}$ ), 7.66-7.62 (1.0H, m,  $\text{H}_{\text{Ar}}$ ), 7.47 (1.0H, d,  $J$  8.32 Hz,  $\text{H}_{\text{Ar}}$ ), 7.29-7.18 (10.0H, m,  $\text{H}_{\text{Ar}}$ ), 6.68 (0.9H, d,  $J$  8.37 Hz,  $\text{H}_{\text{Ar}}$ ), 4.72-4.67 (1.1H, m,  $\text{CH}^*$ ), 4.66-4.60 (1.9H, m,  $\text{OCH}_2$ ), 4.57-4.51 (1.0H, m,  $\text{CH}^*$ ), 3.61 (2.9H, s,  $\text{OCH}_3$ ), 3.37 (10.6H, br s,  $\text{H}_2\text{O}$ ), 3.10-3.02 (2.0H, m,  $\text{PhC}_a\text{H}_b$  and  $\text{PhC}_b\text{H}_a\text{H}_b$ ), 2.97 (1.0H, dd,  $J$  13.78, 8.70 Hz,  $\text{PhC}_b\text{H}_a\text{H}_b$ ), 2.86 (1.0H, dd,  $J$  13.72, 9.60 Hz,  $\text{PhC}_b\text{H}_a\text{H}_b$ ), 2.50 (1.4H, quintet, residual  $\text{DMSO-d}_5$ ).  $\delta_{\text{C}}$  (100 MHz,  $\text{DMSO-d}_6$ ,  $25\text{ }^\circ\text{C}$ ) 171.77, 170.96, and 166.88

(C=O), 152.50, 137.42, 137.01, 130.43, 129.29, 129.10, 128.30, 128.07, 126.62, 126.42, 126.35, 126.09, 125.82, 123.58, 122.52, 122.32, and 105.97 (C<sub>Ar</sub>), 67.21 (OCH<sub>2</sub>), 53.68 (CH<sup>\*</sup>), 53.15 (CH<sup>\*</sup>), 51.92 (OCH<sub>3</sub>), 39.52 (septet, DMSO-d<sub>6</sub>), 37.46 (PhC<sub>b</sub>H<sub>2</sub>), 36.65 (PhC<sub>a</sub>H<sub>2</sub>).

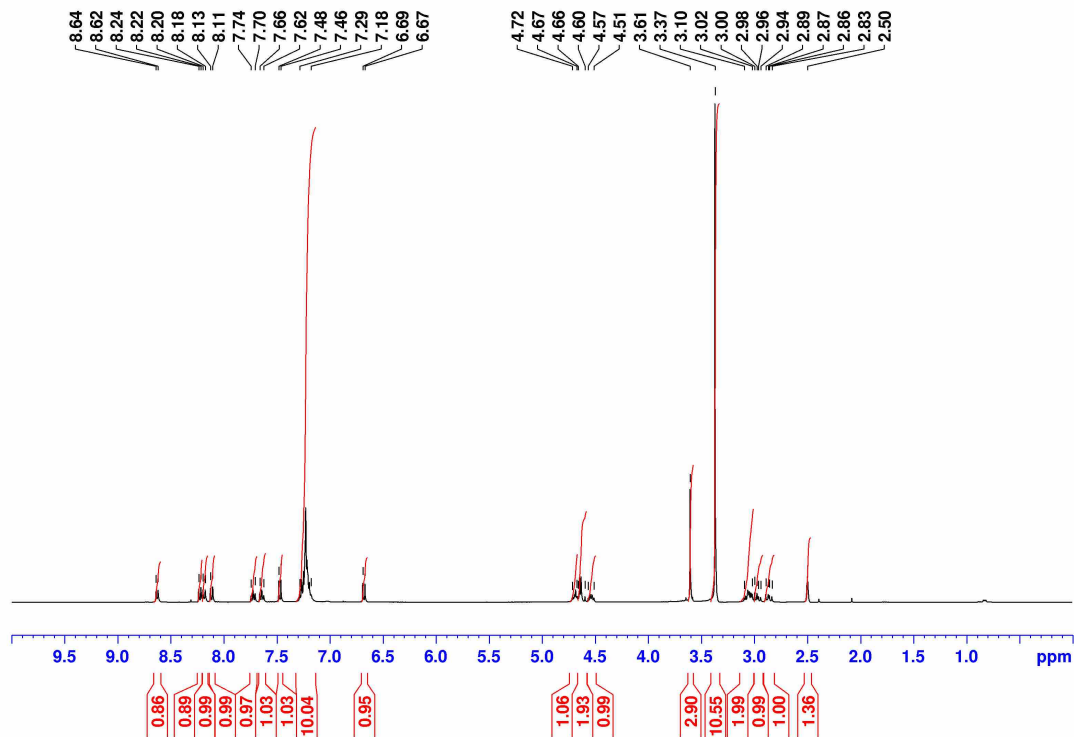


**Figure A3-25.** <sup>1</sup>H NMR spectrum of 4Cl-005 in d<sub>6</sub>-DMSO at 25 °C.

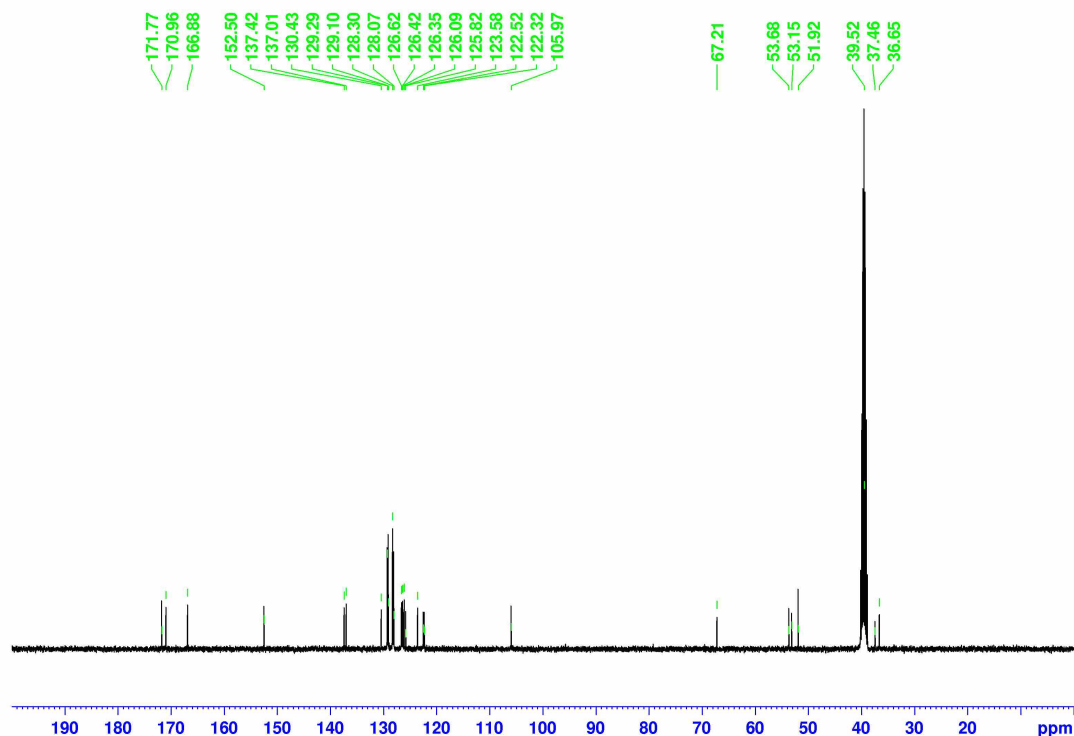
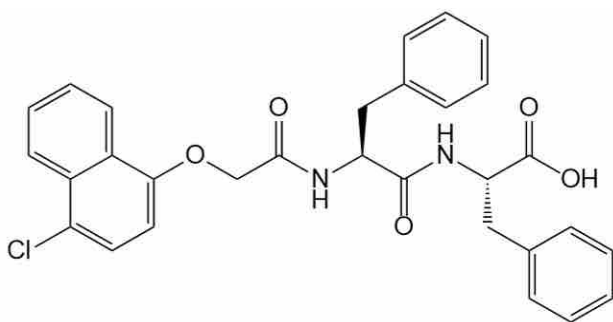


**Figure A3-26.**  $^{13}\text{C}$  NMR spectrum of 4Cl-005 in  $\text{d}_6$ -DMSO at 25 °C.

**(2S)-2-[(2S)-2-{2-[(4-Chloronaphthalen-1-yl)oxy]acetamido}-3-phenylpropanamido]-3-phenylpropanoic acid (4Cl-006)**



$\delta_{\text{H}}$  (400 MHz, DMSO- $\text{d}_6$ , 25 °C) 12.85 (0.9H, br s, COOH), 8.48 (0.9H, d,  $J$  7.87 Hz, NH), 8.22 (1.0H, d,  $J$  8.29 Hz, NH), 8.18 (0.9H, d,  $J$  8.55 Hz,  $\text{H}_{\text{Ar}}$ ), 8.12 (1.0H, d,  $J$  8.37 Hz,  $\text{H}_{\text{Ar}}$ ), 7.74-7.70 (1.1H, m,  $\text{H}_{\text{Ar}}$ ), 7.66-7.62 (1.1H, m,  $\text{H}_{\text{Ar}}$ ), 7.47 (1.3H, d,  $J$  8.30 Hz,  $\text{H}_{\text{Ar}}$ ), 7.26-7.19 (10.4H, m,  $\text{H}_{\text{Ar}}$ ), 6.68 (1.0H, d,  $J$  8.37 Hz,  $\text{H}_{\text{Ar}}$ ), 4.73-4.68 (1.2H, m,  $\text{CH}^*$ ), 4.65-4.60 (1.8H, m,  $\text{OCH}_2$ ), 4.54-4.49 (1.0H, m,  $\text{CH}^*$ ), 3.40 (3.0H, br s,  $\text{H}_2\text{O}$ ), 3.14-3.05 (2.2H, m,  $\text{PhC}_a\text{H}_b$  and  $\text{PhC}_b\text{H}_a\text{H}_b$ ), 2.96 (1.1H, dd,  $J$  13.90, 8.82 Hz,  $\text{PhC}_b\text{H}_a\text{H}_b$ ), 2.88 (1.0H, dd,  $J$  13.74, 9.62 Hz,  $\text{PhC}_b\text{H}_a\text{H}_b$ ), 2.50 (0.6H, quintet, residual DMSO- $\text{d}_5$ ), 2.06 (0.5H, s,  $\text{CH}_3$  in acetonitrile).  $\delta_{\text{C}}$  (100 MHz, DMSO-

d<sub>6</sub>, 25 °C) 172.79, 170.85, and 166.86 (C=O), 152.49, 137.49, 137.42, 130.44, 129.34, 129.18, 128.12, 126.50, 126.42, 126.33, 126.10, 125.83, 123.59, 122.52, 122.34 and 105.98 (C<sub>Ar</sub>), 67.24 (OCH<sub>2</sub>), 53.55 (CH<sup>\*</sup>), 53.21 (CH<sup>\*</sup>), 39.52 (septet, DMSO-d<sub>6</sub>), 37.48 (PhCH<sub>2</sub>), 36.74 (PhCH<sub>2</sub>).

**HRMS (ESI) m/z:** [M+H]<sup>+</sup> accurate mass calculated for C<sub>30</sub>H<sub>27</sub>ClN<sub>2</sub>HO<sub>5</sub>: 531.1608; Found: 531.1684.

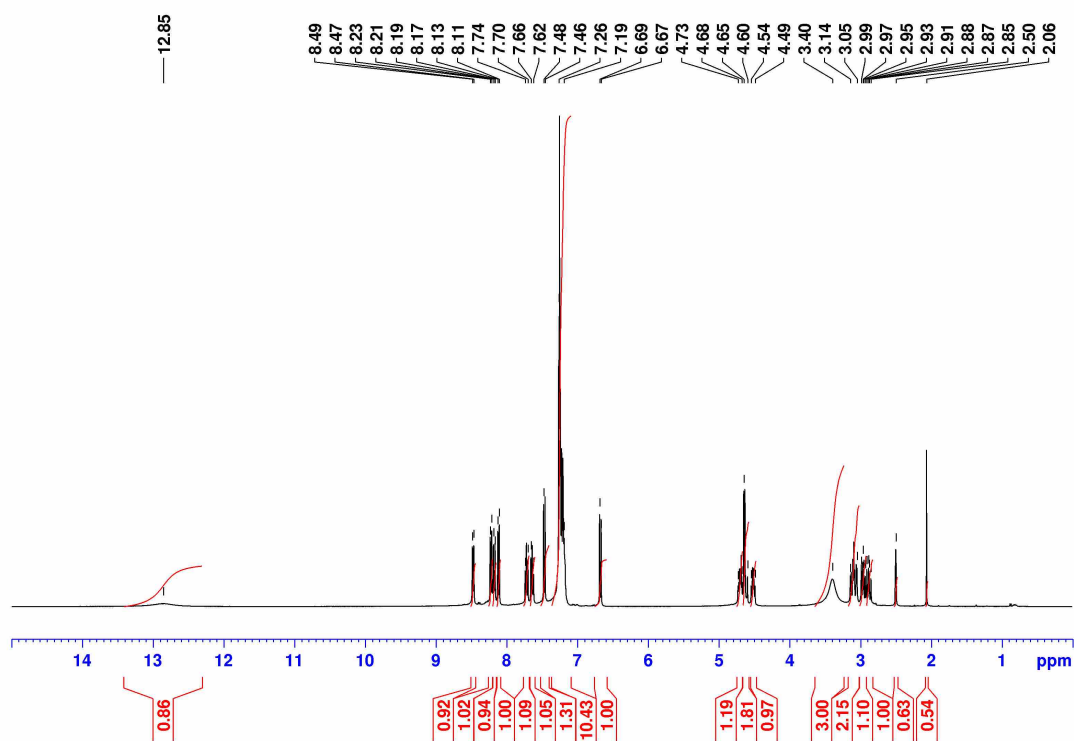


**Figure A3-27.** <sup>1</sup>H NMR spectrum of 4Cl-006 in d<sub>6</sub>-DMSO at 25 °C.

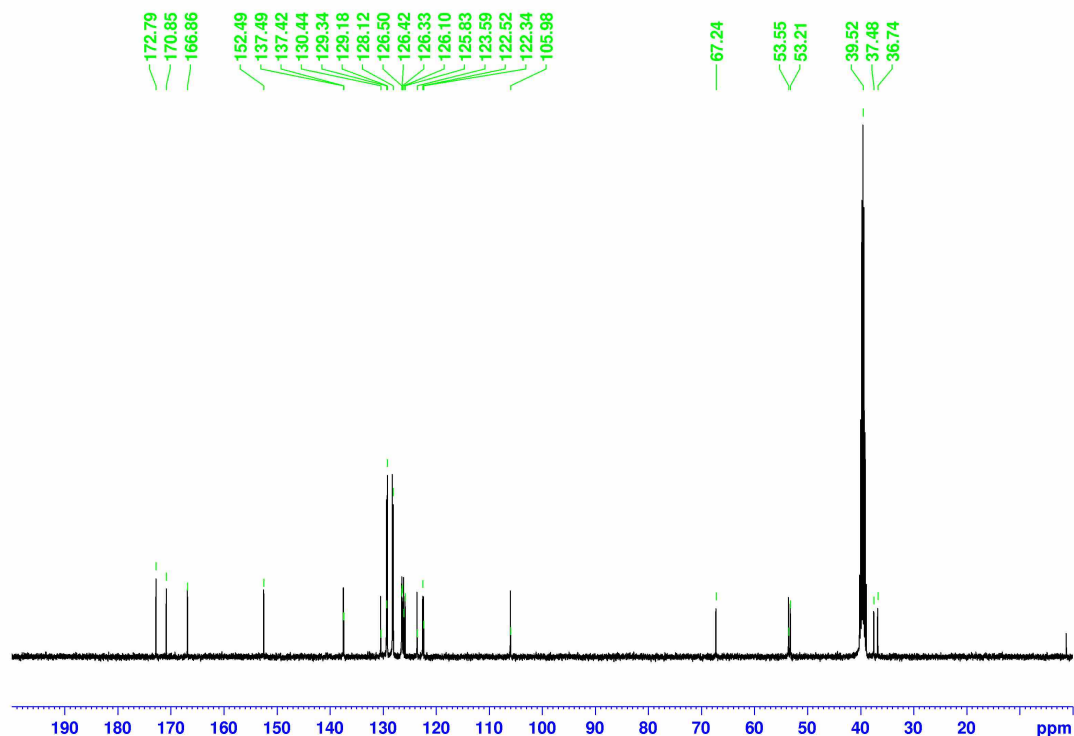
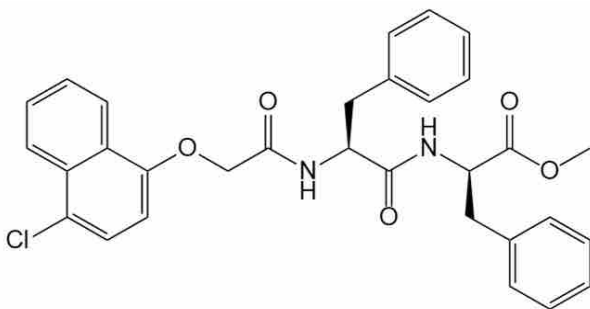


**Figure A3-28.**  $^{13}\text{C}$  NMR spectrum of 4Cl-006 in  $\text{d}_6\text{-DMSO}$  at  $25\text{ }^\circ\text{C}$ .

**Methyl (2R)-2-[(2S)-2-{2-[(4-chloronaphthalen-1-yl)oxy]acetamido}-3-phenylpropanamido]-3-phenylpropanoate (4Cl-007)**



$\delta_{\text{H}}$  (400 MHz,  $\text{DMSO-d}_6$ ,  $25\text{ }^\circ\text{C}$ ) 8.72 (1.0H, d,  $J$  8.19 Hz,  $\text{NH}$ ), 8.21 (1.1H, d,  $J$  8.80 Hz,  $\text{NH}$ ), 8.14-8.10 (2.0H, m,  $\text{H}_{\text{Ar}}$ ), 7.74-7.70 (1.0H, m,  $\text{H}_{\text{Ar}}$ ), 7.65-7.61 (1.0H, m,  $\text{H}_{\text{Ar}}$ ), 7.48 (1.1H, d,  $J$  8.32 Hz,  $\text{H}_{\text{Ar}}$ ), 7.31-7.16 (8.5H, m,  $\text{H}_{\text{Ar}}$ ), 7.04-7.01 (2.0H, m,  $\text{H}_{\text{Ar}}$ ), 6.69 (1.0H, d,  $J$  8.39 Hz,  $\text{H}_{\text{Ar}}$ ), 4.72-4.68 (1.0H, m,  $\text{CH}^*$ ), 4.67-4.61 (2.1H, m,  $\text{OCH}_2$ ), 4.58-4.52 (1.0H, m,  $\text{CH}^*$ ), 3.65 (2.9H, s,  $\text{OCH}_3$ ), 3.37 (10.3H, br s,  $\text{H}_2\text{O}$ ), 3.10 (1.0H, dd,  $J$  13.68, 4.96 Hz,  $\text{PhC}_b\text{H}_a\text{H}_b$ ), 2.89 (1.1H, dd,  $J$  13.68, 10.00 Hz,  $\text{PhC}_b\text{H}_a\text{H}_b$ ), 2.79 (1.0H, dd,  $J$  13.66, 4.26 Hz,  $\text{PhC}_b\text{H}_a\text{H}_b$ ), 2.66 (1.0H, dd,  $J$  13.68, 9.23 Hz,  $\text{PhC}_b\text{H}_a\text{H}_b$ ), 2.50 (1.3H, quintet, residual  $\text{DMSO-d}_5$ ), 2.07 (8.6H, s,

$\text{CH}_3$  in acetonitrile).  $\delta_{\text{C}}$  (100 MHz, DMSO- $d_6$ , 25 °C) 171.93, 170.76, and 166.84 ( $\text{C}=\text{O}$ ), 152.48, 137.24, 137.12, 130.43, 129.28, 129.23, 128.30, 128.12, 128.01, 126.69, 126.42, 126.30, 126.09, 125.81, 123.59, 122.47, 122.33, 118.09 and 105.95 ( $\text{C}_{\text{Ar}}$ ), 67.19 ( $\text{OCH}_2$ ), 53.55 ( $\text{CH}^*$ ), 53.18 ( $\text{CH}^*$ ), 52.04 ( $\text{OCH}_3$ ), 39.52 (septet, DMSO- $d_6$ ), 37.71 ( $\text{PhC}_b\text{H}_2$ ), 36.94 ( $\text{PhC}_a\text{H}_2$ ).

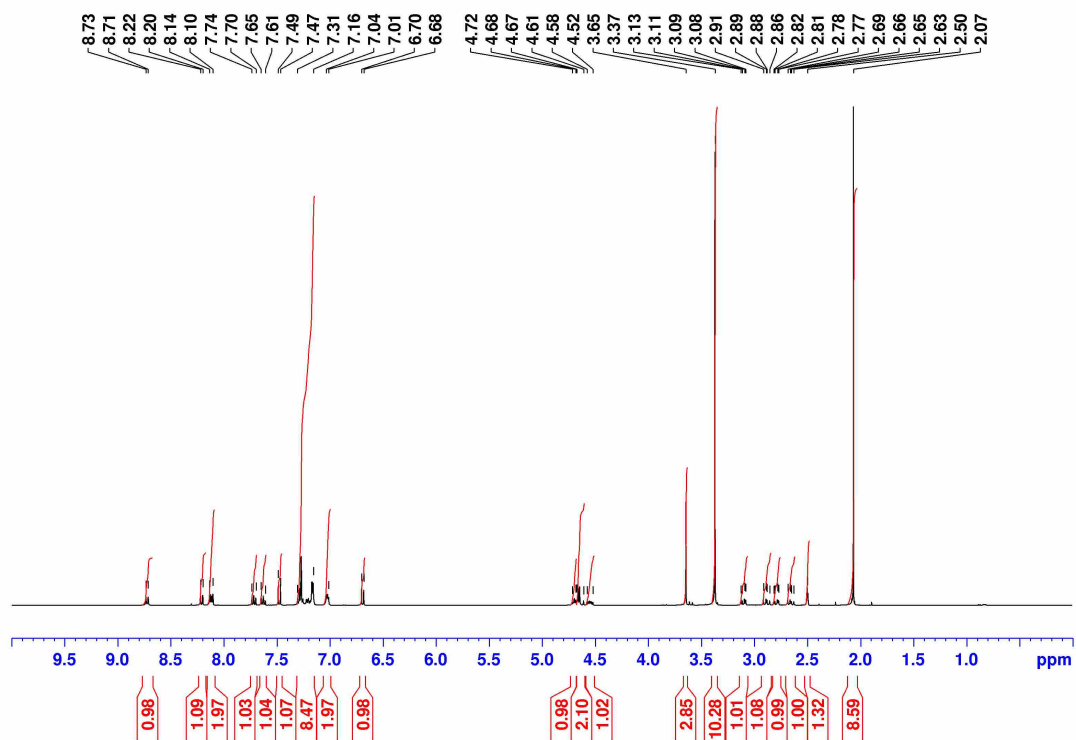


**Figure A3-29.**  $^1\text{H}$  NMR spectrum of 4Cl-007 in  $d_6$ -DMSO at 25 °C.

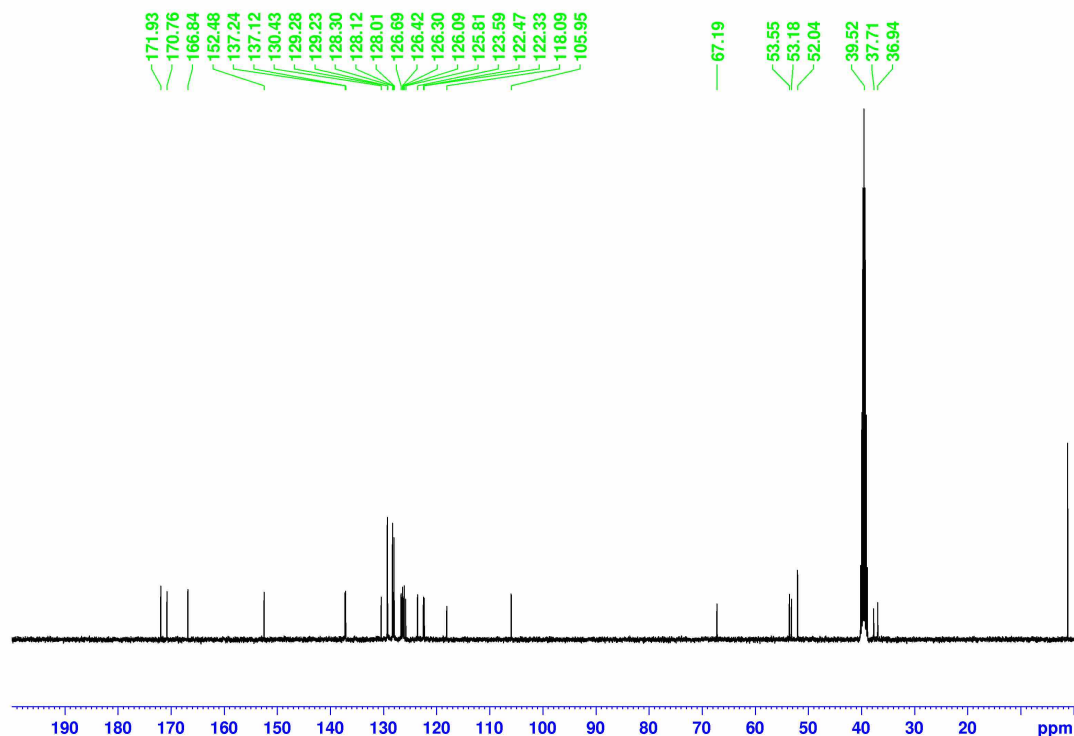
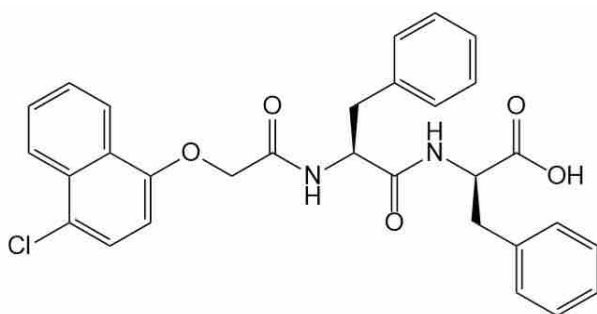


**Figure A3-30.**  $^{13}\text{C}$  NMR spectrum of 4Cl-007 in  $\text{d}_6$ -DMSO at 25 °C.

**(2R)-2-[(2S)-2-{2-[(4-Chloronaphthalen-1-yl)oxy]acetamido}-3-phenylpropanamido]-3-phenylpropanoic acid (4Cl-008)**



$\delta_{\text{H}}$  (400 MHz,  $\text{DMSO-d}_6$ , 25 °C) 12.88 (0.7H, br s,  $\text{COOH}$ ), 8.61 (0.9H, d,  $J$  8.35 Hz,  $\text{NH}$ ), 8.21 (1.1H, d,  $J$  8.24 Hz,  $\text{NH}$ ), 8.11 (1.9H, d,  $J$  8.41 Hz,  $\text{H}_{\text{Ar}}$ ), 7.73-7.69 (1.1H, m,  $\text{H}_{\text{Ar}}$ ), 7.64-7.61 (1.1H, m,  $\text{H}_{\text{Ar}}$ ), 7.48 (1.2H, d,  $J$  8.31 Hz,  $\text{H}_{\text{Ar}}$ ), 7.29-7.15 (8.4H, m,  $\text{H}_{\text{Ar}}$ ), 7.01-6.99 (1.8H, m,  $\text{H}_{\text{Ar}}$ ), 6.69 (0.9H, d,  $J$  8.38 Hz,  $\text{H}_{\text{Ar}}$ ), 4.74-4.69 (1.2H, m,  $\text{CH}^*$ ), 4.66-4.61 (1.8H, m,  $\text{OCH}_2$ ), 4.55-4.49 (1.0H, m,  $\text{CH}^*$ ), 3.41 (2.0H, br s,  $\text{H}_2\text{O}$ ), 3.15 (1.1H, dd,  $J$  13.62, 4.46 Hz,  $\text{PhC}_b\text{H}_a\text{H}_b$ ), 2.88 (1.1H, q,  $J$  10.16 Hz,  $\text{PhC}_b\text{H}_a\text{H}_b$ ), 2.81 (1.0H, dd,  $J$  13.68, 4.08 Hz,  $\text{PhC}_b\text{H}_a\text{H}_b$ ), 2.65 (1.0H, dd,  $J$  13.58, 9.22 Hz,  $\text{PhC}_b\text{H}_a\text{H}_b$ ), 2.50 (0.6H, quintet, residual  $\text{DMSO-d}_5$ ).  $\delta_{\text{C}}$  (100 MHz,

DMSO-d<sub>6</sub>, 25 °C) 172.94, 170.60, and 166.79 (C=O), 152.48, 137.54, 137.29, 130.44, 129.33, 129.27, 128.24, 128.11, 127.98, 126.58, 126.42, 126.10, 125.82, 123.59, 122.47, 122.35, and 105.96 (C<sub>Ar</sub>), 67.22 (OCH<sub>2</sub>), 53.56 (CH\*), 53.19 (CH\*), 39.52 (septet, DMSO-d<sub>6</sub>), 37.80 (PhC<sub>b</sub>H<sub>2</sub>), 37.06 (PhC<sub>a</sub>H<sub>2</sub>).

**HRMS (ESI) m/z:** [M+H]<sup>+</sup> accurate mass calculated for C<sub>30</sub>H<sub>27</sub>ClN<sub>2</sub>HO<sub>5</sub>: 531.1608; Found: 531.1689.

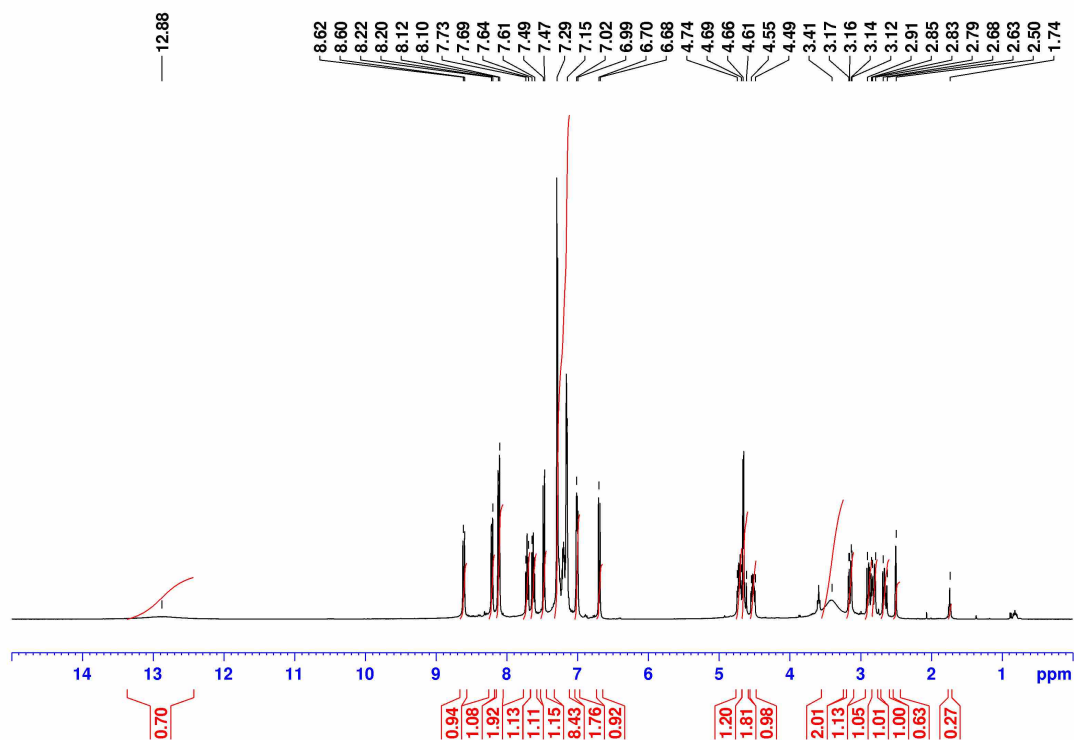


**Figure A3-31.** <sup>1</sup>H NMR spectrum of 4Cl-008 in d<sub>6</sub>-DMSO at 25 °C.

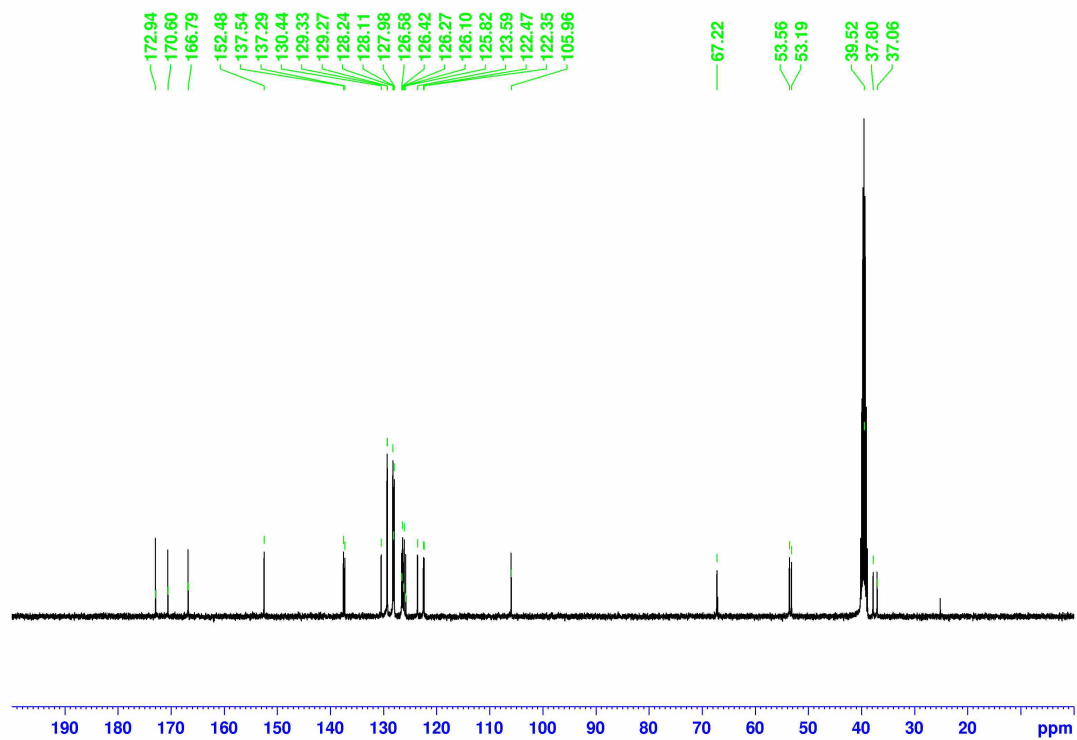
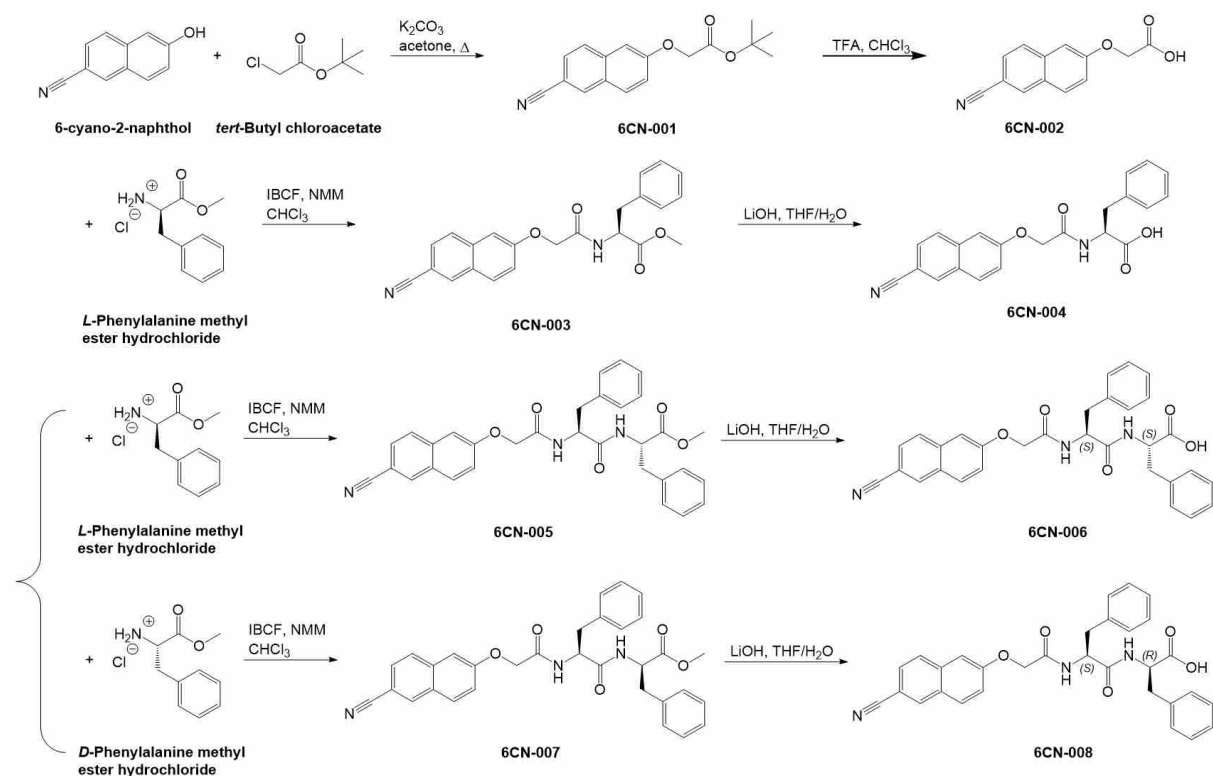


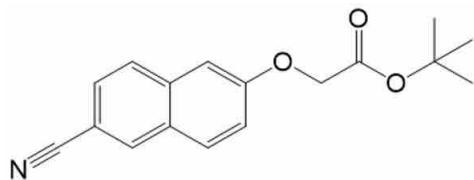
**Figure A3-32.**  $^{13}\text{C}$  NMR spectrum of 4Cl-008 in  $\text{d}_6$ -DMSO at 25 °C.

### A3.2.3 6CN2NapFF



Scheme A3-3. Synthetic route of 6CN2NapFF.

#### Tert-butyl 2-[(6-cyanonaphthalen-2-yl)oxy]acetate (6CN-001)



$\delta_{\text{H}}$  (400 MHz, DMSO- $d_6$ , 25 °C) 8.46 (0.9H, s,  $\underline{\text{H}}_{\text{Ar}}$ ), 7.99 (1.0H, d,  $J$  8.96 Hz,  $\underline{\text{H}}_{\text{Ar}}$ ), 7.94 (1.0H, d,  $J$  8.56 Hz,  $\underline{\text{H}}_{\text{Ar}}$ ), 7.71 (1.0H, dd,  $J$  8.48, 2.01 Hz,  $\underline{\text{H}}_{\text{Ar}}$ ), 7.38-7.34 (2.0H, m,  $\underline{\text{H}}_{\text{Ar}}$ ), 4.83 (2.0H, s,  $\underline{\text{OCH}}_2$ ), 3.39 (2.8H, br s,  $\underline{\text{H}}_2\text{O}$ ), 2.50 (0.4H, quintet, residual DMSO- $d_5$ ), 1.43 (7.1H, s, Rot-2  $\text{C}(\underline{\text{CH}}_3)_3$ ), 1.42 (2.1H, s, Rot-1  $\text{C}(\underline{\text{CH}}_3)_3$ ).  $\delta_{\text{C}}$  (100 MHz, DMSO- $d_6$ , 25 °C) 167.35 ( $\underline{\text{C}}=\text{O}$ ), 157.96, 135.92, 133.95, 130.31, 128.10, 127.55, 126.97, 119.42, 107.49, 106.00 ( $\underline{\text{C}}_{\text{Ar}}$ ), 120.17 ( $\underline{\text{C}}\equiv\text{N}$ ), 81.65 ( $\underline{\text{C}}(\underline{\text{CH}}_3)_3$ ), 65.11 ( $\underline{\text{OCH}}_2$ ), 39.52 (septet, DMSO- $d_6$ ), 27.68 (Rot-2  $\text{C}(\underline{\text{CH}}_3)_3$ ), 27.54 (Rot-1  $\text{C}(\underline{\text{CH}}_3)_3$ ).

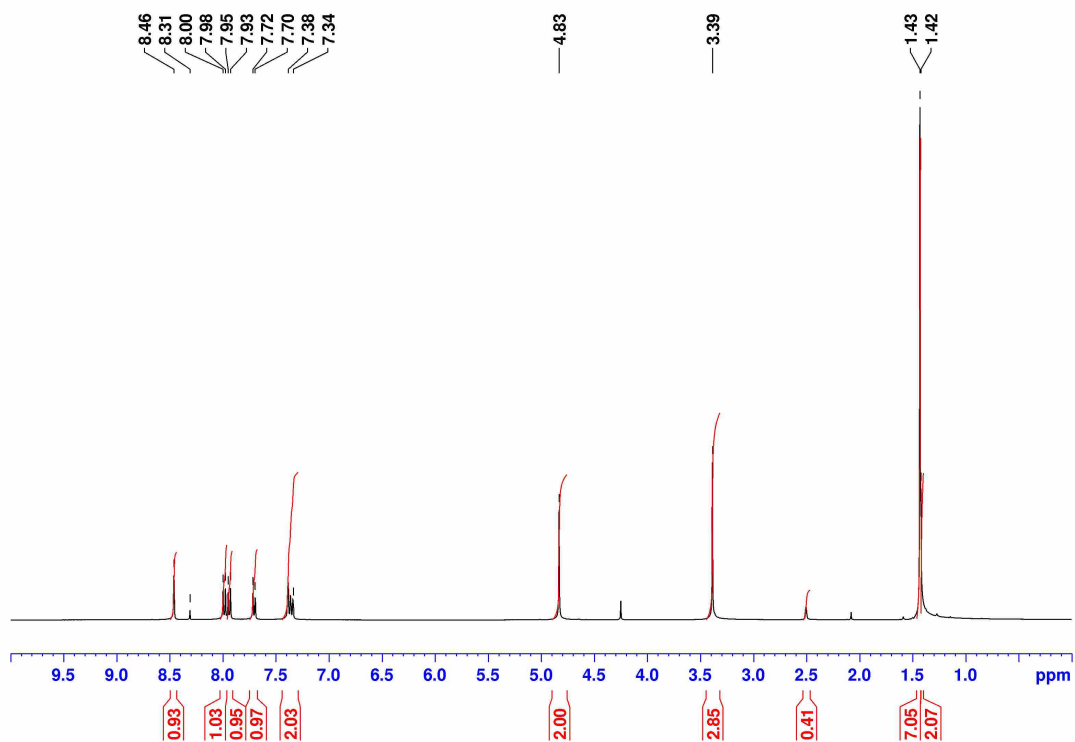


Figure A3-33.  $^1\text{H}$  NMR spectrum of 6CN-001 in  $\text{d}_6\text{-DMSO}$  at  $25\text{ }^\circ\text{C}$ .

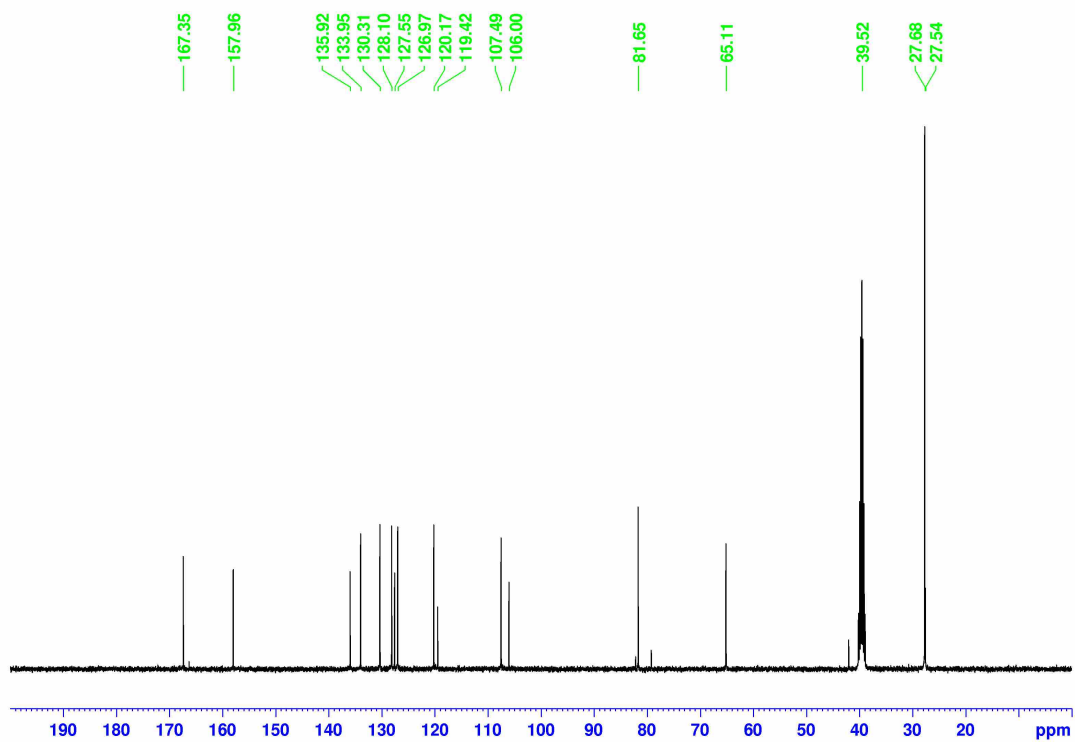
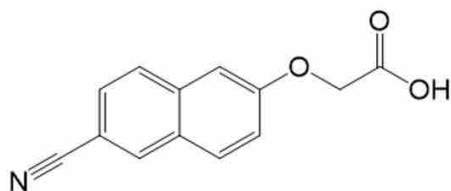
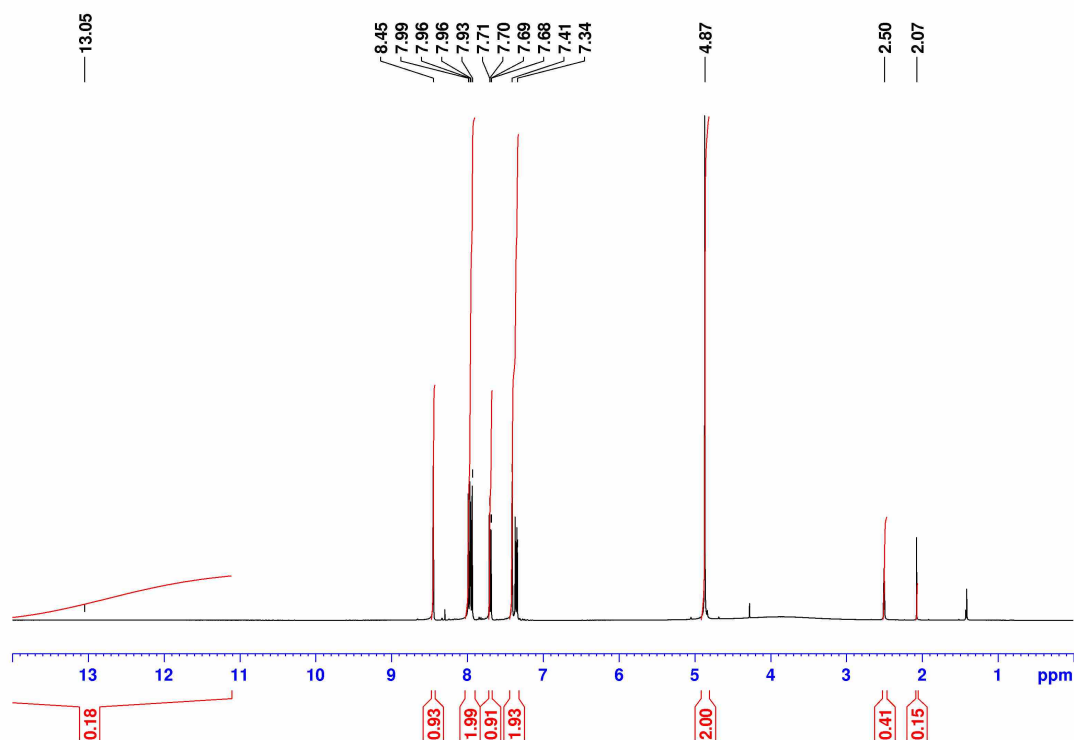


Figure A3-34.  $^{13}\text{C}$  NMR spectrum of 6CN-001 in  $\text{d}_6\text{-DMSO}$  at  $25\text{ }^\circ\text{C}$ .

**2-[(6-Cyanonaphthalen-2-yl)oxy]acetic acid (6CN-002)**

$\delta_{\text{H}}$  (400 MHz, DMSO- $d_6$ , 25 °C) 13.05 (0.2H, br s, COOH), 8.45 (0.9H, s,  $\underline{\text{H}}_{\text{Ar}}$ ), 7.96 (2.0H, dd,  $J$  12.57, 8.86 Hz,  $\underline{\text{H}}_{\text{Ar}}$ ), 7.70 (0.9H, d,  $J$  8.51, 1.65 Hz,  $\underline{\text{H}}_{\text{Ar}}$ ), 7.41-7.34 (1.9H, m,  $\underline{\text{H}}_{\text{Ar}}$ ), 4.87 (2.0H, s, OCH $\underline{2}$ ), 2.50 (0.4H, quintet, residual DMSO- $d_5$ ), 2.07 (0.1H, br s, CH $\underline{3}$  in acetonitrile).  $\delta_{\text{C}}$  (100 MHz, DMSO- $d_6$ , 25 °C) 169.81 (C=O), 158.13, 136.02, 134.01, 130.35, 128.16, 127.58, 127.00, 119.52, 107.40, 105.98 (C $\underline{\text{Ar}}$ ), 120.34 (C $\equiv$ N), 64.66 (OCH $\underline{2}$ ), 39.52 (septet, DMSO- $d_6$ ).



**Figure A3-35.**  $^1\text{H}$  NMR spectrum of 6CN-002 in  $d_6$ -DMSO at 25 °C.

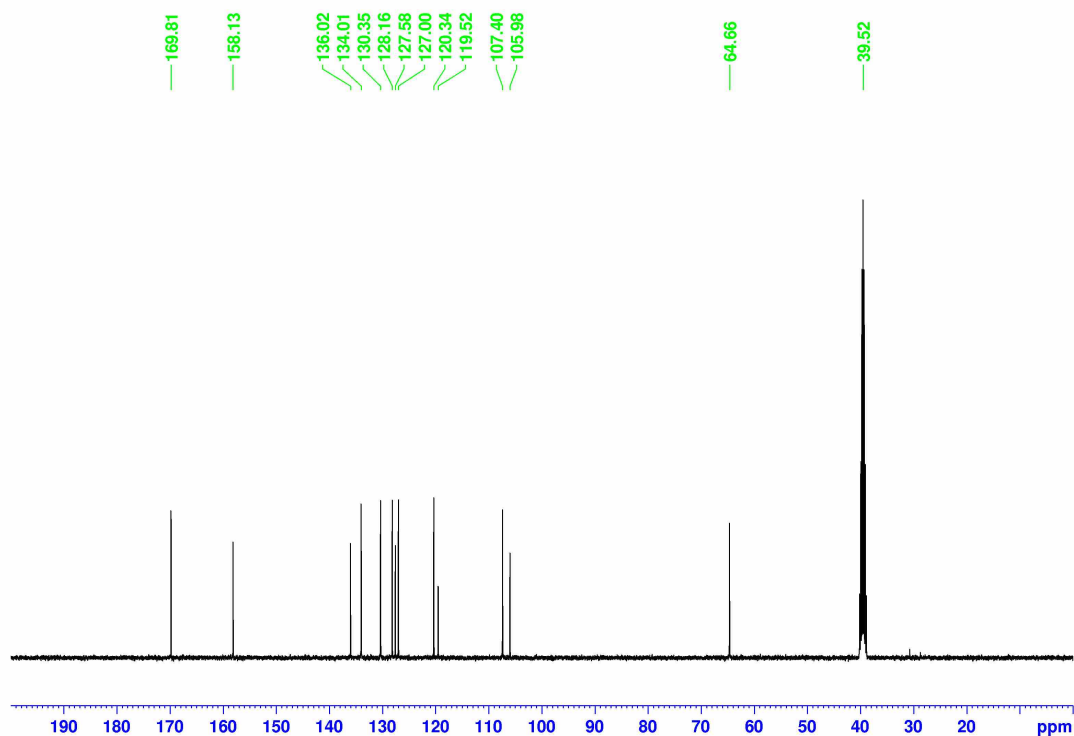
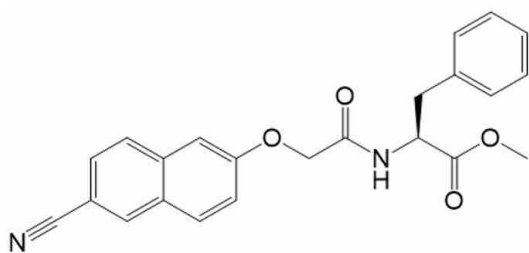


**Figure A3-36.**  $^{13}\text{C}$  NMR spectrum of 6CN-002 in  $\text{d}_6$ -DMSO at 25 °C.

**Methyl (2S)-2-{2-[(6-cyanonaphthalen-2-yl)oxy]acetamido}-3-phenylpropanoate (6CN-003)**



$\delta_{\text{H}}$  (400 MHz,  $\text{DMSO-d}_6$ , 25 °C) 8.61 (0.9H, d,  $J$  7.98 Hz,  $\text{NH}$ ), 8.48 (0.9H, s,  $\text{H}_{\text{Ar}}$ ), 8.00 (0.9H, d,  $J$  9.06 Hz,  $\text{H}_{\text{Ar}}$ ), 7.89 (0.9H, d,  $J$  8.64 Hz,  $\text{H}_{\text{Ar}}$ ), 7.73 (1.0H, dd,  $J$  8.52, 1.65 Hz,  $\text{H}_{\text{Ar}}$ ), 7.38-7.14 (8.3H, m,  $\text{H}_{\text{Ar}}$ ), 4.71-4.63 (1.9H, m,  $\text{OCH}_2$ ), 4.62-4.57 (0.8H, m,  $\text{CH}^*$ ), 3.62 (3.0H, s,  $\text{OCH}_3$ ), 3.37 (4.5H, br s,  $\text{H}_2\text{O}$ ), 3.12 (1.0H, dd,  $J$  13.81, 5.20 Hz,  $\text{PhCH}_a\text{H}_b$ ), 3.01 (1.1H, dd,  $J$  13.78, 9.48 Hz,  $\text{PhCH}_a\text{H}_b$ ), 2.50 (0.8H, quintet, residual  $\text{DMSO-d}_5$ ).  $\delta_{\text{C}}$  (100 MHz,  $\text{DMSO-d}_6$ , 25 °C) 171.68, 167.41 ( $\text{C}=\text{O}$ ), 157.96, 137.13, 135.89, 133.96, 129.16, 129.03, 128.22, 128.12, 127.61, 126.96, 126.53, 119.41, 107.58 and 106.01 ( $\text{C}_{\text{Ar}}$ ), 120.38 ( $\text{C}\equiv\text{N}$ ), 66.65 ( $\text{OCH}_2$ ), 53.26 ( $\text{CH}^*$ ), 52.01 ( $\text{OCH}_3$ ), 39.52 (septet,  $\text{DMSO-d}_6$ ), 36.32 ( $\text{PhCH}_2$ ).

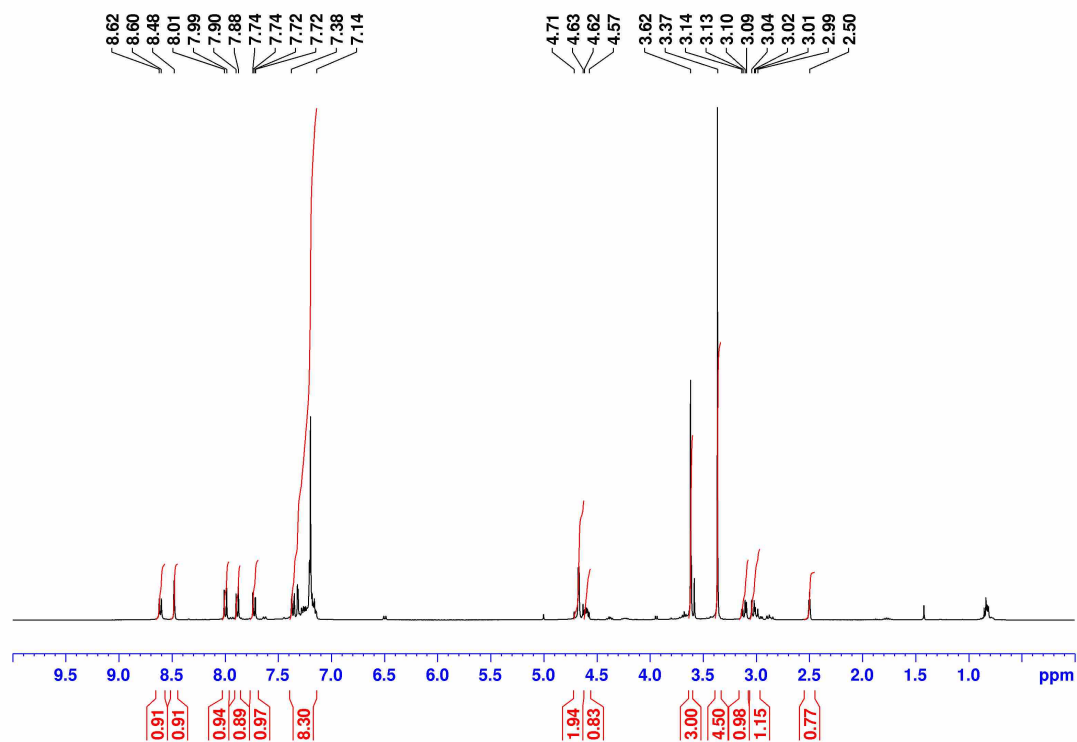


Figure A3-37.  $^1\text{H}$  NMR spectrum of 6CN-003 in  $\text{d}_6$ -DMSO at 25 °C.

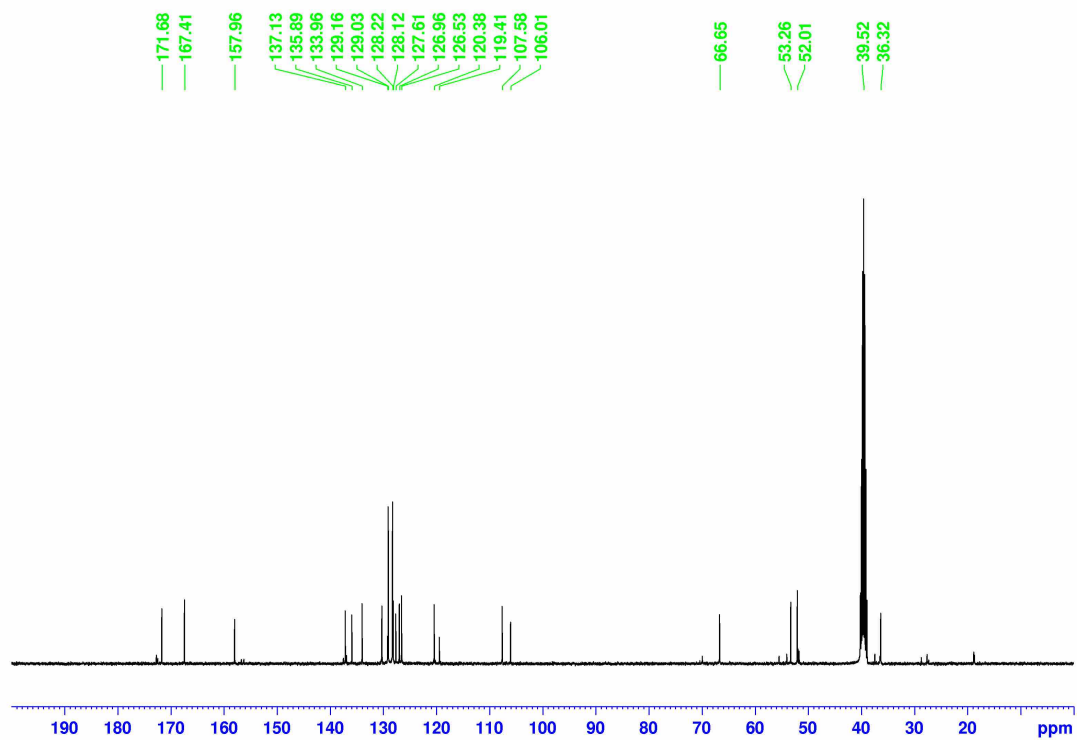
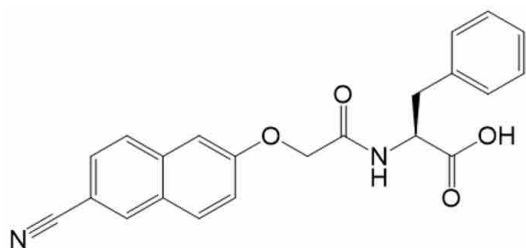
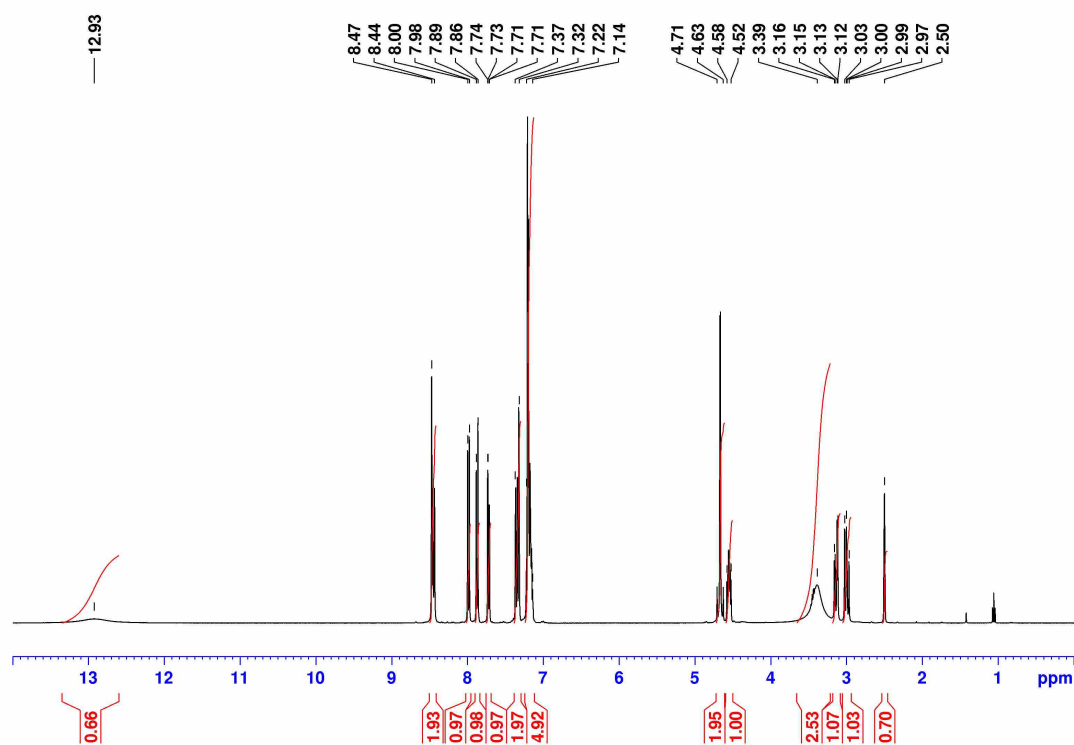


Figure A3-38.  $^{13}\text{C}$  NMR spectrum of 6CN-003 in  $\text{d}_6$ -DMSO at 25 °C.

**(2S)-2-{2-[(6-Cyanonaphthalen-2-yl)oxy]acetamido}-3-phenylpropanoic acid (6CN-004)**

$\delta_{\text{H}}$  (400 MHz, DMSO- $d_6$ , 25 °C) 12.93 (0.7H, br s, COOH), 8.47-8.44 (1.9H, m, NH and  $\text{H}_{\text{Ar}}$ ), 8.00 (1.0H, d,  $J$  9.00 Hz,  $\text{H}_{\text{Ar}}$ ), 7.87 (1.0H, d,  $J$  8.60 Hz,  $\text{H}_{\text{Ar}}$ ), 7.72 (1.0H, dd,  $J$  8.53, 1.53 Hz,  $\text{H}_{\text{Ar}}$ ), 7.37-7.32 (2.0H, m,  $\text{H}_{\text{Ar}}$ ), 7.22-7.14 (4.9H, m,  $\text{H}_{\text{Ar}}$ ), 4.71-4.63 (1.9H, m,  $\text{OCH}_2$ ), 4.58-4.52 (1.0H, m,  $\text{CH}^*$ ), 3.39 (2.5H, br s,  $\text{H}_2\text{O}$ ), 3.14 (1.1H, dd,  $J$  13.85, 4.61 Hz,  $\text{PhCH}_a\text{H}_b$ ), 3.00 (1.0H, dd,  $J$  13.83, 9.59 Hz,  $\text{PhCH}_a\text{H}_b$ ), 2.50 (0.7H, quintet, residual DMSO- $d_5$ ).  $\delta_{\text{C}}$  (100 MHz, DMSO- $d_6$ , 25 °C) 172.83, 167.48 ( $\text{C}=\text{O}$ ), 158.09, 137.59, 136.03, 134.07, 130.37, 129.18, 128.32, 128.29, 127.73, 127.06, 126.58, 119.58, 107.68 and 106.12 ( $\text{C}_{\text{Ar}}$ ), 120.53 ( $\text{C}\equiv\text{N}$ ), 67.16 ( $\text{OCH}_2$ ), 53.36 ( $\text{CH}^*$ ), 39.52 (septet, DMSO- $d_6$ ), 36.49 ( $\text{PhCH}_2$ ).



**Figure A3-39.**  $^1\text{H}$  NMR spectrum of 6CN-004 in  $d_6$ -DMSO at 25 °C.

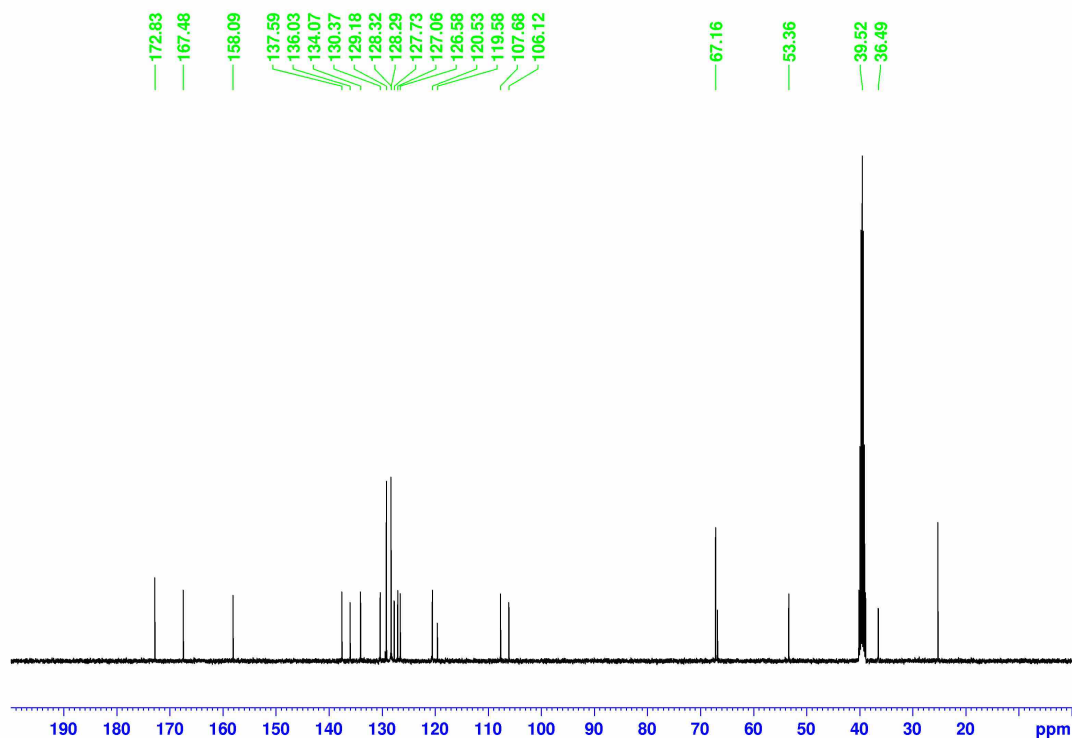
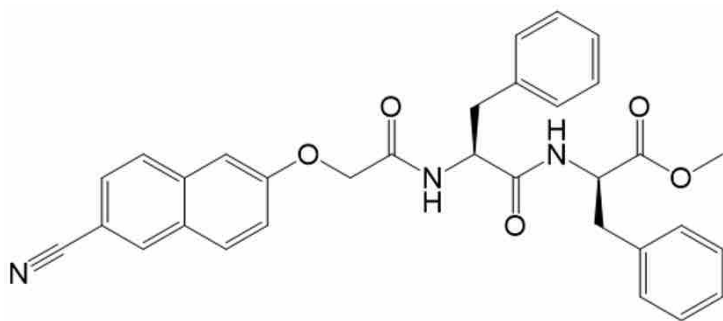


**Figure A3-40.**  $^{13}\text{C}$  NMR spectrum of 6CN-004 in  $\text{d}_6$ -DMSO at 25 °C.

**Methyl (2S)-2-[(2S)-2-{2-[(6-cyanonaphthalen-2-yl)oxy]acetamido}-3-phenylpropanamido]-3-phenylpropanoate (6CN-005)**



$\delta_{\text{H}}$  (400 MHz,  $\text{DMSO-d}_6$ , 25 °C) 8.62 (0.8H, d,  $J$  7.53 Hz,  $\text{NH}$ ), 8.47 (0.9H, s,  $\text{H}_{\text{Ar}}$ ), 8.31 (0.5H, s,  $\text{CH}$  in chloroform), 8.24 (0.8H, d,  $J$  8.55 Hz,  $\text{NH}$ ), 7.98 (0.9H, d,  $J$  9.04 Hz,  $\text{NH}$ ), 7.87 (0.8H, d,  $J$  8.66 Hz,  $\text{H}_{\text{Ar}}$ ), 7.72 (0.9H, dd,  $J$  8.53, 1.61 Hz,  $\text{H}_{\text{Ar}}$ ), 7.34-7.13 (12.1H, m,  $\text{H}_{\text{Ar}}$ ), 4.69-4.63 (1.0H, m,  $\text{CH}^*$ ), 4.60 (1.4H, s,  $\text{OCH}_2$ ), 4.55-4.49 (0.9H, m,  $\text{CH}^*$ ), 3.61-3.59 (3.2H, m,  $\text{OCH}_3$ ), 3.36 (9.2H, br s,  $\text{H}_2\text{O}$ ), 3.07-2.90 (2.9H, m,  $\text{PhCH}_2$ ), 2.84 (1.0H, dd,  $J$  13.77, 9.84 Hz,  $\text{PhCH}_2$ ), 2.50 (1.5H, quintet, residual  $\text{DMSO-d}_5$ ).  $\delta_{\text{C}}$  (100 MHz,  $\text{DMSO-d}_6$ , 25 °C) 171.72, 171.02, and 166.90 ( $\text{C}=\text{O}$ ), 157.98, 137.48, 136.96, 135.92, 133.97, 130.25, 129.19, 129.05, 128.26, 128.22,

128.15, 128.01, 127.59, 126.93, 126.58, 126.30, 119.45, 107.54 and 105.97 ( $C_{Ar}$ ), 120.33 ( $C\equiv N$ ), 66.68 ( $OCH_2$ ), 53.67 ( $CH^*$ ), 53.27 ( $CH^*$ ), 51.89 ( $OCH_3$ ), 39.52 (septet,  $DMSO-d_6$ ), 37.41 ( $PhC_bH_2$ ), 36.61 ( $PhC_aH_2$ ).

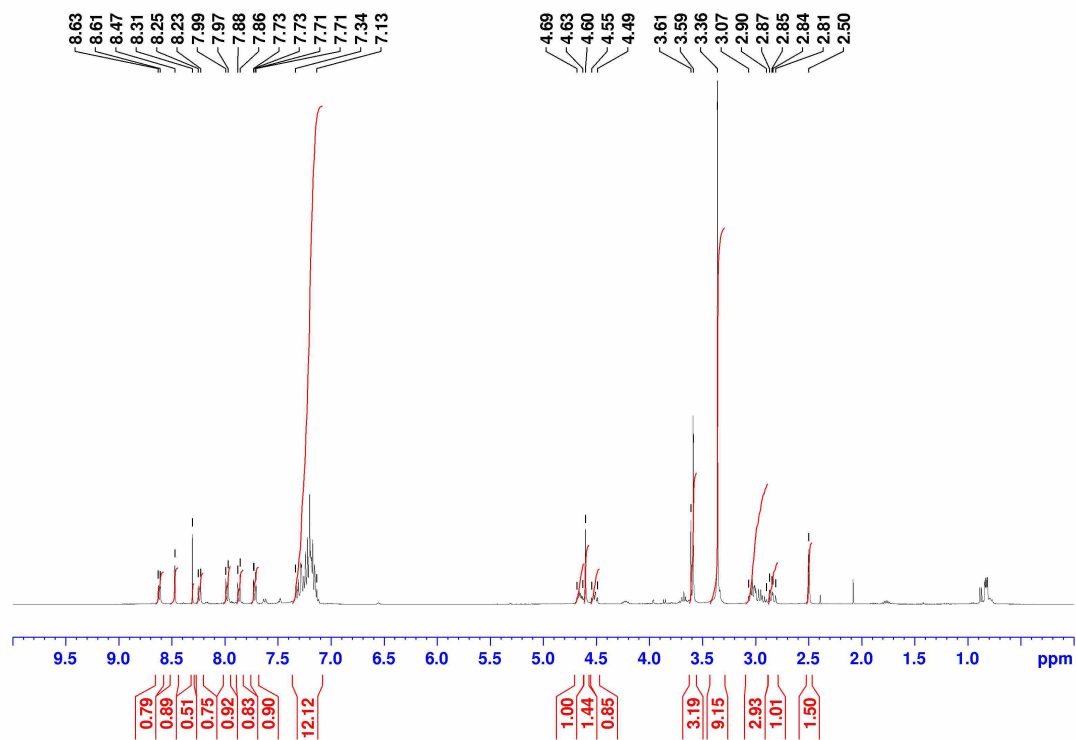


**Figure A3-41.**  $^1H$  NMR spectrum of 6CN-005 in  $d_6$ -DMSO at 25 °C.

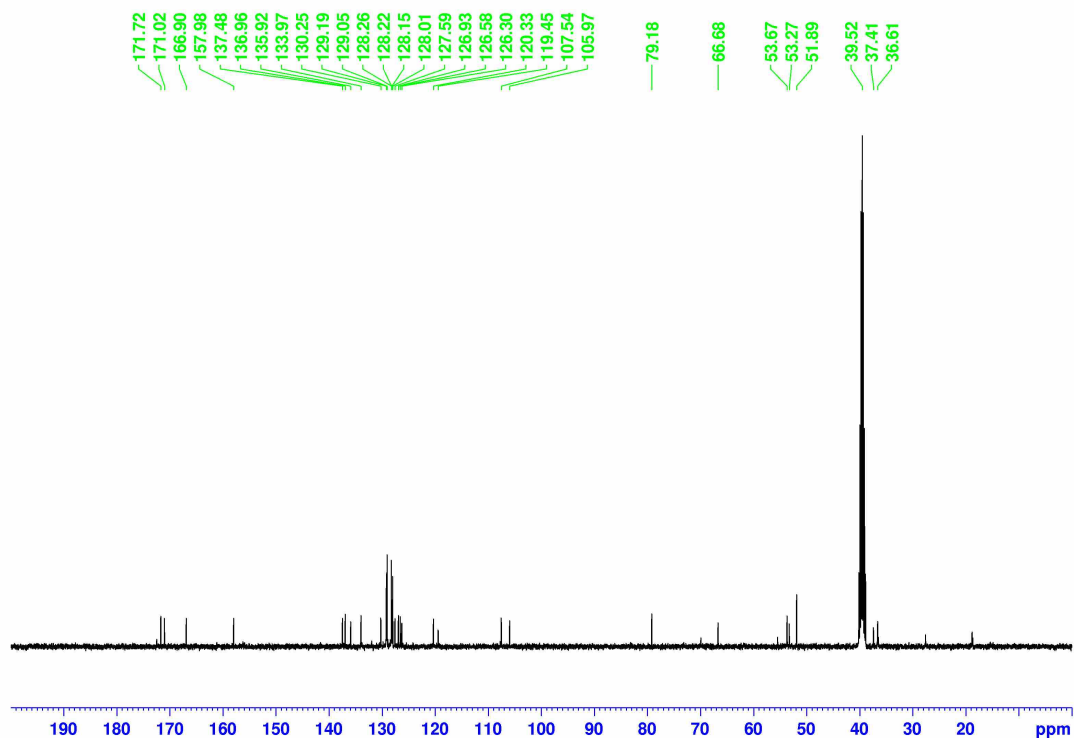
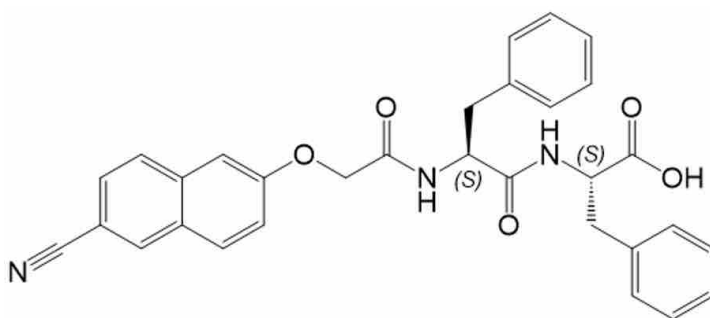


**Figure A3-42.**  $^{13}\text{C}$  NMR spectrum of 6CN-005 in  $\text{d}_6$ -DMSO at 25 °C.

**(2S)-2-[(2S)-2-{2-[(6-Cyanonaphthalen-2-yl)oxy]acetamido}-3-phenylpropanamido]-3-phenylpropanoic acid (6CN-006)**



$\delta_{\text{H}}$  (400 MHz,  $\text{DMSO-d}_6$ , 25 °C) 12.80 (0.7H, br s,  $\text{COOH}$ ), 8.49-8.47 (1.8H, m,  $\text{NH}$  and  $\text{H}_{\text{Ar}}$ ), 8.25 (0.9H, d,  $J$  8.60 Hz,  $\text{NH}$ ), 7.98 (0.9H, d,  $J$  9.08 Hz,  $\text{H}_{\text{Ar}}$ ), 7.87 (0.9H, d,  $J$  8.68 Hz,  $\text{H}_{\text{Ar}}$ ), 7.72 (0.9H, d,  $J$  8.54, 1.66 Hz,  $\text{H}_{\text{Ar}}$ ), 7.33-7.11 (11.9H, m,  $\text{H}_{\text{Ar}}$ ), 4.67 (1.0H, td,  $J$  9.56, 4.04 Hz,  $\text{CH}^*$ ), 4.61 (1.7H, m,  $\text{OCH}_2$ ), 4.49 (0.9H, td,  $J$  8.36, 5.32 Hz,  $\text{CH}^*$ ), 3.43 (1.7H, br s,  $\text{H}_2\text{O}$ ), 3.11-3.02 (2.0H, m,  $\text{PhCH}_2$ ), 2.96-2.82 (2.0H, m,  $\text{PhCH}_2$ ), 2.50 (0.7H, quintet, residual  $\text{DMSO-d}_5$ ).

$\delta_{\text{C}}$  (100 MHz,  $\text{DMSO-d}_6$ , 25 °C) 172.71, 170.90, and 166.87 ( $\text{C}=\text{O}$ ), 157.97, 137.55, 137.38, 135.92, 133.95, 130.24, 129.23, 129.13, 128.17, 127.97, 127.59, 126.92, 126.44, 126.26, 119.44,

107.57 and 105.97 ( $C_{Ar}$ ), 120.31 ( $C\equiv N$ ), 66.71 ( $OCH_2$ ), 53.53 ( $CH^*$ ), 53.34 ( $CH^*$ ), 39.52 (septet, DMSO- $d_6$ ), 37.41 ( $PhCH_2$ ), 36.68 ( $PhCH_2$ ).

**HRMS (ESI) m/z:**  $[M+H]^+$  accurate mass calculated for  $C_{31}H_{27}N_3HO_5$ : 522.1951; Found: 522.2027.

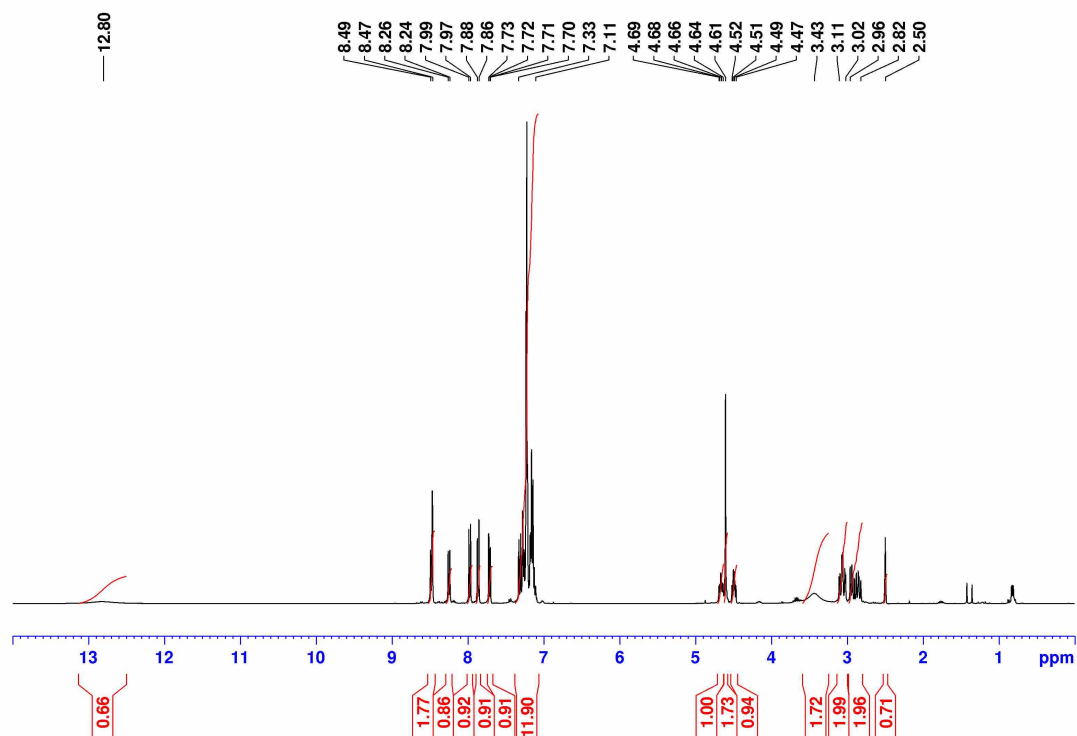


**Figure A3-43.**  $^1H$  NMR spectrum of 6CN-006 in  $d_6$ -DMSO at 25 °C.

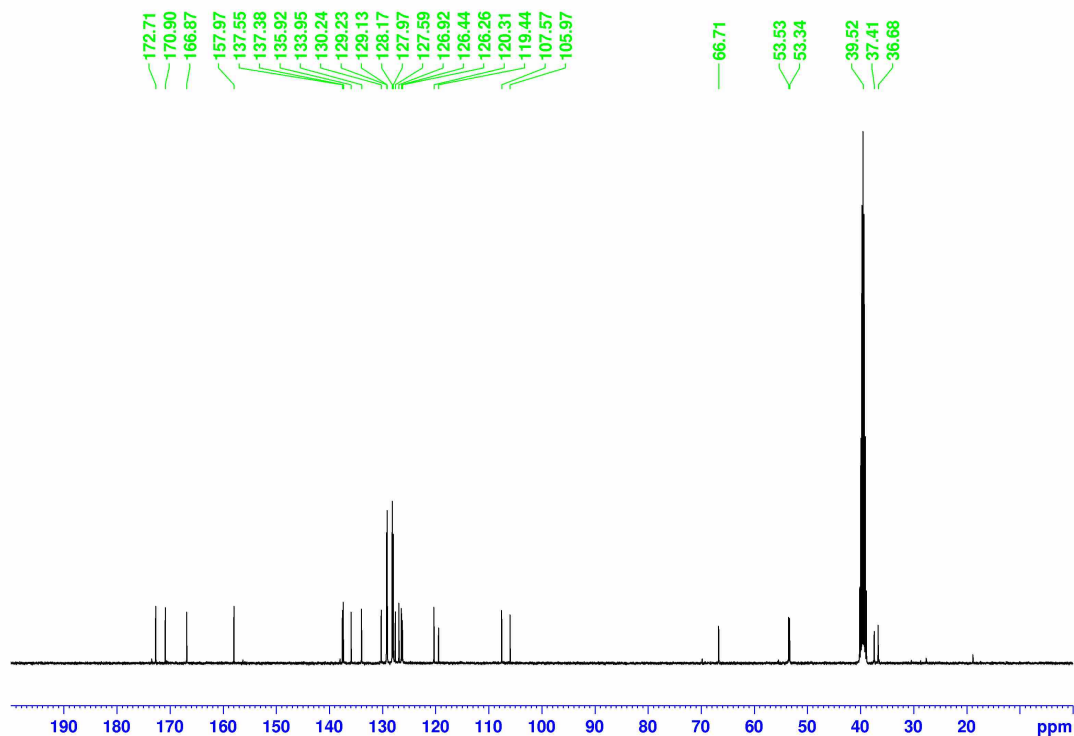
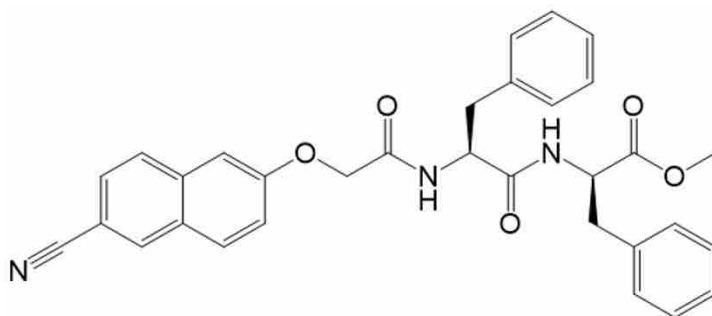


**Figure A3-44.**  $^{13}\text{C}$  NMR spectrum of 6CN-006 in  $\text{d}_6\text{-DMSO}$  at  $25\text{ }^\circ\text{C}$ .

**Methyl (2R)-2-[(2S)-2-{2-[(6-cyanonaphthalen-2-yl)oxy]acetamido}-3-phenylpropanamido]-3-phenylpropanoate (6CN-007)**



$\delta_{\text{H}}$  (400 MHz,  $\text{DMSO-d}_6$ ,  $25\text{ }^\circ\text{C}$ ) 8.73 (0.9H, d,  $J$  8.15 Hz,  $\text{NH}$ ), 8.47 (0.9H, s,  $\text{H}_{\text{Ar}}$ ), 8.19 (0.9H, d,  $J$  8.60 Hz,  $\text{NH}$ ), 7.98 (0.9H, d,  $J$  8.98 Hz,  $\text{NH}$ ), 7.87 (0.9H, d,  $J$  8.61 Hz,  $\text{H}_{\text{Ar}}$ ), 7.72 (0.9H, dd,  $J$  8.53, 1.56 Hz,  $\text{H}_{\text{Ar}}$ ), 7.33-7.02 (12.1H, m,  $\text{H}_{\text{Ar}}$ ), 4.66 (1.0H, d,  $J$  9.38, 4.18 Hz,  $\text{CH}^*$ ), 4.62 (1.6H, s,  $\text{OCH}_2$ ), 4.57-4.51 (0.9H, m,  $\text{CH}^*$ ), 3.62 (3.4H, s,  $\text{OCH}_3$ ), 3.37 (4.8H, br s,  $\text{H}_2\text{O}$ ), 3.11-3.00 (1.2H, m,  $\text{PhCH}_2$ ), 2.87 (1.2H, dd,  $J$  13.57, 10.04 Hz,  $\text{PhCH}_2$ ), 2.76 (0.9H, dd,  $J$  13.68, 4.10 Hz,  $\text{PhCH}_2$ ), 2.64 (0.9H, dd,  $J$  13.62, 9.49 Hz,  $\text{PhCH}_2$ ), 2.50 (0.9H, quintet, residual  $\text{DMSO-d}_5$ ).  $\delta_{\text{C}}$  (100 MHz,  $\text{DMSO-d}_6$ ,  $25\text{ }^\circ\text{C}$ ) 171.90, 170.82, and 166.85 ( $\text{C}=\text{O}$ ), 157.98, 137.36,

137.10, 135.93, 133.96, 130.26, 129.26, 129.15, 129.07, 128.26, 128.14, 127.96, 127.59, 126.93, 126.66, 126.26, 119.44, 107.53, and 105.98 ( $C_{Ar}$ ), 120.32( $C\equiv N$ ), 66.68 ( $OCH_2$ ), 53.52 ( $CH^*$ ), 53.34 ( $CH^*$ ), 52.00 ( $OCH_3$ ), 39.52 (septet,  $DMSO-d_6$ ), 37.67 ( $PhC_bH_2$ ), 36.94 ( $PhC_aH_2$ ).

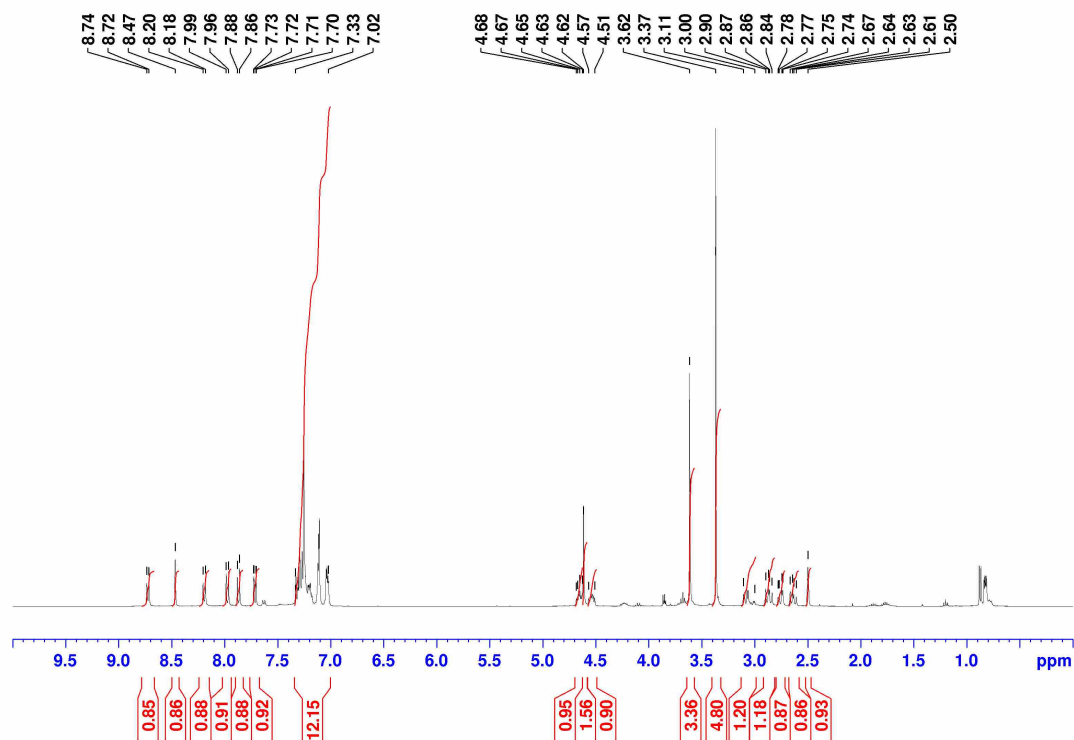


**Figure A3-45.**  $^1H$  NMR spectrum of 6CN-007 in  $d_6$ -DMSO at 25 °C.

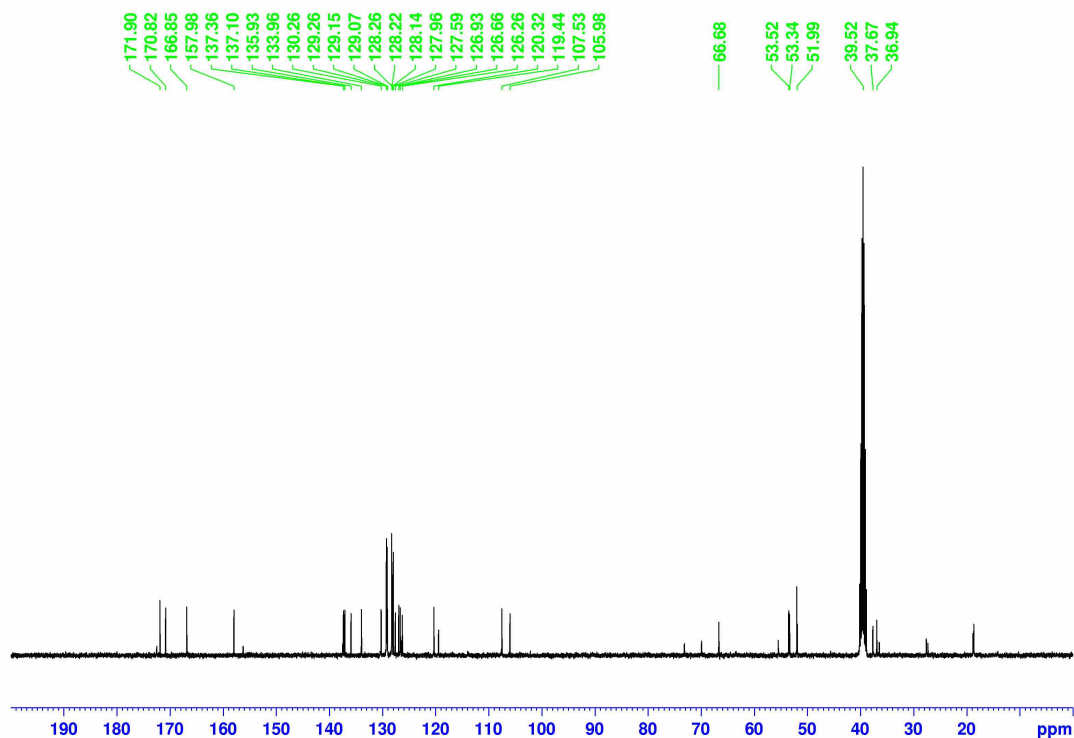
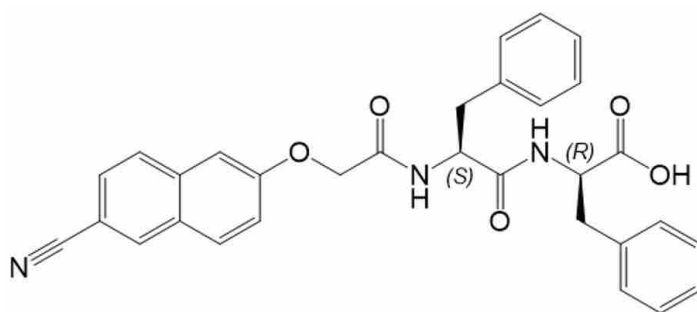


**Figure A3-46.**  $^{13}\text{C}$  NMR spectrum of 6CN-007 in  $\text{d}_6$ -DMSO at 25 °C.

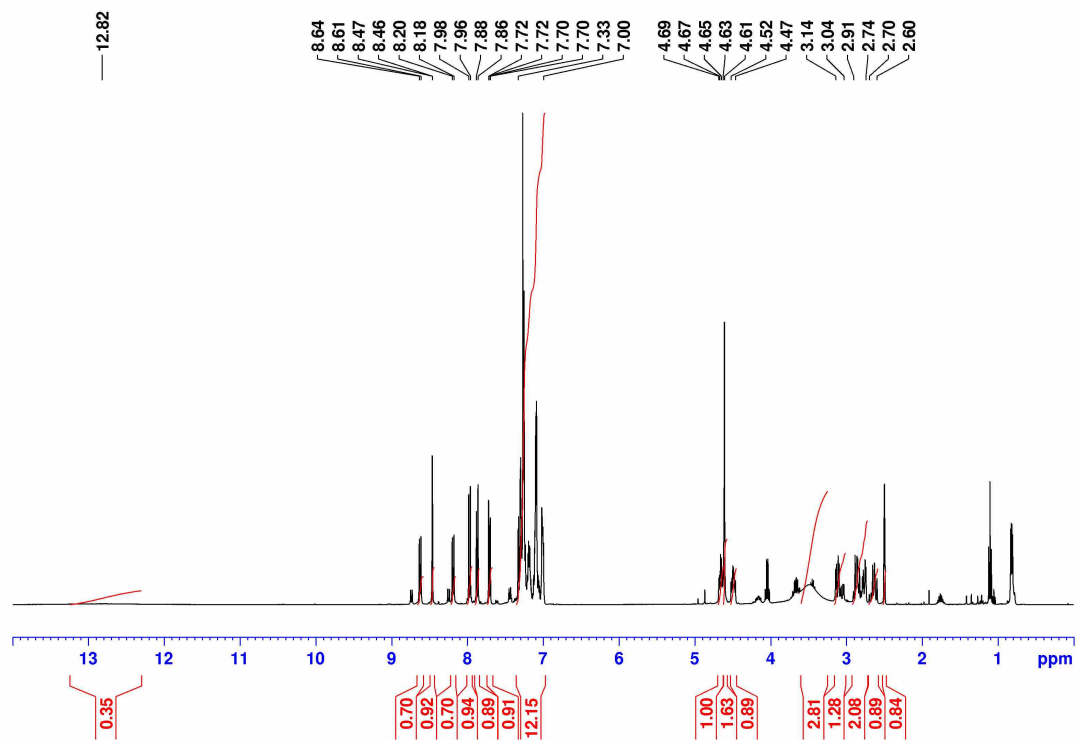
**(2R)-2-[(2S)-2-{2-[(6-Cyanonaphthalen-2-yl)oxy]acetamido}-3-phenylpropanamido]-3-phenylpropanoic acid (6CN-008)**



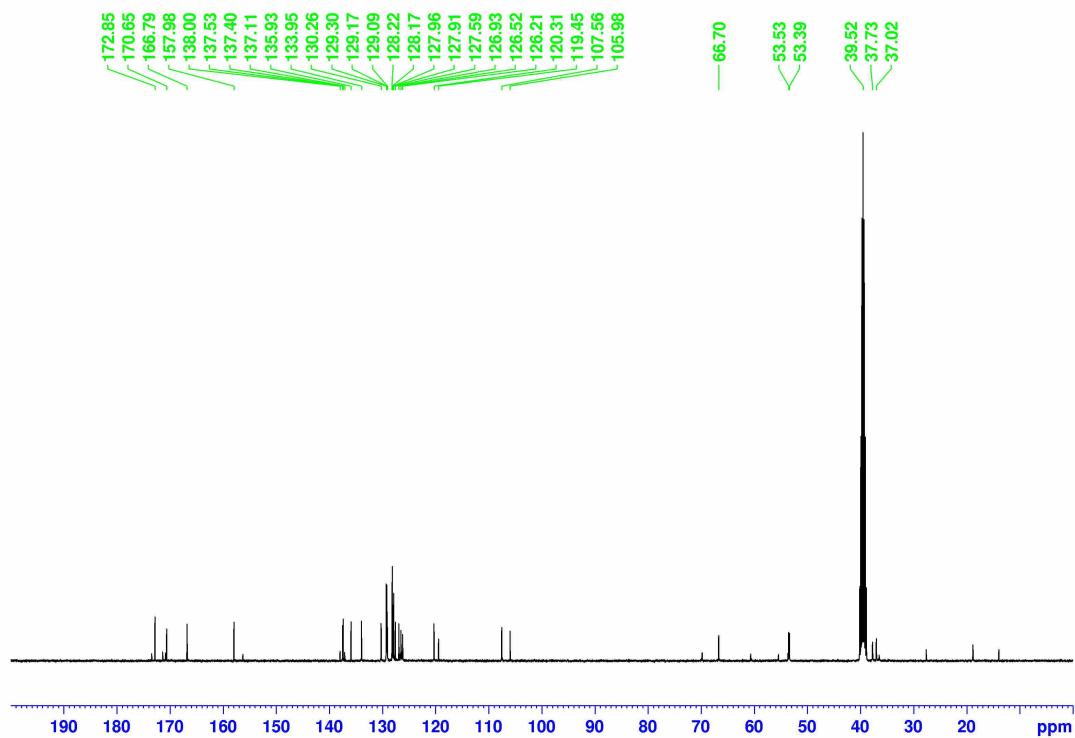
$\delta_{\text{H}}$  (400 MHz,  $\text{DMSO-d}_6$ , 25 °C) 12.82 (0.4H, br s,  $\text{COOH}$ ), 8.62 (0.7H, d,  $J$  8.36 Hz,  $\text{NH}$ ), 8.46 (0.9H, m,  $\text{H}_{\text{Ar}}$ ), 8.19 (0.7H, d,  $J$  8.64 Hz,  $\text{H}_{\text{Ar}}$ ), 7.97 (0.9H, d,  $J$  8.96 Hz,  $\text{H}_{\text{Ar}}$ ), 7.87 (0.9H, d,  $J$  8.64 Hz,  $\text{H}_{\text{Ar}}$ ), 7.71 (0.9H, dd,  $J$  8.52, 1.64 Hz,  $\text{H}_{\text{Ar}}$ ), 7.33-7.00 (12.1H, m,  $\text{H}_{\text{Ar}}$ ), 4.66 (1.0H, td,  $J$  9.16, 4.16 Hz,  $\text{CH}^*$ ), 4.61 (1.6H, s,  $\text{OCH}_2$ ), 4.52-4.47 (0.9H, m,  $\text{CH}^*$ ), 3.14-3.04 (1.3H, m,  $\text{PhCH}_2$ ), 2.91-2.74 (2.1H, m,  $\text{PhCH}_2$ ), 2.70-2.60 (0.9H, m,  $\text{PhCH}_2$ ), 2.50 (0.8H, quintet, residual  $\text{DMSO-d}_5$ ).  $\delta_{\text{C}}$  (100 MHz,  $\text{DMSO-d}_6$ , 25 °C) 172.85, 170.65, and 166.79 ( $\text{C}=\text{O}$ ), 157.98, 138.00, 137.53, 137.40, 137.11, 135.93, 133.95, 130.26, 129.30, 129.17, 129.09, 128.22, 128.17, 127.96,

127.91, 127.59, 126.93, 126.52, 126.21, 119.45, 107.56, and 105.98 ( $C_{Ar}$ ), 120.31 ( $C\equiv N$ ), 66.70 ( $OCH_2$ ), 53.53 ( $CH^*$ ), 53.39 ( $CH^*$ ), 39.52 (septet, DMSO- $d_6$ ), 37.73 ( $Ph_bCH_2$ ), 37.02 ( $Ph_aCH_2$ ).

**HRMS (ESI) m/z:**  $[M+H]^+$  accurate mass calculated for  $C_{31}H_{27}N_3HO_5$ : 522.1951; Found: 522.2015.

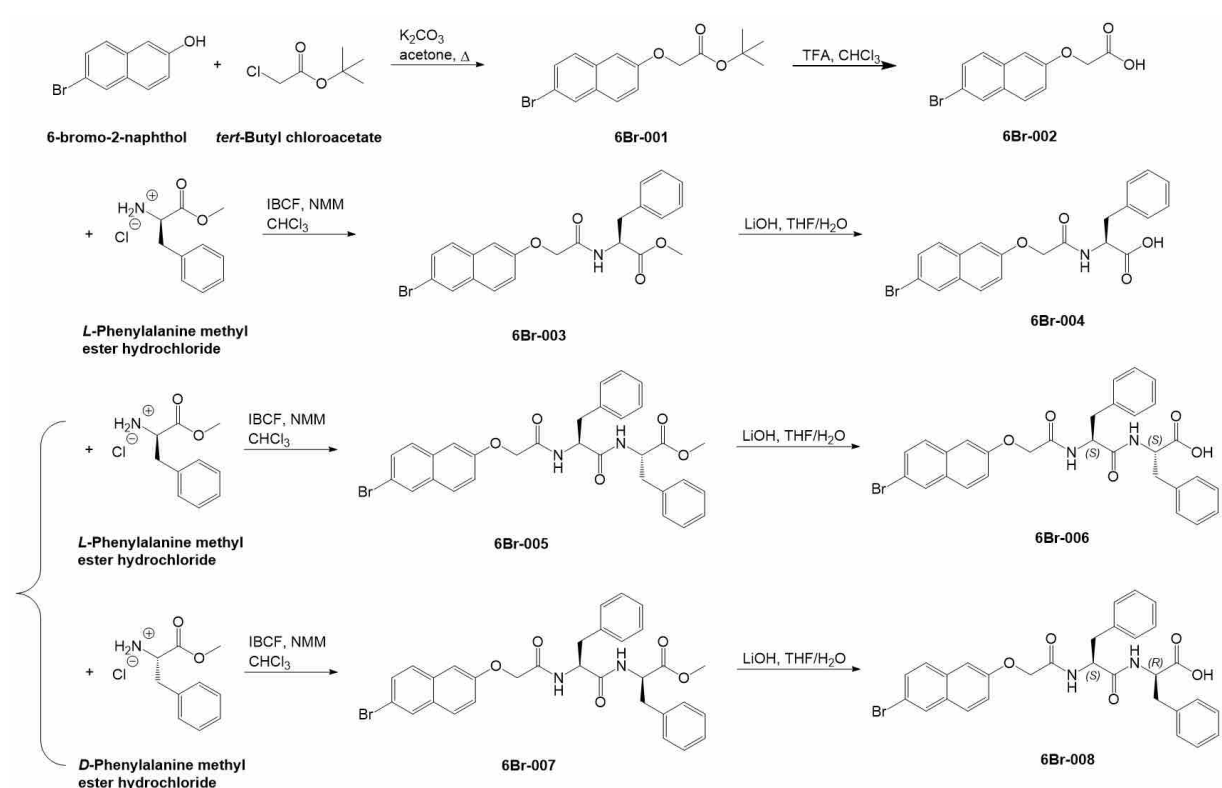


**Figure A3-47.**  $^1H$  NMR spectrum of 6CN-008 in  $d_6$ -DMSO at 25 °C.

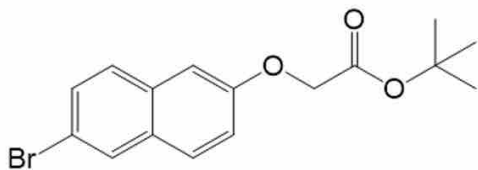


**Figure A3-48.**  $^{13}\text{C}$  NMR spectrum of 6CN-008 in  $\text{d}_6$ -DMSO at 25 °C.

## A3.2.4 6Br2NapFF



Scheme A3-4. Synthetic route of 6Br2NapFF.

**Tert-butyl 2-[(6-bromonaphthalen-2-yl)oxy]acetate (6Br-001)**

$\delta_{\text{H}}$  (400 MHz, DMSO- $d_6$ , 25 °C) 8.101-8.096 (1.1H, m,  $\underline{\text{H}}_{\text{Ar}}$ ), 7.83 (1.1H, d,  $J$  8.93 Hz,  $\underline{\text{H}}_{\text{Ar}}$ ), 7.74 (1.2H, d,  $J$  8.79 Hz,  $\underline{\text{H}}_{\text{Ar}}$ ), 7.55 (1.1H, dd,  $J$  8.75, 2.01 Hz,  $\underline{\text{H}}_{\text{Ar}}$ ), 7.28-7.23 (2.2H, m,  $\underline{\text{H}}_{\text{Ar}}$ ), 4.77 (2.0H, s,  $\underline{\text{OCH}}_2$ ), 3.39 (3.0H, br s,  $\underline{\text{H}}_2\text{O}$ ), 2.50 (0.4H, quintet, residual DMSO- $d_5$ ), 1.424 (7.2H, s, Rot-2  $\text{C}(\underline{\text{CH}}_3)_3$ ), 1.418 (2.2H, s, Rot-1  $\text{C}(\underline{\text{CH}}_3)_3$ ).  $\delta_{\text{C}}$  (100 MHz, DMSO- $d_6$ , 25 °C) 167.56 ( $\underline{\text{C}}=\text{O}$ ), 155.93, 132.64, 129.88, 129.36, 129.33, 128.93, 128.70, 119.52, 116.58, 107.30 ( $\underline{\text{C}}_{\text{Ar}}$ ), 81.49 ( $\underline{\text{C}}(\underline{\text{CH}}_3)_3$ ), 65.09 ( $\underline{\text{OCH}}_2$ ), 39.52 (septet, DMSO- $d_6$ ), 27.68 (Rot-2  $\text{C}(\underline{\text{CH}}_3)_3$ ), 27.53 (Rot-1  $\text{C}(\underline{\text{CH}}_3)_3$ ).

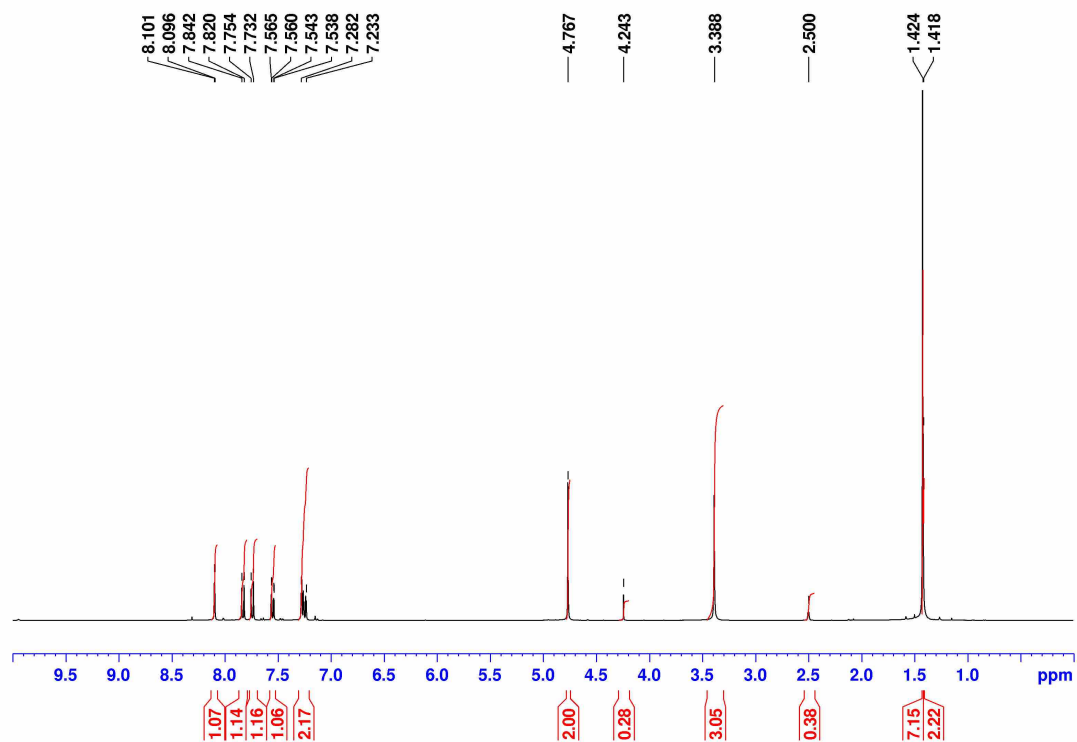


Figure A3-49.  $^1\text{H}$  NMR spectrum of 6Br-001 in  $d_6$ -DMSO at 25 °C.

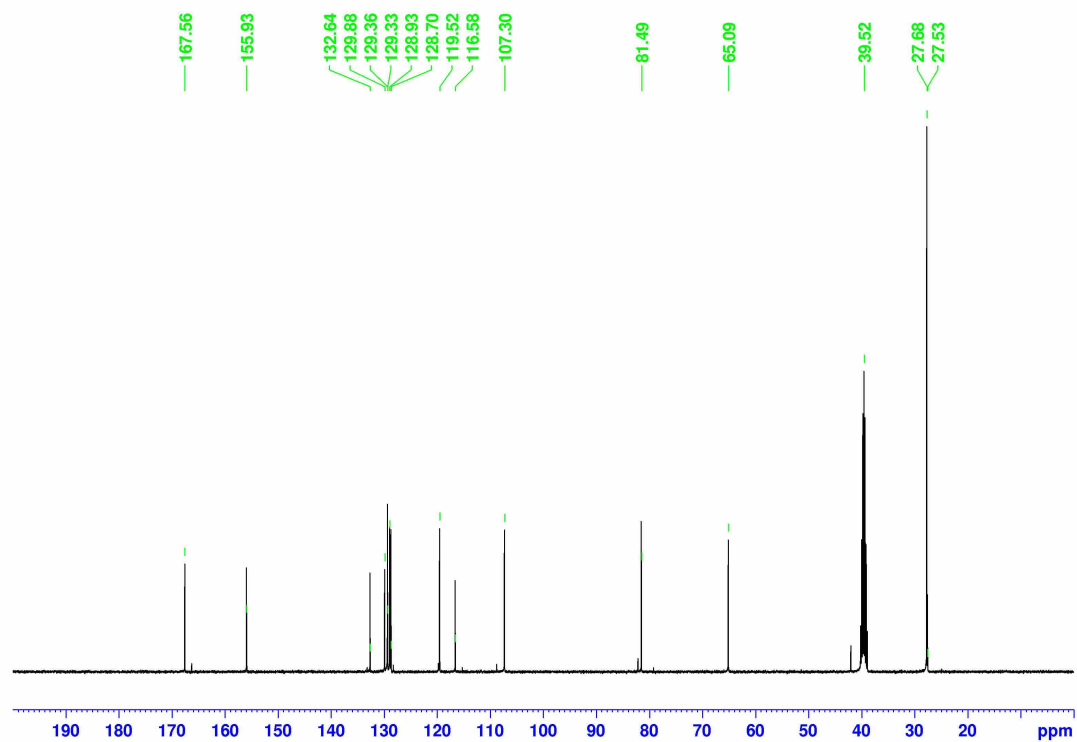
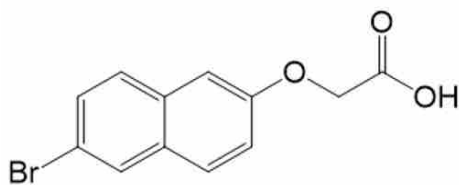
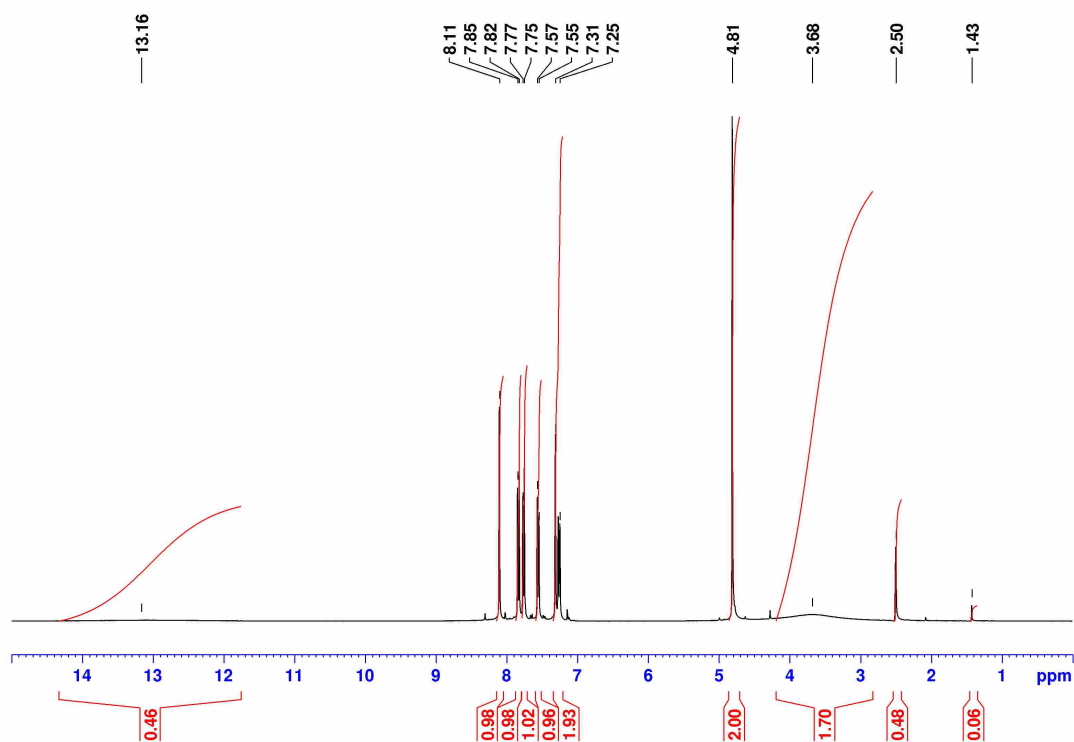


Figure A3-50.  $^{13}\text{C}$  NMR spectrum of 6Br-001 in  $d_6$ -DMSO at 25 °C.

**2-[(6-Bromonaphthalen-2-yl)oxy]acetic acid (6Br-002)**

$\delta_{\text{H}}$  (400 MHz, DMSO- $d_6$ , 25 °C) 13.16 (0.5H, br s, COOH), 8.11 (1.0H, s,  $\underline{\text{H}}_{\text{Ar}}$ ), 7.84 (1.0H, d,  $J$  8.96 Hz,  $\underline{\text{H}}_{\text{Ar}}$ ), 7.76 (1.0H, d,  $J$  8.76 Hz,  $\underline{\text{H}}_{\text{Ar}}$ ), 7.56 (1.0H, d,  $J$  8.72 Hz,  $\underline{\text{H}}_{\text{Ar}}$ ), 7.31-7.25 (1.9H, m,  $\underline{\text{H}}_{\text{Ar}}$ ), 4.81 (2.0H, s, OCH $\underline{2}$ ), 3.68 (1.7H, br s,  $\underline{\text{H}}_2\text{O}$ ), 2.50 (0.5H, quintet, residual DMSO- $d_5$ ).  
 $\delta_{\text{C}}$  (100 MHz, DMSO- $d_6$ , 25 °C) 169.98 ( $\underline{\text{C}}=\text{O}$ ), 156.07, 132.71, 129.89, 129.39, 129.35, 128.99, 128.74, 119.66, 116.56, 107.18 ( $\underline{\text{C}}_{\text{Ar}}$ ), 64.58 (OCH $\underline{2}$ ), 39.52 (septet, DMSO- $d_6$ ).



**Figure A3-51.**  $^1\text{H}$  NMR spectrum of 6Br-002 in  $d_6$ -DMSO at 25 °C.

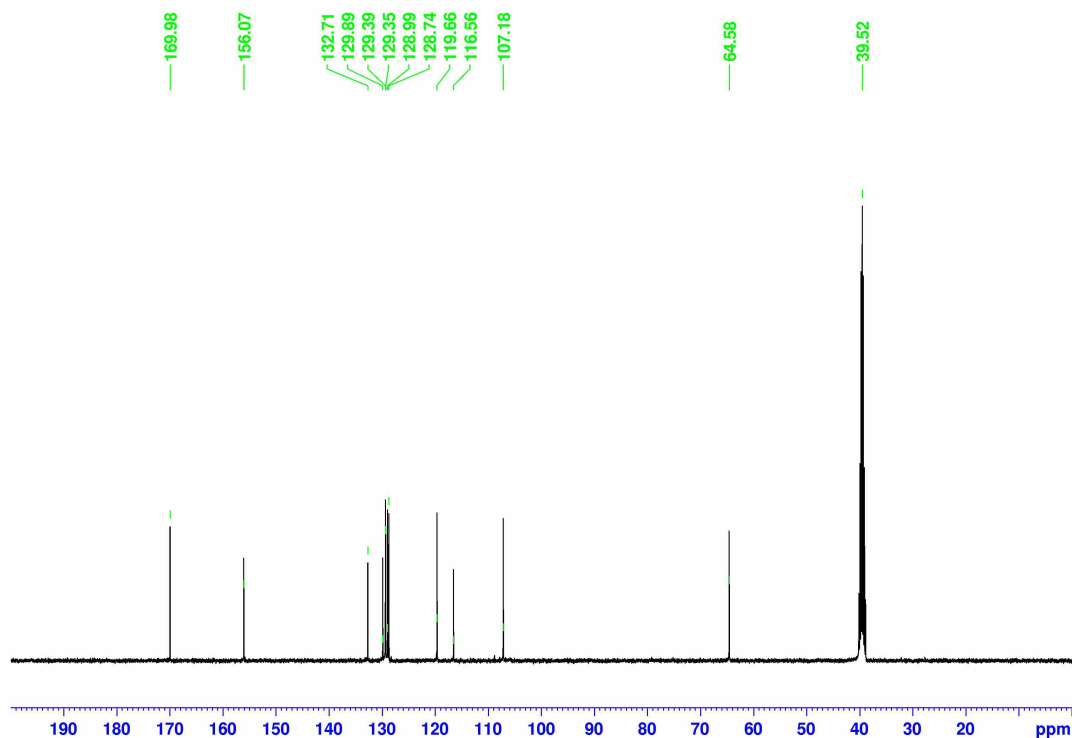
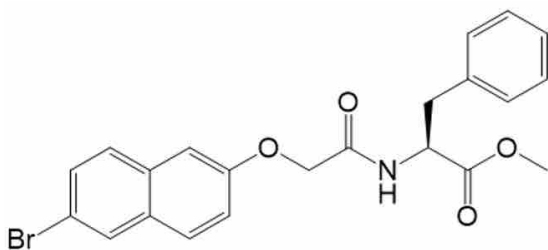


**Figure A3-52.**  $^{13}\text{C}$  NMR spectrum of 6Br-002 in  $\text{d}_6$ -DMSO at 25 °C.

**Methyl (2S)-2-{2-[(6-bromonaphthalen-2-yl)oxy]acetamido}-3-phenylpropanoate (6Br-003)**



$\delta_{\text{H}}$  (400 MHz,  $\text{DMSO-d}_6$ , 25 °C) 8.57 (1.0H, d,  $J$  8.00 Hz,  $\text{NH}$ ), 8.31 (0.05H, s, CH in chloroform), 8.125-8.120 (1.0H, m,  $\text{H}_{\text{Ar}}$ ), 7.85 (1.0H, d,  $J$  8.96 Hz,  $\text{H}_{\text{Ar}}$ ), 7.70 (1.0H, d,  $J$  8.84 Hz,  $\text{H}_{\text{Ar}}$ ), 7.58 (1.0H, dd,  $J$  8.75, 2.02 Hz,  $\text{H}_{\text{Ar}}$ ), 7.28-7.15 (7.2H, m,  $\text{H}_{\text{Ar}}$ ), 4.66-4.58 (2.9H, m,  $\text{OCH}_2$  and  $\text{CH}^*$ ), 3.62 (3.0H, s,  $\text{OCH}_3$ ), 3.37 (2.7H, br s,  $\text{H}_2\text{O}$ ), 3.12 (1.0H, dd,  $J$  13.81, 5.23 Hz,  $\text{PhCH}_2\text{H}_b$ ), 3.02 (1.0H, q,  $J$  9.38 Hz,  $\text{PhCH}_2\text{H}_b$ ), 2.50 (0.6H, quintet, residual  $\text{DMSO-d}_5$ ).  $\delta_{\text{C}}$  (100 MHz,  $\text{DMSO-d}_6$ , 25 °C) 171.71, 167.66 ( $\text{C}=\text{O}$ ), 155.95, 137.16, 132.62, 129.95, 129.39, 129.34, 129.06, 128.97, 128.65, 128.24, 126.54, 119.74, 116.62 and 107.44 ( $\text{C}_{\text{Ar}}$ ), 66.65 ( $\text{OCH}_2$ ), 53.24 ( $\text{CH}^*$ ), 52.02 ( $\text{OCH}_3$ ), 39.52 (septet,  $\text{DMSO-d}_6$ ), 36.33 ( $\text{PhCH}_2$ ).

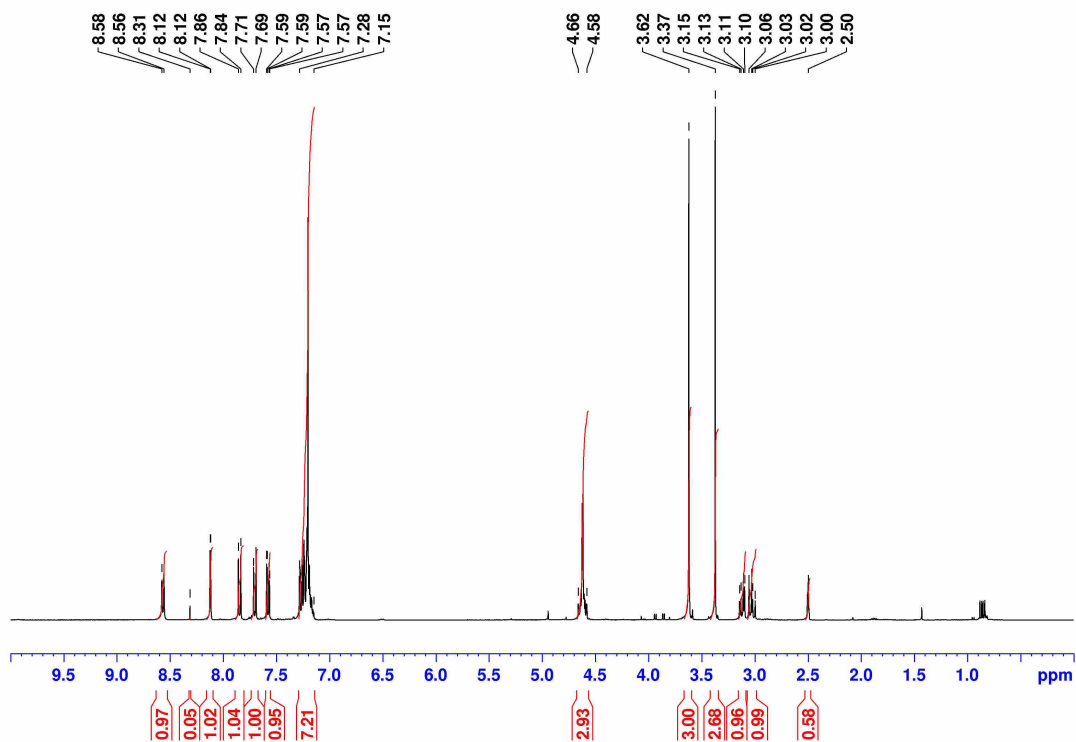


Figure A3-53.  $^1\text{H}$  NMR spectrum of 6Br-003 in  $d_6$ -DMSO at 25 °C.

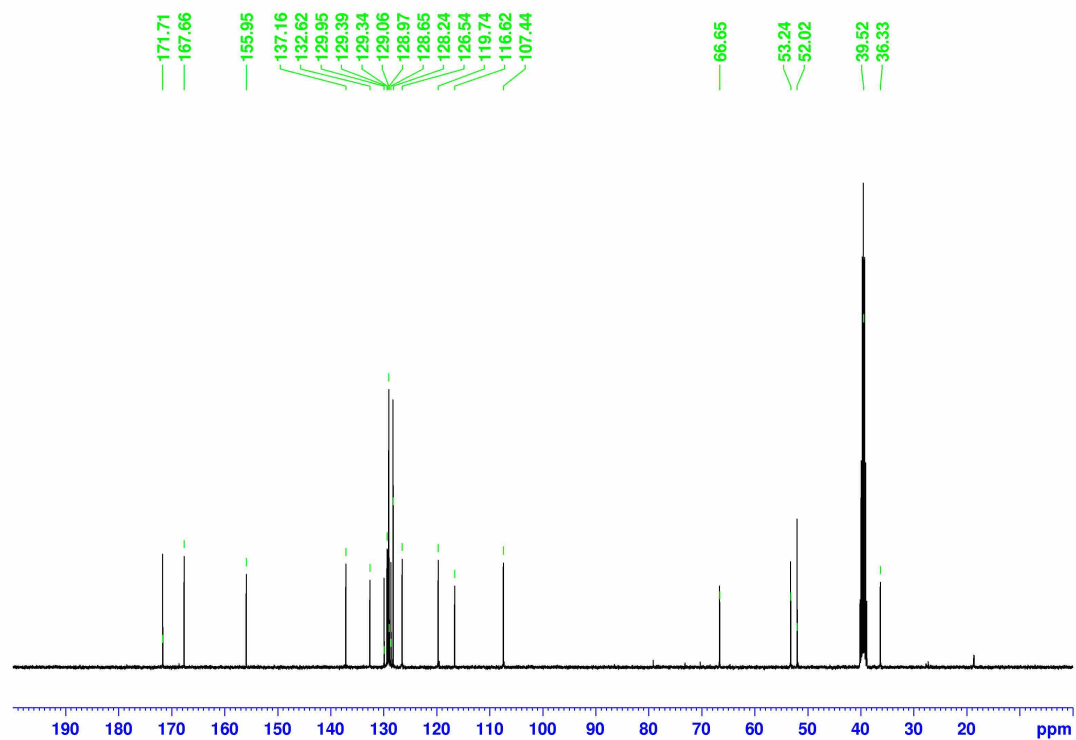
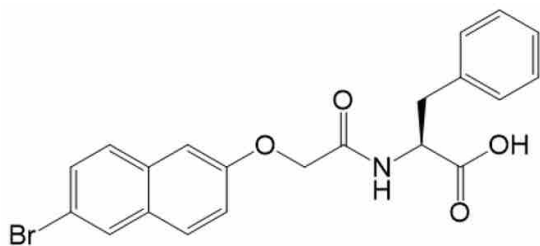
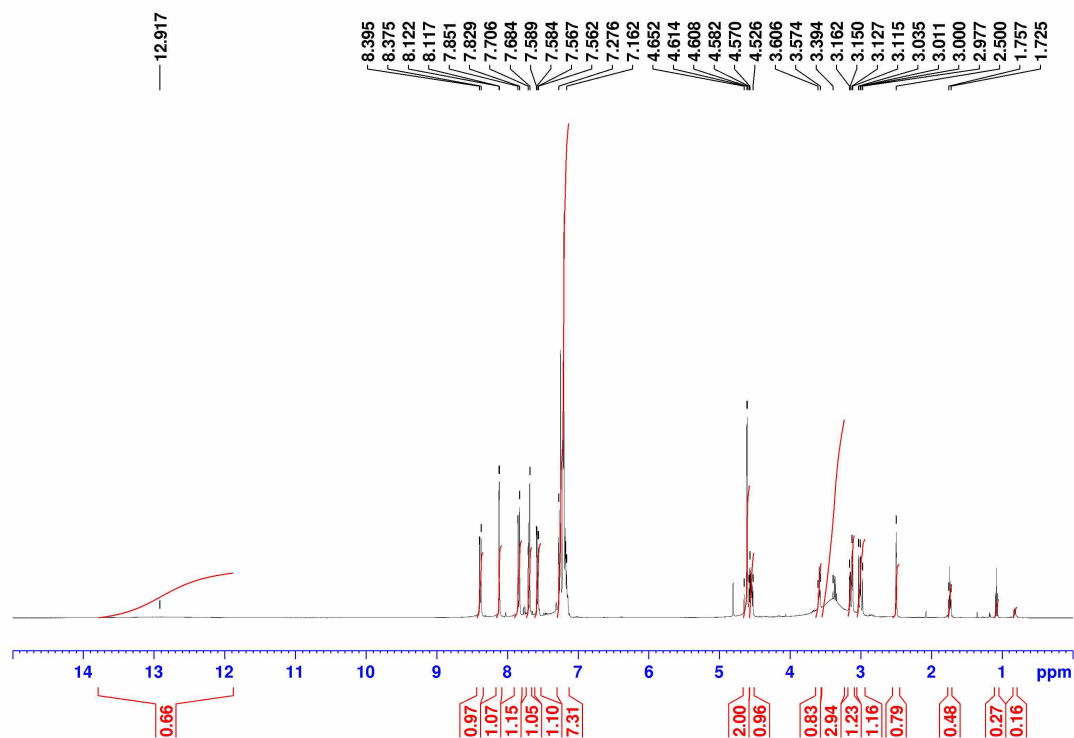


Figure A3-54.  $^{13}\text{C}$  NMR spectrum of 6Br-003 in  $d_6$ -DMSO at 25 °C.

**(2S)-2-{2-[(6-Bromonaphthalen-2-yl)oxy]acetamido}-3-phenylpropanoic acid (6Br-004)**

$\delta_{\text{H}}$  (400 MHz, DMSO- $d_6$ , 25 °C) 12.92 (0.7H, br s, COOH), 8.39 (1.0H, d,  $J$  8.19 Hz, NH), 8.122-8.117 (1.1H, m,  $\text{H}_{\text{Ar}}$ ), 7.84 (1.1H, , d,  $J$  8.73 Hz,  $\text{H}_{\text{Ar}}$ ), 7.70 (1.0H, d,  $J$  8.80 Hz,  $\text{H}_{\text{Ar}}$ ), 7.58 (1.1H, dd,  $J$  8.73, 1.99 Hz,  $\text{H}_{\text{Ar}}$ ), 7.28 (7.3H, m,  $\text{H}_{\text{Ar}}$ ), 4.65-4.58 (2.0H, m,  $\text{OCH}_2$ ), 4.57-4.53 (1.0H, m,  $\text{CH}^*$ ), 3.61-3.57 (0.8H, m,  $\text{CH}_2\text{O}$  in THF), 3.39 (2.9H, br s,  $\text{H}_2\text{O}$ ), 3.14 (1.2H, dd,  $J$  13.84, 4.64 Hz,  $\text{PhCH}_a\text{H}_b$ ), 3.01 (1.2H, dd,  $J$  13.83, 9.46 Hz,  $\text{PhCH}_a\text{H}_b$ ), 2.50 (0.8H, quintet, residual DMSO- $d_5$ ), 1.76-1.73 (0.5H, m,  $\text{CH}_2$  in THF).  $\delta_{\text{C}}$  (100 MHz, DMSO- $d_6$ , 25 °C) 172.74, 167.53 ( $\text{C}=\text{O}$ ), 155.98, 137.63, 132.66, 129.96, 129.40, 129.33, 129.11, 129.02, 128.67, 128.21, 126.47, 119.77, 116.63 and 107.49 ( $\text{C}_{\text{Ar}}$ ), 66.73 ( $\text{OCH}_2$ ), 53.20 ( $\text{CH}^*$ ), 39.52 (septet, DMSO- $d_6$ ), 36.41 ( $\text{PhCH}_2$ ).



**Figure A3-55.**  $^1\text{H}$  NMR spectrum of 6Br-004 in  $d_6$ -DMSO at 25 °C.

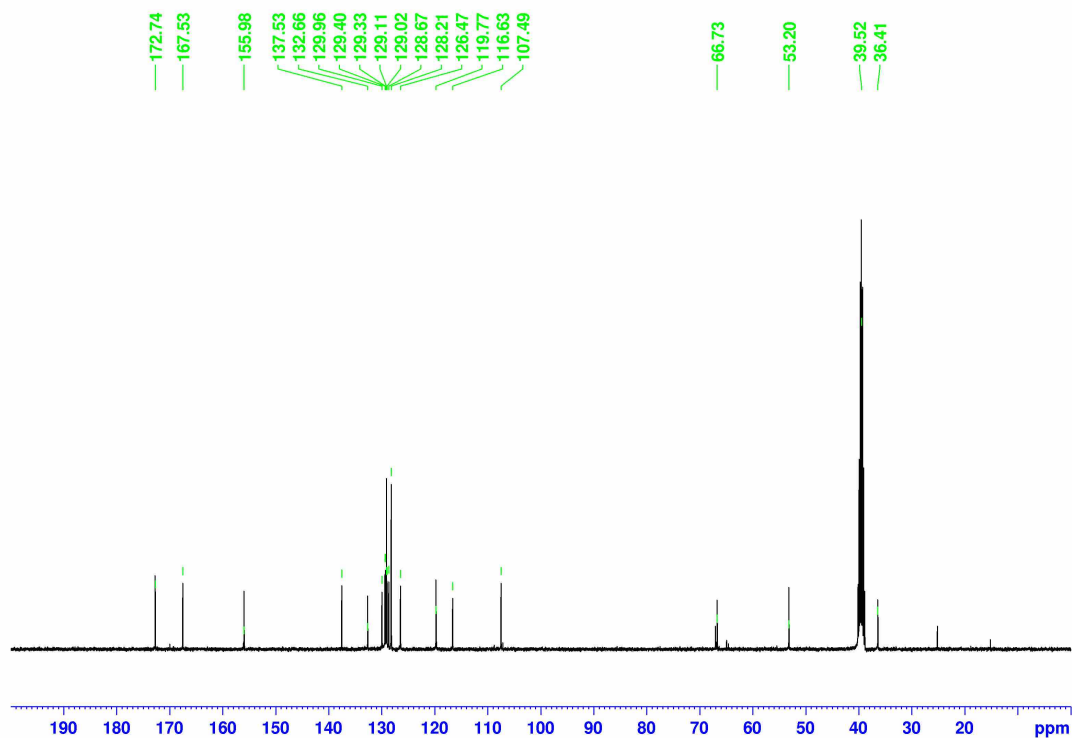
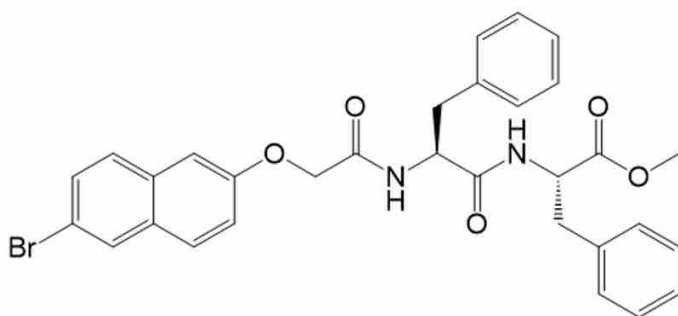


**Figure A3-56.**  $^{13}\text{C}$  NMR spectrum of 6Br-004 in  $\text{d}_6$ -DMSO at 25 °C.

**Methyl (2S)-2-[(2S)-2-{2-[(6-bromonaphthalen-2-yl)oxy]acetamido}-3-phenylpropanamido]-3-phenylpropanoate (6Br-005)**



$\delta_{\text{H}}$  (400 MHz,  $\text{DMSO-d}_6$ , 25 °C) 8.61 (0.6H, d,  $J$  7.56 Hz,  $\text{NH}$ ), 8.30 (0.3H, s,  $\text{CH}$  in chloroform), 8.18 (0.8H, d,  $J$  8.57 Hz,  $\text{NH}$ ), 8.12 (1.1H, m,  $\text{H}_{\text{Ar}}$ ), 7.83 (1.0H, d,  $J$  8.75 Hz,  $\text{H}_{\text{Ar}}$ ), 7.69 (0.9H, d,  $J$  8.79 Hz,  $\text{H}_{\text{Ar}}$ ), 7.58-7.56 (1.0H, m,  $\text{H}_{\text{Ar}}$ ), 7.30-7.00 (12.8H, m,  $\text{H}_{\text{Ar}}$ ), 4.67-4.60 (1.0H, m,  $\text{CH}^*$ ), 4.54 (1.6H, m,  $\text{OCH}_2$ ), 4.51-4.48 (0.8H, m,  $\text{CH}^*$ ), 3.58 (2.7H, s,  $\text{OCH}_3$ ), 3.40 (63.7H, br s,  $\text{H}_2\text{O}$ ), 3.10-2.91 (3.1H, m,  $\text{PhCH}_2$ ), 2.89-2.81 (1.4H, m,  $\text{PhCH}_2$ ), 2.50 (5.1H, quintet, residual  $\text{DMSO-d}_5$ ).  $\delta_{\text{C}}$  (100 MHz,  $\text{DMSO-d}_6$ , 25 °C) 171.76, 171.03, and 167.17 ( $\text{C}=\text{O}$ ), 155.96, 137.48, 136.99, 132.67, 129.95, 129.40, 129.34, 129.23, 129.09, 129.04, 128.71, 128.30, 128.05, 126.63,

126.35, 119.69, 116.62 and 107.44 ( $C_{Ar}$ ), 66.68 ( $OCH_2$ ), 53.70 ( $CH^*$ ), 53.26 ( $CH^*$ ), 51.93 ( $OCH_3$ ), 39.52 (septet,  $DMSO-d_6$ ), 37.43 ( $PhC_bH_2$ ), 36.64 ( $PhC_aH_2$ ).

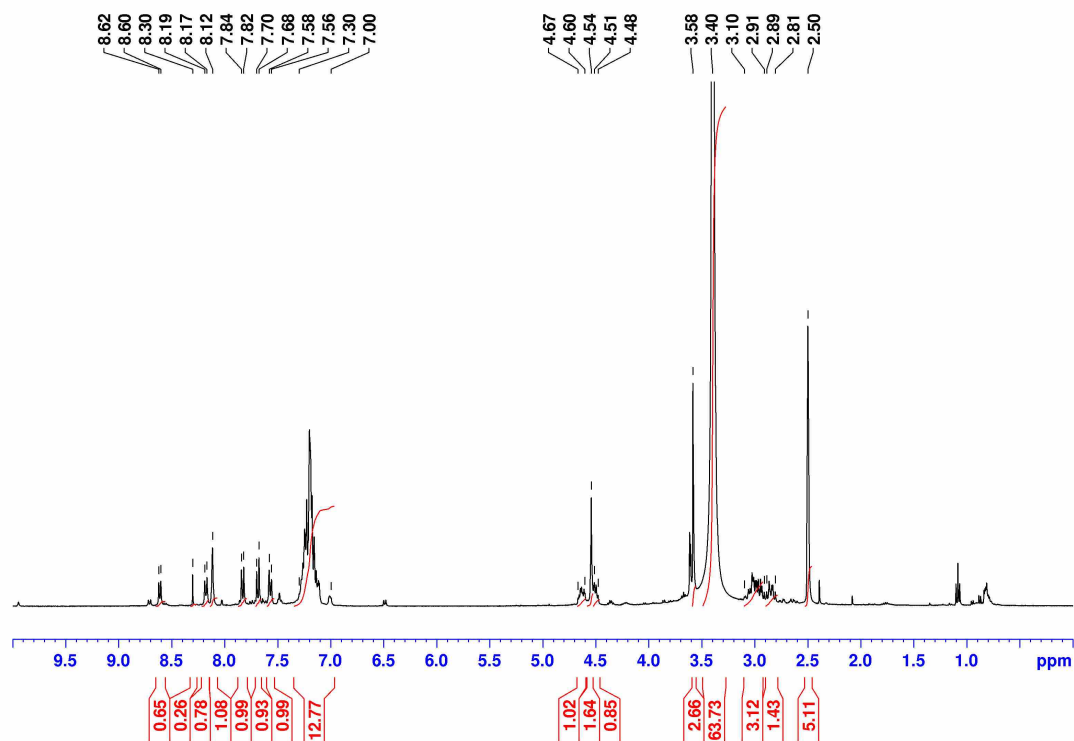


**Figure A3-57.**  $^1H$  NMR spectrum of 6Br-005 in  $d_6$ -DMSO at 25 °C.

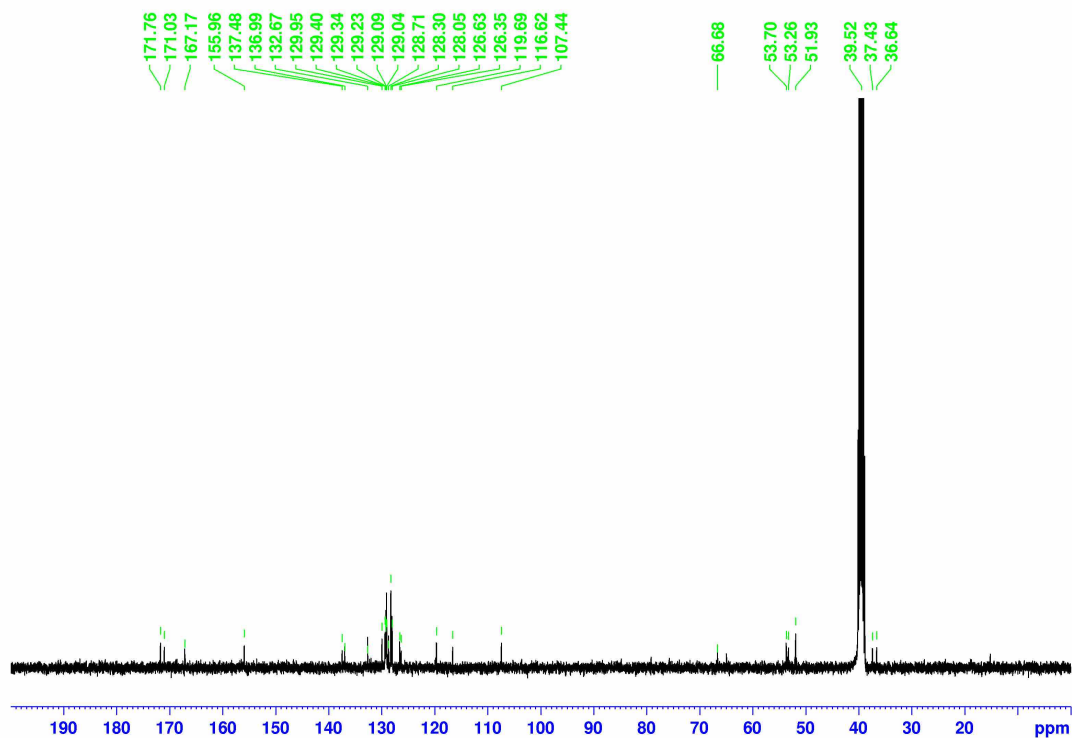
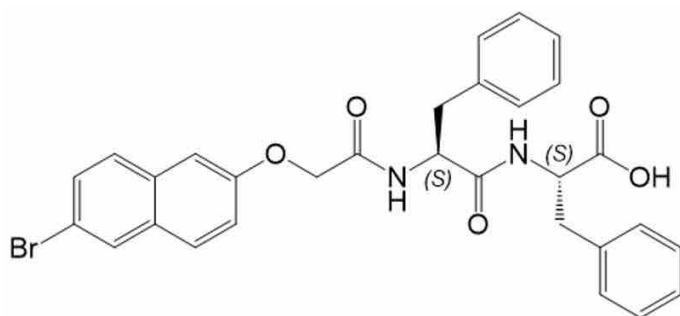


**Figure A3-58.**  $^{13}\text{C}$  NMR spectrum of 6Br-005 in  $\text{d}_6$ -DMSO at 25 °C.

**(2S)-2-[(2S)-2-{2-[(6-Bromonaphthalen-2-yl)oxy]acetamido}-3-phenylpropanamido]-3-phenylpropanoic acid (6Br-006)**



$\delta_{\text{H}}$  (400 MHz, DMSO- $\text{d}_6$ , 25 °C) 12.82 (1.0H, br s, COOH), 8.46 (0.9H, d,  $J$  7.86 Hz, NH), 8.17 (1.0H, d,  $J$  8.58 Hz, NH), 8.12-8.11 (1.0H, m,  $\text{H}_{\text{Ar}}$ ), 7.83 (1.0H, d,  $J$  8.95 Hz,  $\text{H}_{\text{Ar}}$ ), 7.69 (1.0H, d,  $J$  8.87 Hz,  $\text{H}_{\text{Ar}}$ ), 7.57 (1.0H, dd,  $J$  8.76, 2.03 Hz,  $\text{H}_{\text{Ar}}$ ), 7.26-7.12 (12.3H, m,  $\text{H}_{\text{Ar}}$ ), 4.67 (1.0H, td,  $J$  9.31, 4.08 Hz,  $\text{CH}^*$ ), 4.55 (1.9H, m,  $\text{OCH}_2$ ), 4.53-4.47 (1.1H, m,  $\text{CH}^*$ ), 3.38 (1.0H, br s,  $\text{H}_2\text{O}$ ), 3.11-3.02 (2.0H, m,  $\text{PhCH}_2$ ), 2.96-2.83 (2.0H, m,  $\text{PhCH}_2$ ), 2.50 (0.8H, quintet, residual DMSO- $\text{d}_5$ ), 2.07 (0.02H, s,  $\text{CH}_3$  in acetone).  $\delta_{\text{C}}$  (100 MHz, DMSO- $\text{d}_6$ , 25 °C) 172.71, 170.86, and 167.08 ( $\text{C}=\text{O}$ ), 155.93, 137.52, 137.35, 132.63, 129.92, 129.36, 129.29, 129.23, 129.12,

128.99, 128.66, 128.17, 127.97, 126.44, 126.26, 119.63, 116.59 and 107.44 ( $C_{Ar}$ ), 66.70 ( $OCH_2$ ), 53.50 ( $CH^*$ ), 53.25 ( $CH^*$ ), 39.52 (septet, DMSO- $d_6$ ), 37.41 ( $PhCH_2$ ), 36.99 ( $PhCH_2$ ).

**HRMS (ESI) m/z:**  $[M+H]^+$  accurate mass calculated for  $C_{30}H_{27}BrN_2HO_5$ : 575.1103; Found: 575.1168.

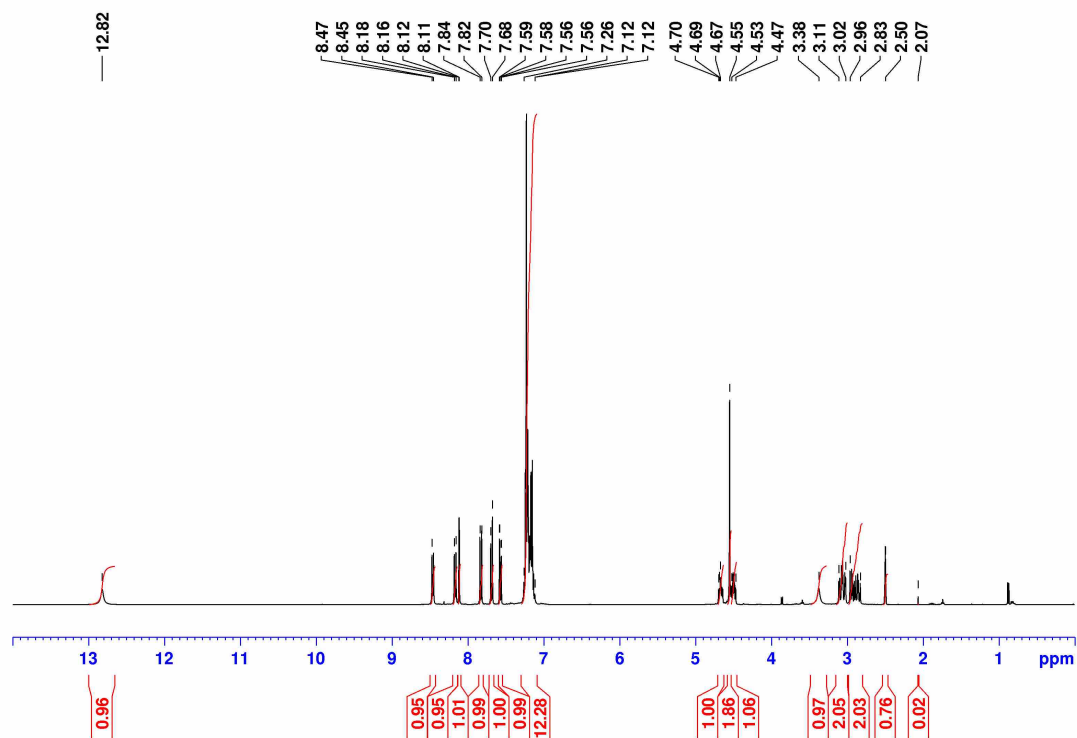


**Figure A3-59.**  $^1H$  NMR spectrum of 6Br-006 in  $d_6$ -DMSO at 25 °C.

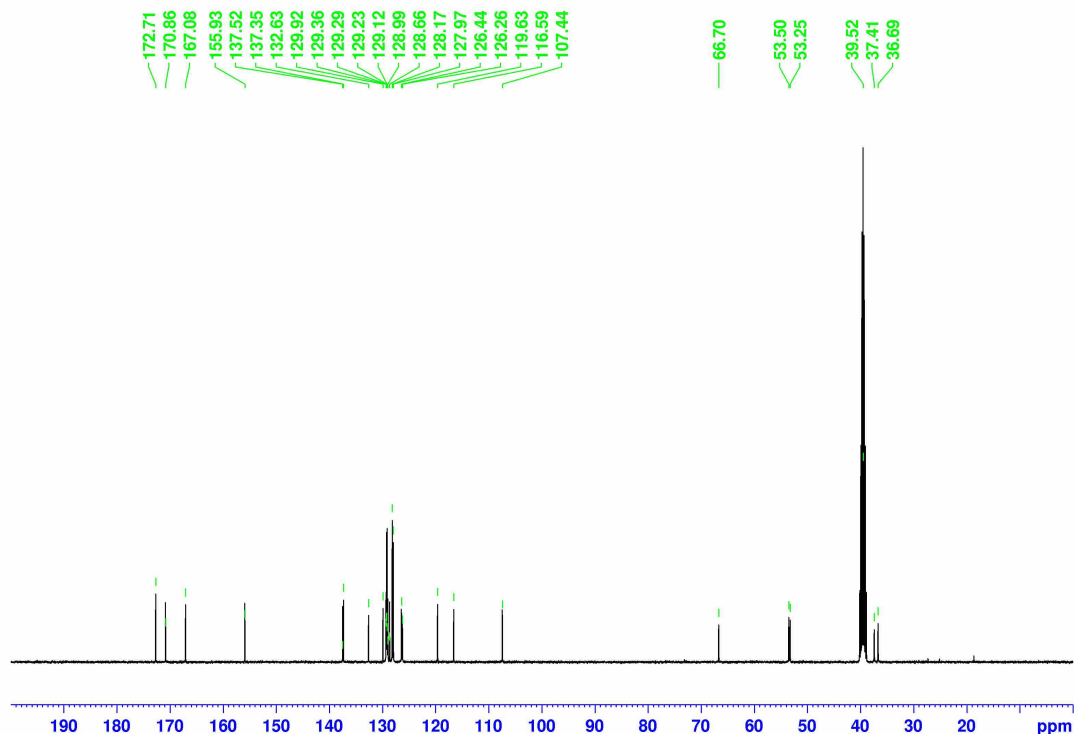
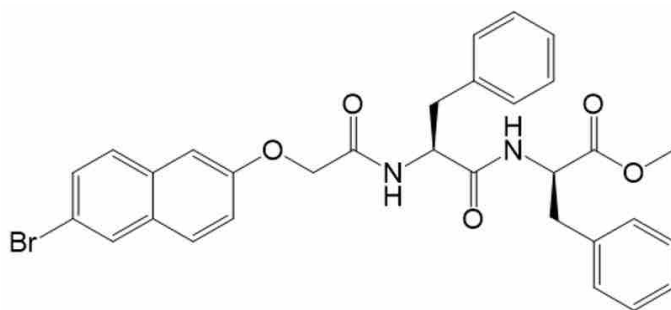


**Figure A3-60.**  $^{13}\text{C}$  NMR spectrum of 6Br-006 in  $\text{d}_6$ -DMSO at 25 °C.

**Methyl (2R)-2-[(2S)-2-{2-[(6-Bromonaphthalen-2-yl)oxy]acetamido}-3-phenylpropanamido]-3-phenylpropanoate (6Br-007)**



$\delta_{\text{H}}$  (400 MHz,  $\text{DMSO-d}_6$ , 25 °C) 8.73 (0.7H, d,  $J$  8.02 Hz,  $\text{NH}$ ), 8.31 (0.4H, s,  $\text{CH}$  in chloroform), 8.21-8.11 (1.8H, m,  $\text{NH}$  and  $\text{H}_{\text{Ar}}$ ), 7.82 (1.0H, d,  $J$  8.70 Hz,  $\text{H}_{\text{Ar}}$ ), 7.69 (1.0H, d,  $J$  8.72 Hz,  $\text{H}_{\text{Ar}}$ ), 7.56 (1.0H, d,  $J$  8.67 Hz,  $\text{H}_{\text{Ar}}$ ), 7.27-7.03 (11.7H, m,  $\text{H}_{\text{Ar}}$ ), 4.74-4.51 (3.6H, m,  $\text{CH}^*$  and  $\text{OCH}_2$ ), 3.62 (3.0H, s,  $\text{OCH}_3$ ), 3.40 (7.3H, br s,  $\text{H}_2\text{O}$ ), 3.11-2.62 (4.2H, m,  $\text{PhCH}_2$ ), 2.50 (0.8H, quintet, residual  $\text{DMSO-d}_5$ ).  $\delta_{\text{C}}$  (100 MHz,  $\text{DMSO-d}_6$ , 25 °C) 171.91, 170.84, and 167.10 ( $\text{C}=\text{O}$ ), 155.94, 137.33, 137.11, 132.66, 129.94, 129.39, 129.32, 129.27, 129.18, 129.08, 129.01, 128.70, 128.28, 127.98, 126.68, 126.29, 119.66, 116.62 and 107.41 ( $\text{C}_{\text{Ar}}$ ), 79.20 ( $\text{CH}$  in chloroform), 66.68

(OCH<sub>2</sub>), 53.55 (CH<sup>\*</sup>), 53.32 (CH<sup>\*</sup>), 52.01 (OCH<sub>3</sub>), 39.52 (septet, DMSO-d<sub>6</sub>), 37.70 (PhC<sub>b</sub>H<sub>2</sub>), 36.95 (PhC<sub>a</sub>H<sub>2</sub>).

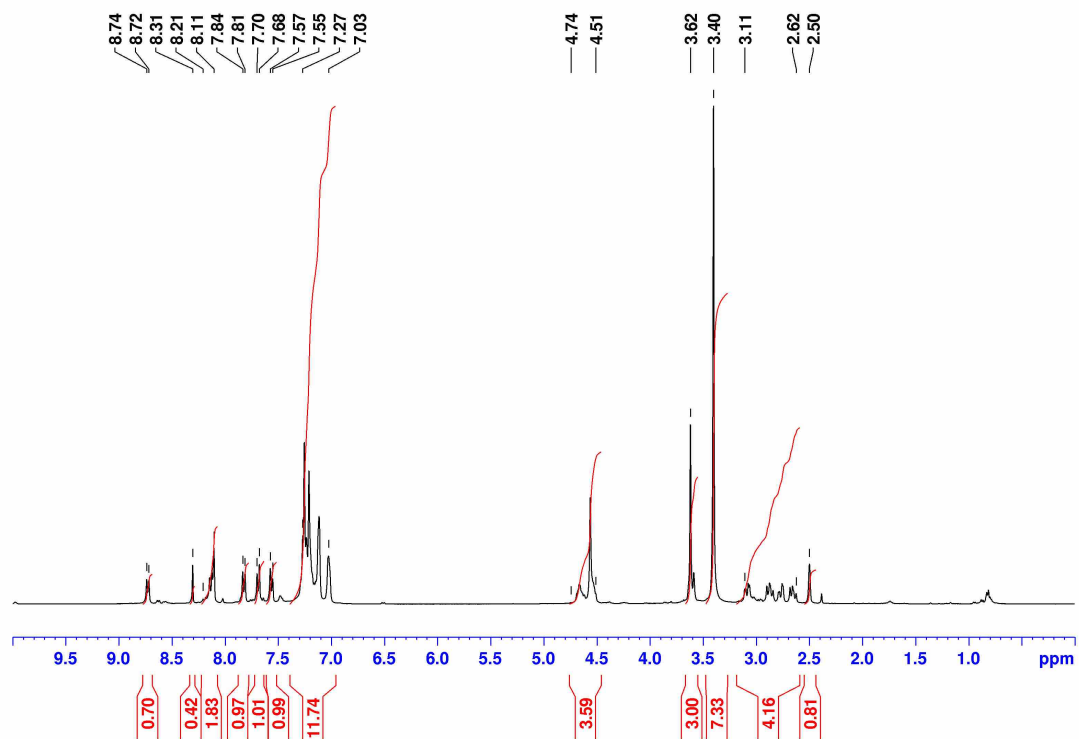


**Figure A3-61.** <sup>1</sup>H NMR spectrum of 6Br-007 in d<sub>6</sub>-DMSO at 25 °C.

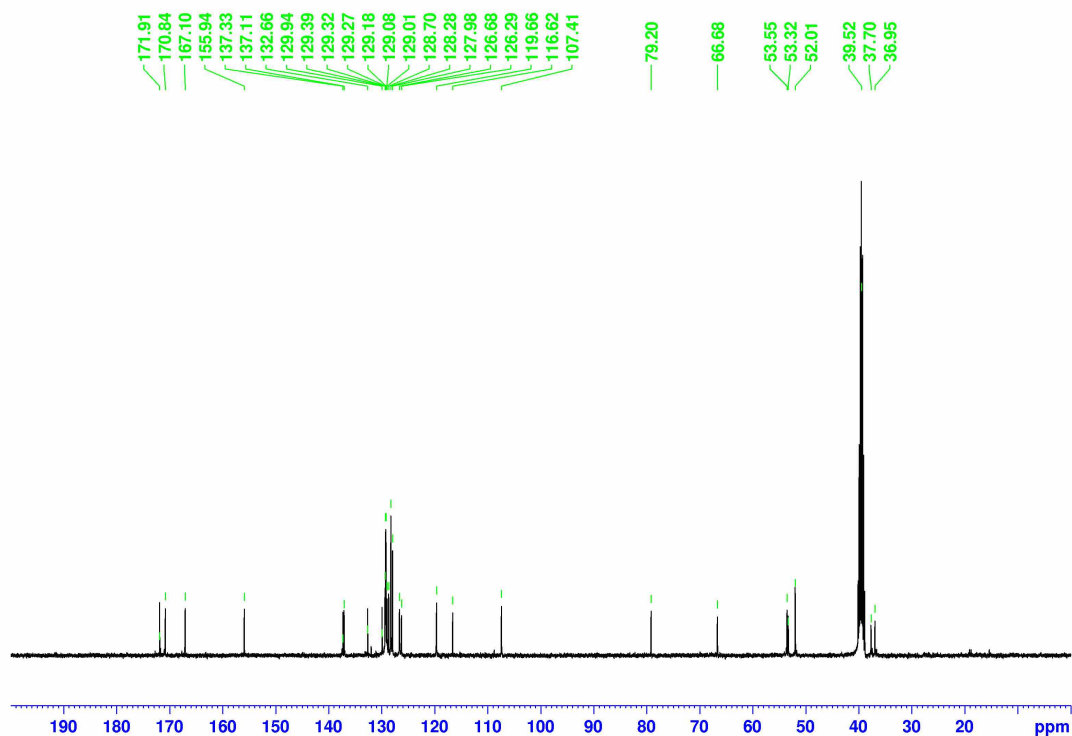
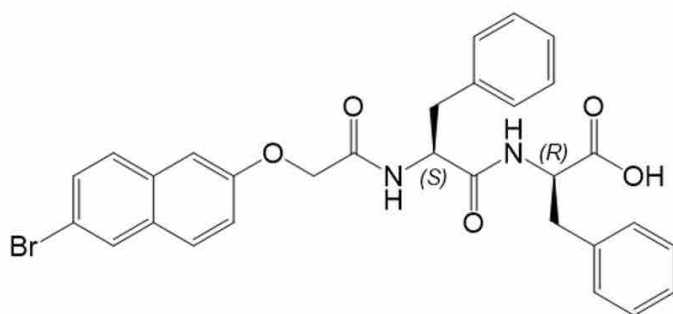


**Figure A3-62.**  $^{13}\text{C}$  NMR spectrum of 6Br-007 in  $\text{d}_6$ -DMSO at 25 °C.

**(2R)-2-[(2S)-2-{2-[(6-Bromonaphthalen-2-yl)oxy]acetamido}-3-phenylpropanamido]-3-phenylpropanoic acid (6Br-008)**



$\delta_{\text{H}}$  (400 MHz, DMSO- $\text{d}_6$ , 25 °C) 12.83 (0.7H, br s, COOH), 8.60 (0.9H, d,  $J$  8.36 Hz, NH), 8.11-8.09 (1.9H, m, NH and  $\text{H}_{\text{Ar}}$ ), 7.84-7.81 (1.0H, m,  $\text{H}_{\text{Ar}}$ ), 7.69 (1.0H, d,  $J$  7.86 Hz,  $\text{H}_{\text{Ar}}$ ), 7.57 (1.0H, dd,  $J$  8.76, 2.03 Hz,  $\text{H}_{\text{Ar}}$ ), 7.28-6.99 (12.6H, m,  $\text{H}_{\text{Ar}}$ ), 4.67 (1.0H, td,  $J$  9.02, 4.12 Hz,  $\text{CH}^*$ ), 4.56 (1.9H, s,  $\text{OCH}_2$ ), 4.53-4.47 (1.0H, m,  $\text{CH}^*$ ), 3.13 (1.1H, dd,  $J$  13.66, 4.56 Hz,  $\text{Ph}_a\text{CH}_a\text{H}_b$ ), 2.86 (1.1H, dd,  $J$  13.67, 10.05 Hz,  $\text{Ph}_a\text{CH}_a\text{H}_b$ ), 2.77 (1.0H, dd,  $J$  13.65, 4.09 Hz,  $\text{Ph}_b\text{CH}_a\text{H}_b$ ), 2.63 (1.0H, dd,  $J$  13.65, 9.30 Hz,  $\text{Ph}_b\text{CH}_a\text{H}_b$ ), 2.50 (0.8H, quintet, residual DMSO- $\text{d}_5$ ).  $\delta_{\text{C}}$  (100 MHz, DMSO- $\text{d}_6$ , 25 °C) 172.87, 170.61, and 166.99 ( $\text{C}=\text{O}$ ), 155.92, 137.50, 137.35,

132.64, 129.92, 129.36, 129.29, 129.17, 129.08, 128.99, 128.67, 128.18, 127.91, 126.53, 126.21, 119.62, 116.60, and 107.43 ( $C_{Ar}$ ), 66.69 ( $OCH_2$ ), 53.50 ( $CH^*$ ), 53.28 ( $CH^*$ ), 39.52 (septet, DMSO- $d_6$ ), 37.75 ( $Ph_bCH_2$ ), 37.04 ( $Ph_aCH_2$ ).

**HRMS (ESI) m/z:**  $[M+H]^+$  accurate mass calculated for  $C_{30}H_{27}BrN_2HO_5$ : 575.1103; Found: 575.1184.

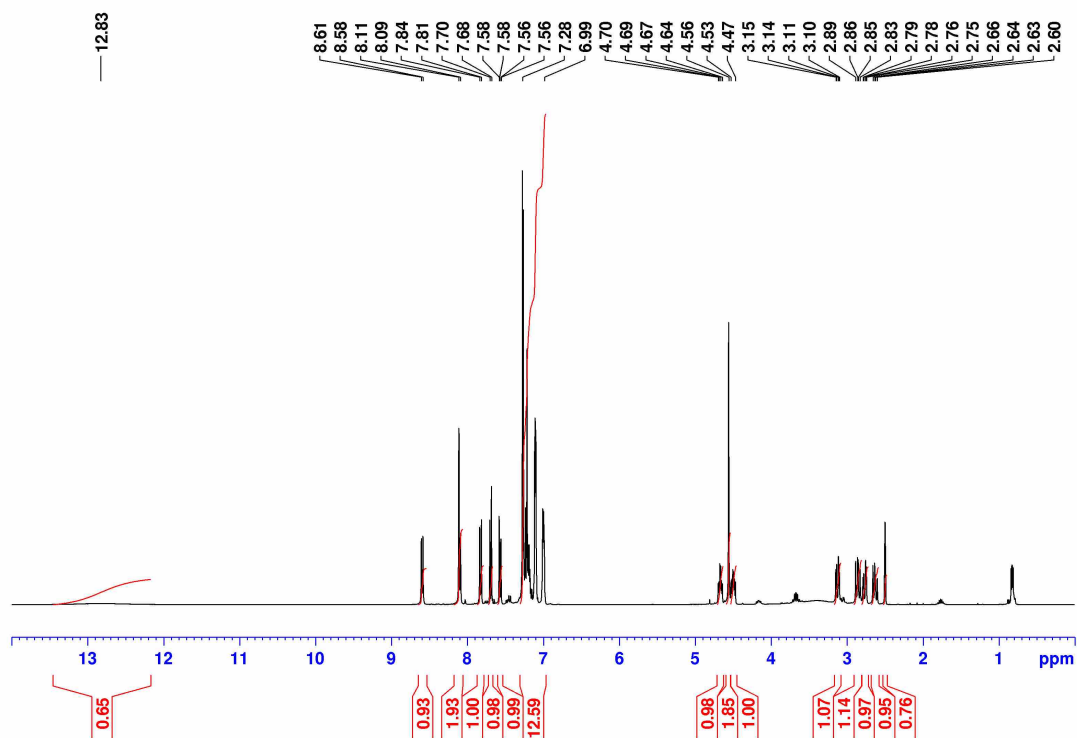


**Figure A3-63.**  $^1H$  NMR spectrum of 6Br-008 in  $d_6$ -DMSO at 25 °C

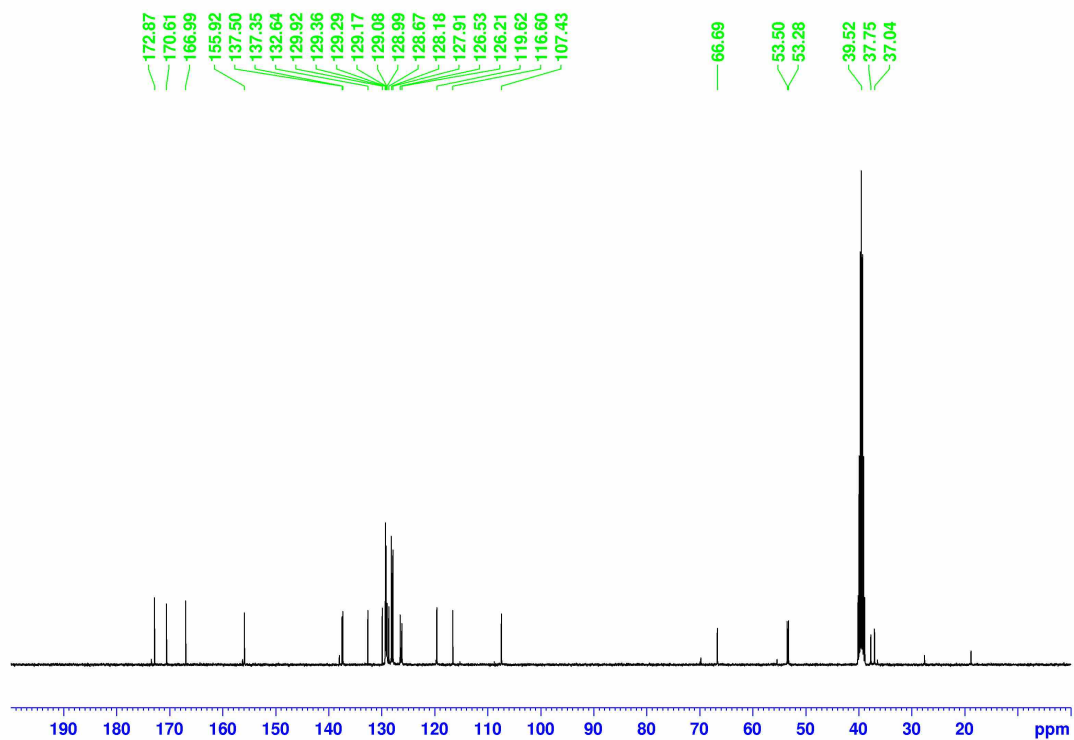
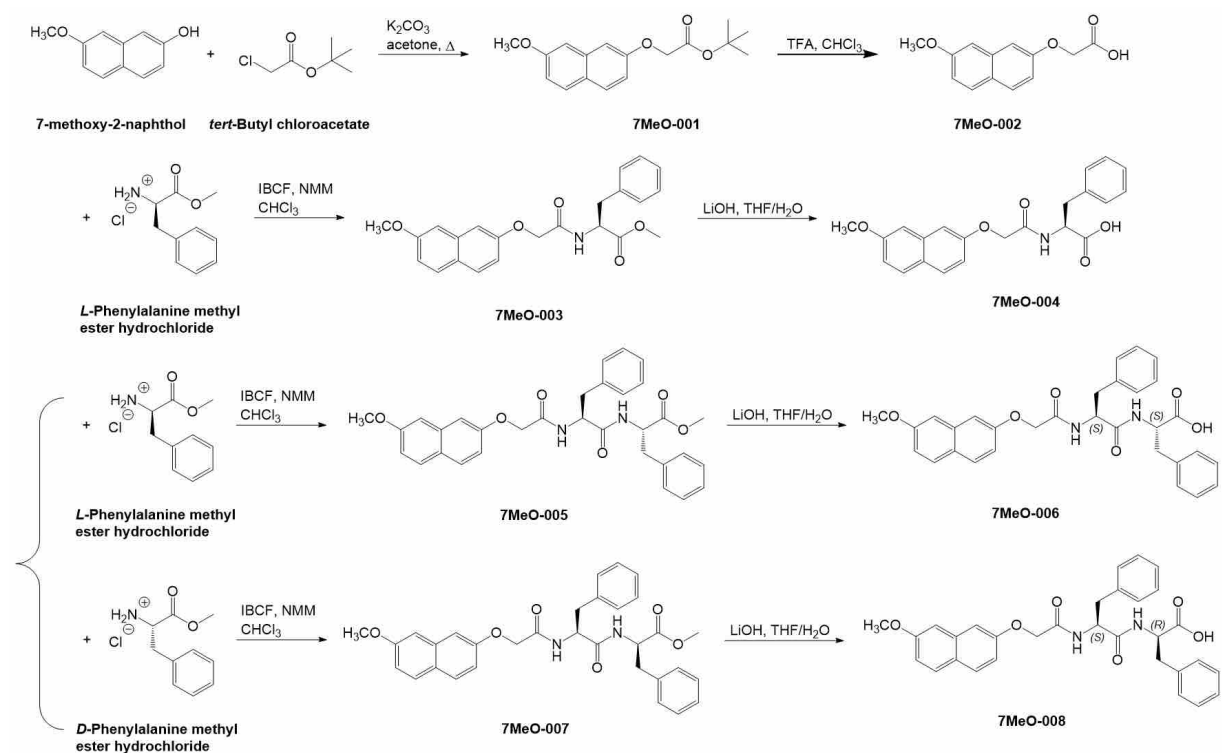


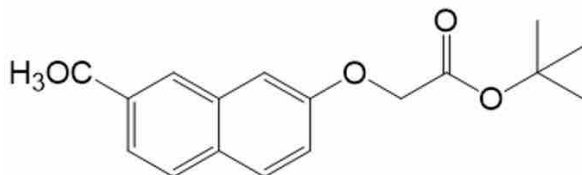
**Figure A3-64.**  $^{13}\text{C}$  NMR spectrum of 6Br-008 in  $\text{d}_6$ -DMSO at 25 °C.

### A3.2.5 7MeO2NapFF



Scheme A3-5. Synthetic route of 7MeO2NapFF.

#### Tert-butyl 2-[7-(hydroxymethyl)naphthalen-2-yl]oxy}acetate (7MeO-001)



$\delta_{\text{H}}$  (400 MHz, DMSO- $d_6$ , 25 °C) 7.73 (1.5H, dd,  $J$  8.90, 5.54 Hz,  $\underline{\text{H}}_{\text{Ar}}$ ), 7.65 (0.5H, d,  $J$  8.80 Hz,  $\underline{\text{H}}_{\text{Ar}}$ ), 7.17 (1.5H, dd,  $J$  10.02, 2.47 Hz,  $\underline{\text{H}}_{\text{Ar}}$ ), 7.07 (0.5H, dd,  $J$  8.43, 2.38 Hz,  $\underline{\text{H}}_{\text{Ar}}$ ), 7.03-6.99 (1.5H, m,  $\underline{\text{H}}_{\text{Ar}}$ ), 6.93-6.88 (0.5H, m,  $\underline{\text{H}}_{\text{Ar}}$ ), 4.74 (1.5H, s,  $\underline{\text{OCH}}_2$ ), 3.84 (2.2H, s, Rot-2  $\underline{\text{OCH}}_3$ ), 3.83 (0.7H, s, Rot-1  $\underline{\text{OCH}}_3$ ), 3.39 (2.3H, m,  $\underline{\text{H}}_2\text{O}$ ), 2.50 (0.3H, quintet, residual DMSO- $d_5$ ), 1.44 (6.3H, s, Rot-2  $\text{C}(\underline{\text{CH}}_3)_3$ ), 1.43 (2.9H, s, Rot-1  $\text{C}(\underline{\text{CH}}_3)_3$ ).  $\delta_{\text{C}}$  (100 MHz, DMSO- $d_6$ , 25 °C) 167.78 ( $\underline{\text{C}}=\text{O}$ ), 166.28 ( $\underline{\text{C}}_{\text{Ar}}-\text{O}$ ), 157.84, 157.43, 156.14, 155.89, 136.07, 135.56, 129.14, 129.03, 124.06, 123.13, 116.11, 115.53, 108.15, 106.70, 105.40, 104.51 ( $\underline{\text{C}}_{\text{Ar}}$ ), 82.14, 81.42 ( $\underline{\text{C}}(\underline{\text{CH}}_3)_3$ ), 65.06 ( $\underline{\text{OCH}}_2$ ), 55.10, 55.01 ( $\text{C}_{\text{Ar}}\underline{\text{OCH}}_3$ ), 39.52 (septet, DMSO- $d_6$ ), 27.70 (Rot-2  $\text{C}(\underline{\text{CH}}_3)_3$ ), 27.54 (Rot-1  $\text{C}(\underline{\text{CH}}_3)_3$ ).

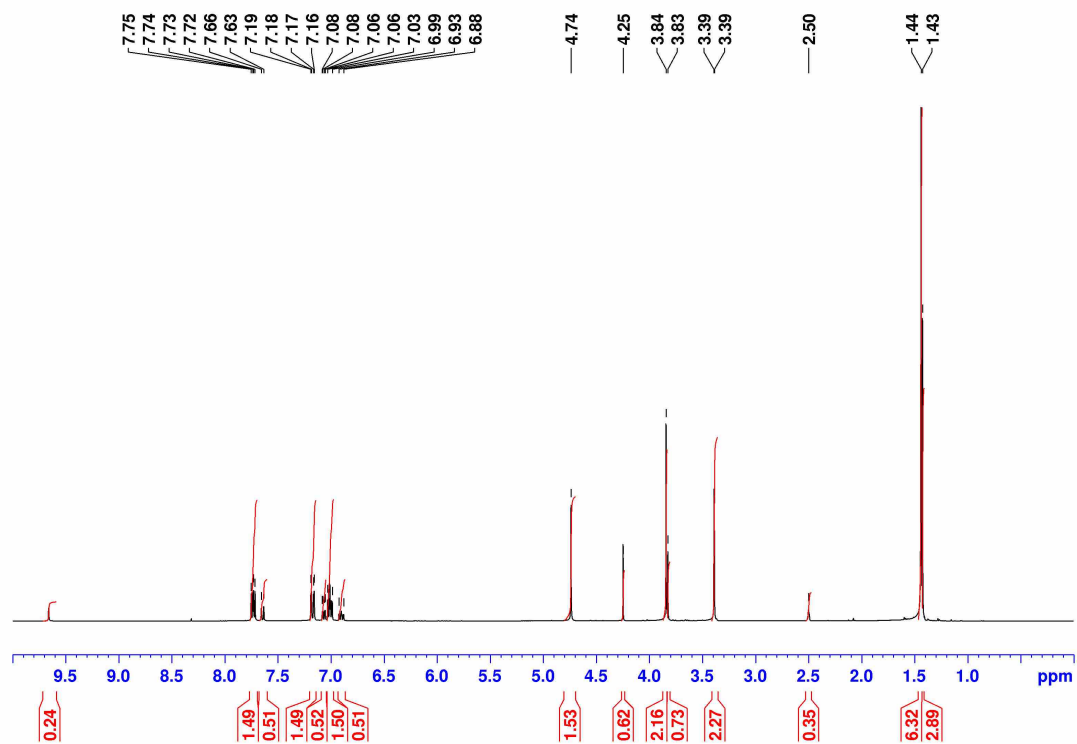


Figure A3-65.  $^1\text{H}$  NMR spectrum of 7MeO-001 in  $d_6$ -DMSO at 25 °C.

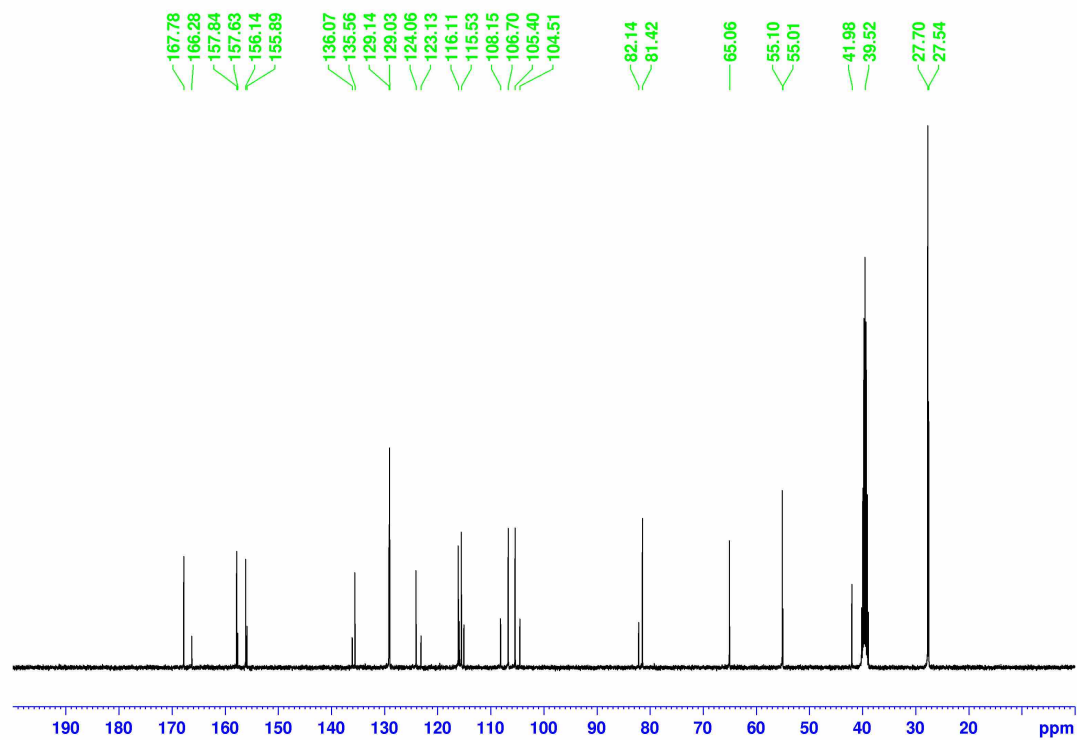
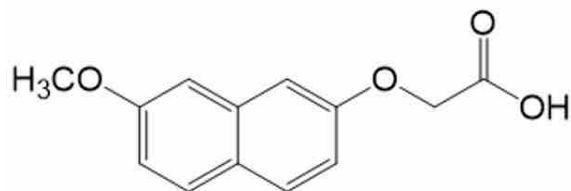
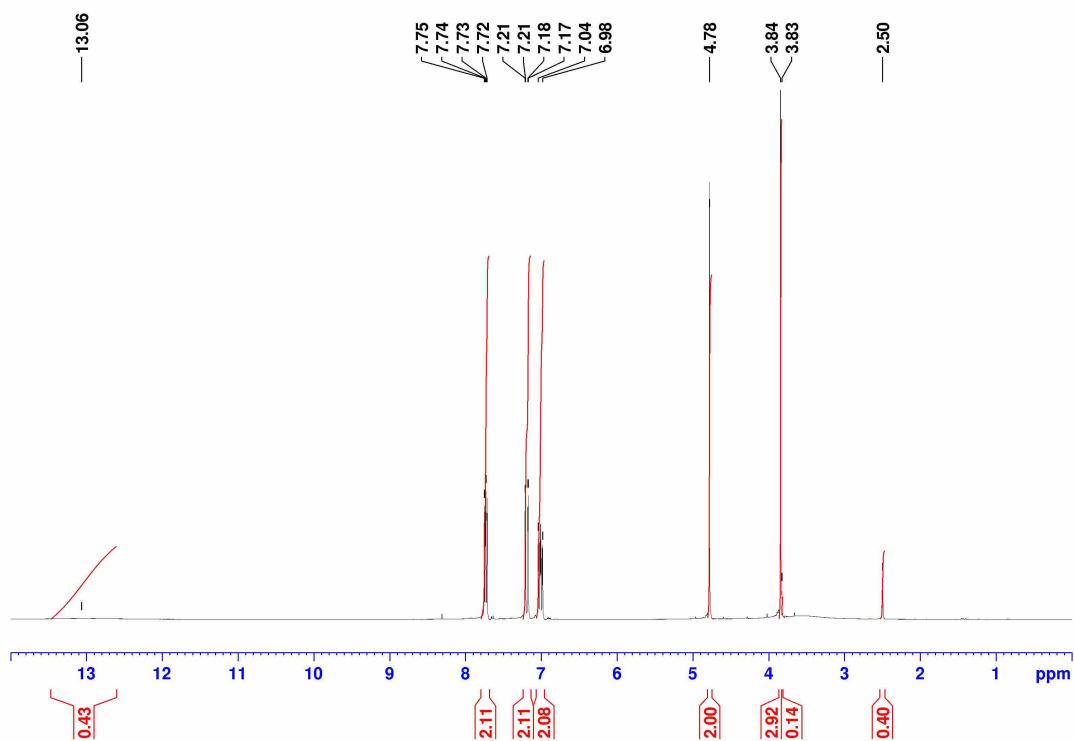


Figure A3-66.  $^{13}\text{C}$  NMR spectrum of 7MeO-001 in  $d_6$ -DMSO at 25 °C.

**2-[(7-Methoxynaphthalen-2-yl)oxy]acetic acid (7MeO-002)**

$\delta_{\text{H}}$  (400 MHz, DMSO- $d_6$ , 25 °C) 13.07 (0.4H, br s, COOH), 7.73 (2.1H, dd,  $J$  8.87, 6.10 Hz,  $\text{H}_{\text{Ar}}$ ), 7.19 (2.1H, dd,  $J$  14.09, 2.40 Hz,  $\text{H}_{\text{Ar}}$ ), 7.04-6.98 (2.1H, m,  $\text{H}_{\text{Ar}}$ ), 4.78 (2.0H, s,  $\text{OCH}_2$ ), 3.84 (2.9H, s, Rot-2  $\text{OCH}_3$ ), 3.83 (0.1H, s, Rot-1  $\text{OCH}_3$ ), 2.50 (0.4H, quintet, residual DMSO- $d_5$ ).  $\delta_{\text{C}}$  (100 MHz, DMSO- $d_6$ , 25 °C) 170.19 ( $\text{C}=\text{O}$ ), 157.87, 156.26 ( $\text{C}_{\text{Ar}}\text{O}$ ), 135.61, 129.18, 129.06, 124.04, 116.16, 115.72, 106.48, 105.43 ( $\text{C}_{\text{Ar}}$ ), 64.53 ( $\text{OCH}_2$ ), 55.14 ( $\text{C}_{\text{Ar}}\text{OCH}_3$ ), 39.52 (septet, DMSO- $d_6$ ).



**Figure A3-67.**  $^1\text{H}$  NMR spectrum of 7MeO-002 in  $d_6$ -DMSO at 25 °C.

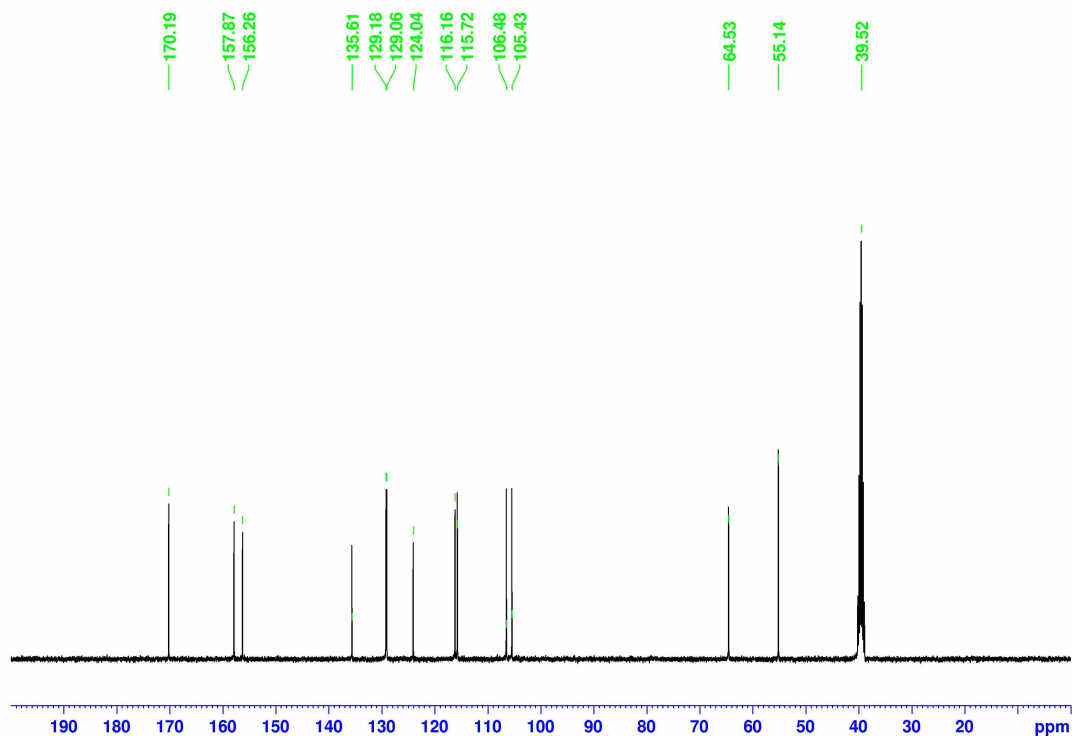
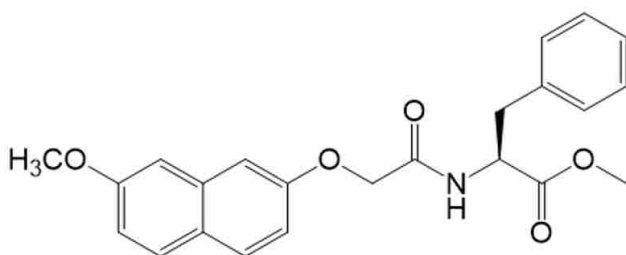


**Figure A3-68.**  $^{13}\text{C}$  NMR spectrum of 7MeO-002 in  $\text{d}_6$ -DMSO at 25 °C.

**Methyl (2S)-2-{2-[(7-methoxynaphthalen-2-yl)oxy]acetamido}-3-phenylpropanoate (7MeO-003)**



$\delta_{\text{H}}$  (400 MHz,  $\text{DMSO-d}_6$ , 25 °C) 8.53 (0.9H, d,  $J$  7.97 Hz,  $\text{NH}$ ), 7.75 (2.0H, dd,  $J$  8.88, 3.31 Hz,  $\text{H}_{\text{Ar}}$ ), 7.24-7.13 (7.1H, m,  $\text{H}_{\text{Ar}}$ ), 7.05-7.00 (2.0H, m,  $\text{H}_{\text{Ar}}$ ), 4.64-4.54 (2.9H, m,  $\text{OCH}_2$  and  $\text{CH}^*$ ), 3.85 (3.0H, s,  $\text{C}_{\text{Ar}}\text{OCH}_3$ ), 3.63 (2.7H, s,  $\text{OCH}_3$ ), 3.38 (4.5H, br s,  $\text{H}_2\text{O}$ ), 3.14-3.01 (2.0H, m,  $\text{PhCH}_2$ ), 2.50 (0.7H, quintet, residual  $\text{DMSO-d}_5$ ).  $\delta_{\text{C}}$  (100 MHz,  $\text{DMSO-d}_6$ , 25 °C) 171.74, 167.86 ( $\text{C}=\text{O}$ ), 157.82, 156.13 ( $\text{C}_{\text{Ar}}\text{O}$ ), 137.19, 135.53, 129.10, 128.26, 126.54, 124.12, 116.18, 115.79, 106.87 and 105.42 ( $\text{C}_{\text{Ar}}$ ), 66.65 ( $\text{OCH}_2$ ), 55.11 ( $\text{CH}^*$ ), 53.24 ( $\text{C}_{\text{Ar}}\text{OCH}_3$ ), 52.03 ( $\text{OCH}_3$ ), 39.52 (septet,  $\text{DMSO-d}_6$ ), 36.34 ( $\text{PhCH}_2$ ).

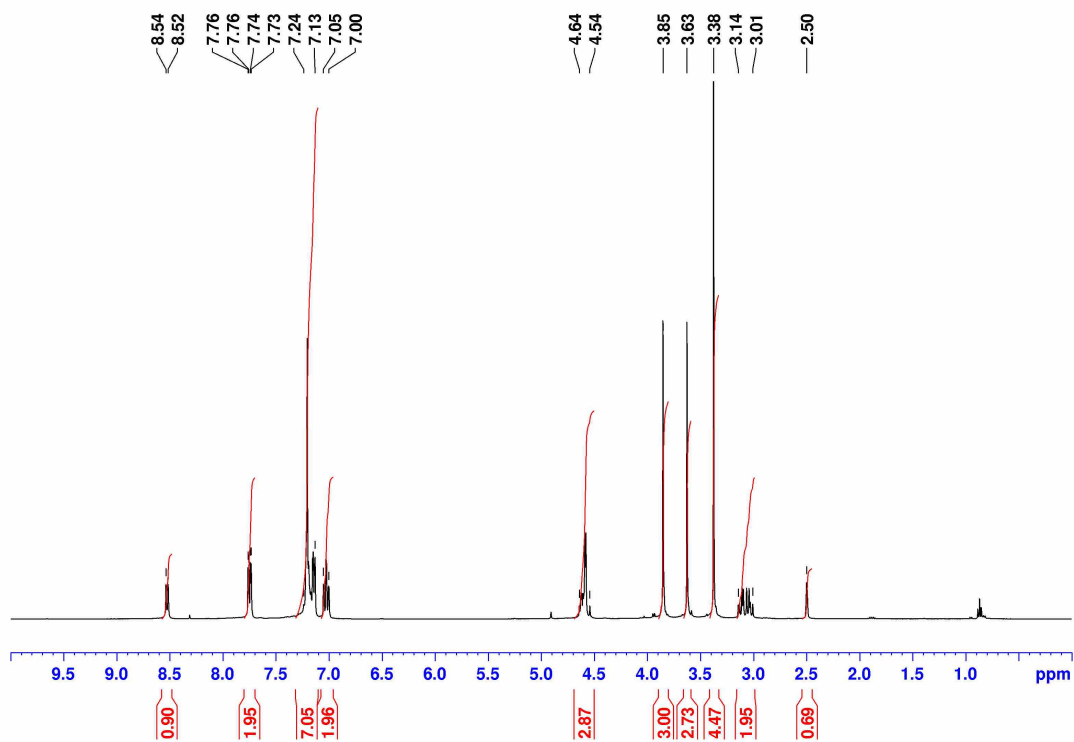


Figure A3-69.  $^1\text{H}$  NMR spectrum of 7MeO-003 in  $d_6$ -DMSO at 25 °C.

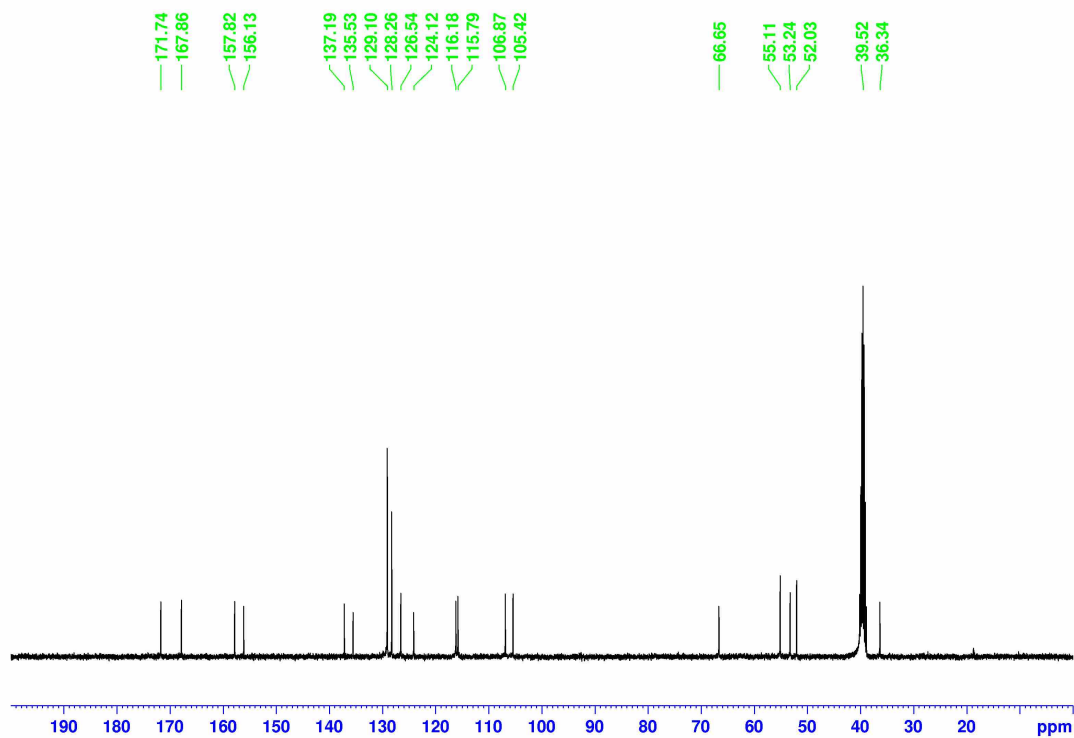
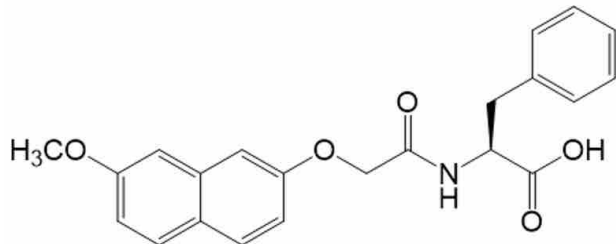
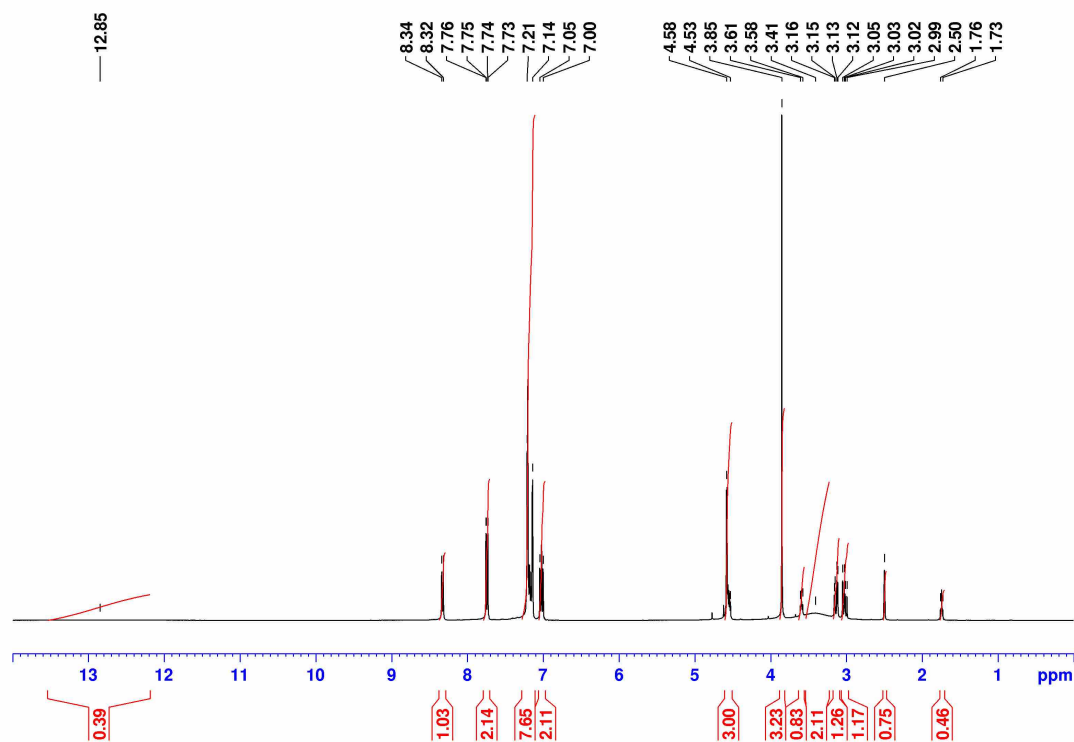


Figure A3-70.  $^{13}\text{C}$  NMR spectrum of 7MeO-003 in  $d_6$ -DMSO at 25 °C.

**(2S)-2-{2-[(7-Methoxynaphthalen-2-yl)oxy]acetamido}-3-phenylpropanoic acid (7MeO-004)**

$\delta_{\text{H}}$  (400 MHz, DMSO- $d_6$ , 25 °C) 12.85 (0.4H, br s, COOH), 8.33 (1.0H, d,  $J$  8.17 Hz, NH), 7.75 (2.1H, dd,  $J$  8.92, 1.60 Hz,  $\text{H}_{\text{Ar}}$ ), 7.21-7.14 (7.7H, m,  $\text{H}_{\text{Ar}}$ ), 7.05-7.00 (2.1H, m,  $\text{H}_{\text{Ar}}$ ), 4.58-4.53 (3.0H, m,  $\text{OCH}_2$  and  $\text{CH}^*$ ), 3.85 (3.2H, s,  $\text{C}_{\text{Ar}}\text{OCH}_3$ ), 3.61-3.58 (0.8H, m,  $\text{CH}_2\text{O}$  in THF), 3.41 (2.1H, br s,  $\text{H}_2\text{O}$ ), 3.14 (1.3H, dd,  $J$  13.83, 4.70 Hz,  $\text{PhCH}_a\text{H}_b$ ), 3.02 (1.2H, dd,  $J$  13.82, 9.28 Hz,  $\text{PhCH}_a\text{H}_b$ ), 2.50 (0.8H, quintet, residual DMSO- $d_5$ ), 1.76-1.73 (0.5H, m,  $\text{CH}_2$  in THF).  $\delta_{\text{C}}$  (100 MHz, DMSO- $d_6$ , 25 °C) 172.74, 167.70 ( $\text{C}=\text{O}$ ), 157.82, 156.16 ( $\text{C}_{\text{Ar}}\text{O}$ ), 137.54, 135.56, 129.15, 129.12, 129.08, 128.21, 126.45, 124.13, 116.18, 115.81, 106.89 and 105.49 ( $\text{C}_{\text{Ar}}$ ), 67.06 ( $\text{CH}_2\text{O}$  in THF), 66.72 ( $\text{OCH}_2$ ), 55.13 ( $\text{CH}^*$ ), 53.20 ( $\text{C}_{\text{Ar}}\text{OCH}_3$ ), 39.52 (septet, DMSO- $d_6$ ), 36.43 ( $\text{PhCH}_2$ ), 25.16 ( $\text{CH}_2$  in THF).



**Figure A3-71.**  $^1\text{H}$  NMR spectrum of 7MeO-004 in  $d_6$ -DMSO at 25 °C.

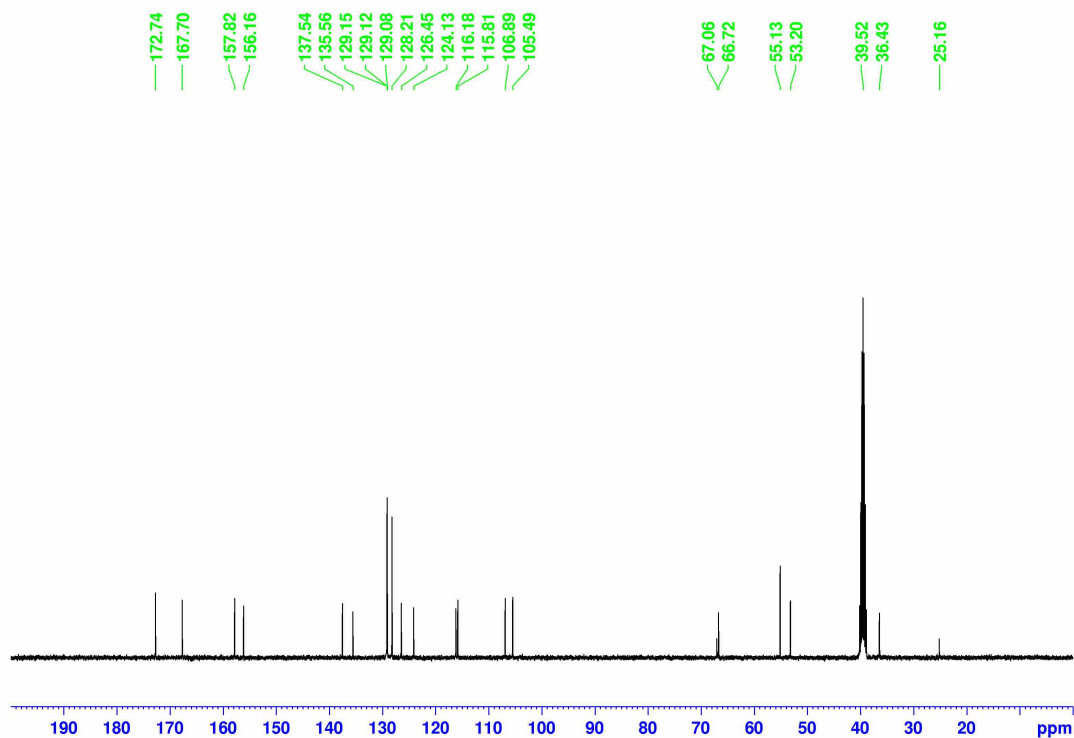
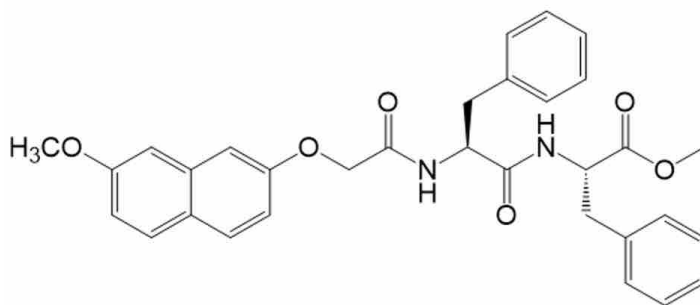


**Figure A3-72.**  $^{13}\text{C}$  NMR spectrum of 7MeO-004 in  $\text{d}_6$ -DMSO at 25 °C.

**Methyl (2S)-2-[(2S)-2-{2-[(7-methoxynaphthalen-2-yl)oxy]acetamido}-3-phenylpropanamido]-3-phenylpropanoate (7MeO-005)**



$\delta_{\text{H}}$  (400 MHz,  $\text{DMSO-d}_6$ , 25 °C) 8.73 (0.8H, d,  $J$  8.15 Hz,  $\text{NH}$ ), 8.08 (0.8H, d,  $J$  8.61 Hz,  $\text{NH}$ ), 7.73 (1.9H, d,  $J$  8.90 Hz,  $\text{H}_{\text{Ar}}$ ), 7.30-7.11 (11.3H, m,  $\text{H}_{\text{Ar}}$ ), 7.02-6.98 (3.5H, m,  $\text{H}_{\text{Ar}}$ ), 4.68-4.63 (1.1H, m,  $\text{CH}^*$ ), 4.56-4.50 (2.5H, m,  $\text{OCH}_2$  and  $\text{CH}^*$ ), 3.85 (0.7H, s, Rot-2  $\text{C}_{\text{Ar}}\text{OCH}_3$ ), 3.83 (0.2H, s, Rot-1  $\text{C}_{\text{Ar}}\text{OCH}_3$ ), 3.62 (2.7H, s, Rot-2  $\text{OCH}_3$ ), 3.58 (0.7H, s, Rot-1  $\text{OCH}_3$ ), 3.37 (7.0H, br s,  $\text{H}_2\text{O}$ ), 3.09 (0.9H, dd,  $J$  13.64, 4.98 Hz,  $\text{PhCH}_b\text{CH}_a$ ), 2.87 (1.2H, dd,  $J$  13.61, 9.97 Hz,  $\text{PhCH}_b\text{CH}_a$ ), 2.77 (0.8H, dd,  $J$  13.68, 4.25 Hz,  $\text{PhCH}_b\text{CH}_a$ ), 2.66 (0.8H, dd,  $J$  13.63, 9.18 Hz,  $\text{PhCH}_b\text{CH}_a$ ), 2.50 (1.2H, quintet, residual  $\text{DMSO-d}_5$ ).  $\delta_{\text{C}}$  (100 MHz,  $\text{DMSO-d}_6$ , 25 °C) 171.90,

170.80, and 167.26 ( $\underline{C=O}$ ), 157.79, 156.09 ( $\underline{C_{Ar}-O}$ ), 137.30, 137.12, 135.55, 129.26, 129.19, 128.27, 126.67, 126.25, 124.08, 116.16, 115.69, 106.80 and 105.43 ( $\underline{C_{Ar}}$ ), 66.64 ( $\underline{OCH_2}$ ), 55.08 ( $\underline{CH^*}$ ), 53.56 ( $\underline{CH^*}$ ), 53.25 ( $\underline{C_{Ar}OCH_3}$ ), 51.98 ( $\underline{OCH_3}$ ), 39.52 (septet,  $\underline{DMSO-d_6}$ ), 37.69 ( $\underline{PhC_bH_2}$ ), 36.93 ( $\underline{PhC_aH_2}$ ).

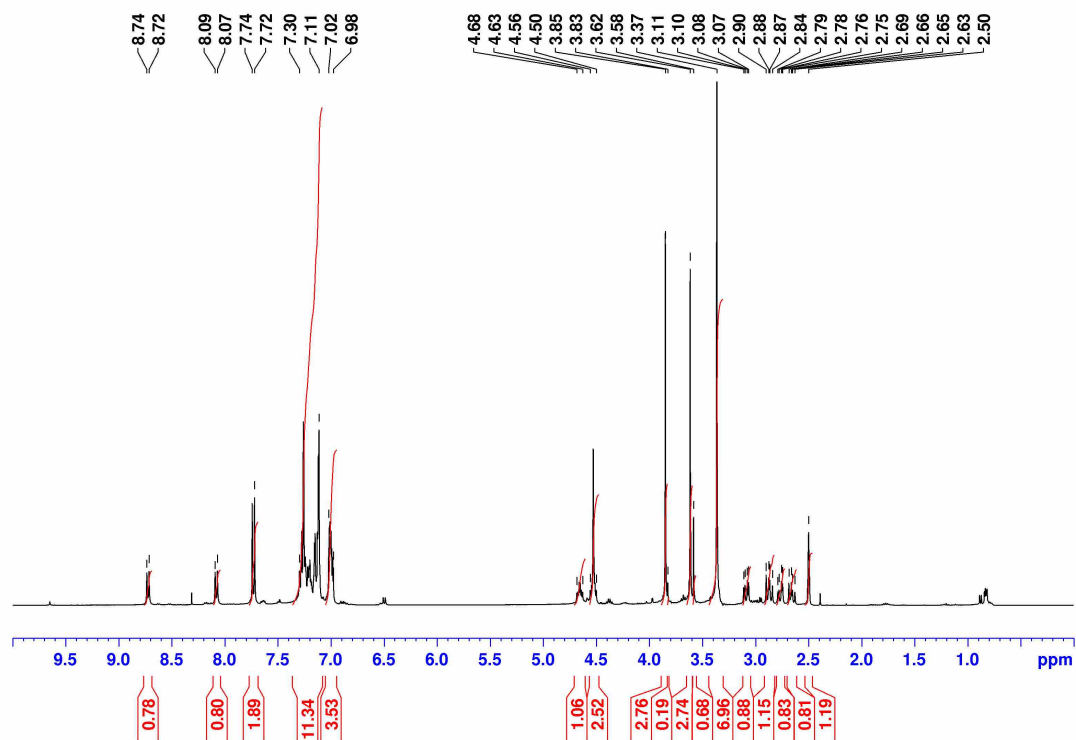


**Figure A3-73.**  $^1\text{H}$  NMR spectrum of 7MeO-005 in  $d_6$ -DMSO at 25 °C.

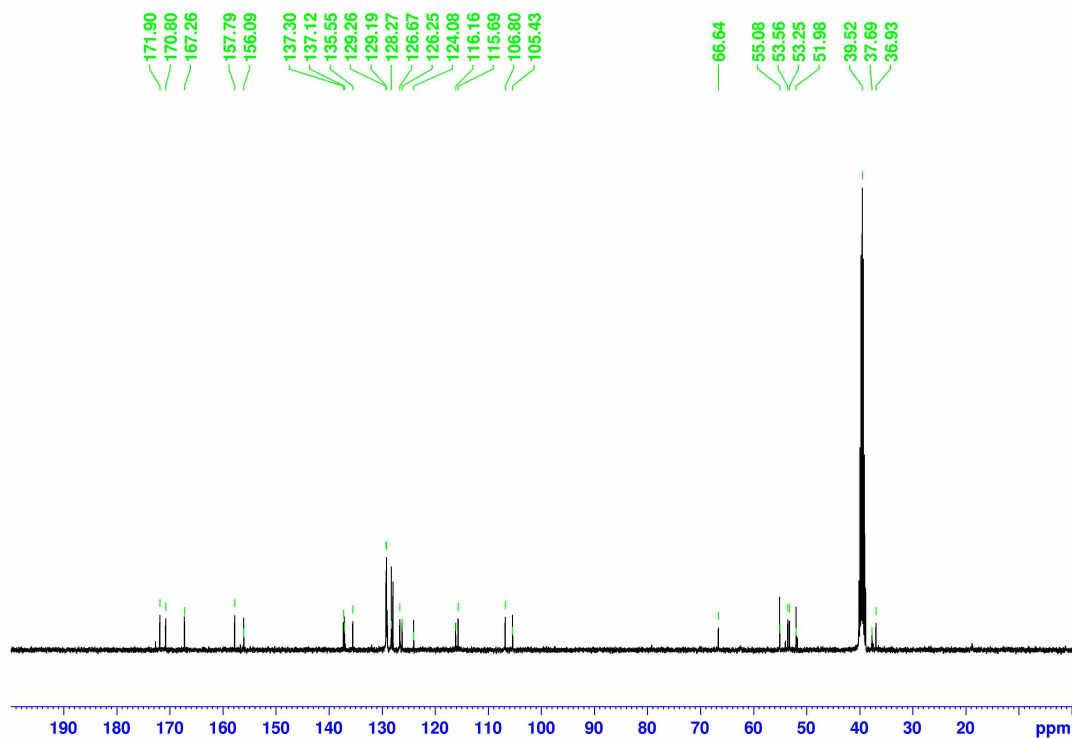
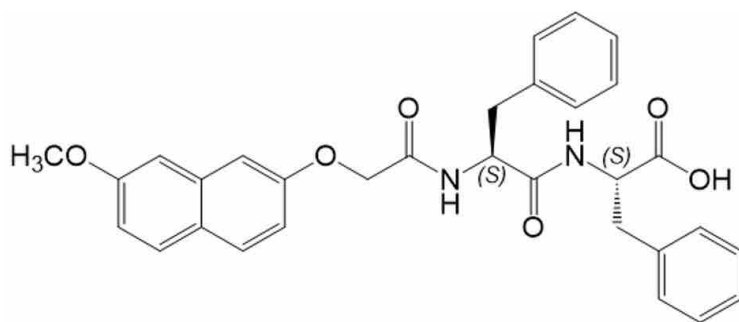


**Figure A3-74.**  $^{13}\text{C}$  NMR spectrum of 7MeO-005 in  $\text{d}_6$ -DMSO at 25 °C.

**(2S)-2-[(2S)-2-{2-[(7-Methoxynaphthalen-2-yl)oxy]acetamido}-3-phenylpropanamido]-3-phenylpropanoic acid (7MeO-006)**



$\delta_{\text{H}}$  (400 MHz, DMSO- $\text{d}_6$ , 25 °C) 12.82 (1.0H, br s, COOH), 8.47 (0.9H, d,  $J$  7.83 Hz, NH), 8.13 (0.9H, d,  $J$  8.58 Hz, NH), 7.74 (2.0H, d,  $J$  8.92 Hz,  $\text{H}_{\text{Ar}}$ ), 7.26-7.12 (12.3H, m,  $\text{H}_{\text{Ar}}$ ), 7.03-6.99 (2.1H, m,  $\text{H}_{\text{Ar}}$ ), 4.66 (1.0H, td,  $J$  9.14, 4.11 Hz,  $\text{CH}^*$ ), 4.56-4.48 (2.9H, m,  $\text{OCH}_2$  and  $\text{CH}^*$ ), 3.85 (2.9H, s, Rot-2  $\text{OCH}_3$ ), 3.83 (0.1H, s, Rot-1  $\text{OCH}_3$ ), 3.38 (0.9H, br s,  $\text{H}_2\text{O}$ ), 3.12-3.03 (2.1H, m,  $\text{PhCH}_2$ ), 2.97-2.85 (2.1H, m,  $\text{PhCH}_2$ ), 2.50 (0.7H, quintet, residual DMSO- $\text{d}_5$ ), 2.06 (0.04H, s,  $\text{CH}_3$  in acetone).  $\delta_{\text{C}}$  (100 MHz, DMSO- $\text{d}_6$ , 25 °C) 172.72, 170.86, and 167.30 ( $\text{C}=\text{O}$ ), 157.79, 156.10, 137.52, 137.35, 135.55, 129.27, 129.12, 129.03, 128.19, 127.98, 126.46, 126.24, 124.10,

116.16, 115.69, 106.87 and 105.45 ( $C_{Ar}$ ), 66.71 ( $OCH_2$ ), 55.09 ( $CH^*$ ), 53.53 ( $CH^*$ ), 53.24 ( $C_{Ar}OCH_3$ ), 39.52 (septet,  $DMSO-d_6$ ), 37.42 ( $PhCH_2$ ), 36.70 ( $PhCH_2$ ).

**HRMS (ESI) m/z:**  $[M+H]^+$  accurate mass calculated for  $C_{31}H_{30}N_2HO_6$ : 527.2104; Found: 527.2190.

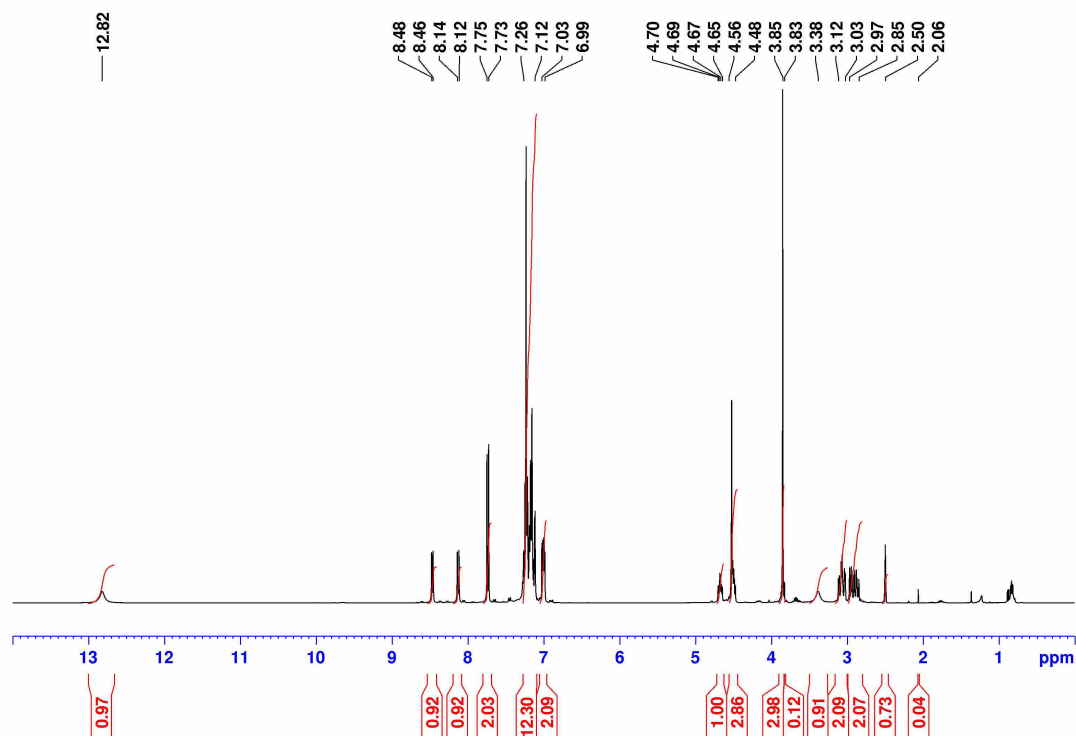


**Figure A3-75.**  $^1H$  NMR spectrum of 7MeO-006 in  $d_6$ -DMSO at 25 °C.

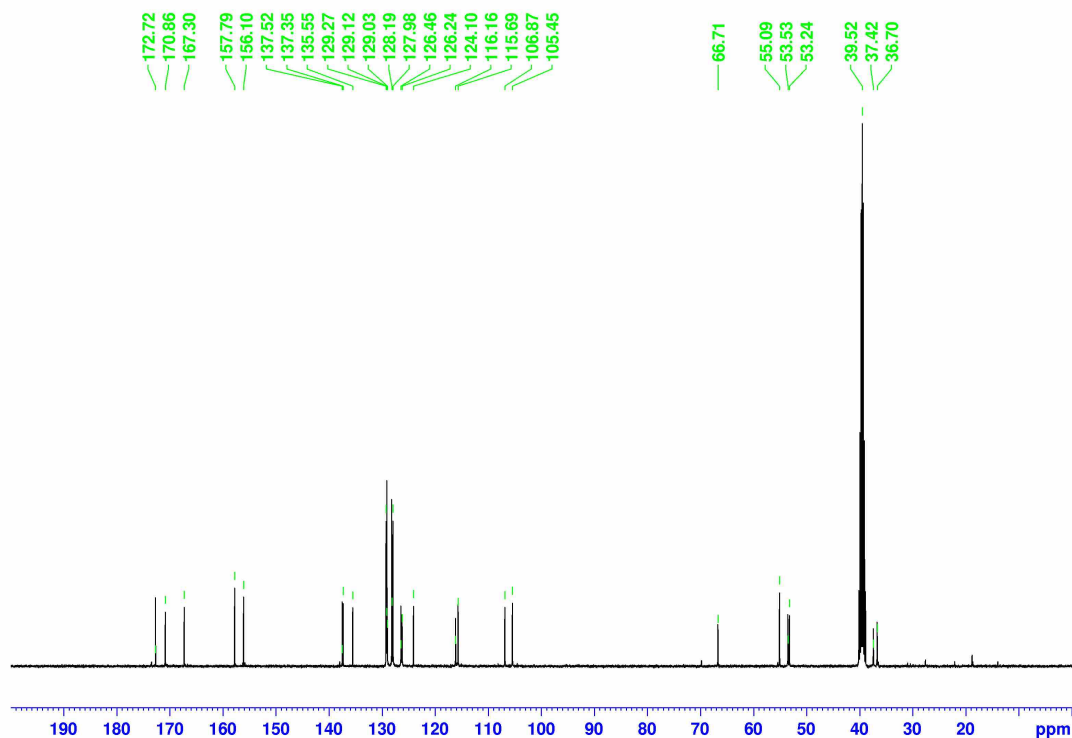
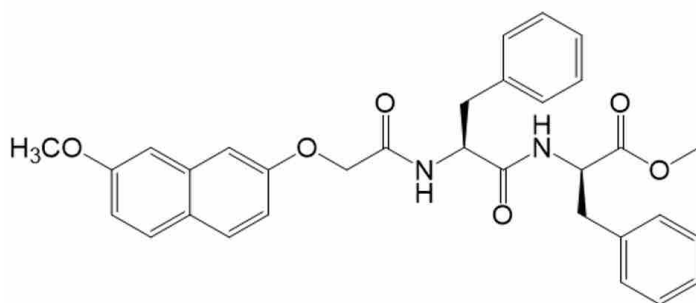


**Figure A3-76.**  $^{13}\text{C}$  NMR spectrum of 7MeO-006 in  $\text{d}_6$ -DMSO at 25 °C.

**Methyl (2R)-2-[(2S)-2-{2-[(7-methoxynaphthalen-2-yl)oxy]acetamido}-3-phenylpropanamido]-3-phenylpropanoate (7MeO-007)**



$\delta_{\text{H}}$  (400 MHz,  $\text{DMSO-d}_6$ , 25 °C) 8.62 (0.7H, d,  $J$  7.49 Hz,  $\text{NH}$ ), 8.31 (0.6H, s,  $\text{CH}$  in chloroform), 8.14 (0.8H, d,  $J$  8.55 Hz,  $\text{NH}$ ), 7.74 (1.7H, d,  $J$  8.91 Hz,  $\text{H}_{\text{Ar}}$ ), 7.30-7.11 (12.4H, m,  $\text{H}_{\text{Ar}}$ ), 7.02-6.98 (1.8H, m,  $\text{H}_{\text{Ar}}$ ), 4.69-4.63 (0.9H, m,  $\text{CH}^*$ ), 4.56-4.48 (2.4H, m,  $\text{CH}^*$  and  $\text{OCH}_2$ ), 3.85 (2.6H, s,  $\text{C}_{\text{Ar}}\text{OCH}_3$ ), 3.58 (2.9H, s,  $\text{OCH}_3$ ), 3.36 (7.7H, br s,  $\text{H}_2\text{O}$ ), 3.07-2.93 (2.9H, m,  $\text{PhCH}_2$ ), 2.90-2.83 (1.2H, m,  $\text{PhCH}_2$ ), 2.50 (1.3H, quintet, residual  $\text{DMSO-d}_5$ ).  $\delta_{\text{C}}$  (100 MHz,  $\text{DMSO-d}_6$ , 25 °C) 171.74, 171.00, and 167.34 ( $\text{C}=\text{O}$ ), 157.79, 156.10, 137.46, 136.95, 135.55, 129.23, 129.19, 129.10, 129.06, 128.27, 128.01, 126.60, 126.29, 124.08, 116.16, 115.71, 106.83, and 105.43

(C<sub>Ar</sub>), 79.19 (CH in chloroform), 66.67 (OCH<sub>2</sub>), 55.08 (CH\*), 53.70 (CH\*), 53.20 (C<sub>Ar</sub>OCH<sub>3</sub>), 51.87(OCH<sub>3</sub>), 39.52 (septet, DMSO-d<sub>6</sub>), 37.43 (PhC<sub>b</sub>H<sub>2</sub>), 36.62 (PhC<sub>a</sub>H<sub>2</sub>).

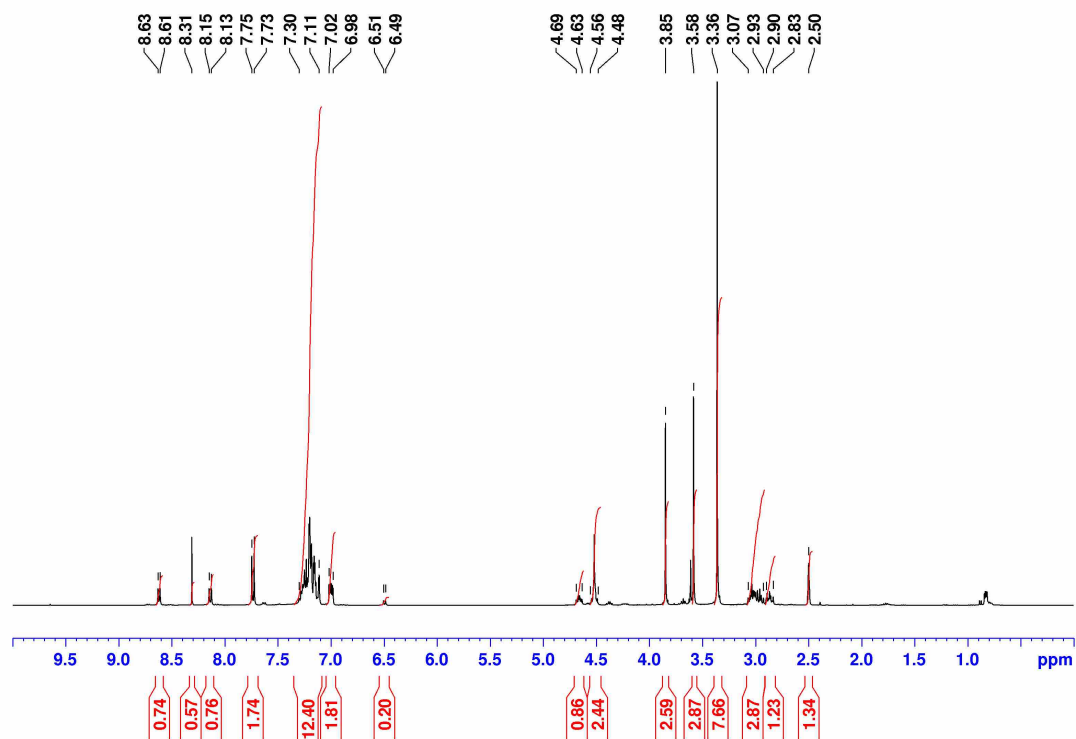


**Figure A3-77.** <sup>1</sup>H NMR spectrum of 7MeO-007 in d<sub>6</sub>-DMSO at 25 °C.

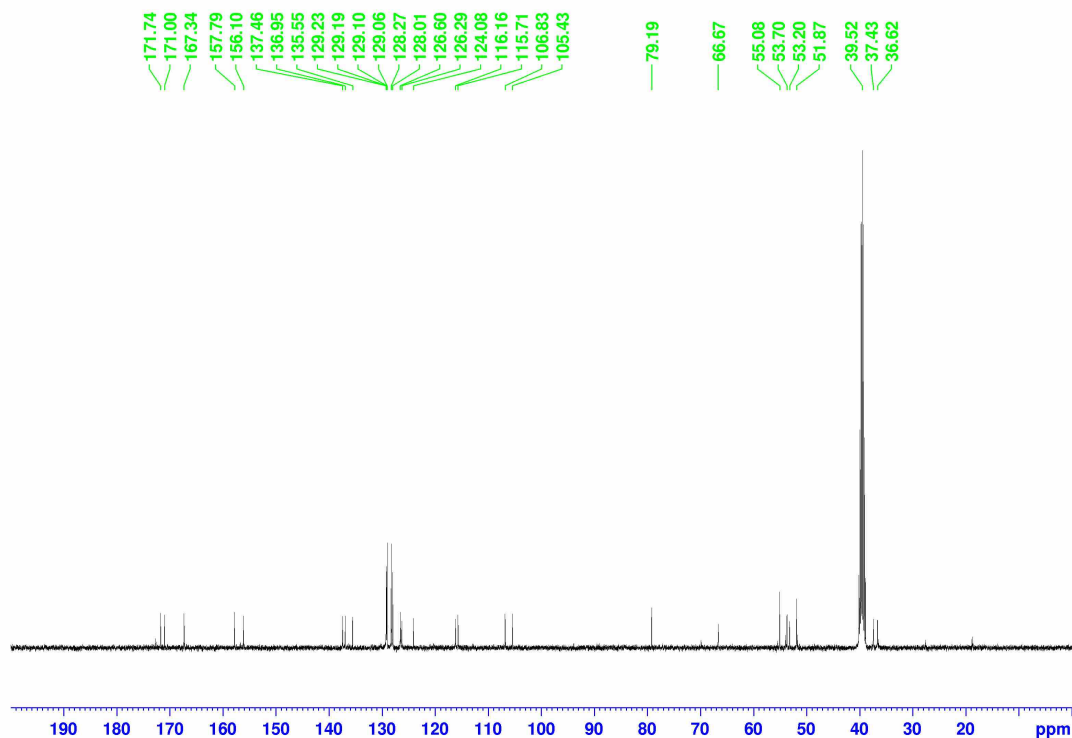
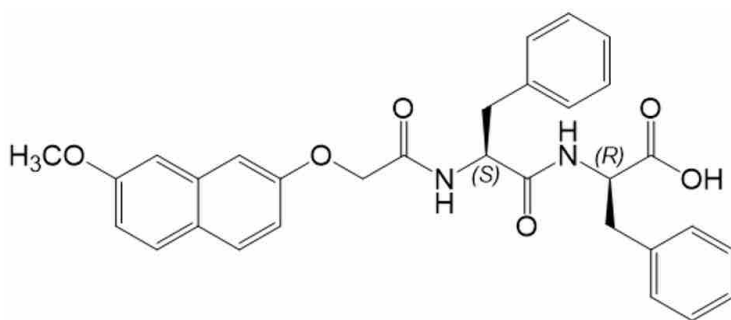


**Figure A3-78.**  $^{13}\text{C}$  NMR spectrum of 7MeO-007 in  $\text{d}_6$ -DMSO at 25 °C.

**(2R)-2-[(2S)-2-{2-[(7-Methoxynaphthalen-2-yl)oxy]acetamido}-3-phenylpropanamido]-3-phenylpropanoic acid (7MeO-008)**



$\delta_{\text{H}}$  (400 MHz,  $\text{DMSO-d}_6$ , 25 °C) 12.87 (0.8H, br s,  $\text{COOH}$ ), 8.61 (0.9H, d,  $J$  8.35 Hz,  $\text{NH}$ ), 8.06 (0.9H, d,  $J$  8.63 Hz,  $\text{NH}$ ), 7.73 (1.9H, d,  $J$  8.94 Hz,  $\text{H}_{\text{Ar}}$ ), 7.28 (3.8H, d,  $J$  4.36 Hz,  $\text{H}_{\text{Ar}}$ ), 7.22-7.10 (5.8H, m,  $\text{H}_{\text{Ar}}$ ), 7.02-6.98 (3.7H, m,  $\text{H}_{\text{Ar}}$ ), 4.67 (1.0H, td,  $J$  8.94, 4.15 Hz,  $\text{CH}^*$ ), 4.53-4.48 (2.8H, m,  $\text{OCH}_2$  and  $\text{CH}^*$ ), 3.85 (2.7H, s,  $\text{OCH}_3$ ), 3.39 (0.7H, br s,  $\text{H}_2\text{O}$ ), 3.13 (0.9H, dd,  $J$  13.65, 4.53 Hz,  $\text{PhCH}_b\text{CH}_a$ ), 2.86 (1.0H, dd,  $J$  13.65, 10.08 Hz,  $\text{PhCH}_b\text{CH}_a$ ), 2.78 (0.9H, dd,  $J$  13.64, 4.08 Hz,  $\text{PhCH}_b\text{CH}_a$ ), 2.65 (0.9H, dd,  $J$  13.65, 9.16 Hz,  $\text{PhCH}_b\text{CH}_a$ ), 2.50 (0.6H, quintet, residual  $\text{DMSO-d}_5$ ).  $\delta_{\text{C}}$  (100 MHz,  $\text{DMSO-d}_6$ , 25 °C) 172.87, 170.61, and 167.20 ( $\text{C}=\text{O}$ ), 157.80,

156.09, 137.51, 137.33, 135.56, 129.29, 129.20, 129.11, 128.02, 127.91, 126.54, 126.19, 124.09, 116.17, 115.67, 106.84 and 105.43 ( $C_{Ar}$ ), 66.68 ( $OCH_2$ ), 55.09 ( $CH^*$ ), 53.53 ( $CH^*$ ), 53.25 ( $C_{Ar}OCH_3$ ), 39.52 (septet,  $DMSO-d_6$ ), 37.76 ( $PhCH_2$ ), 37.05 ( $PhCH_2$ ).

**HRMS (ESI) m/z:**  $[M+H]^+$  accurate mass calculated for  $C_{31}H_{30}N_2HO_6$ : 527.2104; Found: 527.2184.

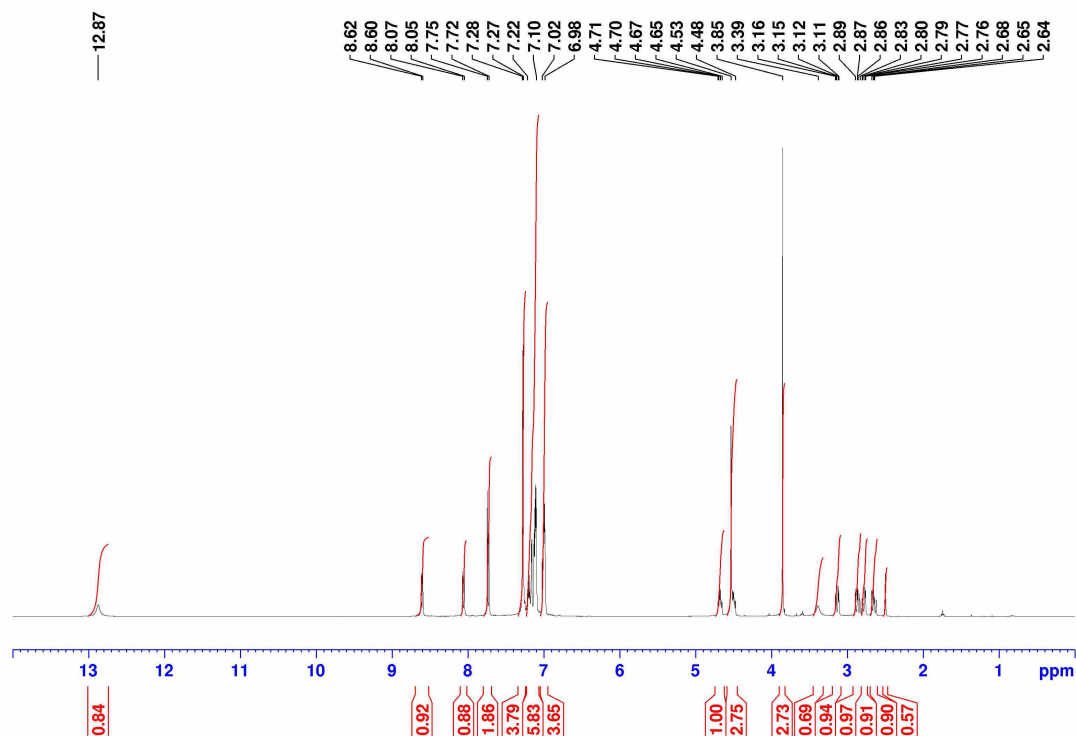


**Figure A3-79.**  $^1H$  NMR spectrum of 7MeO-008 in  $d_6$ -DMSO at 25 °C.

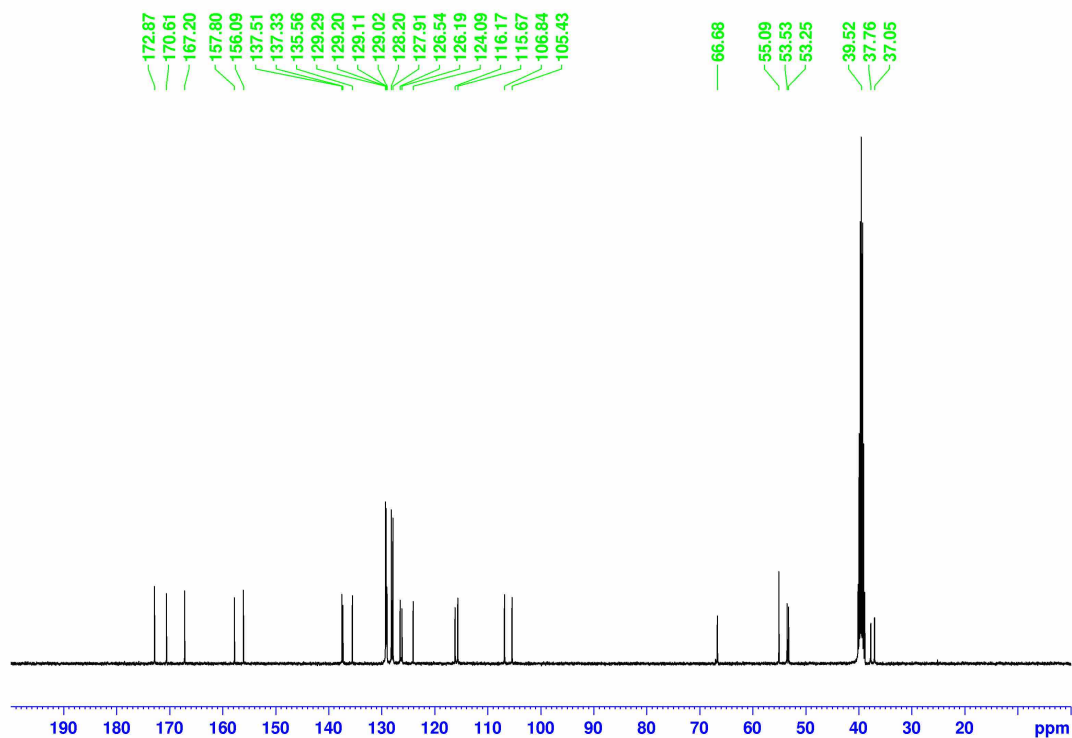


Figure A3-80.  $^{13}\text{C}$  NMR spectrum of 7MeO-008 in  $d_6$ -DMSO at 25 °C.

### A3.3 Additional Figures and Tables

#### A3.3.1 7MeO<sub>2</sub>NapFF

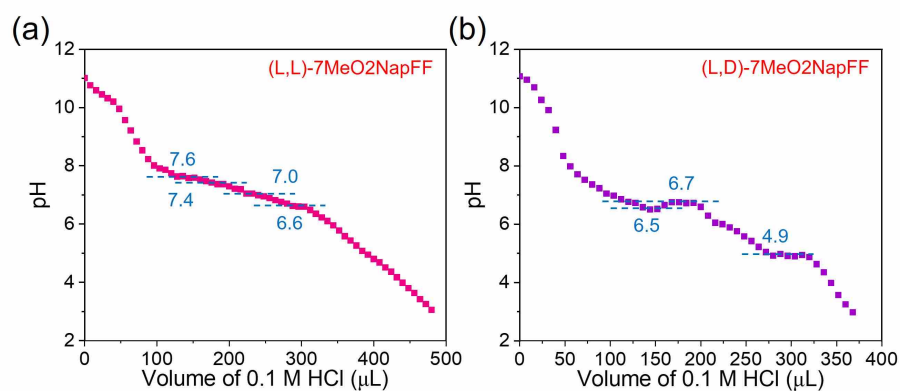
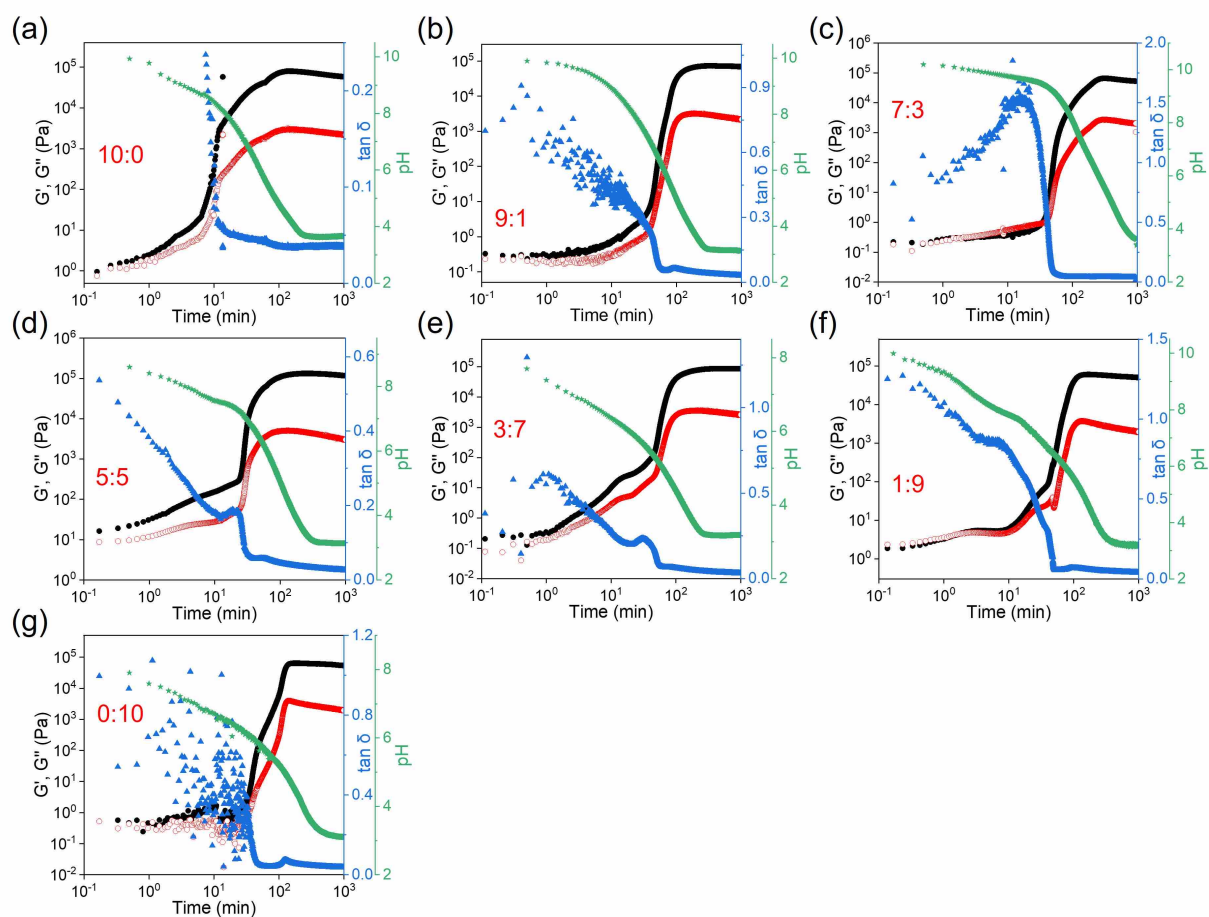
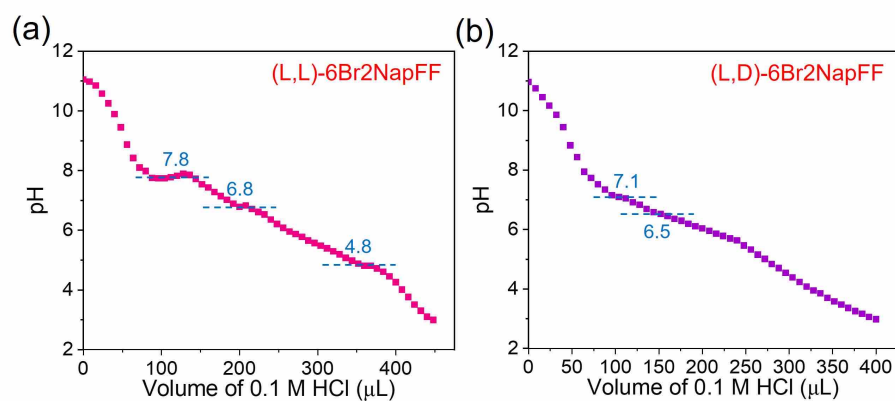


Figure A3-81. Apparent  $pK_a$  titration for 10 mg/mL (L,L)-7MeO<sub>2</sub>NapFF and (L,D)-7MeO<sub>2</sub>NapFF stock solutions at 25 °C.



**Figure A3-82.** Evolution of  $G'$  (black),  $G''$  (red),  $\tan\delta$  (blue), and pH (green) with time for binary solutions with various volume ratios of 10 mg/mL (L,L)-7MeO<sub>2</sub>NapFF:(L,D)-7MeO<sub>2</sub>NapFF stock solutions.

### A3.3.2 6Br<sub>2</sub>NapFF



**Figure A3-83.** Apparent  $pK_a$  titration for 10 mg/mL (L,L)-6Br<sub>2</sub>NapFF and (L,D)-6Br<sub>2</sub>NapFF stock solutions at 25 °C.

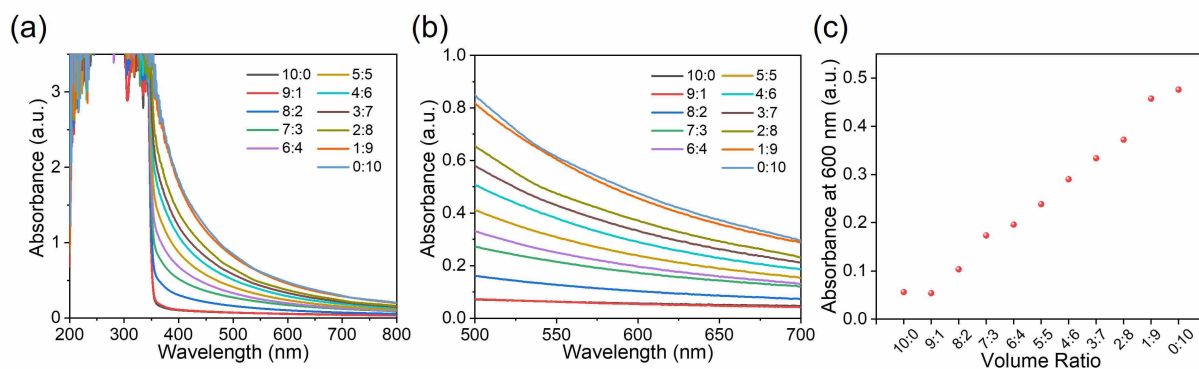


**Figure A3-84.** (a) UV-Vis absorption spectra of solutions containing 10 mg/mL (L,L)-6Br2NapFF:(L,D)-6Br2NapFF at ratios varying from 10:0 to 0:10, recorded using a 2 mm path length quartz cuvette at 25 °C. (b) Enlarged spectra from graph (a) focusing on the wavelength range of 500–700 nm. (c) Variation in turbidity across composition at 600 nm for solutions.

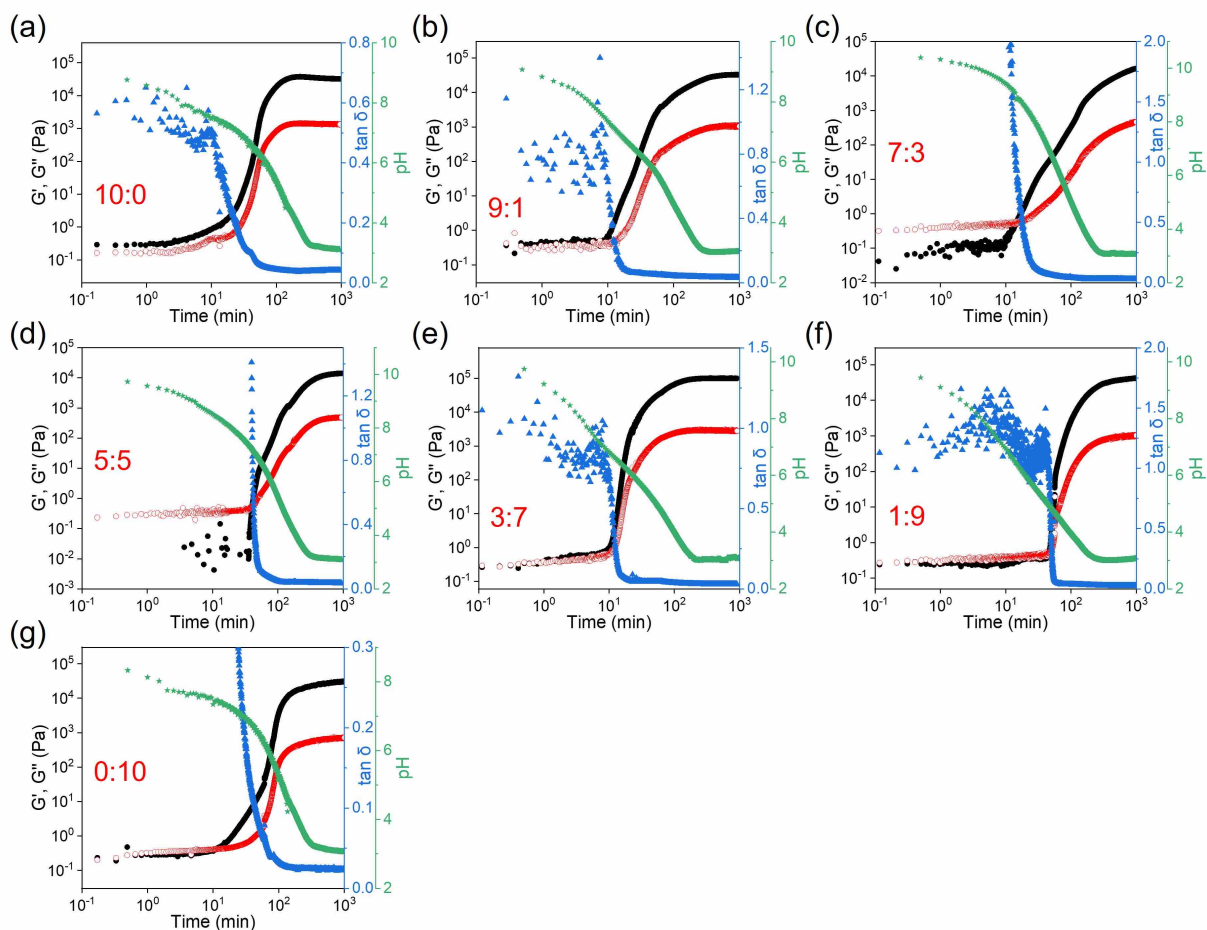


**Figure A3-85.** Evolution of  $G'$  (black),  $G''$  (red),  $\tan\delta$  (blue), and pH (green) with time for binary solutions with various volume ratios of 10 mg/mL (L,L)-6Br2NapFF:(L,D)-6Br2NapFF stock solutions.

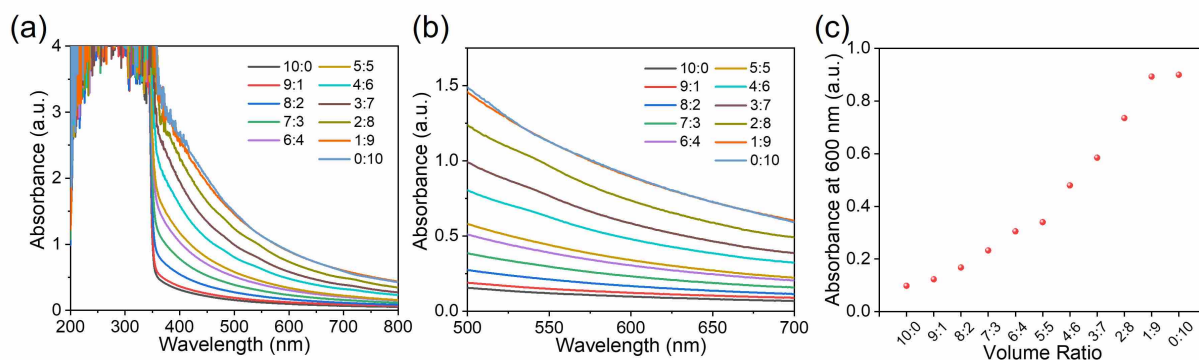


**Figure A3-86.** (a) UV-Vis absorption spectra of gels containing 10 mg/mL (L,L)-6Br2NapFF:(L,D)-6Br2NapFF at ratios varying from 10:0 to 0:10, recorded using a 2 mm path length quartz cuvette at 25 °C. (b) Enlarged spectra from graph (a) focusing on the wavelength range of 500–700 nm. (c) Variation in turbidity across composition at 600 nm for gels.

### A3.3.3 1NapFF

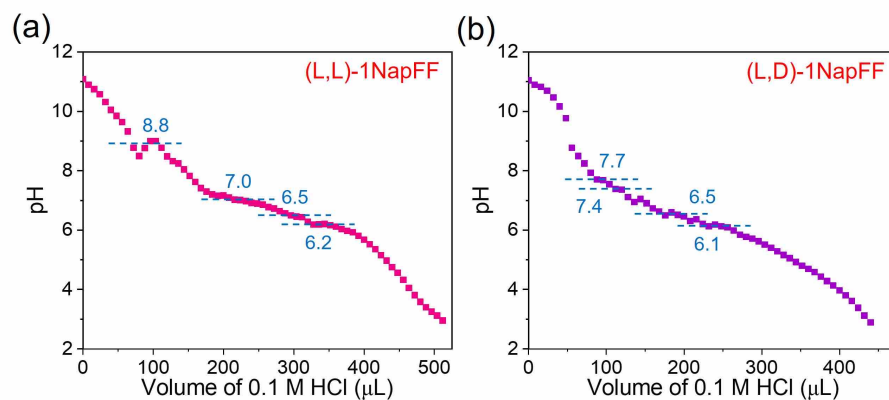


**Figure A3-87.** Apparent  $pK_a$  titration for 10 mg/mL (L,L)-1NapFF and (L,D)-1NapFF stock solutions at 25 °C.

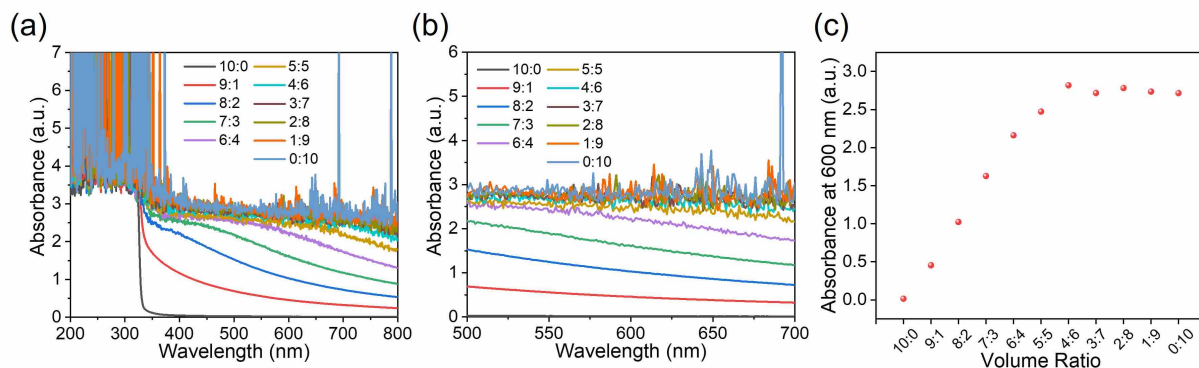


**Figure A3-88.** (a) UV-Vis absorption spectra of solutions containing 10 mg/mL (L,L)-1NapFF:(L,D)-1NapFF at ratios varying from 10:0 to 0:10, recorded using a 2 mm path length quartz cuvette at 25 °C. (b) Enlarged spectra from graph (a) focusing on the wavelength range of 500–700 nm. (c) Variation in turbidity across composition at 600 nm for solutions.

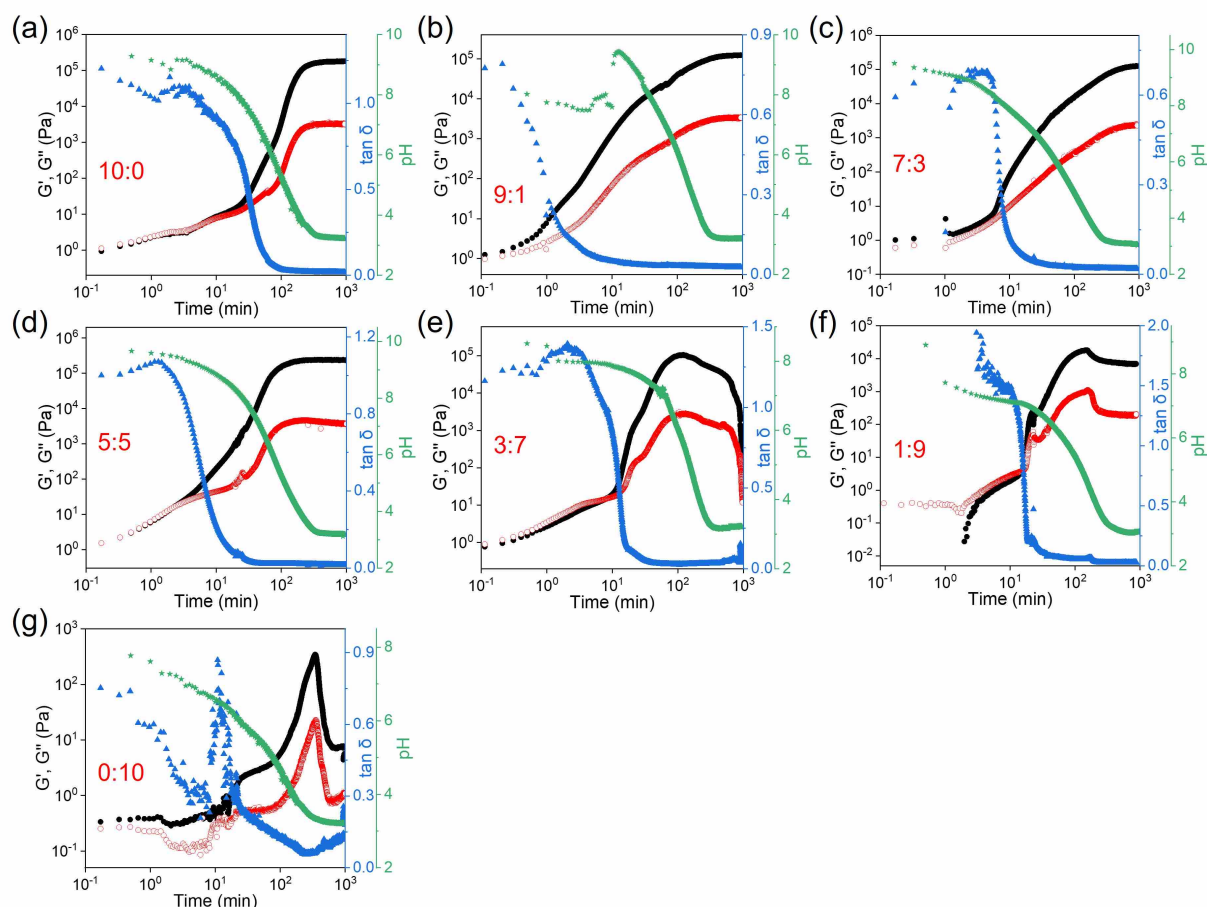


**Figure A3-89.** Evolution of  $G'$  (black),  $G''$  (red),  $\tan\delta$  (blue), and pH (green) with time for binary solutions with various volume ratios of 10 mg/mL (L,L)-1NapFF:(L,D)-1NapFF stock solutions.

**Table A3-2.** List of Materials and Amounts Required for Preparing 12 mL of 1NapFF Solutions of Different Concentrations. Two-component systems of various concentrations were prepared by mixing different concentrations of (L,L)-1NapFF: (L,D)-1NapFF at a volume ratio of 1:1.

Concentration (mg/mL)	Mass of 1NapFF (mg)	Volume of H <sub>2</sub> O (mL)	Volume of 0.1M NaOH (mL)	Mass of GdL (mg)
1	12	11.8	0.2	3.2
2	24	11.5	0.5	6.4
3	36	11.3	0.7	9.6
4	48	11.0	1.0	12.8

5	60	10.8	1.2	16.0
6	72	10.5	1.5	19.2
7	84	10.3	1.7	22.4
8	96	10.1	1.9	25.6
9	108	9.8	2.2	28.8
10	120	9.6	2.4	32.0

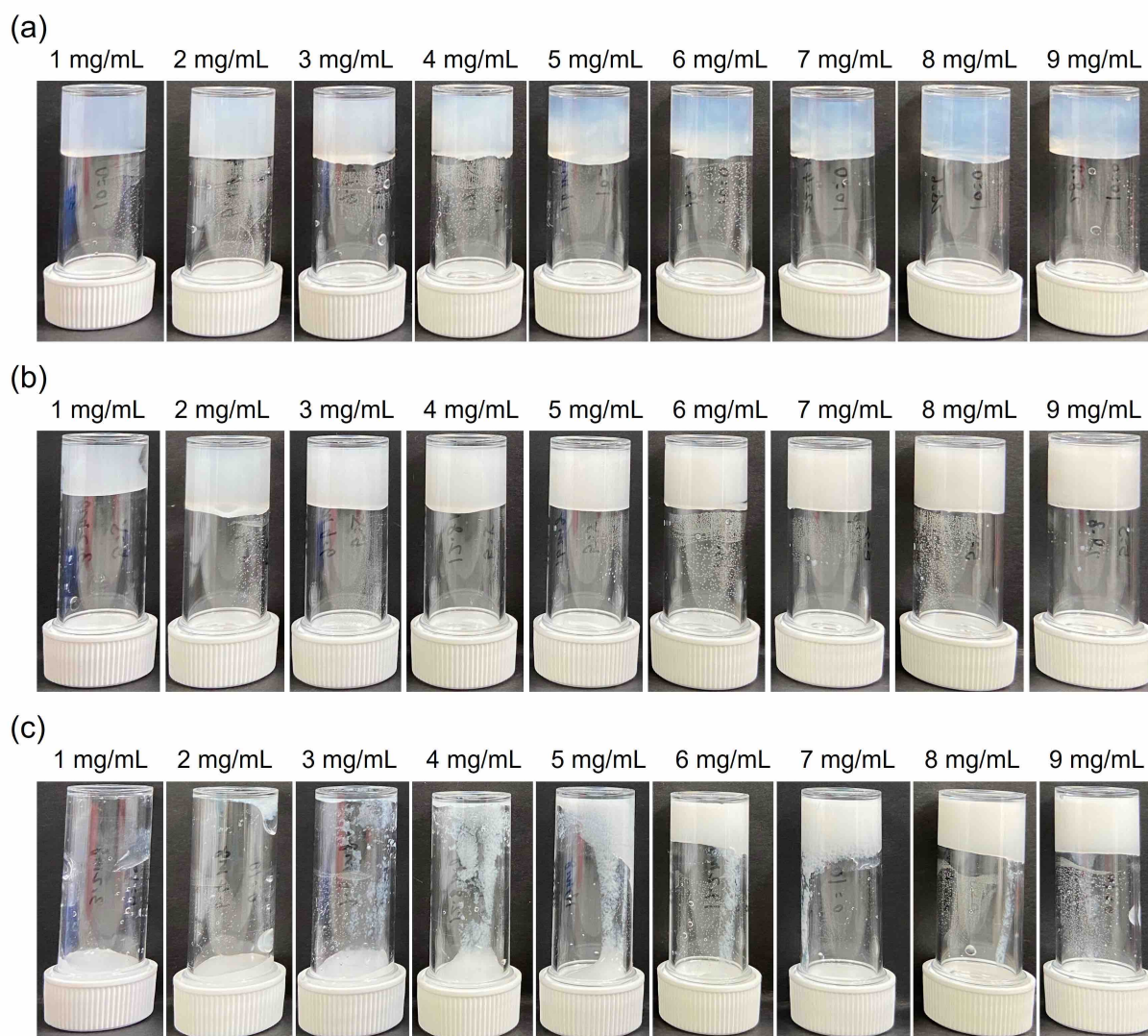


**Figure A3-90.** Photographs of gels at varying concentrations of (a) (L,L)-1NapFF, (b) two-component systems formed by mixing different concentrations of (L,L)-1NapFF: (L,D)-1NapFF at a volume ratio of 1:1, and (c) (L,D)-1NapFF under acidic pH conditions.

**Table A3-3.** pH of gels at varying concentrations of (a) (L,L)-1NapFF, (b) two-component systems formed by mixing different concentrations of (L,L)-1NapFF: (L,D)-1NapFF at a volume ratio of 1:1, and (c) (L,D)-1NapFF under acidic pH conditions.

G'Gelator	1 mg/mL	2 mg/mL	3 mg/mL	4 mg/mL	5 mg/mL	6 mg/mL	7 mg/mL	8 mg/mL	9 mg/mL
(L,L)-1NapFF	3.7	3.5	3.4	3.3	3.3	3.2	3.3	3.3	3.2
	3.7	3.5	3.3	3.3	3.3	3.2	3.3	3.3	3.3
	3.6	3.4	3.3	3.3	3.3	3.2	3.3	3.3	3.2
Two-component system	3.5	3.4	3.3	3.3	3.3	3.2	3.2	3.2	3.2
	3.4	3.3	3.3	3.3	3.3	3.2	3.2	3.2	3.2
	3.4	3.3	3.3	3.3	3.2	3.2	3.2	3.2	3.2
(L,D)-1NapFF	3.5	3.4	3.3	3.3	3.3	3.3	3.2	3.2	3.2
	3.5	3.4	3.3	3.3	3.2	3.3	3.2	3.2	3.2
	3.5	3.4	3.3	3.3	3.2	3.3	3.2	3.2	3.2

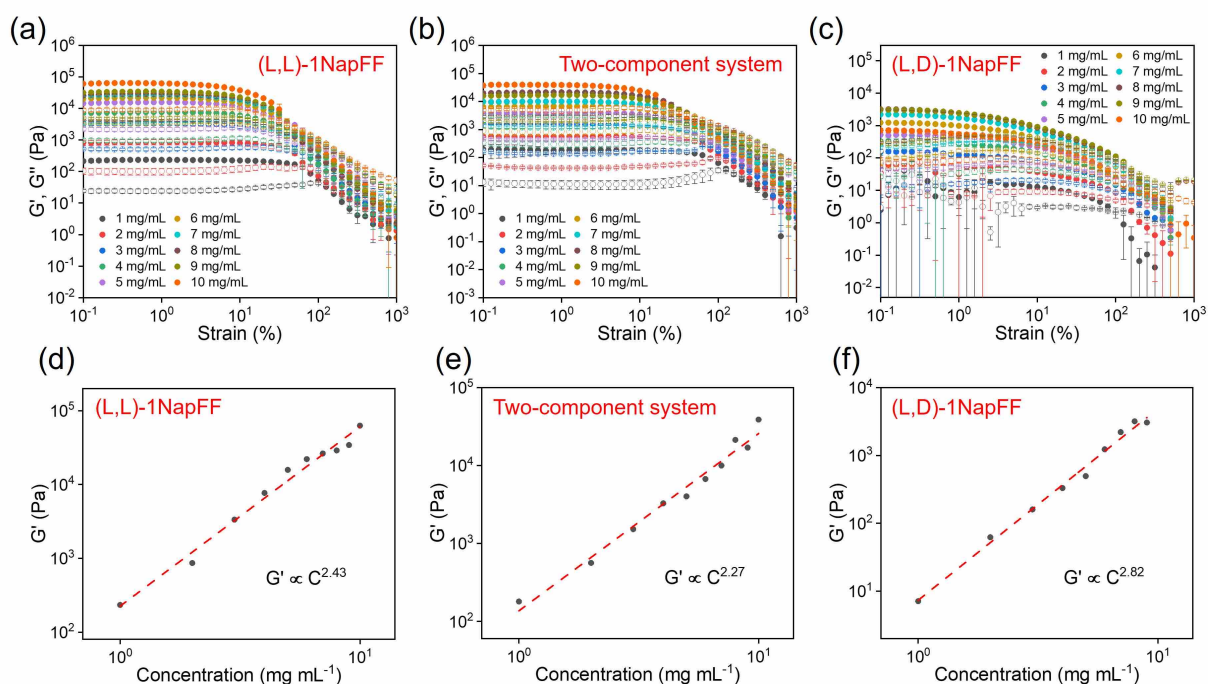


**Figure A3-91.** (a-c) Strain sweep of gels at varying concentrations of (L,L)-1NapFF, two-component systems formed by mixing different concentrations of (L,L)-1NapFF: (L,D)-1NapFF at a volume ratio of 1:1, and (L,D)-1NapFF under acidic pH conditions. (d-f) Plots depict the concentration-dependent storage modulus ( $G'$ ) of gels.

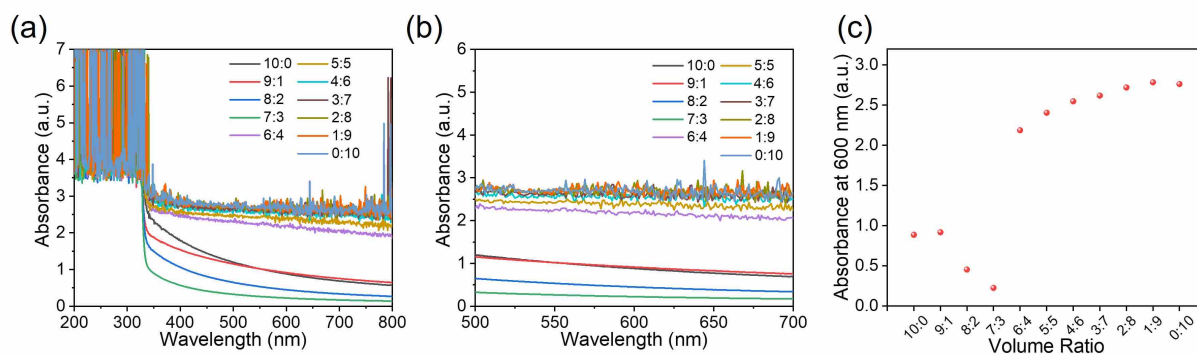


**Figure A3-92.** (a) UV-Vis absorption spectra of gels containing 10 mg/mL (L,L)-1NapFF:(L,D)-1NapFF at ratios varying from 10:0 to 0:10, recorded using a 2 mm path length quartz cuvette at 25 °C. (b) Enlarged spectra from graph (a) focusing on the wavelength range of 500–700 nm. (c) Variation in turbidity across composition at 600 nm for gels.

### A3.3.4 6CN2NapFF

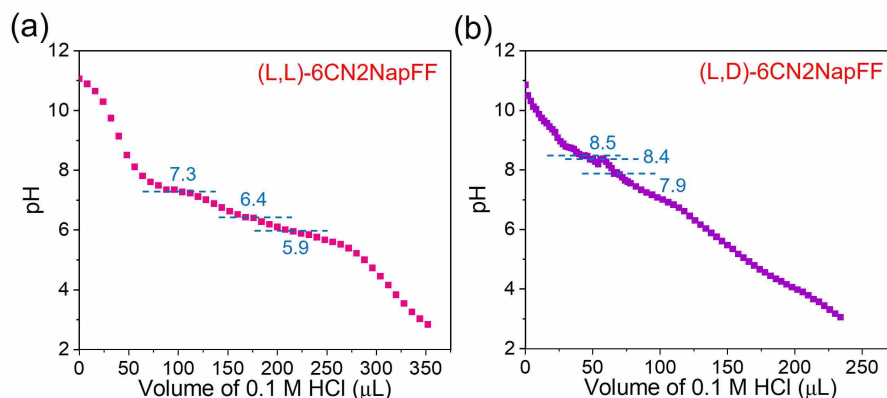


**Figure A3-93.** Apparent  $pK_a$  titration for 10 mg/mL (L,L)-6CN2NapFF and (L,D)-6CN2NapFF stock solutions at 25 °C.

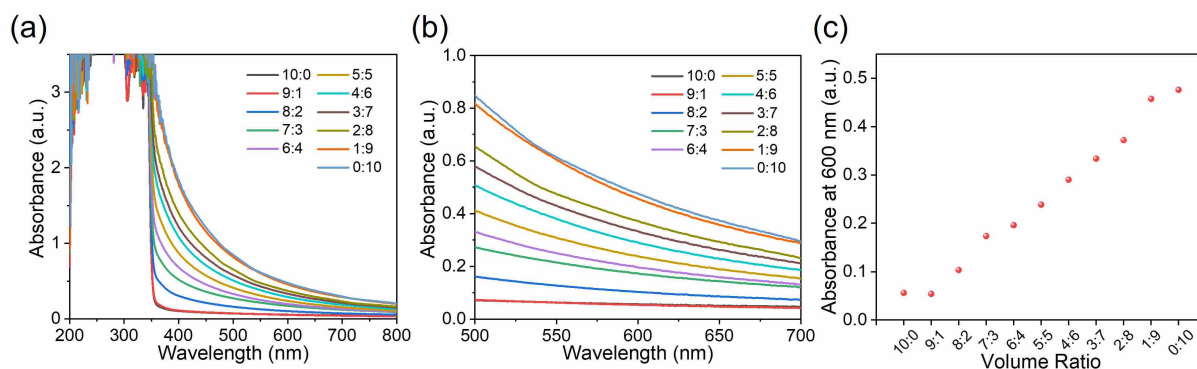


**Figure A3-94.** (a) UV-Vis absorption spectra of solutions containing 10 mg/mL (L,L)-6CN2NapFF:(L,D)-6CN2NapFF at ratios varying from 10:0 to 0:10, recorded using a 2 mm

path length quartz cuvette at 25 °C. (b) Enlarged spectra from graph (a) focusing on the wavelength range of 500–700 nm. (c) Variation in turbidity across composition at 600 nm for solutions.

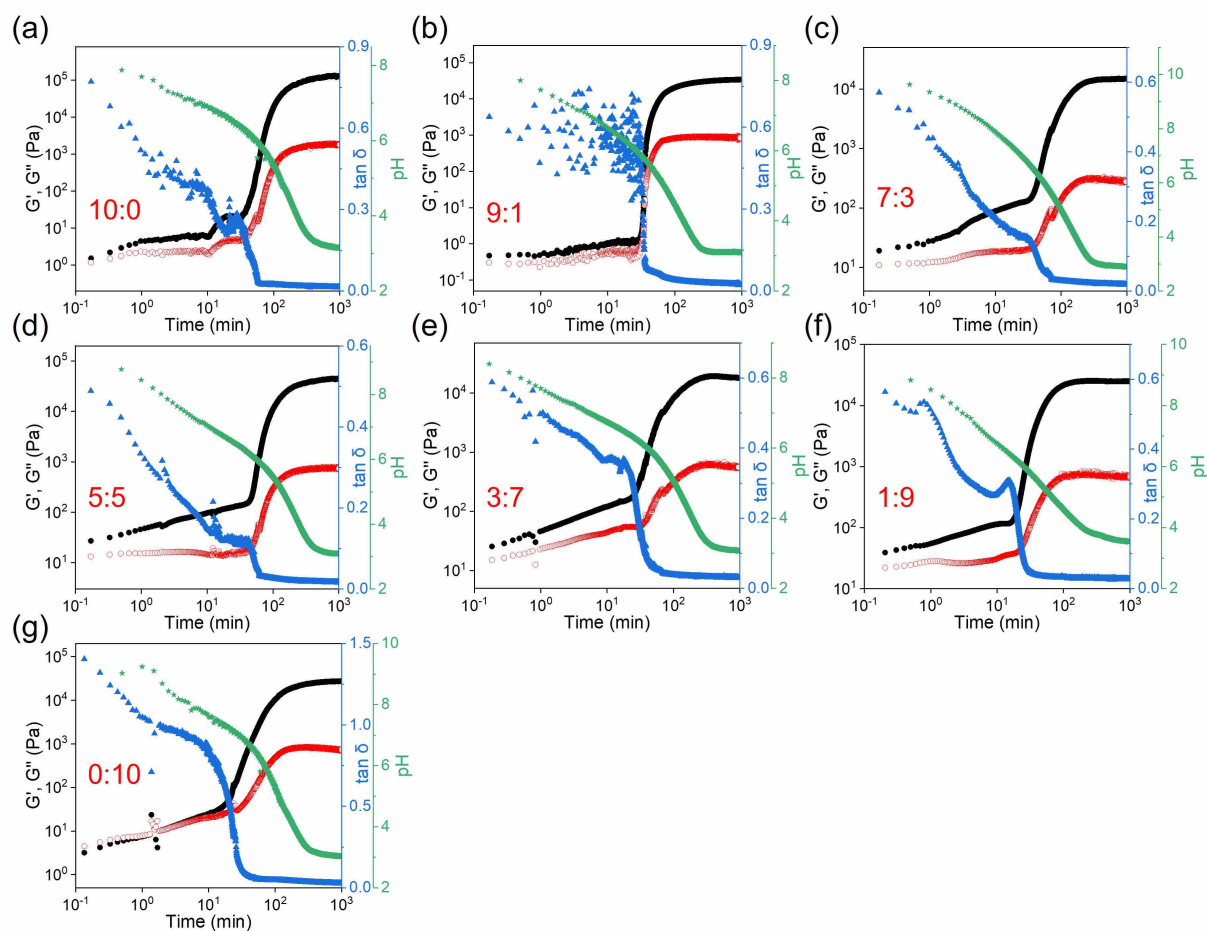


**Figure A3-95.** Evolution of  $G'$  (black),  $G''$  (red),  $\tan\delta$  (blue), and pH (green) with time for binary solutions with various volume ratios of 10 mg/mL (L,L)-6CN2NapFF:(L,D)-6CN2NapFF stock solutions.

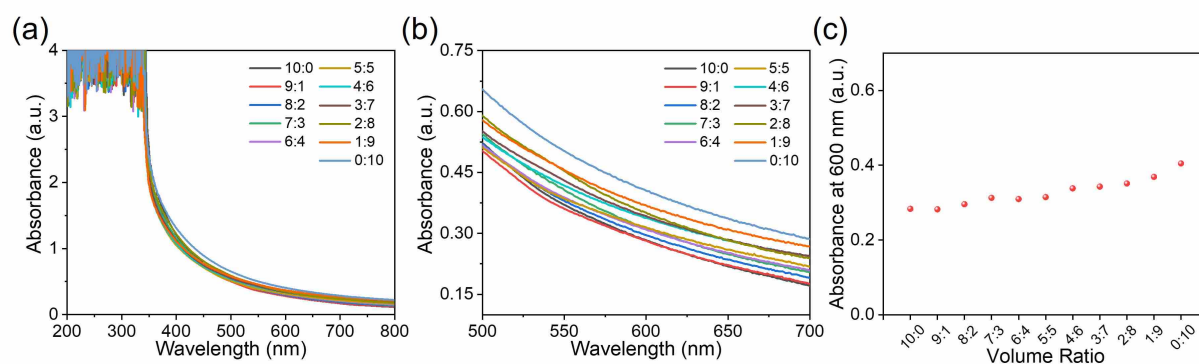


**Figure A3-96.** (a) UV-Vis absorption spectra of gels containing 10 mg/mL (L,L)-6CN2NapFF:(L,D)-6CN2NapFF at ratios varying from 10:0 to 0:10, recorded using a 2 mm

path length quartz cuvette at 25 °C. (b) Enlarged spectra from graph (a) focusing on the wavelength range of 500–700 nm. (c) Variation in turbidity across composition at 600 nm for gels.

### A3.3.5 4Cl1NapFF

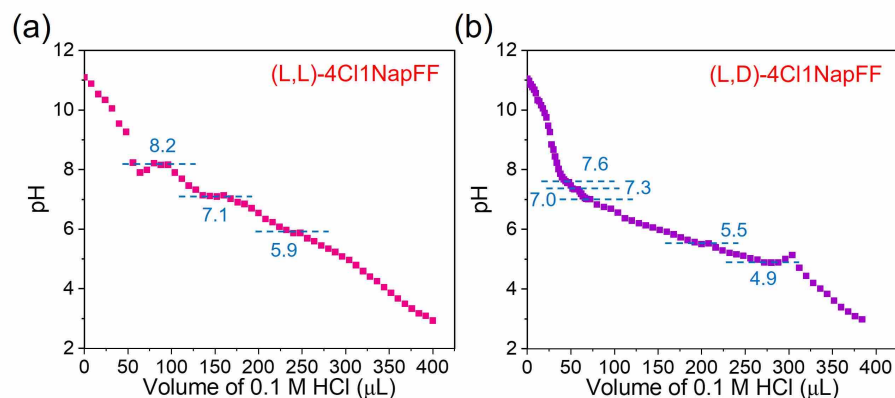


**Figure A3-97.** Apparent  $pK_a$  titration for 10 mg/mL (L,L)-4Cl1NapFF and (L,D)-4Cl1NapFF stock solutions at 25 °C.

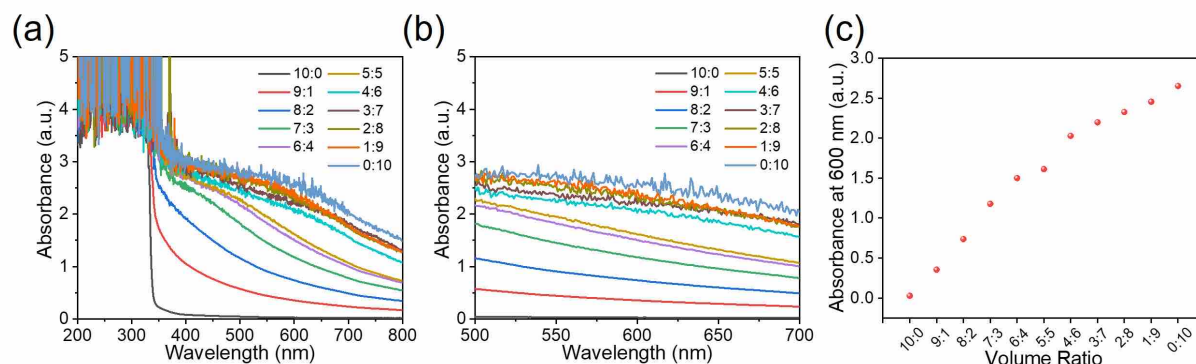


**Figure A3-98.** (a) UV-Vis absorption spectra of solutions containing 10 mg/mL (L,L)-4Cl1NapFF:(L,D)-4Cl1NapFF at ratios varying from 10:0 to 0:10, recorded using a 2 mm path length quartz cuvette at 25 °C. (b) Enlarged spectra from graph (a) focusing on the wavelength range of 500–700 nm. (c) Variation in turbidity across composition at 600 nm for solutions.

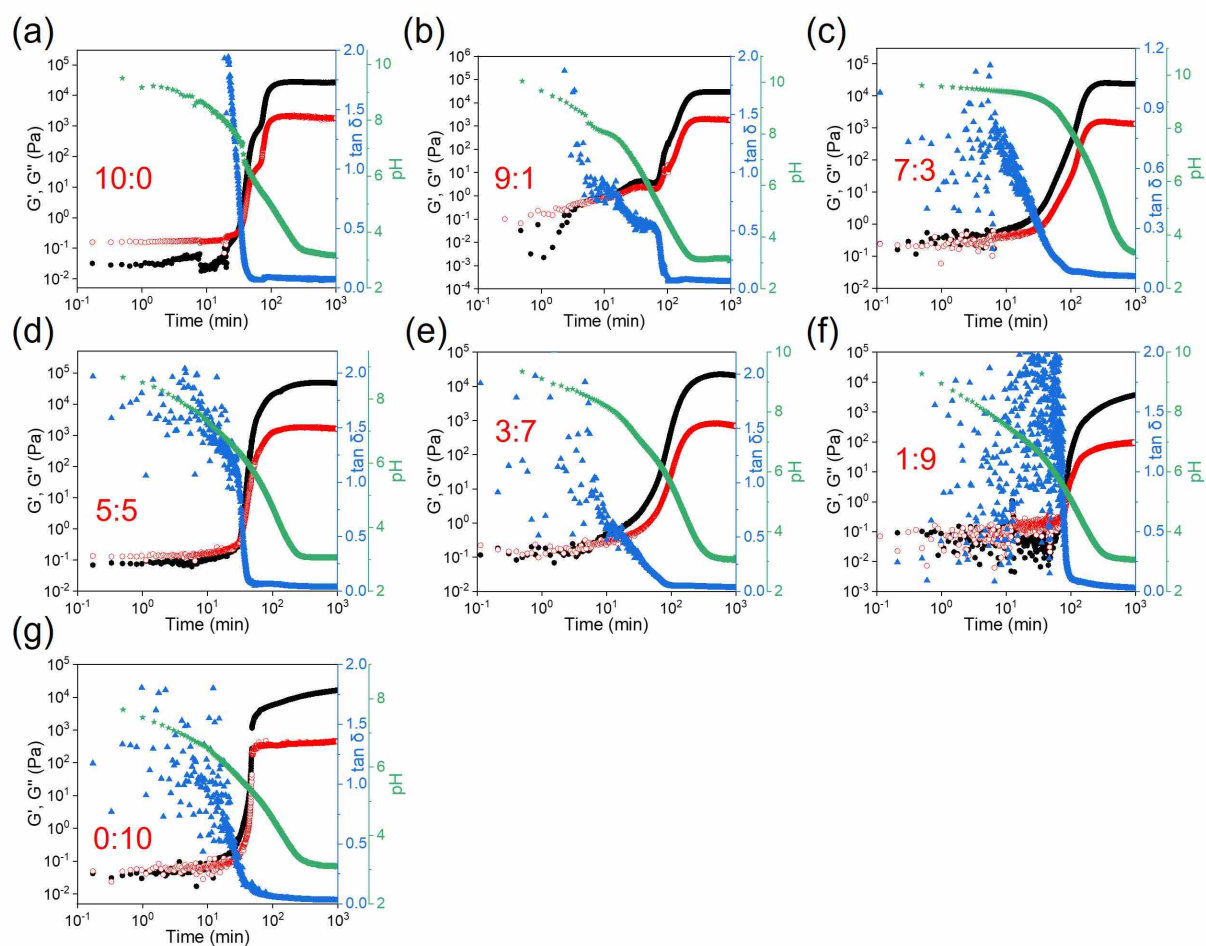


**Figure A3-99.** Evolution of  $G'$  (black),  $G''$  (red),  $\tan\delta$  (blue), and pH (green) with time for binary solutions with various volume ratios of 10 mg/mL (L,L)-4C11NapFF:(L,D)-4C11NapFF stock solutions.

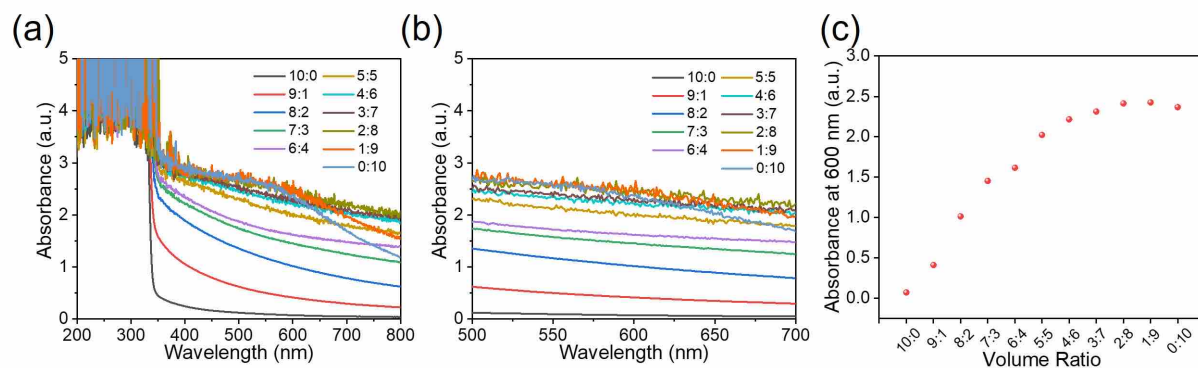


**Figure A3-100.** (a) UV-Vis absorption spectra of gels containing 10 mg/mL (L,L)-4C11NapFF:(L,D)-4C11NapFF at ratios varying from 10:0 to 0:10, recorded using a 2 mm path length quartz cuvette at 25 °C. (b) Enlarged spectra from graph (a) focusing on the wavelength range of 500–700 nm. (c) Variation in turbidity across composition at 600 nm for gels.

## A4 Appendix for Chapter 4

### A4.1 Additional Figures

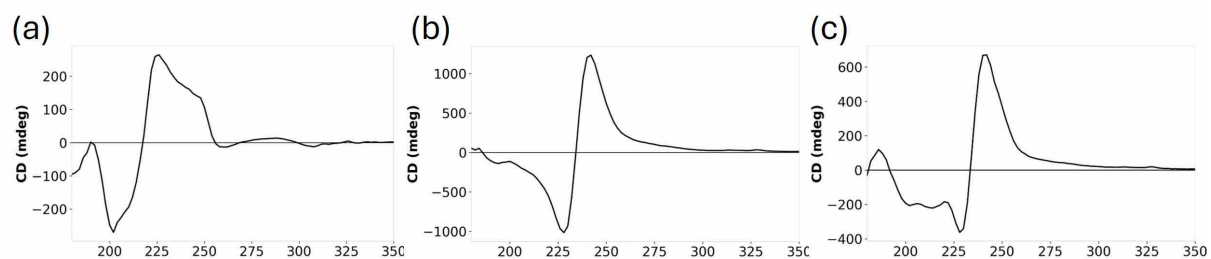


**Figure A4-1.** SRCD spectra of (a) 10 mg/mL (L,L)-7MeO<sub>2</sub>NapFF pre-gel solution, (b) 10 mg/mL (L,D)-7MeO<sub>2</sub>NapFF pre-gel solution, and (c) binary solution of (L,L)-7MeO<sub>2</sub>NapFF and (L,D)-7MeO<sub>2</sub>NapFF each at 10 mg/mL with a 1:1 volume ratio (5:5) at pH 10.5, 25 °C.

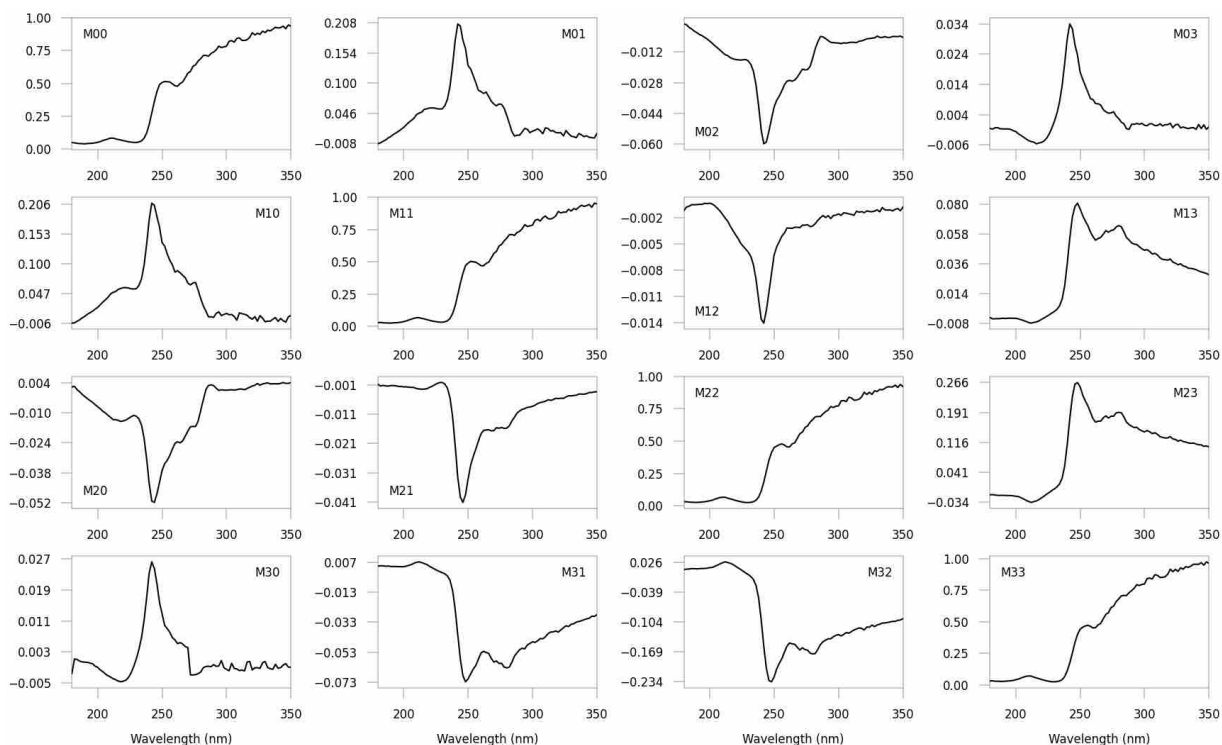


**Figure A4-2.** Preliminary differential Mueller matrix plots of 10 mg/mL (L,D)-2NapFF pre-gel solution at pH 10.5, 25 °C.

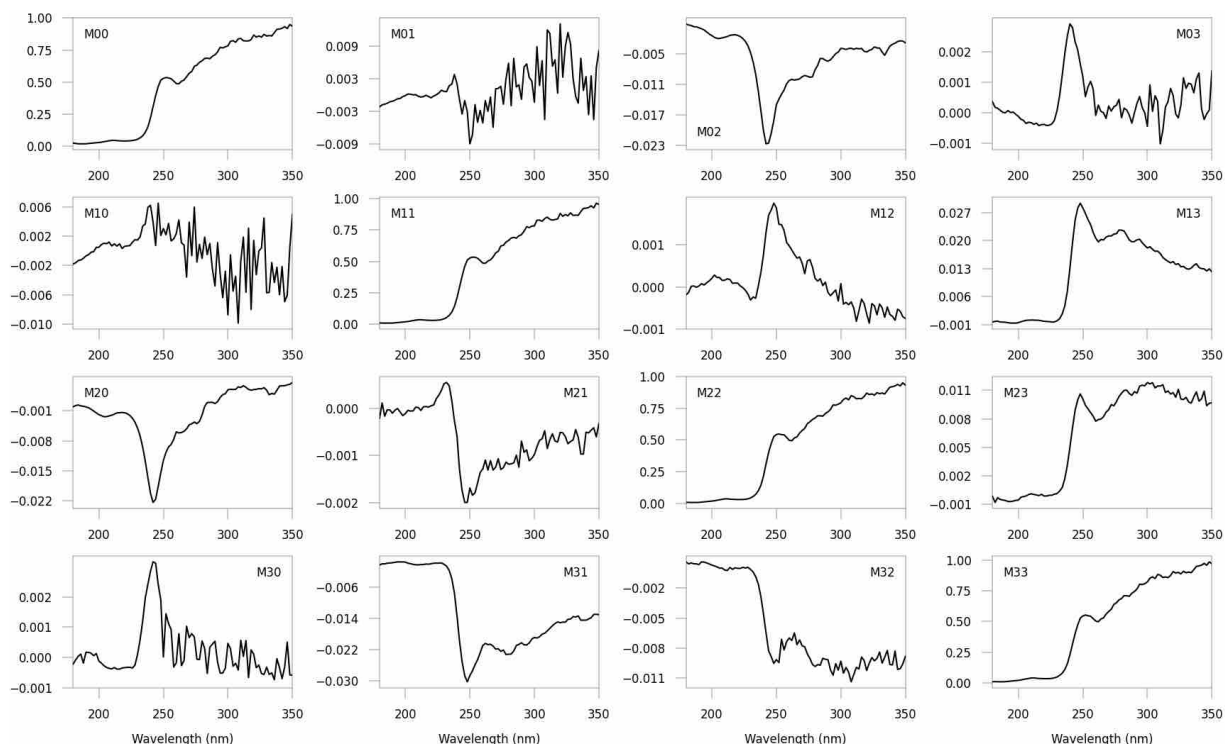


**Figure A4-3.** Preliminary differential Mueller matrix plots of the binary solution composed of (L,L)-2NapFF and (L,D)-2NapFF each at 10 mg/mL with a 1:1 volume ratio (5:5) at pH 10.5, 25 °C.

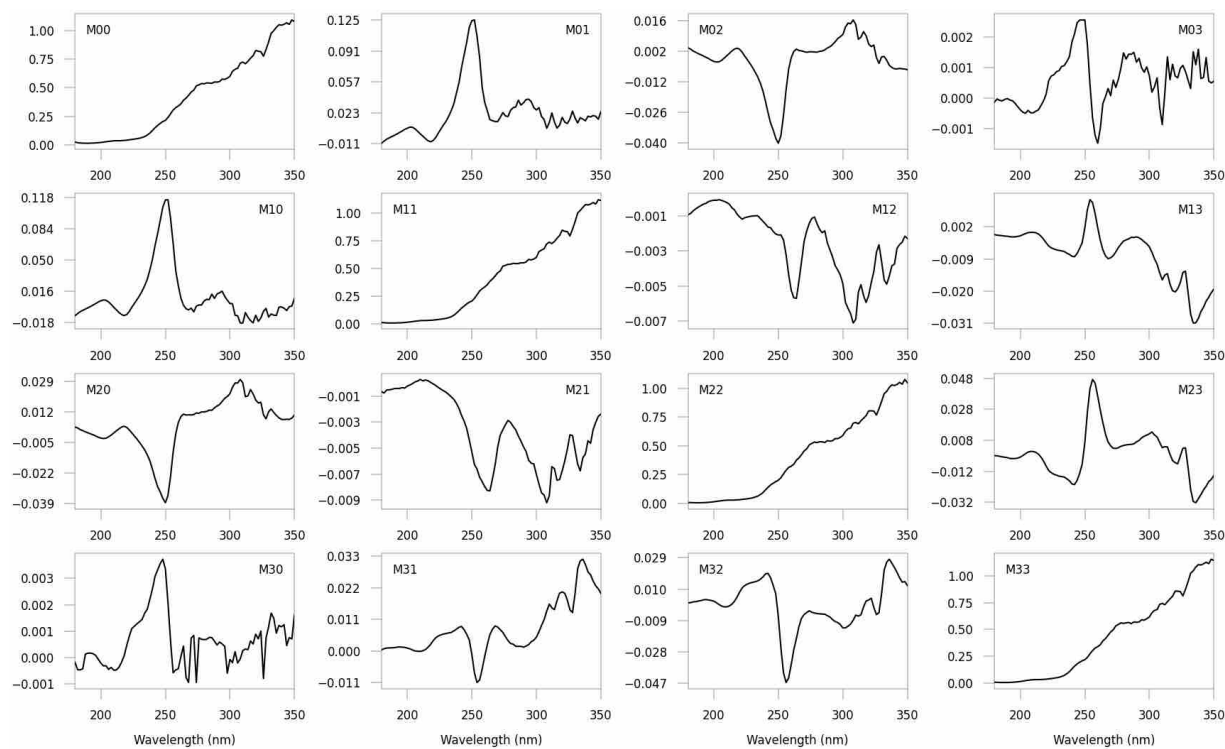


**Figure A4-4.** Preliminary differential Mueller matrix plots of 10 mg/mL (L,L)-7MeO<sub>2</sub>NapFF pre-gel solution at pH 10.5, 25 °C.

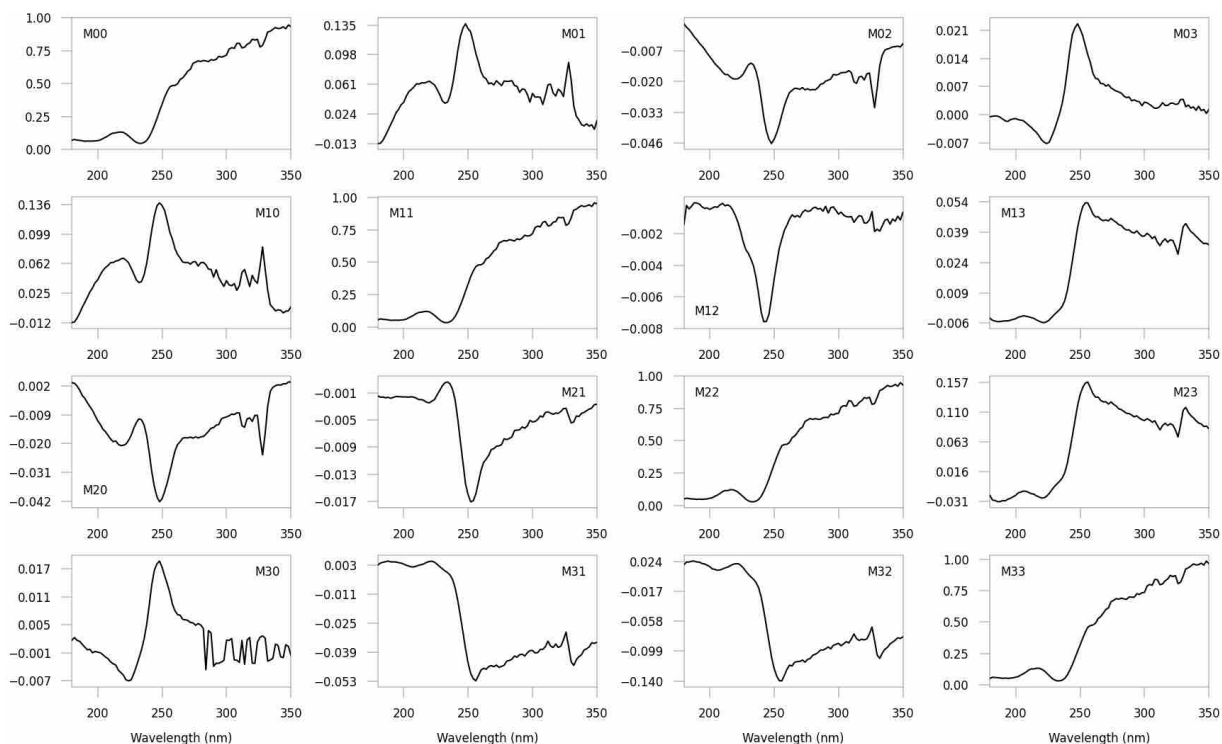


**Figure A4-5.** Preliminary differential Mueller matrix plots of 10 mg/mL (L,D)-7MeO<sub>2</sub>NapFF pre-gel solution at pH 10.5, 25 °C.

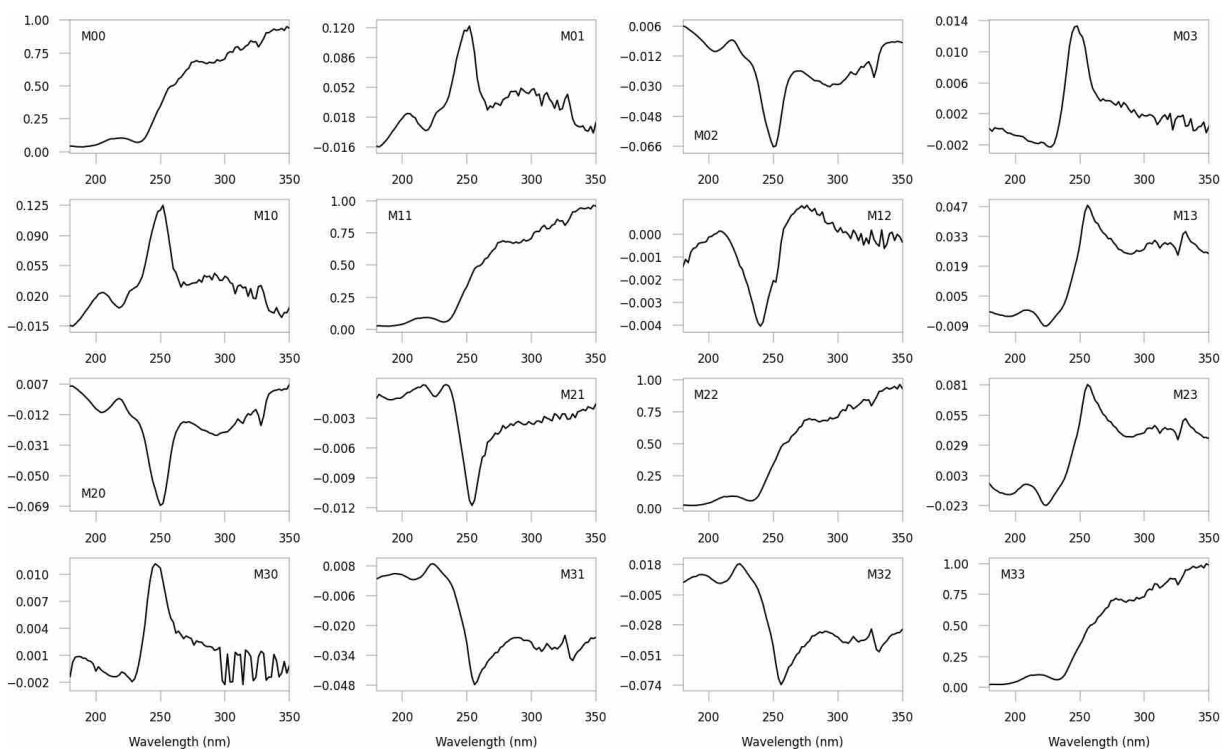


**Figure A4-6.** Preliminary differential Mueller matrix plots of the binary solution composed of (L,L)-7MeO<sub>2</sub>NapFF and (L,D)-7MeO<sub>2</sub>NapFF each at 10 mg/mL with a 1:1 volume ratio (5:5) at pH 10.5, 25 °C.

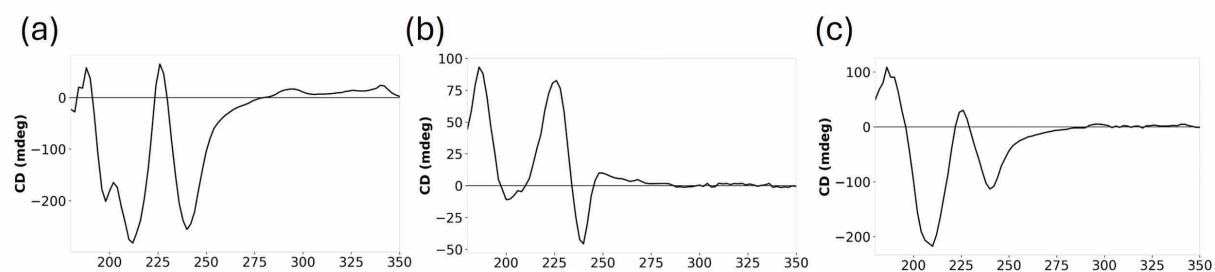


**Figure A4-7.** SRCD spectra of (a) 10 mg/mL (L,L)-6Br<sub>2</sub>NapFF pre-gel solution, (b) 10 mg/mL (L,D)-6Br<sub>2</sub>NapFF pre-gel solution, and (c) binary solution of (L,L)-6Br<sub>2</sub>NapFF and (L,D)-6Br<sub>2</sub>NapFF each at 10 mg/mL with a 1:1 volume ratio (5:5) at pH 10.5, 25 °C.

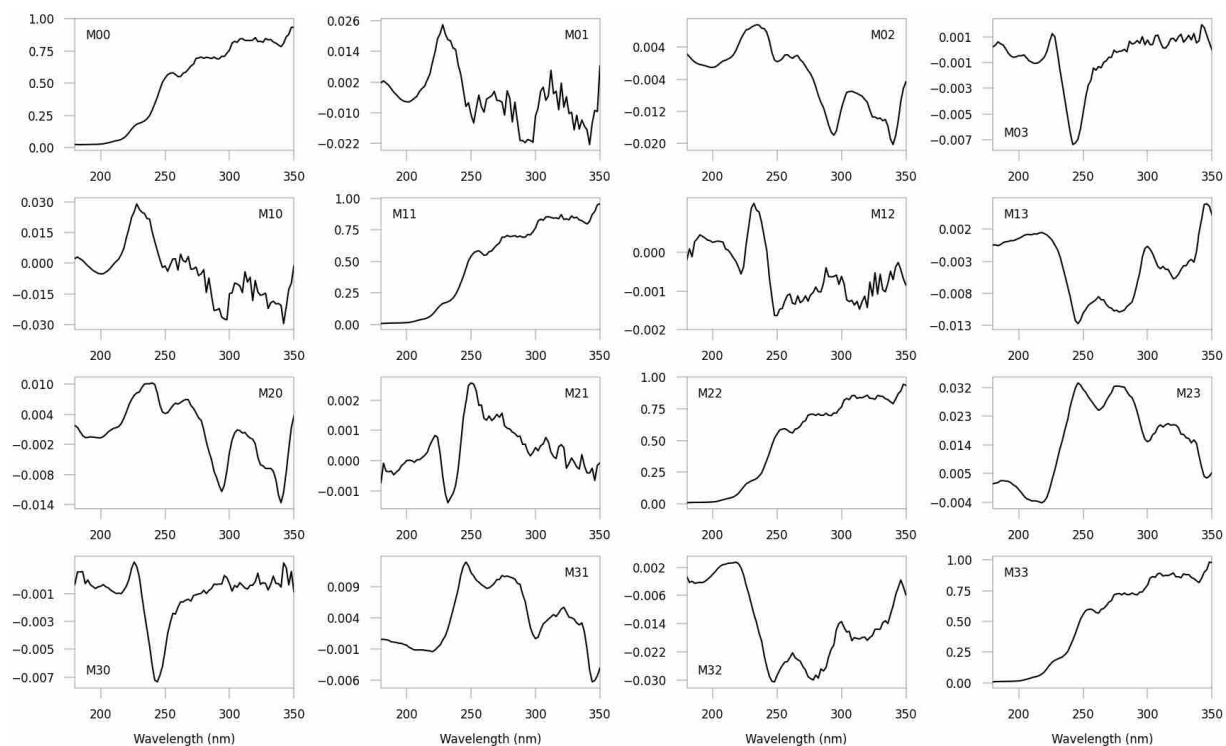


**Figure A4-8.** Preliminary differential Mueller matrix plots of 10 mg/mL (L,L)-6Br<sub>2</sub>NapFF pre-gel solution at pH 10.5, 25 °C.

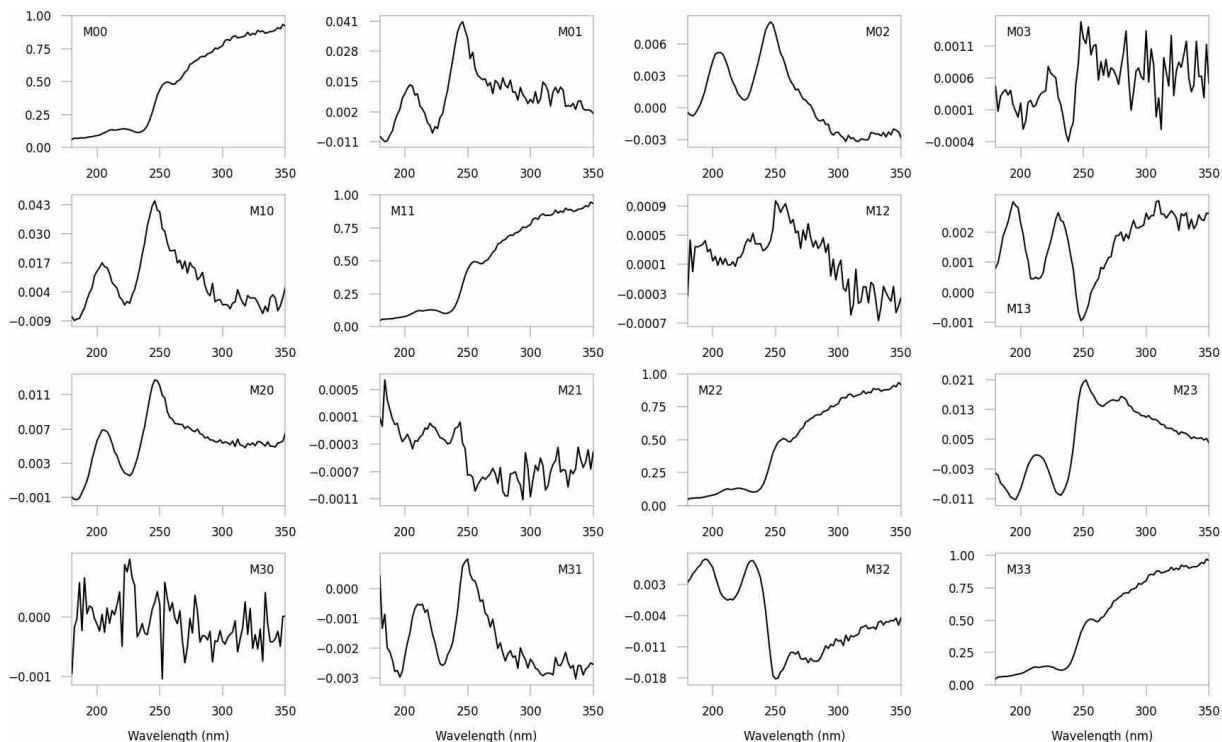


**Figure A4-9.** Preliminary differential Mueller matrix plots of 10 mg/mL (L,D)-6Br<sub>2</sub>NapFF pre-gel solution at pH 10.5, 25 °C.

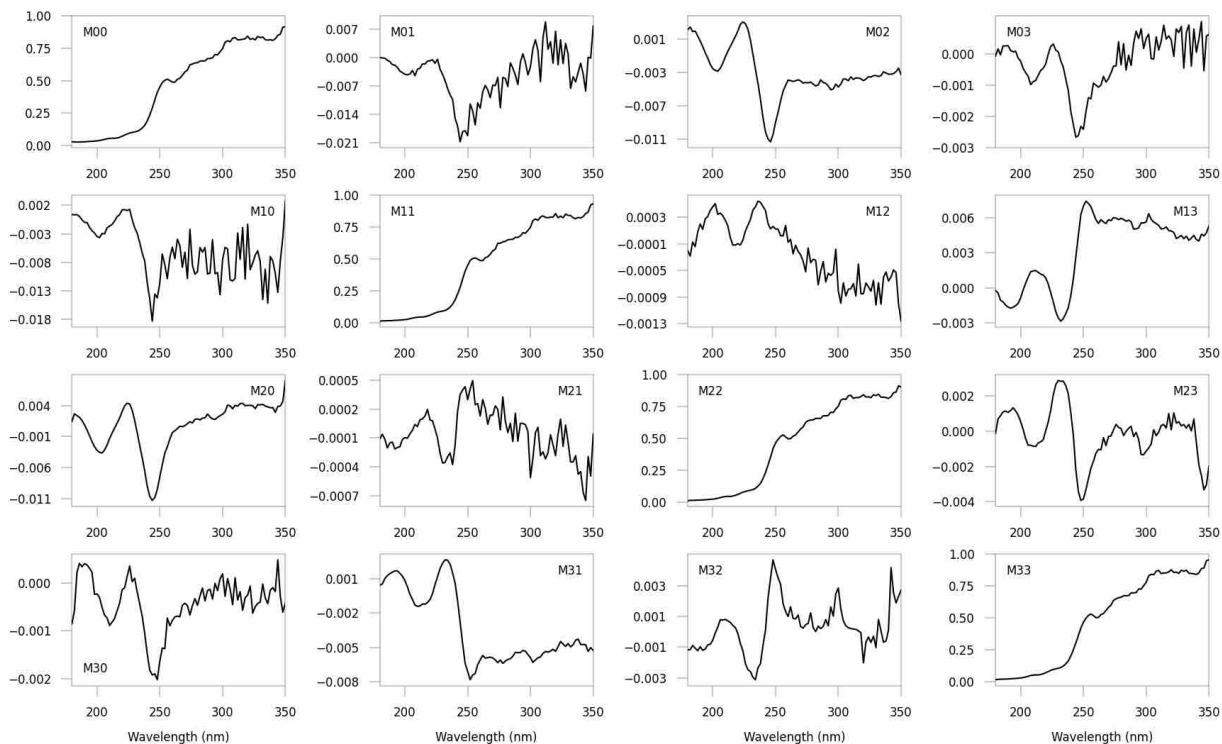


**Figure A4-10.** Preliminary differential Mueller matrix plots of the binary solution composed of (L,L)-6Br<sub>2</sub>NapFF and (L,D)-6Br<sub>2</sub>NapFF each at 10 mg/mL with a 1:1 volume ratio (5:5) at pH 10.5, 25 °C.

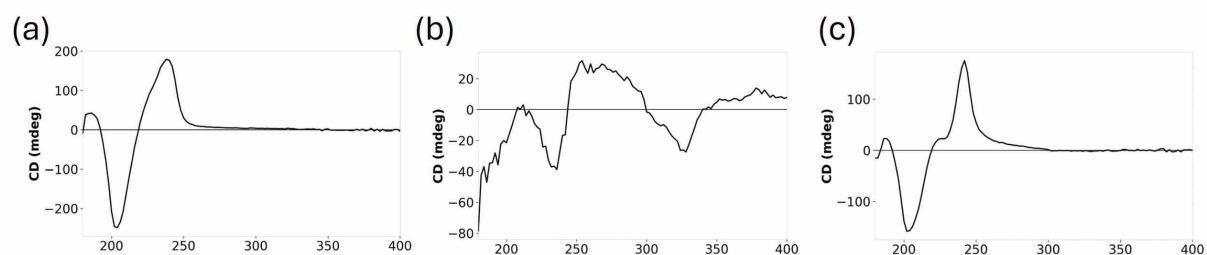


**Figure A4-11.** SRCD spectra of (a) 10 mg/mL (L,L)-1NapFF pre-gel solution, (b) 10 mg/mL (L,D)-1NapFF pre-gel solution, and (c) binary solution of (L,L)-1NapFF and (L,D)-1NapFF each at 10 mg/mL with a 1:1 volume ratio (5:5) at pH 10.5, 25 °C.

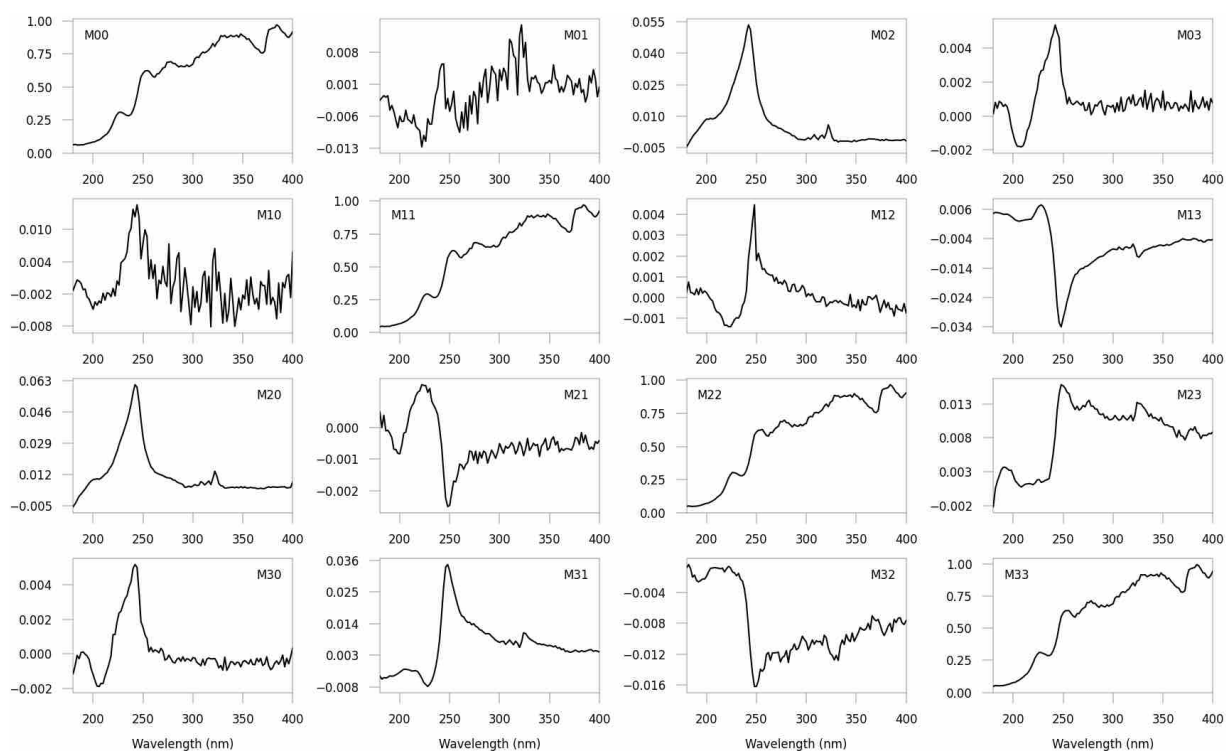


**Figure A4-12.** Preliminary differential Mueller matrix plots of 10 mg/mL (L,L)-1NapFF pre-gel solution at pH 10.5, 25 °C.

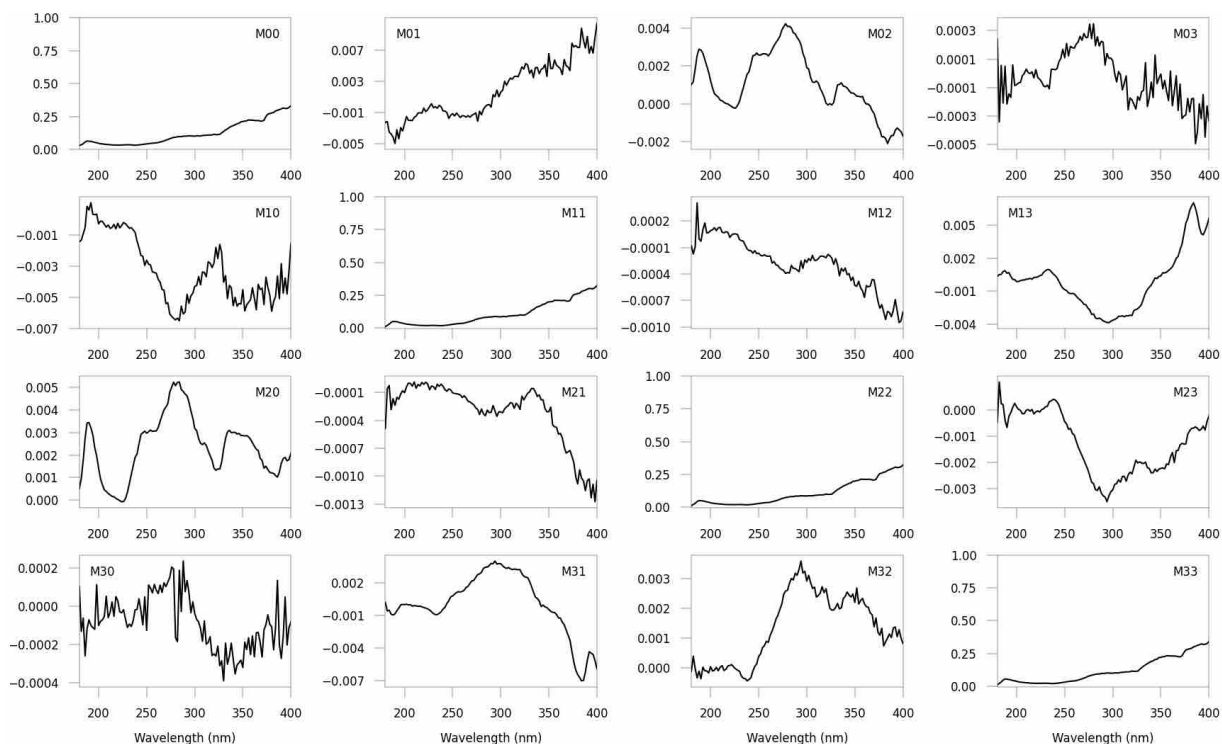


**Figure A4-13.** Preliminary differential Mueller matrix plots of 10 mg/mL (L,D)-1NapFF pre-gel solution at pH 10.5, 25 °C.

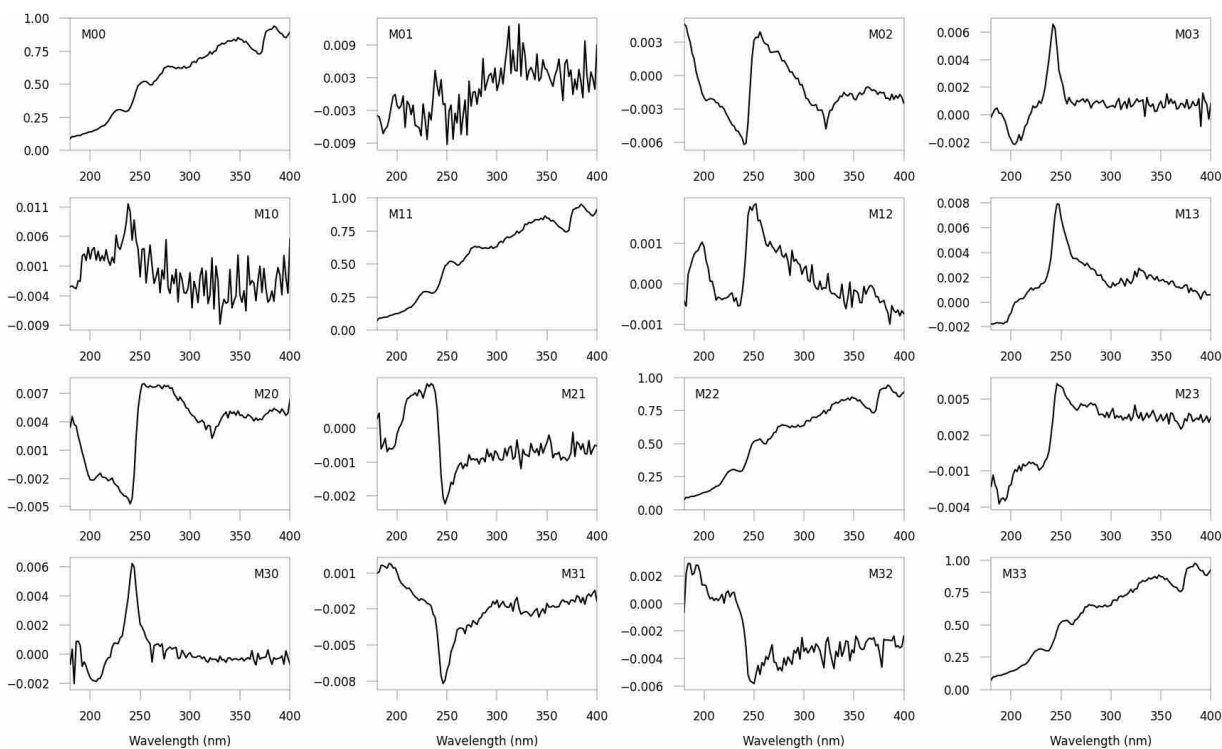


**Figure A4-14.** Preliminary differential Mueller matrix plots of the binary solution composed of (L,L)-1NapFF and (L,D)-1NapFF each at 10 mg/mL with a 1:1 volume ratio (5:5) at pH 10.5, 25 °C.

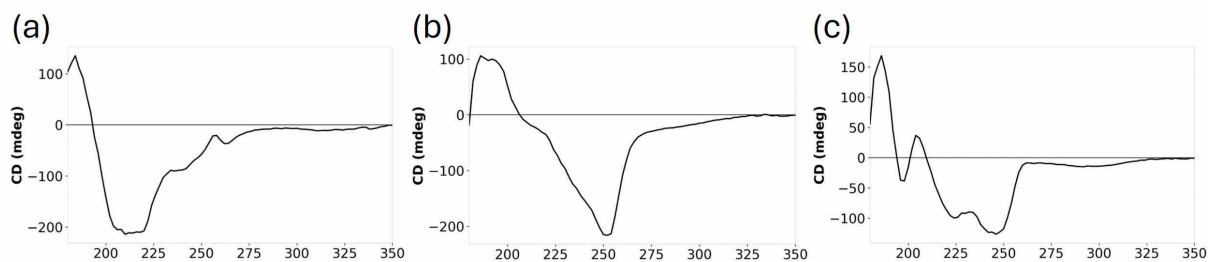


**Figure A4-15.** SRCD spectra of (a) 10 mg/mL (L,L)-6CN2NapFF pre-gel solution, (b) 10 mg/mL (L,D)-6CN2NapFF pre-gel solution, and (c) binary solution of (L,L)-6CN2NapFF and (L,D)-6CN2NapFF each at 10 mg/mL with a 1:1 volume ratio (5:5) at pH 10.5, 25 °C.

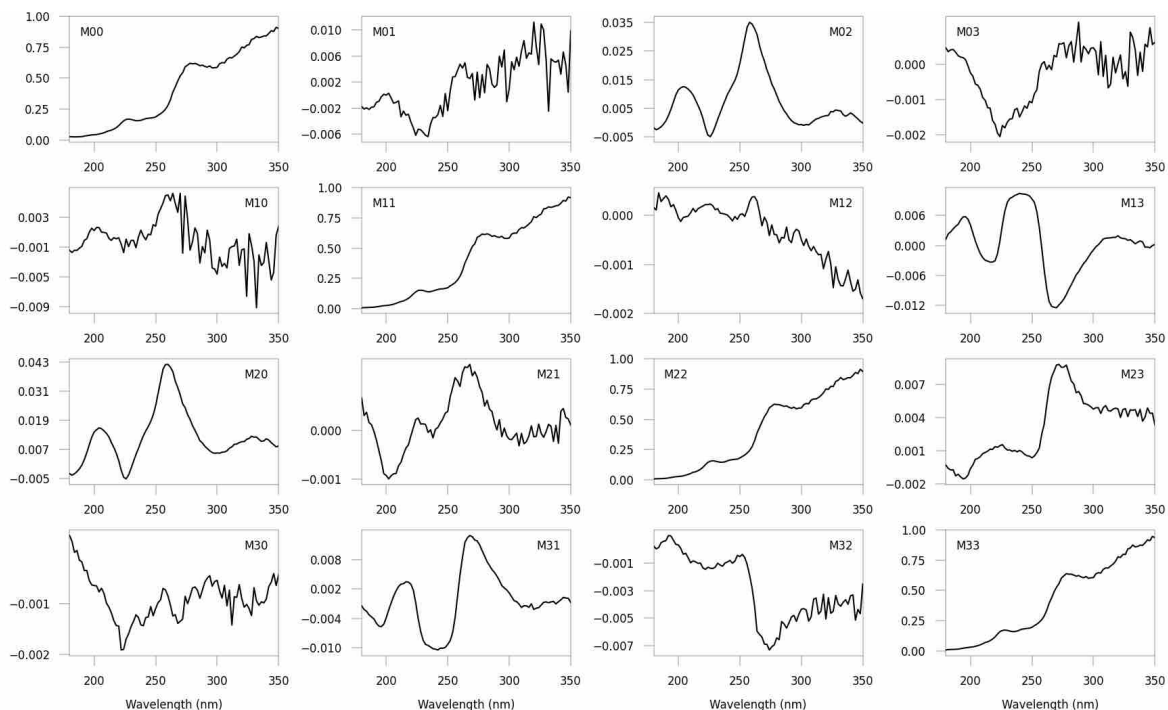


**Figure A4-16.** Preliminary differential Mueller matrix plots of 10 mg/mL (L,L)-6CN2NapFF pre-gel solution at pH 10.5, 25 °C.

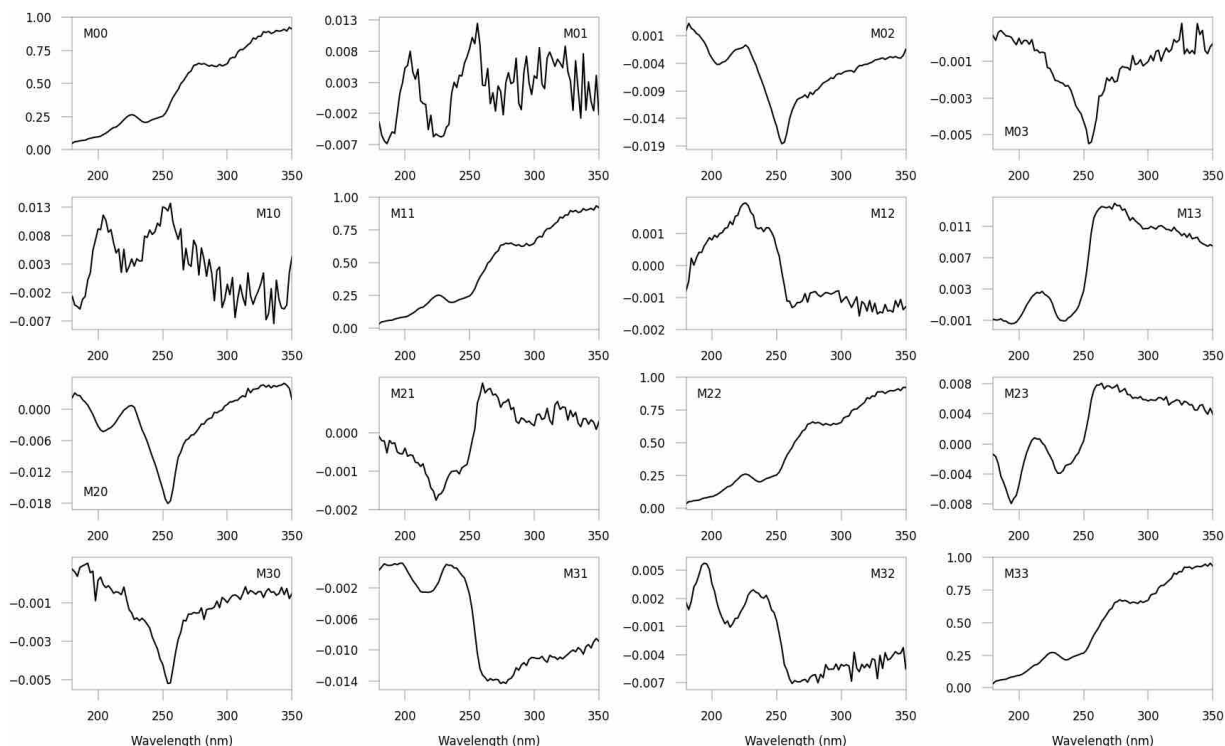


**Figure A4-17.** Preliminary differential Mueller matrix plots of 10 mg/mL (L,D)-6CN2NapFF pre-gel solution at pH 10.5, 25 °C.

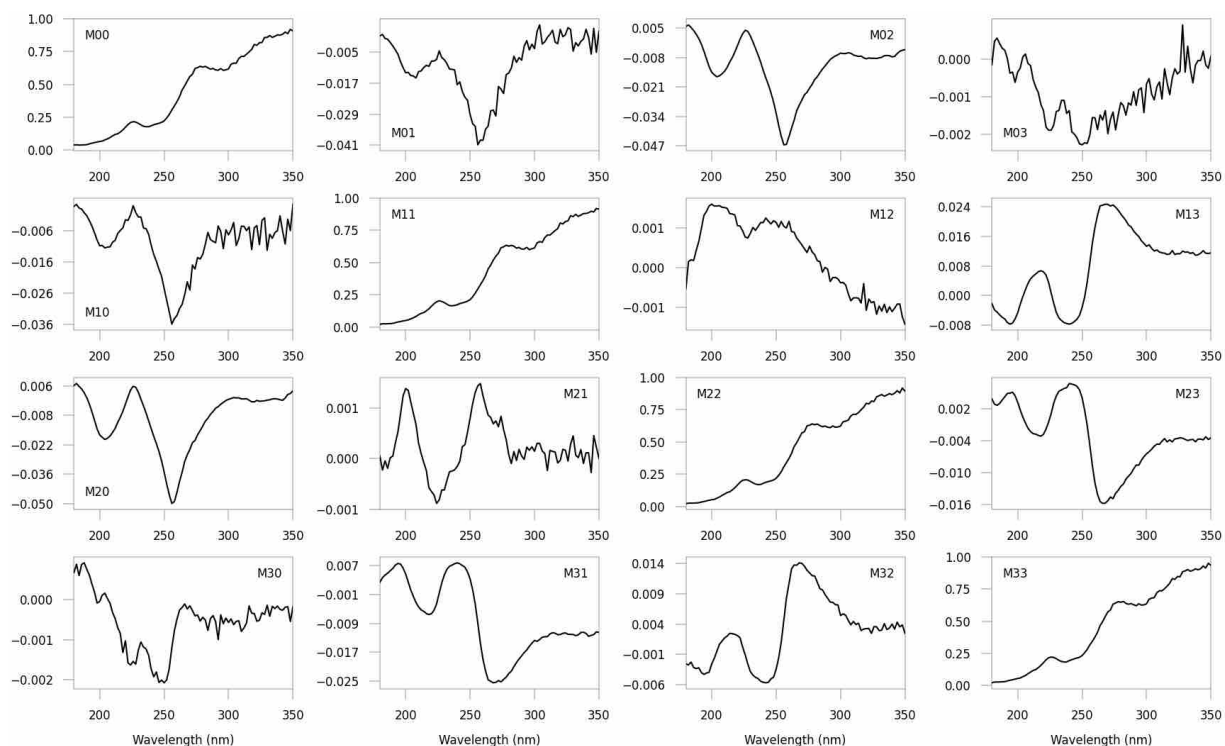


**Figure A4-18.** Preliminary differential Mueller matrix plots of the binary solution composed of (L,L)-6CN2NapFF and (L,D)-6CN2NapFF each at 10 mg/mL with a 1:1 volume ratio (5:5) at pH 10.5, 25 °C.

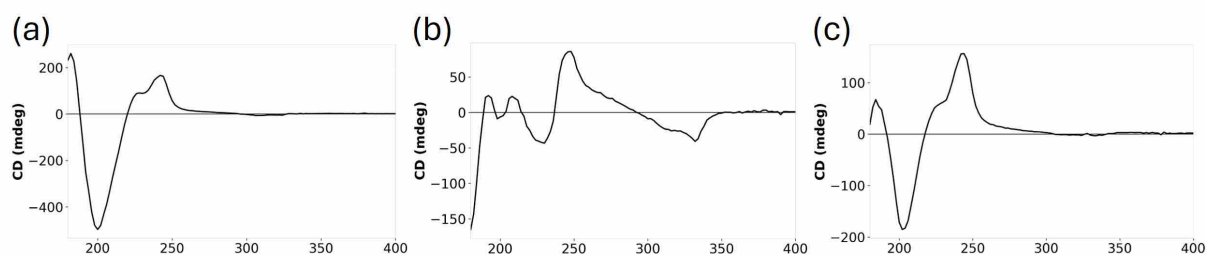


**Figure A4-19.** SRCD spectra of (a) 10 mg/mL (L,L)-4C11NapFF pre-gel solution, (b) 10 mg/mL (L,D)-4C11NapFF pre-gel solution, and (c) binary solution of (L,L)-4C11NapFF and (L,D)-4C11NapFF each at 10 mg/mL with a 1:1 volume ratio (5:5) at pH 10.5, 25 °C.

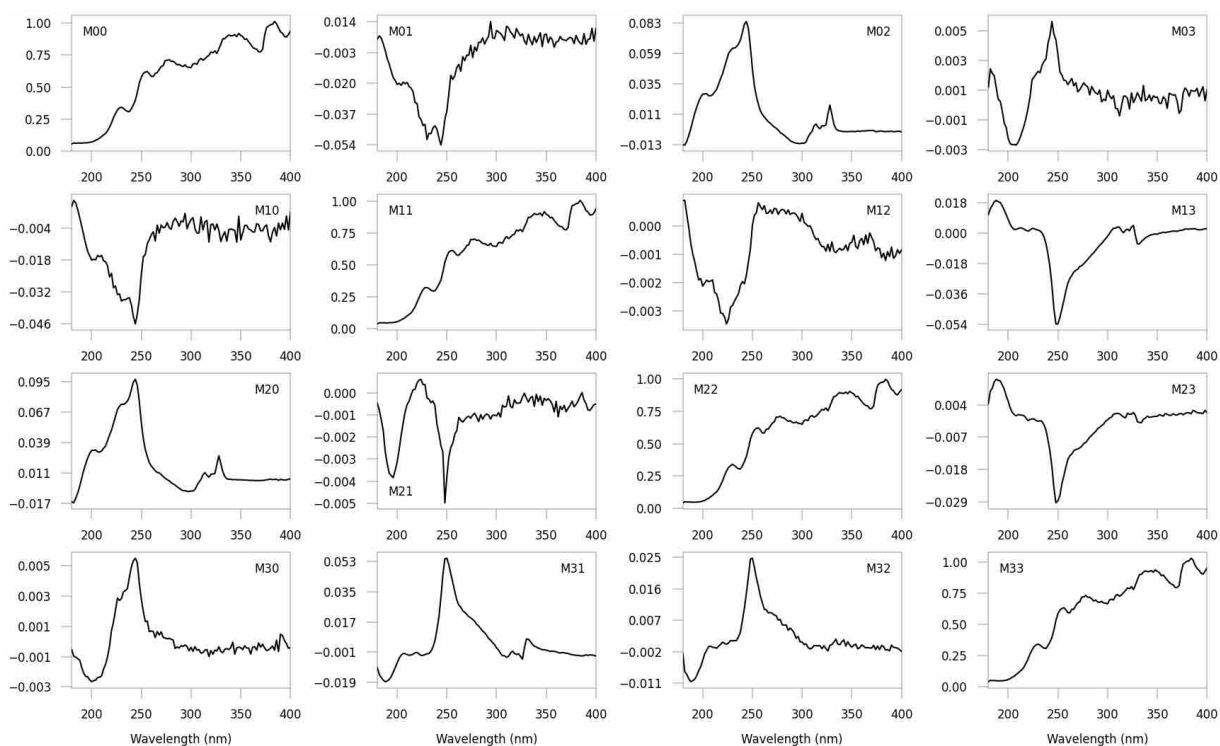


**Figure A4-20.** Preliminary differential Mueller matrix plots of 10 mg/mL (L,L)-4C11NapFF pre-gel solution at pH 10.5, 25 °C.

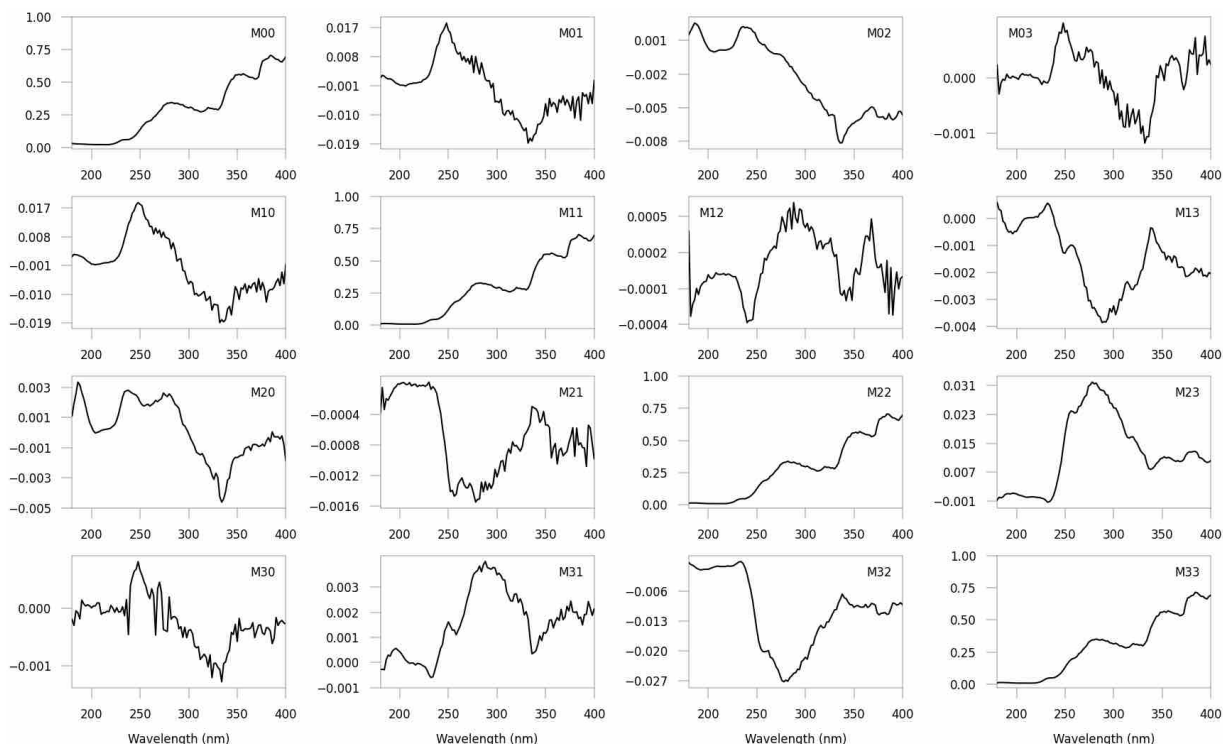


**Figure A4-21.** Preliminary differential Mueller matrix plots of 10 mg/mL (L,D)-4C11NapFF pre-gel solution at pH 10.5, 25 °C.

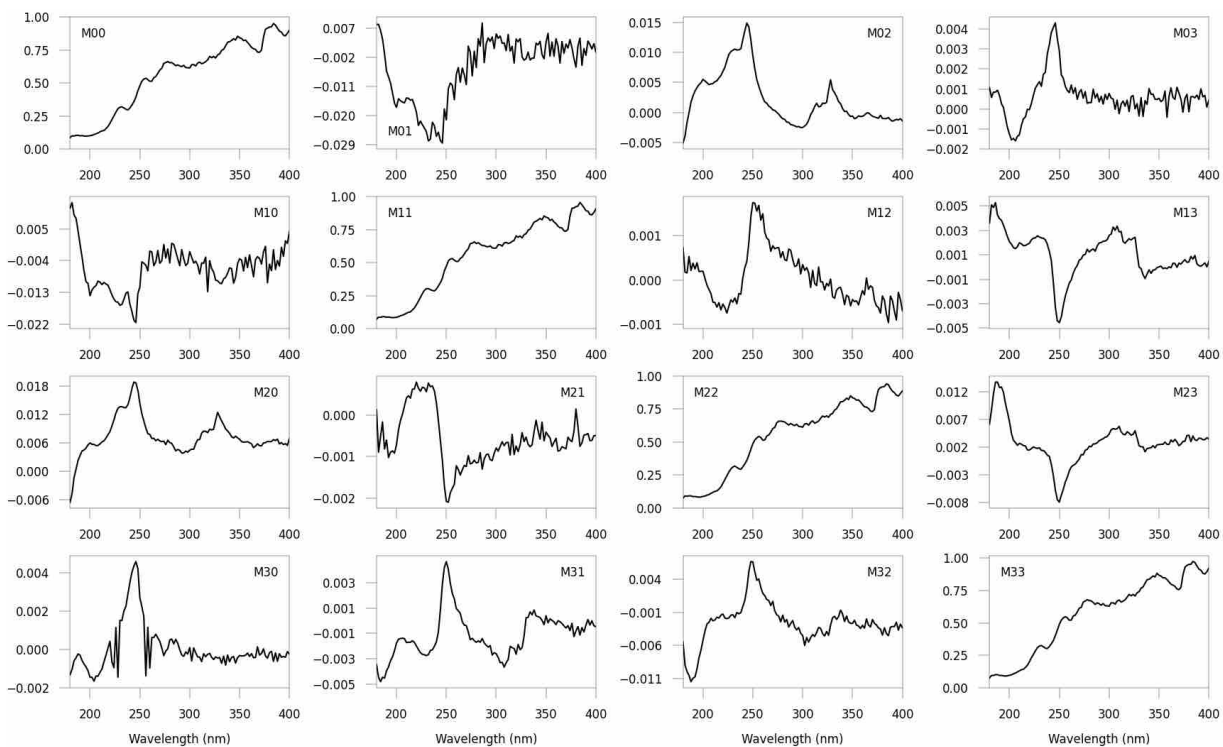


**Figure A4-22.** Preliminary differential Mueller matrix plots of the binary solution composed of (L,L)-4C11NapFF and (L,D)-4C11NapFF each at 10 mg/mL with a 1:1 volume ratio (5:5) at pH 10.5, 25 °C.